ELECTROCORTICOGRAPHIC BRAIN-COMPUTER INTERFACES

EDITED BY: Mikhail Lebedev, Alexei Ossadtchi, Mikhail Sinkin,
Christoph Guger, Alessandro Vato and Eric Leuthardt

PUBLISHED IN: Frontiers in Neuroscience and Frontiers in Neuroinformatics

frontiers Research Topics

frontiers

ISSN 1664-8714
ISBN 978-2-88974-474-9
DOI 10.3389/978-2-88974-474-9

About Frontiers

Frontiers is more than just an open-access publisher of scholarly articles: it is a pioneering approach to the world of academia, radically improving the way scholarly research is managed. The grand vision of Frontiers is a world where all people have an equal opportunity to seek, share and generate knowledge. Frontiers provides immediate and permanent online open access to all its publications, but this alone is not enough to realize our grand goals.

Frontiers Journal Series

The Frontiers Journal Series is a multi-tier and interdisciplinary set of open-access, online journals, promising a paradigm shift from the current review, selection and dissemination processes in academic publishing. All Frontiers journals are driven by researchers for researchers; therefore, they constitute a service to the scholarly community. At the same time, the Frontiers Journal Series operates on a revolutionary invention, the tiered publishing system, initially addressing specific communities of scholars, and gradually climbing up to broader public understanding, thus serving the interests of the lay society, too.

Dedication to Quality

Each Frontiers article is a landmark of the highest quality, thanks to genuinely collaborative interactions between authors and review editors, who include some of the world's best academicians. Research must be certified by peers before entering a stream of knowledge that may eventually reach the public - and shape society; therefore, Frontiers only applies the most rigorous and unbiased reviews.
Frontiers revolutionizes research publishing by freely delivering the most outstanding research, evaluated with no bias from both the academic and social point of view. By applying the most advanced information technologies, Frontiers is catapulting scholarly publishing into a new generation.

What are Frontiers Research Topics?

Frontiers Research Topics are very popular trademarks of the Frontiers Journals Series: they are collections of at least ten articles, all centered on a particular subject. With their unique mix of varied contributions from Original Research to Review Articles, Frontiers Research Topics unify the most influential researchers, the latest key findings and historical advances in a hot research area! Find out more on how to host your own Frontiers Research Topic or contribute to one as an author by contacting the Frontiers Editorial Office: frontiersin.org/about/contact

ELECTROCORTICOGRAPHIC BRAIN-COMPUTER INTERFACES

Topic Editors:
Mikhail Lebedev, Skolkovo Institute of Science and Technology, Russia
Alexei Ossadtchi, National Research University Higher School of Economics, Russia
Mikhail Sinkin, Research Institute of Emergency Care, Russia
Christoph Guger, g.tec medical engineering GmbH, Austria
Alessandro Vato, National Center for Adaptive Neurotechnologies, United States
Eric Leuthardt, Washington University in St. Louis, United States

Topic Editor Christoph Guger is the CEO of Guger Technologies. All other topic editors declare no competing interests with regards to the Research Topic subject.

Citation: Lebedev, M., Ossadtchi, A., Sinkin, M., Guger, C., Vato, A., Leuthardt, E., eds. (2022). Electrocorticographic Brain-Computer Interfaces. Lausanne: Frontiers Media SA. doi: 10.3389/978-2-88974-474-9

Table of Contents

frontiers in Neuroscience

TECHNOLOGY REPORT
published: 13 February 2019
doi: 10.3389/fnins.2018.01030

BCI2000Web and WebFM: Browser-Based Tools for Brain Computer Interfaces and Functional Brain Mapping

Griffin Milsap[1]*, *Max Collard*[2], *Christopher Coogan*[2] and *Nathan E. Crone*[2]

[1] Department of Biomedical Engineering, Johns Hopkins University, Baltimore, MD, United States, [2] Department of Neurology, Johns Hopkins University, Baltimore, MD, United States

BCI2000 has been a popular platform for development of real-time brain computer interfaces (BCIs). Since BCI2000's initial release, web browsers have evolved considerably, enabling rapid development of internet-enabled applications and interactive visualizations. Linking the amplifier abstraction and signal processing native to BCI2000 with the host of technologies and ease of development afforded by modern web browsers could enable a new generation of browser-based BCIs and visualizations. We developed a server and filter module called BCI2000Web providing an HTTP connection capable of escalation into an RFC6455 WebSocket, which enables direct communication between a browser and a BCI2000 distribution in real-time, facilitating a number of novel applications. We also present a JavaScript module, bci2k.js, that allows web developers to create paradigms and visualizations using this interface in an easy-to-use and intuitive manner. To illustrate the utility of BCI2000Web, we demonstrate a browser-based implementation of a real-time electrocorticographic (ECoG) functional mapping suite called WebFM. We also explore how the unique characteristics of our browser-based framework make BCI2000Web an attractive tool for future BCI applications. BCI2000Web leverages the advances of BCI2000 to provide real-time browser-based interactions with human neurophysiological recordings, allowing for web-based BCIs and other applications, including real-time functional brain mapping. Both BCI2000 and WebFM are provided under open source licenses. Enabling a powerful BCI suite to communicate with today's most technologically progressive software empowers a new cohort of developers to engage with BCI technology, and could serve as a platform for internet-enabled BCIs.

Keywords: electrocorticogram (ECoG), functional brain mapping, visualization, web browser, brain computer interface (BCI)

OPEN ACCESS

Edited by:
Christoph Guger,
g.tec Medical Engineering GmbH, Austria

Reviewed by:
Sebastian Halder,
University of Essex, United Kingdom
Hasan Ayaz,
Drexel University, United States

***Correspondence:**
Griffin Milsap
griff@jhmi.edu

Specialty section:
This article was submitted to Neuroprosthetics, a section of the journal Frontiers in Neuroscience

Received: *27 August 2018*
Accepted: *19 December 2018*
Published: *13 February 2019*

Citation:
Milsap G, Collard M, Coogan C and Crone NE (2019) BCI2000Web and WebFM: Browser-Based Tools for Brain Computer Interfaces and Functional Brain Mapping. Front. Neurosci. 12:1030. doi: 10.3389/fnins.2018.01030

1. INTRODUCTION

A brain-computer interface (BCI) is a system that translates brain activity into control signals for a computer. Modern incarnations of BCIs rely on rapid and low-latency brain signal acquisition, preprocessing, feature extraction, classification and/or regression, and frequently, postprocessing of the resultant control signal (Wolpaw et al., 2002). In the case of closed-loop BCI, some

form of visual or auditory feedback is given to the user to inform them of their control performance, typically requiring a low round-trip latency from signal acquisition to output. BCI development typically requires performant implementations of data acquisition and signal processing algorithms, high precision synchronization of external device telemetry, and typically, control of external software, requiring inter-process control or device input emulation (Wolpaw et al., 2000; Vaughan et al., 2003).

These technical requirements make the development of software for this purpose extremely challenging; however, there are a number of existing software platforms that bootstrap this development endeavor. BCI2000 has been a standardized research platform for BCI development for the last 15 years; it has been used by over 400 labs, and has been cited in numerous publications (Schalk et al., 2004). OpenViBE is another platform that has been developed to support real-time BCI research, offering a graphical programming language for signal processing and visualization (Renard et al., 2010). Additionally, a low-level communication protocol supporting signal acquisition and synchronization, called LabStreamingLayer, allows for TCP network streaming and synchronization of multi-modal data streams (Kothe, 2016) and could form the foundation of a BCI platform.

Widespread adoption and advancement of web browser technology makes it an attractive target for a BCI platform. Recent advancements in browser technology and standards have enabled direct access to low-level system resources such as graphics hardware and accelerometry/system sensors with application programming interfaces (APIs) that have exposed this hardware and software functionality via easy-to-use yet powerful and performant JavaScript packages. Network-enabled services also implement publicly available APIs that allow developers to call upon remote computational resources, such as Amazon web services (AWS), or to query information from vast databases of indexed knowledge, such as Wikipedia and Google Image Search. Moreover, many libraries supporting visual presentation of user interfaces and data visualizations have been developed. For example, d3.js (Bostock, 2011) has been used to power interactive data visualizations with impressive performance and an expressive yet functional API.

Many of the technologies readily available in the modern web browser would be useful to have available for the development of a contemporary BCI—for example, the ability to tag data in real-time with a speech transcription, via the WebSpeech API (Shires and Wennborg, 2012), or the ability to present stimuli in 3D using a virtual reality headset, via WebVR (Vukicevic et al., 2016) and three.js (Cabello et al., 2010). Visualization of the resulting data using d3.js (Bostock, 2011) or even sonification using the WebAudio API (Adenot et al., 2018) are fruitful endeavors for understanding realtime BCI output. Existing BCI software suites generally provide some amount of interprocess communication, typically exposed via user datagram protocol (UDP) or shared memory. However, browsers do not typically allow web apps to access UDP natively due to security concerns; further, existing communication schemes like BCI2000's AppConnector interface do not scale well to high data volumes, like those required to transmit human electrocorticography (ECoG) signals. BCI2000's existing interprocess communication tooling was designed with the transmission of control signals in mind, communicating signals using ASCII for simplicity instead of binary at the expense of inflating the data rate by a factor of ∼8-fold—an approach that was successful until the need to transmit raw and processed ECoG data streams was desirable. Modern browsers implement a protocol built on top of TCP called WebSocket (Fette, 2011) that allows an HTTP client to escalate an existing connection to a general purpose real-time bidirectional binary/ASCII communication interface. WebSockets are perfectly situated to facilitate the transfer of raw brain signals, extracted neural features, and processed control signals from a BCI software suite to a web app on a browser-enabled device, as well as the transfer of auxiliary sensor information from the web app back to the native software suite, all in real time. In this article, we present an implementation of the aforementioned interface as a plugin to BCI2000, which we call BCI2000Web.

1.1. ECoG Functional Mapping: A Testbed for Web Technologies

In this report, we additionally demonstrate the utility of this new BCI2000Web interface with an example application that shares many technical requirements with a BCI: a functional mapping tool capable of visualizing cortical activation derived from ECoG recordings in real-time using local processing at the bedside or in the operating room, and of synchronizing the final results to a centrally hosted repository.

Functional mapping of eloquent cortex is a target application of great scientific and clinical impact. About a third of patients with epilepsy have seizures that are resistant to medication therapy. In many of these patients, seizures arise from a focal brain area, and if this area can be safely removed, seizure control can be achieved. When non-invasive testing cannot reliably identify the seizure onset zone as distinct from brain regions needed for normal neurological function, clinicians may choose to surgically implant electrodes in the depths of the brain (stereo-EEG) or on its surface (electrocorticography, or ECoG). These intracranial electrodes may be implanted for a week or more in order to reliably localize the onset of seizures. These electrodes also facilitate the identification of eloquent cortex—i.e., regions that are implicated in speech and language, as well as perception, movement, and other important brain functions. A technique called electrocortical stimulation mapping (ESM) is typically used to map these regions. During ESM, pulse-trains of electrical current are passed between pairs of the implanted electrodes to temporarily disable a small patch of cortex while the patient performs a simple language or motor task. A behavioral change elicited by this temporary lesion indicates that the stimulated area of the brain is necessary for task completion (Ojemann et al., 1989). This testing procedure is time-consuming and uncomfortable for the patient, sometimes eliciting after-discharges (Lesser et al., 1984; Blume et al., 2004); these after-discharges can also evolve into seizures, which can be of questionable utility for diagnosing ictal cortex (Hamberger, 2007).

The limitations of ESM have motivated a complementary mapping technique based upon estimates of task-related changes in the power spectra, especially in high frequencies, of passive recordings of ECoG or stereo-EEG during behavioral tasks. This mapping technique, hereafter referred to as ECoG functional mapping, produces maps of task-related cortical activation, which may include cortex that is recruited by a task but not critical to task performance. In contrast, ESM uses a temporary electrophysiological disruption of cortical function to simulate the acute behavioral effects of tissue resection, and is presumed to be specific to areas critical to task performance. Nevertheless, a number of clinical studies have demonstrated good correspondence between ECoG functional mapping and ESM (Brunner et al., 2009; Wang et al., 2016). Moreover, several studies have shown that ECoG functional mapping can be used to predict post-resection neurological impairments, and in some cases it has predicted impairments that were not predicted by ESM (Wang et al., 2016). For these reasons, some epilepsy surgery centers have begun to use ECoG functional mapping as a complement to ESM, sometimes providing a preliminary map of cortical function that guides the use of ESM. However, most epilepsy centers have not yet adopted ECoG functional mapping because of the lack of technical resources, especially software that can be used with their clinical EEG monitoring systems.

Several ECoG functional mapping packages have been developed in recent years. For example, SIGFRIED acquires a large baseline distribution of neural activity in a calibration block, then rapidly accumulates estimates of cortical activation by averaging neural activity evoked by behavior in blocks of time (Brunner et al., 2009). A commercial product called cortiQ (Prueckl et al., 2013) is capable of performing this block-based mapping paradigm, which makes it possible for minimally trained clinical professionals to perform passive ECoG mapping. Both SIGFRIED and cortiQ are built using the BCI2000 framework and take advantage of the extensive optimizations and development legacy of the platform. A more nuanced mapping technique, termed spatial-temporal functional mapping (STFM), provides time-resolved, trial-locked results during a specific task by collecting a pooled baseline activity from a pre-defined Ĩ s period before the onset of a trial, then performing a statistical test on each time/channel bin in a window of interest relative to trial onset (Wang et al., 2016). Though the results of STFM are more complicated and require more expertise to interpret than the block-based mapping used by SIGFRIED or CortIQ, they provide a more detailed map of the spatial-temporal evolution of task-related activation, which can help clarify the role of different areas activated by a given task, of clear utility in cognitive neuroscience research and of potential clinical utility in planning surgical resections.

ECoG functional mapping relies on high performance signal processing and sophisticated real-time visualization, making it a suitable application example for BCI2000 and BCI2000Web. We saw an opportunity to build an easy-to-deploy-and-use tool for both researchers and clinicians that delivers the time-resolved, trial-locked results of STFM at the bedside in a web application, using BCI2000Web as the underlying communication technology to drive a browser-based interactive visualization. As a demonstration of the potential of the BCI2000Web plugin, in this report we also present WebFM, a software suite built on top of Node.js and BCI2000Web for performing real-time functional mapping in a web browser.

2. DESIGN AND IMPLEMENTATION

We chose to build our BCI WebSocket interface on top of BCI2000 as opposed to the other aforementioned technologies for many reasons, including support for acquisition devices in common use within epilepsy monitoring units and EEG research lab settings, high performance spectral extraction implementations, pedigree within the research community, highly accurate stimulus presentation capabilities, comprehensive documentation, and its ability to replay experimental sessions *post hoc* easily and accurately.

The BCI2000 environment is a general-purpose computational framework, typically used to construct BCIs, built upon four binary executables: the signal source module, which acquires physiological data from a supported amplifier; the signal processing module, which extracts neural features and transforms those features into control signals; an application module, which reacts to those control signals and provides feedback to the subject; and an Operator module, which orchestrates the behavior of all three functional submodules of the system (see **Figure 1**). Signals propagate from the source module to the processing module to the application module, with interconnections facilitated by a network-based protocol (in older versions of BCI2000) or a shared memory interface (in more recent iterations). Each of the modules consists of a series of signal "filters," which accept an incoming signal (as a channels-by-elements array) and output a derived signal, potentially of different dimensionality. A built-in Operator scripting language allows for setup and configuration of filters within an experimental session to occur automatically, and a Telnet interface exists in the Operator module, capable of accepting textual commands in the Operator scripting language from outside BCI2000.

2.1. BCI2000Web

To address remote control of BCI2000 and data transmission between BCI2000 and browsers, we developed a Node.js module called BCI2000Web that accepts Operator scripting language commands via WebSocket and transmits them to the Operator executable via Telnet, returning system output back to the client. It is primarily used to control data acquisition and signal processing parameters remotely via a connected WebSocket-enabled client, typically a browser. BCI2000Web has been developed as a service that runs within the Node.js runtime. Upon starting, it opens a Telnet connection to the Operator module and also functions as a basic HTTP server. While BCI2000's Telnet implementation only supports one client sending one set of instructions that are executed serially, BCI2000Web provides an interface that allows multiple clients to make requests to send commands to the Operator module; these commands are queued and executed sequentially, with responses sent back to the appropriate client

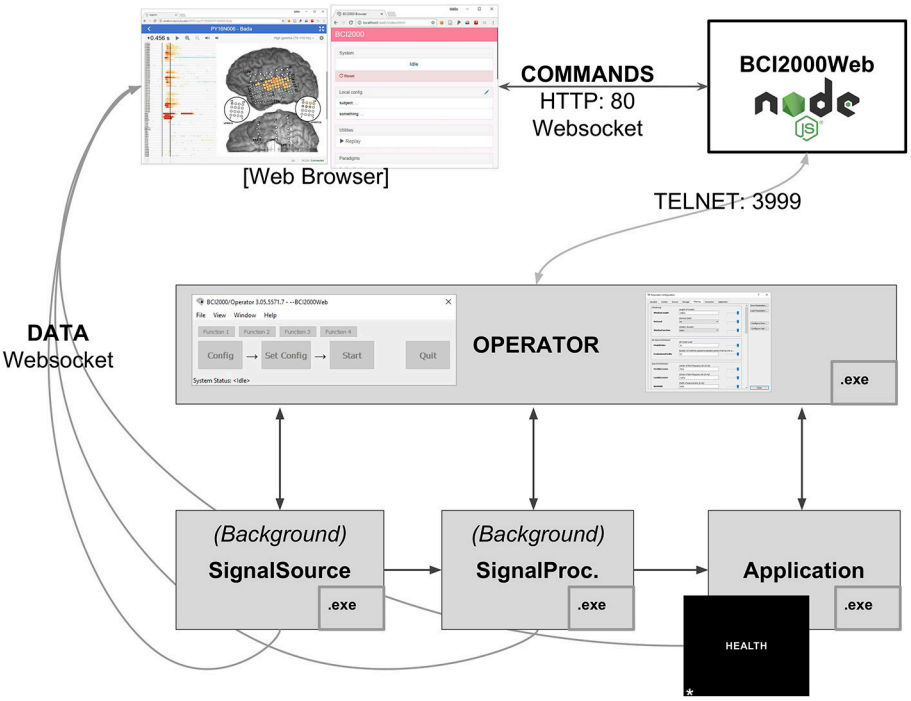

FIGURE 1 | A full BCI2000 stack including a Signal Source, Signal Processing, Application, and Operator module communicates with BCI2000Web, implemented as a Node.js module, via Telnet. Browser-based remote control software and visualization tools interact with BCI2000Web, and receive raw and processed neural signals directly from the BCI2000 system modules, via WebSockets, while the application module presents stimuli to the patient, in this case, the word stimulus "HEALTH" for a word reading paradigm.

asynchronously. BCI2000Web is capable of interfacing with an unmodified BCI2000 distribution and automating system configuration without any further software or modifications to BCI2000 modules.

In order to transmit the raw and processed signal from the BCI2000 filter pipeline to the browser, however, source modifications within the system modules are required. The raw and processed signal is never sent directly to the Operator module, so the signal can only be transmitted to a browser by compiling secondary WebSocket servers into the existing modules at specific locations within the filter chain. This modification has been realized in our implementation as a generic "WSIOFilter" (**W**eb**S**ocket **I**nput/**O**utput Generic**Filter**) that can be instantiated multiple times into the BCI2000 filter chain. Each WSIOFilter defines a parameter specifying the address and port its WebSocket server is hosted on. Once an incoming connection is escalated to a WebSocket, this filter sends packets to the client in the BCI2000 binary format, first describing the dimensionality of the signal and the system state vector via a "SignalProperties" and "StateList" packet, then a "GenericSignal" and "StateVector" packet for the current system signal and state vector once per sample block. These filters can be instantiated several times in the signal processing chain for any particular signal processing module. This filter has also been included as a source module extension that enables transmission of the raw signal in all signal source modules, and an application module extension that enables transmission of the application module input—identical to the signal processing output—in all application modules. In practice, the amount of data being sent/received by instantiations of the WSIOfilter is directly related to CPU usage on the sending and receiving machines, while the latency of system throughput from recording to browser is more a function of the network setup and the number of network interface hops the data has to traverse.

A WebSocket-enabled client is unlikely to natively understand the format of the incoming/outgoing messages on any of the aforementioned connections: our implementation of BCI2000Web adds some decorators to Operator scripting commands and Operator outputs to handle multiple clients, and the WSIOFilter output is implemented in the BCI2000 binary protocol. A JavaScript library, bci2k.js—available as a package on the Node package manager (NPM) registry—contains functions that manage the BCI2000 WebSocket connections and translate the binary BCI2000 format into readily usable data structures within a JavaScript context. Non-browser WebSocket-enabled clients will need to implement this functionality in order to communicate using these interfaces.

2.2. WebFM: Browser-Based ECoG Functional Mapping

Subdural ECoG recordings are the target modality for WebFM, the aforementioned functional mapping application; this modality has different signal processing requirements than scalp EEG. The signal processing module used in the system in the

Johns Hopkins Epilepsy Monitoring Unit is a modification of the default `SpectralSignalProcessing.exe` module. This signal processing module consists of a chain of filters, the first of which is a spatial filter capable of applying a common average reference, a frequently used spatial filter for ECoG recordings (Liu et al., 2015). This is followed by a series of IIR Butterworth filters, including a fourth order low pass at 110 Hz, followed by a second order high pass at 70 Hz and a 4th order notch filter at 60 Hz. After the signal is downsampled to 500 Hz from the native sampling rate, it is passed through a spectral estimator filter, which generates an autoregressive model on a window of filtered data and uses the model coefficients to form an estimate of the signal's power spectrum, using the Burg method (Burg, 1968). A WSIOFilter is instantiated at this point in the filter chain, capable of streaming this estimated spectral content of the neural signals in real-time. A system diagram and description of the system topology is detailed in **Figure 1**.

A language or motor task is parameterized as a BCI2000 `.prm` file and a collection of audio-visual stimuli in a git repository hosted on GitHub, available as packages that remote-control BCI2000 using the BCI2000Web server. Any number of these tasks can be checked out into the BCI2000Web distribution, and the server will automatically present them as startup options within the built-in BCI2000Web browser interface, shown and described in **Figure 2**. These paradigms typically specify a parameterization for `StimulusPresentation.exe`, a BCI2000 application module capable of presenting audio-visual stimuli to the patient with high-precision timing and sequence control. A browser is used to communicate to the bedside data-collection and stimulus-presentation machine, and to set up this system parameterization. (Because of this setup, it is notable that, when high-precision control isn't needed for stimulus presentation, the tasks presented to patients may themselves be interactive web applications, utilizing bci2k.js and BCI2000Web to inject behavioral markers into the data recorded by BCI2000.) A monitor and speaker connected to the bedside computer is set up in front of the patient, and a microphone is connected to the auxiliary analog inputs provided by the acquisition system, to be digitized synchronously with the electrophysiology.

The WebFM/BCI2000Web system currently supports more than 20 possible experimental paradigms, including a task battery used for clinical assessment for functional localization. These paradigms are currently versioned in GitHub repositories with group permissions and access control managed by the authors. A setup script is provided with BCI2000Web that accepts a GitHub login and clones/updates all available task repositories into the proper location.

2.2.1. Patients and Electrode Localization

All aspects of this study were carried out in accordance with the recommendations of the Johns Hopkins Institutional Review Board with written informed consent from all subjects. All subjects gave written informed consent in accordance with the Declaration of Helsinki. The protocol was approved by the Johns Hopkins Institutional Review Board.

Before any functional mapping sessions occur with a patient, a post-operative computed tomography scan containing electrode locations is co-registered to a pre-operative magnetic resonance imaging scan of sufficient resolution (typically with voxel dimensions of 1 mm or less) to render the patient's cortical surface anatomy in high detail, using Freesurfer (Fischl, 2012) or Bioimage Suite (Papademetris et al., 2006). These electrode locations are overlaid on a 2D rendering of the cortical surface. An image file depicting this cortical anatomy and electrode layout, as well as a comma-separated value (`.csv`) file containing the normalized image coordinates of each electrode, is uploaded to the WebFM server via controls within the WebFM browser interface. This layout doesn't typically change during a patient's EMU stay, and it is referenced and retrieved by using a subject identification code, effectively de-identifying the reconstruction for research purposes.

2.2.2. Software

During an ECoG functional mapping session, a browser running on the visualization device contacts the WebFM server and queries the bedside machine for the subject's identification code and what task is currently running. The WebFM server then serves the corresponding cortical reconstruction image and sensor location file in addition to a bolus of javascript code that is capable of opening WebSockets to the BCI2000Web server and WSIOFilters running on the bedside machine. The code also contains statistics packages and graphical libraries necessary for acquiring, analyzing, and visualizing the data. The browser then opens these data streaming WebSockets and performs the mapping without further contacting the WebFM server. After each trial of the task, the visualization is updated and once a full task run has been collected, the resulting map can be saved back to the WebFM server for indexing and *post-hoc* inspection, available on the WebFM Landing page, detailed in **Figure 3**.

The statistics and visualization for WebFM are based on the techniques and methods described in Wang et al. (2016). The baseline window for the tasks is defined as a configurable period from 1,000 to 200 ms before the trial onset and a baseline distribution is formed per channel from the pooled high gamma power values during this period. A two-way t-test is performed between the distribution for each time-channel bin and that channel's baseline distribution. The resulting p-values are corrected for multiple comparisons using the Benjamini-Hochberg (BH) procedure, controlling the false discovery rate at 0.05 (Benjamini and Hochberg, 1995). This correction is used to threshold the results displayed in the WebFM raster and spatial plots: time-channel bins that did not survive the BH correction are hidden from view. Any individual time point in this raster can be dynamically selected and visualized by "scrubbing" the mouse cursor over the raster display; this yields circles drawn on a two dimensional representation of the electrode montage, highlighting which cortical locations were active during that particular time-point across trials. An options dialog allows users to change baseline periods, modify visualization timing parameters and amplitudes, as well as make comparisons across task conditions and contrasts. The visualization is shown and further described in **Figure 4**.

The visualization APIs exposed by WebFM can be used to implement a number of other visualizations as well. One mode of

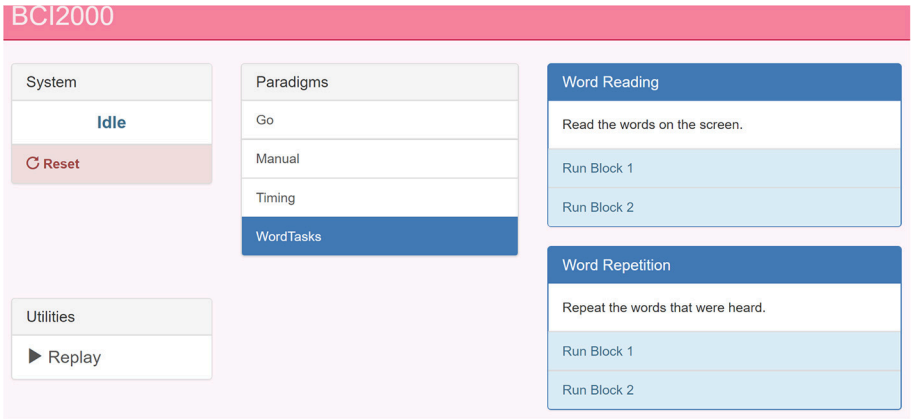

FIGURE 2 | A screenshot of the BCI2000 remote control interface. The paradigm index is hosted by BCI2000Web over HTTP. This page is populated by the experimental paradigms present on the host machine (center) with buttons to start sub-tasks and specific blocks (right). A pane in the top left reads out the current BCI2000 system state, in addition to a system reset button. In the bottom left, a link to the system replay menu allows for recorded BCI2000 `.dat` file playback for system testing and offline mapping.

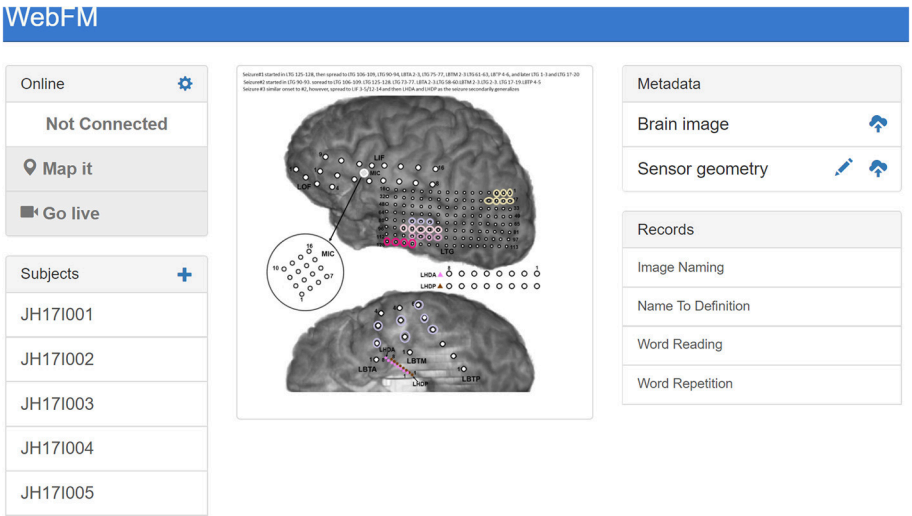

FIGURE 3 | The landing page for WebFM. A pane in the top left shows system state and houses buttons that start trial-based functional mapping paradigms and a "live" mode that visualizes neural activity on the brain in real-time, as visualized in prior studies (Lachaux et al., 2007). A list of subject identifiers on the bottom left pane enables users to pull up previous/current subjects; a list of saved maps for the selected subject appears in the "Records" pane on the bottom right. The "+" in the top left of the "Subjects" pane allows operators to add new subjects to the database, and the "Metadata" pane at the top right allows operators to upload brain reconstruction images and normalized electrode locations for displaying functional mapping results. The brain images used for mapping are often overlaid with information about seizures and/or ESM results, so that functional activation can be easily visually compared with these data; the image shown in the center includes colored circles depicting the hypothesized spread of ictal activity during the subject's seizures.

WebFM provides a visualization of raw high gamma activation in real time, as in (Lachaux et al., 2007); other modifications have also been used to visualize the propagation of interictal spiking and seizure propagation across cortex.

2.3. Deployment

As of the time of writing, the WebFM system has been deployed at two sites: the Johns Hopkins Hospital and the University of Pittsburgh Medical Center. Across these sites, WebFM has been used with three acquisition devices: the NeuroPort system (Blackrock Microsystems, Salt Lake City, UT), a Grapevine system (Ripple, Salt Lake City, UT), and the EEG1200 system (Nihon Kohden, Tomioka, Japan). Between these sites and amplifiers, WebFM has been used to create over 200 functional maps across 33 subjects. The majority of these subjects (19) were hospital inpatients undergoing epilepsy monitoring prior to resective surgery. Clinical staff in the Johns Hopkins Epilepsy Monitoring Unit have a link to the WebFM portal on their desktop machines and frequently use the passive ECoG mapping results when discussing surgical plans. The remaining 14 subjects

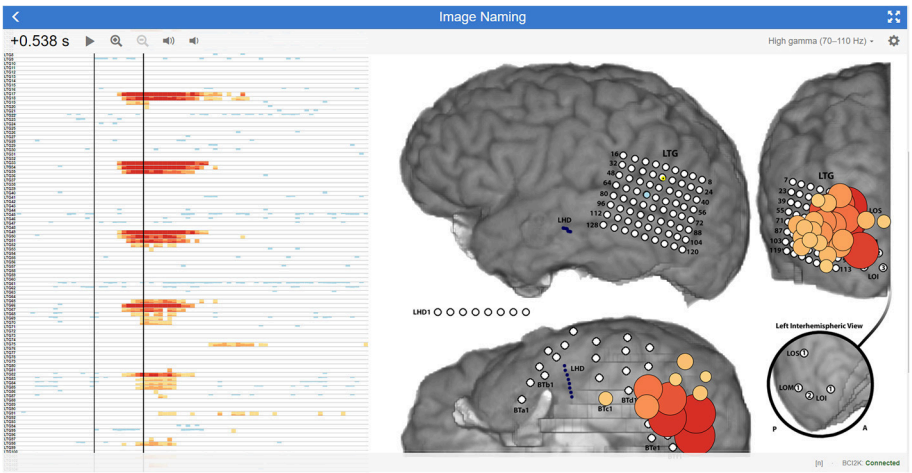

FIGURE 4 | WebFM visualization description An example of WebFM results for an image naming task in a subject with high density (5-mm spacing) temporal-parietal-occipital electrode coverage. A horizon raster Heer et al. (2009) to the left shows a time (*x*-axis) by channels (*y*-axis) plot of trial-averaged task-modulated high gamma power, thresholded for statistical significance with BH correction for a FDR of <0.05. Warm colors represent a statistically significant increase in task-modulated high gamma power, while cool colors indicate a statistically significant decrease in task-modulated high gamma power. The left black vertical bar within the raster indicates the trial-start (t = 0 s) where StimulusCode transitioned from zero to a non-zero value, indicating that a stimulus was being displayed. The right black vertical bar is a temporal cursor that interactively tracks the user's mouse gestures; the current time it indexes is shown in the top left corner, 0.538 s after stimulus onset. Buttons next to the selected time manipulate visualization properties. The current temporal slice is visualized on the brain image (right) as circles with size and color indicating the magnitude of the *z*-score, with the same coloration as in the horizon chart. A button in the top right maximizes the display to occupy the full screen-space of the device; a gear icon next to the fullscreen icon presents a configuration dialog box containing options for saving results, changing visualization parameters, configuring realtime signal or BCI2000 state trial-triggering, and visualizing the raw signal, amongst much more functionality. A drop down menu next to the gear icon turns on/off multiple visualization layers, enabling/disabling display of ESM, functional mapping, connectivity metrics, evoked responses, etc. A status message at the bottom right indicates WebFM has connected to BCI2000Web via bci2k.js and a trial counter, in this image represented with an "[n]", increments as trials are delivered to and visualized by WebFM.

were temporarily implanted with a 64-channel high density ECoG strip during lead implantation for deep brain stimulation; for these subjects, WebFM was used to map sensorimotor cortex in the operating room. WebFM has even been used to generate maps of activity recorded at one site by researchers at another site in real time, utilizing virtual private networks.

3. DISCUSSION

BCI2000Web and WebFM take advantage of several recent technological developments. First and foremost, these packages capitalize on advancements in the modern web browser, which is quickly becoming a platform capable of general purpose computing. With a focus on frontend user interaction, many packages have been written in JavaScript that support the rapid implementation of interactive applications and visualizations. WebFM in particular makes use of d3.js (Bostock, 2011) to provide a high-quality interactive visualization of trial-averaged high gamma modulation directly on the brain.

The key to taking advantage of these web-based technologies is the implementation of BCI2000Web, which utilizes the WebSocket API to transmit binary-formatted brain data directly to the browser over TCP/HTTP, and which allows direct communication to and from BCI2000. While the experimental paradigms presented in conjunction with WebFM utilized the native BCI2000 stimulus presentation module to interact with the subject, the general-purpose access to Operator scripting over WebSockets provided by BCI2000Web easily lends itself to a different system architecture, in which a browser application itself is responsible for interacting with the subject and providing experimental markers sent via WebSocket; this topology is depicted in **Figure 5**. Several paradigm packages for BCI2000Web leveraging this architecture have been authored to date. Some make use of the WebSpeech API (Shires and Wennborg, 2012) to do real-time speech tagging and segmentation for tasks involving freely generated speech; another uses the WebMIDI and WebAudio APIs (Wyse and Subramanian, 2013) to register subject input on musical peripheral devices, and perform high-performance audio synthesis in response. Public JavaScript APIs allow for rich BCI interactions, and experimental paradigms can pull upon web resources such as Google Image search for providing varied and tailored stimuli at run-time. Extending this idea, it is easy to envision a system architecture in which users' neural data is sent to a browser application that communicates with a server backend in real time, allowing cloud-based services to apply sophisticated machine learning techniques that wouldn't be feasible otherwise on the client-side. Even further, one could develop a browser-based application that transmits multiple users' neural data to each other's clients, facilitating brain-based communication.

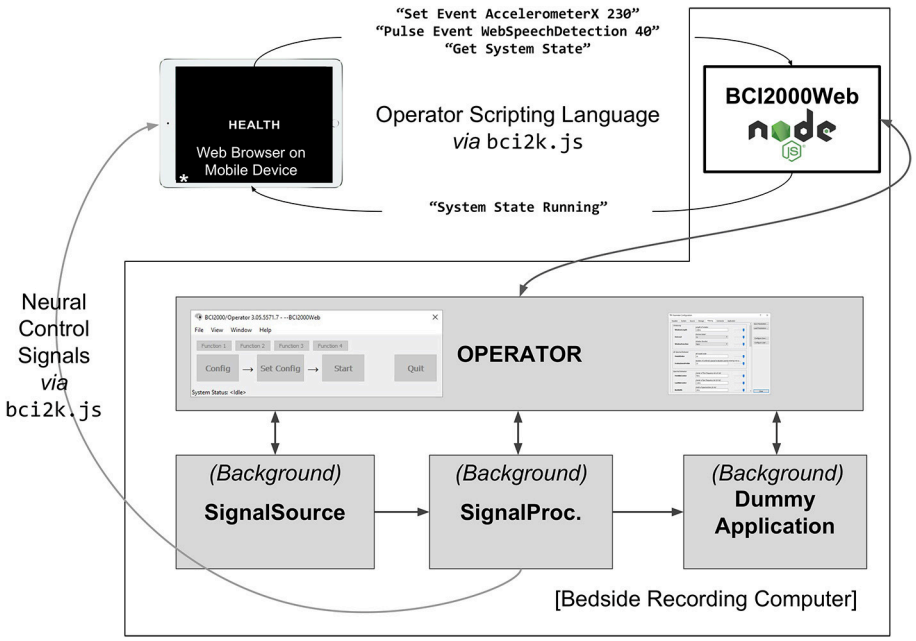

FIGURE 5 | A system diagram depicting an experiment implemented in browser JavaScript running on an independent mobile device. The mobile device is running an experimenter-implemented web-page in fullscreen mode which communicates directly with BCI2000Web for event logging as well as the Signal Processing module for receiving extracted neural control signals. A JavaScript package, bci2k.js, manages WebSocket connections that handle transmission of operator scripting language commands and decodes neural control signals from a binary format. The mobile device is running a word reading paradigm (with the stimulus "HEALTH" currently presented) that has defined asynchronous experimental states including markers for automated vocal transcription onsets using the WebSpeech API. A query for system state is also relayed by the BCI2000Web server. The benefit of such an architecture is that the patient interface is separated from the bedside clinical acquisition machine and can be left with the patient without concern of the patient manipulating the clinical datastream.

Cross-device compatibility is another advantage to using the browser as a visualization and stimulus presentation platform. Any browser-enabled device (smartphone, tablet, PC, or even game console) can be used to present stimuli or visualize output. Because of this "write-once, run-anywhere" development process, WebFM can be used by clinicians to view mapping results in real-time on their smartphones from outside the patient's room while ECoG functional mapping is being run by technicians.

3.1. Drawbacks and Caveats

The rationale behind the division of processing using native binaries and visualization using browser-interpreted javascript is due to current limitations inherent to browsers. Browser-hosted JavaScript is rapidly advancing as a next-generation efficient computational platform with the advent of WebAssembly and ASM.js (Herman et al., 2014), but at the time of writing it is still too computationally demanding to perform real-time feature extraction and signal processing in the browser. Furthermore, browser access to low level computer hardware and connected USB devices is only in the early development stages. Given these limitations, BCI2000Web was designed to take advantage of the device driver access and computational efficiency of the C++ code base that powers BCI2000 for acquisition device abstraction and signal processing/feature extraction. This architecture frees frontend developers from dealing with complicated signal processing code in JavaScript, and instead enables them to focus on user experience and design. In the future, a full-stack BCI2000 analog could be implemented directly within the browser, and BCI2000Web is a glimpse of what that software could empower for web developers with access to neural features.

A significant amount of the development effort for BCI2000 has been spent on implementing high-performance signal processing and stimulus presentation software. Delivering audio-visual stimuli to subjects with a consistent yet minimal latency is a non-trivial task that BCI2000 has accomplished by interfacing with low-level graphics drivers in a nuanced way. Operating system version, bit-width (32 vs. 64), driver versions, compiler optimizations, and varying hardware capabilities collude to make this stimulus presentation problem a fragmented and moving target—one which BCI2000 has historically hit with surprising accuracy, achieving visual presentation latency on the order of one to two frames at a 60 Hz monitor refresh rate and audio latencies on par with modern audio production software (Wilson et al., 2010). The BCI2000 core team encourage developers to implement custom signal processing and stimulus presentation paradigms within this BCI2000 environment using documented C++ code templates in order to benefit from these optimizations. That said, so long as tasks are designed properly and ground truth stimulus and response signals are collected (e.g., screen mounted photodiodes and patient facing microphones connected directly to auxiliary inputs on the amplifier), it is still possible to collect

data of high scientific quality using the browser as the primary stimulus presentation software even if its stimulus display and communication latency are in question.

We benchmarked the visual timing performance of a system with and without BCI2000Web modifications using the procedure in Wilson et al. (2010) on a platform comprising Windows 7 64 bit with BCI2000 r5688, Google Chrome 67.0.3396.99, and a 256 channel 1,000 Hz recording from a Blackrock NeuroPort running with a 20 ms sample-block size; a standard configuration for a moderate-to-high channel-count ECoG recording running on an up-to-date clinical machine as of the time of writing. An unmodified BCI2000 distribution on this system exhibits a visual latency (t_{3v}, as expressed in Wilson et al., 2010) of 52 ms with a standard deviation of 8.0 ms. With BCI2000Web sending neural signals to a browser via WebSocket on the same acquisition machine, a mean visual latency of 60 ms with a standard deviation 9.4 ms was observed. Using the hospital wireless network to send neural signals via WebSocket to a tablet PC running Windows 10 and the same version of Chrome results in a visual latency of 62 ms with a standard deviation of 13.4 ms. These latency metrics indicate a minimal impact to timing performance when using BCI2000Web. In many real-time BCI implementations, spectral feature extraction occurs in windows of 128–256 ms with a slide of 16–32 ms, and single-trial visual timing differences fall well within one windowing period. BCIs reliant upon time-domain features—in particular those that perform trial-averaging of evoked response potentials—will be more sensitive to these latency differences, and it is critically important to run timing benchmarks for specific hardware/software/network configurations in these circumstances. It should be noted that these performance metrics are configuration-specific and are likely to vary significantly across use cases; BCI2000Web comes bundled with an A/V timing paradigm that can be used to collect timing-test data, but analyses of these latencies and interpretation of what constitutes sufficient performance is application specific and is left to the end-user.

4. CONCLUSIONS

The development of a communication protocol that connects one of the most widely adopted BCI research and development suites with the power of modern browser technologies is expected to accelerate the pace of development for BCI technologies. Newer software developers, primarily taught using these modern software development paradigms, can now develop new BCI applications and neural signal visualizations while leveraging the legacy and performance of native BCI2000 modules. We have developed and presented a web-based ECoG functional brain mapping tool using this technology, and we have successfully deployed it at two sites with a cohort of 33 patients over two years. BCI2000Web and WebFM together utilize the relative strengths of a highly optimized C++ code base in BCI2000 and the high level visualization libraries within modern browsers to demonstrate a clinically useful and modern functional mapping tool. We have also used BCI2000Web for ongoing, albeit unpublished, BCI research projects, and we describe herein the advantages and potential uses of BCI2000Web in future BCI applications. This software is documented and released under permissive free and open source software licenses, and is put forward by the authors for use in the research and development of BCIs and multi-site studies on the clinical efficacy of ECoG functional mapping.

DATA AVAILABILITY STATEMENT

A standalone distribution of BCI2000Web is available on GitHub (`github.com/cronelab/bci2000web`). This distribution comes packaged with pre-compiled BCI2000 binaries that contain WSIOFilter taps for data access. The bci2k.js package—which translates BCI2000 binary packets from signal taps to usable data structures, and handles the Operator scripting language protocol—can be installed with NPM (`node install bci2k`); its codebase is available on GitHub (`github.com/cronelab/bci2k.js`). WebFM can also be found on GitHub (`github.com/cronelab/webfm`). All of this software is available under free and open source licenses.

The data used in the live demo at `www.webfm.io` is available via the WebFM API: the subject's brain image, base-64 encoded, is located at `www.webfm.io/api/brain/PY17N009`; the subject's sensor geometry is located, in JSON format, at `www.webfm.io/api/geometry/PY17N009`; the high gamma activation data for the presented task (syllable reading) is located at `www.webfm.io/api/data/PY17N009/SyllableReading`."

AUTHOR CONTRIBUTIONS

BCI2000Web was developed by GM with assistance from MC. Testing and validation of BCI2000Web was performed by CC. WebFM was developed by MC with assistance and maintenance by CC and supervision by NC. Deployment and testing of WebFM in the Johns Hopkins Epilepsy Monitoring Unit was undertaken by GM, MC, and NC. This report was prepared by GM and MC, with input from NC.

FUNDING

Work on this article and the software presented therein has been supported by the National Institutes of Health (R01 NS088606, R01 NS091139).

ACKNOWLEDGMENTS

We would like to thank Dr. Gerwin Schalk, Dr. Peter Brunner, Dr. Juergen Mellenger, and the BCI2000 development community for invaluable contributions to this work.

REFERENCES

Adenot, P., Raymond, T., Wilson, C., and Rogers C. (2018). *Web Audio API Specification, W3C Candidate Recommendation.* Available online at: https://www.w3.org/TR/webaudio/

Benjamini, Y., and Hochberg, Y. (1995). Controlling the false discovery rate: a practical and powerful approach to multiple testing. *J. R. Stat. Soc. B Methodol.* 57, 289–300.

Blume, W. T., Jones, D. C., and Pathak, P. (2004). Properties of after-discharges from cortical electrical stimulation in focal epilepsies. *Clin. Neurophysiol.* 115, 982–989. doi: 10.1016/j.clinph.2003.11.023

Bostock, M., Ogievetsky, V., and Heer, J. (2011). D^3 data-driven documents. *IEEE Trans. Visual. Comput. Graph.* 12, 2301–2309.

Brunner, P., Ritaccio, A. L., Lynch, T. M., Emrich, J. F., Wilson, J. A., Williams, J. C., et al. (2009). A practical procedure for real-time functional mapping of eloquent cortex using electrocorticographic signals in humans. *Epilepsy Behav.* 15, 278-86. doi: 10.1016/j.yebeh.2009.04.001

Burg, J. P. (1968). "A new analysis technique for time series data," in *Paper Presented at NATO Advanced Study Institute on Signal Processing* (Enschede).

Cabello, R. et al. (2010). *Three.js.* Available online at: https://github.com/mrdoob/three.js."

Fette, I., and Melnikov, A. (2011). *The Websocket Protocol.* No. RFC 6455.

Fischl, B. (2012). FreeSurfer. *Neuroimage* 62, 774–781. doi: 10.1016/j.neuroimage.2012.01.021

Hamberger, M. J. (2007). Cortical language mapping in epilepsy: a critical review. *Neuropsychol. Rev.* 17, 477–489.

Heer, J., Kong, N., and Agrawala, M. (2009). "Sizing the horizon: the effects of chart size and layering on the graphical perception of time series visualizations," in *Proceedings of the SIGCHI Conference on Human Factors in Computing Systems, CHI '09,* (New York, NY: ACM), 1303–1312.

Herman, D., Wagner, L., and Zakai, A. (2014). *asm.js-Working Draft.* Available online at: http://asmjs.org/spec/latest/

Kothe, C. (2016). *Lab Streaming Layer.* Available online at: https://github.com/sccn/labstreaminglayer

Lachaux, J. P., Jerbi, K., Bertrand, O., Minotti, L., Hoffmann, D., Schoendorff, B., et al. (2007). BrainTV: a novel approach for online mapping of human brain functions. *Biol. Res.* 40, 401–413.

Lesser, R. P., Lüders, H., Klem, G., Dinner, D. S., Morris, H. H., and Hahn, J. (1984). Cortical afterdischarge and functional response thresholds: results of extraoperative testing. *Epilepsia* 25, 615–621.

Liu, Y., Coon, W. G., Pesters, A. d., Brunner, P., and Schalk, G. (2015). The effects of spatial filtering and artifacts on electrocorticographic signals. *J. Neural Eng.* 12:056008. doi: 10.1088/1741-2560/12/5/056008

Ojemann, G., Ojemann, J., Lettich, E., and Berger, M. (1989). Cortical language localization in left, dominant hemisphere. An electrical stimulation mapping investigation in 117 patients. *J. Neurosurg.* 71, 316–326.

Papademetris, X., Jackowski, M. P., Rajeevan, N., DiStasio, M., Okuda, H., Constable, R. T., et al. (2006). BioImage suite: an integrated medical image analysis suite: an update. *Insight J.* 2006:209.

Prueckl, R., Kapeller, C., Potes, C., Korostenskaja, M., Schalk, G., Lee, K. H., et al. (2013). "cortiQ - Clinical software for electrocorticographic real-time functional mapping of the eloquent cortex," in *2013 35th Annual International Conference of the IEEE Engineering in Medicine and Biology Society (EMBC)*, 6365–6368. doi: 10.1109/EMBC.2013.6611010

Renard, Y., Lotte, F., Gibert, G., Congedo, M., Maby, E., Delannoy, V., et al. (2010). OpenViBE: an open-source software platform to design, test, and use brain–computer interfaces in real and virtual environments. *Presence Teleoperat. Virt. Environ.* 19, 35–53. doi: 10.1162/pres.19.1.35

Schalk, G., McFarland, D. J., Hinterberger, T., Birbaumer, N., and Wolpaw, J. R. (2004). BCI2000: a general-purpose brain-computer interface (BCI) system. *IEEE Trans. Biomed. Eng.* 51, 1034–1043. doi: 10.1109/TBME.2004.827072

Shires, G., and Wennborg H. (2012). *Web Speech API Specification.* W3C Community Group Final Report. Available online at: https://w3c.github.io/speech-api/

Vaughan, T. M., Heetderks, W. J., Trejo, L. J., Rymer, W. Z., Weinrich, M., Moore, M. M. et al. (2003). Brain-computer interface technology: a review of the second international meeting. *IEEE Trans. Neural Syst. Rehabil. Eng.* 11, 94–109.

Vukicevic, V., Jones, B., Gilbert, K., and Wiemeersch, C. (2016). *Webvr.* World Wide Web Consortium.

Wang, Y., Fifer, M. S., Flinker, A., Korzeniewska, A., Cervenka, M. C., Anderson, W. S., et al. (2016). Spatial-temporal functional mapping of language at the bedside with electrocorticography. *Neurology* 86, 1181–1189. doi: 10.1212/WNL.0000000000002525

Wilson, J. A., Mellinger, J., Schalk, G., and Williams, J. (2010). A procedure for measuring latencies in brain-computer interfaces. *IEEE Trans. Biomed. Eng.* 57, 1785–1797. doi: 10.1109/TBME.2010.2047259

Wolpaw, J. R., Birbaumer, N., Heetderks, W. J., McFarland, D. J., Peckham, P. H., Schalk, G., et al. (2000). Brain-computer interface technology: a review of the first international meeting. *IEEE Trans. Rehabil. Eng.* 8, 164–173. doi: 10.1109/TRE.2000.847807H

Wolpaw, J. R., Birbaumer, N., McFarland, D. J., Pfurtscheller, G., and Vaughan, T. M. (2002). Brain-computer interfaces for communication and control. *Clin. Neurophysiol.* 113, 767–791.

Wyse, L., and Subramanian, S. (2013). The viability of the web browser as a computer music platform. *Computer Music J.* 37, 10–23. doi:10.1162/COMJa00213

Conflict of Interest Statement: The authors declare that the research was conducted in the absence of any commercial or financial relationships that could be construed as a potential conflict of interest.

frontiers in Neuroscience

ORIGINAL RESEARCH
published: 19 February 2019
doi: 10.3389/fnins.2019.00060

Keyword Spotting Using Human Electrocorticographic Recordings

Griffin Milsap[1]*, *Maxwell Collard*[2], *Christopher Coogan*[2], *Qinwan Rabbani*[3], *Yujing Wang*[2,4] *and Nathan E. Crone*[2]

[1] Department of Biomedical Engineering, Johns Hopkins University, Baltimore, MD, United States, [2] Department of Neurology, Johns Hopkins University School of Medicine, Baltimore, MD, United States, [3] Department of Electrical Engineering, Johns Hopkins University, Baltimore, MD, United States, [4] Fischell Department of Bioengineering, University of Maryland College Park, College Park, MD, United States

Neural keyword spotting could form the basis of a speech brain-computer-interface for menu-navigation if it can be done with low latency and high specificity comparable to the "wake-word" functionality of modern voice-activated AI assistant technologies. This study investigated neural keyword spotting using motor representations of speech via invasively-recorded electrocorticographic signals as a proof-of-concept. Neural matched filters were created from monosyllabic consonant-vowel utterances: one keyword utterance, and 11 similar non-keyword utterances. These filters were used in an analog to the acoustic keyword spotting problem, applied for the first time to neural data. The filter templates were cross-correlated with the neural signal, capturing temporal dynamics of neural activation across cortical sites. Neural vocal activity detection (VAD) was used to identify utterance times and a discriminative classifier was used to determine if these utterances were the keyword or non-keyword speech. Model performance appeared to be highly related to electrode placement and spatial density. Vowel height (/a/ vs /i/) was poorly discriminated in recordings from sensorimotor cortex, but was highly discriminable using neural features from superior temporal gyrus during self-monitoring. The best performing neural keyword detection (5 keyword detections with two false-positives across 60 utterances) and neural VAD (100% sensitivity, ~1 false detection per 10 utterances) came from high-density (2 mm electrode diameter and 5 mm pitch) recordings from ventral sensorimotor cortex, suggesting the spatial fidelity and extent of high-density ECoG arrays may be sufficient for the purpose of speech brain-computer-interfaces.

Keywords: electrocorticography (ECoG), keyword spotting (KWS), automatic speech recognition (ASR), brain computer interface (BCI), speech, sensorimotor cortex (SMC), superior temporal gyrus (STG), articulation

OPEN ACCESS

Edited by:
Christoph Guger,
g.tec Medical Engineering GmbH, Austria

Reviewed by:
Christian Herff,
Maastricht University, Netherlands
Ivan Volosyak,
Rhine-Waal University of Applied Sciences, Germany

***Correspondence:**
Griffin Milsap
griff@jhmi.edu

Specialty section:
This article was submitted to Neuroprosthetics, a section of the journal Frontiers in Neuroscience

Received: *20 August 2018*
Accepted: *21 January 2019*
Published: *19 February 2019*

Citation:
Milsap G, Collard M, Coogan C, Rabbani Q, Wang Y and Crone NE (2019) Keyword Spotting Using Human Electrocorticographic Recordings. Front. Neurosci. 13:60. doi: 10.3389/fnins.2019.00060

1. INTRODUCTION

Keyword spotting (KWS) has recently come to the forefront of human-computer-interaction with the advent of voice-assist technologies such as Amazon Alexa, Apple's Siri, and Google's Assistant. All of these systems employ local, low-resource acoustic keyword search in real-time to detect a "wake word" that activates server-side speech recognition for interaction with an intelligent agent. These systems have been commercially successful and lauded for their ease of use. There are scenarios where voice-activated system interaction is suboptimal, especially when many speaking

voices make the acoustic speech recognition less reliable and socially awkward to use. The ability to trigger an intelligent agent or perform menu selections with low latency and high specificity using neural control is of great practical interest.

A number of studies of neural speech decoding motivate the selection of electrocorticography (ECoG) for neural keyword spotting. Bouchard et al. (2013) were the first to examine the organization of articulation in ventral sensorimotor cortex (vSMC) using high-density ECoG recordings. Their study revealed that high frequency activity in the high-gamma range (70–110 Hz) encodes precise movements of speech articulators with a high degree of temporal specificity. Mugler et al. (2014, 2015) similarly characterized the articulatory representation in this area and further showed that this activity is more related to the gestural trajectories of specific muscles in the vocal tract than it is related to the specific keywords or phonemes articulated. Kanas et al. (2014) used high frequency content of speech-active areas of the brain to perform voice-activity-detection, or VAD—segmenting periods of speech from non-speech periods. Moreover, high-gamma activity from ECoG arrays was used as input to a language model and a small-vocabulary continuous speech recognition from neural signals was created in a study by Herff et al. (2015). Decoding of phonemic (Pei et al., 2011a; Bouchard and Chang, 2014) and gestural (Lotte et al., 2015; Mugler et al., 2015) content from vSMC has repeatedly been shown as well. These studies provide evidence that the dynamics of speech require the spatiotemporal resolution of intracortical electrophysiological recordings; features derived from non-invasive modalities do not modulate at rates necessary to make short-time inferences about articulatory processes. This study employs subdural ECoG recordings to determine the feasibility of neural keyword spotting using high quality neural recordings as a proof of concept.

In building a neural keyword spotter, we were inspired by acoustic keyword spotting, where this has been accomplished in a variety of ways. Hidden Markov Models (HMM) have been applied to this problem extensively. HMM based real-time keyword spotting tends to use a silent state, a keyword state (or series of states) and a set of "garbage" states that capture typical non-keyword speech. In "whole-word" approaches, each state of the HMM represents an entire word (Rohlicek et al., 1989; Rahim et al., 1997), whereas phonetic-based approaches (Rohlicek et al., 1993; Bourlard et al., 1994; Manos and Zue, 1997) break down the keyword and non-keyword utterances into sequences of phoneme sub-models. A keyword has been identified in the window of interest if the state sequence prediction proceeds through a keyword state (for whole-word modeling) or sequence of phonetic states corresponding to a keyword. Using a phonetic-based model to perform neural keyword spotting is risky: according to Mugler et al. (2014), a full set of American English phonemes has only been decoded at 36% accuracy from implanted ECoG arrays, motivating a whole-word approach.

Keshet et al. (2009) suggested a low-latency acoustic keyword spotting using a discriminative approach rather than a HMM-based probabilistic model. In this approach, a linear classifier is trained to maximize the margin between acoustic feature sequences containing keywords and others that don't. As detailed in the aforementioned study, this approach does not rely on computationally intensive Viterbi decoding and achieves higher keyword spotting performance than HMM-based systems.

We have chosen to use a neural voice-activity detection combined with an adaptation of the aforementioned discriminative (non-HMM-based) approach to perform neural keyword spotting. A flowchart that describes the signal processing chain and two-step discriminative decoding pipeline is described in **Figure 1**. Application of neural features to existing acoustic KWS approaches requires a few modifications. For example, mel-frequency cepstral coefficients derived from a single spectrally-rich microphone recording are sufficient to perform acoustic keyword recognition; by contrast, there are many electrodes in an ECoG recording, each with a single time-varying "activation" signal, corresponding to changes in neural population firing rates, in turn indexed by changes in high frequency activity. These activations capture neural processes necessary to sequence, control, and monitor the production of speech, as opposed to acoustic features that capture discriminable aspects of spoken acoustic waveforms. The motor representations of speech that capture the dynamics of articulators, and the auditory representations of speech that capture phonetic content during self-monitoring but also activate during perceived speech, are of particular interest to a neural keyword spotting system.

A recent study by Ramsey et al. (2017) has significantly influenced the approach we've developed to capture the spatiotemporal dynamics of neural features for the purpose of informing keyword discrimination. In the study, Ramsey discriminated phonemes from high density ECoG recordings of vSMC using the correlation of spatiotemporal matched filters as a means of identifying when the spatiotemporal pattern of high frequency activity matched stereotyped patterns for articulations (or gestural sequence of articulations). This method achieved 75% accuracy in a four-class phoneme discrimination problem, and highlighted the importance of including temporal relationships of high frequency activity between cortical sites in decoding models. We extend this methodology here to the creation of maximally discriminative "neural templates" to identify consonant-vowel "keyword" utterances instead of single phonemes.

"Wake-words" for voice-assist technologies are typically chosen to be low-frequency and phonetically complex to reduce the number of spontaneous detections. To simplify the problem of producing a more neurally detectable keyword, we examine monosyllabic, "consonant-vowel" keywords, varying the place of articulation, the consonant voicing, and the vowel height during phonation. Within the context of this study, any speech following the presentation (either textual or auditory) of a CV syllable stimulus is called an "utterance." Keyword spotter models were trained/tested on one of those utterances, defined as the "keyword" utterance for that particular model, with the rest defined as non-keyword utterances—resulting in the creation of 12 keyword spotter models per subject; each sensitive to a specific monosyllabic keyword. We have chosen to examine keyword detection accuracy with respect to non-keyword speech

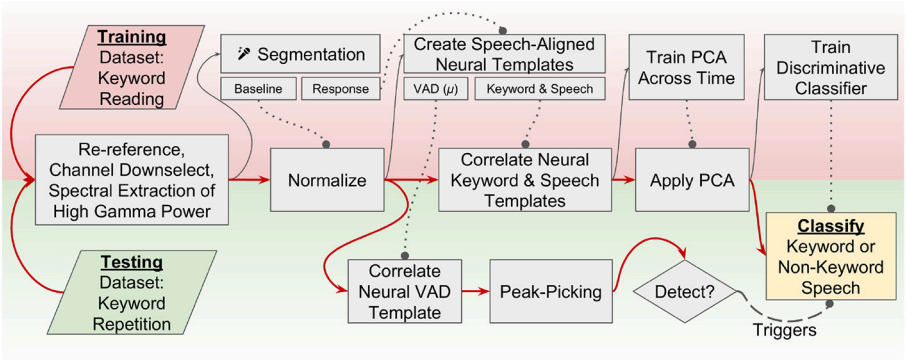

FIGURE 1 | A flowchart representation of the keyword-spotting signal processing pipeline. Red arrows indicate flow of data through the pipeline. Dotted lines with circles indicate models that were trained on the training dataset are used in this step for both the training and testing data. Training is performed using a visually presented keyword reading paradigm, and testing occurs across an auditory keyword repetition task. This study implements a two-stage detector; one neural VAD template is correlated across the testing dataset, and peak-picking indicates a detected utterance. When an utterance is detected, a discriminative classifier is used to decide if the utterance was a keyword or non-keyword speech. Channel downselection, normalization parameters, neural templates, feature dimensionality reduction, and classifiers are all trained on the reading (training) task and applied to the repetition (testing) task to simulate how keyword spotting would realistically perform in a separate recording session.

and silence, as opposed to a multi-keyword decode to further simplify the problem and performance metrics. We will also limit ourselves to causal methods of feature extraction and classification for this study to realize how neural keyword detection would perform if deployed in a low-resource real-time scenario.

This is the first study of neural keyword spotting in ECoG recordings that demonstrates low latency (~1 s) using causal models and feature extraction methods akin to low-resource acoustic KWS implementations. Application of spatiotemporal matched filters, trained/tested in separate ECoG recordings, appeared to strongly influence the specificity of the spotter in single-trials. We found that spatial **and** temporal features from vSMC can be used to discriminate place of articulation and consonant voicing in monosyllabic keywords, and that vowel height (/a/ vs /i/) is much more discriminable using neural features from STG during self-monitoring of overtly produced speech, as opposed to the motor representations that are simultaneously present in vSMC.

2. MATERIALS AND METHODS

Please refer to **Figure 1** for a brief overview of the methodology used in this study, summarized here for convenience, but with more detail provided in subsections 2.1-2.6. Two datasets were collected in separate recording sessions; one used for training model parameters and another used for performance validation. The first step in the signal processing pipeline was a signal re-referencing to the common average followed by a manual channel downselection and spectral extraction of high gamma log-power. High gamma modulation across the training task was normalized (z-scored) per-channel to a pooled baseline period constructed by segmenting baseline periods from across the training task. Response periods in the training dataset were used to train neural templates, and these templates were cross-correlated over the normalized high gamma features before a principal component analysis (PCA) was fit. Discriminative classifiers for each keyword were fit on these "template-PC" features and a decision boundary was chosen for each keyword spotter individually. Similarly, a threshold parameter was selected for a causal peak-picking algorithm applied to the cross-correlation of the grand-average "VAD" template. The same preprocessing steps were applied to the testing dataset, and high gamma log-power was normalized across testing dataset. The templates and PCA that were trained previously were then applied without further calibration to the testing high gamma features, and template-PC features corresponding to super-threshold peaks in the VAD template output were classified using the aforementioned discriminative classifiers.

2.1. Data Collection

Subdural electrocorticographic recordings were made in eight subjects undergoing intracranial monitoring prior to resective surgery for drug-resistant epilepsy. Electrocorticographic (ECoG) arrays of platinum electrodes with varying exposed area and spatial density were placed for a 1–2 week period according to clinical requirements. Subjects performed both syllable-reading and syllable-repetition paradigms as part of a protocol approved by the Johns Hopkins University Institutional Review Board. All subjects gave written informed consent in accordance with the Declaration of Helsinki. Electrode localization was performed by aligning electrode locations from a post-operative computed tomography image with a pre-operative magnetic resonance image using Bioimage Suite (Papademetris et al., 2006). Neuroimaging and electrode locations are shown in **Figure 2**.

Subjects performed two tasks wherein they were asked to overtly produce monosyllabic consonant-vowel (CV) utterances. In the (syllable) reading task, a textual representation of the utterance was visually presented for 1 s (see **Table 2** for details)

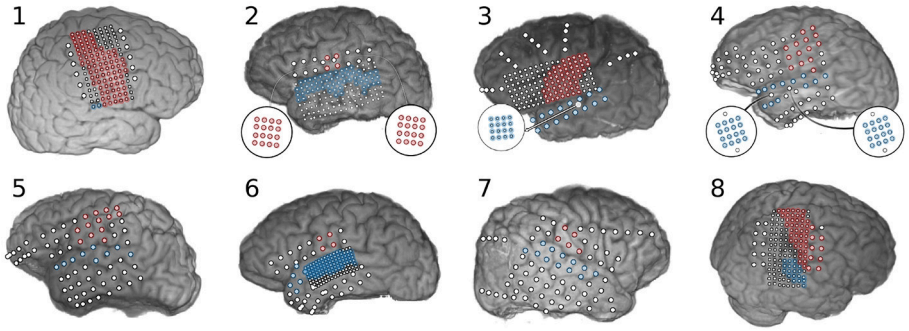

FIGURE 2 | Neuroimaging and electrode localization for eight subjects implanted with subdural electrode arrays. Electrodes positioned over sensorimotor cortex are highlighted in red and electrodes over superior temporal gyrus are highlighted blue. Biographical and experimental details for these subjects can be found in **Table 1**. Subject 1 had a large lesion within pre-central gyrus, from which very little high frequency activity was recorded. Subject 3 had an ictal locus very near sensorimotor cortex with substantial inter-ictal activity that limited observation of neural features in this area. Subject 8 had a lesion in the right supramarginal gyrus.

followed by an intertrial interval of 2–3 s during which the subject was instructed to fixate on a visible fixation cross. The (syllable) repetition paradigm was identical, except that the fixation cross remained on screen throughout the task and the utterance was aurally cued using a speaker. In both tasks, the subject was instructed to speak the prompted syllable aloud after stimulus delivery, and a microphone was used to record the subject's responses to a high quality digital audio file. A monitor-output cable connected the microphone recording device (Zoom H2, Zoom Corporation, Tokyo, Japan) to an auxiliary analog input on the electrophysiological amplifier (Neuroport, Blackrock Microsystems, Salt Lake City, UT; and EEG1200, Nihon Kohden, Tomioka, Japan), recording a lower-resolution version of the subject's speech synchronized with the ECoG data at 1,000 samples per second. BCI2000 (Mellinger and Schalk, 2007) was used to present stimuli and record the data from the amplifier into a standardized format for offline analysis. Data was collected in blocks of 60 trials; 5 trials each for all 12 utterances in a randomized order. The paradigm was split across two blocks of reading and two blocks of repetition for each subject, but time and clinical constraints limited collection to one-block of the tasks for some subjects. Details of data collection for each subject is documented in **Table 1**.

2.2. Preprocessing and Segmentation

Seventy one channels across all subjects (1–18 per subject) were identified as noisy/bad by a neurologist via visual inspection of the raw ECoG signals and were removed from further analysis. Spatial filters were applied to re-reference recordings to the common-average of the included channels. Trial markers from BCI2000 that designated stimulus presentation (auditory or visual) were used to define the trial onset points. The 250–450 Hz band-power in the synchronized low-fidelity microphone recording captured the first formant of speech in each subject, and was thresholded to detect the voice onset time for each trial. These threshold crossings tend to be associated with the voice-onset-time in CV keywords containing a voiced consonant and the plosive release in CV keywords containing an unvoiced consonant, due to the silent nature of consonant articulation. Templates were generated from a 1-s "response" period centered around this threshold crossing to capture differences in the timing of neural features relative to the response onset (Mugler et al., 2014; Jiang et al., 2016; Ramsey et al., 2017). Neural features were normalized within each task individually to a pooled "baseline" period which was created from a 1-s period prior to stimulus presentation across all trials within a single task. All trials from the reading dataset were used for training templates and classifiers that were applied across the repetition dataset. In this way, the training data were entirely separate from the testing data, and the templates generalized feature extraction across tasks.

2.3. Feature Extraction and Electrode Downselection

Electrodes over sensorimotor cortex and superior temporal gyrus were manually identified by a neurologist; see **Figure 2** for a summary. Electrodes lying outside these areas were excluded from further analysis. A 128 ms window sliding by 16 ms increments was used to perform spectral decomposition via the fast Fourier transform. Spectral power was log-transformed and z-scored to the baseline period, per-frequency. Frequency bins between 70 and 110 Hz were averaged together to form a time-varying feature capturing the band power modulations in the "high-gamma" range, a frequency range highly correlated with the firing of local neural populations (Ray et al., 2008). This feature was then re-normalized to the baseline period per-electrode.

2.4. Template Generation and Voice Activity Detection

Previous studies indicate that the timing of high gamma activity contributes significantly to decoding of speech from vSMC (Jiang et al., 2016; Ramsey et al., 2017). Neural templates were trained to capture spatiotemporal relationships of high gamma activity in an efficient, but causal representation. A "response template" was created by calculating the mean of the neural responses from all trials (N = 60–120) in the training dataset. A "keyword

TABLE 1 | Biographical and experimental details for subjects.

ID	Side	Age	Sex	Reading trials	Repetition trials	Grid specifications
1	R	17	M	120	60*	vSMC: 85 (85 HD-5) STG: 2 (2 HD-5) Total: 87
2	L	37	F	60	120	vSMC: 36 (32 μ, 4 SD) STG: 57 (57 HD-5) Total: 93
3	L	25	M	105**	120	vSMC: 30 (30 HD-5) STG: 32 (16 μ, 16 SD) Total: 62
4	L	39	M	120	120	vSMC: 14 (14 SD) STG: 48 (32 μ, 16 SD) Total: 62
5	L	40	M	120	120	vSMC: 13 (13 SD) STG: 9 (9 SD) Total: 22
6	L	40	F	60	120	vSMC: 4 (4 SD) STG: 87 (81 HD-3, 6 SD) Total: 91
7	R	27	M	120	60	vSMC: 5 (5 SD) STG: 12 (12 SD) Total: 17
8	R	19	M	120	120	vSMC: 52 (43 HD-5, 9 SD) STG: 19 (HD-5) Total: 7

The implant hemisphere (side), age, sex, number of reading/repetition trials, and grid specifications for all eight subjects in the study are listed here. Associated neuroimaging and electrode localization can be found in ***Figure 2****. Channels are delineated by region of interest, and further by the diameter of the electrode's exposed area, then by the inter-electrode spacing. SD: Standard macro-array (2 mm diameter, 1 cm pitch). HD-5: High density array (2 mm diameter, 5 mm pitch). HD-3: High density array (1 mm diameter, 3 mm pitch). μ: Micro-ECoG array (75 μm diameter, 1 mm pitch). *120 trials were recorded, but the synchronized microphone recording failed for the second set of 60 trials. Neural keyword spotting can be applied to this second block, but ground truth timing metrics are unavailable. **Recording session ended early.*

TABLE 2 | Utterances and associated axes of articulation.

/IPA/ ("Stim")	Bilabial	Alveolar	Velar
Voiced	/ba/ ("BAH")	/da/ ("DAH")	/ga/ ("GAH")
Unvoiced	/pa/ ("PAH")	/ta/ ("TAH")	/ka/ ("KAH")
/IPA/ ("Stim")	**Bilabial**	**Alveolar**	**Velar**
Voiced	/bi/ ("BEE")	/di/ ("DEE")	/gi/ ("GEE")
Unvoiced	/pi/ ("PEE")	/ti/ ("TEE")	/ki/ ("KEE")

Utterances vary on three axes; three places of articulation, two ways of consonant voicing, and two vowel heights. Utterances are shown with their IPA notation as well as the textual prompt as shown in the reading paradigm. "GEE" would typically be pronounced /ʤi/ but subjects were instructed to respond with /gi/ instead.

template" for each keyword was also created by calculating the mean of the neural responses for each of the keywords individually (5–10 trials). We additionally took advantage of our keyword design to create neural templates composed of higher trial counts across axes of articulation, as described in **Table 2**. The response template was then subtracted from each of these keyword templates, the resulting "discrimination template" captured spatiotemporal relationships that differed from the mean neural responses in the response template. A significance mask was created by z-scoring the condition mean (prior to subtraction of the response template) relative to the baseline period. A temporal smoothing kernel (hamming, 0.1 s) was applied to reduce noise in the template before the significance mask was applied; elements with a z-score of <3.0 were set to zero to further reduce noise. The smoothed and regularized discrimination templates were correlated with the corresponding high-gamma features in both testing and training datasets—these features were further smoothed (hamming, 0.25 s) to reduce the influence that slight timing mismatches could have on keyword discrimination. An example visualization of the generation of a discrimination template for bilabial keywords can be found in **Figure 4A**. A PCA was fit to identify linear combinations of template output features that accounted for 90% of the variance across the entire reading task. Principle components of template outputs were calculated for both the reading and repetition datasets, reducing covariance in the template outputs and creating neural features which can be used for keyword discrimination.

Electrodes from STG were excluded from the response template; the resulting template was used as the neural VAD template. Auditory representations of speech in STG tend to have less specificity to self-generated speech and their inclusion in the VAD model can result in false-positive detections coincident with the *perception* of speech, whether or not it was produced by the subject. Neural VAD was calculated as the squared temporal correlation between the VAD template and the normalized high-gamma power. VAD output was further smoothed using a temporal smoothing kernel (hamming, 1.0 s). A causal peak-picking algorithm was applied to identify utterance onset times—the derivative of the neural VAD signal was thresholded and the zero-crossing that follows a threshold crossing was chosen as the utterance detection time. Example templates and their corresponding correlational output are shown in **Figure 4**. Application of these templates to live neural features results in exactly 1 s of latency for neural VAD and keyword discrimination.

2.5. Discriminative Classification

A discriminative classifier similar to SVM, as described in great mathematical detail by Keshet et al. (2009), was trained on the reading dataset. In broad strokes, the training step attempted to designate a linear discrimination boundary that maintains a constant margin of separation between pairs of feature-vectors corresponding to keyword and non-keyword utterances. For each pair, the training step searched for the feature-vector within $\pm$100 ms of the alignment time for the non-keyword utterance that looked maximally "keyword-like," given the current discrimination boundary. The learning step adjusted the discrimination boundary using the difference between that maximized non-keyword feature-vector and the ground-truth keyword feature-vector. A significant advantage of this classifier is that it can be trained online as new observations become available.

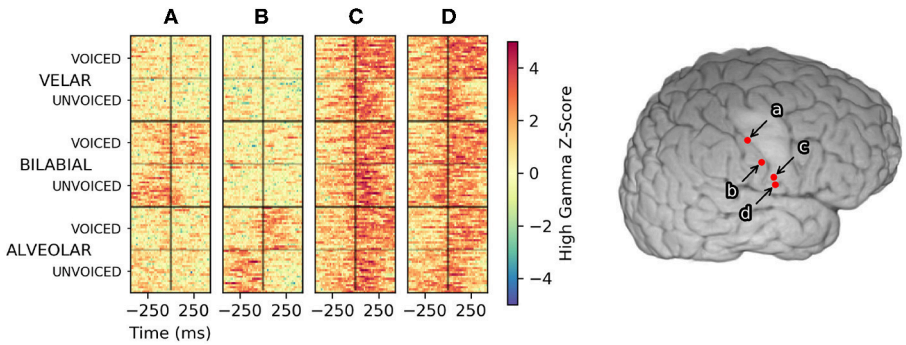

FIGURE 3 | High-gamma single-trial rasters across the reading task from four manually selected electrodes in Subject 1. Trials, plotted along the Y axis, were sorted first by the place of articulation for the consonant, then by consonant voicing. Trials were aligned with response-onset time set to 0 s, denoted by a black vertical line at the center of each raster. Color denotes the high-gamma feature z-score normalized to a pooled pre-trial baseline period. Activity in electrode **(A)** appears to represent a bilabial place of articulation, whereas activity in electrode **(B)** appears to indicate an alveolar place of articulation. Timing differences of high-gamma activity relative to the voice onset time encoded the voicing of bilabial and alveolar consonants in these areas. Electrode **(C)** exhibited consistent high-gamma amplitude and timing for all utterances; informing neural VAD but less useful for keyword discrimination. Electrode **(D)** appeared to encode consonant voicing across all places of articulation. No clear patterns emerged if the trials were sorted by vowel height (/a/ vs /i/) for any electrodes in Subject 1.

Pairs of feature-vectors associated with keyword and non-keyword utterances were assigned within stimulus blocks. Additionally, feature-vectors associated with keyword utterances were paired with feature-vectors corresponding to silent periods (1.0 s before stimulus onset) to adapt the classifier boundary to VAD false-detections during silent periods. In **Figure 5**, classifier output was calculated using ground-truth utterance detections derived from the microphone. During simulated testing, results of which are shown in **Figure 6**, the classifier output was calculated at times when the neural VAD model identified an utterance. The slight temporal misalignments between neural VAD and microphone-derived timing accounts for the different classifier performances between these figures.

2.6. Testing and Performance Metrics

The templates, principle components, and discriminative classifiers were trained on all trials of the reading task. Testing and performance metrics were calculated from the application of these models to the repetition task. A VAD performance metric was calculated by sweeping the aforementioned VAD threshold value from 0 to 20 standard deviations (relative to baseline periods) and comparing the utterance detection times to the ground-truth microphone threshold crossings. An utterance detection within $\pm$100 ms of a microphone event was classified as a true-positive, but subsequent detections for that utterance were considered false-positives.

An ROC curve was created for each of the keyword classifiers using microphone-derived voice onsets in the repetition task. A classifier threshold was swept from -10 to 10 and the resulting keyword detections and false-positives were used to create an ROC curve and derive area-under-curve (AUC) metrics for each keyword classifier. Significance of the AUC statistic was calculated by scrambling the ground-truth utterance labels while training keyword detectors. A bootstrapped null-distribution of 1000 AUC metrics was generated for each keyword classifier, from which statistical significance thresholds for the metric were calculated. Keyword spotting performance using neural VAD times was also calculated for each classifier using a threshold that was chosen to maximize sensitivity while minimizing false detections' in particular, equalizing the error rates for false-negatives and false-positives, the so-called "equal error rate" condition (Motlicek et al., 2012)—on the training dataset.

3. RESULTS

Within the context of this methodology, discrimination between keyword and non-keyword speech relies upon differences in timing and/or amplitude of high-gamma activity. Differences in high-gamma amplitude across keywords are useful in traditional decoding approaches where only single time-points of high-gamma activity are used to make classification decisions. Single-trial plots, as seen in **Figure 3**, suggest high-gamma amplitude in vSMC can be sufficient to decide the place-of-articulation for an utterance. Consonant voicing appears to be encoded in the timing of high-gamma activity relative to voice onset time. The sensation of pressure build-up in the vocal tract prior to plosive release is a plausible explanation for the timing of this discriminable neural activation in electrodes **a** and **b**, especially given the placement of these electrodes in postcentral gyrus; an area typically associated with sensation.

The correlation of neural templates with high-gamma activity created high-level features that appeared to be useful for clustering utterances using these spatiotemporal relationships, as shown in **Figure 4**. The discriminative quality of a neural template appeared to rely primarily upon the number of trials used to create it; a decrease in the template noise was associated with a higher number of trials. A neural template for a particular contrast highlights the difference from the mean template, which can be a problem if there is no discriminable difference between the contrasts. As seen in **Figure 4**, Subject 1 had very little discriminable activity within the vowel height condition (/a/ vs /i/), meaning the trial average across the '/a/' condition and

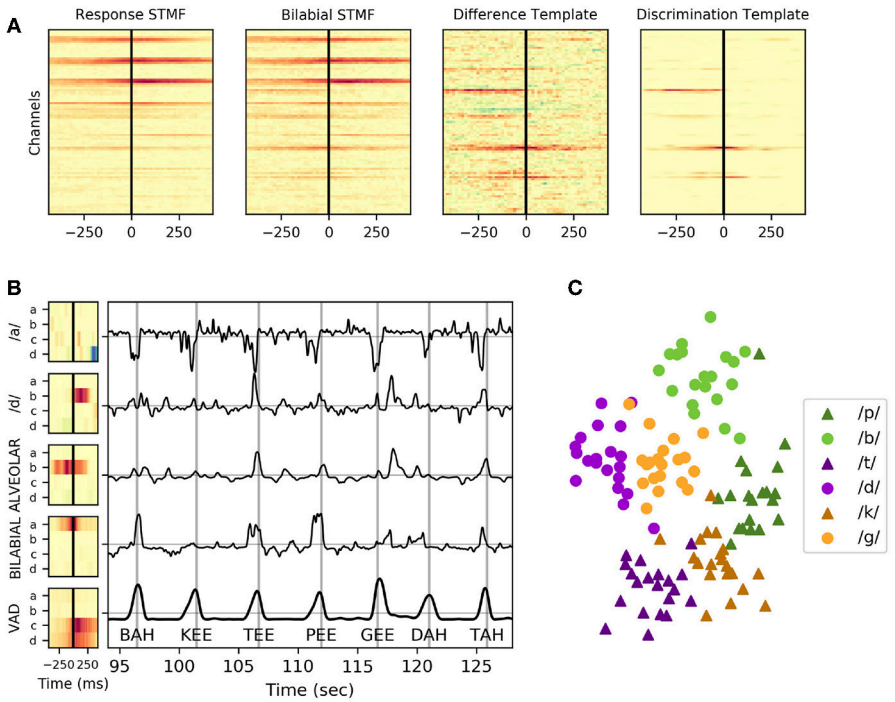

FIGURE 4 | Example neural templates and utterance discrimination in Subject 1. **(A)** From left to right: the response spatiotemporal matched filter; an average of all keyword utterances, the bilabial spatiotemporal matched filter (STMF); an average of just keyword utterances with a bilabial place of articulation, the difference template; the subtraction of the response spatiotemporal matched filter from the bilabial spatiotemporal matched filter, and the discrimination template; the regularized and smoothed/denoised discrimination template for bilabial keywords. **(B)** Neural templates, created as a trial-average of particular keywords or phonemic contrasts followed by regularization and normalization, are shown for the four electrodes (**a**, **b**, **c**, and **d**) depicted in **Figure 3**. The VAD template, shown at the bottom, is the mean across all 120 trials in the task. The correlation of these templates with the high-gamma activity in the same task is shown in the plot to the right of the templates for a contiguous period of ~95 to ~125 s into the reading task. Vertical gray lines in this plot indicate ground truth utterance times as recorded by a microphone, and the associated utterance is indicated at the bottom of these lines. Peaks of the neural VAD output closely matched the utterance times. **(C)** The values of these template features across all templates (including many not pictured) at the utterance onset times were collected and reduced to two dimensions using multi-dimensional scaling, then plotted in the scatter plot, highlighting how these features clearly discriminate place of articulation and consonant voicing.

the '/i/' condition were very similar to the trial grand-average. Subtracting the trial-average from the two condition averages resulted in a template that introduced significant noise to the feature set. The inclusion of these templates was less of a problem due to the following decomposition of these features into principal components; the noisy template outputs tended to be de-emphasized as they did not explain much of the variance of the features across time. Noting that template output appeared to fluctuate around neural VAD timings, temporal alignment was absolutely critical when interpreting these features.

Neural VAD and keyword discriminability appeared to be somewhat decoupled; several subjects showed consistent high-gamma modulation across utterances that was useful for performing VAD, but these features were less useful for keyword discrimination, as shown in **Figure 5**. Subject 1 exhibited exceptional VAD with highly significant discrimination of several keywords. Subject 2 showed similar VAD performance, but demonstrated relatively poor keyword discrimination. Classifiers in Subject 1 leveraged neural features that discriminated consonants well (shown in **Figure 3**), whereas classifiers from Subject 2 were only informed by features that discriminated vowel height and alveolar place of articulation, shown in **Figure 7**. VAD and keyword discrimination results for all subjects are shown in **Supplementary Material**.

4. DISCUSSION

This study is the first to examine keyword spotting using ECoG. A neural keyword spotter could form the basis of a menu-selection BCI for disabled users, or a low latency "neural click" in a virtual reality context where the user is unable to see/use a real-world input device. A BCI-enabled keyword spotter could respond selectively to the user whereas acoustic keyword spotters struggle to operate in multi-speaker conditions. These results were obtained by performing a two-step classification procedure involving neural VAD and keyword vs. non-keyword-speech classification. As mentioned previously, neural voice activity detection has been performed before using spectral decomposition techniques and a discriminative classifier by Kanas et al. (2014). Performing VAD using this method of template-based "matched filtering" has a number of benefits over this prior work. Due to the fact that all utterances are roughly the same length and surrounded by silence, cross

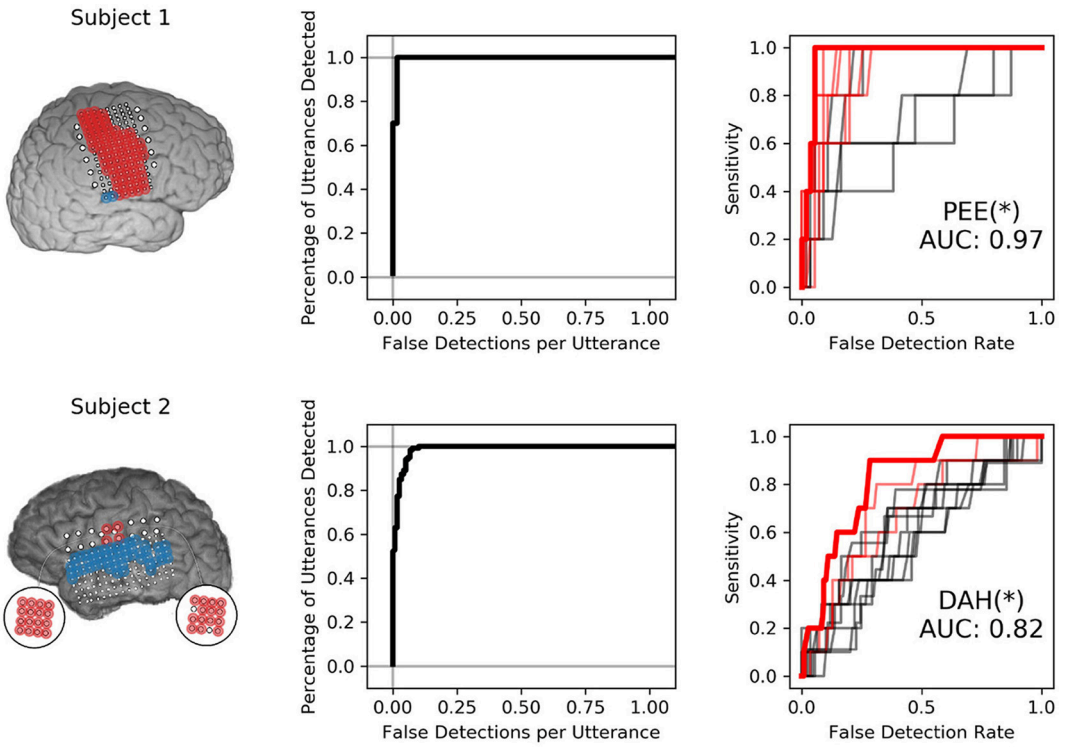

FIGURE 5 | Isolated VAD and keyword discriminability for two subjects. The left-most panel shows the electrodes highlighted in red and blue that were used to discriminate syllables. Only electrodes highlighted in red were used to perform VAD. The center panel shows the VAD performance in sensitivity (percentage of utterance timings correctly identified) against the number of false detections per utterance for various VAD thresholds. The right-most panel shows ROC curves for all 12 keyword detectors. ROC curves with AUC values were significant at the 95% confidence interval are highlighted in red. The keyword detector that produced the highest AUC is highlighted in bold-red and indicated via annotation under the curves, followed by an asterisk that indicates significance at the $p < 0.05$ level with respect to the distribution of maximum AUC models.

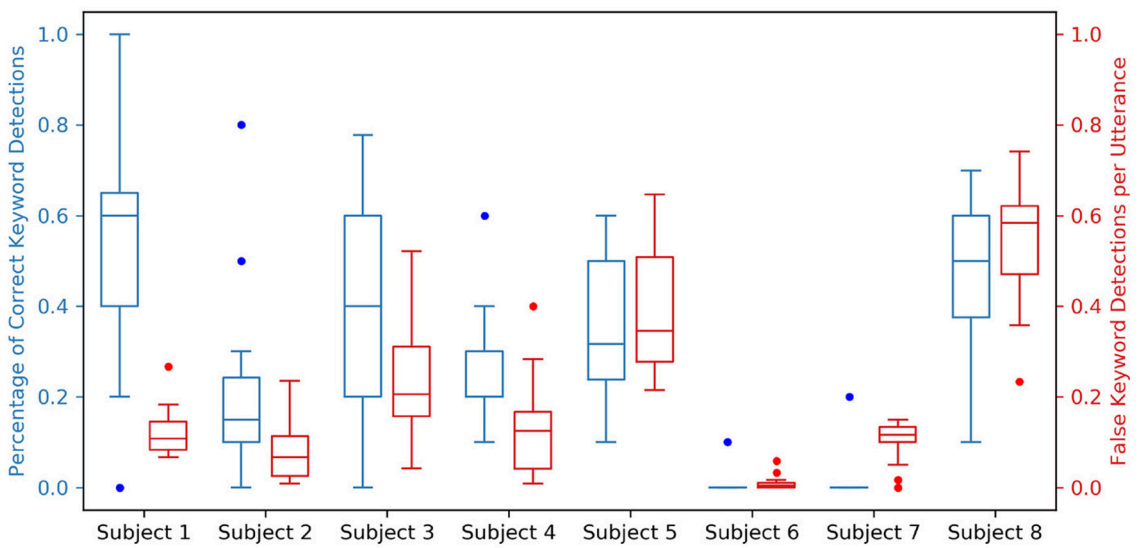

FIGURE 6 | Simulated keyword spotting performance on the testing dataset for all spotters across all subjects. For each subject, two boxplots relating the performance of all 12 keyword spotters are shown; a blue boxplot to the left indicating the percentage of correct keyword detections with a value ideally closer to 1.0, and a red boxplot to the right indicating the percentage of false keyword detections per utterance with a value ideally closer to 0.0. These performance metrics are coupled to neural VAD performance, which is shown in the **Supplementary Material** for all subjects.

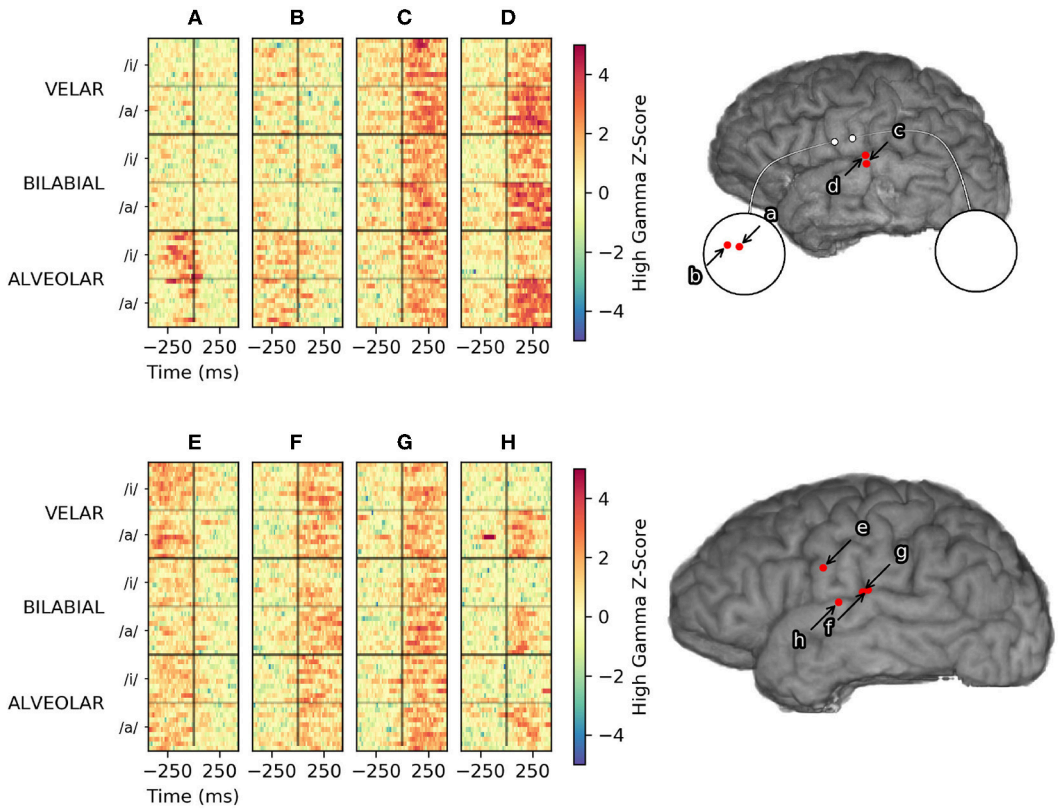

FIGURE 7 | Vowel-specific high gamma activity from Subject 2 (top) and Subject 6 (bottom). Single-trial high-gamma rasters to the left are sorted first by place of articulation, then by vowel height. Electrode **(D)** and **(H)** appear to encode vowel height, in similar areas of STG. Electrode **(A)** and **(B)** are micro-ECoG electrodes over vSMC that appear to encode place of articulation. Electrodes **(C)**, **(F)**, and **(G)** appear to modulate consistently with all utterances and are more useful for VAD, but provide little discriminative information. Modulation recorded by electrode **(E)** appears to be consistently related to articulation, but does not appear to discriminate utterances by place of articulation or vowel height.

correlation with the neural VAD template actually provides a good alignment point for the application of a discriminative classifier. Furthermore, the cross correlation is computationally efficient and only relies on a peak-picking implementation to find utterances. The second-stage discriminative classifier tends to classify VAD false detections as "non-keyword utterances," and serves as a secondary filter before detecting keyword events.

Acoustic "wake word" spotting typically relies on keywords that are low frequency and dissimilar from typical non-keyword utterances, the most popular wake words being words/phrases like "Alexa," "Hey Siri," and "Okay Google." In this study, monosyllabic keywords were chosen to examine what makes keywords more distinguishable neurally as opposed to acoustically. The utterances used in our experiment were exceptionally similar to each-other, varying only by 1–3 distinctive articulatory features. Indeed, a particularly important feature—keyword length—was the same across all utterances, making the keyword detection problem significantly more difficult. The simulated keyword spotting performance for all keyword spotters in Subject 1 is shown in **Supplementary Figure**, and the simulated keyword spotting summary performance metrics are shown for all subjects in **Figure 6**. While this performance is not comparable with the current state of the art in acoustic keyword spotting, neural VAD alone appears to provide a temporally precise 1-bit (silent vs. speech) BCI and the addition of keyword discrimination would allow the user to trigger the BCI while not restricting speech between intended triggerings.

The most striking finding from this study was that vowel height was poorly represented in vSMC. This is consistent with the findings of Bouchard et al. (2013) in which syllable discrimination using a high-density grid in vSMC achieved lower cluster separability of vowel height than manner of consonant articulation. This result also corroborates a finding from Ramsey et al. (2017) that vowels are the least distinguishable phonemes in their test set; the authors speculated that lacking plosives, vowels differ only in lip positions, which may not be well-represented in this area. Our findings suggest that vowel height is well represented in auditory association cortex areas STG, presumably due to self-monitoring, shown in **Figure 7**.

None of the subjects in the study exhibited high gamma activity that significantly encoded vowel height within vSMC. Many studies indicate vowel phones may be decoded from vSMC (Pei et al., 2011a; Bouchard and Chang, 2014; Mugler

et al., 2014; Ramsey et al., 2017), although some studies also note that decoding accuracy is generally worse than consonant phones (Mugler et al., 2014; Ramsey et al., 2017). None of the aforementioned studies report a failure to decode vowel phones from vSMC, which is contrary to our findings. This may be due to the fact that the vowels chosen for this study, /a/ and /i/, result from a slight variation in tongue height and do not involve differential activation of the lips, such as with the vowel contrasts selected for the aforementioned studies, /a/ and /u/, which can recruit sensorimotor areas related to the face. This said, STG has been shown to consistently modulate with differences in vowel height (Mesgarani et al., 2014) during audition and self monitoring. Practically, our results suggest that discrimination of vowels during keyword spotting with a neural interface may be improved by including auditory representations from STG with sensorimotor representations from vSMC. This finding also suggests that modulation and control of vowel height relies on interactions between auditory areas and motor areas more than consonant articulation which seems to be well represented in just suprasylvian cortex.

The subject with electrode coverage most analogous to the implant detailed in Bouchard et al. (2013) had a high-density grid with 2-mm electrode diameter and 5-mm interelectrode distance over somatosensory cortex. Although we showed no significant neural differences between low and high vowel height with this grid placement, the grid in Bouchard et. al. had a slightly smaller pitch and this higher resolution may have captured more information about vowel height than we observed. Similarly, we showed significantly worse performance with lower density coverage of vSMC, demonstrated by subjects with only standard-density (2 mm electrode diameter and 1 cm pitch) coverage, indicating that standard ECoG arrays are likely insufficient for a comprehensive speech neuroprosthesis. Some subjects were also implanted with microelectrode array grommets (75 μm electrode diameter and 1 mm pitch); these arrays have a sensor density similar to what is thought to be the spatial limit of subdural neural recordings (Slutzky et al., 2010). Micro-ECoG was useful in discriminating place of articulation for utterances from Subject 2, but its utility was greatly dependent on placement due to its limited spatial extent. An ideal ECoG array would probably cover all of vSMC with the same 1 mm pitch, but this is not yet technically feasible with clinically approved ECoG electrodes and their connectors. Although our best results came from a subject with a high density grid over vSMC, our inability to observe neural activity associated with velar consonants indicates that even these high density arrays do not capture sufficient detail to distinguish all articulators (and hence, all phones) necessary for a speech neuroprosthesis. Further research into recording devices that cover a similar spatial extent but with higher sensor density and channel counts might be fruitful, but our results indicate that neural features recorded from high density ECoG arrays can, at a minimum, produce a usable neural interface for whole-word keyword spotting in overt speech.

Correlating spatiotemporal templates with streaming high gamma features was primarily motivated by existing keyword search methodology, as well as a recent study by Ramsey et al. (2017). The temporal encoding of consonant voicing in Subject 1 (see **Figure 3**) further motivated the application of spatiotemporal template methodology. To evaluate the contribution of neural templates to keyword discrimination, the templates were replaced with a rectangular window of the same size, resulting in smoothing of the high gamma features on the same order as that of the templates. After making this change, we observed a marked drop in keyword discrimination, highlighted in **Figure 8**, suggesting that temporal relationships between high-gamma events provide information useful for discriminating keywords, and that these templates are an effective way of quantifying these relationships in single trials.

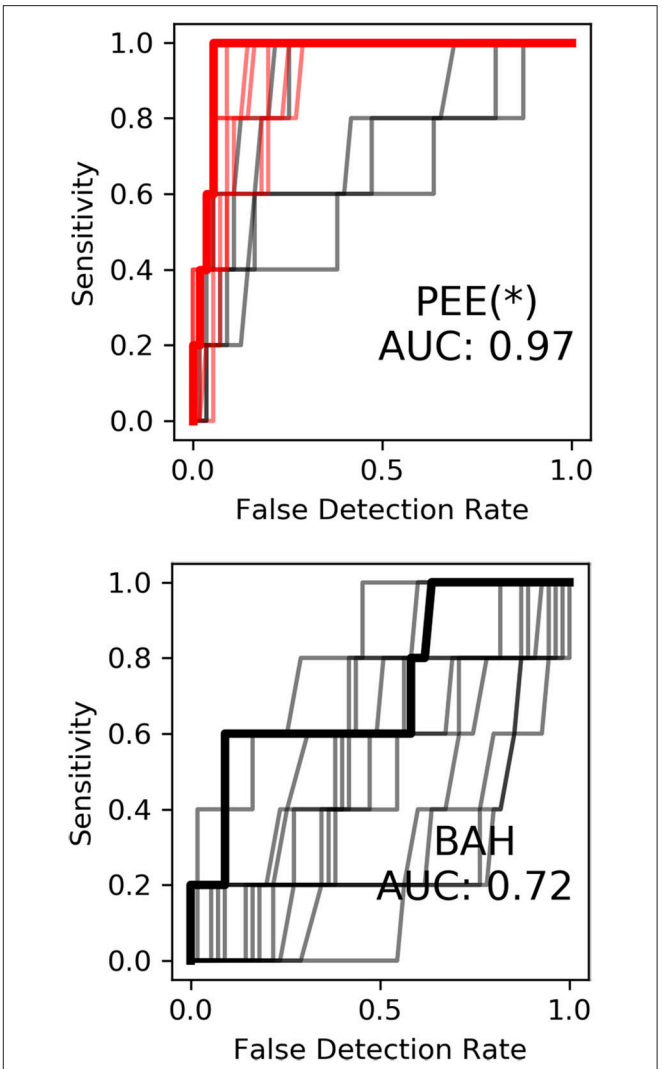

FIGURE 8 | Keyword discrimination ROC curves for Subject 1 before (to the left) and after (to the right) replacement of neural templates with rectangular smoothing windows. Keyword discrimination performance dropped across all models suggesting inclusion of spatiotemporal relationships using neural templates aids keyword discrimination.

A rational application of neural keyword spotting would detect keywords that would have more contextual relevance in the presence of continuous speech. Commercial keyword spotting systems tend to select low-frequency words with more discriminable acoustic features that maximize the probability of keyword detection while minimizing the number of false-positive detections during typical non-keyword speech. The keywords chosen for this particular study were not selected with these considerations in mind, but rather highlight how keyword spotting performance varies primarily with the articulatory representations sampled. For Subject 1, there were no electrodes that showed high gamma modulation during the articulation of syllables with a velar place of articulation—yet within the context of this study—these articulations were readily discriminable *because* of this lack of neural activity. Within the context of **Figure 3**, a keyword that only modulated electrodes **c** and **d**, and not **a** or **b**, can be reasonably deduced to have a velar consonant, but if the keywords were downselected to just "GAH, KAH, GEE, and KEE," these keywords would not be sufficiently discriminable using the coverage from Subject 1. As described earlier, Subject 1 also had no discriminable neural modulation across the vowel contrast in the keyword set, with false detections tending to trigger for the alternative vowel height (see simulated KWS performance for Subject 1 in **Supplementary Material**). These observations demonstrate why whole-word keyword spotting approaches are better suited for neural data. Some phonemic representations may not be sampled by a particular electrode coverage even with high-density spatial sampling—particularly if the neural populations associated with those articulators are located in a sulcus, which surface ECoG has difficulty sampling. They further demonstrate the inherent difficulty of performing phonemic-based automatic speech recognition ala (Herff et al., 2015) using even the high density neural recordings from our best-performing subjects.

Critically, the results of this study suggest that the precise temporal sequencing of neural activity correlated with the subset of neural articulator representations that *are* sampled can be sufficient to discriminate a keyword from non-keyword speech. Furthermore, neural keyword spotting has several significant advantages to an acoustic keyword spotting system. Neural keyword spotting is capable of activating selectively to the intended speaker even in the presence of multiple speakers, and it performs keyword discrimination using features that can discriminate acoustically similar words like "Alexa" and "Balexa" which most commercial keyword spotting systems would struggle with using acoustic features alone—especially in the presence of noise. Although utterance detection using the peak-picking algorithm described in this study would likely need modification to properly trigger for keywords that occur mid-vocalization, our results suggest that neural VAD as described by this study would perform well for interaction with a virtual agent, wherein a period of silence is followed first by the keyword, then the command for the agent. We further propose that our results demonstrate encouraging performance that motivates a follow-up study using practical keywords in a less constrained scenario involving continuous speech.

5. CONCLUSIONS

This study suggests that a high-sensitivity/specificity one-bit neural keyword spotting BCI can be created using ECoG recordings from vSMC and STG. Neural signals capturing speech motor representations from vSMC appear to be useful for low-latency (~1 s) and high-specificity VAD, while a combination of neural signals from vSMC and auditory representations from STG may be useful for discriminating keyword utterances from non-keyword speech. Spatiotemporal relationships of high gamma activity across electrodes, captured and efficiently quantified using a method of neural template correlation, appear to be instrumental for keyword discrimination. In this study, keyword-spotting performance depended on several factors including electrode density and the number of electrodes within vSMC and STG. Our results suggest that high-density ECoG grids may be necessary and sufficient for capturing the spatial layout of cortical speech representations needed for a keyword-spotting neural interface. Neural features that provide information about consonant articulation appear to be best represented in vSMC, with place of articulation primarily encoded by the spatial location of high-gamma activity and consonant voicing encoded by the temporal dynamics of this activity. Vowel height during overt speech appeared to be poorly encoded by vSMC, but better represented in traditionally auditory areas along STG during self-monitoring. Although we did not test whether neural activity in STG during covert speech was sufficient for decoding vowel height, other studies have indicated that this may be possible (Pei et al., 2011b; Leuthardt et al., 2012). Together with these and other studies, our findings support the feasibility of keyword spotting with an ECoG BCI provided that relevant cortical areas are recorded with sufficient spatial sampling and that keywords are composed of neurally discriminable articulatory gestures.

DATA AVAILABILITY

The datasets generated and analyzed for this study, analysis code, and latex source files for this paper can be found in the gigantum project located at: https://gigantum.com/griffinmilsap/ecog-keyword-spotting. Stimulus parameters for BCI2000 and BCI2000 Web are available at https://github.com/cronelab/SyllableTasks.

AUTHOR CONTRIBUTIONS

MC, YW, and NC designed the experiment and utterance contrasts. GM, MC, CC, and YW collected the intracranial recordings. GM conceived and conducted analyses. MC, QR, YW, and NC provided feedback and direction. GM authored the manuscript. GM, MC, CC, QR, YW, and NC reviewed the manuscript and associated submission documents.

FUNDING

This project has been supported by the National Institutes of Health (R01 NS088606, R01 NS091139).

ACKNOWLEDGMENTS

The analysis package is hosted by/created in https://gigantum.com. Analysis was supported by Jupyter Notebook and plots were generated using Matplotlib. Significant editing and support was provided by Philip H. Keck.

SUPPLEMENTARY MATERIAL

The Supplementary Material for this article can be found online at: https://www.frontiersin.org/articles/10.3389/fnins.2019.00060/full#supplementary-material

REFERENCES

Bouchard, K. E., and Chang, E. F. (2014). "Neural decoding of spoken vowels from human sensory-motor cortex with high-density electrocorticography," in *2014 36th Annual International Conference of the IEEE Engineering in Medicine and Biology Society* (Chicago, IL), 6782–6785.

Bouchard, K. E., Mesgarani, N., Johnson, K., and Chang, E. F. (2013). Functional organization of human sensorimotor cortex for speech articulation. *Nature* 495, 327–332. doi: 10.1038/nature11911

Bourlard, H., D'hoore, B., and Boite, J. (1994). "Optimizing recognition and rejection performance in wordspotting systems," in *Proceedings of ICASSP '94. IEEE International Conference on Acoustics, Speech and Signal Processing* (Adelaide), I/373–I/376.

Herff, C., Heger, D., de Pesters, A., Telaar, D., Brunner, P., Schalk, G., et al. (2015). Brain-to-text: decoding spoken phrases from phone representations in the brain. *Front. Neurosci.* 9:217. doi: 10.3389/fnins.2015.00217

Jiang, W., Pailla, T., Dichter, B., Chang, E. F., and Gilja, V. (2016). "Decoding speech using the timing of neural signal modulation," in *2016 38th Annual International Conference of the IEEE Engineering in Medicine and Biology Society (EMBC)* (Orlando, FL), 1532–1535.

Kanas, V. G., Mporas, I., Benz, H. L., Sgarbas, K. N., Bezerianos, A., and Crone, N. E. (2014). "Real-time voice activity detection for ECoG-based speech brain machine interfaces," in *2014 19th International Conference on Digital Signal Processing* (Hong Kong), 862–865.

Keshet, J., Grangier, D., and Bengio, S. (2009). Discriminative keyword spotting. *Speech Commun.* 51, 317–329. doi: 10.1016/j.specom.2008.10.002

Leuthardt, E., Pei, X. M., Breshears, J., Gaona, C., Sharma, M., Freudenburg, Z., et al. (2012). Temporal evolution of gamma activity in human cortex during an overt and covert word repetition task. *Front. Hum. Neurosci.* 6:99. doi: 10.3389/fnhum.2012.00099

Lotte, F., Brumberg, J. S., Brunner, P., Gunduz, A., Ritaccio, A. L., Guan, C., et al. (2015). Electrocorticographic representations of segmental features in continuous speech. *Front. Hum. Neurosci.* 9:97. doi: 10.3389/fnhum.2015.00097

Manos, A. S., and Zue, V. W. (1997). "A segment-based wordspotter using phonetic filler models," in *1997 IEEE International Conference on Acoustics, Speech, and Signal Processing* (Munich), 899–902.

Mellinger, J., and Schalk, G. (2007). "BCI2000: a general-purpose software platform for BCI research," in *Towards Brain-Computer Interfacing,* eds G. Dornhege, J. R. Millán, T. Hinterberger, D. J. McFarland, and K.-R. Müller (Cambridge, MA: MIT Press), 359–368. Available online at: https://ieeexplore.ieee.org/document/6281212

Mesgarani, N., Cheung, C., Johnson, K., and Chang, E. F. (2014). Phonetic feature encoding in human superior temporal gyrus. *Science* 343, 1006–1010. doi: 10.1126/science.1245994

Motlicek, P., Valente, F., and Szoke, I. (2012). "Improving acoustic based keyword spotting using LVCSR lattices," in *2012 IEEE International Conference on Acoustics, Speech and Signal Processing (ICASSP)* (Kyoto), 4413–4416.

Mugler, E. M., Goldrick, M., Rosenow, J. M., Tate, M. C., and Slutzky, M. W. (2015). "Decoding of articulatory gestures during word production using speech motor and premotor cortical activity," in *2015 37th Annual International Conference of the IEEE Engineering in Medicine and Biology Society (EMBC)* (Milan), 5339–5342.

Mugler, E. M., Patton, J. L., Flint, R. D., Wright, Z. A., Schuele, S. U., Rosenow, J., et al. (2014). Direct classification of all American English phonemes using signals from functional speech motor cortex. *J. Neural Eng.* 11:035015. doi: 10.1088/1741-2560/11/3/035015

Papademetris, X., Jackowski, M. P., Rajeevan, N., DiStasio, M., Okuda, H., Constable, R. T., et al. (2006). BioImage suite: an integrated medical image analysis suite: an update. *Insight J.* 2006:209. Available online at: https://scholar.google.com/scholar?cluster=2157595775705786589&hl=en&as_sdt=0,21

Pei, X., Barbour, D. L., Leuthardt, E. C., and Schalk, G. (2011a). Decoding vowels and consonants in spoken and imagined words using electrocorticographic signals in humans. *J. Neural Eng.* 8:046028. doi: 10.1088/1741-2560/8/4/046028

Pei, X., Leuthardt, E. C., Gaona, C. M., Brunner, P., Wolpaw, J. R., and Schalk, G. (2011b). Spatiotemporal dynamics of electrocorticographic high gamma activity during overt and covert word repetition. *Neuroimage* 54, 2960–2972. doi: 10.1016/j.neuroimage.2010.10.029

Rahim, M. G., Lee, C.-H., and Juang, B.-H. (1997). Discriminative utterance verification for connected digits recognition. *IEEE Trans. Speech Audio Process.* 5, 266–277.

Ramsey, N. F., Salari, E., Aarnoutse, E. J., Vansteensel, M. J., Bleichner, M. G., and Freudenburg, Z. V. (2017). Decoding spoken phonemes from sensorimotor cortex with high-density ECoG grids. *Neuroimage* 180(Pt A), 301–311. doi: 10.1016/j.neuroimage.2017.10.011

Ray, S., Crone, N. E., Niebur, E., Franaszczuk, P. J., and Hsiao, S. S. (2008). Neural correlates of high-gamma oscillations (60–200 Hz) in macaque local field potentials and their potential implications in electrocorticography. *J. Neurosci.* 28, 11526–11536. doi: 10.1523/JNEUROSCI.2848-08.2008

Rohlicek, J. R., Jeanrenaud, P., Ng, K., Gish, H., Musicus, B., and Siu, M. (1993). "Phonetic training and language modeling for word spotting," in *1993 IEEE International Conference on Acoustics, Speech, and Signal Processing Vol. 2* (Minneapolis, MN), 459–462.

Rohlicek, J. R., Russell, W., Roukos, S., and Gish, H. (1989). "Continuous hidden Markov modeling for speaker-independent word spotting," in *International Conference on Acoustics, Speech, and Signal Processing, Vol. 1* (Glasgow), 627–630.

Slutzky, M. W., Jordan, L. R., Krieg, T., Chen, M., Mogul, D. J., and Miller, L. E. (2010). Optimal spacing of surface electrode arrays for brain-machine interface applications. *J. Neural Eng.* 7:026004. doi: 10.1088/1741-2560/7/2/026004

Conflict of Interest Statement: The authors declare that the research was conducted in the absence of any commercial or financial relationships that could be construed as a potential conflict of interest.

frontiers in Neuroscience

ORIGINAL RESEARCH
published: 22 May 2019
doi: 10.3389/fnins.2019.00502

Cortical Topography of Error-Related High-Frequency Potentials During Erroneous Control in a Continuous Control Brain–Computer Interface

Nile R. Wilson[1], Devapratim Sarma[1], Jeremiah D. Wander[1], Kurt E. Weaver[2], Jeffrey G. Ojemann[3] and Rajesh P. N. Rao[4]*

[1] Department of Bioengineering, University of Washington, Seattle, WA, United States, [2] Department of Radiology, University of Washington, Seattle, WA, United States, [3] Department of Neurological Surgery, University of Washington, Seattle, WA, United States, [4] Paul G. Allen School of Computer Science & Engineering, University of Washington, Seattle, WA, United States

Brain–computer interfaces (BCIs) benefit greatly from performance feedback, but current systems lack automatic, task-independent feedback. Cortical responses elicited from user error have the potential to serve as state-based feedback to BCI decoders. To gain a better understanding of local error potentials, we investigate responsive cortical power underlying error-related potentials (ErrPs) from the human cortex during a one-dimensional center-out BCI task, tracking the topography of high-gamma (70–100 Hz) band power (HBP) specific to BCI error. We measured electrocorticography (ECoG) in three human subjects during dynamic, continuous control over BCI cursor velocity. Subjects used motor imagery and rest to move the cursor toward and subsequently dwell within a target region. We then identified and labeled epochs where the BCI decoder incorrectly moved the cursor in the direction opposite of the subject's expectations (i.e., BCI error). We found increased HBP in various cortical areas 100–500 ms following BCI error with respect to epochs of correct, intended control. Significant responses were noted in primary somatosensory, motor, premotor, and parietal areas and generally regardless of whether the subject was using motor imagery or rest to move the cursor toward the target. Parts of somatosensory, temporal, and parietal areas exclusively had increased HBP when subjects were using motor imagery. In contrast, only part of the parietal cortex near the angular gyrus exclusively had an increase in HBP during rest. This investigation is, to our knowledge, the first to explore cortical fields changes in the context of continuous control in ECoG BCI. We present topographical changes in HBP characteristic specific to the generation of error. By focusing on continuous control, instead of on discrete control for simple selection, we investigate a more naturalistic setting and provide high ecological validity for characterizing error potentials. Such potentials could be considered as design elements for co-adaptive BCIs in the future as task-independent feedback to the decoder, allowing for more robust and individualized BCIs.

Keywords: brain–computer interface, electrocorticography, error-related potential, error potential, execution error, low-level error

OPEN ACCESS

Edited by:
Christoph Guger, g.tec medical engineering GmbH, Austria

Reviewed by:
Yongtian He, University of Houston, United States
Chadwick Boulay, Ottawa Hospital, Canada

****Correspondence:***
Nile R. Wilson
nilew@uw.edu

Specialty section:
This article was submitted to Neuroprosthetics, a section of the journal Frontiers in Neuroscience

Received: *21 December 2018*
Accepted: *30 April 2019*
Published: *22 May 2019*

Citation:
Wilson NR, Sarma D, Wander JD, Weaver KE, Ojemann JG and Rao RPN (2019) Cortical Topography of Error-Related High-Frequency Potentials During Erroneous Control in a Continuous Control Brain–Computer Interface. Front. Neurosci. 13:502. doi: 10.3389/fnins.2019.00502

INTRODUCTION

Everyone makes mistakes and can learn from them. But the neurophysiological mechanisms behind how we recognize and use these mistakes to learn is still not completely understood. Prior studies have focused on the error-related potential (ErrP), an event-locked electrophysiological response generated during task rule violations. The vast majority of our understanding to date of the ErrP originates from electroencephalography (EEG) studies (Ferrez and Millan, 2008; Iturrate et al., 2013; Spüler and Niethammer, 2015; Zhang et al., 2015; Kreilinger et al., 2016). The typical coverage and high temporal resolution of EEG, relative to fMRI, allow for the identification of wide-spread voltage changes in response to error. However, because EEG is non-invasive, electrical signals from the cortex attenuate and diffuse as they travel up through the skull, leading to lower signal-to-noise ratio (SNR) and challenges in source localization (Jatoi et al., 2014; Olson et al., 2016). To circumvent some of these limitations, we investigate error-related potentials in a one-dimensional brain–computer interface (BCI) task using subdural electrocorticography (ECoG) in human subjects.

Brain–computer interfaces represent a particularly useful opportunity to characterize error-related brain responses. BCIs rely on closed-loop (typically) visual feedback to inform the user of their control and on-going performance. This feedback is hypothesized to be key to the BCI learning process and performance improvement (Green and Kalaska, 2011), analogous to the utility of somatosensory feedback during the acquisition of new motor skills (Newell, 1991). BCI decoders have traditionally been static, in the sense that initial parameters in the algorithm would be set and only changed by manual updates performed by the BCI technician. Recently, however, there has been a push to develop dynamic feedback systems that automatically update over time based on pre-task parameters (DiGiovanna et al., 2009; Orsborn et al., 2014; Pohlmeyer et al., 2014; Merel et al., 2015). However, most efforts so far rely on knowledge of the task and of actuator kinematics, thus limiting BCI co-adaptation to the research setting and do not allow for automatic updating based on signals generated by the user. A co-adaptive BCI may improve the user experience by promoting faster mastery of the BCI and by allowing longer term use through accounting for changes in the brain due to plasticity.

Our motivation in this report was to gain a better understanding of the electrophysiological signatures of error potentials in BCI and whether this will serve to better inform unsupervised co-adaptive BCIs. Specifically, relying on ErrPs as a feedback source to inform adaptive BCI decoders, rather than on specific task data, will allow for BCI use in less constrained environments.

Previous work suggests there are different types of error-related potentials which manifest in different contexts (Milekovic et al., 2012; Spüler and Niethammer, 2015). Such potentials are generally categorized into two classes, high-level error and low-level error (Krigolson and Holroyd, 2007). Krigolson and Holroyd distinguish the two on temporal disparities. Specifically, low-level errors are those immediately correctable in control, and high-level errors as not immediately correctable, which prevent the achievement of a desired goal (Krigolson and Holroyd, 2007). For example, a reactionary turn of the steering wheel to adjust for an unseen bump in the road would be considered low-level error, and failing to reach your destination would be considered high-level error. High-level error, also called outcome error, is thought to be represented by the error-related negativity (ERN), which is often localized to the medial-frontal cortex (Krigolson and Holroyd, 2007; Wessel, 2012) and is believed to be essential to reinforcement learning (Nieuwenhuis et al., 2004). The reinforcement learning theory of the ERN suggests the error signals are generated in the basal ganglia and propagate to the cortex through the anterior cingulate cortex (ACC). Localization of the cortical error-related potentials to the ACC has been suggested in EEG (Krigolson and Holroyd, 2007; O'Connell et al., 2007) and confirmed through ECoG (Bechtereva et al., 2005).

Low-level error, known as target error (Krigolson and Holroyd, 2007; Krigolson et al., 2008) or execution error (Milekovic et al., 2012, 2013), is believed to be represented by positive deflections originating from the posterior parietal cortex (PPC) following commitment of a behaviorally-defined error (Krigolson and Holroyd, 2007; Ladouceur et al., 2007; Krigolson et al., 2008). Although the exact role of this positive activity over PPC is not completely agreed upon, the extent literature converges on a general hypothesis that the PPC is involved with action conflict monitoring, including movement correction (Falkenstein et al., 2000; Nieuwenhuis et al., 2001; Van Veen and Carter, 2002; Krigolson and Holroyd, 2007).

Various EEG studies have identified and investigated ErrPs in the form of ERN (Nieuwenhuis et al., 2001; Ullsperger and von Cramon, 2006; Ladouceur et al., 2007; Krigolson et al., 2008; Iannaccone et al., 2015), P_E (Nieuwenhuis et al., 2001; Ladouceur et al., 2007; Navarro-Cebrian et al., 2016), P300 (Krigolson et al., 2008; MacLean et al., 2015), and other signals (Krigolson and Holroyd, 2007; Ferrez and Millan, 2008; Chavarriaga and Millan, 2010; Kim and Kirchner, 2013; Spüler and Niethammer, 2015).

Here we aimed to expand upon our understanding of ErrPs by bridging EEG efforts and characterizing time-frequency responses through ECoG, cross-referencing evoked power effects to the common cortical-localized sites of evoked response ErrPs. We focus on low-level error and its presentation in the parietal cortex, as clinical requirements of electrode placement often constrain consistent frontal coverage. In addition, low-level error is ultimately more relevant in influencing real-time BCI control on a finer time scale than high-level error, which can only be used to provide feedback on longer time-scales (e.g., once per trial).

A previous ECoG study by Milekovic and colleagues demonstrated the presence of ErrPs across multiple cortical regions in a continuous, overt-movement task in human ECoG (Milekovic et al., 2012, 2013). The researchers observed low-level and high-level ErrPs, described as execution and outcome errors, respectively, in the motor, somatosensory, parietal, temporal, and pre-frontal areas. Here, we utilize ECoG to investigate whether errors induced during a motor-imagery BCI task would also result in the typical ErrP profile. We focused exclusively on high-gamma (70–100 Hz) activity. High frequency broadband power

(HBP) is thought to best reflect local activity (Ray et al., 2008; Manning et al., 2009; Miller et al., 2009) and is reliably recorded through ECoG. We are particularly interested in examining local response activity for error-processing across the surface of the human brain. Rather than examining errors resultant from (1) failed trial outcomes, (2) induced error, or (3) unexpected stimuli beyond the user's control, we took a novel approach by examining naturally occurring errors in the BCI decoder's performance in a continuous control one-dimensional center-out task.

We hypothesize significant HBP changes in error-related detection cortex. This is built on literature and computational models describing ErrPs as a mismatch between sensory expectation from an efference copy and from actual sensory input (in this case, visual) (Holroyd and Coles, 2002; Nieuwenhuis et al., 2004). This mismatch can be thought of as the sensory discrepancy described in Miall and Wolpert's forward model, which is the difference between actual sensory feedback and expected sensory feedback from an efference copy (Miall and Wolpert, 1996). By gaining a better understanding of the contribution of HBP to ErrPs, we eventually hope to enable unsupervised reinforcement learning in the BCI decoder allowing for robust co-adaptation and improvement of BCI usability.

MATERIALS AND METHODS

Participants

Three patients with medically intractable epilepsy (mean age: 19.67 years, one male), undergoing clinical seizure monitoring at either Harborview Medical Center or Seattle Children's Hospital, consented and volunteered to participate in research in accordance with the University of Washington Institutional Review Board (see **Table 1** for demographics).

Data Recording and Electrode Localization

The electrocorticogram was acquired from subdural macro-scale grid electrodes (Ad-Tech 8 × 8 platinum, 10 mm contact spacing). Cortical potentials were recorded at 1200 Hz using g.USBamps (GugerTec, Graz, Austria) through the BCI2000 software suite (Schalk et al., 2004). Pre-operative T1 MRI scans were co-registered with post-operative CT scans (SPM8) to allow for individualized electrode localization through BioImageSuite software imaging package (Papademetris et al., 2006) in accordance with previously published reports (Casimo et al., 2016). Each subjects' electrodes were then normalized to the 1 mm MNI 251 brain coordinate system (Evans et al., 1993) using Freesurfer's ReconAll for multi-subject analysis (Fischl, 2012) and a secondary transform through FSL FLIRT (part of the FMRIB Software Library – FSL[1]) algorithms. Center value MNI coordinates for each electrode were transformed to Talairach space using the MNI anatomical labeling atlas, and Brodmann area (BA) labels were estimated using the Talairach Daemon Client (Talairach and Tournoux, 1988).

[1]www.fmrib.ox.ac.uk/fsl

TABLE 1 | Subject information and task performance separated by trial type.

ID	Sex	Age	Hemisphere	Control channel	# of trials	Successful up trials per run	Successful down trials per run	Overall trial success	# of up error epochs	# of up correct epochs	# of down error epochs	# of down correct epochs
S1	F	11	Left	Hand	49	20.8%	40.0%	30.6%	6	40	39	13
S2	M	13	Left	Tongue	141	28.6%	39.4%	34.0%	31	59	43	32
S3	F	35	Left	Hand	62	20.0%	34.4%	27.4%	21	27	17	22

BCI Task

Subjects were instructed to control the vertical velocity of a cursor in a one-dimensional center-out BCI task, to reach and dwell within a trial target for 1 s using motor imagery (**Figure 1A**). Although trial success was determined by whether the cursor dwelled within the target for 1 s, our investigation focuses on correct and erroneous movements made toward or away from the target (specific details provided below). The control electrode was selected through a prior motor screening task, which was used to identify the channel exhibiting the strongest HBP response to a cued imagined movement task of the contralateral hand or tongue (depending on electrode coverage) as previously described (Wander, 2015; **Table 1**). Consequently the control electrode was always localized to the primary motor cortex.

Each BCI run consisted of four blocks of eight randomly ordered trials. Targets were placed either above or below the starting center point, either large or small (35 or 20% of screen height, respectively) and placed either near or far from the starting center point (20 or 16% of screen height, respectively). This resulted in eight unique trial configurations per block. Each trial was structured to include a 1 s rest period where neither the cursor nor target were displayed [inter-trial interval (ITI)], followed by a 2 s cue period where the target was visible, followed by a feedback period of up to 6 s where subjects would attempt to reach and dwell within the trial target for 1 s. Each trial would terminate either when dwell time was reached or the trial timed out, whichever came first.

For the purposes of these analyses, we grouped trial configurations to only distinguish between trials where the target was placed above or below the starting point, reflecting differences in behavioral task demands.

To drive the cursor up, subjects were required to increase HBP in their control electrode using motor imagery. HBP was estimated using BCI2000's auto-regressive filter on the preceding 500 ms of data. HBP was normalized to 6 s of pre-trial data using the BCI2000 built-in normalizer, and were linearly mapped to cursor velocity as described in Wolpaw and McFarland (2004). To drive the cursor down, they were instructed to rest. The cursor velocity would update every 40 ms.

Offline Analysis for Error-Related Potentials

All signal processing and statistical analyses were conducted in MATLAB (MathWorks, Natick, MA, United States) computing environment. For each subject, we performed common average referencing to account for common noise across all channels in the grid. We then removed 60 Hz noise and isolated the high-gamma frequency band activity (HG, 70–100 Hz) using 4th order Butterworth filters (non-causal), and estimated the amplitude envelope of the signals using a Hilbert transform. Power was calculated by taking the absolute square of the analytical amplitude across the full time series. Then the power for each trial was normalized with respect to the preceding ITI (baseline) by calculating the z-score specifically for HBP. The full normalized power time series was smoothed using a sliding Gaussian window with a window width of 40 samples to match the update rate of the task ran in BCI2000.

Error and Correct Window Extraction

We were specifically interested in the topography of the responsive HBP during periods of BCI error. To accomplish this, we first grouped subject's electrodes by identified Brodmann

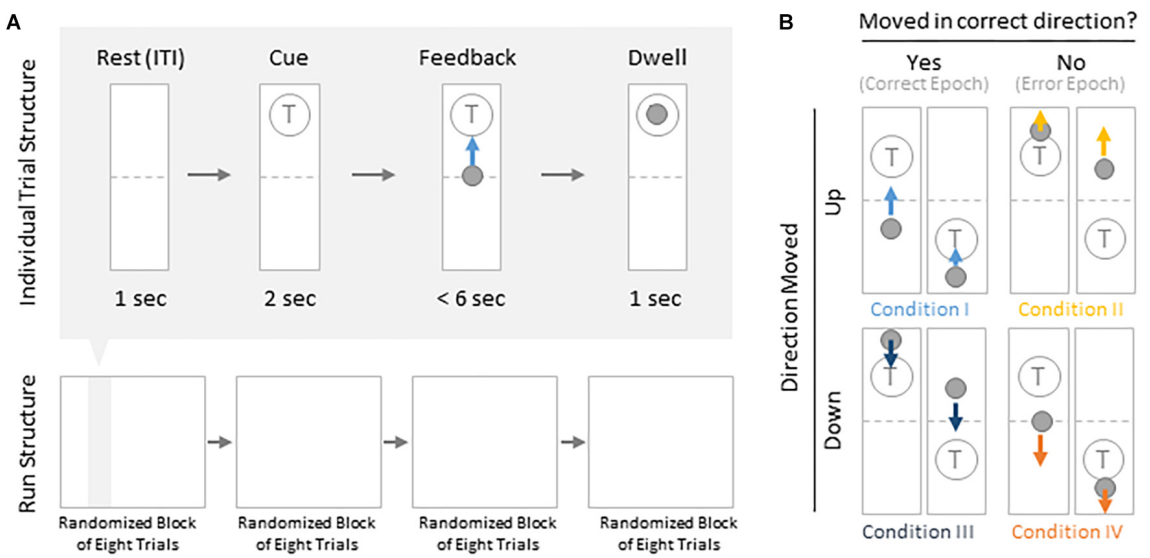

FIGURE 1 | Task structure and epoch conditions. **(A)** Subjects modulated cursor velocity in a one-dimensional center-out BCI task using imagined hand or tongue movement (**Table 1**) in order to reach and dwell within a target. Cursor was re-centered prior to each trial and was not displayed during the inter-trial interval (ITI) and cue period. Trials were randomized to have the target located above or below the start position, near or far, and small or large. Trials were organized into four blocks, each containing eight randomized trials. **(B)** Within trials, data were binned into epochs based on four movement conditions: cursor moved up correctly (I, light blue), moved up erroneously (II, yellow), moved down correctly (III, navy blue), or moved down erroneously (IV, orange).

Areas. Second, we defined decoder error as a mismatch between the decoder assessment of HBP and the subject's goal-directed intention. This was defined operationally as when the slope of the cursor movement (at any junction across the 6000 ms duration of a trial) was in the direction opposite of the target position for a continuous period of 400 ms. This definition allowed for the identification of improper decoding under the assumption that subjects intend to move the cursor toward a target during trial feedback (for clarification, see **Figure 1B**). We reasoned 400 ms duration is sufficient time for the subjects to realize error during real-time continuous feedback (Gerson et al., 2005). We then identified the beginning of this period as $t = 0$ in error identification. Likewise, correct performance windows were extracted where the cursor movement was in the direction toward the target for a 400 ms period, with $t = 0$ at the start of this period. We then extracted error and correct epochs from these error and correct windows, respectively.

To prevent overlap between epochs, we extracted only one epoch per window, where we defined windows of 1000 ms starting from 200 ms prior to our $t = 0$ time points to 800 ms after, based on previously published reports investigating error-related potentials in an overt-movement ECoG task (Milekovic et al., 2012). **Figure 2** shows data of one full length trial from an example electrode with example windows and example epochs. Note that there are often multiple error and/or correct epochs within any given trial, based on our pre-defined states described below.

From these defined windows, we classify epochs into the four conditions presented in **Figure 1B**. Specifically, error epochs were classified as when the cursor moves incorrectly upwards when located above a target (Condition II) and when the cursor moves incorrectly downwards when located below a target (Condition IV). Finally, correct epochs were defined as when the cursor moves correctly upwards when located below a target (Condition I) and when the cursor moves correctly downwards when located above a target (Condition III).

Statistical Analysis Epochs From Windows

To contrast HBP behavior across the cortical sampling space during real-time continuous error detection, we generated statistical analysis epochs from error and correct windows. These epochs were defined as the samples from $t = 100$–500 ms in their respective 1000 ms windows (where $t = 0$ corresponds to the start of 400 ms consecutive movement in one direction, as described above). Previous ErrP work by Milekovic et al. (2012) observed that the window from 100 to 800 ms after error onset engendered ECoG, error-related components during an overt motor control task. We used the length and range of $t = 100$–500 ms after error onset to characterize responsive HBP behavior based on (1) a relatively short, continuous trial period (6000 ms) and (2) previous EEG observations of typical higher-order processing time of visual cues ranging from 150 to 500 ms, depending on the cortical area being examined (Gerson et al., 2005).

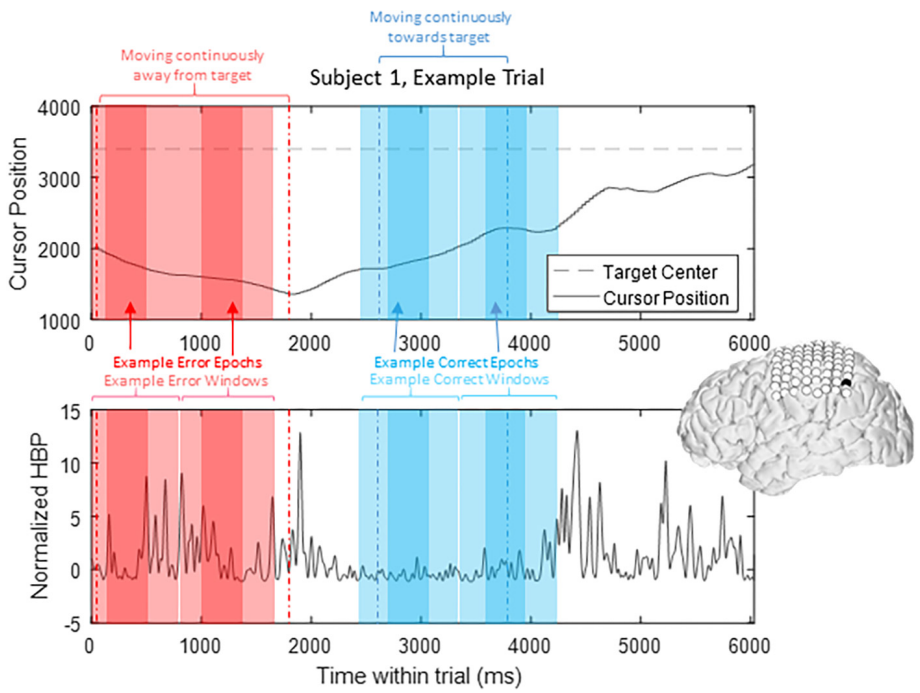

FIGURE 2 | HBP throughout one trial. In this parietal channel in one subject (shown in black), we see a decrease in HBP as the cursor moves correctly toward the target and increase when the cursor is no longer moving as intended. The highlighted light red sections shows example error windows, where their $t = 0$ time points are defined by 400 ms of continuous movement away from the target. The darker red areas represent example error epochs. Likewise, the highlighted light blue sections show example correct windows, and the dark blue sections show example correct epochs, as detailed in Section "Offline Analysis for Error-Related Potentials."

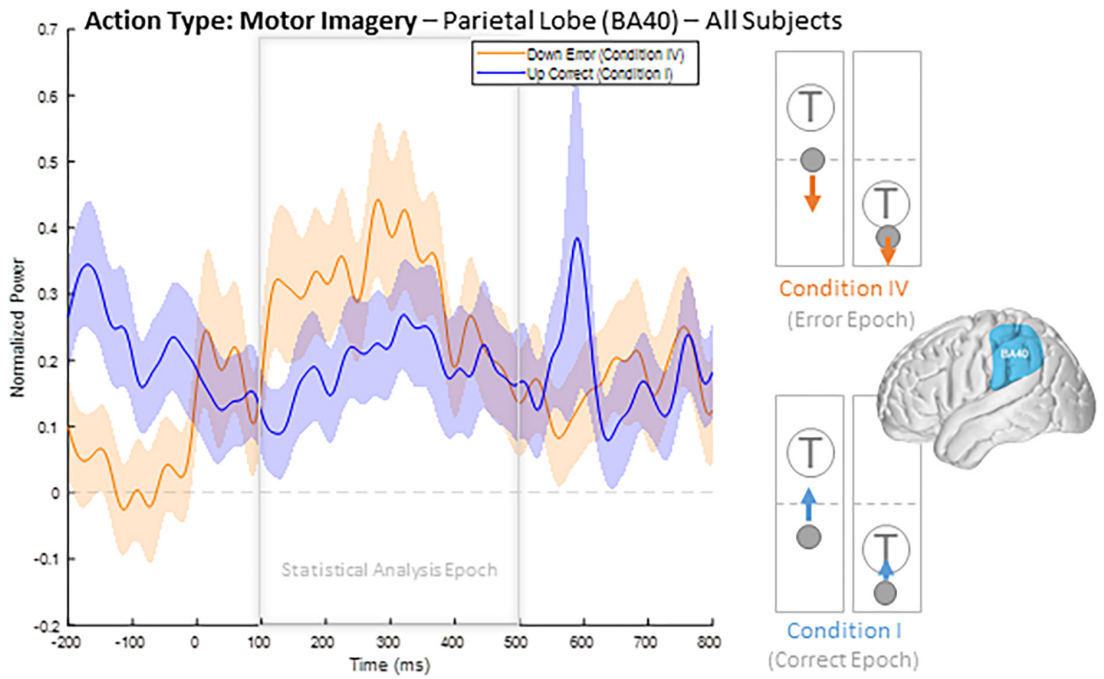

FIGURE 3 | Time series of mean HBP during motor imagery in the decoder error and correct conditions in the parietal lobe (BA 40, highlighted in the brain inset). In these conditions, the subjects were attempting to move the cursor toward the target through eliciting motor imagery. In the erroneous condition, the BCI mistakenly decoded the subject's intention as wanting to move downwards with rest. Error onset begins at time t = 0 ms for the Condition IV plot. Statistical analyses were performed using the time window of t = 100–500 ms (i.e., the statistical analysis window), as indicated by the window on the figure. Shaded region shows standard error of the mean. Dashed gray line represents baseline.

Statistical Analysis

At the group analysis level, we conducted a two-way ANOVA by extracting mean HBP from our defined statistical analysis epochs and estimating main effects of trial type (whether the target was located above or below the center starting position, requiring motor imagery or rest, respectively) and performance [whether the epoch was a correct epoch (Conditions I and III) or an error epoch (Conditions II and IV)] on HBP for each Brodmann Area available.

We utilized *post hoc* two-sample *t*-tests (FDR corrected) to identify significant interactions of correct and erroneous decoder behavior epochs by subject action type (active motor imagery or rest). We present our findings through exploring Error-related Potentials as changes in HBP across cortical areas. That is, our *post hoc* approach compares (1) HBP of all error epochs and (2) HBP of all correct epochs from all channels falling within each Brodmann Area of interest. Finally, at the individual level, we utilized these two-sample *t*-tests.

RESULTS

Task Performance

As common with motor imagery controlled BCIs, the users experienced difficulty in achieving high task performance without an extensive calibration period (Wolpaw and McFarland, 2004; Blankertz et al., 2007, 2008, 2010). The low overall trial success of the subjects (average trial success 30.67%, **Table 1**) may be due to the difficulty of the task requirement to dwell within the target, and the limited amount of time we had with each subject for training (**Table 1**). Overall, all three subjects had greater trial success when the target was below the cursor starting position (average trial success 37.93%, **Table 1**). The effects of task performance on error potentials is discussed in Section "Discussion."

Effect of Trial Type and Performance on Group HBP Responses

To determine the HBP response topography of error performance (whether the cursor moved accurately toward or away from the target) we conducted a two-way ANOVA on HBP across BA regions. Results from all available BA regions are presented in **Supplementary Table 2**. Here we focus on specific BA regions of interest related to ErrPs. **Supplementary Table 1** denotes the number of contributing electrodes from each subject within each BA investigated.

A significant main effect of trial type was observed in BA 4 [primary motor cortex – $F(1,999) = 4.49$, $p = 0.0343$], BA 6 [premotor cortex – $F(1,4258) = 14.01$, $p = 0.0002$], BA 40 ([inferior parietal lobule – $F(1,4918) = 7.21$, $p = 0.0073$], and BA 43 [$F(1,161) = 7.59$, $p = 0.0065$]. A significant main effect of performance was observed in BA 3 [primary somatosensory cortex, $F(1,912) = 5.92$, $p = 0.00152$], BA 40 [$F(1,4918) = 4.48$, $p = 0.0342$], and BA 4 [$F(1,999) = 4.49$, $p = 0.0343$].

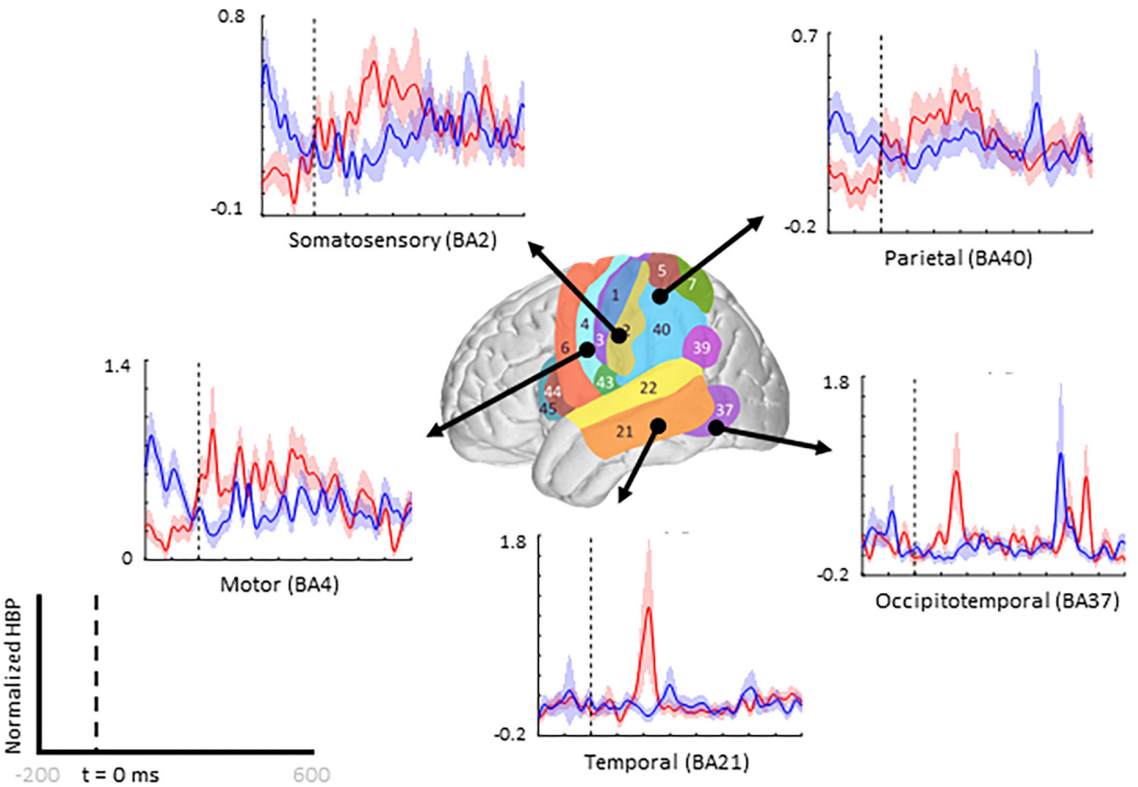

FIGURE 4 | Increased HBP in multiple cortical areas during motor imagery error. The brain in the center shows the spatial range for each Brodmann Area available in our subject population, with each area labeled by their corresponding number. Each plot shows the average response within the specified Brodmann Area during erroneous decoding (red) and during correct decoding (blue), 100 to 500 ms after error onset (indicated by the vertical dashed line).

Importantly, we noted a statistically significant interaction between the trial type, control requirement and performance in primary somatosensory cortex [BA 3; $F(1,912) = 3.97$, $p = 0.0466$], in primary motor cortex [BA 4; $F(1,999) = 8.46$, $p = 0.0037$] as well in the inferior parietal cortex [BA 40; $F(1,4918) = 6.09$, $p = 0.0136$]. For all ANOVA results, please refer to **Supplementary Table 2**.

Error-Related HBP Time Series by Brodmann Areas

To illustrate our overall HBP response profiles, we plotted the mean time-series for all four epoch conditions generated by averaging the responses of all constituent electrodes from all subjects for significant BA regions. **Figure 3** shows the mean time-series during the correct and error windows used to extract our Conditions I and IV epochs in all electrodes placed over the inferior parietal lobule (BA 40). We observed increased HBP after error onset at $t = 0$ ms (red) when the decoder failed to recognize the subject's motor imagery as intent to move the cursor upwards toward the target (Condition IV). Contrarily, we did not see a general increase in HBP when the decoder was correctly decoding the subject's motor imagery (Condition I). During rest, we did not see a change in HBP relative to error onset (**Supplementary Figure 1**). We generated similar plots for all available BAs during both motor imagery and during rest. Note, that $t = 0$ ms is a window-unique classification based on our behavioral mismatch between cursor trajectory and decoder output. Our $t = 0$ is not a phase-resetting, evoked boundary event in the classic sense of evoked potentials. Importantly, because there were typically multiple error and correct epochs within any given trial, $t < 0$ reflects behaviorally heterogeneous conditions.

Collectively, this approach provides a useful description of the overall responsive cortical regions generating ErrPs. We next used *post hoc* tests to determine the specific nature of HBP activity as a function of error and correct condition type. We contrasted two different populations for a given action type, motor imagery or rest for significantly responsive regions: (1) the mean value for each error epoch 100–500 ms following error onset from all electrodes within the specified BA, and (2) the mean value for each epoch during correct decoder performance 100–500 ms following the start of recognized correct performance, from all electrodes within the specified BA. We applied a one-sided *t*-test to test the specific hypothesis that HBP is greater in error than in correct epochs.

When comparing average responses following error onset (100–500 ms) during motor imagery (Condition IV–Condition I), we found motor, somatosensory, temporal, and parietal areas as having greater HBP in error epochs than in correct epochs (**Figure 4**). Specifically, HBP in Condition IV (motor imagery

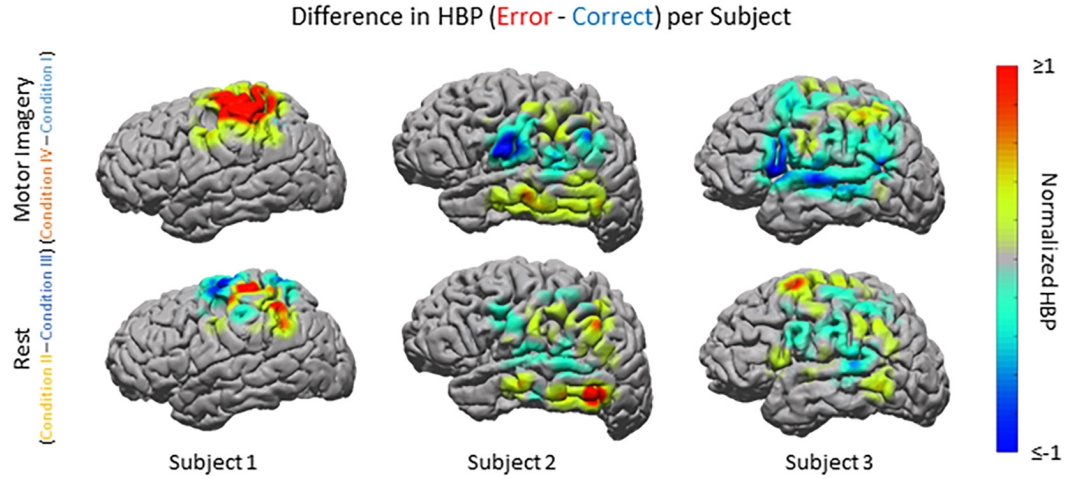

FIGURE 5 | HBP during correct and erroneous BCI decoder performance per individual subject. Difference in high-gamma power during correct and error epochs 100–500 ms after error onset for each subject. Top row shows power of Condition IV–Condition I, bottom row shows power of Condition II–Condition III. Heat maps were scaled to visualize the most robust effects.

error) were significantly greater than in Condition I (motor imagery correct) in BAs 4 and 40 (one-sided Student's *t*-test, FDR-adjusted $p < 0.05$). During rest error (Condition II–Condition III), BA 4 was statistically significant (**Supplementary Figure 2**).

Low Frequency Error-Related Potentials by Brodmann Areas

In addition to investigating increases in HBP in error epochs as compared to correct epochs, we also observed increases in spectral power in lower frequency bands in these same conditions. Although lower frequency activity is not as localized as high-gamma activity, some lower frequency bands have played an important role in ErrP investigations in EEG work (Trujillo and Allen, 2007; Atchley et al., 2017; Glazer et al., 2018).

Like with HBP, we compared the band power between 100 and 500 ms after error onset and correct performance using one-sided Student's *t*-tests (alpha = 0.05) and correcting for multiple comparisons using FDR-adjusted *p*-values. For the delta band (<4 Hz), we observed significantly greater power in error epochs compared to in correct epochs, regardless of movement direction, posterior to the temporoparietal junction (BA 39). For the theta band (4–8 Hz), we observed significantly greater power in error epochs compared to in correct epochs, regardless of movement direction, in Brodmann Area 9 (frontal) and in the temporal lobe (BAs 21, 22, and 37). For the alpha band (8–13 Hz), we observed significantly greater power in error epochs compared to in correct epochs, regardless of movement direction, posterior to the temporoparietal junction (BA 39) and in the temporal lobe (BAs 21 and 22). Lastly, for the beta band (13–30 Hz), we observed significantly greater power in error epochs compared to in correct epochs, regardless of movement direction, only in the temporal lobe (BA 21). For a full table of *t*-test results for all available Brodmann Areas and bands, see **Supplementary Table 3**.

Error-Related Potentials in Individual Subjects

Beyond region of interest event-related error analysis, we also explored individual electrode response topography for each subject. Contributions from each electrode are presented in **Figure 5** as the difference in mean HBP 100–500 ms following error onset in erroneous and correct decoding, during motor imagery. To visualize this topography, we used a Gaussian spatial smoothing kernel across electrodes allowing for the visualization of cortical-response 'heat maps' at the individual level. Warm colors indicate a positive difference where HBP during error is greater than HBP during correct decoding.

As seen in **Figures 5**, **6A**, electrode coverage per subject varies thus yielding variable number of electrodes per Brodmann Area (**Supplementary Table 1**). Similar to the group-wide analysis, we also determined significance of BAs within individual subjects by comparing the respective error and correct epochs applying one-sided Student's *t*-tests (alpha = 0.05) and correcting for multiple comparisons using FDR-adjusted *p*-values.

For Subject 1 (11 years old), the majority of electrodes present within the following areas had statistically significantly greater HBP during error than during correct in the motor imagery case (Condition IV–Condition I): BAs 1, 3, 5–7, and 40 (one-sided Student's *t*-test, FDR-adjusted $p < 0.05$). Brodmann Areas 2 and 4 had a few significant electrodes. There was at least one significant electrode for all observable areas in this subject during motor imagery. During rest (Condition II–Condition III), the number of significant electrodes per respective area was lower than during motor imagery, except for in BA 4. Like during motor imagery, there was always at least one electrode per area that was significant.

For Subject 2 (13 years old), 50% or more of electrodes present within the following areas had statistically significantly greater HBP during error than during correct in the motor imagery case: BAs 2–4, 9, 21, 37, 40, and 42 (one-sided Student's *t*-test,

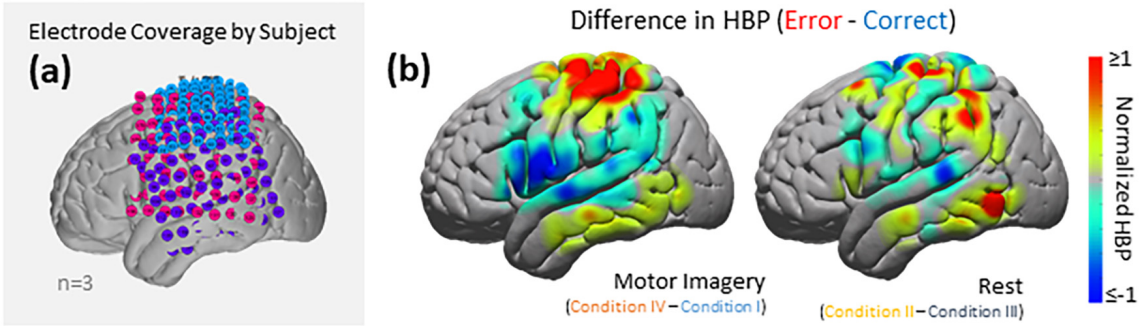

FIGURE 6 | HBP during correct and erroneous BCI decoder performance. **(a)** Electrode coverage by subjects in the left (n = 3), separated by color (Subject 1 in blue, Subject 2 in purple, Subject 3 in pink). **(b)** Difference in high-gamma power during correct and error epochs 100–500 ms after error onset. Left shows power of Condition IV–Condition I, right shows power of Condition II–Condition III. Heat maps were scaled to visualize the most robust effects.

FDR-adjusted $p < 0.05$). Brodmann Area 6 had one significant electrode, BA 22 had three significant electrodes, and BAs 39 and 43 did not have any. During rest, the number of significant electrodes per respective area was typically lower than during motor imagery. Some areas, which had most of their electrodes significant during motor imagery, do not have any significant differences during rest (BAs 3–4, 9, 42).

For Subject 3 (35 years old), 50% or more of electrodes present within the following areas had statistically significantly greater HBP during error than during correct in the motor imagery case: BAs 4 and 5 (one-sided Student's t-test, FDR-adjusted $p < 0.05$). Brodmann Areas 1, 6, 21, and 40 had at least one significant electrode each, and areas 2, 3, 7, 9, 22, 39, 42, 44, and 45 had no significant differences. During rest, the number of significant electrodes per respective area was typically higher than during motor imagery. With the exception of BA 7, all the areas which had no significant electrodes during motor imagery had at least one significant electrode during rest.

Group Analysis: Cortical Topography of Error-Related HBP Responses

Using the data from each electrode of all subjects (**Figure 5**), we generated cortical heat maps to observe the overall activity of the group. **Figure 6** serves to show the contributions by electrodes instead of presenting the mean response of any given Brodmann Area. As seen when we project each subject's electrodes onto the MNI brain, each subject has different coverage and therefore contributes a different number of electrodes to each area of interest.

The areas with the most common coverage were BA 40 (part of the parietal cortex) and BA 6 (posterior-most part of the frontal cortex), with 42 and 38 total electrodes per area, respectively. Areas 2–4 also had common coverage but had 10 electrodes or less per area.

We zoom-in to a portion of the parietal lobe in **Figure 7** to show examples of individual electrode contributions from all subjects in BA 40, one of the few areas with multiple electrodes from each subject.

DISCUSSION

We present the brain topography of HBP changes associated with error processing in the context of visual feedback, closed-loop, motor-imagery BCI. Our novel approach to extracting epochs of behaviorally defined error within a free-running BCI context is likely to be more reflective of naturalistic error processing, provides high ecological validity and is specifically relevant to contemporary co-adaptive BCI design. That is, our *post hoc* identification of error epochs, based on violations of intention, circumvent limitations of artificially-induced error events which do not take subject intention into account. To this end, our results are in agreement with a previous study investigating error-related potentials in ECoG in an overt movement task (Milekovic et al., 2012).

Our BCI task involved using both active motor imagery and rest to control the vertical velocity of a cursor to reach and dwell within a target. We investigated the involvement of different Brodmann Areas and individual electrodes across subjects for these two different control paradigms when the decoder incorrectly decodes the subject's intention and moves the cursor away from the target.

Interpreting Effects of Trial Type and Performance on HBP

The interaction of trial control requirement (whether the subject needed to bring the cursor up to a target placed above the center starting position using motor imagery) and performance (whether the cursor moved correctly toward or erroneously away from the target) had a statistically significant interaction on HBP in Brodmann Areas 3, 4, 40, and 43. In other words, the difference in HBP between correct performance and erroneous performance were affected by whether motor imagery or rest was required as the initial action to reach the target in the trial. The specificity of this significant interaction was clarified by *post hoc* t-test results for the motor imagery conditions and the rest conditions.

Importantly, we noted a statistically significant effect of trial control requirement on HBP in the primary motor cortex (BA 4)

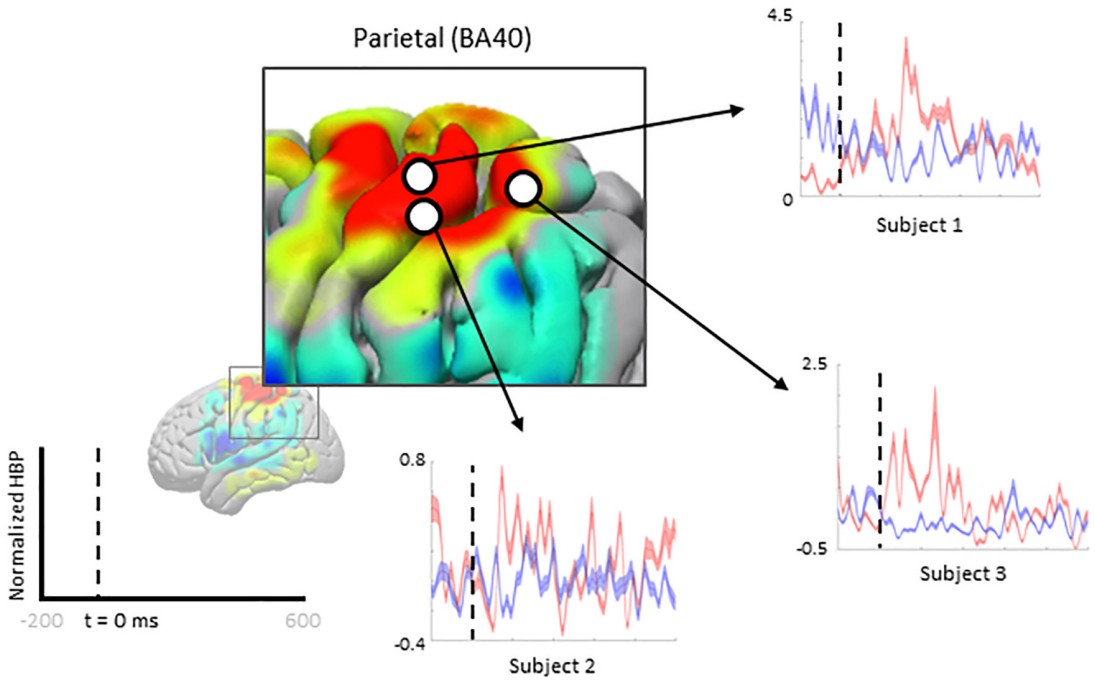

FIGURE 7 | Increased HBP in multiple cortical areas during motor imagery error (parietal). Each plot shows the average response of a single electrode (from one subject, each) within Brodmann Area 40 during erroneous decoding (red) and during correct decoding (blue).

and premotor cortex (BA 6), providing internal validity for our statistical approach. Specifically, the control electrode, located in primary motor cortex, moved the cursor up or down through increasing or decreasing HBP.

Broader Response Observed for Motor Imagery Error Than for Rest Error

Overall, more areas of the cortex exhibited significantly greater HBP during error in motor imagery cursor control rather than in rest cursor control. BA regions which showed more significant HBP changes in both the motor imagery and rest cases, when including all subjects, were the somatosensory (BAs 1 and 5), motor (BA 4), and parietal (BA 7) cortices. Areas which were exclusively significant during motor imagery include part of somatosensory (BAs 2 and 3), temporal (BAs 21 and 37), and parietal (BA 40) cortices. The only area which was significant during rest but not motor imagery was near the angular gyrus in the parietal lobe (BA 39). Note that we did not have much frontal coverage from any of the subjects, preventing investigation of common areas of interest associated with outcome (not execution) error, such as the ACC (**Figure 6A**). In Milekovic and colleagues overt movement ECoG study, ErrPs in the motor, somatosensory, parietal, temporal, and pre-frontal areas were observed when an execution error was induced in the subject's joystick control (Milekovic et al., 2012, 2013).

ErrPs in the motor and somatosensory areas are not unexpected considering they are directly involved in the control and immediate feedback associated with the control. Involvement of other areas may not be as obvious. Previous work has suggested that the parietal lobe is involved with low-level error processing, which cursor control error can be considered (Krigolson and Holroyd, 2007). Although not traditionally explored for error analyses, as there is typically a focus on the ACC and other frontal areas, previous fMRI work suggests the temporal lobe is also involved in error processing (Stevens et al., 2009).

Corrective Movement

The extent literature also suggests the parietal lobe may be involved in the execution of corrective movements in response to error or low-level error (Calhoun et al., 2006; Krigolson et al., 2008; Navarro-Cebrian et al., 2016). It is of note that the temporoparietal junction (TPJ; BA 40) only had significant HBP during motor imagery error, but the more posterior and superior area of the parietal lobe (BA 7) had significant HBP during both motor imagery and rest error conditions. Krigolson et al. (2008) suggest that low-level errors are mediated in the PPC, which may be reflected by the increased HBP in BA 7 for both error conditions. Interestingly, the same group showed that a P300 response from the TPJ would immediately precede corrective movements in response to error in an earlier study (Krigolson and Holroyd, 2007). Instead of being directly responsible for the corrective movement, Krigolson et al. (2008) postulate that the P300 indicates the updating of an internal model of the task at hand. Navarro-Cebrian et al. (2016) instead suggest the P_E from the parietal lobe indicates that enough error information has been gathered to make a decision to change motor output in order to correct for the error. In our current work, the TPJ had significant increases in HBP during motor imagery error, but

not during rest error. This may imply that the parietal lobe elicits a greater response when the corrective action to take requires an increase or change in motor output, in this case, increased motor imagery. Rest error may not have resulted in increased local activity in the TPJ because the corrective action to take would be to suppress motor imagery.

Low Performance and Error Elicitation

Error-related potentials are typically investigated in settings where instances of correct performance greatly outnumber the instances of error. However, recent work by Pezzetta et al. (2018) reverses the correct/error ratio by inducing error events for 70% of the task. In their study, Pezzetta et al. (2018) find that error-related potentials are still elicited even when error occurs during the majority of the task, confirming that the performance-monitoring system engages in the presence of error and not just in the presence of uncommon stimuli.

The subjects of this present investigation had relatively low task performance, with an average trial success rate of 30.67% (**Table 1**). This low trial success rate can be partially explained by task difficulty and/or BCI task novelty, as the targets would be placed at varying distances from the center and would also vary in size. In particular, the success condition of having to dwell within the target made the task more difficult than similar one dimensional cursor control tasks, such as the Right-Justified Box task. Note that our behavioral definition of low-level error is not dependent on trial success, but instead on successful cursor movements within each trial. Overall, subjects performed marginally better on trials where the target was placed below the cursor starting position (**Table 1**). Even with this generally poor performance, we believe our investigation to still be valid as error-related potentials are still elicited in tasks where the majority of actions are erroneous (Pezzetta et al., 2018).

Impact of Age on Error Potentials

Two of the subjects in this investigation were early adolescents of the ages 11 and 13 years old (Subjects 1 and 2, respectively), and the other subject was 35 years old (Subject 3) (**Table 1**). Human brain maturation from childhood to adulthood is characterized by changes in the structure of and activation of various brain structures, including in the ACC in the prefrontal cortex (Casey et al., 1997; Adleman et al., 2002), a structure essential to conflict monitoring.

Previous work by Ladouceur et al. (2007) found that with a more developed ACC, adults (19+ years old) and late adolescents (14–18 years old) had stronger ERN responses than early adolescents (9–13 years old), however, the P_E responses did not differ significantly between any of the groups.

Although most subjects exhibited greater HBP in more areas during motor imagery error, Subject 3 had more electrodes with significantly greater HBP differences between error and correct in rest rather than in motor imagery. While this does not seem to be directly related to the aforementioned developmental changes, it is still possible that error presentation in Subject 3 differed from the younger subjects due to processes related to cortical maturation.

Error Presentation in the Time Domain

Unlike with well-established error potentials in EEG, which are often measured as particular phase-locked negative and positive deflections in the time domain, we explored ErrPs related to specific changes in the band-limited time-frequency domain due to the high temporal/spatial resolution inherent to ECoG. Our use of a *post hoc* defined behavioral marker for detecting error-onset instead of a controlled, elicited error in control may have also led to less distinct, non-event locked ErrP waveforms. As discussed, analyses in the frequency domain do not provide a clean time-stamped waveform present in multiple electrodes in or across any of the subjects. The higher spatial resolution of ECoG, in addition to our unique epoch boundary markers were determined, contributed to the difficulty of relying on time-domain data for ErrP identification in this study.

Regardless, we attempted to compare topographical results more directly with EEG literature by investigating changes in the raw voltage potentials recorded per channel per subject in all conditions. Due to the nature of our task not having an experimentally controlled induced onset of error, we did not expect, nor did we see, as robust a response as in EEG. We only saw significantly greater voltage amplitude during error than during correct in a few select electrodes in two subjects.

Implications for BCI

Although this investigation focused on identifying cortical error-related potentials *post hoc*, online classification of error-related potentials have been demonstrated in a few EEG studies (Iturrate et al., 2015; Zander et al., 2016; Cruz et al., 2018). With online ErrP monitoring, future cortical BCI can infer BCI performance without explicit task information, allowing for automatic adaptation of the system based on estimated performance. The task-independent nature of this method could allow for robust adaptive systems that allow for long-term use of BCI that account for changes in recorded brain signals over time.

As this was a preliminary investigation into error-related potentials in cortical BCI, we did not employ online classification methods. The methods presented here could be adapted to work for online classification by continually calculating HBP via a sliding window, and setting a threshold for channels located on particular regions of interest, such as over BA 7. The baseline may be set as the data prior to the start of the sliding window, of a length longer than the sliding window itself. Alternatively, a machine learning model could be developed and trained to classify error and non-error signals and fed the necessary sliding window information for continual classification.

CONCLUSION

In this study, we examined the cortical activity of human subjects during a one-dimensional center-out BCI task and investigated how different areas of the cortex behaved during erroneous BCI decoding versus during correct performance. Of all the cortical areas available for analysis, the somatosensory (BAs 1 and 5), motor (BA 4), and the parietal lobe (BA 7) showed significantly greater HBP 100–500 ms after error onset than

during correct behavior, regardless of whether the subject was actively imagining movement or resting to achieve their goal. During motor imagery, parts of the somatosensory (BAs 2 and 3), the temporal lobe (BAs 21 and 37), and part of the parietal cortex (BA 40) were exclusively significant. During rest, only part of the parietal cortex near the angular gyrus (BA 39) was exclusively significant. Overall, more areas were involved in error processing during the motor imagery error cases rather than during rest error, although there were differences between subjects, with one subject having more significant electrodes during rest. The observed activity of these areas agrees with previous work suggesting the involvement of the parietal and temporal areas in error processing.

Although our results generally agree with previous work performed with overt movement in ECoG (Milekovic et al., 2012), our error-related potentials (ErrPs) do not present themselves as the well-defined waveforms discussed in the EEG literature, likely due to the diffuse timing of our error events. The presence of ErrPs in both overt- and imagined-movement controlled ECoG tasks suggests error processing is impartial to the method of control in a task.

Our investigation is the first to explore ErrPs in the context of continuous control in a cortical BCI. As the BCI field delves further into understanding error and reinforcement learning, it is critical that we understand error processing at various spatial and temporal levels in a multitude of conditions. This study contributes to the field by focusing on continuous control (instead of discrete control for simple selection) representing a more naturalistic setting for characterizing error potentials in the brain. Additionally, we report the first description of the responsive local high-frequency activity using high-gamma band power in a BCI, instead of more global signals such as theta band activity in EEG.

In addition to exploring error processing in the context of motor BCI, we are also interested in the effects of different forms of feedback during continuous control, not just visual (as is typical with most current BCIs). In the future of BCIs and their adoption into neuroprostheses, we will need to understand the effect of other forms of feedback, which inform volitional control, on BCI learning. Ultimately, the use of ErrPs as an automatic feedback signal to future BCIs will allow for co-adaptation, leading to better and longer-lasting control. Greater performance and longer ability of use will allow these co-adaptive BCIs to break out of the confines of the research setting and make their way into clinics and home settings.

We would like to explore the long-term effects of learning on the error-related potentials, but our limited time with research subjects renders this nearly impossible. A better understanding of ErrPs and their usability over time is crucial for implementing co-adaptive BCI systems which rely on ErrPs for feedback. Longer use in the experimental setting may allow for the development of robust classification techniques which can assist in real-time error detection in the future.

ETHICS STATEMENT

This study was carried out in accordance with the protocol approved by the Seattle Children's Hospital Institutional Review Board for Subjects 1 and 2, and of the University of Washington Institutional Review Board, Human Subjects Division, Committee K for Subject 3. All subjects, or their legal guardians if under age 18, gave written informed consent in accordance with the Declaration of Helsinki.

AUTHOR CONTRIBUTIONS

NW performed the analyses and wrote the manuscript. DS and KW provided input and mentorship through the analysis and writing. JW designed the task and collected the data. JO and RR supervised the work.

FUNDING

This research was supported by National Science Foundation (Grant No. EEC-1028725), National Institute of Neurological Disorders and Stroke (Grant No. 5R01NS065186), Washington Research Foundation *Fund for Innovation in Neuroengineering*, National Institutes of Health Computational Neuroscience Training (Grant No. 5T90DA032436-05), and the Achievement Rewards for College Scientists Fellowship (Seattle Chapter).

SUPPLEMENTARY MATERIAL

The Supplementary Material for this article can be found online at: https://www.frontiersin.org/articles/10.3389/fnins.2019.00502/full#supplementary-material

REFERENCES

Adleman, N. E., Menon, V., Blasey, C. M., White, C. D., Warsofsky, I. S., Glover, G. H., et al. (2002). A developmental fMRI study of the stroop color-word task. *NeuroImage* 16, 61–75. doi: 10.1006/nimg.2001.1046

Atchley, R., Klee, D., and Oken, B. (2017). EEG frequency changes prior to making errors in an easy stroop task. *Front. Hum. Neurosci.* 11:521. doi: 10.3389/fnhum.2017.00521

Bechtereva, N. P., Shemyakina, N. V., Starchenko, M. G., Danko, S. G., and Medvedev, S. V. (2005). Error detection mechanisms of the brain: background and prospects. *Int. J. Psychophysiol.* 58, 227–234. doi: 10.1016/j.ijpsycho.2005.06.005

Blankertz, B., Dornhege, G., Krauledat, M., Müller, K.-R., and Curio, G. (2007). The non-invasive berlin brain–computer interface: fast acquisition of effective performance in untrained subjects. *NeuroImage* 37, 539–550. doi: 10.1016/j.neuroimage.2007.01.051

Blankertz, B., Losch, F., Krauledat, M., Dornhege, G., Curio, G., and Muller, K.-R. (2008). The berlin brain–computer interface: accurate performance from first-session in bci-naive subjects. *IEEE Trans. Biomed. Eng.* 55, 2452–2462. doi: 10.1109/TBME.2008.923152

Blankertz, B., Sannelli, C., Halder, S., Hammer, E. M., Kübler, A., Müller, K.-R., et al. (2010). Neurophysiological predictor of SMR-based BCI performance. *NeuroImage* 51, 1303–1309. doi: 10.1016/j.neuroimage.2010.03.022

Calhoun, V. D., Adali, T., Pearlson, G. D., and Kiehl, K. A. (2006). Neuronal chronometry of target detection: fusion of hemodynamic and event-related potential data. *NeuroImage* 30, 544–553. doi: 10.1016/j.neuroimage.2005.08.060

Casey, B. J., Trainor, R., Giedd, J., Vauss, Y., Vaituzis, C. K., Hamburger, S., et al. (1997). The role of the anterior cingulate in automatic and controlled processes: a developmental neuroanatomical study. *Dev. Psychobiol.* 30, 61–69. doi: 10.1002/(sici)1098-2302(199701)30:1<61::aid-dev6>3.3.co;2-b

Casimo, K., Darvas, F., Wander, J., Ko, A., Grabowski, T. J., Novotny, E., et al. (2016). Regional patterns of cortical phase synchrony in the resting state. *Brain Connect.* 6, 470–481. doi: 10.1089/brain.2015.0362

Chavarriaga, R., and Millan, J. D. R. (2010). Learning from EEG error-related potentials in noninvasive brain-computer interfaces. *IEEE Trans. Neural Syst. Rehabil. Eng.* 18, 381–388. doi: 10.1109/TNSRE.2010.2053387

Cruz, A., Pires, G., and Nunes, U. J. (2018). Double errp detection for automatic error correction in an erp-based BCI speller. *IEEE Trans. Neural Syst. Rehabil. Eng.* 26, 26–36. doi: 10.1109/TNSRE.2017.2755018

DiGiovanna, J., Mahmoudi, B., Fortes, J., Principe, J. C., and Sanchez, J. C. (2009). Coadaptive brain-machine interface via reinforcement learning. *IEEE Trans. Biomed. Eng.* 56, 54–64. doi: 10.1109/TBME.2008.926699

Evans, A. C., Collins, D. L., Mills, S. R., Brown, E. D., Kelly, R. L., and Peters, T. M. (1993). "3D statistical neuroanatomical models from 305 MRI volumes," in *Proceedings of the IEEE Conference Record Nuclear Science Symposium and Medical Imaging Conference*, (Piscataway, NJ: IEEE).

Falkenstein, M., Hoormann, J., Christ, S., and Hohnsbein, J. (2000). ERP components on reaction errors and their functional significance: a tutorial. *Biol. Psychol.* 51, 87–107. doi: 10.1016/s0301-0511(99)00031-9

Ferrez, P. W., and Millan, J. D. R. (2008). Error-related EEG potentials generated during simulated brain-computer interaction. *IEEE Trans. Biomed. Eng.* 55, 923–929. doi: 10.1109/TBME.2007.908083

Fischl, B. (2012). FreeSurfer. *NeuroImage* 62, 774–781. doi: 10.1016/j.neuroimage.2012.01.021

Gerson, A. D., Parra, L. C., and Sajda, P. (2005). Cortical origins of response time variability during rapid discrimination of visual objects. *NeuroImage* 28, 342–353. doi: 10.1016/j.neuroimage.2005.06.026

Glazer, J. E., Kelley, N. J., Pornpattananangkul, N., Mittal, V. A., and Nusslock, R. (2018). Beyond the FRN: broadening the time-course of EEG and ERP components implicated in reward processing. *Int. J. Psychophysiol.* 132, 184–202. doi: 10.1016/j.ijpsycho.2018.02.002

Green, A. M., and Kalaska, J. F. (2011). Learning to move machines with the mind. *Trends Neurosci.* 34, 61–75. doi: 10.1016/j.tins.2010.11.003

Holroyd, C. B., and Coles, M. G. H. (2002). The neural basis of human error processing: reinforcement learning, dopamine, and the error-related negativity. *Psychol. Rev.* 109, 679–709. doi: 10.1037/0033-295X.109.4.679

Iannaccone, R., Hauser, T. U., Staempfli, P., Walitza, S., Brandeis, D., and Brem, S. (2015). Conflict monitoring and error processing: new insights from simultaneous EEG–fMRI. *NeuroImage* 105, 395–407. doi: 10.1016/j.neuroimage.2014.10.028

Iturrate, I., Chavarriaga, R., Montesano, L., Minguez, J., and Millán, J. D. R. (2015). Teaching brain-machine interfaces as an alternative paradigm to neuroprosthetics control. *Sci. Rep.* 5:13893. doi: 10.1038/srep13893

Iturrate, I., Montesano, L., and Minguez, J. (2013). Task-dependent signal variations in EEG error-related potentials for brain-computer interfaces. *J. Neural Eng.* 10:026024. doi: 10.1088/1741-2560/10/2/026024

Jatoi, M. A., Kamel, N., Malik, A. S., Faye, I., and Begum, T. (2014). A survey of methods used for source localization using EEG signals. *Biomed. Signal Process. Control* 11, 42–52. doi: 10.1016/j.bspc.2014.01.009

Kim, S. K., and Kirchner, E. A. (2013). "Classifier Transferability in the Detection of Error Related Potentials from Observation to Interaction," in *Proceedings of the IEEE International Conference on Systems, Man, and Cybernetics*, (Manchester: IEEE).

Kreilinger, A., Hiebel, H., and Müller-Putz, G. R. (2016). Single versus multiple events error potential detection in a BCI-controlled car game with continuous and discrete feedback. *IEEE Trans. Biomed. Eng.* 63, 519–529. doi: 10.1109/TBME.2015.2465866

Krigolson, O. E., and Holroyd, C. B. (2007). Hierarchical error processing: different errors, different systems. *Brain Res.* 1155, 70–80. doi: 10.1016/j.brainres.2007.04.024

Krigolson, O. E., Holroyd, C. B., Van Gyn, G., and Heath, M. (2008). Electroencephalographic correlates of target and outcome errors. *Exp. Brain Res.* 190, 401–411. doi: 10.1007/s00221-008-1482-x

Ladouceur, C. D., Dahl, R. E., and Carter, C. S. (2007). Development of action monitoring through adolescence into adulthood: ERP and source localization. *Dev. Sci.* 10, 874–891. doi: 10.1111/j.1467-7687.2007.00639.x

MacLean, S. J., Hassall, C. D., Ishigami, Y., Krigolson, O. E., and Eskes, G. A. (2015). Using brain potentials to understand prism adaptation: the error-related negativity and the P300. *Front. Hum. Neurosci.* 9:335. doi: 10.3389/fnhum.2015.00335

Manning, J. R., Jacobs, J., Fried, I., and Kahana, M. J. (2009). Broadband shifts in local field potential power spectra are correlated with single-neuron spiking in humans. *J. Neurosci. Off. J. Soc. Neurosci.* 29, 13613–13620. doi: 10.1523/JNEUROSCI.2041-09.2009

Merel, J., Pianto, D. M., Cunningham, J. P., and Paninski, L. (2015). Encoder-decoder optimization for brain-computer interfaces. *PLoS Comput. Biol.* 11:e1004288. doi: 10.1371/journal.pcbi.1004288

Miall, R. C., and Wolpert, D. M. (1996). Forward models for physiological motor control. *Neural Netw.* 9, 1265–1279. doi: 10.1016/s0893-6080(96)00035-4

Milekovic, T., Ball, T., Schulze-Bonhage, A., Aertsen, A., and Mehring, C. (2012). Error-related electrocorticographic activity in humans during continuous movements. *J. Neural Eng.* 9:026007. doi: 10.1088/1741-2560/9/2/026007

Milekovic, T., Ball, T., Schulze-Bonhage, A., Aertsen, A., and Mehring, C. (2013). Detection of error related neuronal responses recorded by electrocorticography in humans during continuous movements. *PloS One* 8:e55235. doi: 10.1371/journal.pone.0055235

Miller, K. J., Sorensen, L. B., Ojemann, J. G., and den Nijs, M. (2009). Power-law scaling in the brain surface electric potential. *PLoS Comput. Biol.* 5:e1000609. doi: 10.1371/journal.pcbi.1000609

Navarro-Cebrian, A., Knight, R. T., and Kayser, A. S. (2016). Frontal monitoring and parietal evidence: mechanisms of error correction. *J. Cogn. Neurosci.* 28, 1166–1177. doi: 10.1162/jocn_a_00962

Newell, K. M. (1991). Motor skill acquisition. *Annu. Rev. Psychol.* 42, 213–237.

Nieuwenhuis, S., Holroyd, C. B., Mol, N., and Coles, M. G. H. (2004). Reinforcement-related brain potentials from medial frontal cortex: origins and functional significance. *Neurosci. Biobehav. Rev.* 28, 441–448. doi: 10.1016/j.neubiorev.2004.05.003

Nieuwenhuis, S., Ridderinkhof, K. R., Blom, J., Band, G. P. H., and Kok, A. (2001). Error-related brain potentials are differentially related to awareness of response errors: evidence from an antisaccade task. *Psychophysiology* 38, 752–760. doi: 10.1017/s0048577201001111

O'Connell, R. G., Dockree, P. M., Bellgrove, M. A., Kelly, S. P., Hester, R., Garavan, H., et al. (2007). The role of cingulate cortex in the detection of errors with and without awareness: a high-density electrical mapping study. *Eur. J. Neurosci.* 25, 2571–2579. doi: 10.1111/j.1460-9568.2007.05477.x

Olson, J. D., Wander, J. D., Johnson, L., Sarma, D., Weaver, K., Novotny, E. J., et al. (2016). Comparison of subdural and subgaleal recordings of cortical high-gamma activity in humans. *Clin. Neurophysiol.* 127, 277–284. doi: 10.1016/j.clinph.2015.03.014

Orsborn, A. L., Moorman, H. G., Overduin, S. A., Shanechi, M. M., Dimitrov, D. F., and Carmena, J. M. (2014). Closed-loop decoder adaptation shapes neural plasticity for skillful neuroprosthetic control. *Neuron* 82, 1380–1393. doi: 10.1016/j.neuron.2014.04.048

Papademetris, X., Jackowski, M. P., Rajeevan, N., DiStasio, M., Okuda, H., Constable, R. T., et al. (2006). BioImage suite: an integrated medical image analysis suite: an update. *Insight J.* 2006:209.

Pezzetta, R., Nicolardi, V., Tidoni, E., and Aglioti, S. M. (2018). Error, rather than its probability, elicits specific electrocortical signatures: a combined EEG-immersive virtual reality study of action observation. *J. Neurophysiol.* 120, 1107–1118. doi: 10.1152/jn.00130.2018

Pohlmeyer, E. A., Mahmoudi, B., Geng, S., Prins, N. W., and Sanchez, J. C. (2014). Using reinforcement learning to provide stable brain-machine interface control despite neural input reorganization. *PLoS One* 9:e87253. doi: 10.1371/journal.pone.0087253

Ray, S., Crone, N. E., Niebur, E., Franaszczuk, P. J., and Hsiao, S. S. (2008). Neural correlates of high-gamma oscillations (60–200 Hz) in macaque local field

potentials and their potential implications in electrocorticography. *J. Neurosci.* 28, 11526–11536. doi: 10.1523/jneurosci.2848-08.2008

Schalk, G., McFarland, D. J., Hinterberger, T., Birbaumer, N., and Wolpaw, J. R. (2004). BCI2000: a general-purpose brain-computer interface (BCI) system. *IEEE Trans. Biomed. Eng.* 51, 1034–1043. doi: 10.1109/tbme.2004.827072

Spüler, M., and Niethammer, C. (2015). Error-related potentials during continuous feedback: using EEG to detect errors of different type and severity. *Front. Hum. Neurosci* 9:155. doi: 10.3389/fnhum.2015.00155

Stevens, M. C., Kiehl, K. A., Pearlson, G. D., and Calhoun, V. D. (2009). Brain Network Dynamics During Error Commission. *Hum. Brain Mapp.* 30, 24–37. doi: 10.1002/hbm.20478

Talairach, J., and Tournoux, T. (1988). *Co-planar Stereotaxic Atlas of the Human Brain: 3-Dimensional Proportional System - an Approach to Cerebral Imaging*. Stuttgart: Thieme Medical Publishers.

Trujillo, L. T., and Allen, J. J. B. (2007). Theta EEG dynamics of the error-related negativity. *Clin. Neurophysiol.* 118, 645–668. doi: 10.1016/j.clinph.2006.11.009

Ullsperger, M., and von Cramon, D. Y. (2006). How does error correction differ from error signaling? An event-related potential study. *Brain Res.* 1105, 102–109. doi: 10.1016/j.brainres.2006.01.007

Van Veen, V., and Carter, C. S. (2002). The timing of action-monitoring processes in the anterior cingulate cortex. *J. Cogn. Neurosci.* 14, 593–602. doi: 10.1162/08989290260045837

Wander, J. (2015). *Neural Correlates of Learning and Intent During Human Brain-Computer Interface Use*. Ph.D. thesis, Washington DC: University of Washington.

Wessel, J. R. (2012). Error awareness and the error-related negativity: evaluating the first decade of evidence. *Front. Hum. Neurosci.* 6:88. doi: 10.3389/fnhum.2012.00088

Wolpaw, J. R., and McFarland, D. J. (2004). Control of a two-dimensional movement signal by a noninvasive brain-computer interface in humans. *Proc. Natl. Acad. Sci. U.S.A.* 101, 17849–17854. doi: 10.1073/pnas.0403504101

Zander, T. O., Krol, L. R., Birbaumer, N. P., and Gramann, K. (2016). Neuroadaptive technology enables implicit cursor control based on medial prefrontal cortex activity. *Proc. Natl. Acad. Sci. U. S. A.* 113, 14898–14903. doi: 10.1073/pnas.1605155114

Zhang, H., Chavarriaga, R., Khaliliardali, Z., Gheorghe, L., Iturrate, I., and Millán, J. D. R. (2015). EEG-based decoding of error-related brain activity in a real-world driving task. *J. Neural Eng.* 12:066028. doi: 10.1088/1741-2560/12/6/066028

Conflict of Interest Statement: The authors declare that the research was conducted in the absence of any commercial or financial relationships that could be construed as a potential conflict of interest.

frontiers in Neuroscience

ORIGINAL RESEARCH
published: 07 August 2019
doi: 10.3389/fnins.2019.00832

Functional Frequency Discrimination From Cortical Somatosensory Stimulation in Humans

Daniel R. Kramer[1,2], Krista Lamorie-Foote[3], Michael Barbaro[3], Morgan Lee[3], Terrance Peng[3], Angad Gogia[3], Charles Y. Liu[1,2], Spencer S. Kellis[2,4,5] and Brian Lee[1,2]*

[1] Department of Neurosurgery, University of Southern California, Los Angeles, CA, United States, [2] Neurorestoration Center, University of Southern California, Los Angeles, CA, United States, [3] Keck School of Medicine, University of Southern California, Los Angeles, CA, United States, [4] Department of Biology and Biological Engineering, California Institute of Technology, Pasadena, CA, United States, [5] Tianqiao and Chrissy Chen Brain-Machine Interface Center, California Institute of Technology, Pasadena, CA, United States

Recently, efforts to produce artificial sensation through cortical stimulation of primary somatosensory cortex (PSC) in humans have proven safe and reliable. Changes in stimulation parameters like frequency and amplitude have been shown to elicit different percepts, but without clearly defined psychometric profiles. This study investigates the functionally useful limits of frequency changes on the percepts felt by three epilepsy patients with subdural electrocorticography (ECoG) grids. Subjects performing a hidden target task were stimulated with parameters of constant amplitude, pulse-width, and pulse-duration, and a randomly selected set of two frequencies (20, 30, 40, 50, 60, and 100 Hz). They were asked to decide which target had the "higher" frequency. Objectively, an increase in frequency differences was associated with an increase in perceived intensity. Reliable detection of stimulation occurred at and above 40 Hz with a lower limit of detection around 20 Hz and a just-noticeable difference estimated at less than 10 Hz. These findings suggest that frequency can be used as a reliable, adjustable parameter and may be useful in establishing settings and thresholds of functionality in future BCI systems.

Keywords: somatosensation, cortical stimulation, brain computer interface, brain machine interface, sensory feedback control, electrocorticography, frequency

OPEN ACCESS

Edited by:
Kai J. Miller, Mayo Clinic, United States

Reviewed by:
Burak Güçlü, Boğaziçi University, Turkey
Sean Kevin Meehan, University of Waterloo, Canada

****Correspondence:***
Daniel R. Kramer
dankramer29@gmail.com

Specialty section:
This article was submitted to Neuroprosthetics, a section of the journal Frontiers in Neuroscience

Received: *31 January 2019*
Accepted: *25 July 2019*
Published: *07 August 2019*

Citation:
Kramer DR, Lamorie-Foote K, Barbaro M, Lee M, Peng T, Gogia A, Liu CY, Kellis SS and Lee B (2019) Functional Frequency Discrimination From Cortical Somatosensory Stimulation in Humans. Front. Neurosci. 13:832. doi: 10.3389/fnins.2019.00832

INTRODUCTION

For the millions of patients with somatosensory deficits from stroke, paralysis, or limb-loss, restoration of function has vast implications for health, and independence recovery. Somatosensory brain-computer interface (BCI) presents a means to restore function in such individuals, where somatosensory input can potentially improve motor BCI (Andersen et al., 2004, 2010; Suminski et al., 2010; Fifer et al., 2012; Chestek et al., 2013; Lee et al., 2013; Aflalo et al., 2015; Bundy et al., 2016; Flesher et al., 2016; Hollins and Risner, 2016; Armenta Salas et al., 2018), or restore basic functions like bladder control. Although stimulation of peripheral nerves can potentially reproduce somatosensation (Raspopovic et al., 2014; Tan et al., 2014), to fully restore function in stroke patients or paralyzed individuals, cortical stimulation would be required. However, somatosensory BCI is at an early stage with limited work establishing the basic utility (Flesher et al., 2016;

Armenta Salas et al., 2018; Lee et al., 2018), functionality (Baumgartner et al., 1991; Tan et al., 2014; Collins et al., 2017), and modalities (Raspopovic et al., 2014; Tan et al., 2014; Vidal et al., 2016; Collins et al., 2017; Armenta Salas et al., 2018; Lee et al., 2018).

Trained non-human primate (NHP) studies have helped to establish foundational parameters and feasibility of discriminating between sensations arising from intracortical micro-stimulation (ICMS) with microelectrodes in the primary somatosensory cortex (PSC). These techniques have produced behavioral responses comparable to those produced by real tactile stimuli (Romo et al., 1998, 2000; O'Doherty et al., 2012; Klaes et al., 2014). Through alterations in amplitude and location of an ICMS, NHPs have demonstrated an ability to differentiate pressure, location, and timing on par with that of tactile stimulation. By varying frequency in ICMS (10–30 Hz, with a minimum absolute difference in comparative frequencies of 2 Hz), NHPs showed similar accuracy to natural sensation produced by mechanical stimulation (80% vs. 89% accuracy) (Romo et al., 1998, 2000). O'Doherty et al. (2012) demonstrated that NHPs could differentiate between periodic and aperiodic pulse-trains in an active exploration task, suggesting that temporally patterned stimulation can lead to noticeable, unique sensations. Stimulation as low as 6 Hz produced perceptible sensations based on behavioral responses (Romo et al., 2000). They also identified that quickly adapting neurons were important in frequency discrimination, and discrimination between sensations was based on frequency alone. When slowly adapting neurons were stimulated, monkeys' performances decreased and were not comparable to mechanical stimulation (Romo et al., 2000).

While NHP studies have demonstrated that artificial sensation through cortical stimulation is achievable (O'Doherty et al., 2011; Tabot et al., 2013, 2015; Kim et al., 2015a,b; Overstreet et al., 2016), clinical studies in humans are needed to fully understand the subjective quality of sensations evoked by modulating these parameters and verify the generalizability. Direct electrical stimulation of PSC, with ICMS and surface electrodes, have yielded reliable and safe results (Flesher et al., 2016; Armenta Salas et al., 2018; Lee et al., 2018) and established basic stimulation parameters (Lee et al., 2018). Changes in amplitude and frequency are primarily perceived as increased intensity, with occasional enlargement of dermatomal areas involved, and rarely a change in perceptual quality (Armenta Salas et al., 2018; Lee et al., 2018). Amplitude increase was most consistent in producing increased intensity (Lee et al., 2018). A study utilizing ECoG electrodes at three frequencies (50, 75, and 100 Hz) exemplified that sensation arising from stimulation at different frequencies can be differentiated in humans when there is at least a 25 Hz difference between frequencies and frequencies are greater than 50 Hz (Johnson et al., 2013). In addition, another high density ECoG study noted that perceiving somatosensation was inconsistent below 20 Hz for absolute perceptual threshold from a single stimuli (Lee et al., 2018). Although lower vibrotactile frequencies are better sensed in the skin (Vardar and Guclu, 2017), and have a wider range of responses (Griffin, 2012), earlier work by this group established a lower threshold in cortical stimulation of 20 Hz in which greater than 50% sensed the stimulation, and subject-described percepts reflected increased intensity and speed from increased cortical stimulation frequencies (Lee et al., 2018). Since the results of cortical stimulation on individual neurons is not well understood, the difference in frequency ranges and percepts likely reflects a difference in how cortical stimulation is interpreted compared to skin-sensed stimulation.

Going forward with BCI, establishing the psychometric thresholds for parameters like frequency will set the groundwork for what "degrees of freedom" are possible in subjects. Here we attempt to establish the perceptual limits of one specific parameter, frequency, during direct cortical stimulation of PSC using ECoG grids in humans with intact somatosensory pathways. We aim to estimate lower limits, and reliable degrees of freedom for frequency changes in stimulation parameters, for the purpose of using ECoG as a delivery method in somatosensory BCI in the future. We also aim to explore the usable limits for detecting the absolute difference between two frequencies.

MATERIALS AND METHODS

Subjects and Implantation

Three patients with intractable epilepsy, of normal intelligence on neuropsychiatric testing, normal somatosensation, and undergoing implantation of subdural ECoG with coverage over PSC, were enrolled in this study (see **Table 1** for demographic details). These patients, as part of their care for epilepsy, required ECoG for seizure localization, and were to receive a craniotomy with access to the PSC hand region. S12 had a cavernous malformation in the parietal lobe. Based on the mapping of PSC, imaging, and results from invasive monitoring, the cavernoma was separate from the PSC hand area, and the seizure focus was not near PSC. S18 was found to have a seizure focus in the interhemispheric portion of the parietal lobe, also distinct from PSC. S30 was found to have seizure foci in the frontal and temporal lobes, also distinct from PSC. This study was approved by the USC Institutional Review Board and all subjects provided written consent. Surgical technique was standard, and has been described elsewhere (Lee et al., 2018), but briefly, a craniotomy was to be performed with access to the frontal, temporal, and parietal regions. Prior to surgery, the motor cortex hand area was identified based on anatomic landmarks, and the hand representation in PSC was marked, using neuronavigation software. During surgery, grids were placed to center over the PSC hand area. This area was not under direct visualization. Grids were high-density, "mini"-ECoG grids (mECoG) with 2 mm contacts, with 1.2 mm exposed surface of platinum-iridium electrodes between silastic sheeting, spaced 3 mm apart from center-to-center (FG64C-MP03, Ad-Tech Medical Instrument Corporation, Wisconsin, WI, United States), except in S12 where a standard spaced ECoG grid (sECoG) was used with 4 mm contacts, with 2.4 mm exposed surface, spaced 10 mm apart from center-to-center (AU4 × 5P2, Integra Life Sciences Corporation, New Jersey, United States). Following implantation, the grids were secured to the dura,

TABLE 1 | Patient Demographics.

Subject	Seizure foci	Radiographic abnormalities	Epilepsy duration (years)	Age (years)	Sex	Dominant hand	Dermatome chosen for stimulation
S12	Right parietal	Prior surgery for right parietal cavernous malformation	3	25	M	R	Digit 5 medial surface
S18	Posterior interhemispheric strip, lateral parietal	N/A	11	32	F	R	Medial palm
S30	Left interhemispheric frontal cortex in area of encephalomalacia	Left frontal/temporal encephalomalacia	11	24	F	R	Medial palm and wrist

Subjects were epilepsy patients who underwent subdural electrode placement for the purpose of seizure localization. An electrocorticography grid was placed over primary somatosensory cortex. Dermatomes for stimulation testing were chosen after mapping by an epileptologist, where the bipolar electrodes had stable dermatomal percepts upon multiple repeat stimulations.

tunneled through the scalp, and secured to the scalp with suture. The dura was closed, bone replaced, and scalp closed; the patient was transported to the epilepsy monitoring unit in the intensive care unit (ICU).

Experimental Set Up

Location of the implanted grid was confirmed by imaging with a computed tomography scan fused to a preoperative magnetic resonance imaging scan (**Figure 1**). Superimposition of grid placement was made using Freesurfer and Statistical Parametric Mapping software SPM12 with the *img_pipe* package described in Hamilton et al. (2017). Functional location of electrodes was confirmed by mapping with cortical stimulation while subjects were in the ICU. Electrode pairs were stimulated with a range of amplitudes, at the discretion of the epileptologist, between 0.5 and 12 mA, with a frequency of 50 Hz, pulse-width of 250 μs, and duration of 1 s. Areas with pure sensory responses (self-reported by the subject), underwent steady increases in amplitude until motor responses were noted. Following mapping, electrode pairs with sensory only responses at 4 mA were retested 25 times to confirm that repeat stimulation did not (1) alter the percept by the subject, (2) alter the location or region of perception, (3) result in motor activity, (4) cause seizures or seizure-like activity, or (5) cause discomfort. All subjects had at least one electrode pair that met these criteria. If more than one electrode pair met these criteria, there was a preference for the ventral side of the hand and for digits on the lateral side of the hand over the medial (see **Table 1**). This electrode pair was then chosen for repeat stimulation with our paradigm.

Subjects explored a 2-dimensional space consisting of a sheet with two circles on it, which the subject placed at a comfortable distance for exploring with the hand contralateral to the implanted grid. The two circles corresponded to two different stimulation frequencies. As the subject moved one hand over the two circles, an epileptologist stimulated PSC with the associated frequency using an FDA-approved, clinically available stimulator (Natus Neurology Incorporated, Warwick, United States). The current, pulse-width, and pulse-duration were held stable (4 mA, 250 μs, and 1 s, respectively). In a two-alternative forced-choice task design, subjects were instructed to report which circle corresponded to the higher frequency, whether they were "guessing" (meaning they were not sure which one was the higher frequency), and whether they felt both stimulations (see **Figure 2** for experimental setup). Frequencies included 20, 30, 40, 50, 60, and 100 Hz and were chosen pseudorandomly. The stimulator did not have parameters between 60 and 100 Hz. Because subjects moved at their own speed, the time between stimuli ranged from 1 to 6 s. Statistical analysis was performed using Matlab software (The Mathworks, Natick, MA, United States). Thresholds and differences in detection were compared using Fisher's exact test.

RESULTS

Electrodes used for stimulation were determined after cortical mapping and somatosensory percepts were reported by the subject and remained stable after repeat stimulations (>50 stimulations). Stimulation parameters included pulse-width of 250 μs, duration of 1 s, and a square-wave, and were chosen based on prior literature (Lee et al., 2018) and to minimize the interplay of the other parameters with frequency (i.e., low, but reliably detected on 25 repeat stimulations at 50 Hz). Amplitude was chosen to be the lowest value that elicited reliable somatosensory percepts on the 50 prior stimulations with a 50 Hz frequency, and that did not elicit motor activity (2 mA for S12, 3 mA for S18, and 5 mA for S30). Selected dermatomes were the medial surface of digit 5 for S12, medial surface of the palm for S18, and medial palm and wrist for S30 (**Table 1**). Twenty-five trials were completed for S12 and 50 trials for S18 and S30. For S12, 50 trials were planned, however, the patient chose to stop half-way through testing due to fatigue. No adverse events occurred. With increased frequency, patients described the sensation as "more intense," "faster," and "faster buzzing."

Overall Accuracy

Altogether, participants identified the higher frequency with 89.76% accuracy. To explore whether the first stimulation might alter the perception of the second stimulation, trials were grouped based on which condition occurred first. Correct responses were statistically equivalent between these groups (91.9% when the higher frequency occurred first vs. 86.8% when it occurred second; $p = 0.39$, Fisher's exact test). The accuracy of trials broken down into the individual categories is included in **Figure 3**.

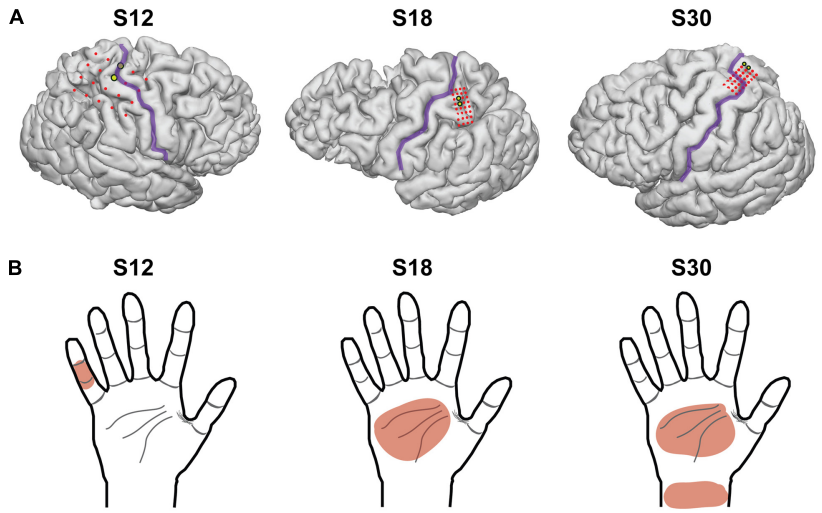

FIGURE 1 | Electrocorticography grid placement. **(A)** 3-dimensional images of each subject's brain from a magnetic resonance image, with the location of the electrodes superimposed. The central sulcus is outlined in purple and electrodes of the grid are shown in red. The electrodes chosen for stimulation in this experimental model are highlighted in yellow. S12 had electrodes with 1 cm of spacing, and S18 and S30 had electrodes with 3 mm of spacing (center-to-center). **(B)** The dermatomal distribution of the percepts used for testing after grid mapping for each subject.

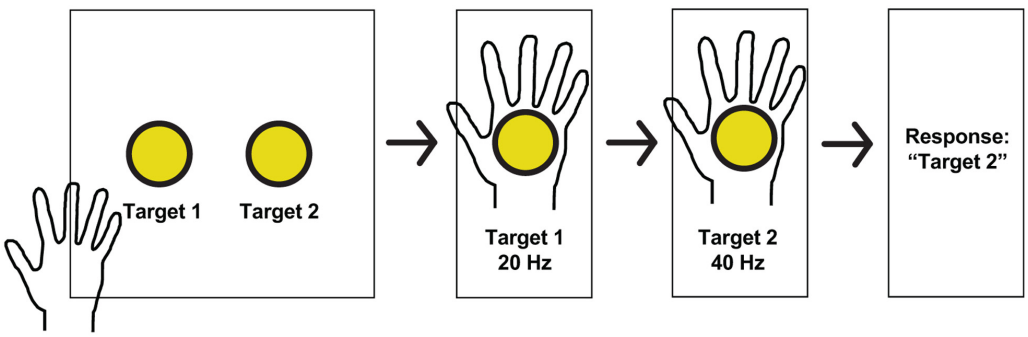

FIGURE 2 | Experimental paradigm and hand receptive fields. Schematic of a typical session. Subjects received stimulation at one of two pseudorandomly determined frequencies when searching for targets in a 2-dimensional space, and reported which target had the higher frequency, whether or not they guessed, and whether or not both stimulations were perceived.

Next, we focused on the absolute difference between two frequencies (see **Figures 4**, **5**). When the frequency difference was equal to 10 Hz, the mean accuracy was 74.29% (S12 71.4%; S18 88.9%; S30 68.4%, see **Figure 5**) compared to a difference larger than 10 Hz, where accuracy increased to 95.65% ($p < 0.001$, individually: S12 100%; S18 100%; S30 87.1%). For S12 and S18, incorrect responses only occurred at a difference of 10 Hz, when both frequencies were equal to or less than 40 Hz.

Using 40 Hz as a cutoff of lower frequencies and higher frequencies, we examined whether small absolute differences were easier to differentiate at lower frequencies or higher frequencies. Separating the trials into those with both frequencies 40 Hz or less vs. those with either frequency greater than 40 Hz, accuracy was 77.8% vs. 93.0% ($p < 0.05$). However, this difference was largely explained by the larger absolute differences of frequencies above 40 Hz. Comparing the absolute difference of 20 Hz or less (since the frequencies at or below 40 Hz had a max absolute difference of 20 Hz) the accuracy was 77.8% vs. 80.0% ($p = 1.0$) for below 40 Hz and above 40 Hz, respectively. When isolating the trials in which the frequency difference was 10 Hz, and then separating them into those with both frequencies 40 Hz or less vs. those with one or both greater than 40 Hz, accuracy was 77.3% vs. 69.2% ($p = 0.69$), respectively. At a frequency difference of 20 Hz, accuracy was 80% when both frequencies were 40 Hz or less compared to 88.2% when at least one was greater than 40 Hz ($p = 0.66$) (**Figure 5**). Frequency differences of 20 Hz had an accuracy of 86.4%, and differences of 30 Hz had an accuracy of 95.0%. All other differences had an accuracy of 100% (see **Figure 5**).

Patient Reported "Guessing"

Subjects reported when they were "guessing," defined as when they could not tell which stimulus was higher. Of all trials, guessing occurred in 18.1% of trials. When subjects reported

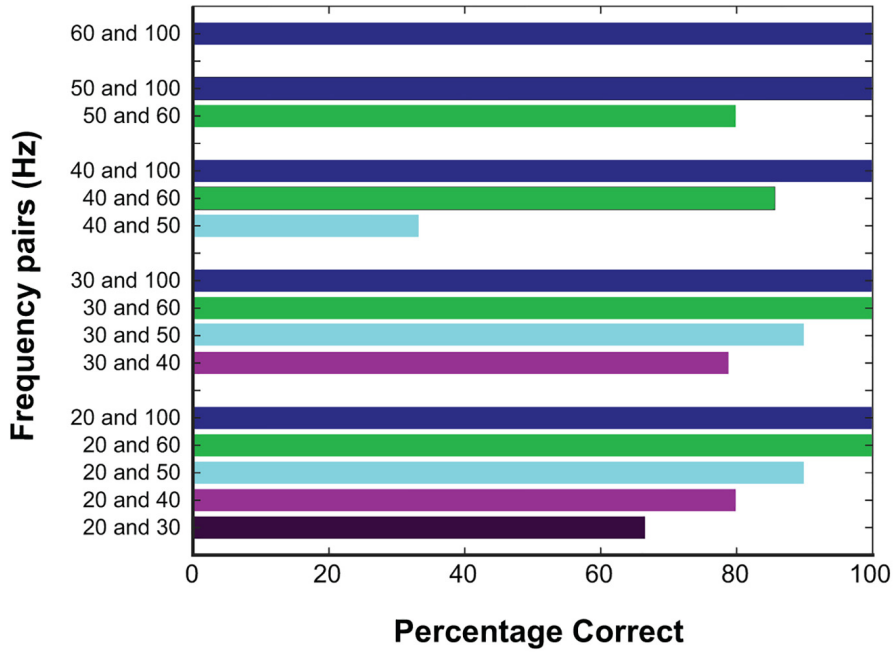

FIGURE 3 | Responses at different frequencies tested. Percentage correct for all trials based on the frequencies being compared, color coded based on the higher frequency. Correct responses were high with larger frequency differences.

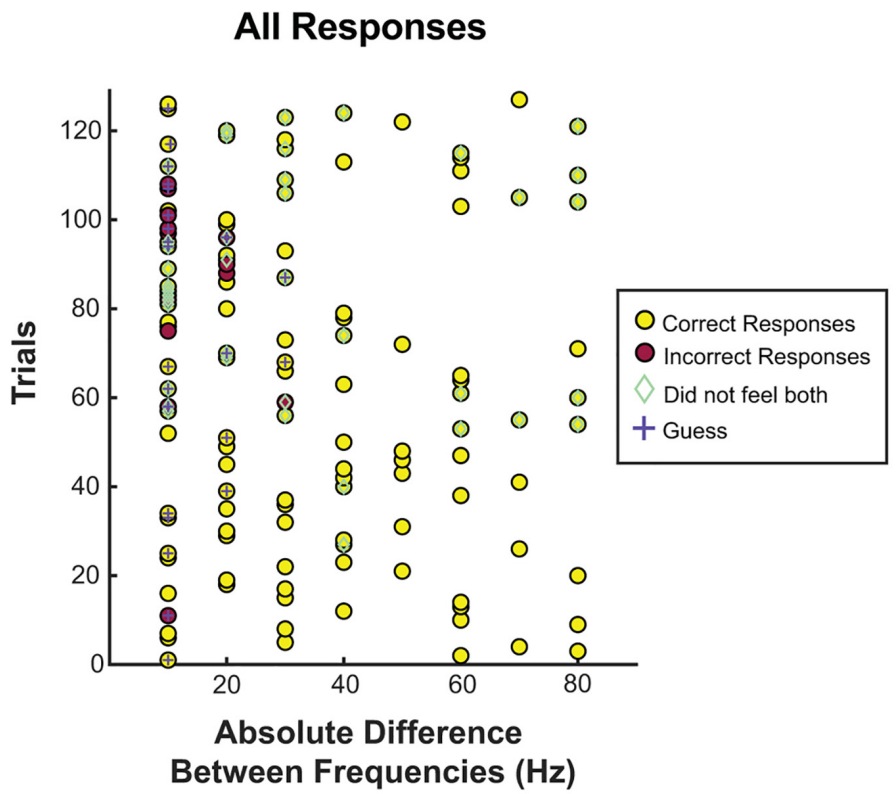

FIGURE 4 | Correct responses organized by absolute difference between two frequencies. All trials separated by the absolute difference in frequency. Correct and incorrect responses, guessing, and whether or not the patient felt both stimuli were recorded for each frequency difference. Most incorrect trials, guessing, and inability to feel both frequencies occurred at or below a difference of 20 Hz.

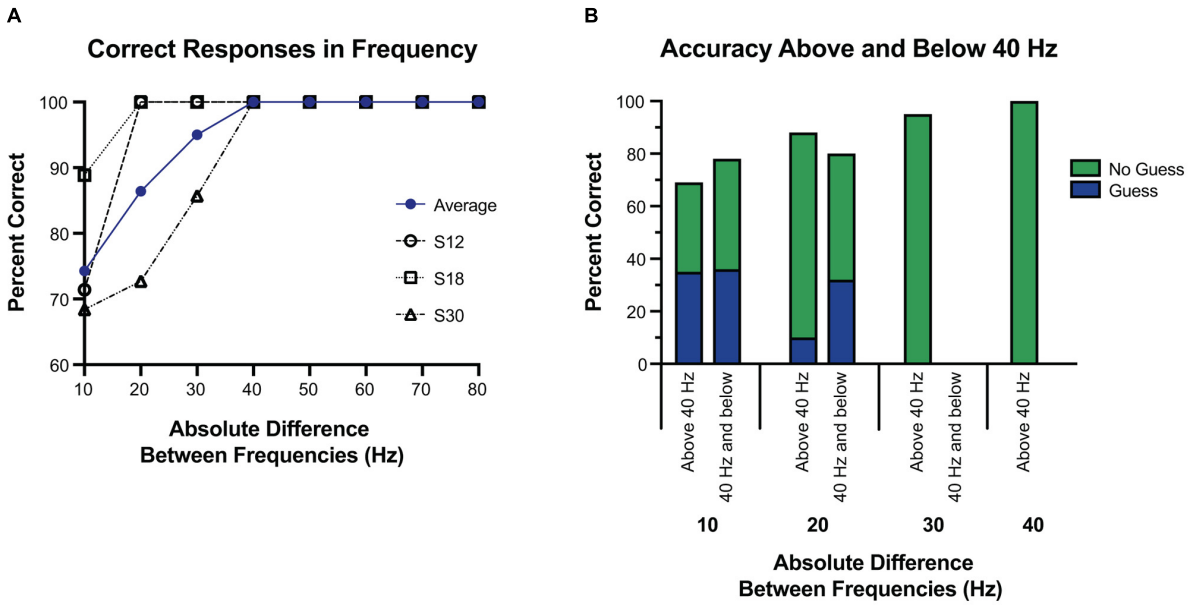

FIGURE 5 | Accuracy at tested frequency differences. **(A)** Overall accuracy for each subject, at each frequency difference. The average of their results is in blue. Above a 30 Hz difference, accuracy was 100%, and well above chance at or below 30 Hz. **(B)** Response accuracy and guessing rate when the tested frequencies were both 40 Hz and below vs. when one or more of the tested frequencies was above 40 Hz. Here the blue and green represent which portions of correct responses were self-reported as a guess, or not a guess, respectively. Overall, subjects were equally accurate regardless of whether the frequencies were above or below 40 Hz, and were more likely to guess if the difference was 10 Hz.

guessing, accuracy was 69.6% vs. 94.2% when they did not report guessing ($p < 0.01$). Limited to trials in which the difference was 20 Hz or less, guessing occurred 36.8% of the time, vs. 2.9% of the time when the difference was greater than 20 Hz ($p < 0.001$). Accuracy for only trials in which the difference was 20 Hz or less was 66.7% when guessing vs. 86.1% when not guessing ($p = 0.10$).

Further, to examine if guessing was more frequent when the frequencies were both low vs. when they were high, we split the 20 Hz differences into those both at or below 40 Hz vs. the rest (see **Figure 4**). For a difference of 20 Hz or less, when both frequencies were at or below 40 Hz, guessing occurred 48.1% of the time vs. 26.7% when one or more frequencies was above 40 Hz ($p = 0.10$), and correct responses were given 77.8% of the time at or below 40 Hz vs. 80.0% of the time above 40 Hz ($p = 1.0$).

When the difference was equal to 10 Hz, guessing occurred 48.6% of the time, vs. 6.5% of the time when the frequency difference was greater than 10 Hz ($p < 0.001$). Among trials with a difference of 10 Hz, accuracy was 64.7% when guessing vs. 83.3% when not guessing ($p = 0.26$). Again, we examined if having both frequencies lower than 40 Hz affected the rate of accuracy or guessing among those that were 10 Hz apart. No difference was seen among subjects' rate of guessing when both frequencies were at or below 40 Hz vs. one or more above 40 Hz (46.1% vs. 50.0%, $p = 1.0$), or subjects' accuracy when guessing (77.2% vs. 69.2%, $p = 0.70$).

Thresholds of Detection

To understand the lower limits of detection thresholds, subjects were asked to report on whether they felt both stimulations, of which 69.3% of trials were reported as perceived for both stimulations (see **Figure 4**). Of the 30.7% in which one or more stimulations were not perceived, 82.1% had one or both frequencies at or below 30 Hz, and 92.3% had one or both frequencies at or below 40 Hz. Correct responses were not significantly different when subjects felt both stimulations (89.8% when both were felt vs. 89.7% when one or both were not felt). No difference was found in whether both stimulations were felt when split for both stimulation frequencies being below 50 Hz vs. both being above 50 Hz (60.0% vs. 75.3%, $p = 0.079$) or both being below 40 Hz vs. both being above 40 Hz (63.0% vs. 71.0%, $p = 0.483$).

DISCUSSION

Here we build upon prior work using ECoG electrodes to establish the thresholds of functionality for somatosensory BCI by adjusting frequency and discerning discrimination thresholds. The ability to detect a difference in frequency from cortical stimulation using an ECoG grid adds an adjustable parameter to the prospect of somatosensory BCI. To this end, we sought to explore the basic psychometric parameters of frequency discrimination in epilepsy patients with already implanted ECoG grids over PSC. Subjectively, when frequency increased, patients perceived a more intense stimulus, similar to other stimulation studies in humans (Johnson et al., 2013; Hiremath et al., 2017; Lee et al., 2018). Even when subjects reported guessing on a forced choice between stimulations of two different frequencies, accuracy was 69.6%. Finally, we show detection of absolute differences between stimulation frequencies above chance at

10 Hz, with reliable differentiation of frequencies at or above 20 Hz and near perfect detection at or above 40 Hz.

Prior ECoG work with cortical stimulation tested frequencies of 50, 75, and 100 Hz and noted that patients were able to identify and differentiate between sensations elicited by these frequencies (Johnson et al., 2013). Our own work showed that intensity was altered with an increase in frequency, but detecting differences was not explicitly tested (Lee et al., 2018). These studies investigating the frequency component of stimulation have mostly studied the feasibility and subjective quality of modulating frequency to produce different sensations, as well as the threshold required for somatosensory percepts (Johnson et al., 2013; Hiremath et al., 2017; Lee et al., 2018). Prior studies in microelectrode stimulation have focused on amplitude, demonstrating alterations in somatosensory category, with the higher amplitudes leading to more proprioceptive sensations, and lower amplitudes leading to cutaneous sensations (Armenta Salas et al., 2018). Further intracortical stimulation with microelectrodes in humans suggested that the "just-noticeable difference" (JND) of amplitude is around 15.4 $\pm$ 3.9 μA with a detection threshold of 39.4 μA (Flesher et al., 2016).

To establish similar baseline parameters in frequency alterations, we built off prior work. With preliminary testing we noted that frequencies below 20 Hz were generally undetectable (Lee et al., 2018), and thus explored 10 Hz differences from 20 to 100 Hz (except 70–90 Hz due to technical constraints). Above a 30 Hz difference, accuracy was 100%, with a high degree of accuracy at all tested differences below 30 Hz. Frequency differences of 20 Hz led to an accuracy of 86.4%, and differences of 10 Hz were still well above chance at 74.3%. S12 and S18 had only two incorrect responses each, both at a 10 Hz difference, with both frequencies at or below 40 Hz. S30 was more varied, but had most incorrect responses at a difference of 10 Hz (60%), and all were when both frequencies were less than 60 Hz.

Although it was more difficult to detect a difference of 10 Hz compared to 20 or 30 Hz, accuracy at a 10 Hz difference was well above chance, and thus we estimate a JND below 10 Hz for cortical stimulation through ECoG electrodes. One exception to this, in **Figure 3**, 40 Hz vs. 50 Hz has a 33.3% accuracy, and may reflect a limited number of trials at that frequency pair, or reflect a true difference. The edges of detection for Meissener corpuscles (flutter sensations at frequencies 10–60 Hz) and Pacinian afferents (vibrational sensations 60–400 Hz) are right around 40 and 50 Hz (Mountcastle et al., 1969), and therefore this may reflect a difficulty in this frequency range for both cortical and peripheral stimulation. Further testing may be warranted.

Weber's law would indicate that the JND would increase proportionally to the increase in the base frequency. Indeed, Weber's law is noted in studies comparing tactile somatosensation (Francisco et al., 2017), however it is not clear if this follows in cortical stimulation. Limited by the testing capabilities of our stimulator, we were unable to explore smaller differences, and thus unable to find a true JND, or the adherence of PSC stimulation to Weber's law. In a NHP microstimulation study, the JND was 3.73 Hz with cortical stimulation (Romo et al., 2000), which may be closer to the real JND or may represent a difference in species, electrode type, or both. Compared to vibrational frequencies of mechanical stimuli, the JND was similar between the two (2.88 Hz for mechanical stimuli). JND could be different with ECoG electrode stimulation vs. microelectrode stimulation given changes in the spread of electricity (bipolar vs. unipolar), size of the electrode (mm vs. μm), or other differences (e.g., mA vs. μA). The JND estimated in this study (<10 Hz) is not far from the JNDs reported for microelectrode stimulation and mechanical stimuli, and although it may abide by Weber's law, all that we can conclude here is that between 50 and 60 Hz (the largest base frequency with the smallest absolute difference), accuracy was well above chance at 80%. Since microelectrode, macroelectrode, and mechanical stimulation appear to have similar JNDs, it may be that the encoding of vibrational frequencies is tied to the frequency of the electrical activity in PSC whether from peripheral nerves or direct stimulation. Indeed, lower vibrational frequencies of mechanical stimuli (<100 Hz) have been seen to stimulate PSC neuron spike rates (Mountcastle et al., 1969; Salinas et al., 2000; Hernandez et al., 2005; Luna et al., 2005). Further testing with stimulators with more finely tuned adjustments will be necessary in the future, and may need to rely on concepts that compare tactile and cortical stimulation thresholds like "psychometric equivalence functions," already shown to be able to estimate these thresholds in amplitude and frequency stimulations in rodents (Devecioglu and Guclu, 2005).

Subject-reported guessing was also evaluated, showing a low rate of guessing across all trials at 18.1%. Most guessing occurred at the lower range of differences, 10 and 20 Hz, however, accuracy was not significantly altered, and correct responses were above 50%. This result indicates that despite self-reports, subjects were still able to differentiate between frequencies. Similarly, subjects reported they could not feel both stimulations approximately 1/3 of the time. Again, this outcome did not diminish correct responses, which were similar when comparing those in which they reported feeling both to those in which they did not (see **Figure 3**). Ninety-two percent of the time that subjects did not sense the stimulation, one frequency was at or below 40 Hz. Taken together, accuracy decreased and guessing increased when both frequencies were less than 30 Hz, and inconsistencies were seen at 30 and 40 Hz. Given these results, 40 Hz is likely the threshold for consistent sensation, and would be a reasonable lower limit for a somatosensory BCI system. From these results, an ECoG BCI system would likely be able to manipulate frequencies at 20 Hz differences from 40 Hz and above, with a high degree of reliability. With training and more fine adjustments, differences of 10 Hz would likely be sufficient. We did see a difference between subjects, with one subject showing decreased accuracy above 30 Hz, suggesting intersubject variability. Additionally, the thresholds were based on fixed parameters of amplitude, pulse-width, and pulse-duration, all factors which independently (Lee et al., 2018), and jointly influence thresholds (Devecioglu and Guclu, 2005). Likely an increased amplitude or pulse-duration would alter the thresholds of frequency discrimination, as well as the perception of the stimulus [as evidenced by changes in the strength of the stimulus noted by Lee et al. (2018)]. A great deal more testing in future studies will be required to elucidate the psychophysical results of the combining parameter variations

and a future BCI system will likely need a range of possible frequencies to adjust for individual variation.

This study has several limitations. First, the stimulator used, an FDA-approved clinical stimulator, can only test differences as small as 10 Hz. Therefore, while the "just-noticeable" difference most likely lies below 10 Hz, we were unable to stimulate smaller changes given that the stimulator settings are unalterable (see **Figure 4**). Similarly, the parameters are limited, without options between 60 and 100 Hz. Testing was carried out in the ICU, limiting time and control, and preventing more trials and further paradigms. Subjects all suffered from epilepsy, which may alter cortical networks in PSC. However, our subjects were still able to perceive sensation in a consistent dermatome upon stimulation and had no known pathology affecting PSC. The other stimulation parameters were not consistent between patients (but rather consistent within patients), introducing bias. Electrode size was different for S12 than S18 and S30, which may have introduced differences into the spread of electricity. Each session only took place in a single day and the results are therefore not generalizable to chronic stimulation. The stability of chronic stimulation for producing somatosensation is unknown, however, reports of chronic stimulation of motor cortex in NHPs shows stability of mapping (Craggs et al., 1976), the safety profile from chronically implanted, stimulating, and surface electrodes in responsive neural stimulators is quite robust (Heck et al., 1976; Bergey et al., 2015; Lee et al., 2015). ICMS use in PSC exhibits stability at 10–12 weeks, without any safety concerns. Since ICMS is invasive, it is likely that the safety profile would be similar or better, but the decay may be more severe (Callier et al., 2015; Chen et al., 2015).

Overall, this study uses ECoG grids to investigate the frequency component of cortical stimulation for use in BCI systems. We estimate a JND value near or below 10 Hz, and show that even when guessing, subjects could correctly identify the higher frequency better than chance. Furthermore, these findings suggest reliable discrimination above 40 Hz, with a difference between frequencies of 20 Hz or above. Future BCI systems utilizing cortical stimulation to produce artificial sensation can utilize frequency to produce a wider range of percepts, empowering users to make better use of artificial sensations.

ETHICS STATEMENT

This study was carried out in accordance with the recommendations of the University of Southern California Health Sciences Campus Institutional Review Board with written informed consent from all subjects. All subjects gave written informed consent in accordance with the Declaration of Helsinki. The protocol was approved by the University of Southern California Health Sciences Campus Institutional Review Board.

AUTHOR CONTRIBUTIONS

DK, BL, SK, and CL conceived the original ideas and experiments. BL and DK carried out the experiments. All authors interpreted the data, edited the manuscript, provided critical feedback, and helped to shape the research and analysis. DK, KL-F, CL, BK, and SK led the writing of the manuscript.

FUNDING

We wish to acknowledge the generous support of Cal-BRAIN: A Neurotechnology Program for California, National Center for Advancing Translational Science (NCATS) of the U.S. National Institutes of Health (KL2TR001854), National Institutes of Health (R25 NS099008-01), the Neurosurgery Research and Education Foundation (NREF), the Tianqiao and Chrissy Chen Brain-Machine Interface Center at Caltech, the Boswell Foundation and the Della Martin Foundation, and the University of Southern California Neurorestoration Center. None of the listed sources of funding had a role in study design, collection, analysis, and interpretation of data, or writing of the manuscript.

REFERENCES

Aflalo, T., Kellis, S., Klaes, C., Lee, B., Shi, Y., Pejsa, K., et al. (2015). Neurophysiology. Decoding motor imagery from the posterior parietal cortex of a tetraplegic human. *Science* 348, 906–910. doi: 10.1126/science.aaa5417

Andersen, R. A., Hwang, E. J., and Mulliken, G. H. (2010). Cognitive neural prosthetics. *Annu. Rev. Psychol.* 61, C1–C3. doi: 10.1146/annurev.psych.093008.100503

Andersen, R. A., Musallam, S., and Pesaran, B. (2004). Selecting the signals for a brain-machine interface. *Curr. Opin. Neurobiol.* 14, 720–726. doi: 10.1016/j.conb.2004.10.005

Armenta Salas, M., Bashford, L., Kellis, S., Jafari, M., Jo, H., Kramer, D., et al. (2018). Proprioceptive and cutaneous sensations in humans elicited by intracortical microstimulation. *eLife* 7:e32904. doi: 10.7554/eLife.32904

Baumgartner, C., Barth, D. S., Levesque, M. F., and Sutherling, W. W. (1991). Functional anatomy of human hand sensorimotor cortex from spatiotemporal analysis of electrocorticography. *Electroencephalogr. Clin. Neurophysiol.* 78, 56–65. doi: 10.1016/0013-4694(91)90019-z

Bergey, G. K., Morrell, M. J., Mizrahi, E. M., Goldman, A., King-Stephens, D., Nair, D., et al. (2015). Long-term treatment with responsive brain stimulation in adults with refractory partial seizures. *Neurology* 84, 810–817. doi: 10.1212/wnl.0000000000001280

Bundy, D. T., Pahwa, M., Szrama, N., and Leuthardt, E. C. (2016). Decoding three-dimensional reaching movements using electrocorticographic signals in humans. *J. Neural. Eng.* 13:026021. doi: 10.1088/1741-2560/13/2/026021

Callier, T., Schluter, E. W., Tabot, G. A., Miller, L. E., Tenore, F. V., and Bensmaia, S. J. (2015). Long-term stability of sensitivity to intracortical microstimulation of somatosensory cortex. *J. Neural. Eng.* 12:056010. doi: 10.1088/1741-2560/12/5/056010

Chen, K. H., Dammann, J. F., Boback, J. L., Tenore, F. V., Otto, K. J., Gaunt, R. A., et al. (2015). The effect of chronic intracortical microstimulation on the electrode-tissue interface. *J. Neural. Eng.* 11:026004. doi: 10.1088/1741-2560/11/2/026004

Chestek, C. A., Gilja, V., Blabe, C. H., Foster, B. L., Shenoy, K. V., Parvizi, J., et al. (2013). Hand posture classification using electrocorticography signals in the gamma band over human sensorimotor brain areas. *J. Neural. Eng.* 10:026002. doi: 10.1088/1741-2560/10/2/026002

Collins, K. L., Guterstam, A., Cronin, J., Olson, J. D., Ehrsson, H. H., and Ojemann, J. G. (2017). Ownership of an artificial limb induced by electrical

brain stimulation. *Proc. Natl. Acad. Sci. U.S.A.* 114, 166–171. doi: 10.1073/pnas.1616305114

Craggs, M. D., Rushton, D. N., and Clayton, D. G. (1976). The stability of the electrical stimulation map of the motor cortex of the anesthetized baboon. *Brain* 99, 575–600. doi: 10.1093/brain/99.3.575

Devecioglu, I., and Guclu, B. (2005). Psychophysical correspondence between vibrotactile intensity and intracortical microstimulation for tactile neuroprostheses in rats. *J. Neural. Eng.* 14:016010. doi: 10.1088/1741-2552/14/1/016010

Fifer, M. S., Acharya, S., Benz, H. L., Mollazadeh, M., Crone, N. E., and Thakor, N. V. (2012). Toward electrocorticographic control of a dexterous upper limb prosthesis: building brain-machine interfaces. *IEEE Pulse* 3, 38–42. doi: 10.1109/MPUL.2011.2175636

Flesher, S. N., Collinger, J. L., Foldes, S. T., Weiss, J. M., Downey, J. E., Tyler-Kabara, E. C., et al. (2016). Intracortical microstimulation of human somatosensory cortex. *Sci. Transl. Med.* 8:361ra141. doi: 10.1126/scitranslmed.aaf8083

Francisco, E., Tannan, V., Zhang, Z., Holden, J., and Tommerdahl, M. (2017). Vibrotactile amplitude discrimination capacity parallels magnitude changes in somatosensory cortex and follows Weber's Law. *Exp. Brain Res.* 191, 49–56. doi: 10.1007/s00221-008-1494-6

Griffin, M. J. (2012). Frequency-dependence of psychophysical and physiological responses to hand-transmitted vibration. *Ind. Health* 50, 354–369. doi: 10.2486/indhealth.ms1379

Hamilton, L. S., Chang, D. L., Lee, M. B., and Chang, E. F. (2017). Semi-automated anatomical labeling and inter-subject warping of high-density intracranial recording electrodes in electrocorticography. *Front. Neuroinform.* 11:62. doi: 10.3389/fninf.2017.00062

Heck, C. N., King-Stephens, D., Massey, A. D., Nair, D. R., Jobst, B. C., Barkley, G. L., et al. (1976). Two-year seizure reduction in adults with medically intractable partial onset epilepsy treated with responsive neurostimulation: final results of the RNS System Pivotal trial. *Epilepsia* 55, 432–441. doi: 10.1111/epi.12534

Hernandez, A., Zainos, A., and Romo, R. (2005). Neuronal correlates of sensory discrimination in the somatosensory cortex. *Proc. Natl. Acad. Sci. U.S.A.* 97, 6191–6196. doi: 10.1073/pnas.120018597

Hiremath, S. V., Tyler-Kabara, E. C., Wheeler, J. J., Moran, D. W., Gaunt, R. A., Collinger, J. L., et al. (2017). Human perception of electrical stimulation on the surface of somatosensory cortex. *PLoS One* 12:e0176020. doi: 10.1371/journal.pone.0176020

Hollins, M., and Risner, S. R. (2016). Evidence for the duplex theory of tactile texture perception. *Percept. Psychophys.* 62, 695–705. doi: 10.3758/bf03206916

Johnson, L. A., Wander, J. D., Sarma, D., Su, D. K., Fetz, E. E., and Ojemann, J. G. (2013). Direct electrical stimulation of the somatosensory cortex in humans using electrocorticography electrodes: a qualitative and quantitative report. *J. Neural. Eng.* 10:036021. doi: 10.1088/1741-2560/10/3/036021

Kim, S., Callier, T., Tabot, G. A., Gaunt, R. A., Tenore, F. V., and Bensmaia, S. J. (2015a). Behavioral assessment of sensitivity to intracortical microstimulation of primate somatosensory cortex. *Proc. Natl. Acad. Sci. U.S.A.* 112, 15202–15207. doi: 10.1073/pnas.1509265112

Kim, S., Callier, T., Tabot, G. A., Tenore, F. V., and Bensmaia, S. J. (2015b). Sensitivity to microstimulation of somatosensory cortex distributed over multiple electrodes. *Front. Syst. Neurosci.* 9:47. doi: 10.3389/fnsys.2015.00047

Klaes, C., Shi, Y., Kellis, S., Minxha, J., Revechkis, B., and Andersen, R. A. (2014). A cognitive neuroprosthetic that uses cortical stimulation for somatosensory feedback. *J. Neural. Eng.* 11:056024. doi: 10.1088/1741-2560/11/5/056024

Lee, B., Kramer, D., Armenta Salas, M., Kellis, S., Brown, D., Dobreva, T., et al. (2018). Engineering artificial somatosensation through cortical stimulation in humans. *Front. Syst. Neurosci.* 12:24. doi: 10.3389/fnsys.2018.00024

Lee, B., Liu, C. Y., and Apuzzo, M. L. (2013). A primer on brain-machine interfaces, concepts, and technology: a key element in the future of functional neurorestoration. *World Neurosurg.* 79, 457–471. doi: 10.1016/j.wneu.2013.01.078

Lee, B., Zubair, M. N., Marquez, Y. D., Lee, D. M., Kalayjian, L. A., Heck, C. N., et al. (2015). A Single-center experience with the NeuroPace RNS system: a review of techniques and potential problems. *World Neurosurg.* 84, 719–726. doi: 10.1016/j.wneu.2015.04.050

Luna, R., Hernandez, A., Brody, C. D., and Romo, R. (2005). Neural codes for perceptual discrimination in primary somatosensory cortex. *Nat. Neurosci.* 8, 1210–1219. doi: 10.1038/nn1513

Mountcastle, V. B., Talbot, W. H., Sakata, H., and Hyvarinen, J. (1969). Cortical neuronal mechanisms in flutter-vibration studied in unanesthetized monkeys. Neuronal periodicity and frequency discrimination. *J. Neurophysiol.* 32, 452–484. doi: 10.1152/jn.1969.32.3.452

O'Doherty, J. E., Lebedev, M. A., Ifft, P. J., Zhuang, K. Z., Shokur, S., Bleuler, H., et al. (2011). Active tactile exploration using a brain-machine-brain interface. *Nature* 479, 228–231. doi: 10.1038/nature10489

O'Doherty, J. E., Lebedev, M. A., Li, Z., and Nicolelis, M. A. (2012). Virtual active touch using randomly patterned intracortical microstimulation. *IEEE Trans. Neural. Syst. Rehabil. Eng.* 20, 85–93. doi: 10.1109/TNSRE.2011.2166807

Overstreet, C. K., Hellman, R. B., Ponce Wong, R. D., Santos, V. J., and Helms Tillery, S. I. (2016). Discriminability of single and multichannel intracortical microstimulation within somatosensory cortex. *Front. Bioeng. Biotechnol.* 4:91. doi: 10.3389/fbioe.2016.00091

Raspopovic, S., Capogrosso, M., Petrini, F. M., Bonizzato, M., Rigosa, J., Di Pino, G., et al. (2014). Restoring natural sensory feedback in real-time bidirectional hand prostheses. *Sci. Transl. Med.* 6:222ra19. doi: 10.1126/scitranslmed.3006820

Romo, R., Hernandez, A., Zainos, A., Brody, C. D., and Lemus, L. (2000). Sensing without touching: psychophysical performance based on cortical microstimulation. *Neuron* 26, 273–278. doi: 10.1016/s0896-6273(00)81156-3

Romo, R., Hernandez, A., Zainos, A., and Salinas, E. (1998). Somatosensory discrimination based on cortical microstimulation. *Nature* 392, 387–390. doi: 10.1038/32891

Salinas, E., Hernandez, A., Zainos, A., and Romo, R. (2000). Periodicity and firing rate as candidate neural codes for the frequency of vibrotactile stimuli. *J. Neurosci.* 20, 5503–5515. doi: 10.1523/jneurosci.20-14-05503.2000

Suminski, A. J., Tkach, D. C., Fagg, A. H., and Hatsopoulos, N. G. (2010). Incorporating feedback from multiple sensory modalities enhances brain-machine interface control. *J. Neurosci.* 30, 16777–16787. doi: 10.1523/JNEUROSCI.3967-10.2010

Tabot, G. A., Dammann, J. F., Berg, J. A., Tenore, F. V., Boback, J. L., Vogelstein, R. J., et al. (2013). Restoring the sense of touch with a prosthetic hand through a brain interface. *Proc. Natl. Acad. Sci. U.S.A.* 110, 18279–18284. doi: 10.1073/pnas.1221113110

Tabot, G. A., Kim, S. S., Winberry, J. E., and Bensmaia, S. J. (2015). Restoring tactile and proprioceptive sensation through a brain interface. *Neurobiol. Dis.* 83, 191–198. doi: 10.1016/j.nbd.2014.08.029

Tan, D. W., Schiefer, M. A., Keith, M. W., Anderson, J. R., Tyler, J., and Tyler, D. J. (2014). A neural interface provides long-term stable natural touch perception. *Sci. Transl. Med.* 6:257ra138. doi: 10.1126/scitranslmed.3008669

Vardar, B., and Guclu, B. (2017). Non-NMDA receptor-mediated vibrotactile responses of neurons from the hindpaw representation in the rat SI cortex. *Somatosens. Mot. Res.* 34, 189–203. doi: 10.1080/08990220.2017.1390450

Vidal, G. W., Rynes, M. L., Kelliher, Z., and Goodwin, S. J. (2016). Review of brain-machine interfaces used in neural prosthetics with new perspective on somatosensory feedback through method of signal breakdown. *Scientifica* 2016:8956432. doi: 10.1155/2016/8956432

Conflict of Interest Statement: The authors declare that the research was conducted in the absence of any commercial or financial relationships that could be construed as a potential conflict of interest.

frontiers in Neuroscience

REVIEW
published: 07 August 2019
doi: 10.3389/fnins.2019.00804

Direct Electrical Stimulation in Electrocorticographic Brain–Computer Interfaces: Enabling Technologies for Input to Cortex

David J. Caldwell[1,2,3], *Jeffrey G. Ojemann*[3,4] *and Rajesh P. N. Rao*[1,3,5]*

[1] *Department of Bioengineering, University of Washington, Seattle, WA, United States,* [2] *Medical Scientist Training Program, University of Washington, Seattle, WA, United States,* [3] *Center for Neurotechnology, University of Washington, Seattle, WA, United States,* [4] *Department of Neurological Surgery, University of Washington, Seattle, WA, United States,* [5] *Paul G. Allen School of Computer Science and Engineering, University of Washington, Seattle, WA, United States*

Electrocorticographic brain computer interfaces (ECoG-BCIs) offer tremendous opportunities for restoring function in individuals suffering from neurological damage and for advancing basic neuroscience knowledge. ECoG electrodes are already commonly used clinically for monitoring epilepsy and have greater spatial specificity in recording neuronal activity than techniques such as electroencephalography (EEG). Much work to date in the field has focused on using ECoG signals recorded from cortex as control outputs for driving end effectors. An equally important but less explored application of an ECoG-BCI is directing input into cortex using ECoG electrodes for direct electrical stimulation (DES). Combining DES with ECoG recording enables a truly bidirectional BCI, where information is both read from and written to the brain. We discuss the advantages and opportunities, as well as the barriers and challenges presented by using DES in an ECoG-BCI. In this article, we review ECoG electrodes, the physics and physiology of DES, and the use of electrical stimulation of the brain for the clinical treatment of disorders such as epilepsy and Parkinson's disease. We briefly discuss some of the translational, regulatory, financial, and ethical concerns regarding ECoG-BCIs. Next, we describe the use of ECoG-based DES for providing sensory feedback and for probing and modifying cortical connectivity. We explore future directions, which may draw on invasive animal studies with penetrating and surface electrodes as well as non-invasive stimulation methods such as transcranial magnetic stimulation (TMS). We conclude by describing enabling technologies, such as smaller ECoG electrodes for more precise targeting of cortical areas, signal processing strategies for simultaneous stimulation and recording, and computational modeling and algorithms for tailoring stimulation to each individual brain.

Keywords: electrocorticography, brain–computer interface (BCI), direct electrical stimulation, intracranial electrodes, plasticity induction, neuroprosthetic, sensory restoration, neuromodulation

OPEN ACCESS

Edited by:
Aysegul Gunduz,
University of Florida, United States

Reviewed by:
Peter Brunner,
Albany Medical College, United States
David Thomas Bundy,
University of Kansas Medical Center Research Institute, United States

***Correspondence:**
Rajesh P. N. Rao
rao@cs.washington.edu

Specialty section:
This article was submitted to Neuroprosthetics, a section of the journal Frontiers in Neuroscience

Received: *01 March 2019*
Accepted: *18 July 2019*
Published: *07 August 2019*

Citation:
Caldwell DJ, Ojemann JG and Rao RPN (2019) Direct Electrical Stimulation in Electrocorticographic Brain–Computer Interfaces: Enabling Technologies for Input to Cortex. Front. Neurosci. 13:804. doi: 10.3389/fnins.2019.00804

INTRODUCTION

Electrocorticography (ECoG) is used clinically as a recording modality for diagnosing specific spatial regions of focal epilepsy onset in individuals suffering from medically intractable epilepsy. By using invasive monitoring, the origins of seizures can be identified, and subsequent surgical removal of the seizure foci can reduce the frequency of or eliminate seizures. After surgical resection, approximately 50% or greater of patients experience significantly improved seizure control following surgical treatment (Englot and Chang, 2014). For monitoring, patients are routinely implanted for 1–2 weeks with electrodes either directly on top of the dura (epidural), beneath the dura (subdural), or implanted in cortex [depth electrodes, or stereo electroencephalography (sEEG)]. The term intracranial EEG, or iEEG, is often used to describe all implanted electrodes. We will use the term ECoG electrodes in this article to encompass surface as well as penetrating depth electrodes. Following electrode implantation, patients remain in the hospital under clinical monitoring by a team of neurologists and epilepsy technicians, until the clinical team has collected enough data to precisely localize the focal seizure zones for surgical resection.

To complement the passive recording of epileptic events, direct electrical stimulation (DES) (Vincent et al., 2016b) [or when applied particularly to cortex, known as direct cortical stimulation (DCS) (Giussani et al., 2010), or direct electrical cortical stimulation (DECS)] through ECoG electrodes is commonly performed for clinical mapping purposes, both intraoperatively and during the patients' clinical observation. For clinical mapping the clinical team electrically stimulates different brain regions to delineate regions of cortex important for language, motor, and sensory function. By stimulating particular brain areas and observing the effects by querying the patient, the clinical team can avoid resecting areas important for cognitive function and preserve these functions in an individual after surgical resection. The combination of recording and mapping through stimulation enables the clinical team to be best informed when making clinical decisions regarding reducing or eliminating seizures through resection, while maintaining cortical function. Clinical teams perform stimulation of both cortical and subcortical structures and pathways. We use the term DES here to refer to general electrical stimulation of any brain region through implanted electrodes, while we consider DCS a subcategory specifically describing stimulation of surface gray matter.

Direct electrical stimulation for clinical uses goes beyond delineating cortical regions of activity. For example, deep brain stimulation (DBS) is a therapy currently being used for therapeutic treatment of movement disorders and psychiatric illnesses. Electrodes similar to those used for sEEG are implanted into deep brain structures, and stimulation helps ameliorate clinical symptoms. The space of DBS research is vast, and we will not go into extensive detail in this review. Instead, we highlight the widespread use of DBS as a demonstration of the therapeutic use of clinical stimulation through implanted electrodes, and we draw from current research in the DBS field to frame future directions for DES.

In this article, we first review the characteristics of implanted electrodes, the effect of electrical stimulation through them on cortex, and the nature of signals recorded through them. We then discuss current clinical uses of DES for disorders such as epilepsy, and briefly cover DBS and its applications for diseases such as Parkinson's disease and essential tremor. We also discuss some of the translational, regulatory, financial, and ethical concerns with ECoG-BCIs. We subsequently describe how ECoG-based DES can be used to provide sensory feedback and to probe and modify cortical connectivity. We then review future applications of DES in ECoG-BCIs, which may draw from invasive animal studies with penetrating and surface electrodes and non-invasive stimulation methods such as transcranial magnetic stimulation (TMS) and transcranial electrical stimulation (TES). We discuss how enabling technologies, such as smaller ECoG electrodes for more precise targeting on smaller spatial scales, software and hardware that allow simultaneous stimulation and recording, and computational modeling for tailoring stimulation to individual patients, could enable the realization of full-fledged bidirectional ECoG-BCIs for a variety of applications.

THE ELECTRICAL-NEURAL INTERFACE

Electrodes

Current clinically used ECoG electrodes are often embedded in a silicone sheet and are made of platinum or stainless steel. The electrodes are 1.5 mm diameter circular contacts with 4 mm spacing ("micro"-ECoG electrodes)[1], to 2.3–3 mm diameter contacts with 10 mm spacing for "macro"-ECoG electrodes (Chang, 2015). Depth electrodes are frequently comprised of platinum, with cylindrical contacts, and can be inserted with or without stereotactic guidance. These are commonly used to localize seizures coming from deep brain structures, such as the hippocampus. DBS electrodes are similar to depth electrodes in that they are linear probes with cylindrical contacts, although they can be of smaller diameter, with tighter electrode spacing and fewer contacts.

Stimulation

Implanted electrodes can be used for direct modulation of neural activity through electrical stimulation. In order to better understand the underlying mechanisms of stimulation, we first consider the effects of stimulation on a single neuron. At the single neuron level, the redistribution of charge, and subsequent depolarization, where the inside of the cell becomes more positive relative to the extracellular fluid, can cause an action potential to be generated which propagates down the cell's axon. Hyperpolarization, which occurs when the inside of the cell becomes more negative relative to the outside of the cell, can inhibit action potentials. Electrical stimulation, through a redistribution of charge within an axon, can result either in hyperpolarization or depolarization. When sufficient

[1]We discuss advances in research-grade microECoG electrodes with much smaller electrode contact size and tighter spacing in the section "Enabling Technologies – Materials and Electronics."

depolarization is achieved, an action potential is generated through the diffusion of ions through sodium, potassium, and calcium channels (Bean, 2007). Subthreshold intracellular stimulation, where an action potential is not generated, can result in the potentiation of synaptic strength with NMDA receptor mediation in the neuron's synapses (Alonso et al., 1990).

In solutions, electrical stimulation results in the redistribution of ions through non-Faradaic reactions, and the transfer of electrons to electrolytes in the solution through Faradaic reactions (Merrill et al., 2005). There exist both reversible and irreversible Faradaic reactions: which one occurs depends on the rate of the electron transfers relative to the mass transport of the reactant. We discuss these reactions further and the impact of stimulation parameters on them in the section "Limitations and Considerations." Through these mechanisms, charge is redistributed. When this redistribution of charge causes depolarization directly beneath the electrode, for the case of a single neuron, the stimulation is often referred to as cathodal stimulation, while electrical stimulation which causes hyperpolarization directly beneath the electrode is referred to as anodal stimulation (**Figure 1A**). On the scale of larger electrodes, such as with ECoG arrays, cathodal stimulation often refers to negative voltages and currents directly beneath the electrode, while anodal stimulation refers to positive voltages and currents.

Stimulation on a local scale can be achieved through intracortical microstimulation (ICMS), where electrical stimulation activates neurons primarily through their axons passing through the region of cortex stimulated (Nowak and Bullier, 1998; Tehovnik et al., 2006). However, other regions of the cell such as the cell body and dendrites may also be activated depending on stimulus polarity and orientation. Anodal pulses best activate cell bodies and terminals, compared to cathodal pulses which best activate axons (McIntyre and Grill, 2000). In both cases, it is the outward flowing current at the axon initial segment or nodes of Ranvier along the axon that results in neuronal excitation (McIntyre and Grill, 2000; Tehovnik et al., 2006). ICMS is thought to sparsely activate a population of cortical neurons, rather than just ones proximal to the stimulation electrode tip (Histed et al., 2009).

The distance of neuron elements from the stimulation source changes whether or not these elements will be hyperpolarized or depolarized by a corresponding cathodic or anodic stimulus. Directly beneath a cathode, a membrane will become depolarized, and hence can generate an action potential. During the case of anodal stimulation, the area directly beneath the electrode is hyperpolarized, but further away from the anode, action potentials may be generated, resulting in a "virtual cathode" (Merrill et al., 2005) (**Figure 1A**). Stimulation beneath the anode can occur with surface anodal stimulation of neocortical cells, where current hyperpolarizes apical dendrites, and subsequently leaves through the axon resulting in depolarization (Ranck, 1975) (**Figure 1B**). For the case of bipolar stimulation, an axon is generally depolarized beneath the cathode and hyperpolarized beneath the anode (Ranck, 1975).

Physiologically, ICMS is thought to activate both inhibitory and excitatory populations of cells (Butovas and Schwarz, 2003), and is not thought to evoke natural patterns of cortical activity (Millard et al., 2015). Functional magnetic resonance imaging (fMRI) along with microstimulation has demonstrated that microstimulation, at least in the visual cortical pathway, suppresses the output activity of neurons which have their afferents stimulated (Logothetis et al., 2010). Further work in microstimulation of the visual cortex has demonstrated that microstimulation in V1 may locally activate cells, but silence neurons further downstream (Klink et al., 2017).

The frequency of ICMS also has an impact on whether neurons are excited or inhibited. High frequency stimulation (>10 Hz) is thought to potentiate neural activity (long-term potentiation) (Bliss and Lomo, 1973; Douglas, 1977), while low frequency stimulation (<1 Hz) is thought to depress neural activity (long-term depression) (Mulkey and Malenka, 1992).

Compared to ICMS, DES of human cortex using larger electrodes, such as ECoG or DBS electrodes, injects current over a larger surface area, and subsequently large amounts of current could lead to greater activation with the potential to spread to a larger area (Vincent et al., 2016a) (**Figures 1C,D**). Additionally, depending on the anatomic location of DES, stimulation can either evoke or inhibit neural activity (Borchers et al., 2012). For example, DES of language areas during a language task can disrupt speech production while DES of somatosensory cortex can evoke sensations and DES of motor cortex can evoke movements. In terms of subdural ECoG stimulation in humans, the patterns and types of cells activated are thought to depend on the intricate details of cortical geometry, cell fiber orientation (Kudela and Anderson, 2015), and whether the pulses are anodal or cathodal (Seo et al., 2015) (**Figures 1C,D**). A finite element model (FEM) of subdural cortical stimulation with integrated neuron models was used to demonstrate that neurons deeper in the bank (buried in cortex) are more activated during cathodal subdural stimulation, while those in the wider crown are activated during anodal stimulation (Seo et al., 2015). DES through ECoG electrodes can result in both local effects, and effects remote to stimulation. The resultant signals at other electrodes are often referred to as cortico-cortico evoked potentials (CCEP) (Keller et al., 2014b). These have been reviewed thoroughly by Keller et al. (2014b, for more details). We will therefore only review some of the relevant physiology here. Pyramidal cells, which are the source of the majority of cortical output, and lie in cortical layers 2, 3, 5, and 6 can have their superficial dendritic trees depolarized. Layer 2/3 inhibitory GABA interneurons can be depolarized, which then synapse preferentially near the soma of pyramidal cells (Brill and Huguenard, 2009) and cause a decrease in pyramidal cell activity due to the inhibitory nature of GABA signaling. If there are axons passing through the region of stimulation, both orthodromic and antidromic stimulation can occur (Keller et al., 2014b). The measured surface potentials are therefore a combination of the initial monosynaptic connections, cortico-cortical pathways, and cortico-subcortical pathways which would explain the polymorphic response lasting hundreds of milliseconds (Matsumoto et al., 2006).

The mechanisms of DBS stimulation are not yet currently understood, and are thought to involve the modulation of the networks targeted by the stimulation, rather than involving solely

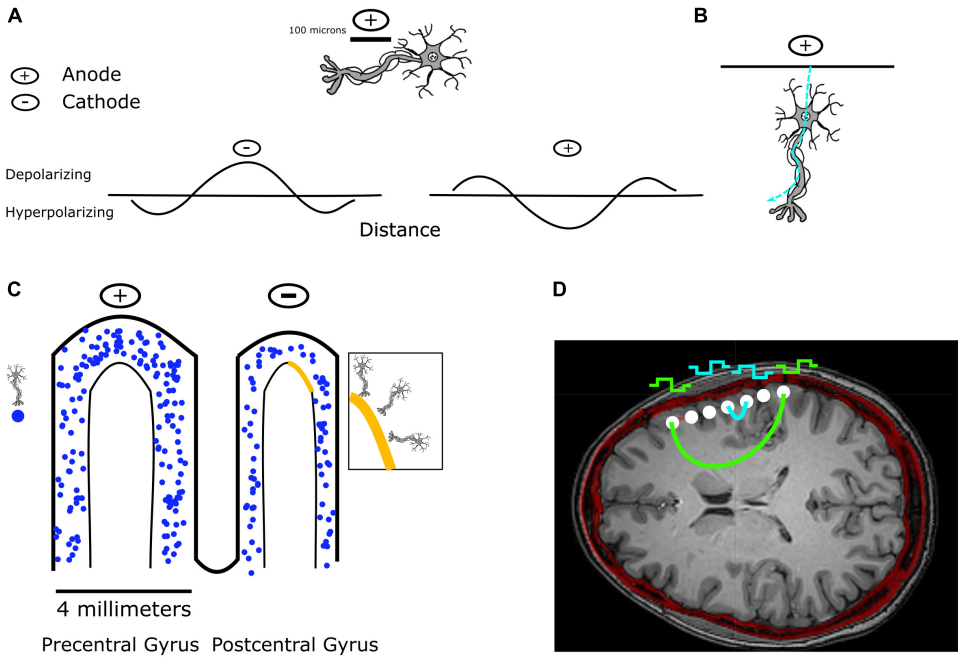

FIGURE 1 | Effect of stimulation on a single neuron and on a population of neurons. **(A)** Stimulation along a nerve fiber results in depolarization beneath the cathode, and hyperpolarization beneath an anode. **(B)** Single neurons can be stimulated by both anodal and cathodal stimulation depending on their orientation. In this example, anodal current enters the dendrites of the neuron and leaves through the axon, which results in depolarization of the axon and an action potential. **(C)** In the case of stimulation through ECoG electrodes, a large population of neurons can be activated by stimulation. Shown are approximate scales of an ECoG electrode relative to the precentral and postcentral gyrus, along with a representative mixed population of pyramidal neurons potentially depolarized by stimulation. In the zoomed-in region, we highlight the multiple orientations of neurons that could be activated. **(D)** An axial slice in a co-registered CT and MRI image following implantation with an ECoG array shows the potential current paths that different stimulation configurations would have to pass through, illustrating the large populations of neurons present within the potential current path. **(A,B)** Inspired by Ranck (1975).

immediate inhibitory effects on the targeted anatomic region (Montgomery and Gale, 2008; Ashkan et al., 2017).

In summary, the results reviewed in this section speak to the immense complexities of engineering stimulation in humans and the work that remains to be done in understanding both its physical and neural effects.

Sensing

A key part of a BCI is the recording of neural activity to use as a control signal in order to successfully modulate the system using stimulation. The summed activity of many hundreds of thousands of neurons in the cortical tissue under an ECoG electrode contributes to the electric voltage recorded from the electrode. The increased firing rate of populations of neurons results in a broad increase in power across all frequencies, which is more easily separable in the broadband gamma band (above 50 Hz), rather than the lower frequency bands (Miller et al., 2008). This is because other frequency bands modulate up and down independently during different tasks and brain states, masking the broadband increase in power. The higher frequency components are more asynchronous, and therefore are not as subject to this masking effect (Hermes et al., 2017). Lower frequency bands, such as the alpha (8–12 Hz) and beta (13–30 Hz) band, are thought to represent pulsed inhibition that serves to gate and coordinate neuronal firing (Schalk, 2015). Therefore, analysis of broadband gamma activity reveals the local neuronal firing dynamics, while analysis of theta (4–8 Hz), alpha, and beta frequency regimes yields insight into the coordinating mechanisms across the brain.

The different oscillatory features discussed above have been explored for advancing our understanding of how different cortical regions function during motor movement and language function (Bouchard et al., 2013; Flint et al., 2017). Measurements of these signals during motor and speech imagery have been employed in ECoG brain–computer interfaces to drive end effectors such as computer cursors (Leuthardt et al., 2004, 2006a,b) and robotic arms (Hotson et al., 2016). Furthermore, non-motor regions can be used to drive ECoG-BCIs as well, illustrating the general utility of oscillatory band driven BCIs (Ramsey et al., 2006; Wilson et al., 2006).

CURRENT CLINICAL USES OF DIRECT ELECTRICAL STIMULATION

Functional Mapping for Epilepsy and Tumors

As detailed in the introduction, DES is frequently used both intraoperatively and during a patient's stay at the hospital for functional mapping and identifying areas of cortex associated

with important cognitive functions (Berger et al., 1989; Ojemann et al., 1989; Berger and Ojemann, 1992). These mapping procedures are done both for epilepsy surgery and tumor resections (Berger et al., 1989; Ojemann et al., 1989; Berger and Ojemann, 1992). Clinicians, using implanted ECoG electrodes or stimulators in the operating room, apply DES to various cortical and subcortical structures and pathways, and observe location dependent effects, including speech arrest in language regions, motor movements in motor cortex, and sensory percepts in somatosensory cortex. The results of these stimulation studies inform where the surgeons will plan to resect; for example, if the seizure focus is close to a language region, the surgeon and patient may decide the surgery is not worth the risk of a permanent language deficit.

Deep Brain Stimulation

Deep brain stimulation is a prominent example of electrical stimulation of the brain. It is currently being used for therapeutic treatment of movement disorders [Parkinson's disease (Bronstein et al., 2011) and Essential Tremor (Della Flora et al., 2010)], and is also being explored for treating psychiatric illnesses (post-traumatic stress disorder, depression, obsessive compulsive disorder, Tourette syndrome, Schrock et al., 2015) and epilepsy treatment. Traditionally, linear probes of cylindrical contacts are inserted into deep brain structures such as the globus pallidus internus (GPi), subthalamic nucleus (STN), or ventral intermediate nucleus of the thalamus (VIM). Following implantation, clinicians may either be guided by intraoperative CT imaging, or wake the patient up intraoperatively to test for adverse effects of stimulation on different contacts, using a monopolar (one stimulating electrode and a distant return electrode), bipolar (two similarly sized electrodes), or multipolar arrangement of electrodes for the steering of current.

Advances in BCI related to DBS have explored the use of closed loop DBS to trigger stimulation of deep brain structures in response to signals recorded from the surface of the cortex (Herron et al., 2017). Herron et al. used threshold crossing in the beta-band regime of recorded ECoG signals over motor cortex as a control decision to trigger DBS stimulation. This enables control of DBS stimulation solely through recorded neural signals. Besides potentially reducing the side-effects of open-loop stimulation, such closed-loop control of stimulation conserves power and helps extend the life of the DBS device, reducing the number of replacement surgeries needed over the life of a user. Adaptive DBS based on recordings in STN has been demonstrated to improve motor scores over traditional open-loop DBS (Little et al., 2013). In addition, primate models of Parkinson's disease demonstrate that closed-loop DBS has a greater effect than open-loop DBS on akinesia and on the neuronal output in both cortical and subcortical structures (Rosin et al., 2011).

Finally, DBS is also being explored for the treatment of particular types of epilepsy. Partial onset seizures often spread through the circuitry of the basal ganglia, and therefore could be controlled using DBS strategies similar to those used for movement disorders (Halpern et al., 2008; Lega et al., 2010).

Closed Loop Stimulation for Epilepsy

Closed loop stimulation to control seizures is currently clinically available to epilepsy patients through the Neuropace RNS system (Morrell, 2011; Lee et al., 2015). A neurosurgeon implants ECoG electrodes either on the cortical surface or in deeper structures near the putative seizure focus. If an impending seizure is detected, high frequency stimulation is triggered near the seizure focus to control the seizure. This is a demonstration of clinically effective and already implemented DES in an ECoG-BCI, where neural control signals are acquired in real time from the brain and used to trigger stimulation.

ADVANTAGES OF DES RELATIVE TO OTHER STIMULATION TECHNIQUES

An advantage of DES relative to non-invasive electrical stimulation modalities is the delivery of much greater amounts of the applied current to neurons. During TES[2], as much as 75% of the current is shunted through the scalp and the skull (Vöröslakos et al., 2018; Widge, 2018). This greatly blunts the efficacy of cortical stimulation, and suggests that some of the published results using TES are due to mechanisms other than direct neuronal excitation. In contrast, by directly stimulating the brain and bypassing the skull and scalp, DES delivers current to cortical structures more effectively. Although the currents applied during TES could be raised to a high enough level to reach a desired electric field strength at a target location in the brain, there would be potential off-target effects and skin damage due to the amount of current required, in contrast to DES through electrodes implanted precisely at the targeted site for this same electric field strength. This reinforces a large advantage of the DES relative to TES, which is the ability to place electrodes close to the target structures, and consequently minimize the amount of current passing through off-target structures.

Even with epidural and subdural stimulation, not all current reaches neurons in the cortex. Epidural stimulation results in current shunting by the dura (Wongsarnpigoon and Grill, 2008), while both epidural and subdural stimulation have some degree of cerebrospinal fluid (CSF) shunting depending on the characteristics of the CSF beneath or surrounding the electrodes (Wongsarnpigoon and Grill, 2008; Guler et al., 2018).

A factor in epidural and subdural stimulation is the presence of pain receptors within the dura which can be activated with dural stimulation (Wirth and Van Buren, 1971). However, previous clinical trials with epidural stimulation made no reports of dural pain with stimulation up to 6.5 mA and 250 μs pulse widths (Levy et al., 2008).

Transcranial magnetic stimulation has primarily been used to induce motor movements, rather than isolated sensory percepts (although phosphenes can often be produced via TMS, and tapping sensations and auditory clicks can accompany TMS) (Sliwinska et al., 2014). A method such as DES affords the ability

[2]We use this term to encompass transcranial direct current stimulation (tDCS) and transcranial alternating current stimulation or (tACS).

to focally and specifically produce sensations that would not be achievable through TMS.

Additionally, traditional figure-8 TMS coils are currently unable to target cortical structures beyond 2–3 cm deep (Roth et al., 1991; Wagner et al., 2009). DES electrodes, on the other hand, can be physically placed in deeper regions of interest in order to elicit the desired stimulation effects. Another advantage of DES over TMS is the fact that the maximum of the electric field strength induced by TMS has to occur at the cortical surface rather than deeper structures (Heller and van Hulsteyn, 1992). This means that off-target effects in cortical layers near the surface are possible when targeting deeper structures. Even with more sophisticated coils, such as the H-coil, the maximum stimulation strength still occurs at the surface and greater depth of stimulation (4–6 cm) is achieved with a loss of focality (Zangen et al., 2005; Wagner et al., 2009). Although the field strength is greatest at the cortical surface for TMS, the orientation of neurons is a critical component in the activation of neurons, as both experimental and modeling work has shown that electric fields tangential to the sulcal walls can activate neurons oriented perpendicularly to them (Fox et al., 2004; Silva et al., 2008; Seo et al., 2016). Similarly, different layered pyramidal neurons are activated differently between the gyral crown and sulcus walls (Silva et al., 2008; Seo et al., 2016). This in total points to the complex physiologic effects of TMS, and the potential difficulties in activating groups of neurons both on the crown of the gyrus and within the sulcus together. A further disadvantage of TMS is that with current hardware, use outside of the lab is limited due to the bulky hardware and the need to maintain a precise spatial relationship between the coil and the head for stimulation.

The fact that DES electrodes can be placed near the deeper structures of interest is vital for the treatment of Parkinson's and Essential Tremor through DBS. As these structures cannot currently be effectively stimulated through alternative methods such as TMS, effective clinical treatment relies upon DES via electrodes near the desired brain regions.

FINANCIAL, TRANSLATIONAL, REGULATORY, AND ETHICAL CONCERNS FOR DES IN ECOG-BCIS

Translational, Regulatory, and Financial Concerns

We expect early applications of ECoG-BCIs to leverage existing clinical devices. This has been a pathway forward for many prior medical devices. Advances in early DBS devices were based largely off of prior work in cardiac pacemaker and spinal cord stimulation devices (Coffey, 2009). We imagine a similar trajectory for DES in ECoG-BCIs. Preliminary use of DES has been enabled by investigational device exemptions (Harvey and Winstein, 2009). Further iterations of Medtronic DBS devices, such as the PC + S device, have been granted an investigational device exemption in research studies, and are improvements upon an already clinically approved device (Herron et al., 2017).

Whenever new technology is implemented for clinical treatment, a question of cost efficacy is raised. However, we suggest that ECoG-BCIs have the potential to be cost effective long-term devices if clinical efficacy is demonstrated, as illustrated by examples such as vagus nerve stimulators and DBS. Vagus nerve stimulation for epilepsy has been show to be effective long-term, and cost benefit analysis has shown that the cost of the treatment pays off within a 2 year period (Boon et al., 1999). Although it is not universally the case, DBS in general is thought to be cost effective, when looking at studies across European and North American Centers (Pereira et al., 2007). It has been noted that during the adoption of DBS large-volume hospitals had lower prices and superior short-term outcomes, which is something to be aware of in the translation of ECoG-BCIs into the clinic (Eskandar et al., 2009).

Ethical Concerns

Ethical concerns are critical to address for any engineered device which is implanted in a patient. A previous review has explored some of the ethical concerns for BCIs (Klein and Ojemann, 2016), and we seek here to highlight some of the concerns which are particularly relevant to ECoG-BCIs with DES.

Articulating the potential risks and long-term requirements for an ECoG-BCI, particularly with DES, is essential for appropriate informed consent. Biologic risks such as infection, seizures, and tissue damage from stimulation (Cogan et al., 2016) are accompanied by technological concerns such as repeated surgeries for battery replacements, heating due to potential wireless charging, and lifetime electrode wear from repeated stimulation (Klein and Ojemann, 2016).

Privacy and security are another key aspect in implantable medical devices, particularly with any BCIs that communicate signals wirelessly or can be programed wirelessly. One can imagine situations where a stimulator could be set to either less than therapeutic levels or to unsafe levels, by malware transmitted to the ECoG-BCI device. Research efforts that build on current security and privacy protocols for medical devices are required to ensure neural signal security and protection against malevolent programing.

RESEARCH DIRECTIONS FOR DES IN ECOG-BCI

We discuss various research directions for ECoG-BCIs, with an emphasis on future engineered applications. A previous review (Wander and Rao, 2014) has explored the use of brain–computer interfaces for investigating scientific questions in the nervous system. Further information on classical ECoG-BCIs and comparison to other types of BCIs can be found in Rao (2013).

Sensory Feedback Through DES

One potential use of ECoG-based stimulation currently being explored is the restoration of sensory feedback for those suffering from disorders such as paralysis. There is a large clinical need, as it is estimated that 5.4 million Americans are living with paralysis, with an estimated 41.8% of people with paralysis unable

to work (Christopher and Dana Reeve Foundation, 2013). The restoration of sensation is a priority for prosthetics users (Biddiss et al., 2007) as well as potential BCI end users such as individuals with paralysis (Anderson, 2004; Collinger et al., 2013). Sensory feedback to cortex would enhance the efficacy of a prosthetic arm to aid with independent tasks, or help an individual better interpret data from body mounted sensors. The lack of sensory feedback in many existing brain–computer interfaces (BCIs) may limit performance (Bensmaia and Miller, 2014; Delhaye et al., 2016). Indeed, integration of somatosensory feedback into BCIs has been demonstrated to improve task performance with BCIs (Suminski et al., 2010; Klaes et al., 2014; Dadarlat et al., 2015; Pistohl et al., 2015; Schiefer et al., 2016).

Prior work has shown that humans can respond to DES of the surface of the primary somatosensory (S1) cortex (Ray et al., 1999; Libet et al., 1964; Johnson et al., 2013; Hiremath et al., 2017), which results in an artificial sensory percept organized according to the standard somatotopy of cortex. Cronin et al. (2016) demonstrated that DES of S1 could be used by an individual in the absence of visual feedback to perform a motor task. Although these percepts would not be mistaken by the individuals for natural touch (Johnson et al., 2013; Cronin et al., 2016; Collins et al., 2017), they are useful for performing closed-loop BCI tasks. An open question is how using DES for feedback compares to a normal somatosensory pathway. One way of assessing this is through response times, which have recently been demonstrated to be slower for DES relative to natural touch (Caldwell et al., 2019). This speaks to the complex effects of stimulation and requires further exploration. Another key consideration for neuroprosthetic use is the embodiment of the prosthetic device. DES through ECoG has been shown to induce prosthetic hand ownership, suggesting that prostheses could be made to feel more natural as a result of DES (Collins et al., 2017).

With recent advances in materials and manufacturing, spatially smaller microECoG arrays are able to target smaller volumes of cortex. More targeted DES through microECoG grids allows higher spatial selectivity relative to larger clinical electrode grids (Hiremath et al., 2017; Lee et al., 2018), opening up the possibility of encoding more complex percepts compared to larger electrodes.

Although short term studies have demonstrated that these percepts induced by DES do not feel natural, the principles of neuroplasticity, which are prevalent in somatosensory cortex and other associated regions, and adaptation within the cortex (Miller and Weber, 2011; Weber et al., 2012; Thomson et al., 2013) will be relevant in the long-term implementation of DES in ECoG-BCIs for sensory restoration.

A BCI application with DES (**Figure 2**) could use signals from motor cortex to drive a sensorized prosthetic arm, which could provide feedback about the task via DES of primary somatosensory cortex (**Figure 2A**). Depending on the potential parameter space of discernible stimulation percepts, a user could learn to map physical contact locations on the prosthetic arm to distinct stimulation percepts (**Figure 2B**) providing feedback from external sensors directly to the brain The recent demonstrations of usable sensory signals in humans via DES brings us a step closer to such closed-loop human BCIs.

Quantification of Cortical Connectivity

An additional application of DES is in quantifying cortical connectivity. DES of a cortical site can produce a cortico-cortical evoked potential (CCEP) at local and remote sites depending on the cortical area stimulated and the intensity of stimulation (Keller et al., 2014b). Studies have explored CCEPs in the context of different cortical networks, including language (Matsumoto et al., 2004) and motor regions (Matsumoto et al., 2006). The connections probed with CCEPs correspond well with known functional networks observed through fMRI as well as white matter pathways confirmed by diffusion tensor imaging (DTI) (Keller et al., 2014a). Such evoked potentials could have utility in BCI applications where depending on the presence or modulation of these CCEPs, an algorithmic decision could be made.

Modification of Cortical Excitability and Induction of Plasticity

Another use for DES currently being explored is the induction of cortical plasticity. This refers to enhancement or other modification of connectivity between different cortical regions, which could aid in the recovery of individuals suffering from disrupted neuronal communication due to injuries such as stroke. To put the clinical need in perspective, there are millions of individuals worldwide who are disabled due to stroke. It is estimated that in the US alone for the year 2016, healthcare and economic costs related to stroke disability totaled $34 billion with stroke being a leading cause of serious long-term disability (CDC, 2015). 50–70% of stroke survivors reach functional independence, but 15–30% of survivors are permanently disabled (Lloyd-Jones et al., 2010). Therapies using targeted activity-dependent neuromodulation may help restore motor recovery (Harvey et al., 2009) but the biological effects of cortical stimulations are not well understood, and the parameters for potentially effective stimulation protocols need further development. Studies with smaller populations of neurons, animal models, and non-invasive stimulation may lend insight into the optimal protocols for plasticity induction.

A persistent theme in cortical connectivity is the idea of Hebbian plasticity, a type of synaptic plasticity first proposed by Hebb (1949): presynaptic firing of one neuron (site A) can strengthen the connection between it and a postsynaptic neuron (site B) that fires soon after A. Bi and Poo demonstrated a version of this plasticity rule, known as spike timing dependent plasticity (STDP), in rat hippocampal slice cells: consistent firing of a presynaptic cell (site A) within a time window of 20–30 ms before another postsynaptic cell (site B) led to a strengthened connection (LTP) from A to B, while B firing in a time window of 20–30 ms before A led to a weakened connection (LTD) (Bi and Poo, 1998). Both of these mechanisms were determined to be dependent on NMDA receptors.

These principles have been applied to induce plasticity in non-human primate (NHP) motor cortex (Jackson et al., 2006) and rodent rehabilitation experiments, where triggering stimulation in somatosensory cortex several milliseconds after premotor cortex firing in rats that suffered from damage to motor

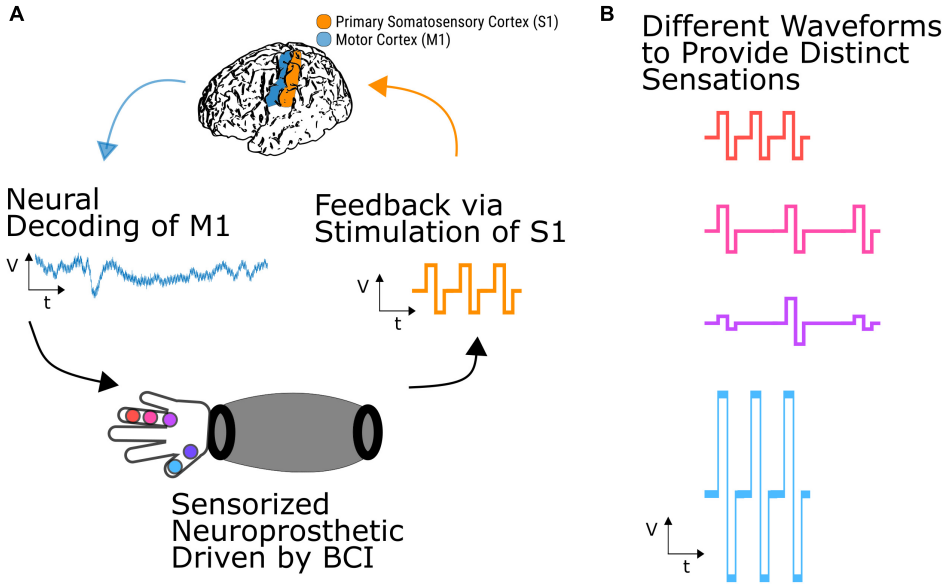

FIGURE 2 | Somatosensory BCI with closed-loop stimulation. **(A)** Neural signals recorded from cortical regions such as primary motor cortex could be used to drive a sensorized prosthetic arm. Feedback about task performance or object manipulation could then be conveyed to the user by DES of primary somatosensory cortex. **(B)** Different stimulation parameters, such as amplitude, frequency, and carrier frequency shape, could convey different percepts which a user could learn to map to locations on the neuroprosthetic arm.

cortex resulted in increased functional performance (Guggenmos et al., 2013). Other work has explored the use of paired-pulse paradigms in NHPs to induce plasticity: where concurrent surface to depth stimulation at one site was consistently followed by stimulation at another site with a fixed time lag (Seeman et al., 2017). The optimal time lag for potentiation was found to be between 10–30 ms, with longer delays not resulting in potentiation. Only a fraction of the sites in this study were potentiated, and effects were often seen globally, illustrating the complex factors influencing cortical plasticity. A recent study in NHPs examined the timing of DES relative to the aggregate activity of neurons: DES delivered during beta oscillations during the depolarizing potential (negative peak as recorded through LFPs) caused potentiation of cortical connectivity, while DES delivered during the hyperpolarizing potential caused depression of cortical connectivity as assessed through cortically evoked potentials (Zanos et al., 2018).

Beyond work in animals, and importantly, for applications such as stroke rehabilitation, recent work has reported improvements in physiological measures of motor function with non-invasive stimulation such as movement triggered TMS compared to random TMS stimulation (Buetefisch et al., 2011). Adding further support to the importance of brain state dependent stimulation for rehabilitation is a recent study that demonstrated TMS delivery during movement-related beta-band (16–22 Hz) desynchronization caused a significant increase in corticospinal excitability, as evaluated through motor evoked potentials, lasting beyond the period of stimulation (Kraus et al., 2016).

Keller et al. (2018) demonstrated that repetitive 10 Hz DES using subdural electrodes induced both potentiation and suppression in different cortical sites, depending on the baseline network characteristics. This suggests that plasticity can indeed be modulated through DES in humans, and that individual patient models of connectivity may inform the optimal sites to target to either enhance or decrease connection strength.

An example BCI application for neuromodulation (**Figure 3**) could include an oscillatory feature at a surface electrode, such as activity in the beta band or high gamma activity representing coordinated neuronal firing, driving stimulation at a damaged cortical region to enhance cortical connectivity and help restore motor function. This activity dependent stimulation could be similar to the activity-dependent DBS paradigms being explored (Herron et al., 2017). A more sophisticated approach, based on the concept of neural co-processors (Rao, 2019), could utilize artificial neural networks to map complex ECoG activity patterns at multiple recording sites to stimulation patterns at multiple stimulation sites to achieve goal-directed rehabilitation.

The combination of theoretical, animal, and human data discussed above suggests that activity-dependent DES is a promising approach to enhance and modify connectivity in humans, offering a new type of therapy for targeted restoration of function after neural injury. ECoG-BCIs are well-suited to acquiring and decoding appropriate control signals and when coupled with DES, can be used to influence cortical activity and induce activity-dependent plasticity.

LIMITATIONS AND CONSIDERATIONS

While ECoG based bi-directional BCIs offer several advantages over other types of BCIs, there are limitations and considerations

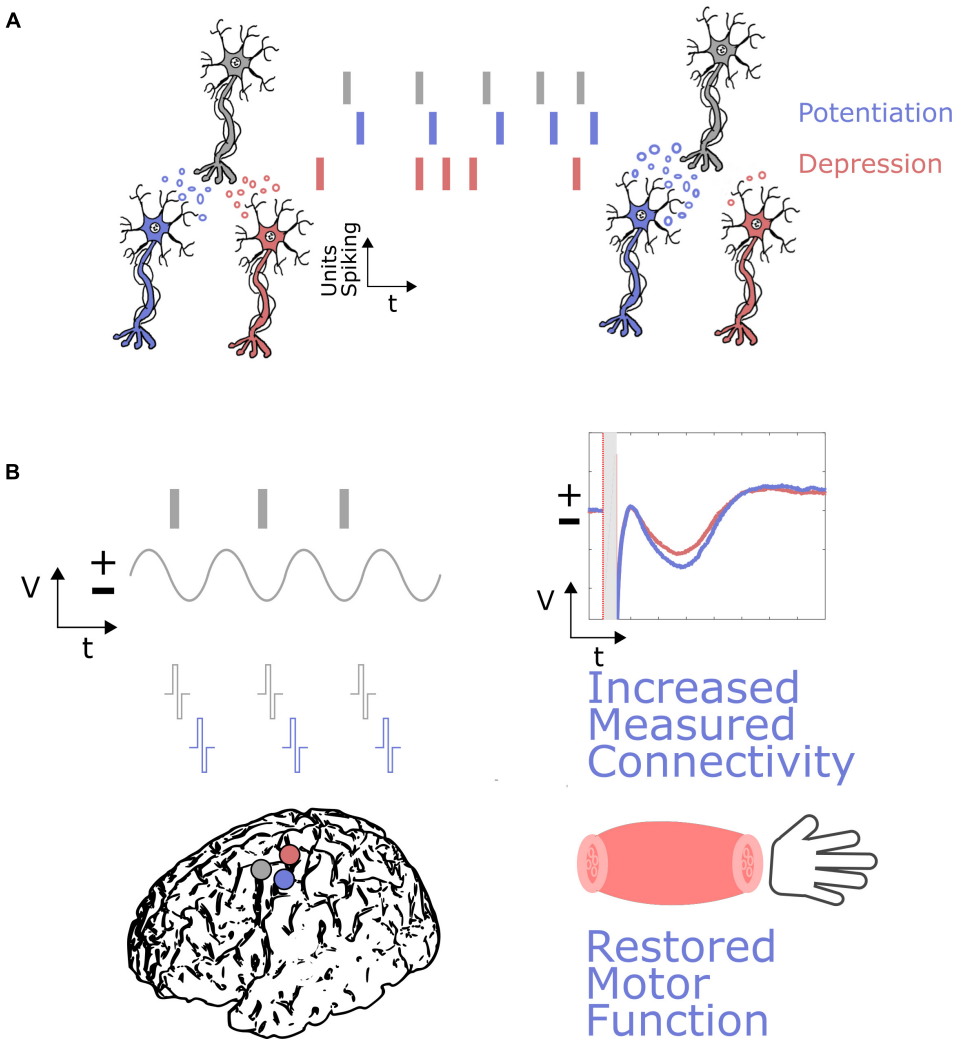

FIGURE 3 | Neural plasticity induction through neuromodulation via DES in ECoG-BCIs. **(A)** The basic principles of neural plasticity involve the timing of activity between neurons resulting in the strengthening of connections, where potentiation occurs if the neurons fire with the appropriate timing in a causal manner, and depression occurs if neurons do not fire with the appropriate timing. **(B)** These principles could be used for neuromodulation through DES and ECoG-BCIs by stimulating near a particular damaged cortical region (purple), based on activity at a spared cortical region (gray). This activity could be a marker of neuronal firing, or a local field potential representing when neurons are more likely to be firing synchronously. Appropriately timed stimulation could then result in increased connectivity, measured through markers such as evoked potentials, and restored motor function relative to baseline. A damaged region not undergoing neuromodulation is shown in red, where evoked potentials are not positively modulated and motor function is not restored.

that must be taken into account. For either subdural or epidural electrodes, neurosurgery is required. The size of the electrodes, relative to other invasive methods such as ICMS, results in larger population of neurons being targeted. Furthermore, there is no ability to target specific types of cells. Additionally, larger neurons with larger diameter axons are more likely to be activated by electrical stimulation (Tehovnik et al., 2006).

The developing field of optogenetics (Deisseroth, 2011; Yizhar et al., 2011) describes the use of genetic modification and optical methods to either activate or inactivate specific neurons *in vivo*. Optogenetics has been demonstrated to change functional connectivity in sensorimotor cortex in NHPs (Yazdan-Shahmorad et al., 2018). Although optogenetics may offer a more targeted approach to activating neurons, progress to humans may be slow due to the technique's reliance on genetic modification of neurons.

Another current consideration when developing technologies and protocols to induce plasticity is our current lack of understanding of the mechanisms of plasticity induction (Feldman, 2012). Beyond the single neuron spiking level, plasticity is a complex phenomenon as discussed above, and in a human brain, the potential factors influencing plasticity can be complex and numerous. Optogenetics, with its ability to selectively target different populations of neurons will help provide critical insight into the mechanisms of plasticity.

Although DES may offer a promising approach to inducing plasticity, it has yet to be demonstrated to be unequivocally effective in a stroke model. Limited subgroups of stroke patients with residual motor function were shown to benefit from open-loop DES in the EVEREST trial, but other groups showed no benefit (Levy et al., 2016). As better animal models of stroke are developed (Sommer, 2017), one can hope to gain a better mechanistic understanding of how DES can be used for stroke rehabilitation, leading to optimized therapies for maximizing functional recovery following cortical injury.

The issue of particular patient subgroup benefit as discussed above speaks to the broader issue of patient variability. Due to anatomic or surgical variations, results from one group of subjects may not necessarily apply to another. Careful consideration of these individual factors will be important for future bidirectional ECoG-BCIs.

An additional consideration is the durability of electrodes with repeated stimulation. As mentioned in section "The Electrical-Neural Interface" above, charge transfer can occur through irreversible Faradaic reactions, where electrolysis occurs, and depending on the polarity of stimulation, either hydrogen gas or oxygen gas are the by products (Merrill et al., 2005). In this electrolytic window, accelerated corrosion and electrode damage can occur. Even below the voltage required for the electrolysis of water, detrimental byproducts such as the formation of metal chloride and hydrogen peroxide can occur, leading to electrode corrosion. Therefore, long-term use of stimulating ECoG electrodes will require careful selection of stimulation parameters and materials to minimize adverse effects. Relative to monophasic pulses, both charge balanced and imbalanced biphasic waveforms result in less electrode potential shift and accumulation of charge. Accumulation of charge during monophasic stimulation can result in additional undesirable Faradaic reactions, and the formation of reactive oxygen species which can cause tissue damage (Merrill et al., 2005). When comparing charge balanced and charge imbalanced biphasic waveforms, charge imbalanced waveforms have the advantage that at the end of each stimulation pulse, the electrode potential is closer to that of the open-circuit potential, resulting in less charge going to irreversible oxidation reactions (Merrill et al., 2005).

Beyond electrode damage, tissue damage induced by stimulation is a key consideration for long-term use of DES. The study of electrical stimulation through platinum electrodes in cats (McCreery et al., 1990) was used to define the Shannon equation (Shannon, 1992), which has been used frequently for assessing safe stimulation levels. Earlier research established a 30 $\mu C/cm^2$ limit on the charge per phase of stimulation for macro-scale electrodes (in particular, DBS electrodes) (Kuncel and Grill, 2004), but tissue damage can occur above and below this threshold (Cogan et al., 2016). There are factors influencing whether or not tissue damage occurs that are not included in the Shannon equation, for example, the scale of the electrode (macro vs. micro), the current density, duty cycle, pulse frequency, and the uniformity of current distribution (Cogan et al., 2016). These complex factors will require further modeling and laboratory testing to establish what the appropriate stimulation parameters are to minimize tissue damage, particularly with the use of novel materials and stimulation patterns.

With penetrating microelectrodes (such as with the Utah array), there is a significant change in the electrode-tissue interface over time (Williams et al., 2007). In addition, stimulation can change the characteristics of the electrode-tissue interface. A recent study analyzing the impedance characteristics of DBS electrodes following implantation and stimulation has shown that DBS electrode impedance increases after implantation and decreases with clinically relevant stimulation (Lempka et al., 2009). Other work has shown that the stimulation parameters used affect the impedance measured for DBS electrodes (Wei and Grill, 2009). ECoG electrode impedance measurements from 191 persons implanted with the Neuropace RNS system, over a median time period of 802 days, did not reveal significant differences between stimulating and non-stimulating electrodes in peri-implant changes in impedance or impedance stability (Ryapolova-Webb et al., 2014). In this study, while there were statistically significant short-term changes in impedance following implantation, long-term impedances were stable. These results suggest that ECoG-BCIs with concurrent DES may prove viable as chronic implants.

ENABLING TECHNOLOGIES

Materials and Electronics

Advances in materials science and electronics are enabling the creation of robust intracranial arrays with thousands of electrode contacts, with closer spacing than is currently used clinically. Current ECoG arrays based on silicone and platinum have been extended to microECoG arrays (Chao et al., 2010). Further reductions in electrode diameter and increases in array density are enabled by micromanufacturing techniques, and in particular, microelectricomechanical systems (MEMS) technologies. Platinum electrodes and polyimide foil substrates similarly have been patterned using micromachining, allowing for electrode contact diameters of 1 mm with electrode spacings between 2 and 3 mm (Rubehn et al., 2009). Through these MEMS technologies, electrode arrays with tighter spacings and smaller diameters can be constructed and placed across large regions of cortex and within sulci (Fukushima et al., 2014). Fukushima et al. (2014) created an array with 0.8 mm diameter electrodes and 1.8 mm spacing.

MicroECoG arrays have recently been used to resolve finer features of cortical activity, particularly in the broadband gamma range, for measurement of phonetic features in single electrodes (Mesgarani et al., 2014). Arrays with electrode diameters of 0.87 mm and spacings of 1.68 mm have resolved cortical activity patterns with response peaks less than the standard clinical spacing of 1 cm apart, pointing to the advantages seen with smaller electrode arrays (Wang et al., 2017). Novel, thin film MEMS arrays are being implanted in humans (Muller et al., 2016), illustrating the translation of these materials and manufacturing techniques to humans. The ability to place more electrodes within a given area could allow for finer patterning of stimulation.

Advances in materials science are enabling electrodes and arrays made of other materials, such as glassy carbon (Kassegne et al., 2015; Goshi et al., 2018). Glassy carbon electrodes have higher charge injection capacities (CIC, which is the amount of charge that can be injected before irreversible chemical reactions take place) than traditional platinum electrodes, and require less stimulation current to activate neurons (Kassegne et al., 2015).

Combinations of ECoG and penetrating electrode arrays are also being constructed for recording and stimulating both surface and deeper structures simultaneously (Orsborn et al., 2015; Goshi et al., 2018; Kleinbart et al., 2018). Currently being used in animal models, such arrays will open the door to a better understanding of network-wide and across cortex effects of stimulation.

Computational Modeling

Computational modeling may help inform the design of DES targeting strategies by delineating which areas of cortex are activated during different polarities of stimulation, and which combinations of electrodes may prove effective. For example, a computational model of subdural cortical stimulation based on anisotropy estimates from DTI revealed that neurons deeper in the cortex are activated more during cathodal subdural stimulation, while those in the wider crown are activated during anodal stimulation (Seo et al., 2015). The influence of anisotropy on neuronal excitation from DES illustrates the importance of detailed, accurate anatomy for understanding and predicting the effects of DES.

A multicompartment computational model for subdural DES illustrated the effect of the neuronal structure, size, and orientation on activation thresholds (Kudela and Anderson, 2015). In the model, the specific parameters of stimulation and structure of the axons influenced the presynaptic terminal activation.

The combination of FEM and patient specific CT and MRI imaging has enabled the optimization of current delivery to various cortical regions depending on desired parameters, such as minimizing current density in particular regions (Guler et al., 2018). Combining individual patient MRIs with accurate computational models of how neurons are activated will allow precise DES targeting, with potentially fewer off-target effects.

The DBS field is replete with examples of new modeling techniques to optimize stimulation of deep cortical targets. These advances could carry over more generally to DES in ECoG-BCIs. Patient specific models of the volume of tissue activated (VTA) enable better understanding of the effects of stimulation at various locations in a given individual (Butson et al., 2007). With the advent of electrodes with many contacts and different geometries, an open question is how to best target the region of interest. Recent algorithmic advances combine electrodes with different contact geometries, including cylindrical and directional leads, and patient specific models, including tissue anisotropy, to best target the sub-thalamic nucleus (STN) (Anderson et al., 2018). A multi-objective particle swarm optimization technique to select a combination of stimulation electrodes was found to be more effective than a single monopolar electrode in targeting the desired efferents from the STN (Peña et al., 2018). As ECoG electrodes become smaller and more numerous, algorithmic techniques such as the ones described above and more advanced ones based on artificial neural networks (Rao, 2019) would enable precisely targeted DES with the right combination of electrodes.

Concurrent Recording and Stimulation

In any closed-loop application involving concurrent stimulation and recording, the electrical artifact due to stimulation is many orders of magnitude greater than the neural signals being recorded. Disentangling the volume conduction of the stimulation pulse from the neural responses is a topic of active research. Different approaches have been used for handling artifacts, ranging from hardware approaches to mitigate artifacts before signal acquisition to post-processing techniques to minimize artifacts after the signals have been acquired.

An example system manufactured with CMOS technology enables both common mode and differential real time artifact cancelation (Smith et al., 2017). In combination with this, new CMOS stimulator front-ends are being developed which could allow for more scalable, integrated BCI devices with wireless, signal processing, and stimulator blocks (Pepin et al., 2016). Advances in this area will permit a better understanding of how the brain responds to electrical stimulation, as well as permit more complex closed loop applications (Zhou et al., 2018a) where neural activity in close temporal and spatial relation to the site of stimulation can be integrated into the control system.

Recent technology development in industry for simultaneous stimulation and recording in DBS applications both illustrates widespread interest in the development of concurrent stimulation and recording devices, and suggests potential combined hardware and software solutions for ECoG-BCIs (Stanslaski et al., 2012; Herron et al., 2018). These techniques include careful consideration of the stimulation and recording configuration to mitigate the measured artifact, front-end filtering, heterodyning to minimize stimulation harmonics in neural frequency bands of interest, and selection of stimulation parameters to aid in the separation of neural signals from stimulation artifacts (Stanslaski et al., 2012). Medtronic's Summit RC + S system extends the previously mentioned approaches to simultaneous stimulation and recording, and further includes oversampling to reduce noise in the signal bands of interest, decimators designed to filter out higher-order harmonics from stimulation, as well as options to only suggest sense-friendly stimulation parameters to the researcher or clinician (Herron et al., 2018). Such techniques could be applied more broadly to include ECoG-BCI systems with DES.

Wireless Technologies

Recent advances in hardware have allowed both real time artifact cancelation and wireless communication with 128 channels of local field potential recording in NHPs (Zhou et al., 2018b). Other implantable devices with microelectrode arrays in NHP model have included wireless charging and data transfer capabilities (Borton et al., 2013), which are critical for an out-of-hospital device. The development of wireless technologies, as well as real time simultaneous stimulation and recording techniques,

opens the door to explorations of the neural basis of naturalistic behavior and long-term effects of closed-loop stimulation. Recent work in non-human primates has demonstrated both wireless recording and stimulation of motor regions over a 6 months time period, with no observed neurological or behavioral consequences (Romanelli et al., 2018). This points to the future translatability of wireless long-term ECoG implants with both recording and stimulation.

CONCLUSION

Direct electrical stimulation of the human brain is currently used clinically for functional mapping, as well as therapeutic treatment of disorders such as epilepsy and movement disorders. In this article, we have explored DES can also be used as a new modality for providing input to cortex in electrocorticographic (ECoG) brain computer interfaces (BCIs). DES offers distinct advantages over other stimulation modalities such as TES and TMS by virtue of delivering electrical stimulation directly to the brain. We discussed some of the barriers for DES translation to ECoG-BCIs, and highlighted the progress being made in the use of DES for restoration of somatosensation and induction of cortical plasticity for targeted rehabilitation in stroke. We also have reviewed how advances in technology, including new materials for electrode design, manufacturing techniques for smaller electrode arrays, and computational modeling for tailoring stimulation to the patient's needs offer opportunities for radically expanding the applications of DES in bi-directional ECoG-BCIs for restoring neurological function.

AUTHOR CONTRIBUTIONS

DC, JO, and RR planned the study and conducted some of the research on the topic of sensation induced by electrocorticographic stimulation described in this manuscript. DC wrote the first draft of the manuscript. DC, JO, and RR edited the draft and finalized the manuscript.

FUNDING

This work was supported by the National Science Foundation (NSF) Center for Neurotechnology (CNT) (Award Number EEC-1028725) and NSF Award Number IIS-1514790. DC was supported by the Big Data for Genomics & Neuroscience Training Grant under Grant Number 1T32CA206089-01A1 and by the Washington Research Foundation Funds for Innovation in Neuroengineering. RR is supported by the CJ and Elizabeth Hwang Endowed Professorship for Computer Science and Engineering and Electrical and Computer Engineering. The content is solely the responsibility of the authors and does not necessarily represent the official views of the National Science Foundation or the National Institutes of Health.

ACKNOWLEDGMENTS

The authors would like to thank the patients who dedicated their time and energy to the experiments which allow the field of electrocortigraphic BCIs to move forward, and without whom, this research would not be possible. The authors would also like to thank Jeffrey Herron for valuable conversation and feedback.

REFERENCES

Alonso, A., De Curtis, M., and Llinast, R. (1990). Postsynaptic Hebbian and non-Hebbian long-term potentiation of synaptic efficacy in the entorhinal cortex in slices and in the isolated adult guinea pig brain (synaptic plasticity/intracellular recording/N-methyl-n-aspartate/ionic channels). *Neurobiology* 87, 9280–9284. doi: 10.1073/pnas.87.23.9280

Anderson, D. N., Osting, B., Vorwerk, J., Dorval, A. D., and Butson, C. R. (2018). Optimized programming algorithm for cylindrical and directional deep brain stimulation electrodes. *J. Neural Eng.* 15:026005. doi: 10.1088/1741-2552/aaa14b

Anderson, K. D. (2004). Targeting recovery: priorities of the spinal cord-injured population. *J. Neurotrauma* 21, 1371–1383. doi: 10.1089/neu.2004.21.1371

Ashkan, K., Rogers, P., Bergman, H., and Ughratdar, I. (2017). Insights into the mechanisms of deep brain stimulation. *Nat. Rev. Neurol.* 13, 548–554. doi: 10.1038/nrneurol.2017.105

Bean, B. P. (2007). The action potential in mammalian central neurons. *Nat. Rev. Neurosci.* 8, 451–465. doi: 10.1038/nrn2148

Bensmaia, S. J., and Miller, L. E. (2014). Restoring sensorimotor function through intracortical interfaces: progress and looming challenges. *Nat. Rev. Neurosci.* 15, 313–325. doi: 10.1038/nrn3724

Berger, M. S., Kincaid, J., Ojemann, G. A., and Lettich, E. (1989). Brain mapping techniques to maximize resection, safety, and seizure control in children with brain tumors. *Neurosurgery* 25, 786–792. doi: 10.1227/00006123-198911000-00015

Berger, M. S., and Ojemann, G. A. (1992). Intraoperative brain mapping techniques in neuro-oncology. *Stereotact. Funct. Neurosurg.* 58, 153–161. doi: 10.1159/000098989

Bi, G. Q., and Poo, M. M. (1998). Synaptic modifications in cultured hippocampal neurons: dependence on spike timing, synaptic strength, and postsynaptic cell type. *J. Neurosci.* 18, 10464–10472. doi: 10.1038/25665

Biddiss, E., Beaton, D., and Chau, T. (2007). Consumer design priorities for upper limb prosthetics. *Disabil. Rehabil. Assist. Technol.* 2, 346–357. doi: 10.1080/17483100701714733

Bliss, T. V. P., and Lomo, T. (1973). Long-lasting poteniation of synpatic transmission in the dentate area of the anaesthetized rabbit following stimulation fo the perforant path. *J. Physiol.* 232, 331–356. doi: 10.1113/jphysiol.1973.sp010273

Boon, P., Vonck, K., Vandekerckhove, T., D'have, M., Nieuwenhuis, L., Michielsen, G., et al. (1999). Vagus nerve stimulation for medically refractory epilepsy; efficacy and cost-benefit analysis. *Acta Neurochir.* 141, 447–453. doi: 10.1007/s007010050324

Borchers, S., Himmelbach, M., Logothetis, N., and Karnath, H.-O. (2012). Direct electrical stimulation of human cortex — the gold standard for mapping brain functions? *Nat. Rev. Neurosci.* 13, 63–70. doi: 10.1038/nrn3140

Borton, D. A., Yin, M., Aceros, J., and Nurmikko, A. (2013). An implantable wireless neural interface for recording cortical circuit dynamics in moving primates. *J. Neural Eng.* 10:026010. doi: 10.1088/1741-2560/10/2/026010

Bouchard, K. E., Mesgarani, N., Johnson, K., and Chang, E. F. (2013). Functional organization of human sensorimotor cortex for speech articulation. *Nature* 495, 327–332. doi: 10.1038/nature11911

Brill, J., and Huguenard, J. R. (2009). Robust short-latency perisomatic inhibition onto neocortical pyramidal cells detected by laser-scanning photostimulation. *J. Neurosci.* 29, 7413–7423. doi: 10.1523/jneurosci.6098-08.2009

Bronstein, J. M., Tagliati, M., Alterman, R. L., Lozano, A. M., Volkmann, J., Stefani, A., et al. (2011). Deep brain stimulation for Parkinson disease. *Arch. Neurol.* 68, 165–171. doi: 10.1001/archneurol.2010.260

Buetefisch, C., Heger, R., Schicks, W., Seitz, R., and Netz, J. (2011). Hebbian-type stimulation during robot-assisted training in patients with stroke. *Neurorehabil. Neural Repair* 25, 645–655. doi: 10.1177/1545968311402507

Butovas, S., and Schwarz, C. (2003). Spatiotemporal effects of microstimulation in rat neocortex: a parametric study using multielectrode recordings. *J. Neurophysiol.* 90, 3024–3039. doi: 10.1152/jn.00245.2003

Butson, C. R., Cooper, S. E., Henderson, J. M., and McIntyre, C. C. (2007). Patient-specific analysis of the volume of tissue activated during deep brain stimulation. *Neuroimage* 34, 661–670. doi: 10.1016/j.neuroimage.2006.09.034

Caldwell, D. J., Cronin, J. A., Wu, J., Weaver, K. E., Ko, A. L., Rao, R. P. N., et al. (2019). Direct stimulation of somatosensory cortex results in slower reaction times compared to peripheral touch in humans. *Sci. Rep.* 9:3292. doi: 10.1038/s41598-019-38619-2

CDC, (2015). *Stroke Facts*. Available at: https://www.cdc.gov/stroke/facts.htm%5Cnhttp://www.cdc.gov/stroke/index.htm (accessed February 11, 2016).

Chang, E. F. (2015). Towards large-scale, human-based, mesoscopic neurotechnologies. *Neuron* 86, 68–78. doi: 10.1016/j.neuron.2015.03.037

Chao, Z. C., Nagasaka, Y., and Fujii, N. (2010). Long-term asynchronous decoding of arm motion using electrocorticographic signals in monkey. *Front. Neuroeng.* 3:3. doi: 10.3389/fneng.2010.00003

Christopher and Dana Reeve Foundation (2013). *Stats About Paralysis*. Available at: https://www.christopherreeve.org/living-with-paralysis/stats-about-paralysis (accessed March 1, 2019).

Coffey, R. J. (2009). Deep brain stimulation devices: a brief technical history and review. *Artif. Organs* 33, 208–220. doi: 10.1111/j.1525-1594.2008.00620.x

Cogan, S. F., Ludwig, K. A., Welle, C. G., and Takmakov, P. (2016). Tissue damage thresholds during therapeutic electrical stimulation. *J. Neural Eng.* 13:021001. doi: 10.1088/1741-2560/13/2/021001

Collinger, J. L., Wodlinger, B., Downey, J. E., Wang, W., Tyler-Kabara, E. C., Weber, D. J., et al. (2013). High-performance neuroprosthetic control by an individual with tetraplegia. *Lancet* 381, 557–564. doi: 10.1016/S0140-6736(12)61816-9

Collins, K. L., Guterstam, A., Cronin, J., Olson, J. D., Ehrsson, H. H., and Ojemann, J. G. (2017). Ownership of an artificial limb induced by electrical brain stimulation. *Proc. Natl. Acad. Sci. U.S.A.* 114, 166–171. doi: 10.1073/pnas.1616305114

Cronin, J. A., Wu, J., Collins, K. L., Sarma, D., Rao, R. P. N., Ojemann, J. G., et al. (2016). Task-specific somatosensory feedback via cortical stimulation in humans. *IEEE Trans. Haptics* 9, 515–522. doi: 10.1109/TOH.2016.2591952

Dadarlat, M. C., O'Doherty, J. E., and Sabes, P. N. (2015). A learning-based approach to artificial sensory feedback leads to optimal integration. *Nat. Neurosci.* 18, 138–144. doi: 10.1038/nn.3883

Deisseroth, K. (2011). Optogenetics. *Nat. Methods* 8, 26–29. doi: 10.1038/nmeth.f.324

Delhaye, B. P., Saal, H. P., and Bensmaia, S. J. (2016). Key considerations in designing a somatosensory neuroprosthesis. *J. Physiol. Paris* 110, 402–408. doi: 10.1016/j.jphysparis.2016.11.001

Della Flora, E., Perera, C. L., Cameron, A. L., and Maddern, G. J. (2010). Deep brain stimulation for essential tremor: a systematic review. *Mov. Disord.* 25, 1550–1559. doi: 10.1002/mds.23195

Douglas, R. M. (1977). Long lasting synaptic potentiation in the rat dentate gyrus following brief high frequency stimulation. *Brain Res.* 126, 361–365. doi: 10.1016/0006-8993(77)90733-8

Englot, D. J., and Chang, E. F. (2014). Rates and predictors of seizure freedom in resective epilepsy surgery: an update. *Neurosurg. Rev.* 37, 389–405. doi: 10.1007/s10143-014-0527-9

Eskandar, E. N., Flaherty, A., Cosgrove, G. R., Shinobu, L. A., and Barker, F. G. (2009). Surgery for Parkinson disease in the United States, 1996 to 2000: practice patterns, short-term outcomes, and hospital charges in a nationwide sample. *J. Neurosurg.* 99, 863–871. doi: 10.3171/jns.2003.99.5.0863

Feldman, D. E. (2012). The Spike-timing dependence of plasticity. *Neuron* 75, 556–571. doi: 10.1016/j.neuron.2012.08.001

Flint, R. D., Rosenow, J. M., Tate, M. C., and Slutzky, M. W. (2017). Continuous decoding of human grasp kinematics using epidural and subdural signals. *J. Neural Eng.* 14:016005. doi: 10.1088/1741-2560/14/1/016005

Fox, P. T., Narayana, S., Tandon, N., Sandoval, H., Fox, S. P., Kochunov, P., et al. (2004). Column-based model of electric field excitation of cerebral cortex. *Hum. Brain Mapp.* 22, 1–14. doi: 10.1002/hbm.20006

Fukushima, M., Saunders, R. C., Mullarkey, M., Doyle, A. M., Mishkin, M., and Fujii, N. (2014). An electrocorticographic electrode array for simultaneous recording from medial, lateral, and intrasulcal surface of the cortex in macaque monkeys. *J. Neurosci. Methods* 233, 155–165. doi: 10.1016/j.jneumeth.2014.06.022

Giussani, C., Roux, F. E., Ojemann, J., Sganzerla, E. P., Pirillo, D., and Papagno, C. (2010). Is preoperative functional magnetic resonance imaging reliable for language areas mapping in brain tumor surgery? Review of language functional magnetic resonance imaging and direct cortical stimulation correlation studies. *Neurosurgery* 66, 113–120. doi: 10.1227/01.NEU.0000360392.15450.C9

Goshi, N., Castagnola, E., Vomero, M., Gueli, C., Cea, C., Zucchini, E., et al. (2018). Glassy carbon MEMS for novel origami-styled 3D integrated intracortical and epicortical neural probes. *J. Micromech. Microeng.* 28:065009. doi: 10.1088/1361-6439/aab061

Guggenmos, D. J., Azin, M., Barbay, S., Mahnken, J. D., Dunham, C., Mohseni, P., et al. (2013). Restoration of function after brain damage using a neural prosthesis. *Proc. Natl. Acad. Sci. U.S.A.* 110, 21177–21182. doi: 10.1073/pnas.1316885110

Guler, S., Dannhauer, M., Roig-Solvas, B., Gkogkidis, A., Macleod, R., Ball, T., et al. (2018). Computationally optimized ECoG stimulation with local safety constraints. *Neuroimage* 173, 35–48. doi: 10.1016/j.neuroimage.2018.01.088

Halpern, C. H., Samadani, U., Litt, B., Jaggi, J. L., and Baltuch, G. H. (2008). Deep brain stimulation for epilepsy. *Neurotherapeutics* 5, 59–67.

Harvey, R. L., and Winstein, C. J. (2009). Design for the everest randomized trial of cortical stimulation and rehabilitation for arm function following stroke. *Neurorehabil. Neural Repair* 23, 32–44. doi: 10.1177/1545968308317532

Harvey, R. L., Winstein, C. J., and Everest Trial, G. (2009). Design for the everest randomized trial of cortical. *Neurorehabil. Neural Repair* 23, 32–44. doi: 10.1177/1545968308317532

Hebb, D. O. (1949). *The Organization of Behavior; A Neuropsychological Theory*. Oxford: Wiley, doi: 10.2307/1418888

Heller, L., and van Hulsteyn, D. B. (1992). Brain stimulation using electromagnetic sources: theoretical aspects. *Biophys. J.* 63, 129–138. doi: 10.1016/S0006-3495(92)81587-4

Hermes, D., Nguyen, M., and Winawer, J. (2017). Neuronal synchrony and the relation between the blood-oxygen-level dependent response and the local field potential. *PLoS Biol.* 15:e2001461. doi: 10.1371/journal.pbio.2001461

Herron, J., Stanslaski, S., Chouinard, T., Corey, R., Denison, T., and Orser, H. (2018). "Bi-directional brain interfacing instrumentation," in *Proceedings of the I2MTC 2018 - 2018 IEEE International Instrumentation and Measurement Technology Conference: Discovering New Horizons in Instrumentation and Measurement*, (houston, TX: IEEE), 1–6. doi: 10.1109/TNSRE.2012.2183617

Herron, J., Thompson, M., Brown, T., Chizeck, H., Ojemann, J., and Ko, A. (2017). Cortical brain computer interface for closed-loop deep brain stimulation. *IEEE Trans. Neural Syst. Rehabil. Eng.* 25, 1–1. doi: 10.1109/TNSRE.2017.2705661

Hiremath, S. V., Tyler-Kabara, E. C., Wheeler, J. J., Moran, D. W., Gaunt, R. A., Collinger, J. L., et al. (2017). Human perception of electrical stimulation on the surface of somatosensory cortex. *PLoS One* 12:e0176020. doi: 10.1371/journal.pone.0176020

Histed, M. H., Bonin, V., and Reid, R. C. (2009). Direct activation of sparse, distributed populations of cortical neurons by electrical microstimulation. *Neuron* 63, 508–522. doi: 10.1016/j.neuron.2009.07.016

Hotson, G., McMullen, D. P., Fifer, M. S., Johannes, M. S., Katyal, K. D., Para, M. P., et al. (2016). Individual finger control of a modular prosthetic limb using high-density electrocorticography in a human subject. *J. Neural Eng.* 13:026017. doi: 10.1088/1741-2560/13/2/026017

Jackson, A., Mavoori, J., and Fetz, E. E. (2006). Long-term motor cortex plasticity induced by an electronic neural implant. *Nature* 444, 56–60. doi: 10.1038/nature05226

Johnson, L. A., Wander, J. D., Sarma, D., Su, D. K., Fetz, E. E., and Ojemann, J. G. (2013). Direct electrical stimulation of the somatosensory cortex in humans

using electrocorticography electrodes: a qualitative and quantitative report. *J. Neural Eng.* 10:036021. doi: 10.1088/1741-2560/10/3/036021

Kassegne, S., Vomero, M., Gavuglio, R., Hirabayashi, M., Özyilmaz, E., Nguyen, S., et al. (2015). Electrical impedance, electrochemistry, mechanical stiffness, and hardness tunability in glassy carbon MEMS μECoG electrodes. *Microelectron. Eng.* 133, 36–44. doi: 10.1016/j.mee.2014.11.013

Keller, C. J., Honey, C. J., Entz, L., Bickel, S., Groppe, D. M., Toth, E., et al. (2014a). Corticocortical evoked potentials reveal projectors and integrators in human brain networks. *J. Neurosci.* 34, 9152–9163. doi: 10.1523/JNEUROSCI.4289-13.2014

Keller, C. J., Honey, C. J., Mégevand, P., Entz, L., Ulbert, I., and Mehta, A. D. (2014b). Mapping human brain networks with cortico-cortical evoked potentials. *Philos. Trans. R. Soc. Lond. Ser. B Biol. Sci.* 369:20130528. doi: 10.1098/rstb.2013.0528

Keller, C. J., Huang, Y., Herrero, J. L., Fini, M., Du, V., Lado, F. A., et al. (2018). Induction and quantification of excitability changes in human cortical networks. *J. Neurosci.* 38, 5384–5398. doi: 10.1523/JNEUROSCI.1088-17.2018

Klaes, C., Shi, Y., Kellis, S., Minxha, J., Revechkis, B., and Andersen, R. A. (2014). A cognitive neuroprosthetic that uses cortical stimulation for somatosensory feedback. *J. Neural Eng.* 11:056024. doi: 10.1088/1741-2560/11/5/056024

Klein, E., and Ojemann, J. (2016). Informed consent in implantable BCI research: identification of research risks and recommendations for development of best practices. *J. Neural Eng.* 13:043001. doi: 10.1088/1741-2560/13/4/043001

Kleinbart, J. E., Orsborn, A. L., Choi, J. S., Wang, C., Qiao, S., Viventi, J., et al. (2018). "A Modular Implant System for Multimodal Recording and Manipulation of the Primate Brain," in *Proceedings of the 2018 40th Annual International Conference of the IEEE Engineering in Medicine and Biology Society (EMBC)*, (Honolulu: IEEE), 3362–3365. doi: 10.1109/EMBC.2018.8512993

Klink, P. C., Dagnino, B., Gariel-Mathis, M. A., and Roelfsema, P. R. (2017). Distinct feedforward and feedback effects of microstimulation in visual cortex reveal neural mechanisms of texture segregation. *Neuron* 95, 209.e–220.e. doi: 10.1016/j.neuron.2017.05.033

Kraus, D., Naros, G., Bauer, R., Khademi, F., Leão, M. T., Ziemann, U., et al. (2016). Brain state-dependent transcranial magnetic closed-loop stimulation controlled by sensorimotor desynchronization induces robust increase of corticospinal excitability. *Brain Stimul.* 9, 415–424. doi: 10.1016/j.brs.2016.02.007

Kudela, P., and Anderson, W. S. (2015). computational modeling of subdural cortical stimulation: a quantitative spatiotemporal analysis of action potential initiation in a high-density multicompartment model. *Neuromodulation* 18, 552–565. doi: 10.1111/ner.12327

Kuncel, A. M., and Grill, W. M. (2004). Selection of stimulus parameters for deep brain stimulation. *Clin. Neurophysiol.* 115, 2431–2441. doi: 10.1016/j.clinph.2004.05.031

Lee, B., Kramer, D., Armenta Salas, M., Kellis, S., Brown, D., Dobreva, T., et al. (2018). Engineering artificial somatosensation through cortical stimulation in humans. *Front. Syst. Neurosci.* 12:24. doi: 10.3389/fnsys.2018.00024

Lee, B., Zubair, M. N., Marquez, Y. D., Lee, D. M., Kalayjian, L. A., Heck, C. N., et al. (2015). A Single-center experience with the neuropace RNS system: a review of techniques and potential problems. *World Neurosurg.* 84, 719–726. doi: 10.1016/j.wneu.2015.04.050

Lega, B. C., Halpern, C. H., Jaggi, J. L., and Baltuch, G. H. (2010). Neurobiology of Disease Deep brain stimulation in the treatment of refractory epilepsy?: update on current data and future directions. *Neurobiol. Dis.* 38, 354–360. doi: 10.1016/j.nbd.2009.07.007

Lempka, S. F., Miocinovic, S., Johnson, M. D., Vitek, J. L., and McIntyre, C. C. (2009). In vivo impedance spectroscopy of deep brain stimulation electrodes. *J. Neural Eng.* 6:046001. doi: 10.1088/1741-2560/6/4/046001

Leuthardt, E. C., Miller, K. J., Schalk, G., Rao, R. P. N., and Ojemann, J. G. (2006a). Electrocorticography-based brain computer interface — the seattle experience. *IEEE Trans. Neural Syst. Rehabil. Eng.* 14, 194–198. doi: 10.1109/TNSRE.2006.875536

Leuthardt, E. C., Schalk, G., Moran, D., and Ojemann, J. G. (2006b). The emerging world of motor neuroprosthetics: a neurosurgical perspective. *Neurosurgery* 59, 1–13. doi: 10.1227/01.NEU.0000221506.06947.AC

Leuthardt, E. C., Schalk, G., Wolpaw, J. R., Ojemann, J. G., and Moran, D. W. (2004). A brain-computer interface using electrocorticographic signals in humans. *J. Neural Eng.* 1, 63–71. doi: 10.1088/1741-2560/1/2/001

Levy, R., Ruland, S., Weinand, M., Lowry, D., Dafer, R., and Bakay, R. (2008). Cortical stimulation for the rehabilitation of patients with hemiparetic stroke: a multicenter feasibility study of safety and efficacy. *J. Neurosurg.* 108, 707–714. doi: 10.3171/JNS/2008/108/4/0707

Levy, R. M., Harvey, R. L., Kissela, B. M., Winstein, C. J., Lutsep, H. L., Parrish, T. B., et al. (2016). Epidural electrical stimulation for stroke rehabilitation: results of the prospective, multicenter, randomized, single-blinded everest trial. *Neurorehabil. Neural Repair* 30, 107–119. doi: 10.1177/1545968315575613

Libet, B., Alberts, W. W., Wright, E. W., Delattre, L. D., Levin, G., and Feinstein, B. (1964). Production of threshold levels of conscious sensation by electrical stimulation of human somatosensory cortex. *J. Neurophysiol.* 27, 546–578. doi: 10.1152/jn.1964.27.4.546

Little, S., Pogosyan, A., Neal, S., Zavala, B., Zrinzo, L., Hariz, M., et al. (2013). Adaptive deep brain stimulation in advanced Parkinson disease. *Ann. Neurol.* 74, 449–457. doi: 10.1002/ana.23951

Lloyd-Jones, D., Adams, R. J., Brown, T. M., Carnethon, M., Dai, S., De Simone, G., et al. (2010). Heart disease and stroke statistics–2010 update: a report from the American heart association. *Circulation* 121, e46–e215. doi: 10.1161/CIRCULATIONAHA.109.192667

Logothetis, N. K., Augath, M., Murayama, Y., Rauch, A., Sultan, F., Goense, J., et al. (2010). The effects of electrical microstimulation on cortical signal propagation. *Nat. Neurosci.* 13, 1283–1291. doi: 10.1038/nn.2631

Matsumoto, R., Nair, D. R., LaPresto, E., Bingaman, W., Shibasaki, H., and Luders, H. O. (2006). Functional connectivity in human cortical motor system: a cortico-cortical evoked potential study. *Brain* 130, 181–197. doi: 10.1093/brain/awl257

Matsumoto, R., Nair, D. R., LaPresto, E., Najm, I., Bingaman, W., Shibasaki, H., et al. (2004). Functional connectivity in the human language system: a cortico-cortical evoked potential study. *Brain? J. Neurol.* 127(Pt 10), 2316–2330. doi: 10.1093/brain/awh246

McCreery, D. B., Agnew, W. F., Yuen, T. G. H., and Bullara, L. (1990). Charge density and charge per phase as cofactors in neural injury induced by electrical stimulation. *IEEE Trans. Biomed. Eng.* 37, 996–1001. doi: 10.1109/10.102812

McIntyre, C. C., and Grill, W. M. (2000). Selective microstimulation of central nervous system neurons. *Ann. Biomed. Eng.* 28, 219–233. doi: 10.1114/1.262

Merrill, D. R., Bikson, M., and Jefferys, J. G. R. (2005). Electrical stimulation of excitable tissue: design of efficacious and safe protocols. *J. Neurosci. Methods* 141, 171–198. doi: 10.1016/j.jneumeth.2004.10.020

Mesgarani, N., Cheung, C., Johnson, K., and Chang, E. F. (2014). Phonetic feature encoding in human superior temporal gyrus. *Science* 43, 1006–1010. doi: 10.1126/science.1245994

Millard, D. C., Whitmire, C. J., Gollnick, C. A., Rozell, C. J., and Stanley, G. B. (2015). Electrical and optical activation of mesoscale neural circuits with implications for coding. *J. Neurosci.* 35, 15702–15715. doi: 10.1523/JNEUROSCI.5045-14.2015

Miller, K. J., Shenoy, P., den Nijs, M., Sorensen, L. B., Rao, R. P. N., and Ojemann, J. G. (2008). Beyond the Gamma band: the role of high-frequency features in movement classification. *IEEE Trans. Biomed. Eng.* 55, 1634–1637. doi: 10.1109/TBME.2008.918569

Miller, L. E., and Weber, D. J. (2011). Guest editorial brain training: cortical plasticity and afferent feedback in brain-machine interface systems. *IEEE Trans. Neural Syst. Rehabil. Eng.* 19, 465–467. doi: 10.1109/tnsre.2011.2168989

Montgomery, E. B., and Gale, J. T. (2008). Mechanisms of action of deep brain stimulation (DBS). *Neurosci. Biobehav. Rev.* 32, 388–407. doi: 10.1016/J.NEUBIOREV.2007.06.003

Morrell, M. J. (2011). Responsive cortical stimulation for the treatment of medically intractable partial epilepsy. *Neurology* 77, 1295–1304. doi: 10.1212/WNL.0b013e3182302056

Mulkey, R. M., and Malenka, R. C. (1992). Mechanisms underlying induction of homosynaptic long-term depression in area CA1 of the hippocampus. *Neuron* 9, 967–975. doi: 10.1016/0896-6273(92)90248-C

Muller, L., Felix, S., Shah, K. G., Lee, K., Pannu, S., and Chang, E. F. (2016). "Thin-film, high-density micro-electrocorticographic decoding of a human cortical gyrus," in *Proceedings of the 2016 38th Annual International Conference of the IEEE Engineering in Medicine and Biology Society (EMBC)*, (Orlando, FL: IEEE), 1528–1531. doi: 10.1109/EMBC.2016.7591001

Nowak, L. G., and Bullier, J. (1998). Axons, but not cell bodies, are activated by electrical stimulation in cortical gray matter. I. Evidence from chronaxie measurements. *Exp. Brain Res.* 118, 477–488. doi: 10.1007/s002210050304

Ojemann, G., Ojemann, J., Lettich, E., and Berger, M. (1989). Cortical language localization in left, dominant hemisphere. An electrical stimulation mapping investigation in 117 patients. *J. Neurosurg.* 71, 316–326. doi: 10.3171/jns.1989.71.3.0316

Orsborn, A. L., Wang, C., Chiang, K., Maharbiz, M. M., Viventi, J., and Pesaran, B. (2015). "Semi-chronic chamber system for simultaneous subdural electrocorticography, local field potentials, and spike recordings," in *Proceedings of the International IEEE/EMBS Conference on Neural Engineering, NER, 2015*, (Montpellier: IEEE), 398–401. doi: 10.1109/NER.2015.7146643

Peña, E., Zhang, S., Patriat, R., Aman, J. E., Vitek, J. L., Harel, N., et al. (2018). Multi-objective particle swarm optimization for postoperative deep brain stimulation targeting of subthalamic nucleus pathways. *J. Neural Eng.* 15:066020. doi: 10.1088/1741-2552/aae12f

Pepin, E., Uehlin, J., Micheletti, D., Perlmutter, S. I., and Rudell, J. C. (2016). "A high-voltage compliant, electrode-invariant neural stimulator front-end in 65nm bulk-CMOS," in *Proceedings of the ESSCIRC Conference 2016: 42nd European Solid-State Circuits Conference*, (Ecublens: IEEE), 229–232. doi: 10.1109/ESSCIRC.2016.7598284

Pereira, E. A., Green, A. L., Nandi, D., and Aziz, T. Z. (2007). Deep brain stimulation: indications and evidence. *Expert Rev. Med. Devices* 4, 591–603. doi: 10.1586/17434440.4.5.591

Pistohl, T., Joshi, D., Ganesh, G., Jackson, A., and Nazarpour, K. (2015). Artificial proprioceptive feedback for myoelectric control. *IEEE Trans. Neural Syst. Rehabil. Eng.* 23, 498–507. doi: 10.1109/TNSRE.2014.2355856

Ramsey, N. F., Heuvel, M. P. V. D., Kho, K. H., and Leijten, F. S. S. (2006). Towards human BCI applications based on cognitive brain systems: an investigation of neural signals recorded from the dorsolateral prefrontal cortex. *IEEE Trans. Neural Syst. Rehabil. Eng.* 14, 214–217. doi: 10.1109/TNSRE.2006.875582

Ranck, J. B. (1975). Which elements are excited in electrical stimulation of mammalian central nervous system: a review. *Brain Res.* 98, 417–440. doi: 10.1016/0006-8993(75)90364-9

Rao, R. P. (2019). Towards neural co-processors for the brain: combining decoding and encoding in brain–computer interfaces. *Curr. Opin. Neurobiol.* 55, 142–151. doi: 10.1016/j.conb.2019.03.008

Rao, R. P. N. (2013). *Brain-Computer Interfacing: An Introduction*. New York, NY: Cambridge University Press.

Ray, P. G., Meador, K. J., Smith, J. R., Wheless, J. W., Sittenfeld, M., and Clifton, G. L. (1999). Physiology of perception: cortical stimulation and recording in humans. *Neurology* 52, 1044–1049. doi: 10.1212/WNL.52.5.1044

Romanelli, P., Piangerelli, M., Ratel, D., Gaude, C., Costecalde, T., Puttilli, C., et al. (2018). A novel neural prosthesis providing long-term electrocorticography recording and cortical stimulation for epilepsy and brain-computer interface. *J. Neurosurg.* 1, 1–14. doi: 10.3171/2017.10.jns17400

Rosin, B., Slovik, M., Mitelman, R., Rivlin-Etzion, M., Haber, S. N., Israel, Z., et al. (2011). Closed-loop deep brain stimulation is superior in ameliorating parkinsonism. *Neuron* 72, 370–384. doi: 10.1016/j.neuron.2011.08.023

Roth, B. J., Saypol, J. M., Hallett, M., and Cohen, L. G. (1991). A theoretical calculation of the electric field induced in the cortex during magnetic stimulation. *Electroencephalogr. Clin. Neurophysiol.* 81, 47–56. doi: 10.1016/0168-5597(91)90103-5

Rubehn, B., Bosman, C., Oostenveld, R., Fries, P., and Stieglitz, T. (2009). A MEMS-based flexible multichannel ECoG-electrode array. *J. Neural Eng.* 6:036003. doi: 10.1088/1741-2560/6/3/036003

Ryapolova-Webb, E., Afshar, P., Stanslaski, S., Denison, T., de Hemptinne, C., Bankiewicz, K., et al. (2014). Chronic cortical and electromyographic recordings from a fully implantable device: preclinical experience in a nonhuman primate. *J. Neural Eng.* 11:016009. doi: 10.1088/1741-2560/11/1/016009

Schalk, G. (2015). A general framework for dynamic cortical function: the function-through-biased-oscillations (FBO) hypothesis. *Front. Hum. Neurosci.* 9:352. doi: 10.3389/fnhum.2015.00352

Schiefer, M., Tan, D., Sidek, S. M., and Tyler, D. J. (2016). Sensory feedback by peripheral nerve stimulation improves task performance in individuals with upper limb loss using a myoelectric prosthesis. *J. Neural Eng.* 13:016001. doi: 10.1088/1741-2560/13/1/016001

Schrock, L. E., Mink, J. W., Woods, D. W., Porta, M., Servello, D., Visser-Vandewalle, V., et al. (2015). Tourette syndrome deep brain stimulation: a review and updated recommendations. *Mov. Disord.* 30, 448–471. doi: 10.1002/mds.26094

Seeman, S. C., Mogen, B. J., Fetz, E. E., and Perlmutter, S. I. (2017). Paired stimulation for spike-timing-dependent plasticity in primate sensorimotor cortex. *J. Neurosci.* 37, 1935–1949. doi: 10.1523/JNEUROSCI.2046-16.2017

Seo, H., Kim, D., and Jun, S. C. (2015). Computational study of subdural cortical stimulation: effects of simulating anisotropic conductivity on activation of cortical neurons. *PLoS One* 10:e0128590. doi: 10.1371/journal.pone.0128590

Seo, H., Schaworonkow, N., Jun, S. C., and Triesch, J. (2016). A multi-scale computational model of the effects of TMS on motor cortex. *F1000Research* 5:1945. doi: 10.12688/f1000research.9277.1

Shannon, R. V. (1992). A model of safe levels for electrical stimulation. *IEEE Trans. Biomed. Eng.* 39, 424–426. doi: 10.1109/10.126616

Silva, S., Basser, P. J., and Miranda, P. C. (2008). Elucidating the mechanisms and loci of neuronal excitation by transcranial magnetic stimulation using a finite element model of a cortical sulcus. *Clin. Neurophysiol.* 119, 2405–2413. doi: 10.1016/j.clinph.2008.07.248

Sliwinska, M. W., Vitello, S., and Devlin, J. T. (2014). Transcranial magnetic stimulation for investigating causal brain-behavioral relationships and their time course. *J. Vis. Exp.* 89:e51735. doi: 10.3791/51735

Smith, W. A., Uehlin, J. P., Perlmutter, S. I., Rudell, J. C., and Sathe, V. S. (2017). "A scalable, highly-multiplexed delta-encoded digital feedback ECoG recording amplifier with common and differential-mode artifact suppression," in *Proceedings of the 2017 IEEE Symposium on VLSI Circuits, Digest of Technical Papers*, (Kyoto: IEEE), C172–C173. doi: 10.23919/VLSIC.2017.8008470

Sommer, C. J. (2017). Ischemic stroke: experimental models and reality. *Acta Neuropathol.* 133, 245–261. doi: 10.1007/s00401-017-1667-0

Stanslaski, S., Afshar, P., Cong, P., Giftakis, J., Stypulkowski, P., Carlson, D., et al. (2012). Design and validation of a fully implantable, chronic, closed-loop neuromodulation device with concurrent sensing and stimulation. *IEEE Trans. Neural Syst. Rehabil. Eng.* 20, 410–421. doi: 10.1109/TNSRE.2012.2183617

Suminski, A. J., Tkach, D. C., Fagg, A. H., and Hatsopoulos, N. G. (2010). Incorporating feedback from multiple sensory modalities enhances brain-machine interface control. *J. Neurosci.* 30, 16777–16787. doi: 10.1523/JNEUROSCI.3967-10.2010

Tehovnik, E. J., Tolias, A. S., Sultan, F., Slocum, W. M., and Logothetis, N. K. (2006). Direct and indirect activation of cortical neurons by electrical microstimulation. *J. Neurophysiol.* 96, 512–521. doi: 10.1152/jn.00126.2006

Thomson, E. E., Carra, R., and Nicolelis, M. A. L. (2013). Perceiving invisible light through a somatosensory cortical prosthesis. *Nat. Commun.* 4:1482. doi: 10.1038/ncomms2497

Vincent, M., Rossel, O., Duffau, H., Bonnetblanc, F., and Guiraud, D. (2016a). "A measure of cortico-cortical potentials evoked by 10Hz direct electrical stimulation of the brain and by means of a differential recording mode of electrocorticographic signals," in *Proceedings of the Annual International Conference of the IEEE Engineering in Medicine and Biology Society, EMBS*, (Orlando, FL: IEEE), 4543–4546. doi: 10.1109/EMBC.2016.7591738

Vincent, M., Rossel, O., Hayashibe, M., Herbet, G., Duffau, H., Guiraud, D., et al. (2016b). The difference between electrical microstimulation and direct electrical stimulation - Towards new opportunities for innovative functional brain mapping? *Rev. Neurosci.* 27, 231–258. doi: 10.1515/revneuro-2015-0029

Vöröslakos, M., Takeuchi, Y., Brinyiczki, K., Zombori, T., Oliva, A., Fernández-Ruiz, A., et al. (2018). Direct effects of transcranial electric stimulation on brain circuits in rats and humans. *Nat. Commun.* 9:483. doi: 10.1038/s41467-018-02928-3

Wagner, T., Rushmore, J., Eden, U., and Valero-Cabre, A. (2009). Biophysical foundations underlying TMS: setting the stage for an effective use of neurostimulation in the cognitive neurosciences. *Cortex* 45, 1025–1034. doi: 10.1016/j.cortex.2008.10.002

Wander, J. D., and Rao, R. P. N. (2014). Brain-computer interfaces: a powerful tool for scientific inquiry. *Curr. Opin. Neurobiol.* 25, 70–75. doi: 10.1016/j.conb.2013.11.013

Wang, X., Gkogkidis, A., Iljina, O., Fiederer, L., Henle, C., Mader, I., et al. (2017). Mapping the fine structure of cortical activity with different micro-ECoG electrode array geometries. *J. Neural Eng.* 265, 197–212. doi: 10.1088/1741-2552/aa785e

Weber, D. J., Friesen, R., and Miller, L. E. (2012). Interfacing the somatosensory system to restore touch and Proprioception: essential considerations. *J. Mot. Behav.* 44, 403–418. doi: 10.1080/00222895.2012.735283

Wei, X. F., and Grill, W. M. (2009). Impedance characteristics of deep brain stimulation electrodes in vitro and in vivo. *J. Neural Eng.* 6:046008. doi: 10.1088/1741-2560/6/4/046008

Widge, A. S. (2018). Cross-Species neuromodulation from high-intensity transcranial electrical stimulation. *Trends Cogn. Sci.* 22, 372–374. doi: 10.1016/j.tics.2018.03.006

Williams, J. C., Hippensteel, J. A., Dilgen, J., Shain, W., and Kipke, D. R. (2007). Complex impedance spectroscopy for monitoring tissue responses to inserted neural implants. *J. Neural Eng.* 4, 410–423. doi: 10.1088/1741-2560/4/4/007

Wilson, J. A., Felton, E. A., Garell, P. C., Schalk, G., and Williams, J. C. (2006). ECoG factors underlying multimodal control of a brain-computer interface. *IEEE Trans. Neural Syst. Rehabil. Eng.* 14, 246–250. doi: 10.1109/TNSRE.2006.875570

Wirth, F. P., and Van Buren, J. M. (1971). Referral of pain from dural stimulation in man. *J. Neurosurg.* 34, 630–642. doi: 10.3171/jns.1971.34.5.0630

Wongsarnpigoon, A., and Grill, W. M. (2008). Computational modeling of epidural cortical stimulation. *J. Neural. Eng.* 5, 443–454. doi: 10.1088/1741-2560/5/4/009

Yazdan-Shahmorad, A., Silversmith, D. B., Kharazia, V., and Sabes, P. N. (2018). Targeted cortical reorganization using optogenetics in non-human primates. *eLife* 7, 1–21. doi: 10.7554/elife.31034

Yizhar, O., Fenno, L. E., Davidson, T. J., Mogri, M., and Deisseroth, K. (2011). Optogenetics in Neural Systems. *Neuron* 71, 9–34. doi: 10.1016/j.neuron.2011.06.004

Zangen, A., Roth, Y., Voller, B., and Hallett, M. (2005). Transcranial magnetic stimulation of deep brain regions: evidence for efficacy of the H-Coil. *Clin. Neurophysiol.* 116, 775–779. doi: 10.1016/j.clinph.2004.11.008

Zanos, S., Rembado, I., Chen, D., and Fetz, E. E. (2018). Phase-locked stimulation during cortical beta oscillations produces bidirectional synaptic plasticity in awake Monkeys. *Curr. Biol.* 28, 2515.e–2526.e. doi: 10.1016/j.cub.2018.07.009

Zhou, A., Johnson, B. C., and Muller, R. (2018a). Toward true closed-loop neuromodulation: artifact-free recording during stimulation. *Curr. Opin. Neurobiol.* 50, 119–127. doi: 10.1016/j.conb.2018.01.012

Zhou, A., Santacruz, S. R., Johnson, B. C., Alexandrov, G., Moin, A., Burghardt, F. L., et al. (2018b). A wireless and artefact-free 128-channel neuromodulation device for closed-loop stimulation and recording in non-human primates. *Nat. Biomed. Eng.* 3, 15–26. doi: 10.1038/s41551-018-0323-x

Conflict of Interest Statement: The authors declare that the research was conducted in the absence of any commercial or financial relationships that could be construed as a potential conflict of interest.

frontiers in Neuroscience

ORIGINAL RESEARCH
published: 21 August 2019
doi: 10.3389/fnins.2019.00847

Long-Term Sheep Implantation of WIMAGINE®, a Wireless 64-Channel Electrocorticogram Recorder

F. Sauter-Starace[1], D. Ratel[1], C. Cretallaz[1], M. Foerster[1], A. Lambert[1], C. Gaude[1], T. Costecalde[1], S. Bonnet[2], G. Charvet[1], T. Aksenova[1], C. Mestais[1], Alim-Louis Benabid[1] and N. Torres-Martinez[1]*

[1] Univ. Grenoble Alpes, CEA, Leti, CLINATEC, Grenoble, France, [2] Univ. Grenoble Alpes, CEA, Leti, DTBS, Grenoble, France

OPEN ACCESS

Edited by:
Christoph Guger, G.tec Medical Engineering GmbH, Austria

Reviewed by:
Ewan Nurse, The University of Melbourne, Australia
Tonio Ball, University Hospital Freiburg, Germany

***Correspondence:**
F. Sauter-Starace
fabien.sauter@cea.fr

Specialty section:
This article was submitted to Neuroprosthetics, a section of the journal Frontiers in Neuroscience

Received: *31 January 2019*
Accepted: *30 July 2019*
Published: *21 August 2019*

Citation:
Sauter-Starace F, Ratel D, Cretallaz C, Foerster M, Lambert A, Gaude C, Costecalde T, Bonnet S, Charvet G, Aksenova T, Mestais C, Benabid A-L and Torres-Martinez N (2019) Long-Term Sheep Implantation of WIMAGINE®, a Wireless 64-Channel Electrocorticogram Recorder. Front. Neurosci. 13:847. doi: 10.3389/fnins.2019.00847

This article deals with the long-term preclinical validation of WIMAGINE® (Wireless Implantable Multi-channel Acquisition system for Generic Interface with Neurons), a 64-channel wireless implantable recorder that measures the electrical activity at the cortical surface (electrocorticography, ECoG). The WIMAGINE® implant was designed for chronic wireless neuronal signal acquisition, to be used e.g., as an intracranial Brain–Computer Interface (BCI) for severely motor-impaired patients. Due to the size and shape of WIMAGINE®, sheep appeared to be the best animal model on which to carry out long-term *in vivo* validation. The devices were implanted in two sheep for a follow-up period of 10 months, including idle state cortical recordings and Somato-Sensory Evoked Potential (SSEP) sessions. ECoG and SSEP demonstrated relatively stable behavior during the 10-month observation period. Information recorded from the SensoriMotor Cortex (SMC) showed an SSEP phase reversal, indicating the cortical site of the sensorimotor activity was retained after 10 months of contact. Based on weekly recordings of raw ECoG signals, the effective bandwidth was in the range of 230 Hz for both animals and remarkably stable over time, meaning preservation of the high frequency bands valuable for decoding of the brain activity using BCIs. The power spectral density (in dB/Hz), on a log scale, was of the order of 2.2, –4.5 and –18 for the frequency bands (10–40), (40–100), and (100–200) Hz, respectively. The outcome of this preclinical work is the first long-term *in vivo* validation of the WIMAGINE® implant, highlighting its ability to record the brain electrical activity through the dura mater and to send wireless digitized data to the external base station. Apart from local adhesion of the dura to the skull, the neurosurgeon did not face any difficulty in the implantation of the WIMAGINE® device and post-mortem analysis of the brain revealed no side effect related to the implantation. We also report on the reliability of the system; including the implantable device, the antennas module and the external base station.

Keywords: long-term implantation, wireless communications, brain–computer interface, electrocorticogram (ECoG), signal quality, local tolerance, sheep

INTRODUCTION

Brain–Computer Interface (BCI) encompass various types of system, which have the common function of establishing a direct communication link between the brain and an external device. The large majority of these systems are non-invasive using a wearable cap to record brain activity from the scalp using either wet or dry Electroencephalography (EEG) electrodes. These systems have become very popular and range from single electrode systems (NeuroSky MindWave; Katona et al., 2016), to high-density EEG [up to 256 contacts (He and Sohrabpour, 2016)]. Among the BCI community, a large number of researchers are struggling to meet the needs of biofeedback-based applications and/or of clinical research, using non-invasive EEG recording systems with centimeter pitched contacts (Schwartz et al., 2006). These contacts record noisy signals generated by large cortical surfaces. In contrast, microelectrode-based systems tend to record single neurons or multi-unit activity. These systems became popular due to the first chronically implanted patients in the Braingate® project (Hochberg et al., 2006), using UTAH arrays (Maynard et al., 1997) and the Cereport® connector now retailed by BlackRock (Salt Lake City, UT, United States). However, due to mechanical mismatch between silicon and brain tissues, and volume displacement of the tissue following silicon needle introduction, glial encapsulation of the probe and neurodegeneration are likely (Schwartz et al., 2006). Accordingly, the number of usable contacts decreases dramatically with time (Rousche and Normann, 1998). Presenting a trade-off between invasiveness and signal quality, surface electrodes placed above (epidural) and below (subdural) the dura mater [electrocorticography (ECoG)] were reported to provide promising performances in BCI (Chao et al., 2010; Eliseyev and Aksenova, 2013; Wang et al., 2013). More recently in the framework of clinical trials, ECoG devices long-term assessment or set-up were reported, respectively for epileptic seizure detection (Cook et al., 2013; Sillay et al., 2013), closed-loop DBS (Swann et al., 2017) or BCI for a locked-in syndrome patient (Vansteensel et al., 2016).

Our team decided to explore the potential of epidural ECoG for chronic medical applications (e.g., motor BCI) using implanted electrodes at the surface of the dura mater to reduce glial reactions produced by penetrating microelectrodes, and to mitigate the lack of resolution of scalp electrodes (Schwartz et al., 2006). For the sake of patient safety and comfort, the implantable BCI recording device should be without wires. Consequently, we designed the wireless ECoG recording implant WIMAGINE® using two antennas, one for the remote power supply at 13.56 MHz and the other for data communication in the Medical Implant Communication Service (MICS) band (402–405) MHz. Thanks to an overmolding of silicone rubber, the titanium housing looks like a cylinder of 50 mm in diameter, whose thickness varies between 7.5 and 12 mm at the center of the pseudo-spherical top surface, whereas the flat bottom surface is covered by 64 contacts for epidural ECoG plus 5 references. The WIMAGINE® implant was developed as the starting point of a BCI platform which includes data processing, a Virtual Reality avatar and finally complex effectors such as a four-limb exoskeleton. The implant's detailed description is given in a previous article (Mestais et al., 2015), including biocompatibility data resulting from the implantation of a semi-scaled and passive device over a 6-month period in a non-human primate model.

This article presents the ultimate step toward a clinical trial, the evaluation of a set of WIMAGINE® implants for long-term functional assessment, and determination of the performance and stability of the WIMAGINE® implant with a remote power supply and wireless data communication during chronic implantation in a large animal model. Experiments were carried out for more than 10 months, in freely moving animals to ensure stable functioning and to evaluate the signal quality.

To assess both the signal and the influence of surgical strategy on signal resolution, several long-term studies of epidural/subdural (Sillay et al., 2013; Gierthmuehlen et al., 2014; Ryapolova-Webb et al., 2014; Schendel et al., 2014; Degenhart et al., 2016; Kohler et al., 2017; Swann et al., 2017; Nurse et al., 2018), and even endovascular electrodes were carried out on large animals (Oxley et al., 2016). These studies lasted at least 4 months and could continue for up to 2 years. Considering the shape and size of the implant, we chose sheep for long-term implantation and monitoring, inspired by a previous 4-month sheep implantation experiment (Gierthmuehlen et al., 2014). Skull size in the adult sheep allows easy surgical implantation of WIMAGINE® on the dura mater above sensorimotor areas. Moreover, these animals are easy to handle and are used to men, which allowed us to perform weekly recordings without anesthesia.

The quality of the signal recorded with a WIMAGINE® implant and its evolution over time were investigated and compared to published clinical ECoG based studies (Sillay et al., 2013; Oxley et al., 2016; Swann et al., 2017; Nurse et al., 2018). Using the same experimental platform as that developed for the clinical trial, we recorded weekly raw ECoG signals and additional Somatosensory Evoked Potential sessions (SSEPs) every other month.

MATERIALS AND METHODS

Wireless ECoG Recorder

The WIMAGINE® implant (**Figure 1**), consists of an array of 64 biocompatible epidural electrodes (Platinum iridium 90/10, 2.3 mm in diameter, pitches of 4 and 4.5 mm on the lateral and antero-posterior directions, respectively) fixed under a titanium housing including electronic boards, and two antennas for wireless transmission of data and a remote power supply. For this purpose, our team designed and handled the implant manufacture according to ISO 13485, as well as qualification tests according to the European directive 2007/47/EC and ISO standards (risk analysis ISO 14971, ISO14708-1 for electrical and mechanical safety of implantable devices, NF EN 60601-1 for electrical safety and electromagnetic compatibility of the external unit). A complete description of the WIMAGINE® implant is given in Mestais et al. (2015).

The design of the WIMAGINE® implant is adapted to a craniotomy with a trephine (50 mm in diameter) and the upper

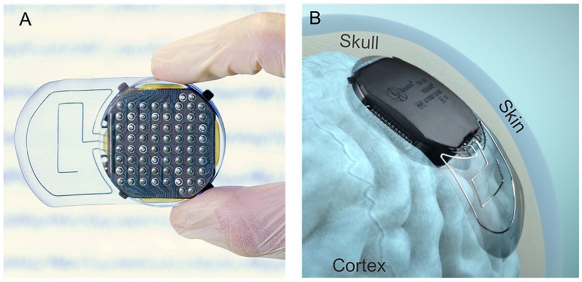

FIGURE 1 | (A) View of the cortical electrode array. **(B)** Lateral implantation of a WIMAGINE® implant on an anatomical model.

surface of the implant has a spherical shape (90 mm in curvature) that matches most of the patient's skull. The implant is designed to replace the bone of the craniotomy. Four little titanium wings were added to prevent any mechanical damage to the brain in the case of mechanical pressure or shocks to the implant through the skin.

Antenna Adaptation to Sheep

In **Figure 2**, we sketched the experimental set-up of the ovine campaign. This consisted of a base station enabling communication between the implant and a laptop running the data recording software (WISCI) developed for the WIMAGINE® platform: a telemetric antenna (402–405 MHz) and a remote power antenna (13.56 MHz) both included in a leather pocket attached to the sheep's front to allow the recording awake animals in an idle state.

Animals

Chronic implantation experiments were conducted on two female sheep (*Ovis Aries*) (Charollais breed, 80–90 kg, 5 and 8 years old). All experiments were carried out following the recommendations of the European Community Council Directives of 1986 (86/609/EEC), the National Institutes of Health Guide for the Care and Use of Laboratory Animals. The Ethics Committee COMETH of Lyon, France approved the experimental protocol which was registered to the national committee under reference number 1504_V2.

Animals were housed and kept together in an air-conditioned room under stable conditions of temperature (20 ± 2°C), humidity (50%), light (12 h light/dark cycle) and food/water was available *ad libitum*.

Sheep were observed daily and were clinically evaluated and weighed once a week by veterinary personnel.

Implantation (Surgical Procedure)

After premedication (Diazepam 4.5 ml and Morphine 0.9 ml), anesthesia was induced with intravenously applied Propofol (4 mg/kg, 1/4 dose) and maintained using vaporized isoflurane (2%) in oxygen. Following endotracheal intubation, animals were maintained in volume-controlled ventilators at a respiratory rate of 12–14 breaths per minute. Fluid requirements were substituted by Ringer's solution (Baxter, Deer Field, IL, United States) infused at 10 mg/kg. ECG, rectal body temperature and oxygen saturation were all monitored and the sheep were kept in a prone position during the procedure. A local anesthetic (2% Lidocaine) was injected prior to skin incision.

Only one device could be implanted – partially covering left and right hemispheres because of the implant size

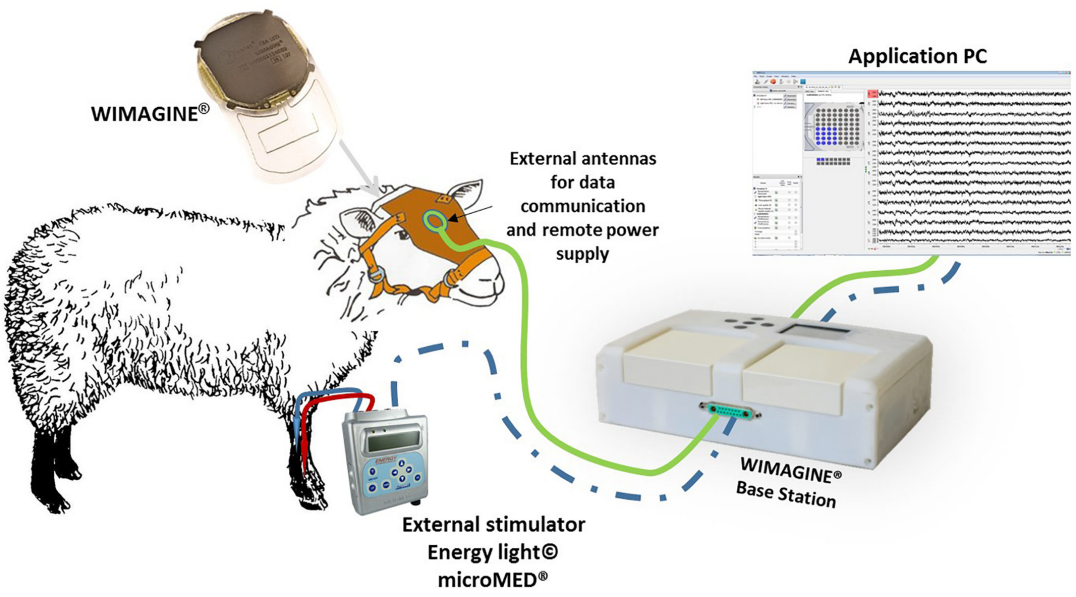

FIGURE 2 | Experimental set-up for ovine experiments. The connection from the stimulator to the base station in dashed blue since it was only used to trig the stimulations to the recordings during the SSEP sessions.

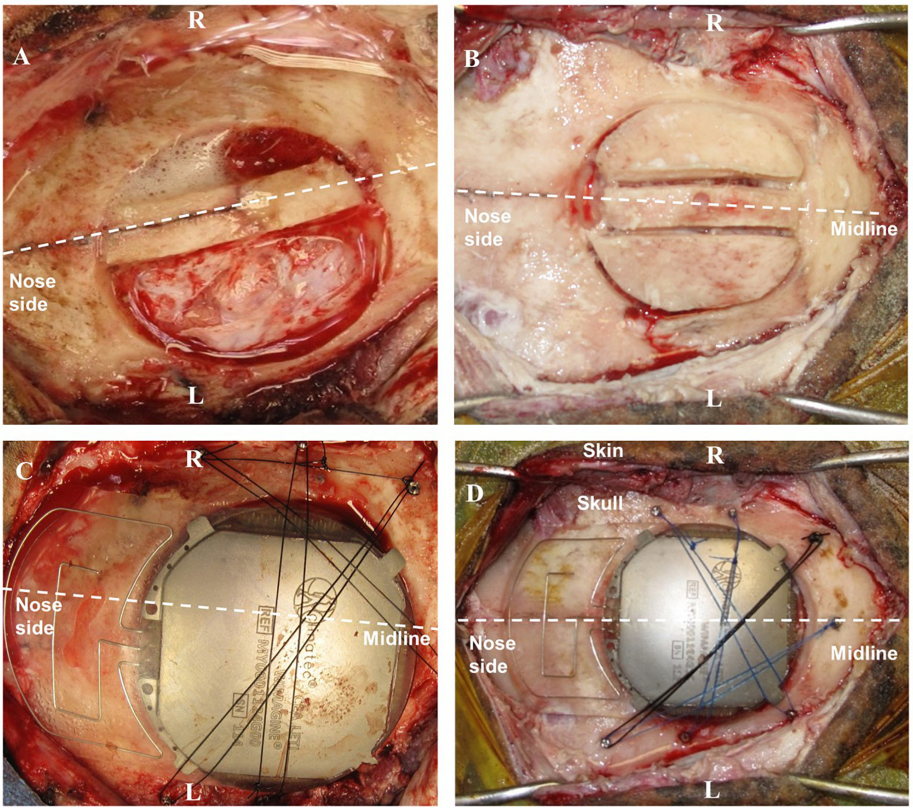

FIGURE 3 | Surgery for WIMAGINE® implantation in the ovine model. **(A,B)** Trepanation and division of the bone disk into 3 parts (**A:** sheep#1, **B:** sheep#2); **(C,D)** WIMAGINE® implant craniotomy fixation during surgery (**C:** sheep#1, **D:** sheep#2). (R: right side, L: left side).

(50 mm in diameter). The craniotomy to expose the epidural space was carried out in several steps. After antisepsis and draping, a linear incision was made between the nasion and the occipital bone in the midline, and the bone surface was extensively exposed. Using the midline and Bregma as an anatomical reference, we performed the craniotomy with a custom-made bone trephine (50 mm in diameter; SMAO, France) with a 1 cm shift for sheep#1 and centered for sheep#2. Because of the presence of the Superior Sagittal Sinus (SSS), the trephine was only used to cut the external table of the skull. The rest of the craniotomy was divided into three parts using a drill (Midas Rex®; Medtronic Inc.) so as to isolate the SSS and to avoid vascular damage (see **Figures 3A,B**). In sheep, the SSS has a deep groove in the internal table of the skull, presenting an additional risk of bleeding. Finally, the dura mater was adherent in several places, requiring careful removal of the last part of the disk and repairs after bone extraction.

After appropriate drilling to avoid any skull fragment between the electrodes and the dura mater, the WIMAGINE® implant was inserted into the craniotomy and the antennas were aligned between the sheep orbits. The small lateral titanium wings helped to keep the implant in position, avoiding rotation of the device. As shown in **Figures 3C,D**, additional fixation points were provided using custom-made titanium screws and Prolene® 2.0 sutures (Ethicon®, Johnson & Johnson, NJ, United States). Control ECoG recordings were performed throughout the surgery, both before and after skin closure. Using a sterile pouch for the base station antenna, we performed intraoperative communication tests. The implant was successfully powered and communication functions were checked. Analgesia (Buprenorphine 0.1 mg/kg) and prophylactic antibiotics (Borgal 24% trimethoprim/sulfadoxine 1 ml/15 kg) were also used postoperatively.

After hemostasis and suture of the surgical plans, a dressing (10 mm thick compress) was applied with Betadine and Tensoplast® at the end of surgery. Finally, we checked the wireless communication after extubation and once the animal woke.

Brain scans were carried out under anesthesia 3 days after surgery (see **Figure 4**), 6 months later, and just before euthanasia at 10 months. There is slight angular tilt on the CT scan but it is still possible to check the position of the WIMAGINE® implant in the skull. In addition, we display on this figure the locations of the four 16-contact phases.

Experimental Design

Sessions started on the first day after surgery. Two different protocols were applied. First, once a week, we performed a session in which awake animals were trained to be calm in a sheep enclosure. In such a session, a 12-min electrocorticogram was recorded in an idle state. Second, every 2 months a SSEP

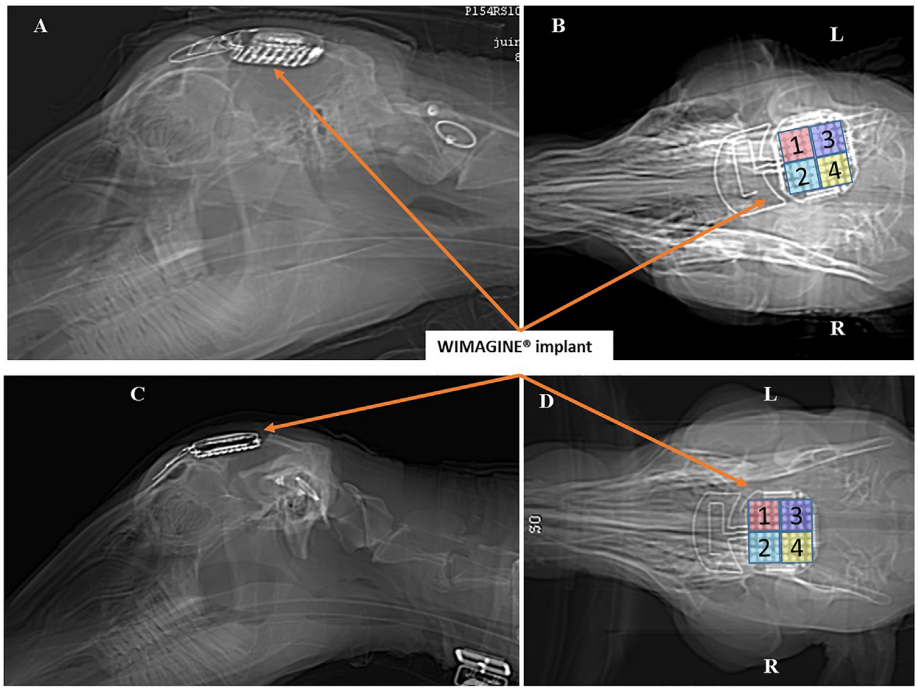

FIGURE 4 | Scanner controls 3 days after surgery: Left sagittal view and right bottom view. Panels **(A,B)** for sheep #1 and Panels **(C,D)** for sheep #2. (R: right side, L: left side).

session was performed under general anesthesia. We kept the anesthetic protocol chosen for the implantation since according to Baines et al. (1985), halothane which is similar to isoflurane has a limited impact on SSEP magnitude (10 to 30% decrease on peak magnitude for less than 35% of the sheep). Consequently, premedication was started with Diazepam 4.5 ml and Morphine 0.9 ml, anesthesia was induced with intravenously applied Propofol (4 mg/kg, 1/4 dose) and maintained using vaporized isoflurane (2%) in oxygen.

The tibial and median nerves of each limb were stimulated by a peripheral nerve stimulator (Energy Light©, MicroMED®, Italy) using two subdermal electrodes (anode proximal, cathode distal) and the SSEP were recorded using WIMAGINE®. For electrical stimulation, we increased the amplitude of the current until visible limb contraction was obtained between 2 and 20 mA, 100 μs pulse width and 2 Hz-train of 150–350 biphasic stimuli.

After a 10-month implantation period, the WIMAGINE® implants were explanted and the brains fixed for immunohistochemical analysis.

Signal Recording and Analysis

Signal Recording

Both cortical activity in an idle state and evoked potentials were recorded using the platform approved for CLINATEC's clinical trial (Mestais et al., 2015). To ensure a robust RF communication link, we chose the 2-FSK mode of the Microsemi component (ZL70102). In this configuration the wireless data transmission is about 250 kb/s. As the Analog Digital Converter has a 12-bit resolution and the sampling frequency (SF) 976 Hz, we decided to sequentially record four 3-min long sessions for each 16-contact phases.

Chronic signal quality was quantified using raw signal power spectral density (PSD) (Bundy et al., 2014), signal-to-noise ratios (SNRs) (Nurse et al., 2018), group level signal power (P_{band}) (Nurse et al., 2018), and maximum/effective bandwidth (BW) (Oxley et al., 2016; Nurse et al., 2018).

Raw Signal Power Spectral Density

Power spectral density of raw signal was estimated (pwelch spectral analysis, 5-s window length, 80% overlap) for each channel. The mean PSD across channels was computed for implants.

Group Level Signal Power P_{band}

Group level signal power P_{band} was computed as the mean PSD per band for the frequency bands (0–10), (10–40), (40–100), and (100–200) Hz. The P_{band} was averaged across channels for each Phase (Phases 1–4) of each implant and is presented in 10 $\log_{10}$ scale. Frequency bands are chosen following to previous studies (Nurse et al., 2018), and as relevant frequency bands for ECoG based BCI (Wang et al., 2013).

Group Signal-to-Noise Ratio (SNR_{band})

Group signal-to-noise ratio (SNR_{band}) was calculated as ratio of mean PSD per band P_{band} and mean PSD of noise P_{noise} in 10 $\log_{10}$ scale:

$$SNR_{band} = 10 \log_{10} \frac{P_{band}}{P_{noise}}.$$

We estimate P_{noise} in (250–260) Hz band due to the digital filter of the Integrated Circuit (cut-off frequency 300 Hz) which start altering the signal above ∼250/260 Hz (**Figure 6**). The use of higher band may bias the SNRs. 10 Hz large bandwidth corresponds to Nurse et al. (2018).

Finally, the *Effective BW* was computed. Upper limit was estimated (Nurse et al., 2018) for cumulative/total noise power CP_{noise}, calculated for band (250 – $f_{\max}$) Hz, $f_{\max}$ is a Nyquist frequency:

$$CP^{+}_{\text{noise}} = 1.5\,[Q_{75}\,(CP_{\text{noise}}) - Q_{25}\,(CP_{\text{noise}})] + Q_{75}\,(CP_{\text{noise}})\,,$$

where $Q_n()$ is n^{th} quantile. Then the frequency, below which x percent ($x = (P - CP^{+}_{\text{noise}})/P$) of the total power P of the signal are located, is computed. Effective BW is thus similar to the Spectral Edge Frequency SEFx[1] .

All statistical analyses were undertaken using GraphPad Prism (version 7.00 for Windows; GraphPad Software, La Jolla, CA, United States). In comparison to Nurse's work for each spectrogram measured and classified in frequency bands [(0–10), (10–40), (40–100), and (100–200) Hz], a linear regression model was used to determine a linear model of the measure as a function of time (Nurse et al., 2018). The coefficients of the linear fit (intercept and slope) were then analyzed to determine the rate of change with time.

Tissue Preparation and Histological Analysis of Brain Reactivity

At the end of this chronological study, histological investigations were performed *post mortem* to evaluate long-term effects of implantation. After freezing, two device areas were cut coronally using a freezing microtome (Leica Microsystem). Sections were collected and processed for Nissl staining and immunohistochemistry for glial fibrillary acidic protein (GFAP), and macrophage detection and microglial activation (CD11b). For the measurement of Dura mater thickness, a sample of Dura mater distant from the implantation area served as a control for the implant-covered Dura mater analysis. Three sections of Dura mater from the implant-covered area and three sections from control Dura mater were cut (30 μm thick) for Nissl staining. A measurement of the dura mater thicknesses (n = 100 per group) was performed using Cell Sens Science Imaging Software (Olympus). The results were represented as mean ± SD. For immunohistochemical analysis, sections were incubated with the following primary antibody solutions overnight at 4°C: anti-GFAP (1:500, monoclonal mouse IgG2b; BioRad Hercules, CA, United States) to identify astrocytes, and anti-CD11b (1/500, monoclonal mouse IgG2b; BioRad Hercules, CA, United States) to identify macrophage/microglia. Secondary antibodies (Molecular Probes – Alexa 488) were diluted to detect anti-GFAP and anti-CD11b antibodies. All sections were counterstained by incubation with the nuclear dye Propidium Iodide (Sigma-Aldrich). Sections treated only with secondary antibody served to determine non-specific binding. Tissue sections were mounted with Fluorsave reagent (Merck Millipore, France) and bound primary antibodies were visualized on a set of arbitrary defined slices, using a confocal microscope.

[1]https://en.wikipedia.org/wiki/Spectral_edge_frequency

RESULTS

In vivo Recording Evaluation

Idle State ECoG Recordings

WIMAGINE® allowed us to perform wireless chronic ECoG recordings up until the end of the scheduled period of 300 days. The procedure and post-operatory events proceeded without problems. The sheep recovered immediately and were able to resume all their normal activities (walking and feeding unassisted) within a few hours. An example of the time-course ECoG is shown in **Figure 5**. We faced no difficulties either to connect the base station to the implant or to record from the ECoG electrodes, except for chewing artifacts (**Supplementary Figure S1**). Signal review demonstrated little effect of line noise in the 50 Hz band (confirmed by **Figure 6**) and in harmonics, so we did not apply a notch filter.

Four and a half months after implantation, sheep #2 accidentally hit one of the bars of its enclosure. The increased overall noise in ECoG recordings was a clue of implant dislodgement. From CT scans, we confirmed a significant reduction in the contact between electrode array and the dura mater. We decided to explant this WIMAGINE® device, ending recording sessions with this implant at day-135 for sheep#2, which stayed until the end of the 10-month period to keep company to sheep#1 in accordance with animal husbandry best practices.

Power Spectral Density and Signal to Noise Ratio

To estimate signal quality, we plotted the mean PSD for the two sheep, and compared these signals to the baseline, which consists of the intrinsic noise of the electronic components. Application Specific Integrated Circuit [ASIC named Cinesic and described in Robinet et al. (2011)] stands for the electronic components in **Figure 6**. The Nyquist frequency is 488 Hz (SF = 976 Hz) but above 250 Hz the signal spectrum is impaired by the digital band pass filter of the ASIC, and cannot be discriminate from noise.

The median signal power and SNR, calculated weekly across the 16 channels for each phase of each animal are shown in **Figure 7** demonstrating moderate decrease in high frequencies (**Supplementary Tables S1, S2**).

Effective Bandwidth

The effective bandwidth is in the range of 230 Hz for sheep #1 and #2 (**Figure 8**). We end the plot for sheep#2 after day 135, when the animal hit its head on one bar of the enclosure, as this dislodged the implant from the craniotomy which corresponds to a dramatic drop of the effective bandwidth. The trends of effective bandwidth for sheep #1 and #2 remained remarkably steady throughout the experiment (at least until day 135); slopes are not significantly different from zero (**Supplementary Table S2**).

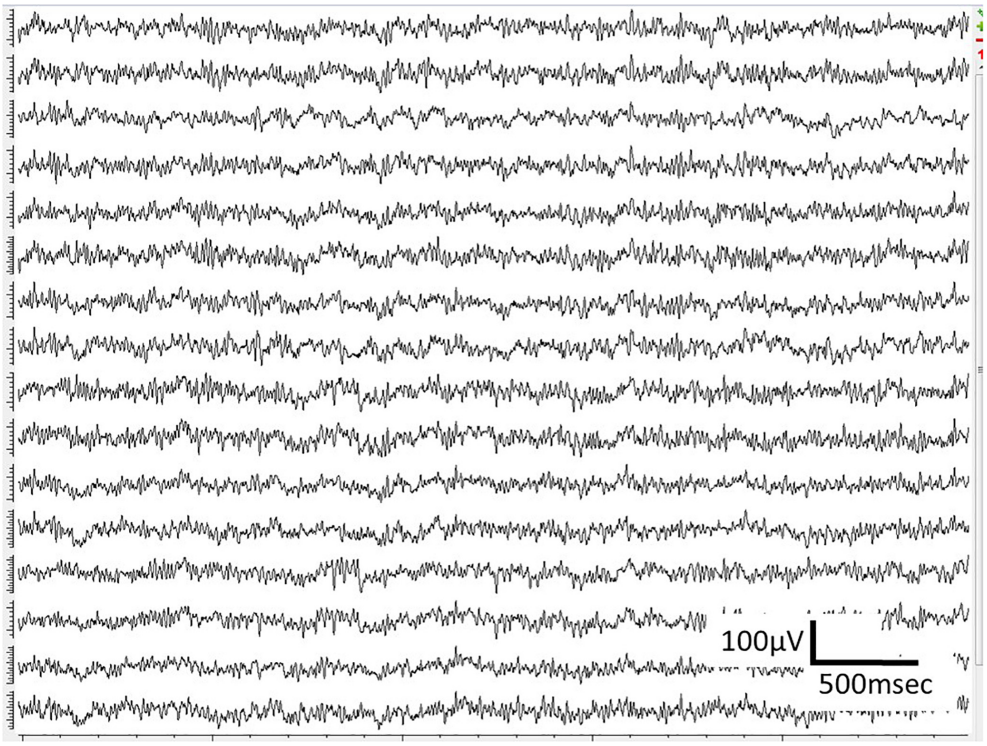

FIGURE 5 | Examples of ECoG recordings in awake sheep, using the WIMAGINE® platform.

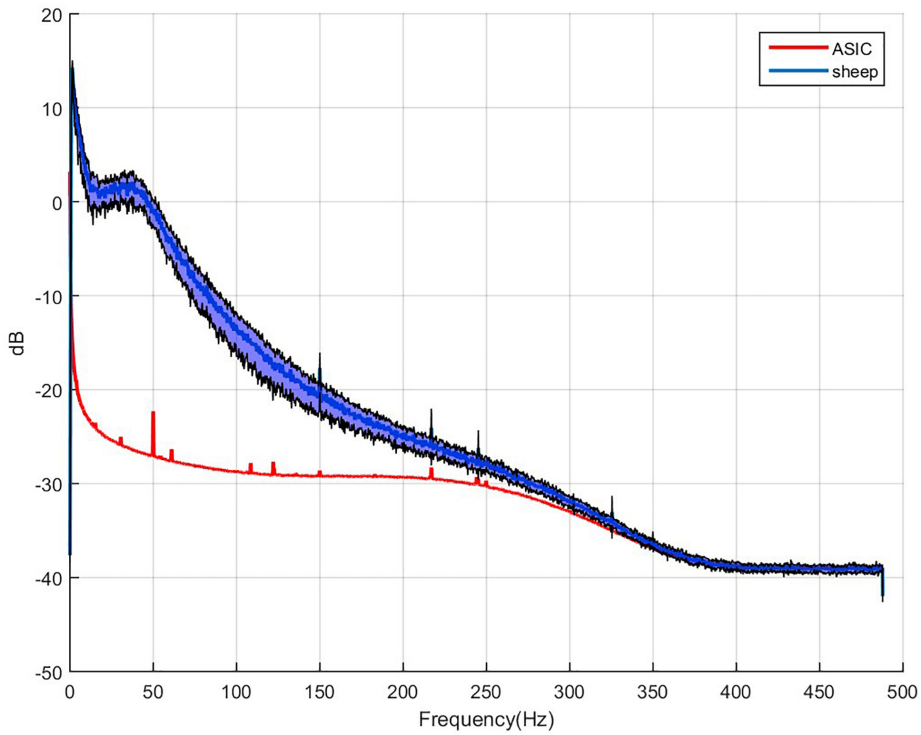

FIGURE 6 | Example of 64 averaged electrode power spectral densities of ECoG during a period without chewing. *X*-axis: frequencies in Hertz, *Y*-axis: logarithm of spectral power in dB. Mean value for sheep in blue, black curves stand for the standard deviation for both animals compared to the intrinsic noise of the electronic components (labeled ASIC) with grounded electrodes.

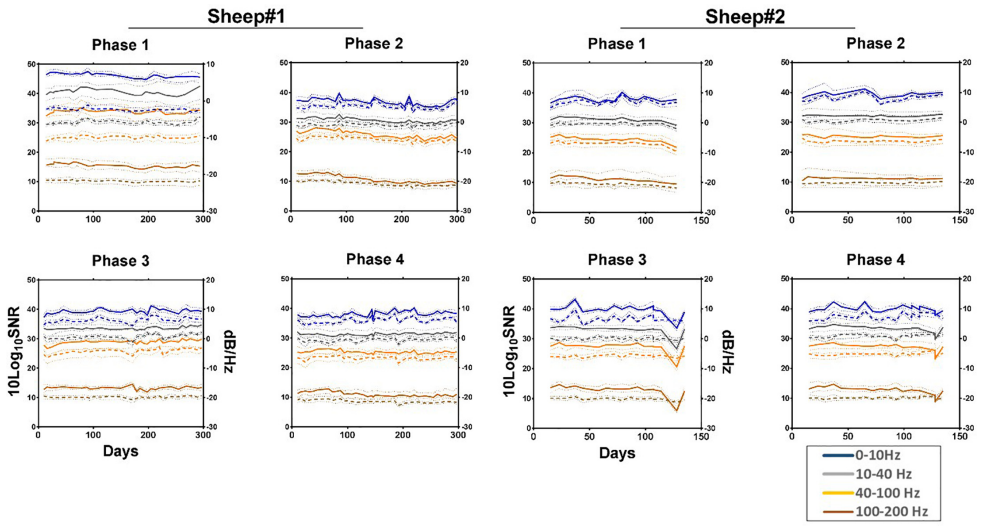

FIGURE 7 | Median normalized power spectral density (solid line) and SNR (dashed line) showing their respective 95% confidence intervals (pointed lines) for each phase across four frequency bands as a function of time. All values are normalized to the size of the band. Estimated noise band: 250–260 Hz. Each line represents the median of the 16 channels across the given bands. Phase 1: left anterior, Phase 2: right anterior, Phase 3: left posterior, and Phase 4: right posterior area of the electrode array.

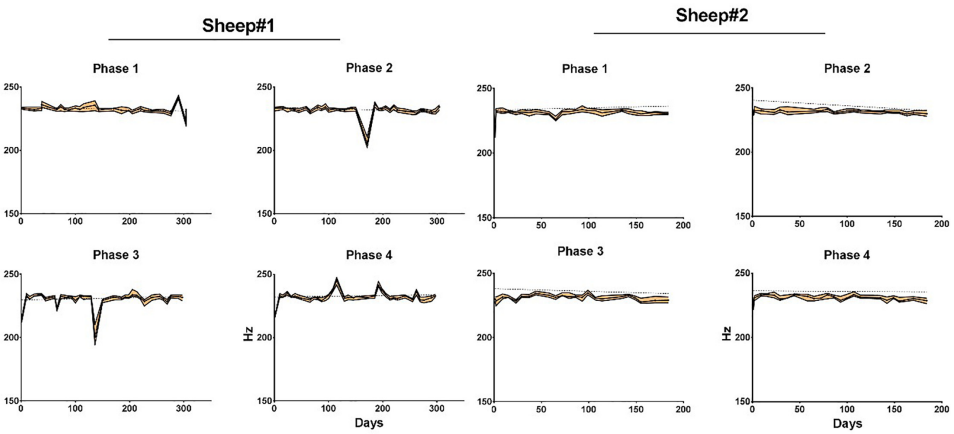

FIGURE 8 | Median effective bandwidth for each phase and animal as a function of time. Areas in orange represent the 95% confidence intervals. Dotted line represents linear regression fit for each phase. Phase 1: left anterior, Phase 2: right anterior, Phase 3: left posterior, and Phase 4: right posterior area of the electrode array.

Somato Sensory Evoked Potentials

Somato sensory evoked potentials are likely to arise with a latency of about 25 ms for thoracic limb stimulation according to Sanborn et al. (2011). Moreover, an inversion of the signal is expected when comparing the lower and the upper side of Rolando's sulcus. In **Figure 9** (left), a right thoracic limb activation triggered the SSEP peaks and the expected inversion in the proper cortical areas. This confirms the biological relevance of the recorded signal, in particular when studying an implant for a BCI. The location of the area recorded by the WIMAGINE® implant is symbolized by a dotted rectangle (**Figure 9**, right). A set of three SSEP experiments with sheep#1 is presented (see **Supplementary Table S3**).

Long-Term Biocompatibility Evaluation

Histological examinations were performed post-mortem, 10 months after implantation. After euthanasia of animals and removal of skin and muscles covering the implants, observation of the implantation sites showed no encapsulation of the WIMAGINE® implants (**Figure 10B**). Interestingly the implants were still functional after explantation. The adhesion of the electrode array and the MED-6210 over-molding silicone with tissues in contact was also tested. The WIMAGINE® implants could be freely removed without damaging the dura mater. As is shown in **Figure 10C**, we did not observe any macroscopic sign of tissue defect but only surgical sutures used to repair adhesion spots of dura mater when the bone flap was removed. After

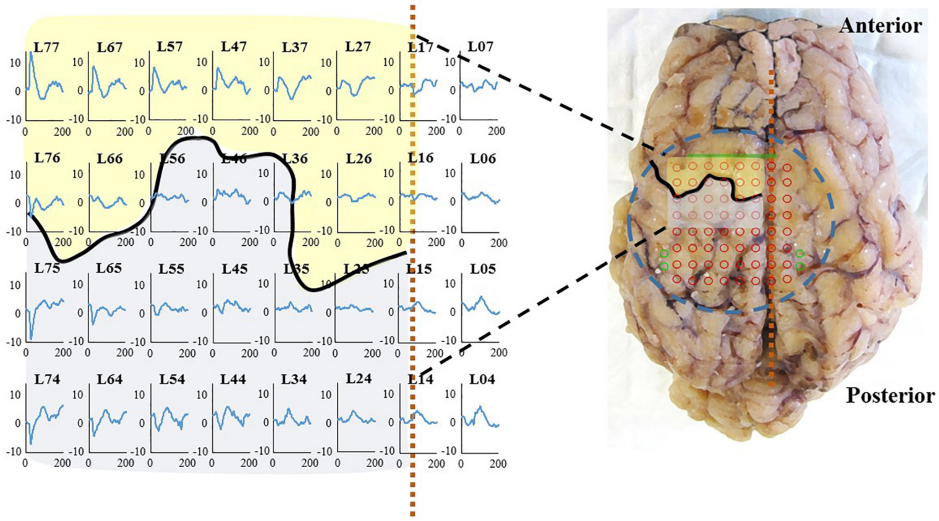

FIGURE 9 | (Left): SSEP at 2 months on sheep #1, right thoracic limb (right forelimb) stimulation on sheep #1: 100 μs, 2 Hz, 4 mA **(Right)**: Brain after explantation the dashed blue circle represents the contact with the inferior face of WIMAGINE® with projection of the recording contacts in red and reference electrodes in green. The black curve and the dashed vertical orange line locate, respectively the central sulcus and the SSS. Primary motor cortex and somatosensory cortex are represented in transparency in yellow and gray, respectively.

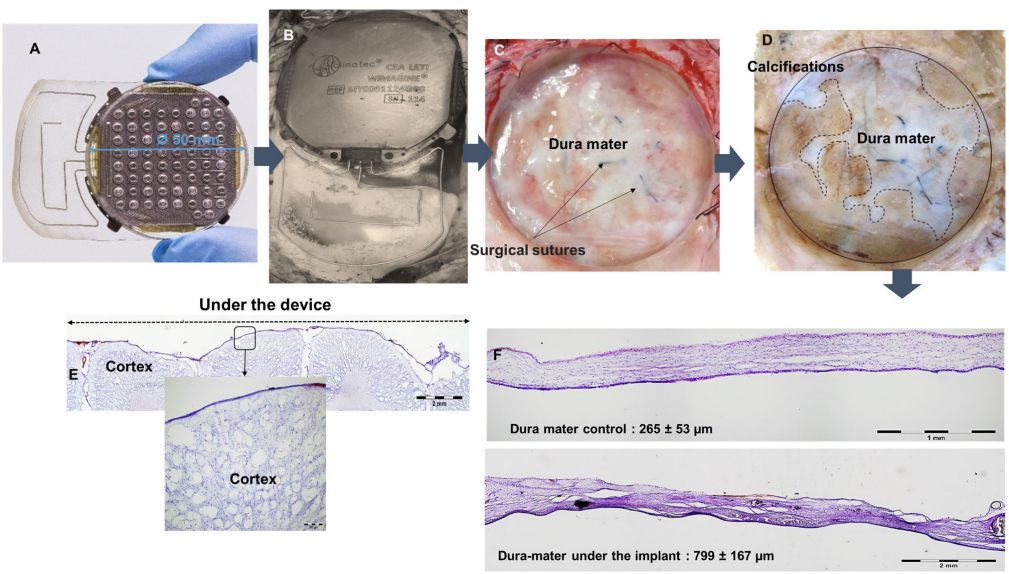

FIGURE 10 | (A) WIMAGINE® before implantation, **(B)** WIMAGINE® before explantation, **(C)** aspect of the duramater after implant withdrawal, **(D)** duramater after chemical fixation. Microscopic analysis Nissl staining **(E)** control of the thickness of the duramater **(F)** cross section of the brain under the device. Data of sheep #1 after a 10-month implantation.

removal of the skull, brain tissues were prepared by chemical fixation for microscopic examination in order to evaluate tissue response in contact with the WIMAGINE® implant (dura mater and leptomeninges structures) and at distance (glia limitans and brain cortex). On the first part of the brain below the implant, the dura mater was removed from the brain surface and transversally cut to evaluate its thickness. As shown in **Figure 10D**, observations of the dura mater and the leptomeninges covered by the epidural implant revealed histopathological changes. The thickness of the implant covered dura mater was 799 ± 167 mm, whereas that of the implant-uncovered dura mater was 265 ± 53 mm (**Figures 10A,E,F**). As shown in **Figure 10D**, we observed calcification areas extending from the edges of the craniotomy to the center and these covered nearly 50% of the surface under the electrode array.

A second part of the histological studies was conducted to evaluate brain cortex reactions beneath the epidural WIMAGINE® implant and to detect signs of inflammation.

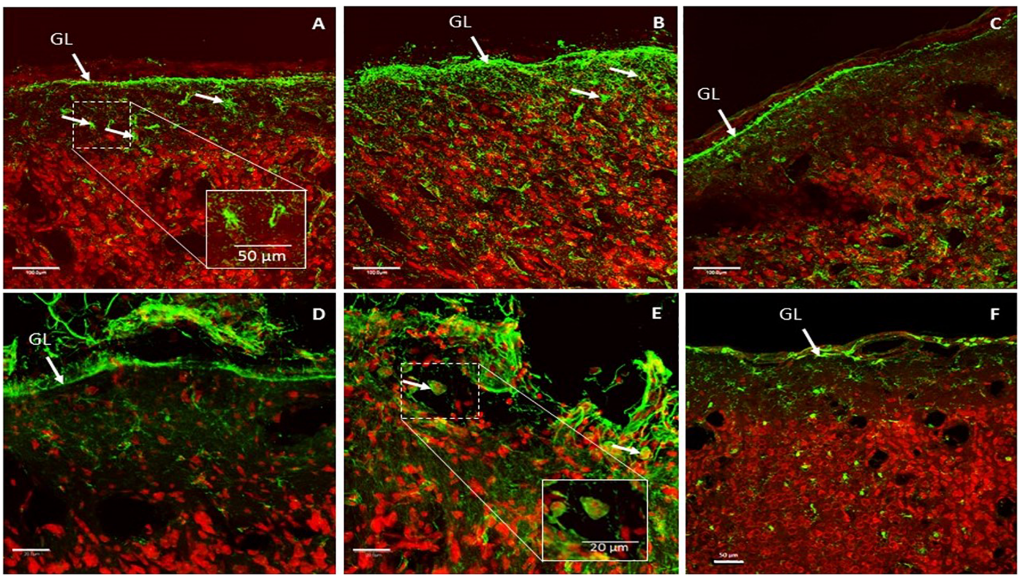

FIGURE 11 | Representative glial fibrillary acidic protein (GFAP) expression patterns in implant-covered brain cortex **(A,B)** and in control brain cortex **(C)**. Scale bar = 100 µm. Representative CD11b expression patterns in implant-covered brain cortex **(D,E)** and uncovered brain cortex **(F)**. Scale bar = 20 µm **(D,E)**, 50 µm **(F)**. GL: glia limitans.

Reactive gliosis is the endogenous response of brain tissue to aggression and this corresponds to the accumulation and/or recruitment of glial cells (astrocytes and microglia). Glial activation is the release of glial factors that will act on target cells in the same way as the cellular immune response, and thus promote peripheral monocyte infiltration (especially macrophages and lymphocytes). Immunohistochemical studies were performed to detect signs of reactive gliosis and monocyte infiltration in the brain cortex. The results are shown in **Figure 11**.

GFAP is a commonly used marker to evaluate reactive gliosis as an astrocytic reaction to injury. Implant-covered brain cortex areas were characterized by elevated GFAP intensity in Glia Limitans and in layer I of the brain cortex, compared to normal cortical tissue far away from contact areas. As presented in **Figures 11A,B**, implant-covered brain cortex areas showed a substantial increase in GFAP reactivity, extending from Glia Limitans to layer I of the cerebral cortex. Staining revealed that astrocytes became hypertrophic; elongated with thick processes (**Figures 11A,B**) as compared to those in the intact brain region, which were more stellate in appearance (**Figure 11C**). GFAP immunoreactivity was maximum at the periphery of the contact site (**Figure 11B**) and declined progressively as a function of the distance from the periphery to the center of the contact area. Such elevation was observed up to 400 µm from the cortical surface.

Activated microglia and macrophages were identified via CD11b staining. The implant-covered site was characterized by a substantial increase in CD11b reactivity above Glia Limitans (**Figure 11D**). As is shown in **Figure 11E**, CD11b reactivity was increased in the peripheral contact area revealing macrophages and activated microglial cells. Some of the CD11b + cells had the appearance of large, round, blood-borne monocytes/macrophages. Smaller, process-bearing microglia were also seen at various distances from the contact site. Staining in the intact brain zone revealed resting microglia with small rod-shaped somata from which numerous thin and highly ramified processes emerged (**Figure 11F**).

DISCUSSION

The design and manufacture of cortical implants for medical use required long and expensive endeavors. Kohler et al. (2017) only identified seven teams world-wide at this level of technological readiness. Indeed, for a device to be approved for clinical trials, it is mandatory to justify the compliance of the design and manufacturing standards. In particular, Active Implantable Medical Devices directive 90/385/EEC or ISO14708-1 and ISO 13485 for quality management must be respected. Moreover, while accelerated aging tests may be interesting to determine the physical limits of the materials or the packaging hermeticity, long-term preclinical tests are mandatory to assess the implant behavior in real conditions *in vivo*. In this study, our first goal was a long-term validation of the functionality of the WIMAGINE® implant and the assessment of the quality of the ECoG signal with time.

Kohler et al.'s study shares many similarities with ours. After a previous mapping experiment on sheep, this species was chosen as a model for long-term assessment of their wireless device, for which recording performances were assessed using SSEP or Auditory Evoked Potential (Gierthmuehlen et al., 2014). As far as we are concerned, we successfully recorded SSEP.

In previous preclinical studies, we published validation results of the electrode array using a semi-scale device (without electronics) on non-human primates. The signal quality and the

algorithms were tested in depth using epidural electrode arrays that were wired to external WIMAGINE® implants (Mestais et al., 2015). In addition, inspired by implantation for 4 months in the sheep model (Oxley et al., 2016; Torres et al., 2017) and clinical studies (Nurse et al., 2018), we extensively investigated ECoG signals over time (SNR, effective bandwidth) to validate its compliance with long-term implantation and with our final goal: enabling the "BCI and tetraplegia" clinical trial at CLINATEC (NCT02550522).

Sheep Model Relevance for WIMAGINE® Testing

In preclinical testing, implant size is important when evaluating a clinical device: a scaled-down version adapted to fit small animal models does not usually fully reflect final human models. Device size reduction could have been detrimental when extracting general conclusions prior to clinical trials. Hence, there is a need for the use of larger species when dealing with medical devices (Torres et al., 2017).

Minipigs are commonly used for preclinical studies of cuff electrodes (Bonnet et al., 2013) or brain recordings (Gierthmuehlen et al., 2011). Unfortunately, for chronic experiments in minipigs, the frontal sinus, which is an open cavity connected to the paranasal sinuses above the brain is a major technical problem for the neurosurgeon and is an obvious source of infection.

The main advantage of the sheep model is the relative compatibility of the sheep skull (biparietal distance of 80 mm) with WIMAGINE® (50 mm in diameter). This set-up mimicked the implantation of the clinical device, even if only one WIMAGINE® implant was placed above the sagittal sinus instead of a bilateral implantation in the clinical protocol which may limit the interest of the phases above the sinus (phase 2 for sheep#1 and phase 1 and 3 for sheep#2, see **Figure 4**). Moreover, the mismatch between the electrode array planar surface and the curvature of the sheep brain is more than three times larger than for human brain. Consequently the contact between the electrode array and the dura is less homogeneous. However, there is no significative difference in the effective bandwidth of the four phases.

Even though the sheep head size was adequate, cranial implantation was more arduous than expected. Indeed, the craniotomy was initiated with a 50 mm large trephine, but finished with a small drill, to smoothen the relatively rough edges of the craniotomy. Moreover, the thickness of sheep skulls ranged from 4 to 7 mm at the edges of the craniotomy, the greater thickness lying above the parietal cortex. As a consequence, the contact between the electrode array and the cortex is less homogeneous than expected for humans. Furthermore, we reported a strong adhesion of the dura to the bone flap. These difficulties are unlikely to be encountered in human surgery, because the craniotomy does not cross the midline, avoiding additional manipulations.

We oriented the implants so that the implant antennas are placed anteriorly between the eyes. In this configuration the distance between the primary (external) and secondary (implant) was less than 20 mm, whereas the wireless link was designed for a distance of between 20 and 30 mm. We never faced communication issues either in post-operative conditions or during recording sessions: wireless links sent usable neural signals during the whole protocol.

ECoG Quality Assessment

To compare this result to the literature, we list several articles dealing with ECoG results either in preclinical or clinical long-term implantation. Using the Activa PC+S from Medtronic Inc., Swann et al. (2017) reported a decrease of the signal power for the beta and gamma band on a 1 year timeframe. Ung et al. (2017) using the NeuroVista device with subdural strip electrodes also reported a decrease in the mean values that reaches an inflection point roughly 100 days after implantation. Nurse et al. (2018) who also used subdural electrodes and the NeuroVista® device reported on mean power relatively steady behavior with low variation but individual changes are far more complex, highlighting the influence of electrode location on the cortex or contact quality. Sillay et al. (2013) using RNS® from NeuroPace® and subdural strip reported, on a median 868-day timeframe, an impedance increase within the first 84 days followed by a stabilization of the subdural electrode impedance. Apart Schendel et al. (2014), there are very few long-term assessment of epidural signal quality in the literature. For macrocontacts (2 mm in diameter), Bundy et al. (2014) reported significantly higher PSD for epidural recordings compared to epidural between 0 and 60 Hz and the opposite above 100 Hz. But this comparison was limited to a few weeks since their patients underwent temporary placement of intracranial electrode grids to identify epileptic seizure foci.

Firstly, once implanted the WIMAGINE® devices had a low sensitivity to the 50 Hz noise and its harmonics artifacts; artifacts did not increase with time. The main artifact recorded by the implant was muscular chewing activity, see **Supplementary Figure S1**. This is a specific characteristic of all ruminant species and was recently well-described (Oxley et al., 2016). Obviously, clinical extrapolation of the chewing artifact is not relevant.

Secondly, tissue reaction surrounding WIMAGINE® did not significantly alter ECoG signals over 10 months. The ECoG signal amplitude remained relatively stable during the 10-month period (see **Figure 7** and **Supplementary Table S1**).

The analysis of the maximum effective bandwidth showed a stable longitudinal behavior at levels of 230 Hz for both animals (**Supplementary Table S2**) and compare favorably with those described in the literature [level of 230 Hz vs. 100 Hz (Nurse et al., 2018); and vs. 200 Hz (Oxley et al., 2016) for epidural recording] and SNR for higher frequencies (2.6 vs. ∼1 for (40–100) Hz; 1.4 vs ∼0.2 for (100–200) Hz).

At the same time, eligibility of SNR comparison or effective bandwidth is limited by the difference in the recording device features, such as sampling rate, integrated digital filters, etc. It may be less favorable for lower sampling rate systems, or lower-pass filter (both influencing noise level estimation). Indeed, WIMAGINE device was designed for ECoG recording in the (0.5–300) Hz bandwidth. **Figure 6** shows that the

digital low pass filter alters the recordings above 250 Hz, 300 Hz being the cut-off frequency of this filter. Whereas Oxley et al. (2016) reported 227 and 200 ± 6 Hz, respectively for subdural and epidural contact using a Twente Medical Systems International (TMSI, Netherlands) amplifier with a low-pass filter of 553 Hz (Tinkhauser et al., 2018). Nurse et al. (2018) used the NeuroVista® device with a sampling frequency of 400 Hz and band-pass filter (0.1–195) Hz and obtained an effective bandwidth in the range of 100 Hz.

SSEP Assessment

The analysis of time evolution of epidural ECoG demonstrated a stable behavior. As the electrodes recorded information from the sensorimotor cortex (SMC) we tried to show – with anesthetized animals- phase reversal in SSEP, allowing identification of the central sulcus. We were able to identify evoked potentials on several SSEP sessions at months 2, 4 and 6 (see **Supplementary Table S3**). Topographical areas belonging to hind limbs and fore limbs were detected and central sulcus were also delineated at month 2 as shown in **Figure 9**.

Biocompatibility Evaluation

Macroscopic post-mortem analysis confirmed the presence of tissue reactions, as previously seen in several implantable neural devices (Kozai et al., 2015). The tissue response represented here has an increase in the dura mater thickness (by a factor of 3 compared to the control), separating the recording matrix from the signal source. As discussed above, signal attenuation in this case did not alter the transmission of relevant physiological information (SSEP).

These *in vivo* trials enabled us to demonstrate the benefits of epidural implantation for an appropriate brain tissue response. The end-stage healing response to materials is usually a fibrous reaction reducing device performances. We only observed a dura mater reaction consisting of a significant thickening of this external meningeal layer. This thickening may be due to the fact that the dura mater was injured and sutured when the bone flap was removed and meningeal fibroblasts were activated. The presence of fibrotic scar tissue was confirmed by microscopic investigation. In addition to dura mater changes below the WIMAGINE® implant, we observed calcifications extending from the edges of the craniotomy to the center. These calcifications could be a consequence of the craniotomy and could be explained by an osteogenic action *via* osteoforming-cells, namely osteoblasts. These cells are present in the internal periosteum and could be activated during removal of the bone flap by a regenerative process including blood factors (released upon injury of blood vessels). Due to the small curvature of sheep brain, the contact between the implant and the dura was probably too weak at the edges of the craniotomy. This could also explain the calcification.

Then we studied the effect of the WIMAGINE® implant on astrocytes and microglia/macrophages *in vivo*. To study the brain cortex response below the WIMAGINE® implant, we performed GFAP and CD11b labeling to detect astrogliosis and microglial activation, respectively. In this study, we observed the presence of reactive astrocytes and macrophages/activated microglia at the implantation site. In our study, GFAP + astrocytes and CD11-B + macrophages/activated microglia were observed predominantly in the periphery of the contact area and at a depth which did not exceed cortical layer 1. As a result of vascular damage, macrophages derived from the bloodstream are recruited to the injury site, and microglia – the resident immune cells of the brain-become activated.

Importantly, the effective ECoG signal bandwidth remained remarkably stable despite this observed partial calcification, combined with dura-mater thickening and superficial astrogliosis (**Figure 8**).

CONCLUSION

This article deals with the first long-term implantation of WIMAGINE®, a proprietary fully implantable wireless ECoG device which compliance with the safety requirements was previously described (Mestais et al., 2015).

We highlight:

- Surgery was successfully performed on two large animals (adult sheep) and ECoG signals were recorded weekly for 10 months. For the first time, long-term SSEP and signal recordings were obtained using the WIMAGINE® implant in an awake ovine model, using the acquisition platform developed for clinical trials;
- Relatively stable power spectra and SNRs of these epidural recordings. The effective bandwidth was observed at a level of 230 Hz, meaning that the high frequency bands useful for BCI decoding were preserved;
- Post-mortem analysis was carried out and showed as expected a thickening of the dura-mater below the implant but no significant inflammation or glial activation in the cortex.

The sheep animal model is different from humans in terms of anatomy and brain activity. Even if, the reported analysis of signal quality cannot be directly translated to human studies, similar methodology could be carried out on human ECoG. The outcome of this preclinical work is the first long-term *in vivo* validation of the WIMAGINE® implant, confirming its ability to record brain electrical activity through the dura mater, and send digitized data wirelessly through the skin. It represents a major step toward conducting clinical trials.

ETHICS STATEMENT

Chronic implantation experiments were conducted on two female sheep (Ovis Aries) (80–90 kg, 5 and 8 years old). All experiments were carried out following the recommendations of the European Community Council Directives of 1986 (86/609/EEC), the National Institutes of Health Guide for the Care and Use of Laboratory Animals. The Ethics Committee COMETH of Lyon, France approved the experimental protocol which was registered to the national committee under reference number 1504_V2.

AUTHOR CONTRIBUTIONS

FS-S, NT-M, DR, and TA wrote the manuscript. FS-S, NT-M, and CC designed the study. AL, MF, GC, and CM contributed to the experiments and provided technical support. SB, TA, TC, and A-LB contributed to the data analysis. CG and DR designed and performed the histological studies.

FUNDING

This work received financial support through grants from the French National Research Agency (ANR-Carnot Institute), Fondation Motrice, Fondation Nanosciences, Fondation de l'Avenir, Fonds de dotation Clinatec, Expleo, KLESIA, and Fondation Philanthropique Edmond J. Safra.

ACKNOWLEDGMENTS

Preclinical studies were performed at the veterinary school of Lyon, France. The authors thank the Vetagro Sup team for their help and contributions and are grateful to all members of CEA-LETI-CLINATEC. The authors would additionally like to thank the reviewers for their insightful comments and suggestions, which have helped to improve the quality of this manuscript.

SUPPLEMENTARY MATERIAL

The Supplementary Material for this article can be found online at: https://www.frontiersin.org/articles/10.3389/fnins.2019.00847/full#supplementary-material

REFERENCES

Baines, D. B., Whittle, I. R., Chaseling, R. W., Overton, J. H., and Johnston, I. H. (1985). Effect of halothane on spinal somatosensory evoked potentials in Sheep. *Br. J. Anaesth.* 57, 896–899. doi: 10.1093/bja/57.9.896

Bonnet, S., Rubeck, C., Agache, V., Bourgerette, A., Fuchs, O., Gharbi, S., et al. (2013). "Selective ENG recordings using a multi-contact cuff electrode," in *2013 6th International IEEE/EMBS Conference on Neural Engineering (NER)*, (Piscataway, NJ: IEEE), 923–926. doi: 10.1109/NER.2013.6696086

Bundy, D. T., Zellmer, E., Gaona, C. M., Sharma, M., Szrama, N., Hacker, C., et al. (2014). Characterization of the effects of the human dura on macro- and micro-electrocorticographic recordings. *J. Neural Eng.* 11:016006. doi: 10.1088/1741-2560/11/1/016006

Chao, Z. C., Nagasaka, Y., and Fujii, N. (2010). Long-term asynchronous decoding of arm motion using electrocorticographic signals in monkey. *Front. Neuroeng.* 3:3. doi: 10.3389/fneng.2010.00003

Cook, M. J., O'Brien, T. J., Berkovic, S. F., Murphy, M., Morokoff, A., Fabinyi, G., et al. (2013). Prediction of seizure likelihood with a long-term, implanted seizure advisory system in patients with drug-resistant epilepsy: a first-in-man study. *Lancet Neurol.* 12, 563–571. doi: 10.1016/S1474-4422(13)70075-9

Degenhart, A. D., Eles, J., Dum, R., Mischel, J. L., Smalianchuk, I., Endler, B., et al. (2016). Histological evaluation of a chronically-implanted electrocorticographic electrode grid in a non-human primate. *J. Neural Eng.* 13:046019. doi: 10.1088/1741-2560/13/4/046019

Eliseyev, A., and Aksenova, T. (2013). Recursive N-Way partial least squares for brain-computer interface. *PLoS One* 8:e69962. doi: 10.1371/journal.pone.0069962

Gierthmuehlen, M., Ball, T., Henle, C., Wang, X., Rickert, J., Raab, M., et al. (2011). Evaluation of μECoG electrode arrays in the minipig: experimental procedure and neurosurgical approach. *J. Neurosci. Methods* 202, 77–86. doi: 10.1016/j.jneumeth.2011.08.021

Gierthmuehlen, M., Wang, X., Gkogkidis, A., Henle, C., Fischer, J., Fehrenbacher, T., et al. (2014). Mapping of sheep sensory cortex with a novel microelectrocorticography grid: micro-ECoG in sheep. *J. Comp. Neurol.* 522, 3590–3608. doi: 10.1002/cne.23631

He, B., and Sohrabpour, A. (2016). Imaging epileptogenic brain using high density EEG source imaging and MRI. *Clin. Neurophysiol.* 127, 5–7. doi: 10.1016/j.clinph.2015.04.074

Hochberg, L. R., Serruya, M. D., Friehs, G. M., Mukand, J. A., Saleh, M., Caplan, A. H., et al. (2006). Neuronal ensemble control of prosthetic devices by a human with tetraplegia. *Nature* 442, 164–171. doi: 10.1038/nature04970

Katona, J., Ujbanyi, T., Sziladi, G., and Kovari, A. (2016). "Speed control of festo robotino mobile robot using neurosky mindwave EEG headset based brain-computer interface," in *2016 7th IEEE International Conference on Cognitive Infocommunications (CogInfoCom)*, (Wrocław: IEEE).

Kohler, F., Gkogkidis, C. A., Bentler, C., Wang, X., Gierthmuehlen, M., Fischer, J., et al. (2017). Closed-loop interaction with the cerebral cortex: a review of wireless implant technology. *Brain Comput. Interfaces* 4, 146–154. doi: 10.1080/2326263X.2017.1338011

Kozai, T. D. Y., Jaquins-Gerstl, A. S., Vazquez, A. L., Michael, A. C., and Cui, X. T. (2015). Brain tissue responses to neural implants impact signal sensitivity and intervention strategies. *ACS Chem. Neurosci.* 6, 48–67. doi: 10.1021/cn500256e

Maynard, E. M., Nordhausen, C. T., and Normann, R. A. (1997). The utah intracortical electrode array: a recording structure for potential brain-computer interfaces. *Electroencephalogr. Clin. Neurophysiol.* 102, 228–239. doi: 10.1016/s0013-4694(96)95176-0

Mestais, C. S., Charvet, G., Sauter-Starace, F., Foerster, M., Ratel, D., and Benabid, A. L. (2015). WIMAGINE: wireless 64-channel ECoG recording implant for long term clinical applications. *IEEE Trans. Neural Syst. Rehabil. Eng.* 23, 10–21. doi: 10.1109/TNSRE.2014.2333541

Nurse, E. S., John, S. E., Freestone, D. R., Oxley, T. J., Ung, H., Berkovic, S. F., et al. (2018). Consistency of long-term subdural electrocorticography in humans. *IEEE Trans. Biomed. Eng.* 65, 344–352. doi: 10.1109/TBME.2017.2768442

Oxley, T. J., Opie, N. L., John, S. E., Rind, G. S., Ronayne, S. M., Wheeler, T. L., et al. (2016). Minimally invasive endovascular stent-electrode array for high-fidelity, chronic recordings of cortical neural activity. *Nat. Biotechnol.* 34, 320–327. doi: 10.1038/nbt.3428

Robinet, S., Audebert, P., Regis, G., Zongo, B., Beche, J., Condemine, C., et al. (2011). A low-power 0.7μVrms 32-channel mixed-signal circuit for ECoG recordings. *IEEE J. Emerg. Sel. Top. Circuits Syst.* 1, 451–460. doi: 10.1109/JETCAS.2011.2180835

Rousche, P. J., and Normann, R. A. (1998). Chronic recording capability of the utah intracortical electrode array in cat sensory cortex. *J. Neurosci. Methods* 82, 1–15. doi: 10.1016/s0165-0270(98)00031-4

Ryapolova-Webb, E., Afshar, P., Stanslaski, S., Denison, T., de Hemptinne, C., Bankiewicz, K., et al. (2014). Chronic cortical and electromyographic recordings from a fully implantable device: preclinical experience in a nonhuman primate. *J. Neural Eng.* 11:016009. doi: 10.1088/1741-2560/11/1/016009

Sanborn, M. R., Balzer, J., Gerszten, P. C., Karausky, P., Cheng, B. C., and Welch, W. C. (2011). Safety and efficacy of a novel ultrasonic osteotome device in an ovine model. *J. Clin. Neurosci.* 18, 1528–1533. doi: 10.1016/j.jocn.2011.04.016

Schendel, A. A., Nonte, M. W., Vokoun, C., Richner, T. J., Brodnick, S. K., Atry, F., et al. (2014). The effect of micro-ECoG substrate footprint on the meningeal tissue response. *J. Neural Eng.* 11:046011. doi: 10.1088/1741-2560/11/4/046011

Schwartz, A. B., Cui, X. T., Weber, D. J., and Moran, D. W. (2006). Brain-controlled interfaces: movement restoration with neural prosthetics. *Neuron* 52, 205–220. doi: 10.1016/j.neuron.2006.09.019

Sillay, K. A., Rutecki, P., Cicora, K., Worrell, G., Drazkowski, J., Shih, J. J., et al. (2013). Long-term measurement of impedance in chronically implanted depth and subdural electrodes during responsive neurostimulation in humans. *Brain Stimul.* 6, 718–726. doi: 10.1016/j.brs.2013.02.001

Swann, N. C., De Hemptinne, C., Miocinovic, S., Qasim, S., Ostrem, J. L., Galifianakis, N. B., et al. (2017). Chronic multisite brain recordings from a totally implantable bidirectional neural interface: experience in 5 patients

with Parkinson's disease. *J. Neurosurg.* 128, 605–616. doi: 10.3171/2016.11.JNS161162

Tinkhauser, G., Torrecillos, F., Duclos, Y., Tan, H., Pogosyan, A., Fischer, P., et al. (2018). Beta burst coupling across the motor circuit in Parkinson's disease. *Neurobiol. Dis.* 117, 217–225. doi: 10.1016/j.nbd.2018.06.007

Torres, N., Molet, J., Moro, C., Mitrofanis, J., and Benabid, A. L. (2017). Neuroprotective surgical strategies in Parkinson's disease: role of preclinical data. *Int. J. Mol. Sci.* 18:E2190. doi: 10.3390/ijms18102190

Ung, H., Baldassano, S. N., Bink, H., Krieger, A. M., Williams, S., Vitale, F., et al. (2017). Intracranial EEG fluctuates over months after implanting electrodes in human brain. *J. Neural Eng.* 14:056011. doi: 10.1088/1741-2552/aa7f40

Vansteensel, M. J., Pels, E. G. M., Bleichner, M. G., Branco, M. P., Denison, T., Freudenburg, Z. V., et al. (2016). Fully implanted brain–computer interface in a locked-in patient with ALS. *N. Engl. J. Med.* 375, 2060–2066. doi: 10.1056/NEJMoa1608085

Wang, W., Collinger, J. L., Degenhart, A. D., Tyler-Kabara, E. C., Schwartz, A. B., Moran, D. W., et al. (2013). An electrocorticographic brain interface in an individual with tetraplegia. *PLoS One* 8:e55344. doi: 10.1371/journal.pone.0055344

Conflict of Interest Statement: The authors declare that the research was conducted in the absence of any commercial or financial relationships that could be construed as a potential conflict of interest.

frontiers in Neuroscience

ORIGINAL RESEARCH
published: 24 September 2019
doi: 10.3389/fnins.2019.01019

Somatosensation Evoked by Cortical Surface Stimulation of the Human Primary Somatosensory Cortex

St. Clair Kirin[1,2], Takufumi Yanagisawa[3,4,5], Satoru Oshino[3], Kohtaroh Edakawa[3], Masataka Tanaka[3], Haruhiko Kishima[3] and Yukio Nishimura[1,2,6]**

[1] Department of Developmental Physiology, National Institute for Physiological Sciences, Okazaki, Japan, [2] Department of Physiological Sciences, School of Life Sciences, The Graduate University for Advanced Studies (SOKENDAI), Hayama, Japan, [3] Department of Neurosurgery, Graduate School of Medicine Osaka University, Suita, Japan, [4] Center for Information and Neural Networks, National Institute of Information and Communications Technology, Suita, Japan, [5] Institute for Advanced Co-Creation Studies, Osaka University, Suita, Japan, [6] Neural Prosthesis Project, Department of Dementia and Higher Brain Function, Tokyo Metropolitan Institute of Medical Science, Tokyo, Japan

OPEN ACCESS

Edited by:
Alexei Ossadtchi,
National Research University Higher School of Economics, Russia

Reviewed by:
Burak Güçlü,
Boğaziçi University, Turkey
Patrick Haggard,
University College London, United Kingdom

***Correspondence:**
Takufumi Yanagisawa
tyanagisawa@nsurg.med.osaka-u.ac.jp;
takufumiy@gmail.com
Yukio Nishimura
nishimura-yk@igakuken.or.jp

Specialty section:
This article was submitted to Neuroprosthetics, a section of the journal Frontiers in Neuroscience

Received: 24 January 2019
Accepted: 09 September 2019
Published: 24 September 2019

Citation:
Kirin SC, Yanagisawa T, Oshino S, Edakawa K, Tanaka M, Kishima H and Nishimura Y (2019) Somatosensation Evoked by Cortical Surface Stimulation of the Human Primary Somatosensory Cortex. Front. Neurosci. 13:1019. doi: 10.3389/fnins.2019.01019

Electrical stimulation of the primary somatosensory cortex using intracranial electrodes is crucial for the evocation of artificial somatosensations, typically tactile sensations associated with specific regions of the body, in brain-machine interface (BMI) applications. The qualitative characteristics of these artificially evoked somatosensations has been well documented. As of yet, however, the quantitative aspects of these evoked somatosensations, that is to say the quantitative relationship between intensity of electrical stimulation and perceived intensity of the resultant somatosensation remains obscure. This study aimed to explore this quantitative relationship by surface electrical stimulation of the primary somatosensory cortex in two human participants undergoing electrocorticographic monitoring prior to surgical treatment of intractable epilepsy. Electrocorticogram electrodes on the primary somatosensory cortical surface were stimulated with varying current intensities, and a visual analogue scale was employed to provide a quantitative measure of intensity of the evoked sensations. Evoked sensations included those of the thumb, tongue, and hand. A clear linear relationship between current intensity and perceived intensity of sensation was observed. These findings provide novel insight into the quantitative nature of primary somatosensory cortex electrical stimulation-evoked sensation for development of somatosensory neuroprosthetics for clinical use.

Keywords: artificial sensation, primary somatosensory cortex, electrocorticography, electrical stimulation, human

INTRODUCTION

Artificial somatosensory feedback will be critical for execution of fine motor control using brain-machine interface (BMI). Under natural conditions, the brain relies on online somatosensory feedback to guide limb movements. Those with impaired somatosensory function often make gross errors in motor output (Gandevia et al., 1990; Sainburg et al., 1993, 1995; Darian-Smith and Ciferri, 2005). Moreover, spinal cord injury and stroke, which are major targets for clinical BMI (Yanagisawa et al., 2011, 2012), are common causes of somatosensory as well as motor impairment

(Yanagisawa et al., 2016). Artificial somatosensory feedback via neuroprosthesis is necessary in order to accomplish natural movements with a clinically plausible BMI (Suminski et al., 2010; Dadarlat et al., 2015; Pistohl et al., 2015; Schiefer et al., 2016).

Human and animal studies have indicated that somatosensory function can be restored using neuroprosthetics. Electrical stimulation of S1 evokes artificial somatosensation (Penfield and Boldrey, 1937; Lueders et al., 1983; Johnson et al., 2013). Some studies using monkeys implanted with intra-cortical microelectrodes demonstrated that electrical stimulation through the electrodes allowed the monkey to discriminate different stimulation frequencies to S1 (Romo et al., 1998; O'Doherty et al., 2011). Further work in humans using electrodes implanted in the somatosensory cortex allowed patients with lost sensation in the hand to discriminate sensations on different fingers (Johnson et al., 2013; Flesher et al., 2016; Hiremath et al., 2017; Caldwell et al., 2019). For both intracortical microelectrodes and surface planar electrodes, electrical stimulation has been successfully used to evoke sensation of the upper limbs dependent on stimulus parameters such as frequency and intensity (Flesher et al., 2016; Hiremath et al., 2017). However, the nature of this artificially evoked somatosensation for different body parts, such as the hand and tongue, and its relationship to the physiological somatosensation experienced as a result of peripheral sensory inputs have yet to be fully elucidated.

In order to design somatosensory neuroprosthesis for long term use in human patients, it is critical to fully characterize the subjective sensation evoked by S1 stimulation. However, a quantitative psychophysical analysis of these S1 electrical stimulation-evoked sensations for different body parts remain obscure. The present study employed a visual analogue scale (VAS) (Zealley and Aitken, 1969; McCormack et al., 1988; Bijur et al., 2001) to quantify the strength of somatosensation experienced by two participants, who were undergoing ECoG monitoring prior to surgical treatment of intractable epilepsy, during electrical stimulation of S1, in order to elucidate the quantitative relationship between S1 stimulation current intensity and perceived intensity of evoked sensation. It was found that stimulation current intensity shares a linear relationship with perceived intensity of somatosensation, within the ranges of current intensities tested, for both the hand and tongue. These results advance toward the goal of understanding the subjective experience of S1 electrical stimulation in order to realize a clinically plausible BMI.

MATERIALS AND METHODS

Participants

Two participants undergoing pre-operative electrocorticographic (ECoG) examination for surgical treatment of intractable epilepsy took part in this study. This experimental protocol was approved by the Ethics Committees of the Osaka University Hospital (Approval No. 14353), the National Institutes for Physiological Sciences (Approval No. 16B004), and the Tokyo Metropolitan Institute of Medical Science (Approval No. 17-2) and carried out in accordance with the Declaration of Helsinki. Participants or their guardians provided written, informed consent to the experimental procedures and to the use of their data for academic study.

Participant A, age 35–40 years old, was undergoing treatment for epilepsy due to cavernous malformation on his left precentral gyrus. Participant B, age 15–20 years old, was undergoing treatment for right frontal lobe epilepsy. Subdural ECoG arrays were implanted across the primary somatosensory (S1) and primary motor (M1) cortices. Participant A was implanted with ECoG arrays on the left hemisphere (**Figure 1A**) and participant B (**Figure 1B**) on the right hemisphere. Throughout this report, participant B's data is mirrored to match participant A's for the sake of comparison. The ECoG electrodes used in this study were implanted exclusively under clinical considerations for the treatment of participants' diseases. Electrical stimulation to the sensorimotor cortex was performed under the clinical necessity to map the sensorimotor cortex.

Electrode Localization

The ECoG electrode arrays analyzed in this study were composed of grids of 20 planar-surface 3 mm diameter platinum electrodes with 1 cm grid spacing. S1 and M1 mapping and identification of electrode location were performed based on preoperative MRI scans, postoperative CT scans, and neurophysiological evidence. First, the preoperative MRI scans were coregistered with postoperative CT scans using established techniques (Dykstra et al., 2012) via EpiSurg software in an anatomical assessment of electrode location (**Figure 1**). To identify the central sulcus and to map and identify the locations of electrodes on S1 and M1 (**Figures 2B–D**, **3A–D**, **5A,B**), peripheral transcutaneous electrical stimulation and/or mechanical stimulation to the surface of the body was/were applied. Peripheral mechanical stimulation experiments were carried out for both participants while recording ECoG signals. These signals were analyzed to find electrodes that detected an increase in neural activity a response to the peripheral mechanical stimulation, and

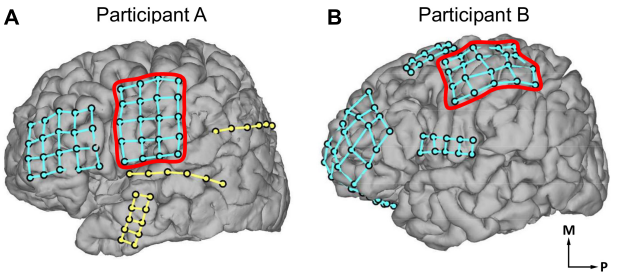

FIGURE 1 | Locations of electrocorticogram electrodes on participants' cortical surfaces as determined by coregistration of MRI and CT images. Electrode locations are visualized with dots, with different electrode grids distinguished by the presence of grid lines between those dots. **(A)** Electrode locations in participant A. **(B)** Electrode locations in participant B. In **(A,B)**, red outlines indicate the electrode grids analyzed in the current study. The outlined electrode grid was on the left hemisphere of the brain for participant A, and the right hemisphere for participant B; participant B's data has been mirrored throughout this report for comparison. Axes labels indicate medial (M) and posterior (P) directions.

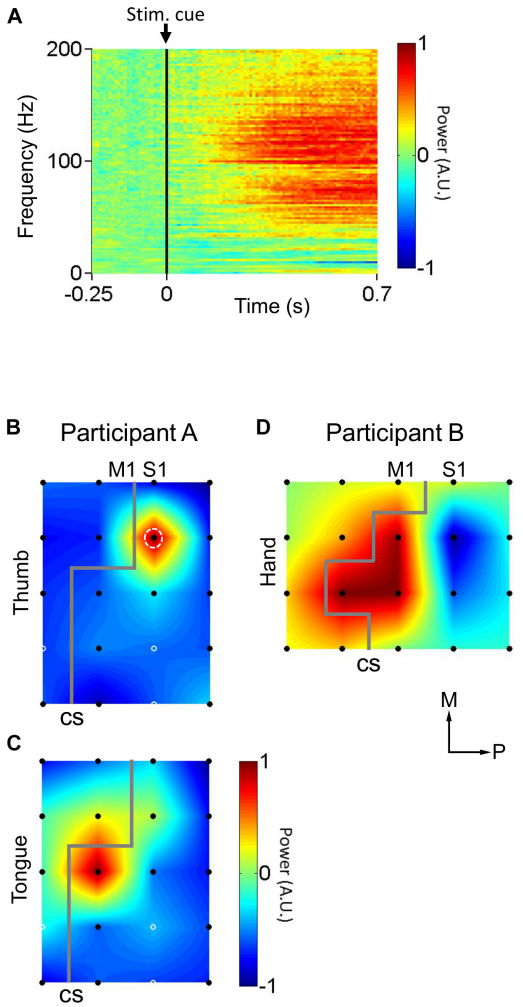

FIGURE 2 | Cortical responses to peripheral mechanical stimulation. **(A)** Average cortical responses upon mechanical stimulation of the thumb in participant A (n = 50 trials). Participant A's thumb were rubbed by a cotton swab. Black vertical lines indicate stimulus instruction onset (Stim. cue). **(B)** Distribution of cortical responses (n = 50 trials) to mechanical stimulation of the thumb in participant A. White dashed circle indicates the electrode whose cortical response is detailed in **(A)**. **(C)** Distribution of cortical responses (n = 50 trials) to mechanical stimulation of the tongue in participant A. **(D)** Distribution of cortical responses (n = 40 trials) to mechanical stimulation of the hand in participant B. Gray lines indicate estimated location of central sulci (CS). Black filled circles indicate electrodes where cortical responses were calculated. White solid circles indicate electrodes where the signal was corrupted by noise, and for where for display purposes the cortical response was taken as the mean of the neighboring electrodes' responses. Axes labels indicate medial (M) and posterior (P) directions. The color scale in **(B–D)** is the same as in **(A)**. A.U. stands for arbitrary units.

thus to help ascertain the location of the electrodes with S1 (**Figure 2**). Participant A also underwent transcutaneous electrical stimulation of the median nerve, which innervates the palmar surface of the thumb, as an additional localization technique. By analyzing the results of obtained by these various experiments together, the locations of the electrodes relative to the central sulcus, S1, and M1 were ascertained. These peripheral mechanical stimulation experiments are explained in more detail below.

Peripheral Mechanical Stimulation

To identify S1 somatotopy, peripheral mechanical stimulation tests were performed while recording participants' cortical responses. Every 2 s, the software Presentation® (Neurobehavioral Systems, Albany, CA, United States) generated a TTL pulse signaling stimulus instruction onset (Stim. Cue in **Figure 2A**) and presented the experimenter with one of two instructions: "Stim" or "Rest." These indicated whether to mechanically stimulate the participant or to refrain from doing so, respectively. "Stim" and "Rest" instructions were presented randomly. During "Stim" trials, Participant A's thumb (n = 50 trials) or tongue (n = 50 trials) were rubbed by a cotton swab, in two separate tests. Participant B's hand was tapped by the fingers of an experimenter (n = 40). The TTL pulses marking stimulus instruction onset (stim. Cue in **Figure 2A**), the point at which the experimenter was presented with the "Stim" or "Rest" instruction, were recorded alongside the physiological data described below and used to align said physiological data indirectly with the onset of the peripheral mechanical stimulation for each 2 s trial.

During the peripheral mechanical stimulation test, ECoG signals were recorded at 1000 Hz via EEG-2000 (Nihon Kohden, Tokyo, Japan). The ECoG signals during the mechanical stimulation were analyzed from -250 ms before to 750 ms after each stimulus instruction onset. The signals for each trial were transformed into the frequency-time domain through a 512 point (512 ms at a 1000 Hz sampling rate) fast Fourier transform (FFT) sliding window that passed down the length of each trial. For speed of computation, FFT was only calculated for every 10th point of the data. This resulted in a 2-dimensional time series representing neural activity, represented in logarithmic scale, over time across the range of frequencies between 0 and 200 Hz. For each frequency in this range, the baseline activity, defined as the mean value of that particular frequency's activity during the baseline time window of -250 to 0 ms prior to stimulus instruction onset, was calculated. This frequency-specific baseline value was then subtracted from the corresponding frequency-time signal, for every individual frequency, in order to normalize the data relative to the pre-stimulus baseline activity (**Figure 2A**). Then, the neural response to the mechanical stimulation was calculated as the average neural activity between 200 and 700 ms post stimulus instruction onset and between 80 and 160 Hz; the high-gamma activity band associated with activation in response to somatosensory stimulation in S1 (**Figures 2B–D**). Power was normalized within each experiment to the range −1 to 1, in arbitrary units, such that the electrode with the highest neural response to mechanical stimulation was 1 and the lowest was −1, for purposes of simplicity in the localization process.

S1 Electrical Stimulation

Pairs of electrodes in which at least one electrode was located on S1 were selected based on the results of the anatomical

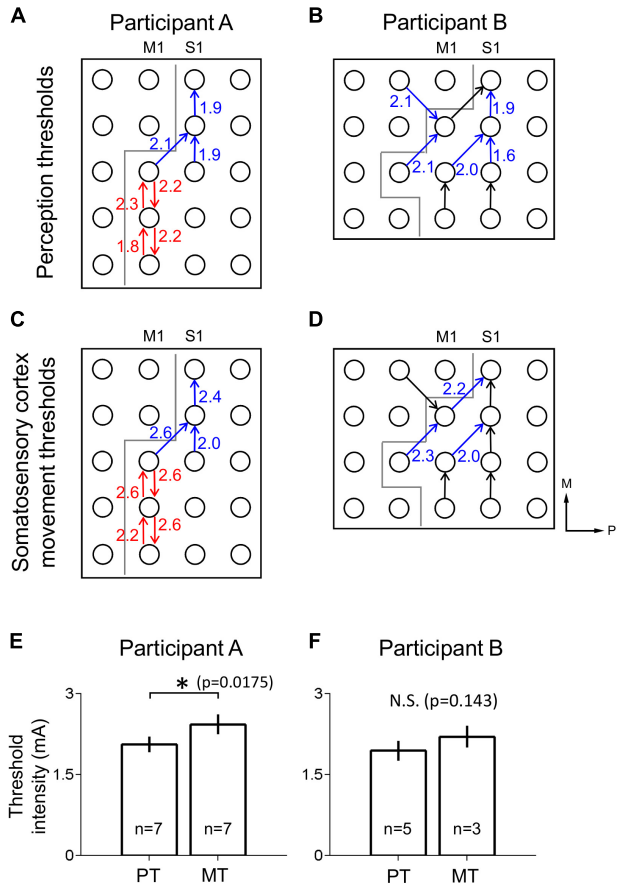

FIGURE 3 | Thresholds for perception and movement evoked by S1 stimulation. **(A,B)** Perception thresholds (PT) at different electrodes for participants A **(A)** and B **(B)** in mA. Arrows point from anode to cathode indicating stimulation polarity (blue: the electrode pairs which induced thumb sensation, red: the electrode pairs which induced tongue sensation, black: no response). Gray line indicates estimated location of central sulcus, dividing M1 and S1. **(C,D)** As in **(A,B)**, but with movement threshold (MT) under S1 stimulation. Axes labels indicate medial (M) and posterior (P) directions for **(A–D)**. **(E)** Comparison of perception (PT) and movement (MT) thresholds in S1 for participant A using a two-tailed Mann–Whitney *U*-test with a significance criterion of $p < 0.05$. Bars and error bars indicate mean and standard error respectively. **(F)** As in **(E),** for participant B. *Indicates significance at the 0.05 level, and N.S. indicates non-significance.

electrode localization. These electrode pairs were electrically stimulated one at a time at a range of current intensities with bipolar 50 Hz pulse trains of 200 μs biphasic pulse width pulses lasting for 3 s each. During the stimulation test, the ECoG signals of all non-stimulated electrodes were monitored to assess the presence of after-discharges. If after-discharges occurred following stimulation, the examination was stopped until a few minutes after the after-discharges disappeared, in order to prevent evoking an epileptic seizure. In general, stimulus current intensity was incrementally increased from low to high. Current intensity ranged from 1.0 to 3.2 mA in participant A and from 0.5 to 3.5 mA in participant B. Notably, we did not perform catch trials (stimulation with 0 mA), although the sensory threshold might be biased without the catch trials. Because we did this experiment as a part of the clinical evaluation, making the implementation of the catch trials difficult. The initial maximum current intensity was set at 3.0 mA for both participants, but when after-discharges were not observed, current intensity was increased beyond this limit after getting permission from the doctors caring for the participants. The current intensity was set to less than 10.0 mA, which corresponds to the charge of 2 μC/phase and charge density of 28.3 μC/phase*cm^2, so as not to exceed the Shannon criteria (1.75 < 1.85; Shannon, 1992). A reversal of polarity in an electrode pair was considered a distinct electrode pair; any two electrodes could produce two electrode pairs taking polarity into account. Any movement apparently evoked by the stimulation was recorded via video. Furthermore, experimenters visually observing the participant during the electrical stimulation watched for any movements apparently evoked by the stimulation and made note of the qualitative nature of said movements.

During this test, participants were instructed to verbally describe the sensations they felt upon stimulation and to mark on a 100 mm VAS the intensity of any sensations they felt upon stimulation. The VAS was a horizontal line with the left side endpoint labeled "no sensation" and the right endpoint labeled "strongest sensation". Participant A was instructed to mark the weakest perceivable sensation at a pre-marked point 10 mm from the left "no sensation" endpoint. This was not done with participant B.

The lowest stimulus current to a given electrode pair at which participants gave a VAS score above 0 mm was defined as the perception threshold (PT) for that electrode pair. The lowest stimulus current to a given electrode pair that apparently evoked visible movement in the participant was defined as the movement threshold (MT) for that electrode pair.

Analysis of VAS Response Characteristics

VAS scores corresponding to S1 electrical stimulation-evoked sensation were linearly fitted for each electrode pair. Electrode pairs that lacked sub-threshold data, defined as current intensities that resulted in 0 mm VAS scores, or that lacked any VAS score above 0 mm, indicating no sensation was perceived, were ignored for this analysis. For fitting purposes, only the highest sub-threshold current intensity was used to calculate the best fit line. The slopes of these best fit lines were defined as the sensitivities of VAS score to current intensity. Electrode pairs in participant A were divided into thumb-related and tongue-related electrode pairs based on verbal descriptions of the electrically evoked sensations given by that participant.

Statistics

PT and MT were tested for mean difference, in participant A (PT: $n = 7$ electrode pairs, MT: $n = 7$), participant B (PT: $n = 5$, MT: $n = 3$), and in the population of both participants (PT: $n = 12$, MT: $n = 10$), using two-tailed Mann–Whitney

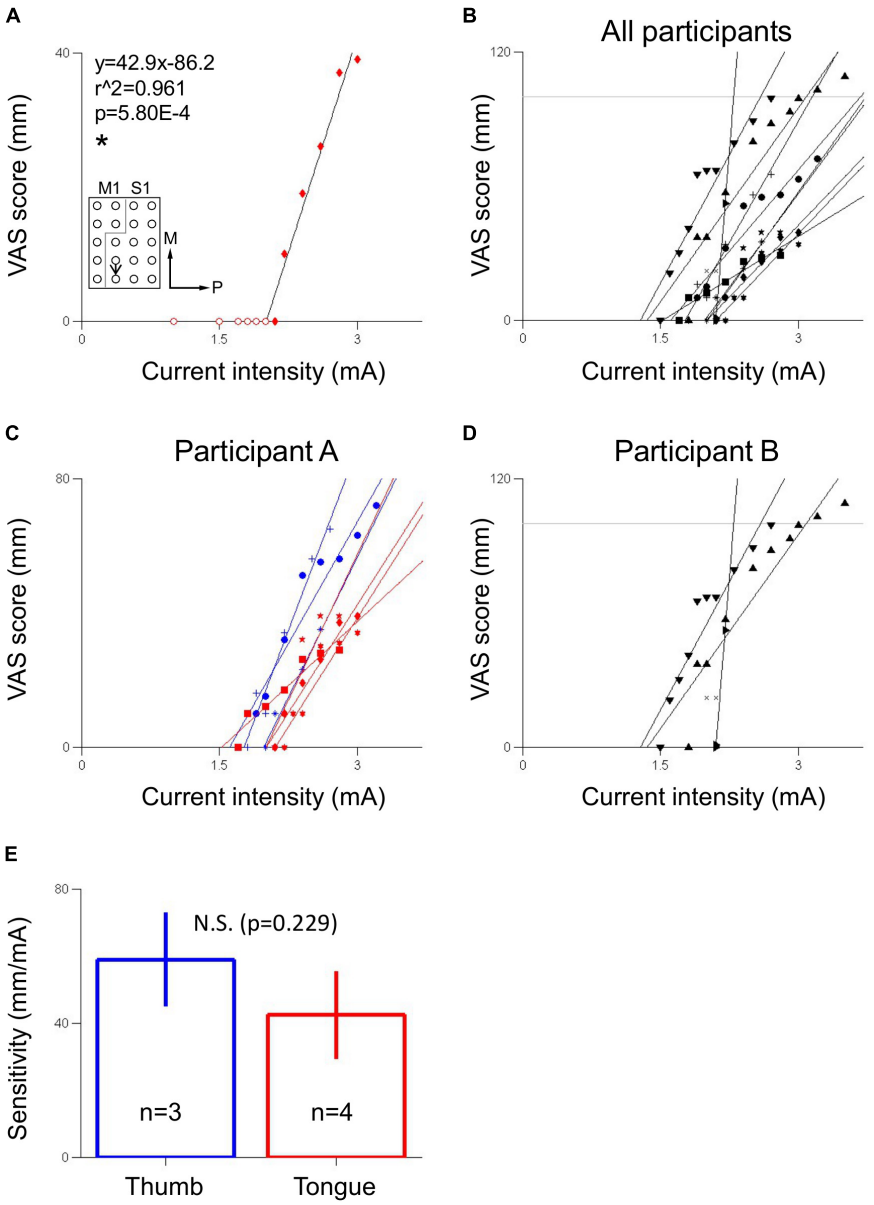

FIGURE 4 | Relationship between S1 stimulation current intensity and VAS score of evoked sensation. **(A)** Electrode pair showing a linear relationship between visual analogue scale (VAS) score, which corresponded to sensation of a hard object on the tongue, and current intensity in participant A. Inset indicates location of stimulated electrode pair. Black arrow points from anode to cathode indicating stimulation polarity. Gray line indicates estimated location of central sulcus. Numerals in inset indicate coefficient of correlation (r^2) and *p*-value (p). Equation describes VAS score (y) in mm as a function of current intensity (x) in mA. The slope of the line is the sensitivity of the electrode pair in mm/mA. *Indicates significance at the $p < 0.05$ level. Fitting ignores redundant-pre threshold points, indicated by hollow circles. Axes labels indicate medial (M) and posterior (P) directions. **(B)** VAS score versus current intensity for electrodes across both participants. **(C)** VAS score versus current intensity for electrodes in participant A, differentiated by perceived body area (blue: thumb, red: tongue). **(D)** VAS score versus current intensity for electrodes in participant B, corresponding to hand sensation. In **(B,D)**, horizontal gray line indicates the 100 mm "strongest sensation" endpoint of the VAS. In **(C,D)**, redundant pre-threshold points (open circles in **A**) have been removed for clarity. **(E)** Comparison of sensitivities between thumb and tongue areas in participant A using a two-tailed Mann–Whitney *U*-test with a significance criterion of $p < 0.05$. Bars and error bars indicates mean and standard error, respectively. N.S. indicates non-significance.

U-tests with a significance criterion of $p < 0.05$. This non-parametric test was selected due to its applicability to data with small sample sizes.

Sensitivities of thumb-related ($n = 3$) and tongue-related ($n = 4$) electrode pairs in participant A were tested for mean difference using a two-tailed Mann–Whitney *U*-test with a significance criterion of $p < 0.05$.

Correlation coefficients and corresponding significance values between stimulation current intensity and VAS scores were calculated using Pearson correlation for all electrode pairs that

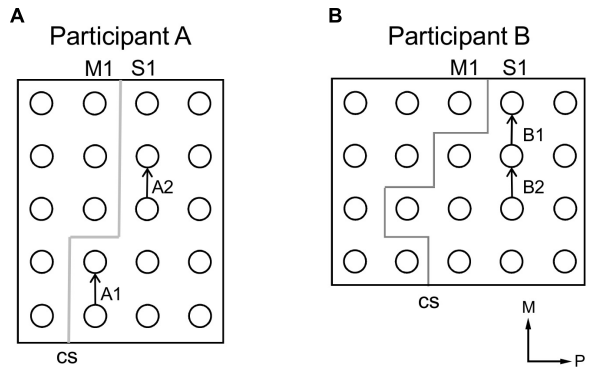

FIGURE 5 | Electrode pairs selected for samples of participants' verbal description of stimulation-evoked sensation (see **Table 1**). **(A)** Selected electrode pairs for participant A. **(B)** Selected electrode pairs for participant B. In **(A,B)**, arrows point from anode to cathode indicating stimulation polarity and gray lines indicate estimated locations of central sulci (CS). Axes labels indicate medial (M) and posterior (P) directions.

had at least two supra-threshold VAS scores and at least one sub-threshold VAS score of 0 mm. Within each electrode pair, all sub-threshold VAS scores except that with the highest current intensity were ignored for statistical purposes.

RESULTS

Electrode Localization

Peripheral mechanical stimulation evoked clear cortical responses in both participants (**Figure 2A**), allowing estimation of the functional locations of electrodes. The cortical responses (thumb sensation in **Figure 2B**; tongue sensation in **Figure 2C**) in participant A demonstrated a clear division between the more medial thumb-associated area and the more lateral tongue-associated area. Also, the types of somatosensations evoked by electrical stimulation to the different electrodes in participant A demonstrated a similar division between thumb-associated (blue arrows in **Figure 3A**) and tongue-associated (red arrows in **Figure 3A**) areas. PTs in participant A ranged from 1.9 to 2.2 mA (**Figure 3A**). PTs in participant B ranged from 1.6 to 2.1 mA, and 3 out of 8 electrode pairs stimulated did not evoke any reported sensation (**Figure 3B**).

Even under S1 stimulation, higher current intensities evoked movements which might be a result of current spread to the motor cortex. Evoked movements were typically muscle twitches or small movements. MTs in participant A ranged from 2.0 to 2.6 mA (**Figure 3C**). MTs in participant B ranged from 2.0 to 2.3 mA, and 5 of the 8 electrode pairs stimulated did not evoke any visible movement (**Figure 3D**).

In participant A, polarity-dependent differences in both PTs and MTs, of up to 0.3 and 0.4 mA, respectively, were observed within particular pairs of electrodes (**Figures 3A,C**). In participant A, PTs (mean ± SE 2.06 ± 7.19E-2 mA) were lower than MTs (2.43 ± 9.18E-2 mA) (two-tailed Mann–Whitney *U*-test, $p = 0.0175$, $U = 6.00$) (**Figure 3E**). Participant B's PTs (1.94 ± 9.27E-2 mA) tended to be lower than her MTs (2.20 ± 0.100 mA), but the mean difference did not meet significance (two-tailed Mann–Whitney *U*-test, $p = 0.143$, $U = 2.5$) (**Figure 3F**).

Linear Relationship Between Current Intensity and VAS Score

There was a clear, positive linear relationship between current intensity and VAS score in both participants within the range of current intensities tested (**Figure 4**). Out of all 11 electrode pairs analyzed, 10 were significantly correlated at the $p < 0.05$ level, while 1, which had three VAS-current intensity data points, did not. In all significantly correlated electrode pairs, r was greater than 0.9, and r^2 was greater than 0.85, indicating a strong, positive linear relationship. In participant A, thumb sensation-related electrode pairs (mean ± SE 58.9 ± 7.10 mm/mA) tended to be more sensitive to current intensity than tongue sensation-related electrode pairs (42.4 ± 6.64 mm/mA) (**Figure 4E**), though this difference did not meet significance at the $p < 0.05$ level (two-tailed Mann–Whitney *U*-test, $p = 0.229$, $U = 2.00$). For electrode pair B1 (**Figure 5**), participant B exceeded the "strongest sensation" endpoint of the VAS, reporting a sensation corresponding to 109 mm at 3.5 mA (**Figure 4D**). Some electrode pairs, particularly those associated with tongue sensation, seemed to exhibit a saturation effect around the higher end of the range of the current intensities tested, showing a decreasing sensitivity as current intensity increased. However this phenomenon was not robust enough in the range of current intensities tested to warrant further analysis.

Current Intensity-Dependent Differences in Evoked Sensation

Participant A described electrically-evoked sensations largely in terms of feelings of touch and numbness. He described qualitative features of the sensations that changed with current intensity, for both thumb-related and tongue-related sites. Participant B described electrically-evoked sensations largely in terms of pressure on the hand. Increases to current intensity generally caused her to describe increases in the intensity of the sensation; increased current would evoke sensation of stronger, wider, or faster pressure on the hand. It was demonstrated that current intensity has an impact on both intensity-related features such as and size and pressure, as well as more qualitative aspects corresponding to different types of somatosensation (**Figure 5** and **Table 1**).

DISCUSSION

These results demonstrate a quantitative analysis of sensation evoked by S1 electrical stimulation using ECoG arrays in humans. A linear relationship between stimulation current intensity and intensity of sensation was observed in both for hand and tongue representation of S1; increasing supra-threshold stimulation current intensity resulted in a proportional increase in intensity of sensation. This opens the potential for clinical application in developing somatosensory neuroprosthetics for clinically plausible BMI.

TABLE 1 | Selected verbal descriptions of stimulation-evoked sensation given by participants.

Participant	Electrode pair	Current intensity (mA)	Description of sensation
A	A1	1.8^{T}	*Sense of a flick on a narrow portion of the right side of the tip of my tongue. Feels like movement [on my tongue].*
A	A1	2.0	*The surface of the right side of the tip of my tongue feels numb. It's as if I'm eating pineapple, but there's no taste. The surface feels numb.*
A	A1	2.2	*The feeling [of numbness] on the right-side of the tip of my tongue spread from front to back.*
A	A1	2.8	*It feels like my tongue is swollen like after being bitten.*
A	A2	1.9^{T}	*Not a feeling of being touched; a bad feeling [around the second joint of the thumb].*
A	A2	2.0	*Feels like a blood vessel pulsing [in my thumb], not like anything I've felt in the past. Feels like stimulation by a low frequency electrical stimulation therapy device around the second joint of the thumb.*
A	A2	2.5	*Outer side of my thumb feels anaesthetized.*
A	A2	2.7	*A slow dull touch on the opposite hand. Also, my finger feels swollen and thick.*
B	B1	1.9^{T}	*The palm under my left little finger is being pressed. The spot moved a little inwards [to the center of my palm].*
B	B1	2.0	*It's being pressed down in a few spots [on my palm] but the overall width is the same [as 1.9 mA].*
B	B1	2.5	*It feels faster. The width is the same.*
B	B1	3.0	*The width increased.*
B	B2	1.6^{T}	*[no verbal description given by participant; VAS response only]*
B	B2	1.7	*I feel pressure at two spots on the [ulnar] side of my palm.*
B	B2	2.3	*It sped up, and got stronger [than at 1.9 mA]. The width is unclear.*
B	B2	2.7	*It got even faster, but the width is the same. It feels like something is really strongly pressing [into my skin].*

*For electrode pair definitions (see **Figure 5**). Original responses were given in Japanese. Text in square brackets was not said by participants but is included for clarity. ^{T}Indicates PT for that electrode pair.*

VAS response curves enable a quantitative determination of what intensity of sensation should be expected for a given stimulation current intensity before stimulation is applied, allowing for easier calibration of stimulation parameters in design of somatosensory neuroprosthetics. The sensitivity of VAS response to current intensity could inform what current intensity to use in different somatotopic regions of S1 to evoke sensation of a particular desired intensity; the non-significant tendency in participant A of thumb-related electrode pairs to be more sensitive than tongue-related electrode pairs suggests that different somatotopic regions of S1 may have different sensitivities to electrical stimulation (**Figure 4**), although a larger sample size and testing of more somatotopic regions of S1 are needed to elucidate this phenomenon more fully. Although ethical and safety considerations, including avoiding inducing epilepsy by monitoring for after-discharges, necessitated the current intensity be generally increased from low to high, it is possible that randomizing the order of the current intensities to be tested may provide more robust results. Furthermore, especially for the evaluation of sensory threshold, more detailed psychophysical methods, such as two-alternative forced-choice or yes/no task (Flesher et al., 2016; Devecioglu and Guclu, 2017), might be used to derive psychometric functions and to minimize or control cognitive bias. However, because such psychophysical methods necessitate a larger number of stimulation trials and a longer experiment time, such methods may be difficult to implement, both practically and ethically, in the clinical context of epilepsy patients with implanted electrodes for preoperative evaluation. Additionally, VAS was suitable here because this experiment focused on the quantitative relationship between the intensity of electrical stimulation and the perceived intensity and quality of the evoked sensation. Perhaps in future experiments a range of non-epileptogenic current intensities could be preliminarily ascertained by gradual increase of the current intensity as was done here, and then current intensities could be randomly selected from within that range for another round of stimulation, the results of which could then be used to construct the VAS response curve and/or another psychophysical method.

A study on S1 stimulation via ECoG in humans (Johnson et al., 2013) found that changing either stimulation frequency or current intensity changed only the intensity of the sensation, without significant change in the quality of the sensation. The results in this study seem to partially conflict with those findings; participant B indeed described mainly changes to intensity, but participant A described clear differences in quality of sensation as current intensity was varied (**Figure 5** and **Table 1**). These results are commonly observed in some recent studies using intracortical microelectrode and surface microelectrode (Flesher et al., 2016; Hiremath et al., 2017). More rigorous investigation of the relationship between stimulation parameters, electrode characteristics, and stimulation sites, neural recruitment by stimulation, and quality of evoked sensation is needed to determine the factors that contribute to the presence or absence of these qualitative changes at a given stimulation site.

Ethical and clinical considerations limited the range of current intensities that could be used for S1 stimulation. Despite the overall linearity of VAS response to current intensity, there was some indication toward the upper limit of the ranges of current intensity tested that as current intensity increased, there was a decrease in slope of the VAS response curve, especially in participant A's tongue-related sites (**Figure 4C**) and participant B (**Figure 4D**). This is suggestive of a saturation effect; as current intensity increases and a wider area of the

S1 containing the somatotopy of the associated body area is activated (Haglund et al., 1993), the number of somatotopically relevant neurons still available for recruitment may decrease as the percentage of recruited neurons tends toward 100%. The resultant decrease in the number of additional neurons recruited by every increase in stimulation current intensity, then, may lead to a decrease in the perceived difference in intensity of subsequent evoked sensations. This could explain why, in participant A, this saturation phenomenon was observed more in tongue-related electrode pairs than in thumb-related ones: the tongue-related area in the human S1 is physically smaller than the thumb-related area (Nakamura et al., 1998), and thus would approach 100% recruitment at a lower current intensity.

In addition to evoking sensation of particular body areas, S1 electrical stimulation also drove small movements of the same general body areas, in accordance with previous findings (Penfield and Boldrey, 1937). In participant A the threshold current intensity for evoked movement was higher than that for evoked sensation (**Figure 3E**). In participant B this relationship appeared to exist as in participant A, but, likely owing to the relatively small number of electrodes pairs that evoked either sensation or movement, this relationship was not found to be statistically significant (**Figure 3F**). Assessment of this phenomenon could prove critical in the calibration of S1 stimulation parameters for neuroprosthetics or psychophysical experiments; to produce a target level of sensation per unit of input sensory signal, the mathematical transformation of that sensory signal into current intensity would require knowledge of the sensitivity of the VAS response curve, including any non-linearity such as saturation effects. The potential for a motor response puts a limit on the current intensity that can be applied when the only desired effect of stimulation is evoked sensation. This, along with the saturation considerations detailed above, could be crucial factors to consider in designing future S1 stimulation experiments or neuroprosthetics for clinical use.

It should be noted that some of the stimulation below the motor threshold might have evoked some very weak muscle contractions which that were not noticed by the experimenter. Although the possibility that the evoked sensations originated from these weak muscle contractions cannot be ruled out completely, the verbal descriptions of the evoked sensations seem consistent with pressure or cutaneous mechanoreceptor-type sensations, which are unlikely to be stimulated by such weak muscle contractions. Furthermore, the established physiological role of S1 suggests that the evoked sensations at least primarily originated from the electrical stimulation to S1.

Notably, some electrode pairs did not induce artificial sensation. Electrical conditions may differ between electrode pairs. For example, some electrodes might not contact the cortical well as well as others. This larger distance between the electrode and the cortical surface might lead to more current spread over the cortex via the cerebrospinal fluid. Moreover, as seen in the case of stimulation using intracortical electrodes, stimulation in deeper layer tends to decrease detection thresholds (DeYoe et al., 2005; Tehovnik and Slocum, 2009; Koivuniemi and Otto, 2012). The distance between the cortex and the electrode might also affect the effective depth of the electrical stimulation. For these electrode pairs, artificial sensation might have been potentially evoked using higher current intensity. However, stimulation current intensity was limited by the clinical factors such as the need to avoid epileptic discharges as a result of stimulation. Although in practice it is difficult to control surface electrode location precisely, these results demonstrated that electrical stimulation via surface electrodes induced artificial sensation with properties similar to those of artificial sensation induced by electrical stimulation via intracortical microelectrodes.

In participant A, S1 stimulation revealed a clear division between more medial thumb-related areas and more lateral tongue-related areas (**Figures 3A,C**), corresponding to the widely known somatosensory homunculus (Penfield and Boldrey, 1937). This general layout was also observed in the spatial distribution of cortical responses evoked by mechanical stimulation (**Figures 2B,C**). However it is clear that the tongue-related areas as determined by cortical responses to mechanical stimulation were more medial than those determined by S1 electrical stimulation. There is a reasonable explanation for this discrepancy. At some cortical sites, for example the more posterior electrodes in participant A, the cortical response to mechanical stimulation appeared to be a decrease in high-gamma power (**Figure 2D**), rather than the increase observed elsewhere. Further, stimulation via ECoG electrodes recruits a large number of neurons en masse, whereas external mechanical stimulation produces more nuanced recruitment patterns, which may include the aforementioned suppression effects, which correspond to physiological somatosensation. Thus, it is difficult to compare, from both mathematical and physiological perspectives, the recording of physiological activity at single electrodes versus data based on bipolar stimulation of electrode pairs. This difference can also explain the somewhat unusual sensations evoked by S1 stimulation (**Table 1**). The polarity-dependent differences in both PT and MT in individual electrode pairs observed in subject A (**Figures 3A,C**) suggest that stimulation polarity has an effect on neural recruitment, presumably based on the cytoarchitecture of the cortex.

It is difficult to induce artificial somatosensation using non-invasive percutaneous cortical stimulation such as transcranical magnetic or electrical stimulation. Invasive cortical stimulation using penetrating electrodes has been demonstrated to induce artificial sensation in a spinal cord injury patient (Flesher et al., 2016). Electrical stimulations through the intracortical micro-electrode arrays requires a lower current intensity less than 100 μA to evoke somatosensory sensations (Flesher et al., 2016), while cortical surface stimulations required mA order to induce somatosensory sensation (**Figure 3**). The intracortical micro-electrodes were also useful to evoke precise and discrete somatosensory sensations (Flesher et al., 2016) and to decode motor information, but the stability of the electrodes makes their implementation in a clinical context difficult. The stimulation area is also limited with intracortical micro-electrodes while ECoG allows coverage of a larger cortical area beyond different body representations. ECoG therefore appears to be a well-balanced technique that allows greater cortical coverage while remaining less invasive than cortex-penetrating

needle electrodes, and as such is useful in medical contexts where minimal invasiveness is desired (Yanagisawa et al., 2012; Matsushita et al., 2018). Therefore, ECoG offers one of the most clinically feasible options, being less invasive, having superior long-term stability, and being less technically difficult to implement (Rubehn et al., 2009; Chao et al., 2010; Shin et al., 2012; Nakanishi et al., 2017) compared with other invasive stimulation methods. These advantages should facilitate the development of the clinically plausible somatosensory BMI.

ETHICS STATEMENT

This experimental protocol was approved by the Ethics Committees of the Osaka University Hospital (Approval No. 14353), the National Institutes for Physiological Sciences (Approval No. 16B004), and the Tokyo Metropolitan Institute of Medical Science (Approval No. 17-2) and carried out in accordance with the Declaration of Helsinki. Participants or their guardians provided written, informed consent to the experimental procedures and to the use of their data for academic study.

AUTHOR CONTRIBUTIONS

YN and TY conceived and designed the experiments. TY, YN, SO, KE, MT, and HK performed the experiments. SK, YN, and TY analyzed the data and wrote the manuscript. SK and YN prepared the figures.

FUNDING

This work was supported by grants from the "Brain Machine Interface Development" and performed under the Strategic Research Program for Brain Sciences from MEXT and the Japan Agency for Medical Research and Development, Japan Science and Technology Agency, a Ministry of Education, Culture, Sports, Science, and Technology Grant-in-Aid for Scientific Research (KAKENHI 23680061) to YN. This work was partly supported by the Japan Science and Technology Agency (JST) PRESTO (JPMJPR1506), CREST (JPMJCR18A5), and ERATO (JPMJER1801); the Brain/MINDS from AMED; and Grants-in-Aid for Scientific Research KAKENHI (JP17H06032 and JP15H05710) to TY.

REFERENCES

Bijur, P. E., Silver, W., and Gallagher, E. J. (2001). Reliability of the visual analog scale for measurement of acute pain. *Acad. Emerg. Med.* 8, 1153–1157. doi: 10.1111/j.1553-2712.2001.tb01132.x

Caldwell, D. J., Cronin, J. A., Wu, J., Weaver, K. E., Ko, A. L., Rao, R. P. N., et al. (2019). Direct stimulation of somatosensory cortex results in slower reaction times compared to peripheral touch in humans. *Sci. Rep.* 9:3292. doi: 10.1038/s41598-019-38619-2

Chao, Z. C., Nagasaka, Y., and Fujii, N. (2010). Long-term asynchronous decoding of arm motion using electrocorticographic signals in monkeys. *Front. Neuroeng.* 3:3. doi: 10.3389/fneng.2010.00003

Dadarlat, M. C., O'doherty, J. E., and Sabes, P. N. (2015). A learning-based approach to artificial sensory feedback leads to optimal integration. *Nat. Neurosci.* 18, 138–144. doi: 10.1038/nn.3883

Darian-Smith, C., and Ciferri, M. M. (2005). Loss and recovery of voluntary hand movements in the macaque following a cervical dorsal rhizotomy. *J. Comp. Neurol.* 491, 27–45. doi: 10.1002/cne.20686

Devecioglu, I., and Guclu, B. (2017). Psychophysical correspondence between vibrotactile intensity and intracortical microstimulation for tactile neuroprostheses in rats. *J. Neural Eng.* 14:016010. doi: 10.1088/1741-2552/14/1/016010

DeYoe, E. A., Lewine, J. D., and Doty, R. W. (2005). Laminar variation in threshold for detection of electrical excitation of striate cortex by macaques. *J. Neurophysiol.* 94, 3443–3450. doi: 10.1152/jn.00407.2005

Dykstra, A. R., Chan, A. M., Quinn, B. T., Zepeda, R., Keller, C. J., Cormier, J., et al. (2012). Individualized localization and cortical surface-based registration of intracranial electrodes. *Neuroimage* 59, 3563–3570. doi: 10.1016/j.neuroimage.2011.11.046

Flesher, S. N., Collinger, J. L., Foldes, S. T., Weiss, J. M., Downey, J. E., Tyler-Kabara, E. C., et al. (2016). Intracortical microstimulation of human somatosensory cortex. *Sci. Transl. Med.* 8:361ra141.

Gandevia, S. C., Macefield, G., Burke, D., and Mckenzie, D. K. (1990). Voluntary activation of human motor axons in the absence of muscle afferent feedback. The control of the deafferented hand. *Brain* 113(Pt 5), 1563–1581. doi: 10.1093/brain/113.5.1563

Haglund, M. M., Ojemann, G. A., and Blasdel, G. G. (1993). Optical imaging of bipolar cortical stimulation. *J. Neurosurg.* 78, 785–793. doi: 10.3171/jns.1993.78.5.0785

Hiremath, S. V., Tyler-Kabara, E. C., Wheeler, J. J., Moran, D. W., Gaunt, R. A., Collinger, J. L., et al. (2017). Human perception of electrical stimulation on the surface of somatosensory cortex. *PLoS One* 12:e0176020. doi: 10.1371/journal.pone.0176020

Johnson, L. A., Wander, J. D., Sarma, D., Su, D. K., Fetz, E. E., and Ojemann, J. G. (2013). Direct electrical stimulation of the somatosensory cortex in humans using electrocorticography electrodes: a qualitative and quantitative report. *J. Neural Eng.* 10:036021. doi: 10.1088/1741-2560/10/3/036021

Koivuniemi, A. S., and Otto, K. J. (2012). The depth, waveform and pulse rate for electrical microstimulation of the auditory cortex. *Conf. Proc. IEEE Eng. Med. Biol. Soc.* 2012, 2489–2492. doi: 10.1109/EMBC.2012.6346469

Lueders, H., Lesser, R. P., Hahn, J., Dinner, D. S., and Klem, G. (1983). Cortical somatosensory evoked potentials in response to hand stimulation. *J. Neurosurg.* 58, 885–894. doi: 10.3171/jns.1983.58.6.0885

Matsushita, K., Hirata, M., Suzuki, T., Ando, H., Yoshida, T., Ota, Y., et al. (2018). A fully implantable wireless ecog 128-channel recording device for human brain-machine interfaces: W-HERBS. *Front. Neurosci.* 12:511. doi: 10.3389/fnins.2018.00511

McCormack, H. M., Horne, D. J., and Sheather, S. (1988). Clinical applications of visual analogue scales: a critical review. *Psychol. Med.* 18, 1007–1019. doi: 10.1017/s0033291700009934

Nakamura, A., Yamada, T., Goto, A., Kato, T., Ito, K., Abe, Y., et al. (1998). Somatosensory homunculus as drawn by MEG. *Neuroimage* 7, 377–386. doi: 10.1006/nimg.1998.0332

Nakanishi, Y., Yanagisawa, T., Shin, D., Kambara, H., Yoshimura, N., Tanaka, M., et al. (2017). Mapping ECoG channel contributions to trajectory and muscle activity prediction in human sensorimotor cortex. *Sci. Rep.* 7:45486. doi: 10.1038/srep45486

O'Doherty, J. E., Lebedev, M. A., Ifft, P. J., Zhuang, K. Z., Shokur, S., Bleuler, H., et al. (2011). Active tactile exploration using a brain-machine-brain interface. *Nature* 479, 228–231. doi: 10.1038/nature10489

Penfield, W., and Boldrey, E. (1937). Somatic motor and sensory representation in the cerebral cortex of man as studied by electrical stimulation. *Brain* 60, 389–443. doi: 10.1093/brain/60.4.389

Pistohl, T., Joshi, D., Ganesh, G., Jackson, A., and Nazarpour, K. (2015). Artificial proprioceptive feedback for myoelectric control. *IEEE Trans. Neural Syst. Rehabil. Eng.* 23, 498–507. doi: 10.1109/TNSRE.2014.2355856

Romo, R., Hernandez, A., Zainos, A., and Salinas, E. (1998). Somatosensory discrimination based on cortical microstimulation. *Nature* 392, 387–390. doi: 10.1038/32891

Rubehn, B., Bosman, C., Oostenveld, R., Fries, P., and Stieglitz, T. (2009). A MEMS-based flexible multichannel ECoG-electrode array. *J. Neural Eng.* 6:036003. doi: 10.1088/1741-2560/6/3/036003

Sainburg, R. L., Ghilardi, M. F., Poizner, H., and Ghez, C. (1995). Control of limb dynamics in normal subjects and patients without proprioception. *J. Neurophysiol.* 73, 820–835. doi: 10.1152/jn.1995.73.2.820

Sainburg, R. L., Poizner, H., and Ghez, C. (1993). Loss of proprioception produces deficits in interjoint coordination. *J. Neurophysiol.* 70, 2136–2147. doi: 10.1152/jn.1993.70.5.2136

Schiefer, M., Tan, D., Sidek, S. M., and Tyler, D. J. (2016). Sensory feedback by peripheral nerve stimulation improves task performance in individuals with upper limb loss using a myoelectric prosthesis. *J. Neural Eng.* 13:016001. doi: 10.1088/1741-2560/13/1/016001

Shannon, R. V. (1992). A model of safe levels for electrical stimulation. *IEEE Trans. Biomed. Eng.* 39, 424–426. doi: 10.1109/10.126616

Shin, D., Watanabe, H., Kambara, H., Nambu, A., Isa, T., Nishimura, Y., et al. (2012). Prediction of muscle activities from electrocorticograms in primary motor cortex of primates. *PLoS One* 7:e47992. doi: 10.1371/journal.pone.0047992

Suminski, A. J., Tkach, D. C., Fagg, A. H., and Hatsopoulos, N. G. (2010). Incorporating feedback from multiple sensory modalities enhances brain-machine interface control. *J. Neurosci.* 30, 16777–16787. doi: 10.1523/JNEUROSCI.3967-10.2010

Tehovnik, E. J., and Slocum, W. M. (2009). Depth-dependent detection of microampere currents delivered to monkey V1. *Eur. J. Neurosci.* 29, 1477–1489. doi: 10.1111/j.1460-9568.2009.06695.x

Yanagisawa, T., Fukuma, R., Seymour, B., Hosomi, K., Kishima, H., Shimizu, T., et al. (2016). Induced sensorimotor brain plasticity controls pain in phantom limb patients. *Nat. Commun.* 7:13209. doi: 10.1038/ncomms13209

Yanagisawa, T., Hirata, M., Saitoh, Y., Goto, T., Kishima, H., Fukuma, R., et al. (2011). Real-time control of a prosthetic hand using human electrocorticography signals. *J. Neurosurg.* 114, 1715–1722. doi: 10.3171/2011.1.JNS101421

Yanagisawa, T., Hirata, M., Saitoh, Y., Kishima, H., Matsushita, K., Goto, T., et al. (2012). Electrocorticographic control of a prosthetic arm in paralyzed patients. *Ann. Neurol.* 71, 353–361. doi: 10.1002/ana.22613

Zealley, A. K., and Aitken, R. C. (1969). Measurement of mood. *Proc. R. Soc. Med.* 62, 993–996.

Conflict of Interest: The authors declare that the research was conducted in the absence of any commercial or financial relationships that could be construed as a potential conflict of interest.

frontiers in Neuroscience

ORIGINAL RESEARCH
published: 26 September 2019
doi: 10.3389/fnins.2019.00901

Time-Variant Linear Discriminant Analysis Improves Hand Gesture and Finger Movement Decoding for Invasive Brain-Computer Interfaces

Johannes Gruenwald[1,2]*, *Andrei Znobishchev*[3], *Christoph Kapeller*[1], *Kyousuke Kamada*[4], *Josef Scharinger*[2] *and Christoph Guger*[1,5]

[1] *g.tec Medical Engineering GmbH, Schiedlberg, Austria,* [2] *Institute of Computational Perception, Johannes Kepler University, Linz, Austria,* [3] *Skolkovo Institute of Science and Technology, Moscow, Russia,* [4] *Neurosurgery, Megumino Hospital, Eniwa, Japan,* [5] *Guger Technologies OG, Graz, Austria*

Invasive brain-computer interfaces yield remarkable performance in a multitude of applications. For classification experiments, high-gamma bandpower features and linear discriminant analysis (LDA) are commonly used due to simplicity and robustness. However, LDA is inherently static and not suited to account for transient information that is typically present in high-gamma features. To resolve this issue, we here present an extension of LDA to the time-variant feature space. We call this method *time-variant linear discriminant analysis* (TVLDA). It intrinsically provides a feature reduction stage, which makes external approaches thereto obsolete, such as feature selection techniques or common spatial patterns (CSPs). As well, we propose a time-domain whitening stage which equalizes the pronounced $1/f$-shape of the typical brain-wave spectrum. We evaluated our proposed architecture based on recordings from 15 epilepsy patients with temporarily implanted subdural grids, who participated in additional research experiments besides clinical treatment. The experiments featured two different motor tasks involving three high-level gestures and individual finger movement. We used log-transformed bandpower features from the high-gamma band (50–300 Hz, excluding power-line harmonics) for classification. On average, whitening improved the classification performance by about 11%. On whitened data, TVLDA outperformed LDA with feature selection by 11.8%, LDA with CSPs by 13.9%, and regularized LDA with vectorized features by 16.4%. At the same time, TVLDA only required one or two internal features to achieve this. TVLDA provides stable results even if very few trials are available. It is easy to implement, fully automatic and deterministic. Due to its low complexity, TVLDA is suited for real-time brain-computer interfaces. Training is done in less than a second. TVLDA performed particularly well in experiments with data from high-density electrode arrays. For example, the three high-level gestures were correctly identified at a rate of 99% over all subjects. Similarly, the decoding accuracy of individual fingers was 96% on average over all subjects. To our knowledge, these mean accuracies are the highest ever reported for three-class and five-class motor-control BCIs.

Keywords: brain-computer interface, electrocorticography, movement decoding, linear discriminant analysis, spectral whitening

OPEN ACCESS

Edited by:
Cuntai Guan,
Nanyang Technological University, Singapore

Reviewed by:
Kazutaka Takahashi,
University of Chicago, United States
Chadwick Boulay,
Ottawa Hospital, Canada

***Correspondence:**
Johannes Gruenwald
gruenwald@gtec.at

Specialty section:
This article was submitted to Neuroprosthetics, a section of the journal Frontiers in Neuroscience

Received: *28 February 2019*
Accepted: *12 August 2019*
Published: *26 September 2019*

Citation:
Gruenwald J, Znobishchev A, Kapeller C, Kamada K, Scharinger J and Guger C (2019) Time-Variant Linear Discriminant Analysis Improves Hand Gesture and Finger Movement Decoding for Invasive Brain-Computer Interfaces. Front. Neurosci. 13:901. doi: 10.3389/fnins.2019.00901

1. INTRODUCTION

A brain-computer interface (BCI) establishes a communication pathway from a person's mind to the environment via brain activity alone (Wolpaw et al., 2002; Wolpaw and Wolpaw, 2012). BCIs operate on brain waves that are usually recorded from the electroencephalogram (EEG), the electrocorticogram (ECoG), or depth electrodes. Many types of task-related information (or features) can be extracted from brain waves, depending on the specific experimental protocol and expected neurophysiological activation pattern. Prominent examples include event-related potentials (ERP) (Blankertz et al., 2011), steady-state evoked potentials (SSEP) (Prueckl and Guger, 2009), event-related (de-)synchronization (Pfurtscheller and Lopes da Silva, 1999), and high-gamma activation (Miller et al., 2009; Kapeller et al., 2018). The latter refers to power changes in frequencies above 50 Hz, which can only be computed from invasively recorded data, such as from ECoG or depth electrodes. Invasive BCIs that operate on high-gamma based features have gained considerable attention and are subject to intensive research. For example, this encompasses real-time passive functional mapping in the course of surgery planning (Ogawa et al., 2014), visual categorization tasks (Kapeller et al., 2018), or the development of BCI prototypes for prosthetic limb, hand, or finger control (Shenoy et al., 2007; Kubánek et al., 2009; Onaran et al., 2011; Yanagisawa et al., 2011; Pistohl et al., 2012; Chestek et al., 2013; Kapeller et al., 2014; Xie et al., 2015; Bleichner et al., 2016; Hotson et al., 2016; Branco et al., 2017; Jiang et al., 2017; Li et al., 2017; Pan et al., 2018).

It is known that high-gamma based invasive BCIs can yield very high classification accuracies, depending on the complexity of the experiment, the electrode location and density, and the processing methods and parameters. For example, Yanagisawa et al. (2011) classified hand movement vs. rest in one patient with an accuracy of 79.6%. Pistohl et al. (2012) achieved an average accuracy of 87.8% over three subjects for two different types of grasp movements. In another study, two high-level hand gestures were correctly identified at an average rate of 95.5% over four subjects (Xie et al., 2015). All these results entailed standard ECoG grids. Performance increases considerably when high-density electrode arrays are employed. Among others, this was shown by Jiang et al. (2017), who achieved 100% accuracy for two subjects in a two-class experiment involving hand gestures.

Three or more different hand gestures can also be identified by high-gamma based BCIs. Yanagisawa et al. (2011) reported 68.3% in one subject for three different hand postures. For the same experiment, Kapeller et al. (2014) published accuracies up to 95.9% averaged over two subjects, and Li et al. (2017) scored on average 80.0% in three subjects. In a similar setup, Xie et al. (2015) obtained correct classification rates of 92.7% over three hand gestures in four subjects on average. Whereas, these experiments were obtained from standard ECoG grids, several studies with hand posture classification were conducted with subjects having high-density grids implanted. Using both high-density and standard electrode arrays, Chestek et al. (2013) conducted experiments to discriminate four hand postures and rest at an accuracy rate of 77.7% on average over three subjects. Using only high-density grids, Pan et al. (2018) reported up to 90% for three different hand gestures over 5 subjects. Involving four different hand gestures, Bleichner et al. (2016) achieved 85.5% accuracy over two subjects, and Branco et al. (2017) attained 85.0% over five subjects.

Many efforts have also gone into decoding individual finger movements. Using standard ECoG grids, Shenoy et al. (2007) achieved an average accuracy of 77.0% for classifying each of the five fingers over six subjects. Kubánek et al. (2009) reported 80.3% over five subjects for the same experiment, whereas Onaran et al. (2011) got 86.3% over three subjects. Four fingers vs. rest were correctly decoded at a rate of 79.3% in three subjects by Chestek et al. (2013). One subject with high-density electrodes implanted achieved 96.5% accuracy for each finger in a study conducted by Hotson et al. (2016).

Table 1 summarizes these results and provides a comprehensive overview of the state of the art.

A variety of classifiers for both offline and real-time BCIs exist. Besides linear programming machines (Shenoy et al., 2007), Bayesian approaches (Chestek et al., 2013), pattern matching (Bleichner et al., 2016; Branco et al., 2017; Kapeller et al., 2018), neural networks (Pan et al., 2018), and support vector machines (Onaran et al., 2011; Yanagisawa et al., 2011; Li et al., 2017), linear discriminant analysis (LDA) is widely used for both non-invasive and invasive BCI and all types of features (Bostanov, 2004; Scherer et al., 2004; Blankertz et al., 2008, 2011; Hoffmann et al., 2008; Prueckl and Guger, 2009; Onaran et al., 2011; Yanagisawa et al., 2011; Pistohl et al., 2012; Kapeller et al., 2014; Xu et al., 2014; Lotte et al., 2015; Xie et al., 2015; Hotson et al., 2016; Gruenwald et al., 2017a; Jiang et al., 2017; Li et al., 2017). LDA is robust, has low complexity due to linearity and performs well in line with more sophisticated methods (Garrett et al., 2003; Lee et al., 2005; Lotte et al., 2007).

If the dimension of the feature space is high, a spatial filter must be employed to reduce the number of features and to prevent the classifier from overfitting. The most straightforward approach is feature selection, either manual from a-priori data inspection or automatized via statistical algorithms (Kapeller et al., 2014; Xie et al., 2015; Bleichner et al., 2016; Hotson et al., 2016; Li et al., 2017; Pan et al., 2018). Another approach for feature reduction in invasive and non-invasive bandpower-based BCIs is common spatial patterns (CSPs), a linear projection scheme that optimizes class separation within a pre-defined window (Blankertz et al., 2008; Onaran et al., 2011; Wu et al., 2013; Kapeller et al., 2014, 2018; Lotte et al., 2015; Gruenwald et al., 2017a).

To underline the popularity of the aforementioned methods, 5 out of 14 setups as listed in **Table 1** utilize LDA while scoring top results, and all feature reduction approaches (9 out of 15) are either selection-based or CSP-based.

Despite their striking advantages, all of the three outlined techniques (LDA, CSP, and feature selection) suffer from substantial drawbacks.

First of all, LDA is inherently static, since it is designed to operate on two multidimensional point clouds. However, the trials of (synchronous) BCIs are usually given as spatiotemporal feature matrices that also contain transient information. This transient information cannot be exploited by LDA in a

TABLE 1 | State-of-the art summary of hand-motor decoding experiments involving high-gamma based invasive BCIs.

Reference	No. of subjects	Electrode spacing[a]	Frequency bands (Hz)	Feature reduction[b]	Classifier[c]	Trial alignment	Trial length (s)[d]	Protocol[e]	Classes[f]	Mean accuracy (%)
Shenoy et al., 2007	6	Macro	11 – 40 71 – 100 101 – 150	None	LPM	None	Not reported	Finger	5	77.0
Kubánek et al., 2009	5	Macro	8 – 12 18 – 24 75 – 115 125 – 159 159 – 175	None	LMD	Data glove	[−1.0, +1.0]	Finger	5	80.3
Onaran et al., 2011	3	Macro	65 – 200	CSP	SVM	Data glove	[−0.75, +1.0]	Finger	5	86.3
Yanagisawa et al., 2011	1	Macro	1 – 8 25 – 40 80 – 150	None	SVM	None	n/a (online)	Move RPS	1 + 1 3	79.6 68.3
Pistohl et al., 2012	3	Macro	2 – 6 14 – 46 54 – 114	None	rLDA	Data glove	[−1.0, +0.5]	Grasp	2	87.8
Chestek et al., 2013	3	Mixed	66 – 114	None	NB	Data glove	[−0.5, +1.5]	Gesture Finger	4 + 1 4 + 1	77.7 79.3
Kapeller et al., 2014	2	Macro	60 – 90 110 – 140 160 – 190	FS CSP	LDA	None	[−0.5, +1.5]	RPS	3	83.8 95.8
Xie et al., 2015	4	Macro	Auto	FS	LDA	None	Various	Gesture	2 3	95.5 92.7
Bleichner et al., 2016	2	Micro	70 – 125	FS	PM	Data glove	[−1.0, +2.0]	Gesture	4	85.5
Hotson et al., 2016	1	Micro	72 – 110	FS	LDA	Data glove	[−0.4, +1.0]	Finger	5	96.5
Branco et al., 2017	5	Micro	70 – 125	None	PM	High-gamma	[−1.0, +2.6]	Gesture	4	85.0
Jiang et al., 2017	2	Micro	60 – 200	CSP	LDA	Not reported	[−0.15, +0.35]	Gesture	2	100.0
Li et al., 2017	3	Macro	4 – 12 70 – 135	FS	SVM	None	[±0.0, +0.9]	RPS	3	80.0
Pan et al., 2018	5	Micro	4 – 12 12 – 40 40 – 70 70 – 135 135 – 200	FS	RNN	Data glove	[±0.0, +0.5] [±0.0, +1.2]	RPS	3	≈ 80 ≈ 90

[a] *Macro, standard ECoG grid; Micro, high-density ECoG grid; Mixed, standard and high-density ECoG grids.*
[b] *CSP, common spatial patterns; FS, algorithm-based or manual channel/feature selection.*
[c] *LPM, linear programming machine; LMD, linear multivariate decoder; SVM, support vector machine; (r)LDA, (regularized) LDA; NB, naive Bayes; PM, pattern matching; RNN, recurrent neural network.*
[d] *Specified relative to cue, movement onset, or high-gamma onset (depending on trial alignment).*
[e] *Finger, finger movement or tapping; Move, movement vs. rest; RPS, rock-paper-scissors; Gesture, arbitrary hand gestures.*
[f] *Inclusion of a resting-state class denoted by "+1".*

straightforward manner. Sometimes, it is feasible to vectorize the feature matrices and apply LDA on the resulting vectors. This approach however inflates the dimension of the feature space dramatically. It therefore requires a large amount of trials to maintain statistical robustness, which are only available in particular BCI protocols (such as in P300-based experiments; Hoffmann et al., 2008). If the statistics are too weak for this approach, a regularized version of LDA may be used. In the current context of invasive BCIs for motor control, this approach was followed by Li et al. (2017), whose feature space was spanned by the vectorized power samples from the time × frequency × channel cube. Another attempt to explicitly account for feature transients was pursued by Pan et al. (2018), who employed recursive neural networks. In general, however, LDA is usually employed such that it is applied to the features at a given point in time within the trial that promises to yield good performance. In turn, this creates the challenge of robustly identifying this time point. Furthermore, the features are usually temporally smoothed to enhance performance—the appropriate smoothing level must thus be found empirically as well.

To reduce the dimension of the feature space, feature selection is straightforward and seems to deliver satisfying performance. However, the nature of *selecting* a feature entirely dismisses information in unselected features. Moreover, feature selection

is unable to combine joint information from coherent features, leading to redundancy in the final feature set. The search for the optimal set of features may be computationally demanding, if statistically robust results should be obtained. In any case, not only identifying the features themselves, but also determining the appropriate *number* of features is an additional degree of freedom of this method that must be properly taken care of.

In contrast to feature selection, CSPs inherently overcome the two main issues of feature selection, such as information redundancy and feature dismissal. However, finding the optimal location and size of the CSP window may be challenging and requires manual intervention. To the best of our knowledge, no automatized approaches thereto exist. As well, the optimal number of features to be selected for optimal performance needs to be determined in advance.

In view of the shortcomings of state-of-the art methods delineated above, we here present a novel classification method for machine-learning systems with spatiotemporal features in general, and for high-gamma based invasive BCIs for motor control in particular. Our method extends LDA such that it accounts for the time-varying nature of features, we thus name it *time-variant* linear discriminant analysis (TVLDA). Since TVLDA is applied to one trial as a whole, it avoids the need of estimating the optimal time point for classification as was necessary for LDA. We will also describe an intrinsic property of TVLDA that allows for straightforward and powerful feature reduction via principal component analysis (PCA). Additionally, we investigate the impact of a simple time-domain spectral whitening stage during preprocessing. The resulting system is still linear and of low complexity, which enables it for future real-time experiments. We quantitatively assess and compare the performance of our method by means of recordings from 15 subjects with temporarily implanted ECoG electrodes.

2. MATERIALS AND METHODS

2.1. Subjects

2.1.1. Original Study

In the original study conducted for this publication, we evaluated data from six epilepsy patients undergoing surgical treatment at Asahikawa Medical University, Asahikawa, Japan. For surgery planning, the patients had a variety of ECoG grids of different types, sizes, and channel counts implanted over the course of several weeks. Besides the standard clinical procedure, all of them volunteered to participate in additional research experiments. The study was approved by the institutional review board of Asahikawa Medical University and received certificate number 245 in June 2012. Written informed consent was obtained from each patient before participating in the study.

Table 2 summarizes the most important data and recordings from the patients, which we subsequently refer to as subjects S1 through S6. Their ages ranged between 17 and 37 years at the day of electrode implantation. S1 and S4 (one third) are female, whereas S2, S3, S5, and S6 are male. S4 is the only left-handed subject. Covered hemispheres are left for S3 and S4 and right for the others.

From the total number of implanted ECoG grids, we only used the ones covering sensorimotor areas for further evaluation. These were standard 20-channel grids (Unique Medical Co., Ltd., Tokyo, Japan; diameter 3 mm, spacing 10 mm, geometry 4×5) for S1 and S6, and 60-channel high-density ECoG grids (Unique Medical Co., Ltd.; diameter 1.5 mm, spacing 5 mm, geometry 6×10) for the others. Based on MRI and CT scans, we reconstructed a three-dimensional model of the brain via *FreeSurfer* (Martinos Center for Biomedical Imaging, Harvard University) and co-registered electrode locations. Based on this and a functional parcellation of the brain, we roughly estimated the electrode coverage on the primary motor cortex and the somatosensory cortex. At this stage, it turned out that the electrodes of S5 were actually only covering somatosensory areas. **Figure 1** provides an overview of the electrode placement.

2.1.2. Public Dataset

In order to make our analyses reproducible by other researchers, we also evaluated the publicly available *fingerflex* dataset[1] from Kai Miller.

2.1.2.1. Ethics statement

All patients participated in a purely voluntary manner, after providing informed written consent, under experimental protocols approved by the Institutional Review Board of the University of Washington (no. 12193). All patient data was anonymized according to IRB protocol, in accordance with HIPAA mandate. These data originally appeared in the manuscript *Human Motor Cortical Activity Is Selectively Phase- Entrained on Underlying Rhythms* published in PLoS Computational Biology in 2012 (Miller et al., 2012).

This dataset contains nine subjects, which we integrate as S7 through S15 in this context. A brief summary is given in **Table 3**. All subjects used implanted platinum arrays (Ad-Tech Medical Instrument Corporation, Wisonsin, USA) with 2.3 mm exposed surface and 10 mm inter-electrode distance. The datasets comprised a variable number of channels, which all seemed to contain good ECoG data. In contrast to the data from our study in Asahikawa, it was difficult to assess the exact coverage of S7–S15; we thus used all channels for further processing. Please see the original publication for more details regarding the exact electrode locations.

We recognized that the recordings from S7 to S9 are identical with Subject 1–3 from the BCI Competition IV, respectively, which is another highly popular public ECoG dataset (Tangermann et al., 2012).

2.2. Experiments

Table 2 summarizes the conducted experiments, which all relate to hand motor functions at different abstraction levels. The *rock-paper-scissors* (RPS) experiment addresses high-level gestures, whereas the *finger-tapping* experiment aims at decoding individual finger movement. The latter is divided into the two variants *palm down* (FTPD) and *palm up* (FTPU). We will use

[1] https://stacks.stanford.edu/file/druid:zk881ps0522/fingerflex.zip

TABLE 2 | Subjects S1–S6 and experiment overview of the original study conducted in Asahikawa, Japan.

ID	Age	Gender	Handedness	Covered hemisphere	Electrode spacing[a]	Electrodes total	Electrodes selected	Coverage motor[b]	Coverage somatosensory[b]	Protocol[c]	Trials per class
S1	35	Female	Right	Right	Macro	98	20	7–8	5–7	RPS	30
S2	26	Male	Right	Right	Micro	140	60	26–32	19–24	FTPU	40
										RPS	40
S3	26	Male	Right	Left	Micro	187	60	29–36	22–26	FTPU	20
S4	17	Female	Left	Left	Micro	164	60	29–37	12–17	FTPD	75
										FTPU	86
										RPS	65
S5	22	Male	Right	Right	Micro	158	60	5–7	27–34	FTPU	97
										RPS	76
S6	37	Male	Right	Right	Macro	100	18	7–9	4–7	RPS	60

[a] *Macro, standard ECoG grid; Micro, high-density ECoG grid.*
[b] *Estimated number of electrodes, based on* ***Figure 1****.*
[c] *RPS, rock-paper-scissors; FTPD, finger tapping, palm down; FTPU, finger tapping, palm up.*

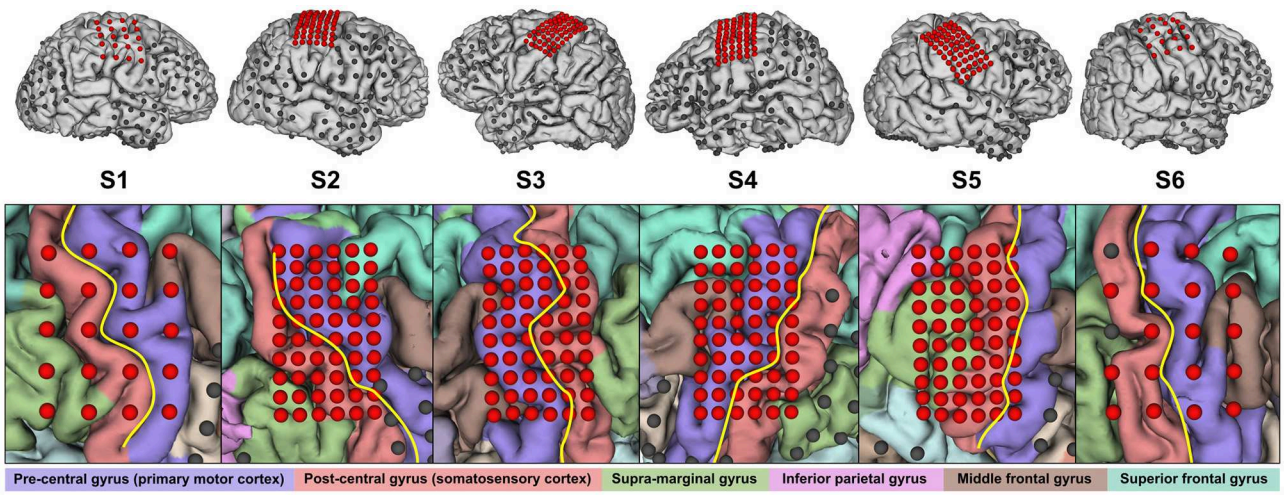

FIGURE 1 | Electrode placement overview. Electrodes reported in **Table 2** are highlighted in red. Not all of the remaining electrodes in the top row are visible due to occlusion. In the close-up view, the central sulcus is indicated in yellow and the identified gyri are shaded in respective colors.

TABLE 3 | Subjects S7–S15 and experiment overview of the public ECoG dataset (S7–S9 are identical with Subject 1–3 from the BCI Competition IV, respectively).

ID	Patient code[a]	BCI comp. IV	Age	Gender	Handedness	Covered hemisphere	Electrode spacing[b]	No. of electrodes	Protocol[c]	Trials per class
S7	bp	Subject 1	18	Female	Right	Left	Macro	46	FTPU	28
S8	cc	Subject 2	21	Male	Right	Right	Macro	63	FTPU	28
S9	zt	Subject 3	27	Female	Right	Left	Macro	61	FTPU	28
S10	jp		35	Female	Right	Left	Macro	58	FTPU	18
S11	ht		26	Male	Right	Left	Macro	64	FTPU	27
S12	mv		45	Female	Right	Left	Macro	43	FTPU	6
S13	wc		32	Male	Right	Left	Macro	64	FTPU	28
S14	wm		19	Female	Right	Right	Macro	38	FTPU	14
S15	jc		18	Female	Right	Left	Macro	47	FTPU	23

[a] *As stated in the dataset documentation.*
[b] *Macro, standard ECoG grid.*
[c] *FTPU, finger tapping, palm up.*

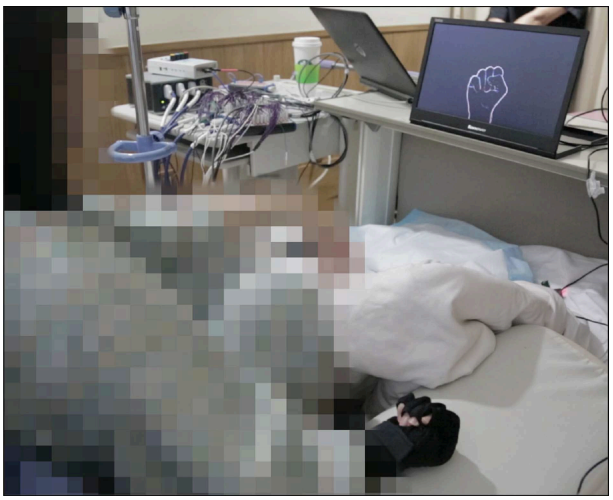

FIGURE 2 | Setup of the rock-paper-scissors experiment.

the terms finger movement and finger tapping interchangeably throughout this publication.

All experiments were conducted at the bedside of the patient. Before each experiment, the patients received and confirmed all necessary instructions to successfully perform it. The respective tasks were triggered by a visual cue, shown on a computer monitor placed in front of the patient. A data glove (5DT Inc., Florida, USA) was used to capture the hand movements of all subjects. In all experiments, the contralateral hand relative to the implantation site carried out the movements. **Figure 2** gives a visual impression of the setup. The experiments conducted with S1–S6 were repeated over the course of several days, depending on the condition and motivation of the subjects.

In the following, we describe the individual experiments more in detail.

2.2.1. Rock-Paper-Scissors

The different hand poses involved in this experiment were inspired by the well-known hand game *rock-paper-scissors* (RPS), constituting a three-class experiment. The visual cues were shown on the screen for one second, interleaved by a scrambled picture distractor of randomized duration between 1.5 and 2.5 seconds. The subjects were instructed to form the requested gesture with their hand once the stimulus appeared, and to return into a relaxed hand position once the distractor showed up. One run included 20 trials per class. The rock-paper-scissors experiment was only conducted with S1–S6.

2.2.2. Finger Tapping, Palm Down and Palm Up

2.2.2.1. Original study (S1–S6)

Here, the subjects were asked to perform two taps with the finger indicated on the screen for one second. Between the cues, a scrambled picture was shown for a randomized duration between 1.7 and 2.5 seconds, indicating that the subject should stay at rest. In the easier version, the palm-up version (FTPU), the subjects executed two repeated finger flexions, whereas in the palm-down version (FTPD), the subjects performed actual taps on a solid, planar surface. One run of this five-class experiment consisted of 10 trials per class. The palm-down version turned out to require a certain level of fine motor skills that was not present in all subjects, so only S4 completed it successfully.

Due to misunderstanding of the task instructions, S3 executed this experiment differently: instead of executing two discrete taps, he kept flexing the finger until a new instruction showed up on the screen. As described below, this required some additional processing steps to obtain usable data.

2.2.2.2. Public dataset (S7–S15)

As described in Miller et al. (2012), the subjects were cued with a word shown on a bedside monitor, indicating which finger to move. Each task lasted for two seconds, during which the subjects typically performed between two and five repeated finger flexions. A blank screen, shown for another two seconds, was interleaved between each task as a resting trial. Only the palm-up variant of the experiment was performed.

2.3. Data Acquisition

2.3.1. Original Study (S1–S6)

We captured the raw ECoG data with the *g.HIamp* biosignal amplifier (g.tec medical engineering GmbH, Austria) and used *Simulink* (The MathWorks, Inc., Massachusetts, USA) as the recording environment. Depending on the overall number of channels, we set the sampling rate to either 1.2 or 2.4 kHz. We used the *g.HIsys Highspeed Online Processing* toolbox (g.tec medical engineering GmbH) for the stimulus presentation and synchronous data acquisition and storage. The recorded data were saved on a hard drive and re-processed offline in *MATLAB* (The MathWorks, Inc.) for this study as described in this section.

2.3.2. Public Dataset (S7–S15)

As communicated by Miller et al. (2012), the ECoG data were recorded with the *Synamps 2* biosignal amplifier (Compumedics Neuroscan, North Carolina, USA) at a sampling rate of 1 kHz and internal bandpass-filter from 0.3 to 200 Hz. The general-purpose software environment *BCI2000* was used for stimulus presentation and synchronous data acquisition.

2.4. Preprocessing and Feature Extraction

This subsection closely follows the concept of Gruenwald et al. (2017b), which outlines optimal bandpower estimation for real-time BCIs. If not otherwise mentioned, we processed data from all subjects regardless of their origin in the exactly same manner.

After excluding channels that were notably bad due to high impedance, we re-referenced the data by the common average. After that, a notch-filter cascade (recursive 6th-order Butterworth, bandwidth: 5 Hz) up to the 6th harmonic was used to remove interference peaks from the spectrum at integer multiples of the power line frequency.

Next, an optional spectral whitening filter (Oppenheim and Schafer, 2010) was applied to each channel. While the

concept of whitening (or spectral equalization) is frequently used in time-frequency analysis (Miller et al., 2009; Yanagisawa et al., 2011; Pistohl et al., 2012), it is less known that it can also be performed in time domain by a simple finite-impulse response filter. This enables whitening for real-time applications, where time-frequency transformation is not an option.

The underlying principle of a whitening filter is that the input signal can be modeled as a Pth-order autoregressive (AR) process, e.g.,

$$\sum_{p=0}^{P} a_p y[n-p] \;=\; v[n] \tag{1}$$

with $v[n] \;\sim\; \mathcal{N}(0, \sigma_v^2)$ i.i.d. being a zero-mean white Gaussian noise with variance σ_v^2. In this publication, we use the tilde notation to link a random variable with its particular distribution and the term i.i.d. to indicate independent and identically distributed samples. The AR coefficients a_p can be determined by the *Yule-Walker equations* that are applied to a sufficiently long signal fragment of $y[n]$ (e.g., a few seconds). Equation 1 can now be seen as a linear time-invariant filter with impulse response a_p:

$$\bar{y}[n] = \sum_{p=0}^{P} a_p y[n-p]\,. \tag{2}$$

It is intuitive that the filter output $\bar{y}[n]$ resembles the white noise $v[n]$ and therefore has a flat spectrum.

The positive effect of whitening on the signal-to-noise ratio of ECoG bandpower features was anticipated previously (Gruenwald et al., 2017b). **Figure 3** provides an illustration, where the dynamic range of the signal within the cut-off frequencies can be roughly estimated to 25 dB. Whitening equalizes the pronounced $1/f$-shape of the spectrum, which balances the frequency-specific contributions to the overall bandpower and thus increases signal fidelity.

Since an ECoG spectrum is rather smooth in absence of interference peaks, the filter order can be low. In practice, we found a 10th-order whitening filter sufficient.

After the optional whitening stage, we band-passed the signal (recursive 6th-order Butterworth) to our high-gamma frequency band of interest. We assessed several bands with respect to classification performance, and finally chose 50 to 300 Hz as our target. This may seem inappropriate in view of the fact that the data of S7–S15 was pre-filtered by a bandpass between 0.3 and 200 Hz. However, we observed that the whitening procedure was able to recover high-gamma components well above 200 Hz.

Given the bandpass signals, we then estimated the bandpower via a sliding variance window of 50 ms length, without overlap. A log-transform was appended, to improve signal stationarity and Gaussianity.

Then, the data were triggered, i.e., cut into signal fragments for each trial and class. Since S3 and S7–S15 exhibited a large movement onset jitter, we applied a trial-based correction. To this end, we used the signals captured by the data glove for aligning the individual trials of S3. Likewise, we corrected the onset jitter

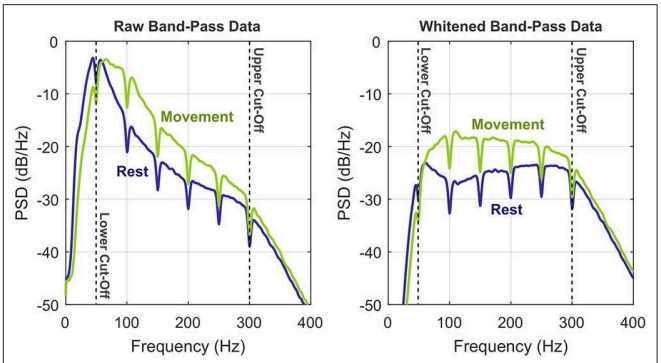

FIGURE 3 | Illustration of the whitening procedure by means of power spectral densities of the preprocessed bandpass signals (S6, RPS, exemplary channel). To illustrate the benefits of whitening, the two conditions *rest* vs. *movement* (any class) are shown separately. Upper and lower corner frequencies of the bandpass filter are indicated by the vertical dashed lines.

of S7 to S15 by a movement trigger already contained in the data. For the other subjects (S1, S2, and S4–S6), no explicit trial alignment was performed, since the onset jitter was already small enough for good classification results. However, we compensated for the systematic reaction and execution latency by shifting the grand average high-gamma onset to the center of the trial to guarantee symmetry.

We set our trial length to 0.75 seconds pre- and post-onset, respectively. Trials that were contaminated with pathological brain activity (such as inter-ictal spiking) were removed. No further trial exclusion was performed.

At this point, it is reasonable to establish a mathematical model that facilitates subsequent methodological derivations. To this end, we refer to the number of samples and channels as N_S and N_Ch, respectively. The preprocessed and triggered data then constitute spatiotemporal feature matrices $\mathbf{X}_\mathsf{c}^{(i)} \in \mathbb{R}^{N_\mathrm{S}\times N_\mathrm{Ch}}$ for trials i and classes c. Both trials and classes are expected to stem from a pool of N_T trials and N_C classes, respectively, e.g., $\mathcal{T} = \{1, \ldots, N_\mathrm{T}\}$ and $\mathcal{C} = \{\mathsf{A}, \mathsf{B}, \mathsf{C}, \ldots\}$ with $|\mathcal{C}| = N_\mathrm{C}$. For the typical machine-learning scenario, we are further partitioning the set of trials into a training set $\mathcal{T}_\mathrm{Train}$ (with known class labels) and a test set $\mathcal{T}_\mathrm{Test}$ (with unknown class labels), which are disjoint. Formally, these sets can be expressed as

$$\mathcal{Y}_\mathrm{Train} = \left\{ \mathbf{X}_\mathsf{c}^{(i)} \;\middle|\; \mathsf{c} \in \mathcal{C}, i \in \mathcal{T}_\mathrm{Train} \right\} \tag{3}$$

$$\mathcal{Y}_\mathrm{Test} = \left\{ \mathbf{X}_\mathsf{c}^{(i)} \;\middle|\; \mathsf{c} \in \mathcal{C}, i \in \mathcal{T}_\mathrm{Test} \right\}. \tag{4}$$

Toward mathematical tractability, we decompose $\mathbf{X}_\mathsf{c}^{(i)}$ into row vectors $\mathbf{y}_\mathsf{c}^{(i)}[n]$ with discrete-time index n:

$$\left(\mathbf{X}_\mathsf{c}^{(i)}\right)_{n,\cdot} = \mathbf{y}_\mathsf{c}^{(i)}[n], \quad n \in \{0, 1, \ldots, N_\mathrm{S}-1\}\,. \tag{5}$$

2.5. Feature Reduction (Standard)

The number of recorded channels may be high, particularly in ECoG experiments. This increases the computational demands and the risk of classifier overfitting. Consequently,

a feature projection or selection stage usually precedes the classifier. Especially for ECoG, this can decrease dimensionality tremendously without losing information, since (1) only a limited amount of channels significantly contributes to class separation and (2) correlation across contributing channels may be high. Mathematically, this feature projection is implemented by a generic matrix $\mathbf{P} \in \mathbb{R}^{N_{\mathrm{Ch}} \times N_{\mathrm{F}}}$ with $N_{\mathrm{F}} \ll N_{\mathrm{Ch}}$, such that

$$\mathbf{x}_{\mathsf{c}}^{(i)}[n] = \mathbf{y}_{\mathsf{c}}^{(i)}[n]\mathbf{P}\,. \tag{6}$$

Following a likewise decomposition as in (5), we denote the contracted spatiotemporal feature matrices by $\mathbf{X}_{\mathsf{c}}^{(i)} \in \mathbb{R}^{N_{\mathrm{S}} \times N_{\mathrm{F}}}$ and write for the training and test sets

$$\mathcal{X}_{\mathrm{Train}} = \left\{ \mathbf{X}_{\mathsf{c}}^{(i)} \mid \mathsf{c} \in \mathcal{C}, i \in \mathcal{T}_{\mathrm{Train}} \right\} \tag{7}$$

$$\mathcal{X}_{\mathrm{Test}} = \left\{ \mathbf{X}_{\mathsf{c}}^{(i)} \mid \mathsf{c} \in \mathcal{C}, i \in \mathcal{T}_{\mathrm{Test}} \right\}. \tag{8}$$

The subsections below describe strategies how to populate the projection matrix $\mathbf{P}$.

2.5.1. Common Spatial Patterns

Common spatial patterns (CSPs) are the de-facto standard for dimension reduction in EEG signal processing (Blankertz et al., 2008; Lotte et al., 2015) and are also popular in ECoG signal processing (Onaran et al., 2011; Kapeller et al., 2014; Xie et al., 2015; Jiang et al., 2017). This approach expects multivariate distributions of two classes A and B with covariances $\mathbf{\Sigma}_{\mathsf{A}}$ and $\mathbf{\Sigma}_{\mathsf{B}}$, respectively. The CSP transformation matrix then simultaneously diagonalizes both $\mathbf{\Sigma}_{\mathsf{A}}$ and $\mathbf{\Sigma}_{\mathsf{B}}$, where the element-wise ratio along the diagonals is strictly monotonic. Consequently, the first and the last CSP component maximize the variance for one class, while minimizing it for the other. Additional CSP components further contribute to this.

In the given context, CSPs operate on the triggered bandpass data within a pre-defined window, i.e., *before* power computation. For all datasets, we have located the peak of the grand high-gamma activation over trials and classes, and centered the CSP window about this peak. We set the window length to 0.3 seconds, since this yielded the best classification results. Denoting the CSP transformation by $\mathbf{R} \in \mathbb{N}^{N_{\mathrm{Ch}} \times N_{\mathrm{Ch}}}$, the projection matrix $\mathbf{P}_{\mathrm{CSP}}$ is then column-wise populated with the first $\lceil N_{\mathrm{F}}/2 \rceil$ and the last $\lfloor N_{\mathrm{F}}/2 \rfloor$ columns of $\mathbf{R}$. As will be discussed in section 2.8, we computed CSPs pairwise for each binary classification in a multi-class scenario.

2.5.2. Feature Selection

Another common approach to reduce the dimensionality is a discrete feature (or channel) selection process. While the individual implementations differ considerably, feature selection is heavily used in the ECoG community (Kapeller et al., 2014; Xie et al., 2015; Bleichner et al., 2016; Hotson et al., 2016; Li et al., 2017; Pan et al., 2018).

Here, we use a straightforward approach for feature selection. First, we compute an activation score for each class and channel, which is the trial-averaged relative band-power increase from baseline (before high-gamma onset) to activation (after high-gamma onset). For each pair of classes, we then calculate the absolute difference of this activation score for each channel and sort the result in descending order. This way, the channels exhibiting the largest high-gamma activation *difference* for the two classes are ranked top. Consequently, the projection matrix $\mathbf{P}_{\mathrm{FS}}$ (which is more a *selection* matrix now) is established such that its N_{F} columns logically index the first N_{F} channels in the given ranking, respectively.

2.6. Classification

We now assume that, for each class, the feature matrices $\mathbf{X}_{\mathsf{c}}^{(i)}$ comprise a unique underlying activation pattern that is identical over trials. However, each repetition is subject to noise, most prominently from imperfect task execution and the uncertainty of feature estimation. We thus employ a multivariate Gaussian distribution to describe these components as follows:

$$\mathbf{x}_{\mathsf{c}}^{(i)}[n] \sim \mathcal{N}\big(\boldsymbol{\mu}_{\mathsf{c}}[n], \mathbf{\Sigma}_{\mathsf{c}}[n]\big) \text{ i.i.d.} \tag{9}$$

In general, $\boldsymbol{\mu}_{\mathsf{c}}[n] \in \mathbb{R}^{1 \times N_{\mathrm{F}}}$ and $\mathbf{\Sigma}_{\mathsf{c}}[n] \in \mathbb{R}^{N_{\mathrm{F}} \times N_{\mathrm{F}}}$ are not known.

The independence constraint is expected to hold over samples n, trials i and classes c. While this requirement is intuitively hold over trials and classes, in fact it may be violated over samples. We have shown in Gruenwald et al. (2017b) that the signal processing pipeline yields high-gamma features with estimation noise that can be considered white; however, imperfect trial execution may impose temporally correlated noise on the data. We will also address this issue in section 4.

2.6.1. Linear Discriminant Analysis

A standard tool to separate features of two classes is linear discriminant analysis (LDA). In a nutshell, LDA expects multivariate Gaussian distributions from two classes A and B and finds a projection vector that simultaneously maximizes the mean distance whilst minimizing the individual variances of the projected populations (Bishop, 2006). LDA-based classifiers are optimal in the maximum-likelihood sense if the two distributions are homoscedastic.

For convenience and if applicable, we hereafter use the generic class label $\mathsf{c} \in \{\mathsf{A}, \mathsf{B}\}$ to denote either of the two classes. In case we know the class associated with a particular variable, we denote this by subscript notation.

A common approach to classify spatiotemporal features with LDA is the training of several LDA instances over time and selecting the classifier which yields best performance. Thus, after introducing the well-known difference of means and pooled covariance matrix

$$\mathbf{\Delta\mu}[n] = \boldsymbol{\mu}_{\mathsf{B}}[n] - \boldsymbol{\mu}_{\mathsf{A}}[n] \tag{10}$$

$$\mathbf{\Sigma}[n] = \tfrac{1}{2}\big(\mathbf{\Sigma}_{\mathsf{A}}[n] + \mathbf{\Sigma}_{\mathsf{B}}[n]\big), \tag{11}$$

the standard LDA projection vector equates to

$$\mathbf{w}[n] = \mathbf{\Delta\mu}[n]\mathbf{\Sigma}^{-1}[n]\,. \tag{12}$$

Given an arbitrary input $\mathbf{x}^{(i)}[n]$, the symmetric LDA score $p^{(i)}[n]$ is computed as

$$p^{(i)}[n] = \mathbf{w}[n]\mathbf{x}^{(i)}[n]^{\mathsf{T}} - d[n]\,, \tag{13}$$

where the superscript $(\cdot)^\mathsf{T}$ denotes matrix transposition and the offset

$$d[n] = \tfrac{1}{2}\mathbf{w}[n]\left(\boldsymbol{\mu}_\mathsf{A}[n] + \boldsymbol{\mu}_\mathsf{B}[n]\right)^\mathsf{T} \tag{14}$$

centers the two projected class populations about zero. This can be verified by equating the means $\mu_{p_\mathsf{C}}[n] = \mathbb{E}\{p_\mathsf{C}^{(i)}[n]\}$ via Equations (13) and (14), where $\mathbb{E}\{\cdot\}$ denotes the expectation operator over trials. It is now evident that $\mu_{p_\mathsf{A}}[n] = -\mu_{p_\mathsf{B}}[n]$, since

$$\mu_{p_\mathsf{A}}[n] = -\tfrac{1}{2}\mathbf{w}[n]\boldsymbol{\Delta\mu}[n]^\mathsf{T} \tag{15}$$

$$\mu_{p_\mathsf{B}}[n] = +\tfrac{1}{2}\mathbf{w}[n]\boldsymbol{\Delta\mu}[n]^\mathsf{T}\,. \tag{16}$$

2.6.1.1. Training

There are different approaches to apply an LDA classifier to spatiotemporal features. The most common strategy is to smooth the features over time, train the LDA classifier for each point in time, and then select the one which gives best performance. In the present context, best performance for LDA was achieved if the features within a trial were symmetrically smoothed by three samples in each direction. Toward the decision which classification time point to use, we investigated several options. Most robust results were obtained by adaptively selecting the time point of maximum high-gamma activation over all classes and trials. We subsequently denote this time point as n_LDA.

Summarizing the LDA training procedure, the sample means $\hat{\boldsymbol{\mu}}_\mathsf{C}[n_\mathrm{LDA}]$ and covariances $\hat{\boldsymbol{\Sigma}}_\mathsf{C}[n_\mathrm{LDA}]$ are computed first, given labeled training data $\mathbf{X}_\mathsf{C}^{(i)} \in \mathcal{X}_\mathrm{Train}$. Via Equations (10), (11), (12), and (14), the set $\{\hat{\mathbf{w}}[n_\mathrm{LDA}], \hat{d}[n_\mathrm{LDA}]\}$ then constitutes the LDA classifier.

2.6.1.2. Test

Given a test trial $\mathbf{X}^{(i)} \in \mathcal{X}_\mathrm{Test}$ and $\{\hat{\mathbf{w}}[n_\mathrm{LDA}], \hat{d}[n_\mathrm{LDA}]\}$ as the classifier, the LDA score $\hat{p}^{(i)}$ is simply computed analogously to (13):

$$\hat{p}^{(i)} = \hat{\mathbf{w}}[n_\mathrm{LDA}]\mathbf{x}^{(i)}[n_\mathrm{LDA}]^\mathsf{T} - \hat{d}[n_\mathrm{LDA}]\,. \tag{17}$$

Since the two classes in question lead to LDA scores symmetric about zero, the natural threshold for classification is zero as well:

$$\hat{\mathsf{C}}_\mathrm{LDA}^{(i)} = \begin{cases} \mathsf{A} & \hat{p}^{(i)} < 0 \\ \mathsf{B} & \hat{p}^{(i)} \geq 0 \end{cases}\,. \tag{18}$$

2.6.2. Regularized Linear Discriminant Analysis

Computing the LDA weight vector requires the inversion of the pooled covariance matrix. This can become numerically unstable if the number of samples is not much larger than the feature dimensionality. To overcome this problem, a regularized LDA (rLDA) can be used where only the main diagonal of the sample covariance matrices is accounted for (also known as *shrinking*). Since this allows stable inversion even in high-dimensional feature space, rLDA is particularly appealing when applied to vectorized features $\overline{\mathbf{x}}_\mathsf{C}^{(i)} \in \mathbb{R}^{1\times N_\mathrm{S}N_\mathrm{F}}$, such that

$$\overline{\mathbf{x}}_\mathsf{C}^{(i)} = \left[\mathbf{x}_\mathsf{C}^{(i)}[0], \mathbf{x}_\mathsf{C}^{(i)}[1], \ldots, \mathbf{x}_\mathsf{C}^{(i)}[N_\mathrm{S}-1]\right] \tag{19}$$

$$\sim \mathcal{N}\left(\overline{\boldsymbol{\mu}}_\mathsf{C}, \overline{\boldsymbol{\Sigma}}_\mathsf{C}\right) \text{ i.i.d.} \tag{20}$$

to account for all spatiotemporal information at once.

2.6.2.1. Training

Training the rLDA classifier is straightforward. After computing sample means and sample covariance matrices from the vectorized training data, the off-diagonal elements of the sample covariance matrices are set to zero. Equations (10), (11), (12), and (14) yield the rLDA classifier $\{\hat{\mathbf{w}}^\star, \hat{d}^\star\}$. Note that the temporal index n has now vanished.

2.6.2.2. Test

Applying the rLDA classifier $\{\hat{\mathbf{w}}^\star, \hat{d}^\star\}$ to test data follows analogously to section 2.6.1.2.

2.6.3. Time-Variant Linear Discriminant Analysis

The major improvement of time-variant linear discriminant analysis (TVLDA) over standard LDA is that it utilizes information of *all* individually trained LDA classifiers over the whole trial, which makes it inherently time-*variant*. To derive the concept of TVLDA mathematically, we first interpret $p^{(i)}[n]$ (13) as an N_S-dimensional vector:

$$\mathbf{p}^{(i)} = \left[p^{(i)}[0], p^{(i)}[1], \ldots, p^{(i)}[N_\mathrm{S}-1]\right]^\mathsf{T}\,. \tag{21}$$

In this notation, each class establishes the multivariate Gaussian distribution

$$\mathbf{p}_\mathsf{C}^{(i)} \sim \mathcal{N}\left(\boldsymbol{\mu}_{\mathbf{p}_\mathsf{C}}, \boldsymbol{\Sigma}_{\mathbf{p}_\mathsf{C}}\right) \text{ i.i.d.} \tag{22}$$

with means $\boldsymbol{\mu}_{\mathbf{p}_\mathsf{C}} \in \mathbb{R}^{N_\mathrm{S}\times 1}$ and covariances $\boldsymbol{\Sigma}_{\mathbf{p}_\mathsf{C}} \in \mathbb{R}^{N_\mathrm{S}\times N_\mathrm{S}}$ equating to

$$\boldsymbol{\mu}_{\mathbf{p}_\mathsf{C}} = \left[\mu_{p_\mathsf{C}}[0], \mu_{p_\mathsf{C}}[1], \ldots, \mu_{p_\mathsf{C}}[N_\mathrm{S}-1]\right]^\mathsf{T} \tag{23}$$

$$\boldsymbol{\Sigma}_{\mathbf{p}_\mathsf{C}} = \mathrm{diag}\left\{\left[\sigma^2_{p_\mathsf{C}}[0], \sigma^2_{p_\mathsf{C}}[1], \ldots, \sigma^2_{p_\mathsf{C}}[N_\mathrm{S}-1]\right]\right\}\,. \tag{24}$$

The assumed temporal independence of the feature noise (cf. (9)) implicates the fact that $\boldsymbol{\Sigma}_{\mathbf{p}_\mathsf{C}}$ must be diagonal. The elements of $\boldsymbol{\mu}_{\mathbf{p}_\mathsf{C}}$ are given by Equations (15) and (16), and the elements of $\boldsymbol{\Sigma}_{\mathbf{p}_\mathsf{C}}$ are obtained after short calculus as

$$\sigma^2_{p_\mathsf{C}}[n] = \mathbf{w}[n]\boldsymbol{\Sigma}_\mathsf{C}[n]\mathbf{w}[n]^\mathsf{T}\,. \tag{25}$$

We now want to separate the two class populations $\left\{\mathbf{p}_\mathsf{A}^{(i)}\right\}$ and $\left\{\mathbf{p}_\mathsf{B}^{(i)}\right\}$ again in the LDA-sense. Consequently, the difference of means and pooled covariance are given as

$$\boldsymbol{\Delta\mu}_\mathbf{p} = \boldsymbol{\mu}_{\mathbf{p}_\mathsf{B}} - \boldsymbol{\mu}_{\mathbf{p}_\mathsf{A}} \tag{26}$$

$$\boldsymbol{\Sigma}_\mathbf{p} = \tfrac{1}{2}\left(\boldsymbol{\Sigma}_{\mathbf{p}_\mathsf{A}} + \boldsymbol{\Sigma}_{\mathbf{p}_\mathsf{B}}\right)\,. \tag{27}$$

To find an expression for the LDA projection vector $\boldsymbol{\Sigma}_\mathbf{p}^{-1}\boldsymbol{\Delta\mu}_\mathbf{p}$, we trace back Equations (23) and (24), Equations (15), (16), and (25), and Equations (11) and (12), to finally arrive at the elegant result

$$\boldsymbol{\Sigma}_\mathbf{p}^{-1}\boldsymbol{\Delta\mu}_\mathbf{p} = \mathbf{1}\,. \tag{28}$$

In other words, the overall *TVLDA score*, denoted by $z^{(i)}$, is simply the sum of all intermediate LDA scores (13):

$$z^{(i)} = \sum_{n=0}^{N_\mathrm{S}-1} p^{(i)}[n]\,. \tag{29}$$

It is evident that $\mu_{p\mathsf{B}}[n] - \mu_{p\mathsf{A}}[n] = \mathbf{\Delta\mu}[n]\mathbf{\Sigma}^{-1}[n]\mathbf{\Delta\mu}[n]^{\mathsf{T}}$, which can be shown by inserting (12) into Equations (15) and (16). Consequently, the difference of the expected TVLDA scores yields via (29)

$$\mathbb{E}\left\{z_{\mathsf{B}}^{(i)}\right\} - \mathbb{E}\left\{z_{\mathsf{A}}^{(i)}\right\} = \sum_{n=0}^{N_{\mathrm{S}}-1} \mathbf{\Delta\mu}[n]\mathbf{\Sigma}^{-1}[n]\mathbf{\Delta\mu}[n]^{\mathsf{T}}\,, \tag{30}$$

which is the accumulated Kullback-Leibler divergence of the classes A and B under the homoscedasticity assumption of the (TV)LDA.

2.6.3.1. Training

From the training data $\mathbf{X}_{\mathsf{c}}^{(i)} \in \mathcal{X}_{\mathrm{Train}}$, the TVLDA parameters $\{\hat{\mathbf{w}}[n], \hat{d}[n]\}$ are computed based on the sample means $\hat{\boldsymbol{\mu}}_{\mathsf{c}}[n]$ and covariances $\hat{\mathbf{\Sigma}}_{\mathsf{c}}[n]$ via Equations (10), (11), (12), and (14).

2.6.3.2. Test

For a test trial $\mathbf{X}^{(i)} \in \mathcal{X}_{\mathrm{Test}}$ and a set of TVLDA parameters $\{\hat{\mathbf{w}}[n], \hat{d}[n]\}$, the TVLDA score $\hat{z}^{(i)}$ follows according to Equations (29) and (13):

$$\hat{z}^{(i)} = \sum_{n=0}^{N_{\mathrm{S}}-1} \hat{\mathbf{w}}[n]\mathbf{x}^{(i)}[n]^{\mathsf{T}} - \hat{d}[n]\,. \tag{31}$$

Evidently, also the TVLDA score is symmetric about zero, which leads to the classification scheme

$$\hat{\mathsf{c}}_{\mathrm{TVLDA}}^{(i)} = \begin{cases} \mathsf{A} & \hat{z}^{(i)} < 0 \\ \mathsf{B} & \hat{z}^{(i)} \geq 0 \end{cases}\,. \tag{32}$$

2.7. Feature Reduction (TVLDA-Specific)

We here resume section 2.5 by proposing a novel feature dimensionality reduction approach that is intrinsic to TVLDA, based on principal component analysis (PCA).

We can interpret the time-variant TVLDA weight vector as a spatiotemporal weight matrix $\mathbf{W} \in \mathbb{R}^{N_{\mathrm{S}} \times N_{\mathrm{F}}}$, whose rows are given by $\mathbf{w}[n]$:

$$\left(\mathbf{W}\right)_{n,\cdot} = \mathbf{w}[n]\,. \tag{33}$$

Motivated by the nature of PCA, we now restrict the generic transformation matrix $\mathbf{P}$ to be orthogonal, i.e., $\mathbf{P} \in \mathbb{R}^{N_{\mathrm{Ch}} \times N_{\mathrm{F}}}$ with $N_{\mathrm{F}} = N_{\mathrm{Ch}}$ and $\mathbf{P}^{-1} = \mathbf{P}^{\mathsf{T}}$. Consequently, any transformation of $\mathbf{y}_{\mathsf{c}}^{(i)}[n]$ by $\mathbf{P}$ transparently affects the TVLDA weight matrices $\mathbf{W_x}$ and $\mathbf{W_y}$:

$$\mathbf{x}_{\mathsf{c}}^{(i)}[n] = \mathbf{y}_{\mathsf{c}}^{(i)}[n]\mathbf{P} \;\Rightarrow\; \mathbf{W_x} = \mathbf{W_y}\mathbf{P}\,, \tag{34}$$

where the subscripts indicate which variable $\mathbf{W}$ is associated with. This relationship can be shown by substituting the projection scheme into the computation of the weight vector (12) via Equations (10) and (11).

The idea now is to find $\mathbf{P}$, such that the weights in $\mathbf{W_y}$ are compressed into very few columns of $\mathbf{W_x}$. Only these columns of $\mathbf{W_x}$ are then kept, leading to an effective reduction in dimensionality.

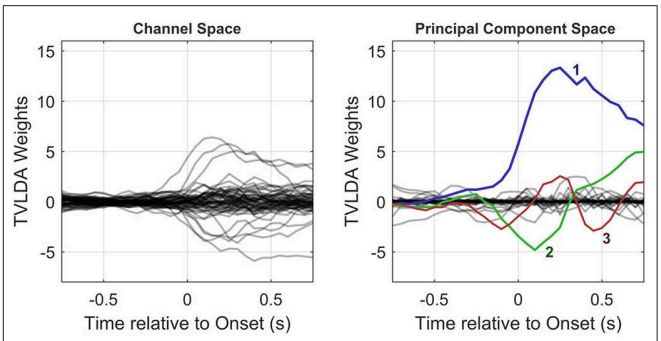

FIGURE 4 | Column-wise visualization of the original and PCA-transformed spatiotemporal weight matrices **$\mathbf{W_y}$ (left)** and **$\mathbf{W_x}$ (right)**, respectively. As illustrated in the right subplot, only few principal components with large amplitudes remain. This allows for substantial dimension reduction, as detailed in the text.

The standard solution to this problem is PCA, which we implement as a singular value decomposition (SVD) of $\mathbf{W_y}$. In short, we factorize $\mathbf{W_y} = \mathbf{USV}^{\mathsf{T}}$ where $\mathbf{U} \in \mathbb{R}^{N_{\mathrm{S}} \times N_{\mathrm{S}}}$ and $\mathbf{V} \in \mathbb{R}^{N_{\mathrm{Ch}} \times N_{\mathrm{Ch}}}$ are orthogonal matrices, and $\mathbf{S} \in \mathbb{R}^{N_{\mathrm{S}} \times N_{\mathrm{Ch}}}$ is a matrix with zeros, except for the non-negative, decreasing singular values on the diagonal. The desired scores in the principal-component space of $\mathbf{W_x}$ are now given by the product $\mathbf{US}$, such that we require

$$\mathbf{W_x} = \mathbf{USV}^{\mathsf{T}}\mathbf{P} \stackrel{!}{=} \mathbf{US} \tag{35}$$

and obtain simply

$$\mathbf{P} = \mathbf{V}\,. \tag{36}$$

Since $\mathbf{V}$ establishes an orthonormal projection, which can be seen as a rotation in high-dimensional space, all information is preserved. The principal components are ordered by their impact, so the projection matrix $\mathbf{P}_{\mathrm{PCA}}$ is simply populated by the first N_{F} columns of $\mathbf{V}$. **Figure 4** provides an example of the PCA-based feature reduction method.

Importantly, the number of channels may be too high to yield invertible covariance matrices (i.e., $N_{\mathrm{Ch}} \gg N_{\mathrm{T}}$). Even if the covariance matrices are nonsingular, their inversion may be numerically unstable. To find a robust PCA decomposition and unless many more trials than channels are available, we therefore recommend smoothing the sample means and covariances over time before computing the weight matrix $\mathbf{W_y}$ that is subject to the SVD. In our case, we used bidirectional averaging of two samples in each direction to obtain the best results. For datasets comprising many trials, this bidirectional averaging did not impair results, and hence we recommend using it whenever applicable.

The number of trials may be extremely low, and thus even temporal averaging does not yield a usable PCA decomposition. In this case—and only in this case—we suggest adding a certain level of regularization to PCA: here, the off-diagonal elements of the TVLDA sample covariances are weighted with a factor between 0 and 1, where 0 is identical to complete diagonalization.

We have observed that setting this factor to 0.75 (which equals a regularization of 25%) can substantially improve results, especially for datasets with particularly low trial count and a small number of channels capturing task-related activation. We will address this issue further in section 4.

Note that the proposed temporal averaging and regularization only apply for computing the initial $\mathbf{W_y}$, but not for $\mathbf{W_x}$ after transformation.

2.8. Multi-Class Extension

So far, we have only addressed binary classification problems. Since many experiments entail more than two classes, the decision rules defined in Equations (18) and (32) must be extended. We do so by employing a one-vs.-one classification scheme. Consequently, each class is tested against each other class, yielding $N_C(N_C-1)/2$ binary classification results. It would be straightforward to implement a voting approach that elects the winner based on the most votes; however, this approach would lead to frequent ties. Moreover, the quantitative information in the (TV)LDA scores would be lost. We thus propose to use a min-max approach for multi-class discrimination. First, we refer to the (TV)LDA score for class c_p vs. c_q as $\hat{z}^{(i)}_{\mathsf{c}_p\mathsf{c}_q}$ ($\mathsf{c}_p, \mathsf{c}_q \in \mathcal{C}, \mathsf{c}_p \neq \mathsf{c}_q$). The smaller this value gets, the more certain (TV)LDA is that trial i belongs to class c_p rather than to class c_q. Taking the worst score over all classes (i.e., the maximum of $\hat{z}^{(i)}_{\mathsf{c}_p\mathsf{c}_q}$ over all q) then indicates how likely it is that trial i stems from class c_p, relative to all other classes (the lower the more likely). Finally, the class that minimizes this score is elected:

$$\hat{\mathsf{c}}^{(i)}_{\text{(TV)LDA}} = \arg\min_{\mathsf{c}_p}\{\max_{p\neq q}\{\hat{z}^{(i)}_{\mathsf{c}_p\mathsf{c}_q}\}\}\,. \tag{37}$$

Evidently, the feature-reduction techniques discussed in sections 2.5 and 2.7 follow this one-vs.-one scheme as well.

2.9. Performance Evaluation

Here, we describe our framework for performance evaluation.

2.9.1. Cross-Validation

We performed 20 repetitions of a randomized 10×10 cross-validation to assess the expected performance of the system. All components (such as feature reduction and classification) were subject to this cross-validation to ensure that testing was done on completely unseen data.

2.9.2. Assessed Method Variants

In this publication, we mainly want to investigate the potentials of our proposed improvements, such as (1) spectral whitening, (2) PCA-based feature reduction instead of CSP and feature selection, and (3) TVLDA instead of LDA or rLDA. To this end, we identified seven method variants (or simply methods) that logically follow this path: for LDA with CSP and feature selection, we investigate the effect of whitening. Then, for whitened data, we incorporate rLDA and PCA as a feature reduction technique for LDA. Finally, for whitened data and PCA-based feature reduction, LDA is switched to TVLDA to arrive at the complete set of proposed improvements.

2.9.3. Performance Quantification

We quantify the performance of the respective methods by means of accuracy rates (or simply accuracies). This is the true positive rate, defined as the ratio between correctly classified trials and total number of trials, averaged over all classes. Since our evaluation framework is of statistical nature, a rigorous comparison between methods by means of accuracies is inappropriate. To resolve this, we here define a margin, within which we consider two methods to perform equal. Intuitively, we set this margin to $1/N_T$ [%], since this represents the accuracy range that relates to one trial per class. This in turn is the actual quantization level of the respective dataset, and we hereafter refer to it as the *quantization margin*.

To facilitate interpretation and comparison further, we also introduce the term *representative accuracy*. The representative accuracy is an acceptable trade-off between classification accuracy and number of features needed. Since, at some point, increasing N_F may only marginally contribute to better performance, we chose the smallest N_F whose corresponding (i.e., representative) accuracy still lies within the quantization margin of the best result.

3. RESULTS

In this section, we present the results of the classifier performance evaluation. For the most comprehensive comparison, we included the number of features N_F from 1 to 15 and evaluated the accuracies for each method variant and dataset.

Figure 5 gives a qualitative overview of the performance evaluation for S1–S6. At this stage, it is already evident that whitening dramatically improves decoding performance, regardless of the feature reduction technique. For CSP and feature selection, a gradual improvement can be observed in most datasets as N_F increases. This is plausible as new information is added to the system. It is remarkable that this characteristic is different for PCA-based feature reduction: more features only slightly improve performance, if there is any improvement at all. For many datasets, the best performance is already achieved for very few PCA components and degrades as more are added to the system. The representative accuracy is indicated by the large dots. Note that the concept of representative accuracy does not apply to rLDA, since it directly operates on the vectorized feature space.

Table 4 lists the representative mean accuracies, standard deviations, and respective number of features versus methods and datasets. For better reading, we ordered the presentation by protocol and electrode grid density. Below, we summarize the most important findings. For brevity, we refer to TVLDA with PCA-based feature reduction and whitening just as TVLDA.

3.1. Relative Performance

As summarized in **Table 4**, the accuracies increase systematically from the standard methods to TVLDA. Whitening already has a dramatic impact on the performance. For CSP and LDA, the improvement peaks at +22.9% (S6, RPS) with +12.3% on average. A similar trend can be observed for feature selection and LDA, where we improved by up to +20.3% (S6, RPS) and +10.4% on average.

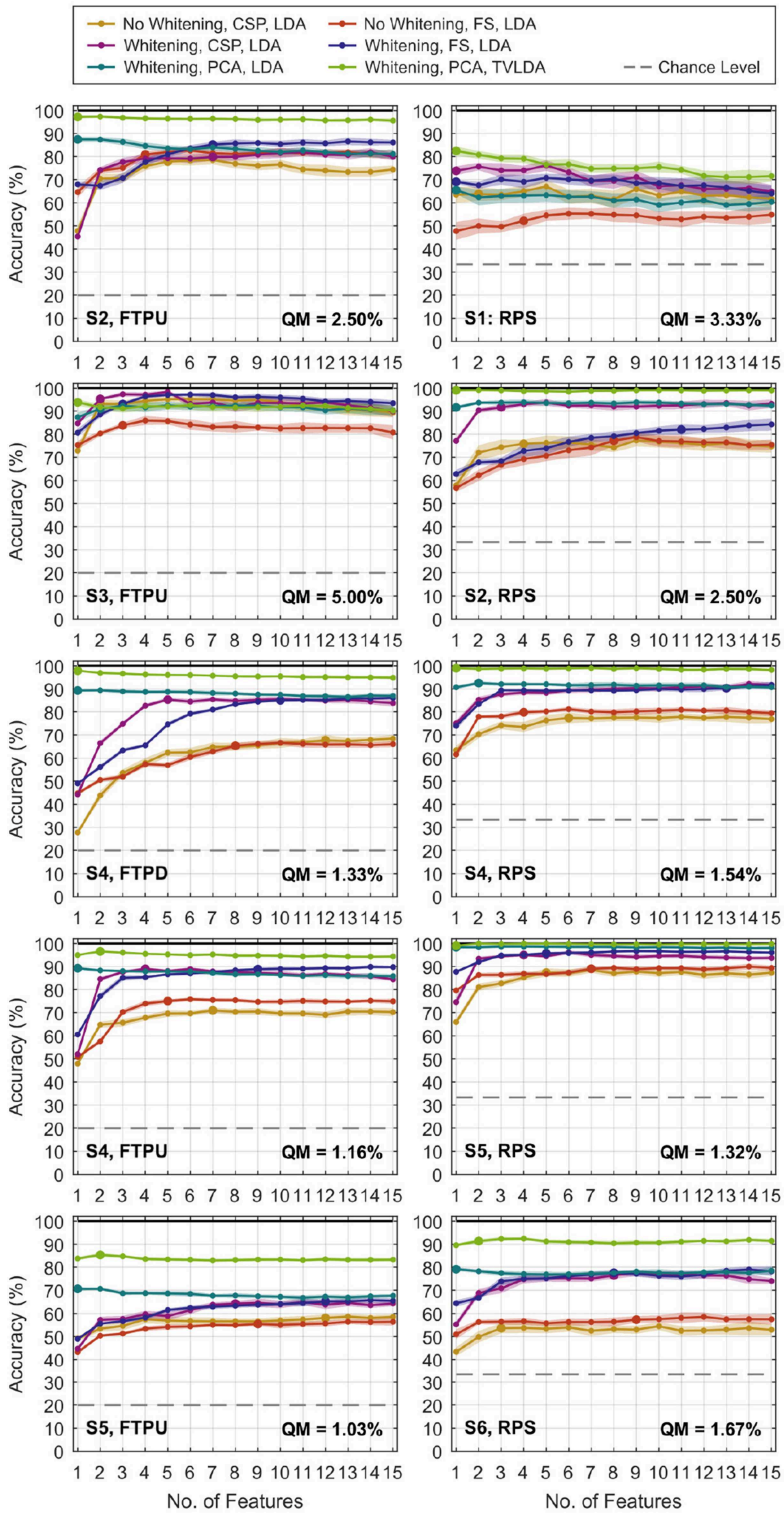

FIGURE 5 | Classification accuracies versus number of features N_F for selected finger-tapping **(left)** and rock-paper-scissors **(right)** datasets. Results for rLDA are not shown since N_F does not apply. The dots represent the average of 20 repetitions of the randomized cross-validation, and the shaded area indicates the standard deviation. The pronounced dots relate to the representative accuracy, which is defined in the text. Feature selection is abbreviated by "FS" in the legend. The quantization margin is abbreviated by "QM".

TABLE 4 | Performance overview of all assessed methods on all datasets.

Dataset			No Whitening				Whitening								
			LDA				rLDA[c]	LDA						TVLDA		
			CSP		Channel Sel.			CSP		Channel Sel.		PCA[d]		PCA[d]		
Protocol[a]	Grids[b]	ID	Acc. (%)	N_F	Acc. (%)	N_F	Acc. (%)	Acc. (%)	N_F	Acc. (%)	N_F	Acc. (%)	N_F	Acc. (%)	N_F	
RPS	Macro	S1	63.8 ± 3.0	2	52.2 ± 3.1	4	68.8 ± 2.5	73.8 ± 2.0	1	69.1 ± 0.9	1	65.4 ± 1.5	1	**82.4 ± 2.0**	**1**	
RPS	Macro	S6	53.6 ± 2.2	3	57.3 ± 1.5	9	79.9 ± 0.8	76.5 ± 1.4	8	77.6 ± 1.0	8	79.2 ± 0.8	1	**91.3 ± 0.9**	**2**	
Average			58.7 ± 2.6	2.5	54.7 ± 2.4	6.5	74.4 ± 1.9	75.2 ± 1.7	4.5	73.4 ± 0.9	4.5	72.3 ± 1.2	1.0	**86.9 ± 1.6**	**1.5**	
RPS	Micro	S2	75.9 ± 1.7	4	77.3 ± 2.2	8	89.2 ± 1.0	91.7 ± 1.2	3	82.0 ± 2.4	11	91.6 ± 0.8	1	**99.0 ± 0.3**	**1**	
RPS	Micro	S4	77.4 ± 2.3	6	79.8 ± 1.2	4	67.8 ± 1.5	90.7 ± 1.0	11	90.3 ± 1.0	13	92.5 ± 0.7	2	**98.9 ± 0.2**	**1**	
RPS	Micro	S5	87.4 ± 1.8	5	89.0 ± 1.1	7	96.3 ± 0.4	95.0 ± 0.6	4	95.7 ± 0.6	5	**98.4 ± 0.3**	**1**	**99.0 ± 0.4**	**1**	
Average			80.2 ± 2.0	5.0	82.0 ± 1.6	6.3	84.4 ± 1.1	92.5 ± 1.0	6.0	89.4 ± 1.5	9.7	94.2 ± 0.7	1.3	**99.0 ± 0.3**	**1.0**	
FTPU	Macro	S7	54.9 ± 3.6	4	60.2 ± 3.0	7	79.3 ± 1.7	65.3 ± 3.5	2	65.6 ± 2.3	4	76.0 ± 2.1	1	**89.4 ± 1.3**	**1**	
FTPU	Macro	S8	56.6 ± 1.7	1	63.5 ± 2.3	4	71.8 ± 1.9	75.6 ± 2.4	2	**79.4 ± 1.6**	**5**	69.1 ± 2.2	1	**82.8 ± 1.2**	**1**	
FTPU	Macro	S9	53.5 ± 3.4	1	70.8 ± 3.6	7	**83.3 ± 1.1**	72.9 ± 2.1	2	75.4 ± 2.1	3	78.6 ± 2.3	1	**85.7 ± 1.2**	**1**	
FTPU	Macro	S10	55.8 ± 3.2	4	62.8 ± 2.1	2	60.8 ± 1.6	57.7 ± 1.9	1	**73.9 ± 1.8**	**2**	71.0 ± 1.9	1	**77.3 ± 2.0**	**1**	⋆
FTPU	Macro	S11	27.0 ± 2.9	1	38.0 ± 2.5	3	50.4 ± 1.6	39.3 ± 2.1	1	50.8 ± 2.7	5	50.4 ± 1.9	1	**64.5 ± 3.2**	**1**	
FTPU	Macro	S12	40.0	1	53.3	1	70.0	60.0	1	63.3	1	**80.0**	**1**	**90.0**	**1**	⋆
FTPU	Macro	S13	49.9 ± 2.7	3	57.4 ± 2.0	1	74.6 ± 1.8	66.0 ± 1.5	1	72.4 ± 1.8	3	68.1 ± 2.8	1	**80.1 ± 1.7**	**2**	
FTPU	Macro	S14	55.7	2	67.1	2	71.4	60.0	3	64.3	5	**78.6**	**1**	**81.4**	**1**	⋆
FTPU	Macro	S15	53.5 ± 1.7	1	58.9 ± 2.3	2	58.9 ± 2.0	68.7 ± 1.4	1	68.9 ± 1.8	2	70.9 ± 1.4	1	**77.5 ± 1.7**	**1**	⋆
Average			49.6 ± 2.8	2.0	59.1 ± 2.6	3.2	68.9 ± 1.7	62.8 ± 2.2	1.6	68.2 ± 2.1	3.3	71.4 ± 2.1	1.0	**81.0 ± 1.9**	**1.1**	
FTPU	Micro	S2	77.8 ± 1.5	5	80.9 ± 1.4	4	80.2 ± 1.3	79.8 ± 1.7	7	85.3 ± 1.2	7	87.5 ± 1.1	1	**97.2 ± 0.6**	**1**	
FTPU	Micro	S3	**93.3 ± 1.8**	**2**	83.8 ± 1.1	3	85.8 ± 1.2	**95.3 ± 0.6**	**2**	**93.1 ± 0.7**	**3**	**91.0 ± 1.4**	**2**	**93.8 ± 1.4**	**1**	
FTPD	Micro	S4	67.7 ± 2.4	12	65.3 ± 1.3	8	50.5 ± 0.9	85.3 ± 0.9	5	85.0 ± 0.7	10	89.3 ± 0.5	1	**97.9 ± 0.3**	**1**	
FTPU	Micro	S4	71.0 ± 1.1	7	75.0 ± 0.9	5	51.7 ± 1.0	89.0 ± 0.7	4	88.8 ± 0.6	9	89.2 ± 0.6	1	**96.6 ± 0.3**	**2**	
FTPU	Micro	S5	58.1 ± 1.5	12	55.4 ± 1.0	9	68.2 ± 0.9	64.3 ± 1.1	8	65.2 ± 0.9	12	70.6 ± 0.8	1	**85.3 ± 0.8**	**2**	
Average			73.6 ± 1.7	7.6	72.1 ± 1.2	5.8	67.3 ± 1.1	82.7 ± 1.0	5.2	83.5 ± 0.9	8.2	85.5 ± 0.9	1.2	**94.2 ± 0.8**	**1.4**	

The table is organized in four blocks, such that the rock-paper-scissor experiments with standard and high-density electrode grids are clustered in the first and second block, respectively. Likewise, the finger-tapping experiments with standard and high-density electrode grids are presented in the third and fourth block, respectively. Accuracies and corresponding number of features N_F are representative values, as described in the text. The percentages are given as means ± standard deviation over 20 cross-validation repetitions. If the standard deviation is missing, it was zero due to the low number of trials. Emphasized values are considered the best for each dataset, which lie within the quantization margin of the best result (cf. section 2.9.3).

[a] *RPS, rock-paper-scissors; FTPD, finger tapping, palm down; FTPU, finger tapping, palm up.*

[b] *Macro, standard ECoG grid; Micro, high-density ECoG grid.*

[c] *rLDA operates on vectorized features, so N_F is not applicable (cf. section 2.6.2).*

[d] *For rows marked with an asterisk (⋆), a regularization of 25% was used for PCA (cf. section 2.7).*

For whitened data, rLDA performed worst on average with 71.5%. LDA with CSP and feature selection was slightly better with 74.0 and 76.1% on average. LDA with PCA was the best on average with 78.8%. At the same time, PCA turned out to be the most efficient feature reduction technique by far, needing only 1.1 components on average instead of 3.5 (CSP), 5.7 (feature selection), or the whole vectorized feature space (rLDA).

Overall, the best results were seen for whitened data and TVLDA, where TVLDA outperformed rLDA by +16.4%, LDA and CSP by +13.9%, and LDA and feature selection by +11.8% on average. Investigating the impact of using TVLDA instead of LDA for PCA-based feature reduction and whitened data, we obtained an improvement of +9.1% on average. To assess the robustness of each evaluated method, we computed the standard deviation of the accuracies over 20 repetitions of the randomized cross-validation. For the non-whitened data and LDA, we obtained an average standard deviation of ±2.2 and ±2.0% for CSP and feature selection, respectively. Whitening decreased these values to ±1.6% and ±1.5%, respectively, whereas rLDA showed an overall standard deviation of ±1.4%. TVLDA slightly diminished the overall standard deviation further to ±1.3%.

3.2. Absolute Performance

TVLDA performed best not only on average, but for every single dataset (within the quantization margin relative to the overall maximum). Only one or two PCA features (1.1 on average) are needed to achieve top performance. For the subsequent discussion, we thus refer to the results yielded by TVLDA.

Combining the results of the rock-paper-scissors experiment for the subjects with standard ECoG grids implanted, an overall accuracy of 86.9% was achieved. In contrast, the accuracy increases tremendously for subjects with high-density grids implanted, who scored 99.0% on average.

S7–S15, all with standard electrode grids implanted, scored 81.0% on average in the finger-tapping experiments. In general, all these data comprised fewer trials; for S12, even only 6 trials were available. The entries marked with an asterisk in **Table 4** were thus obtained with a regularized PCA to avoid overfitting (cf. section 2.7).

For the patients with high-density grids implanted, the classification accuracy in the finger-tapping experiment was 94.2% over all subjects. Accounting only for the subjects with substantial sensorimotor coverage (thus excluding S5), the overall score increased to 96.4%.

4. DISCUSSION

4.1. Classification Performance

Spectral whitening during the preprocessing stage has a tremendous impact on decoding performance. On average, the accuracy rises by +12.3% for CSP and LDA and by +10.4% for feature selection and LDA. **Figure 3** illustrates the reason for this huge leap: whitening balances the information with respect to frequency and therefore substantially increases the signal-to-noise ratio. Employing multi-band features in the high-gamma band (Shenoy et al., 2007; Kubánek et al., 2009; Kapeller et al., 2014; Pan et al., 2018) may have a similar positive effect on the classification performance as whitening, but this comes at the cost of an expanded feature space.

When ECoG signals are offline analyzed in the time-frequency domain, spectral whitening is well established (Miller et al., 2009). Yanagisawa et al. (2011) and Pistohl et al. (2012) directly extracted bandpower features for classification from a time-frequency signal representation (such as short-time Fourier or wavelet transforms). However, this approach is computationally demanding and may not meet real-time constraints. We therefore strongly promote the proposed time-domain whitening filter to save valuable resources.

The evidence that TVLDA outperforms LDA on high-gamma features is overwhelming: for every single dataset, TVLDA delivers the best results. The grand average accuracy improvement relative to standard methods is +16.4% (vs. rLDA), +13.9% (vs. CSP and LDA) and +11.8% (vs. feature selection and LDA). These results were obtained with mostly one (sometimes two) internal PCA components for TVLDA, whereas CSP and feature selection require 3.5 and 5.7 components, respectively. Performance thus not only gets better, but is also achieved at lower system complexity. The fact that only few PCA components are necessary to achieve maximum performance leads to remarkable robustness against overfitting; TVLDA with PCA delivers 10×10 cross-validation results with a standard deviation of ±1.3% on average. If very few trials are available, a regularization term to PCA as discussed in section 2.7 can be applied to further enhance stability.

Before putting our results into the context of state-of-the art research, we want to emphasize that it was not our focus to maximize the *absolute* performance of our system, but rather to investigate the impact of structural and methodological advances proposed in this manuscript. In other words, we did not employ multiple frequency bands or add other features to improve overall performance, unlike other studies to which we compare our results. We did not reject badly or differently executed trials from the datasets. In view of good responsiveness of a real-time BCI, we kept our trial window short (±0.75 seconds, relative to movement onset), whereas longer trials would have increased classification accuracies for some datasets most certainly.

The three-class rock-paper-scissors experiment with standard electrodes yielded an average accuracy of 86.9%. In view of the experiment settings, this compares best to 68.3% (Yanagisawa et al., 2011), 83.8% and 95.8% (Kapeller et al., 2014), 92.7% (Xie et al., 2015), and 80.0% (Li et al., 2017). Whereas the cited reference results relate to the same protocol in general, they were obtained from multi-band features and substantially longer trial durations. Xie et al. (2015) also used alternative features besides bandpower.

For the rock-paper-scissors experiment with high-density electrodes, TVLDA delivered almost perfect accuracies of 99.0% on average over three subjects. A similar experiment was recently conducted by Pan et al. (2018), who reported an accuracy of up to 90%. Bleichner et al. (2016) achieved 85.5% and Branco et al. (2017) attained 85.0% accuracy with high-density grids, but for an experiment involving four gestures.

For standard electrode grids and the finger-tapping experiment, TVLDA scored 81.0% on average over all subjects.

This is well in line with state-of-the art results, such as such as 86.3% (Onaran et al., 2011), 80.3% (Kubánek et al., 2009), and 77.0% (Shenoy et al., 2007). For solid differentiation of five individual fingers, however, the spatial sampling of standard-sized grids may be too coarse. In particular, we observed considerable confusion between the ring finger and little finger, which are in fact difficult to move independently. Combining these two classes improved decoding performance to 88.1% in a four-class scenario, which seems a more usable setup in this context. Interestingly, this result with 88.1% is higher than the 86.9% we obtained for only three classes. We thus suspect that the electrode coverage of S1 was not particularly fortunate for the rock-paper-scissors experiment, or the movements were not executed consistently or pronounced enough. Based on our experimental evidence, we believe that the rock-paper-scissors experiment with proper sensorimotor coverage of standard-sized electrodes and good subject participation should yield around 90% accuracy and above with TVLDA (as in S6).

The finger-tapping experiment with high-density sensorimotor coverage resulted in 96.4% on average. This is comparable to Hotson et al. (2016), who scored a maximum of 96.5% in a single subject, but with posterior selection of the best LDA evaluation time point. With both standard and high-density electrodes implanted, Chestek et al. (2013) reported 79.3% in a similar experiment.

TVLDA with PCA has further advantages beyond high classification accuracy. The architecture needs only minor extensions compared to standard LDA. Additionally required components encompass a time-domain whitening filter for preprocessing, the summation over several LDA scores, temporal smoothing of sample means and covariances for PCA, and an SVD of the spatiotemporal TVLDA weight matrix. All of these elements are strictly deterministic and can be implemented easily. Training a system that implements TVLDA is fully automatic and done in less than a second. Moreover, all shortcomings and difficulties of CSPs and feature-selection approaches disappear, since no external feature reduction is required. TVLDA is more robust than any other assessed approach, even when only few trials are available. With only one or two PCA components, TVLDA already attains maximum performance.

4.2. Extensions, Limitations, and Outlook

Choosing the optimal number of principal components for TVLDA may be straightforward in the given context, where performance vs. number of features was evaluated via cross-validation. In fact, one could have chosen just the first principal component for all datasets with still very good results. TVLDA may however be applied to more complicated datasets, where more than one principal component is required. In this case, cross-validation is still an option to determine the optimal number of principal components. A more theoretical approach that efficiently estimates the true number of underlying principal components via Bayesian model selection was proposed by Minka (2001).

We already mentioned that the temporal independence of the noise as stated in (9) may be violated by inconsistent trial repetitions of the subject. In this case, the assumptions of a diagonal covariance matrix for TVLDA as in (24) is not justified any more. In fact, a good estimate of the *true* covariance matrix can be obtained from the training statistics of the LDA scores (22) with considerable effort. We tested this option, but it did not yield any improvements. On the contrary, TVLDA turned out to become less stable. We therefore resorted to the variant proposed in this manuscript, which can also be seen as a form of regularization.

As evidenced by **Figure 3**, our high-gamma band of choice covered several harmonics of the power-line frequency. Since power-line interference can be huge, especially for ECoG data, it must be addressed. Applying notch filters is a robust solution, although they remove the complete signal within the specified frequency band. As a consequence, we expect to have lost up to 10% of the signal power (harmonic spacing: 50/60 Hz, notch filter bandwidth: 5 Hz). In reality, it may be much less than 10% though, since the filter cut-offs are not infinitely steep. A more sophisticated interference cancelation approach that removes only unwanted signal components could have maintained a higher signal-to-noise ratio. This may have led to slightly better performance, especially for whitened data.

Our evaluation is based on retrospective analysis of offline data. However, since the signal processing pipeline is strictly causal, we are confident that the whole system can be put to the online context in a straightforward manner, yielding comparable results. Based on the experimental evidence and our experience with TVLDA, 20 trials per class for training should already be enough for reasonable online classification performance, provided that the coverage is good and high-density grids are used. Of course, more training data can often improve results.

It should be noted that TVLDA is trial-based per se, so it needs a trigger to perform classification. An interesting undertaking would be the adaptation of TVLDA for asynchronous BCIs. For training, triggered and labeled data will still be necessary (as for most supervised classifiers). During a free run, the previously trained, asynchronous TVLDA may then continuously process the incoming data stream in sliding windows. This yields one classification result at a time, including idle time periods. To reduce this large number of produced false positives, we suggest two strategies. First, the TVLDA scores themselves may be taken into account, such that only scores that exceed a minimum of certainty actually trigger a classifier output. This threshold may be determined during training. As an alternative, a baseline class could be added to the framework to explicitly account for the idle state.

In any case, TVLDA is a window-based classifier and thus requires a consistent spatiotemporal activation pattern for successful classification. Truly continuous BCI control may be difficult to implement with TVLDA.

In its design as proposed here, TVLDA requires each trial to be completed until it is classified. For real-time applications, the trial window should therefore be as short as possible. We can imagine however an adaptive TVLDA that does not necessarily accumulate the LDA scores over the whole trial. Rather, it would raise a classification output whenever the accumulated LDA scores up to the current time point exceed a certain threshold that allows a reliable decision.

TVLDA may also find usage in different application fields apart from classification. For example, as shown in (30), the TVLDA score relates to the accumulated Kullback-Leibler divergence, which can be used for statistical evaluation such as in trial-based functional brain mapping. Here, a particular task is usually compared to a resting condition. Applying TVLDA at each channel separately would then yield a robust measure how much the respective channel is involved in carrying out the task.

Another potential use case of TVLDA would be the reconstruction of task-related activation patterns. The PCA of the TVLDA weight matrix readily provides a decoupled spatial and temporal representation of the underlying cortical processes that are specifically discriminating between the two classes. A similar tool was published by Kobak et al. (2016), who proposed a demixing PCA (dPCA). Here, PCA was extended with task-related information to reduce data dimensionality and to reveal unique activation patterns specific to each task. Unlike TVLDA, dPCA was designed to simplify the analysis and visualization of multi-dimensional neural recordings in animals, but it may also be used for classification.

One fundamental assumption of TVLDA is that each trial is the exact repetition of each other trial. While this leads to a convenient signal model, it may not reflect reality. Most likely, the overall amplitude of the underlying activation curve may vary over trials due to adaptation, high-gamma attenuation, learning, or fatigue. It may be worthwile to study a potential extension of TVLDA that allows for these fluctuations or trends. This may be inspired by Williams et al. (2018), who have recently shown that tensor component analysis (TCA)—a multilinear extension of PCA—provides a powerful framework for decomposing triggered neural data into electrode factors, time factors, and *trial* factors.

5. CONCLUSIONS

In this work, we have outlined a novel classification method for invasive motor-control BCIs that extends LDA to account for time-variant features. We named it TVLDA, for time-variant linear discriminant analysis. At the same time, we proposed an optimized feature extraction path for high-gamma bandpower that utilizes time-domain whitening for improved performance. We assessed the performance of TVLDA by evaluating data from 15 epilepsy patients with implanted subdural grids. Based on 19 experiments involving three high-level gestures and individual finger movement, we systematically demonstrated the superiority of TVLDA over several reference methods based on LDA.

TVLDA establishes a new benchmark for invasive motor-control BCIs, especially for those with high-density electrodes implanted on sensorimotor areas. To our knowledge, 99.0% for the recognition of three high-level gestures and 96.4% for individual finger identification are the highest consistent accuracies ever reported for these kinds of experiments.

Among the strengths of TVLDA is its ability to dramatically reduce feature dimensionality through a novel projection scheme based on PCA. This leads to robust performance, even for experiments with very few trials. As a valuable consequence, TVLDA makes any preceding feature reduction stage obsolete. The implementation of TVLDA is straight forward and requires only few adaptations compared to standard LDA.

It is evident that TVLDA is not limited to motor-based classification tasks. Rather, it can be used for any experimental setup that produces spatio-temporal activation patterns for classification—potentially even in EEG or other non-brain imaging approaches, such as electrooculography (EOG), electrocardiography (ECG), electromyography (EMG), and the like. TVLDA may also find use in different ECoG applications, such trial-based functional brain mapping.

Overall, we believe that we have developed a valuable tool that will open the door for invasive brain-computer interfaces with almost perfect multi-class control in the near future. However, additional work is necessary to further validate TVLDA with different ECoG environments, as well as with EEG and other imaging methods for clinical and scientific applications.

DATA AVAILABILITY

The recordings of S7–S15 analyzed for this study can be found in the *fingerflex* dataset provided by Kai Miller (https://stacks.stanford.edu/file/druid:zk881ps0522/fingerflex.zip).

ETHICS STATEMENT

This study was carried out in accordance with the recommendations of the institutional review board of Asahikawa Medical University with written informed consent from all subjects. All subjects gave written informed consent in accordance with the Declaration of Helsinki. The protocol was approved by the institutional review board of Asahikawa Medical University.

AUTHOR CONTRIBUTIONS

JG developed the methods, was involved in data acquisition, performed data processing, and prepared the manuscript. AZ assisted in data processing, results evaluation, and interpretation. CK was involved in data acquisition and contributed to methods development. KK supervised the clinical study. JS provided scientific input. CG founded g.tec medical engineering GmbH and supervised the project.

FUNDING

This work was funded by the Eurostars RapidMaps 2020 project.

ACKNOWLEDGMENTS

The authors want to thank Michael Jordan for preparing the renderings in **Figure 1**, Brendan Z. Allison for proofreading, and the reviewers for their valuable comments.

REFERENCES

Bishop, C. M. (2006). "Fisher's linear discriminant analysis," in *Pattern Recognition and Machine Learning, Information Science and Statistics*, eds M. Jordan, J. Kleinberg, and B. Schoelkopf (New York, NY: Springer), 186–189.

Blankertz, B., Lemm, S., Treder, M., Haufe, S., and Mueller, K.-R. (2011). Single-trial analysis and classification of ERP components–A tutorial. *NeuroImage* 56, 814–825. doi: 10.1016/j.neuroimage.2010.06.048

Blankertz, B., Tomioka, R., Lemm, S., Kawanabe, M., and Mueller, K.-R. (2008). Optimizing spatial filters for robust EEG single-trial analysis. *IEEE Signal Process. Mag.* 25, 41–56. doi: 10.1109/MSP.2008.4408441

Bleichner, M. G., Freudenburg, Z. V., Jansma, J. M., Aarnoutse, E. J., Vansteensel, M. J., and Ramsey, N. F. (2016). Give me a sign: decoding four complex hand gestures based on high-density ECoG. *Brain Struct. Funct.* 221, 203–216. doi: 10.1007/s00429-014-0902-x

Bostanov, V. (2004). BCI competition 2003–data sets Ib and IIb: feature extraction from event-related brain potentials with the continuous wavelet transform and the t-value scalogram. *IEEE Trans. Biomed. Eng.* 51, 1057–1061. doi: 10.1109/TBME.2004.826702

Branco, M. P., Freudenburg, Z. V., Aarnoutse, E. J., Bleichner, M. G., Vansteensel, M. J., and Ramsey, N. F. (2017). Decoding hand gestures from primary somatosensory cortex using high-density ECoG. *NeuroImage* 147, 130–142. doi: 10.1016/j.neuroimage.2016.12.004

Chestek, C. A., Gilja, V., Blabe, C. H., Foster, B. L., Shenoy, K. V., Parvizi, J., et al. (2013). Hand posture classification using electrocorticography signals in the gamma band over human sensorimotor brain areas. *J. Neural Eng.* 10:026002. doi: 10.1088/1741-2560/10/2/026002

Garrett, D., Peterson, D. A., Anderson, C. W., and Thaut, M. H. (2003). Comparison of linear, nonlinear, and feature selection methods for EEG signal classification. *IEEE Trans. Neural Syst. Rehabil. Eng.* 11, 141–144. doi: 10.1109/TNSRE.2003.814441

Gruenwald, J., Kapeller, C., Guger, C., Ogawa, H., Kamada, K., and Scharinger, J. (2017a). "Comparison of alpha/beta and high-gamma band for motor-imagery based BCI control: a qualitative study," in *2017 IEEE International Conference on Systems, Man, and Cybernetics (SMC)* (IEEE) (Banff, AB), 2308–2311.

Gruenwald, J., Kapeller, C., Kamada, K., Scharinger, J., and Guger, C. (2017b). "Optimal bandpower estimation and tracking via Kalman filtering for real-time brain-computer interfaces," in *2017 8th International IEEE/EMBS Conference on Neural Engineering (NER)* (Shanghai), 605–608.

Hoffmann, U., Vesin, J.-M., Ebrahimi, T., and Diserens, K. (2008). An efficient P300-based brain–computer interface for disabled subjects. *J. Neurosci. Methods* 167, 115–125. doi: 10.1016/j.jneumeth.2007.03.005

Hotson, G., McMullen, D. P., Fifer, M. S., Johannes, M. S., Katyal, K. D., Para, M. P., et al. (2016). Individual finger control of a modular prosthetic limb using high-density electrocorticography in a human subject. *J. Neural Eng.* 13:026017. doi: 10.1088/1741-2560/13/2/026017

Jiang, T., Jiang, T., Wang, T., Mei, S., Liu, Q., Li, Y., et al. (2017). Characterization and decoding the spatial patterns of hand extension/flexion using high-density ECoG. *IEEE Trans. Neural Syst. Rehabil. Eng.* 25, 370–379. doi: 10.1109/TNSRE.2016.2647255

Kapeller, C., Ogawa, H., Schalk, G., Kunii, N., Coon, W. G., Scharinger, J., et al. (2018). Real-time detection and discrimination of visual perception using electrocorticographic signals. *J. Neural Eng.* 15:036001. doi: 10.1088/1741-2552/aaa9f6

Kapeller, C., Schneider, C., Kamada, K., Ogawa, H., Kunii, N., Ortner, R., et al. (2014). "Single trial detection of hand poses in human ECoG using CSP based feature extraction," in *2014 36th Annual International Conference of the IEEE Engineering in Medicine and Biology Society (EMBC)* (Chicago, IL), 4599–4602.

Kobak, D., Brendel, W., Constantinidis, C., Feierstein, C. E., Kepecs, A., Mainen, Z. F., et al. (2016). Demixed principal component analysis of neural population data. *eLife* 5:e10989. doi: 10.7554/eLife.10989

Kubánek, J., Miller, K. J., Ojemann, J. G., Wolpaw, J. R., and Schalk, G. (2009). Decoding flexion of individual fingers using electrocorticographic signals in humans. *J. Neural Eng.* 6:066001. doi: 10.1088/1741-2560/6/6/066001

Lee, FY-T., Scherer, R., Leeb, R., Neuper, C., Bischof, H., and Pfurtscheller, G. (2005). "A comparative analysis of multi-class EEG classification for brain computer interface," in *Computer Vision Winter Workshop* (Zell an der Pram), 195–204. Available online at: https://graz.pure.elsevier.com/en/publications/a-comparative-analysis-of-multi-class-eeg-classification-for-brai

Li, Y., Zhang, S., Jin, Y., Cai, B., Controzzi, M., Zhu, J., et al. (2017). Gesture decoding using ECoG signals from human sensorimotor cortex: a pilot study. *Behav. Neurol.* 2017:3435686. doi: 10.1155/2017/3435686

Lotte, F., Bougrain, L., and Clerc, M. (2015). "Electroencephalography (EEG)-based brain–computer interfaces," in *Wiley Encyclopedia of Electrical and Electronics Engineering*, ed J. G. Webster (Hoboken, NJ: John Wiley & Sons, Inc), 44.

Lotte, F., Congedo, M., Lécuyer, A., Lamarche, F., and Arnaldi, B. (2007). A review of classification algorithms for EEG-based brain-computer interfaces. *J. Neural Eng.* 4, R1–R13. doi: 10.1088/1741-2552/aab2f2

Miller, K. J., Hermes, D., Honey, C. J., Hebb, A. O., Ramsey, N. F., Knight, R. T., et al. (2012). Human motor cortical activity is selectively phase-entrained on underlying rhythms. *PLoS Comput. Biol.* 8:e1002655. doi: 10.1371/journal.pcbi.1002655

Miller, K. J., Zanos, S., Fetz, E. E., den Nijs, M., and Ojemann, J. G. (2009). Decoupling the cortical power spectrum reveals real-time representation of individual finger movements in humans. *J. Neurosci.* 29, 3132–3137. doi: 10.1523/JNEUROSCI.5506-08.2009

Minka, T. P. (2001). "Automatic choice of dimensionality for PCA," in *Advances in Neural Information Processing Systems*, eds T. G. Dietterich, S, Becker, and Z. Ghahramani (Vancouver, BC: MIT Press), 598–604. Available online at: http://www.cs.cmu.edu/Groups/NIPS/NIPS2001/

Ogawa, H., Kamada, K., Kapeller, C., Hiroshima, S., Prueckl, R., and Guger, C. (2014). Rapid and minimum invasive functional brain mapping by real-time visualization of high gamma activity during awake craniotomy. *World Neurosurg.* 82, 912.e1–912.e10. doi: 10.1016/j.wneu.2014.08.009

Onaran, I., Ince, N. F., and Cetin, A. E. (2011). "Classification of multichannel ECoG related to individual finger movements with redundant spatial projections," in *2011 Annual International Conference of the IEEE Engineering in Medicine and Biology Society* (IEEE) (Boston, MA), 5424–5427.

Oppenheim, A. V., and Schafer, R. W. (2010). "Chapter 11.2.2: Modeling of random signals," in *Discrete-Time Signal Processing: International Edition*, eds M. J. Horton and A. Gilfillan (Upper Saddle River, NJ: Pearson Education, Inc.), 921.

Pan, G., Li, J.-J., Qi, Y., Yu, H., Zhu, J.-M., Zheng, X.-X., et al. (2018). Rapid decoding of hand gestures in electrocorticography using recurrent neural networks. *Front. Neurosci.* 12:555. doi: 10.3389/fnins.2018.00555

Pfurtscheller, G., and Lopes da Silva, F. (1999). Event-related EEG/MEG synchronization and desynchronization: basic principles. *Clin. Neurophysiol.* 110, 1842–1857. doi: 10.1016/S1388-2457(99)00141-8

Pistohl, T., Schulze-Bonhage, A., Aertsen, A., Mehring, C., and Ball, T. (2012). Decoding natural grasp types from human ECoG. *NeuroImage* 59, 248–260. doi: 10.1016/j.neuroimage.2011.06.084

Prueckl, R., and Guger, C. (2009). "A brain-computer interface based on steady state visual evoked potentials for controlling a robot," in *Bio-Inspired Systems: Computational and Ambient Intelligence*, eds J. Cabestany, F. Sandoval, A. Prieto, and J. M. Corchado (Berlin; Heidelberg: Springer), 690–697.

Scherer, R., Mueller, G., Neuper, C., Graimann, B., and Pfurtscheller, G. (2004). An asynchronously controlled EEG-based virtual keyboard: improvement of the spelling rate. *IEEE Trans. Biomed. Eng.* 51, 979–984. doi: 10.1109/TBME.2004.827062

Shenoy, P., Miller, K. J., Ojemann, J. G., and Rao, R. P. (2007). "Finger movement classification for an electrocorticographic BCI," in *2007 3rd International IEEE/EMBS Conference on Neural Engineering* (IEEE) (Kohala Coast), 192–195.

Tangermann, M., Müller, K.-R., Aertsen, A., Birbaumer, N., Braun, C., Brunner, C., et al. (2012). Review of the BCI competition IV. *Front. Neurosci.* 6:55. doi: 10.3389/fnins.2012.00055

Williams, A. H., Kim, T. H., Wang, F., Vyas, S., Ryu, S. I., Shenoy, K. V., et al. (2018). Unsupervised discovery of demixed, low-dimensional neural dynamics across multiple timescales through tensor component analysis. *Neuron* 98, 1099–1115.e8. doi: 10.1016/j.neuron.2018.05.015

Wolpaw, J. R., Birbaumer, N., McFarland, D. J., Pfurtscheller, G., and Vaughan, T. M. (2002). Brain–computer interfaces for communication and control. *Clin. Neurophysiol.* 113, 767–791. doi: 10.1016/S1388-2457(02)00057-3

Wolpaw, J. R., and Wolpaw, E. W. (2012). *Brain-Computer Interfaces: Principles and Practice, 1st Edition*. Oxford; New York, NY: Oxford University Press.

Wu, S.-L., Wu, C.-W., Pal, N. R., Chen, C.-Y., Chen, S.-A., and Lin, C.-T. (2013). "Common spatial pattern and linear discriminant analysis for motor imagery classification," in *2013 IEEE Symposium on Computational Intelligence, Cognitive Algorithms, Mind, and Brain (CCMB)* (IEEE) (Singapore), 146–151.

Xie, T., Zhang, D., Wu, Z., Chen, L., and Zhu, X. (2015). Classifying multiple types of hand motions using electrocorticography during intraoperative awake craniotomy and seizure monitoring processes–case studies. *Front. Neurosci.* 9:353. doi: 10.3389/fnins.2015.00353

Xu, R., Jiang, N., Lin, C., Mrachacz-Kersting, N., Dremstrup, K., and Farina, D. (2014). Enhanced low-latency detection of motor intention from EEG for closed-loop brain-computer interface applications. *IEEE Trans. Biomed. Eng.* 61, 288–296. doi: 10.1109/TBME.2013.2294203

Yanagisawa, T., Hirata, M., Saitoh, Y., Goto, T., Kishima, H., Fukuma, R., et al. (2011). Real-time control of a prosthetic hand using human electrocorticography signals. *J. Neurosurg.* 114, 1715–1722. doi: 10.3171/2011.1.JNS101421

Conflict of Interest Statement: Several authors of this publication are employed at g.tec medical engineering GmbH, Austria. As part of a Ph.D. program, our motivation for conducting the study and developing the methods was entirely scientific. However, the described algorithms may be commercialized by g.tec medical engineering GmbH in the future.

frontiers in Neuroscience

ORIGINAL RESEARCH
published: 01 October 2019
doi: 10.3389/fnins.2019.01017

μECoG Recordings Through a Thinned Skull

*Sarah K. Brodnick[1], Jared P. Ness[1], Thomas J. Richner[1], Sanitta Thongpang[2], Joseph Novello[1], Mohammed Hayat[1], Kevin P. Cheng[1], Lisa Krugner-Higby[3], Aaron J. Suminski[1,4], Kip A. Ludwig[1,4] and Justin C. Williams[1,4]**

[1] Department of Biomedical Engineering, University of Wisconsin–Madison, Madison, WI, United States, [2] Department of Biomedical Engineering, Mahidol University, Salaya, Thailand, [3] Department of Surgical Sciences, School of Veterinary Medicine, University of Wisconsin–Madison, Madison, WI, United States, [4] Department of Neurological Surgery, University of Wisconsin–Madison, Madison, WI, United States

OPEN ACCESS

Edited by:
Christoph Guger,
g.tec Medical Engineering GmbH,
Austria

Reviewed by:
Amy L. Orsborn,
University of Washington,
United States
Nitish V. Thakor,
Johns Hopkins School of Medicine,
United States
Patrick Ruther,
Albert Ludwigs Universität Freiburg,
Germany
Ki Yong Kwon,
Plexon Inc., United States

***Correspondence:**
Justin C. Williams
jwilliams@engr.wisc.edu

Specialty section:
This article was submitted to Neuroprosthetics, a section of the journal Frontiers in Neuroscience

Received: 28 February 2019
Accepted: 06 September 2019
Published: 01 October 2019

Citation:
Brodnick SK, Ness JP, Richner TJ, Thongpang S, Novello J, Hayat M, Cheng KP, Krugner-Higby L, Suminski AJ, Ludwig KA and Williams JC (2019) μECoG Recordings Through a Thinned Skull. Front. Neurosci. 13:1017. doi: 10.3389/fnins.2019.01017

The studies described in this paper for the first time characterize the acute and chronic performance of optically transparent thin-film micro-electrocorticography (μECoG) grids implanted on a thinned skull as both an electrophysiological complement to existing thinned skull preparation for optical recordings/manipulations, and a less invasive alternative to epidural or subdurally placed μECoG arrays. In a longitudinal chronic study, μECoG grids placed on top of a thinned skull maintain impedances comparable to epidurally placed μECoG grids that are stable for periods of at least 1 month. Optogenetic activation of cortex is also reliably demonstrated through the optically transparent μECoG grids acutely placed on the thinned skull. Finally, spatially distinct electrophysiological recordings were evident on μECoG electrodes placed on a thinned skull separated by 500–750 μm, as assessed by stimulation evoked responses using optogenetic activation of cortex as well as invasive and epidermal stimulation of the sciatic and median nerve at chronic time points. Neural signals were collected through a thinned skull in mice and rats, demonstrating potential utility in neuroscience research applications such as *in vivo* imaging and optogenetics.

Keywords: thinned skull, μECoG, local field potenitals, optogenetics, somatosensory evoked potentials

INTRODUCTION

Electrophysiological recordings of brain activity using high density electrode arrays are a staple of neuroscience research and have become increasingly prevalent for the clinical diagnosis of epileptic seizure foci as well as the clinical deployment of brain–machine interfaces (BMI) (Osorio et al., 2002; Leuthardt et al., 2004, 2006; Viventi et al., 2011). Traditional electrophysiological recording methods involve the implantation of invasive electrode arrays either indwelling within cortex (Kipke et al., 2003; Normann and Fernandez, 2016), beneath the dura (subdural) (Wyler et al., 1984; Henle et al., 2011; Khodagholy et al., 2014), on top of the dura (epidural) (Thongpang et al., 2011; Park et al., 2014; Spuler et al., 2014), or non-invasively on the skin directly above the exterior of the skull (Myrden and Chau, 2015). It is generally accepted that electrode placement closer to the neural signal sources of interest within the brain yields a more information rich and spatially distinct signal (Fernández et al., 2014), whereas activity measured at a distance non-invasively is attenuated in part by the high impedance skull, yielding less spatially distinct information in the recorded signal from electrode to electrode (Grill et al., 2009; Uriguen and Garcia-Zapirain, 2015).

More recently, there has been a growing appreciation that surgical methods to open the skull, and/or the placement of an indwelling electrode grid on or within cortex, may cause adverse effects that impact the neural circuitry of interest (Fernández et al., 2014; Goss-Varley et al., 2017; Falcone et al., 2018). For example, increased glial scarring (Grill et al., 2009; Marin and Fernández, 2010; Salatino et al., 2017), large increases in temperature of cortex (Shoffstall et al., 2018), changes in intracranial pressure (Onal et al., 2003), intracranial hemorrhage and/or physical depression of cortex (Onal et al., 2003; Marin and Fernández, 2010; Degenhart et al., 2016), and bacterial infection (Onal et al., 2003) have all been linked to the surgical procedure and implantation of electrocorticography (ECoG) or indwelling cortical arrays. These adverse events cause subtle changes to the neural circuitry of interest that have been shown to cause long-lasting deficit in performance of fine motor tasks among other consequences (Goss-Varley et al., 2017).

Concurrently there has been an increasing interest in neuroscience experiments that thin the skull instead of removing it, and that use optical methods to record and manipulate both neuronal and non-neuronal cells within the brain (Yang et al., 2010; Shih et al., 2012; Bonder and McCarthy, 2014). Removal of the skull in rodents has been shown to create glial scarring in the area under the craniotomy (Yang et al., 2010). Unlike the outer compact layer of the skull which has low conductivity, the spongy bone of the skull closer to the brain is low impedance (Akhtari et al., 2002) and if thinned appropriately is optically transparent (Drew et al., 2010). However, the performance of μECoG grids placed chronically on a thinned skull preparation has yet to be evaluated.

To address this gap, a series of acute and chronic studies was performed where the skull was thinned to a translucent layer and implanted with a μECoG electrode array. μECoG arrays were used in the experiments described because of their flexibility, transparency, and well-characterized epidural signal profile (Thongpang et al., 2011; Park et al., 2014). In rats chronically implanted for 1 month, impedance values and somatosensory evoked potentials (SSEPs) were recorded at regular intervals to assess stability of electrical function and spatial resolution of recordings through the thinned skull. Cortical signals from optogenetic stimulation in a ChR2 mouse were recorded in an acute terminal session through a thinned skull and were compared to recordings through the dura after removal of the thinned skull. These studies tested multiple common stimulation paradigms for neuroscience research in multiple species, mice, and rats, to characterize the reliability and spatial resolution of electrophysiological recordings through a thinned skull.

MATERIALS AND METHODS

Ethics Statement

All animal procedures were approved by the Institutional Animal Care and Use Committee (IACUC) at the University of Wisconsin–Madison, Madison, WI, United States. All efforts were made to minimize animal discomfort.

Device Fabrication

Micro-electrocorticography array advanced measurement testing has been published previously and validated to record neural signals (Thongpang et al., 2011; Park et al., 2014; Richner et al., 2014). μECoG devices were fabricated following protocols previously described for polyimide (Thongpang et al., 2011) and parylene C (Schendel et al., 2013) arrays. Briefly, photodefinable polyimide was used to pattern polyimide and a chemical vapor deposition system was used to pattern parylene C onto silicon wafers. Photolithography, metal deposition (Cr/Au/Pt), and lift off and plasma etching allowed for patterning of the electrodes, traces, and array shape. Final thickness of arrays was 25 μm. Rat sized polyimide (spacing between recording sites: 750 μm, 250 μm site diameter) (**Figures 1A,B**) or parylene C (spacing between recording sites: 750 μm, 200 μm site diameter) (**Figure 1C**)-based μECoG electrode arrays were custom fabricated with 16 platinum sites (one or two 4 mm × 4 mm grids) and implanted unilaterally or bilaterally between bregma and lambda in Sprague-Dawley rats. Similarly, for experiments with mice, a smaller, 2 mm × 2 mm 16 platinum site parylene-C μECoG array (500 μm spacing, 150 μm site diameter) (**Figure 2**) was fabricated and used for optogenetic experiments (**Figures 2A,B**). Parylene C was chosen for optogenetic and imaging studies due to its flexibility and translucent properties (**Figure 2C**). A density of 16 electrode sites was chosen along with specific interelectrode site spacings in order to visualize the somatosensory cortex forelimb and hindlimb areas, and to visualize where signals were no longer recorded on the periphery of the array (Sakatani et al., 1990). Extensive bench top testing of μECoG arrays

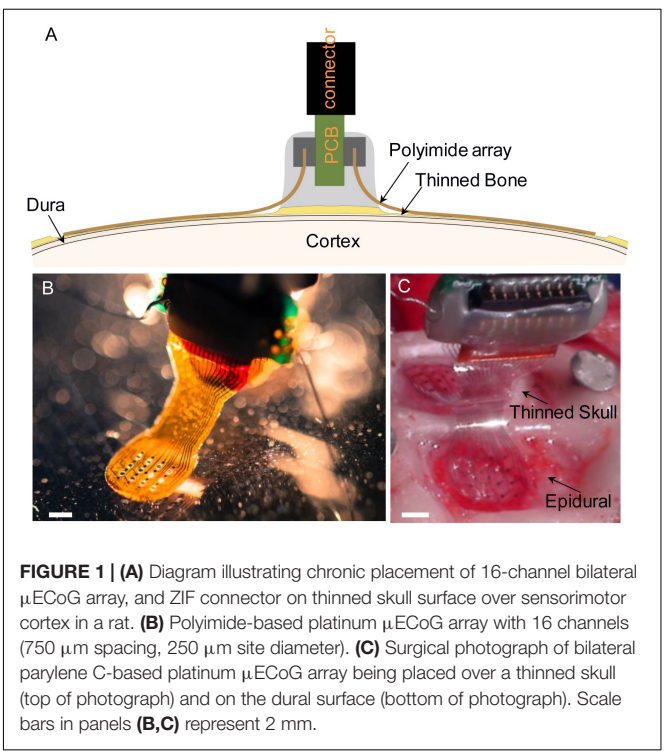

FIGURE 1 | (A) Diagram illustrating chronic placement of 16-channel bilateral μECoG array, and ZIF connector on thinned skull surface over sensorimotor cortex in a rat. **(B)** Polyimide-based platinum μECoG array with 16 channels (750 μm spacing, 250 μm site diameter). **(C)** Surgical photograph of bilateral parylene C-based platinum μECoG array being placed over a thinned skull (top of photograph) and on the dural surface (bottom of photograph). Scale bars in panels **(B,C)** represent 2 mm.

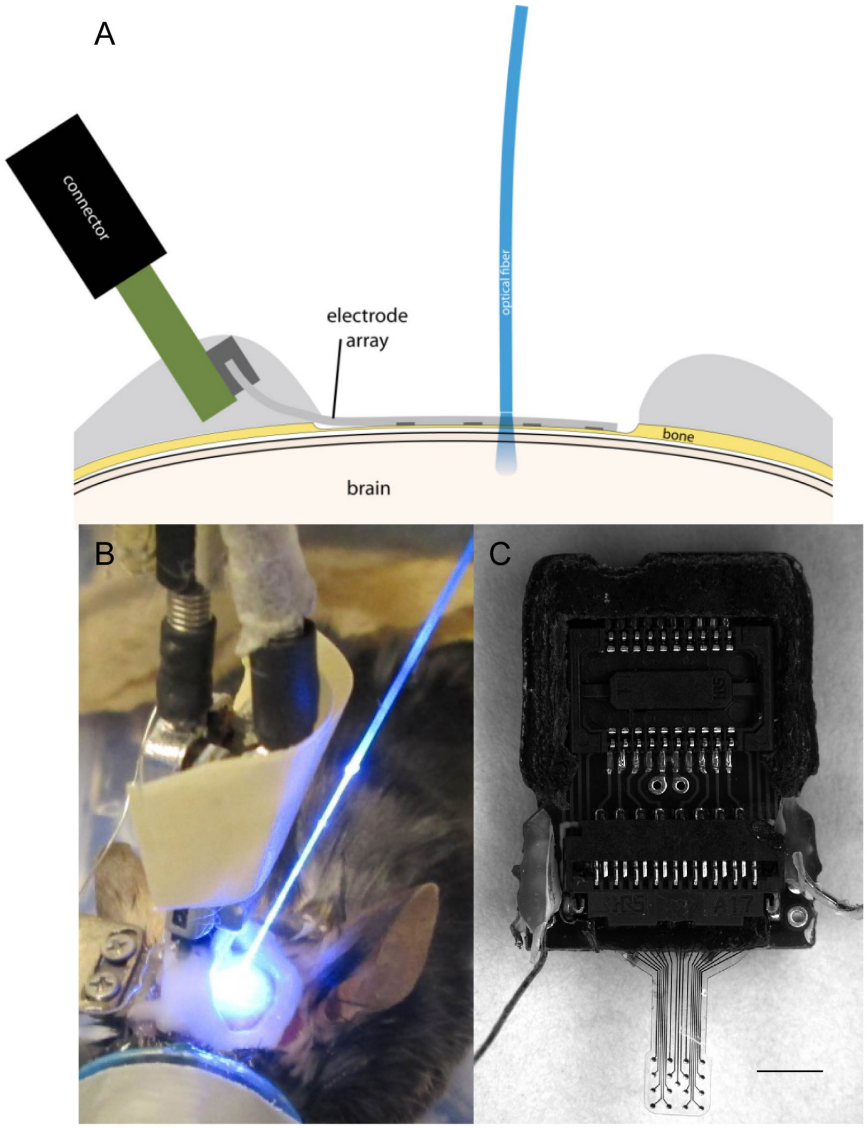

FIGURE 2 | (A) Illustration of μECoG electrode array placement over a thinned skull in a mouse with optical fiber positioning. **(B)** Optogenetic stimulation of cortex with optical fiber placed on a μECoG array over thinned skull. **(C)** Parylene C-based platinum μECoG array with 16 channels (500 μm spacing, 150 μm site diameter) and ZIF connector. Scale bar in panel **(C)** represents 2 mm.

has been preformed in previous publications to validate neural signal recordings.

Surgical Preparation

Chronic Experiments

Male Sprague-Dawley rats (n = 7, Envigo, Indianapolis, IN, United States) 2–4 months old were chronically implanted with custom built polyimide or parylene C μECoG arrays with metal electrodes (**Figure 1A**). Three rats were implanted with bilateral arrays over thinned skull, three rats were implanted with bilateral arrays over the dural surface, and one rat was implanted with a bilateral array, one over thinned skull and one over the dura. The electrode array on the dural hemisphere for this animal was damaged during implantation and not viable therefore electrophysiology and impedance data were not included in this paper; however, histological staining was performed and included. One possible failure mechanism may have been that the flat-flex connector between the array and PCB resulted in the signals of the epidural array being an open circuit and therefore noisy. Surgical procedures were based on previously published methods (Park et al., 2016). Before surgery, buprenorphine hydrochloride (0.05 mg kg^{-1}, Reckitt Benckiser Healthcare) was administered for analgesia and dexamethasone (2 mg kg^{-1}, AgriLabs) to prevent cerebral edema. Rats were induced with 5% isoflurane gas in O_2 and maintained on 1.0–2.5% throughout the duration of the surgery. Following induction, rats were placed into a stereotaxic frame with the scalp shaved and prepped

with alternating povidone iodine and alcohol. The skin was incised, and the exposed skull was cleaned and dried. Three stainless steel screws (stainless steel, 00–80 × 1/8 inch), two for attachment of a ground wire, and another for reference and mechanical support, were attached to the rostral and caudal areas of the skull. Next, UV curable dental acrylic (Fusio, Pentron Clinical) was placed on the periphery of the exposed skull to provide an anchor for the attachment of future acrylic, and two craniotomies (∼5 mm × 5 mm) or thin skull areas were drilled over somatosensory cortex. A thinned skull area was made by drilling through the top layer of compact bone, through the spongy layer, and slightly into the lower compact bone where it became transparent. We estimate the final thickness of the lower compact bone layer as ∼100–200 μm as the adult rat skull at 90 days is ∼700 μm thick (Gefen et al., 2004). #106 and #107 spherical drill burrs were used. Saline irrigation was used to remove debris and to lessen the effect of heating from the drill. The μECoG arrays were placed epidurally or over a thinned skull area and covered with a thin layer of GelFoam (Pharmacia and Upjohn Co., New York, NY, United States) and saline before being covered by dental acrylic. GelFoam was used to prevent acrylic from covering the electrode array and was only placed on top of the arrays and not beneath. The ZIF connector was then secured to the skull and a purse string suture (3–0 vicryl) closed the skin wound. Triple antibiotic ointment was applied to the wound during closing to prevent infection. Rats were monitored post-surgically until they were ambulatory and showed no signs of pain or distress. Another dose of buprenorphine was administered 8–12 h after the initial dose to relieve any pain the animal may have been experiencing following the surgery. Ampicillin [50 mg kg^{-1} subcutaneous injection (SC), Sage Pharmaceutical] was administered twice daily for 7 days postoperatively to prevent infection.

Acute Terminal Experiments

Three Thy1::ChR2/H134R-YFP (ChR2) mice (Jackson Laboratory; stock number 012350) ∼6–16 weeks old were implanted during acute terminal recording sessions with clear parylene C μECoG arrays implanted over the dura or a thinned skull area to compare neural signals recorded from light stimulation (**Figures 2A,B**). Evoked potential data from optogenetic stimulation were collected from three mice and strength duration curve data were collected from one mouse. Arrays were placed onto a thinned skull first, and then placed epidurally after removing the thinned skull. Mouse surgical procedures were similar to previously published methods (Richner et al., 2014). Briefly, mice were administered buprenorphine hydrochloride (0.05 mg kg^{-1}) and dexamethasone (1 mg kg^{-1} SC) before induction, induced, and maintained with 1–2.5% isoflurane. The animal was placed in a stereotaxic-like frame and a craniotomy or thinned skull was performed. A μECoG array was placed on the dura or thinned skull and ground and reference wires were coiled and placed on a small area of thinned skull on the contralateral hemisphere. The skull was thinned in the mice to the lower compact bone similar to the rat but using #105 and #106 spherical drill burrs. After drilling the skull was optically transparent and thickness was ∼50 μm or thinner (Shih et al., 2012). GelFoam was not used in optogenetic studies. Instead the cortical surface was continually kept wet with a saline drip.

Heart rate and blood oxygen concentration in both species were monitored throughout the surgery using a pulse oximeter. Body temperature was monitored with a digital thermometer and regulated with a water-circulated heating blanket.

Electrophysiological Testing

Periodic Chronic Electrophysiology Testing

Sensorimotor evoked potentials were recorded periodically for up to 1 month under sedation in rats with chronic μECoG implants to assess signal stability and uniqueness/spatial resolution of information recorded on nearby sites. Dexmedetomidine (50 μg/kg SC) was used to achieve sedation. Atipamezole (0.5 mg/kg SC) was administered at the end of the procedure as a reversal agent. Dexmedetomidine sedation was supplemented with small amounts of isoflurane (0–0.5%) throughout the procedure to deepen sedation. The sciatic or median nerve, hindlimb or forelimb, respectively, were stimulated weekly to evoke SSEPs. Needle or surface stimulation electrodes were used. Needle electrodes were placed on either side of the sciatic nerve, 3 mm apart. Surface electrodes were placed on shaved skin above the sciatic or median nerve, with a reference electrode placed below the leg. Stimulation pulses were applied using needle electrodes (monophasic 0–0.8 mA for 2 ms), or surface electrodes (monophasic 0.5–3.5 mA for 1 ms) both at approximately 0.5 Hz. The cortical responses were recorded and digitized simultaneously at 3 kHz using a PZ2 Preamplifier and a RZ2 BioAmp Processor (Tucker-Davis Technologies, Alachua, FL, United States).

Acute Terminal Optogenetic Electrophysiological Testing

Optogenetically evoked potentials were recorded during a terminal procedure by shining light through a fiber-coupled LASER system or LED through an optically transparent parylene μECoG onto the dura or thinned skull of ChR2 mice using previously reported methods (Uriguen and Garcia-Zapirain, 2015; **Figure 2**). Photostimulation was accomplished by using an optical fiber (200 μm in diameter, 0.22 NA, flat cleaved, and polished, Thorlabs, Newton, NJ, United States) connected to a 100 mW 473 nm LASER (Laserglow, Toronto, ON, Canada) and controlled by a multichannel system (TDT, Alachua, FL, United States). 2.5 ms pulses, varying power settings, and random interstimulus intervals were used. Power 1 mm from the tip of the optical fiber was approximately 80 mW/mm^2. The optical fiber was placed approximately 1 mm from the cortical or thinned skull surface. 3 kHz recordings were obtained and digitized using a PZ2 Preamplifier and a RZ2 BioAmp Processor (Tucker-Davis Technologies, Alachua, FL, United States), and sampled with a high impedance headstage. A photostimulus delivered by an LED (465 nm, RGB MC-E, Cree, Durham, NC, United States) approximately 2 cm away from the cortical or thinned skull surface was used to create photostimulus duration vs. amplitude peak to peak potential contour plots (**Figure 7**). Voltage pulses were changed to current pulses

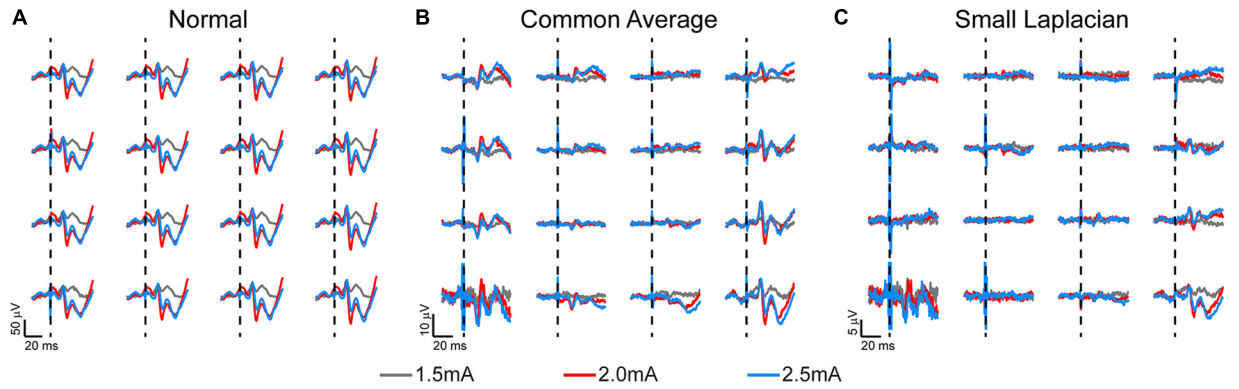

FIGURE 3 | Somatosensory evoked potentials (SSEPs) recorded on week 3 post-implantation from a rat implanted with a 16-channel μECoG array placed on thinned skull over left sensorimotor cortex. Biphasic current pulses (1 ms, varied amplitude) were used to stimulate the right hindlimb with surface electrodes over the sciatic nerve. **(A)** Stainless-steel bone screw, **(B)** common average, and **(C)** small Laplacian referencing strategies are shown to increase the signal-to-noise ratio, and to reveal spatial signaling from the predicted hindlimb anatomical region. Dashed lines represent onset of electrical stimulus.

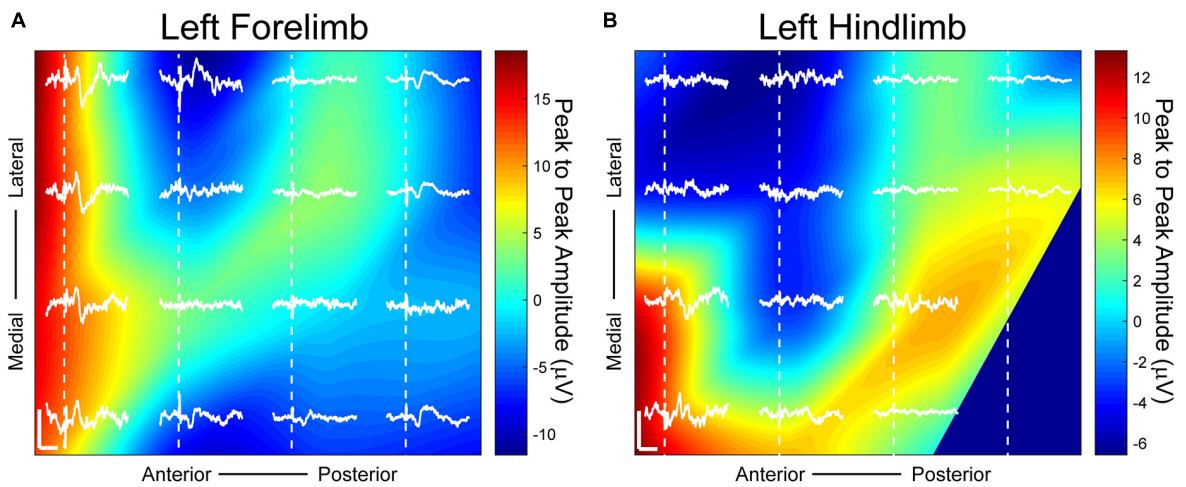

FIGURE 4 | Somatosensory evoked potentials (SSEPs) on day 38 post-implantation with small Laplacian referencing from forelimb and hindlimb electrical surface stimulation using a 16-channel μECoG array placed over a thinned skull portion of rat sensorimotor cortex. Plots represent spatial recordings from the same electrode array, demonstrating LFPs from **(A)** biphasic forelimb stimulation and **(B)** monophasic hindlimb stimulation. Stimuli were applied for 1ms at 1.25 mA. Activity is represented by 2D interpolated heat maps. The portions closer to the red spectrum show evoked activity higher than baseline when averaged over at least 25 trials, and closer to blue shows negative activity. The *x* scale bar, 20 ms; *y* scale bar, 20 μV. Dashed lines represent onset of electrical stimulus.

(0–1000 mA, 0.5–12 ms) with an LED driver (BuckBlock, LEDdynamics, Randolph, VT, United States). Irradiance was calculated by measuring optical power (PM100D, S130C, Thor Labs, Newton, NJ, United States) 2 cm from the LED, and the result was divided by the commercially available photo sensor's area (S370 Optometer, United Detector Technology, Hawthorne, CA, United States).

Electrophysiology Analysis

To examine the efficacy of the evoked responses through the thin skull prep, local-field potentials (LFPs) obtained from varying stimulation, both optogenetic and electric, were analyzed and checked against epidural implants. LFPs were band limited using a combination of a second order, Butterworth lowpass filter (cutoff frequency = 1000 Hz), a Butterworth high pass filter (cutoff frequency = 3Hz), and a third order notch filter (cutoff frequencies = 55 and 65 Hz) to remove line noise. Evoked potentials were computed from the average of evoked responses from the same stimulus amplitude and channel. Positive signal amplitudes reflected positive voltages. To increase signal-to-noise ratios, two known post processing referencing techniques, common average referencing (CAR) and small Laplacian referencing, were employed and compared (**Figure 3**). Each were incorporated as described in the literature (McFarland et al., 1997; Ludwig et al., 2009). Heatmaps were created to describe the spatial organization of the cortical activity based on the small Laplacian referencing technique (**Figures 4**, **7**). Each heatmap was obtained by taking the maximum peak to peak SSEP from each μECoG electrode. Peaks were defined as the average of seven data points centered on the maximums

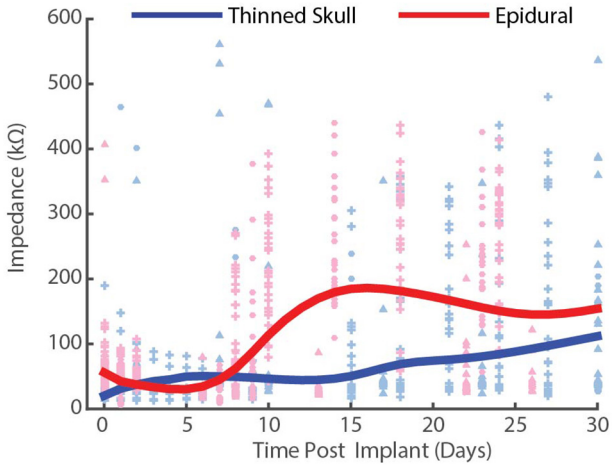

FIGURE 5 | Chronic impedance spectral data at 1 kHz from thinned skull (blue) and epidurally (red) implanted μECoG electrodes in rats. Each interpolation curve represents three animals per group, and 32 electrode sites per animal. Individual data points represent individual electrode site impedance spectra measurements. Each shape represents an individual animal. Epidural impedances increase until ∼2 weeks and plateau, while thinned skull impedances remain lower and more stable.

of the response from a given response window (latency of 10–35 ms). Responses were interpolated using a cubic interpolation algorithm (Matlab griddata) to a meshgrid with 1 μm resolution (Sakatani et al., 1990; Bazley et al., 2012). Peak latencies were measured as the time from the onset of the stimulus to the first contralateral potential peak. We manually selected the peak using a custom GUI in Matlab.

Channels above 600 kΩ were considered to be non-functional and removed from analysis. For the 2 day map interpolation plot (**Figure 7**), 30 pulse shapes with varying width and duration were applied with interleaved trials. Each pulse shape was repeated at least 20 times. The averaged optogenetic evoked potentials were calculated for each pulse shape and the peak amplitude was measured. The contour plots were then interpolated to find isopotential lines.

Chronic Impedance Recordings and Analysis

Electrical impedance spectra were collected from arrays before implantation, and periodically after implantation to assess electrical characteristics using a potentiostat (Autolab PGSTAT 128N, Metrohm, Riverview, FL, United States) and following previously published methods (**Figure 5**; Williams et al., 2007). Arrays that were determined viable for implantation had values of approximately 50–100 kΩ at 1 kHz. Animals were trained to sit still with treats and were not anesthetized or sedated for chronic impedance measurements. Analysis consisted of data from six rats, three with thinned skull implants and three with epidural implants for comparison. Each rat had a bilateral implant consisting of 32 electrode sites. Impedance measurements were gathered from each electrode for 30 days post implantation. Resistive values at 1 kHz were plotted for each of the 32 channels corresponding to length of time of the implant. Single channels with a resistance >600 kΩ were considered outliers and eliminated from calculations for that day. Outliers were considered to be broken or due to an inadequate connection. Average resistance was plotted for each day and fitted to a curve across days using cubic spline interpolation to account for measurements potentially not lining up exactly on individual days across animals. The thinned skull implants interpolation curves were averaged together and plotted against the epidural implants averaged interpolation curves. Impedance values were not recorded after implantation in acute mice experiments, although pre-implantation impedance values were comparable to those of the devices implanted for chronic recordings in rats.

RESULTS AND DISCUSSION

Chronic Periodic Sensory Evoked Potential Recordings in Rats

Chronic SSEP recordings were obtained weekly during electrical stimulation of the sciatic or median nerve in three rats to compare the spatial resolution of thinned skull μECoG arrays vs. traditional epidural arrays. Thinned skull μECoG arrays were implanted bilaterally in sensorimotor cortex in each rat and SSEPs were recorded in each contralateral hemisphere from a cutaneous electrical stimulus of hindlimb or forelimb. A representative plot of thinned skull SSEPs on the left hemisphere from right hindlimb stimulation is shown in **Figure 3**. Using the stainless-steel bone screw as a reference, which was implanted cranial and contralateral to the μECoG array (**Figure 3A**), recorded signals contained common noise, and differences in SSEPs from nearby electrode locations were not readily apparent. Two post process referencing techniques were used to reduce both common noise and common signal to highlight spatially distinct differences in neural signals. Employing a common average reference (CAR) (**Figure 3B**) successfully recovered spatially distinct hindlimb SSEPs on adjacent electrode sites. Similarly, employing a small Laplacian (**Figure 3C**) reference *post hoc* further highlighted spatially distinct SSEP responses on adjacent sites. Consequently, we chose to use the small Laplacian *post hoc* referencing strategy for the remainder of the recording data, because it visually increased unique highlighted spatial information present in the SSEP on adjacent sites (McFarland et al., 1997). Epidural signals are similarly plotted in **Supplementary Figure S1**, although they are recorded at slightly different post-operative time periods and use different stimulation amplitudes.

Distinct somatotopic signals were recorded 38 days post-implantation from μECoG arrays placed on a thinned skull area of the rat's right sensorimotor cortex from both left hindlimb and forelimb stimulation (**Figure 4**). Small Laplacian referencing methods were also applied. Highest peak to peak SSEP values from forelimb stimulation, according to the heatmap, are positioned at the anterior portion of the electrode with peaks spanning both medially and laterally (**Figure 4A**). When switching the area of stimulation to the hindlimb, SSEPs shifted medially similar to previously mapped rat sensorimotor cortex

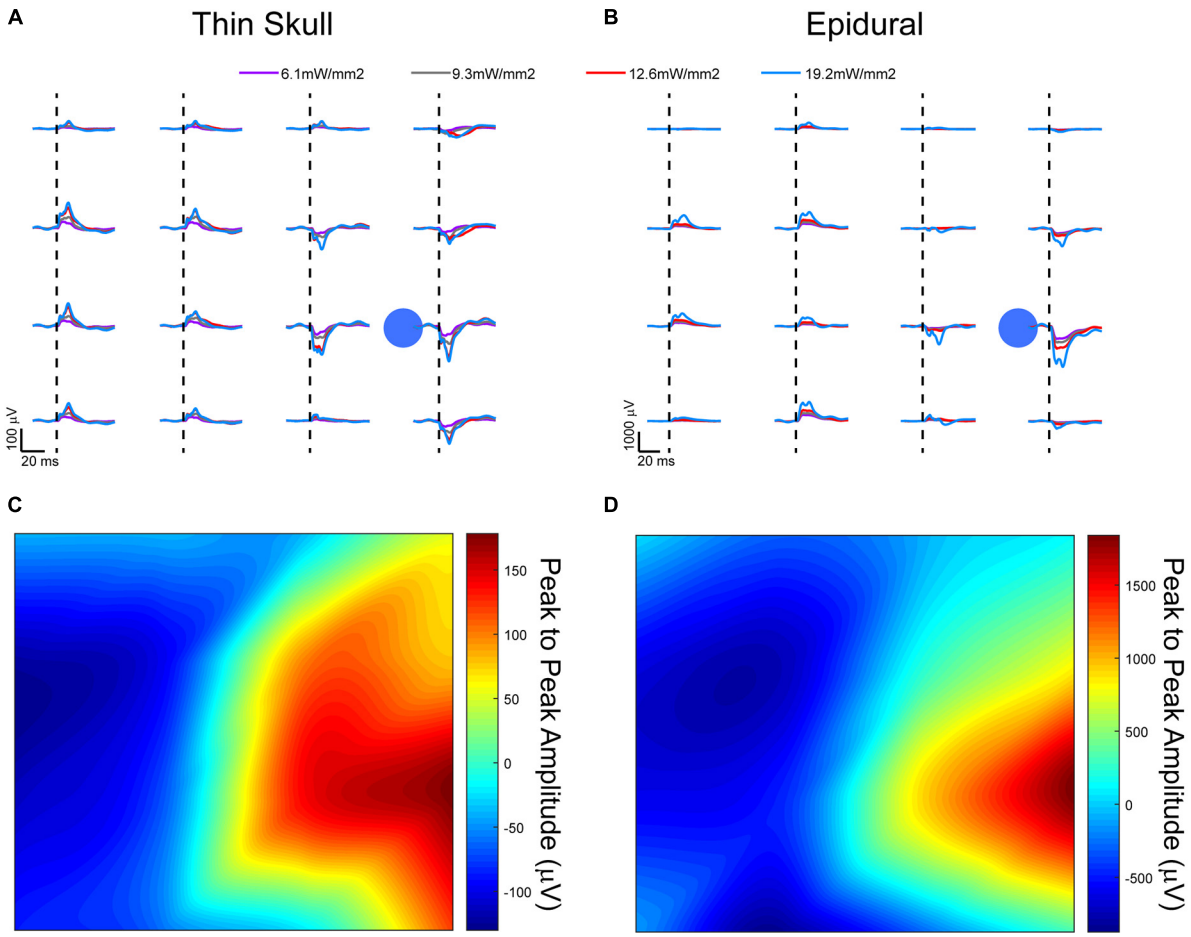

FIGURE 6 | Optically evoked local field potentials from **(A)** thinned skull and **(B)** epidurally implanted μECoG arrays in an acute, terminal Thy1-ChR2 mouse. Amplitude heat maps show the 545.5 mW/mm^2 optically evoked potentials using small Laplacian referencing from both the **(C)** thin skull and **(D)** epidural preparations. Each can be processed to illustrate the spatial resolution of the recordings, although the difference in scale is smaller in the thinned skull preparation by approximately a magnitude of 10. Dashed lines represent onset of electrical stimulus.

(**Figure 4B**; Sakatani et al., 1990). The recorded sensory responses are consistent with the response latencies for myelinated sensory fiber conduction, around 13 ms for forelimb and 17 ms for hindlimb according to previously published data (Sakatani et al., 1990; Bazley et al., 2012).

Thinned skull μECoG electrode arrays not surprisingly have lower signal amplitudes recorded during evoked responses in comparison to historical studies using the same arrays placed epidurally which are closer to the source of the neural signal (Park et al., 2014). As a result, it becomes more important to employ CAR and small Laplacian referencing strategies to eliminate common signal/noise to uncover spatially distinct spatial information for neuroscience applications. Given a similar SSEP was recorded across all electrode sites with appropriate conduction latency prior to *post hoc* referencing, this may suggest the common signal was recorded at the stainless-steel bone screws in contact with the surface of the brain used for the reference and ground, respectively. This referencing strategy was utilized because the ECoG signal recorded from the bone screws has historically been insignificant compared to signals recorded epidurally from μECoG. Therefore, in previous studies *post hoc* referencing was not required to reveal spatially distinct information from site to site. The attenuation of signal through the thin skull in studies described here made the small common signal putatively recorded from the stainless-steel screws more problematic. Consequently, *post hoc* referencing was necessary before spatially distinct SSEPs were observed on adjacent electrode sites.

Thinned skull μECoG electrode arrays also have been shown in this study to record information on a temporal scale similar to epidurally placed arrays. At the relatively low frequencies found in electrophysiological signals, the temporal resistive-capacitive filtering of the bone under the array is minimal. For example, the timing of the SSEP peaks were not appreciably delayed when compared to epidural. Currently, GCaMP6f is a popular genetically coded calcium indication (GECI) that is commonly used to observe neural activity at an onset of approximately 45 ms (Wang et al., 2019). This suggests that the incorporation

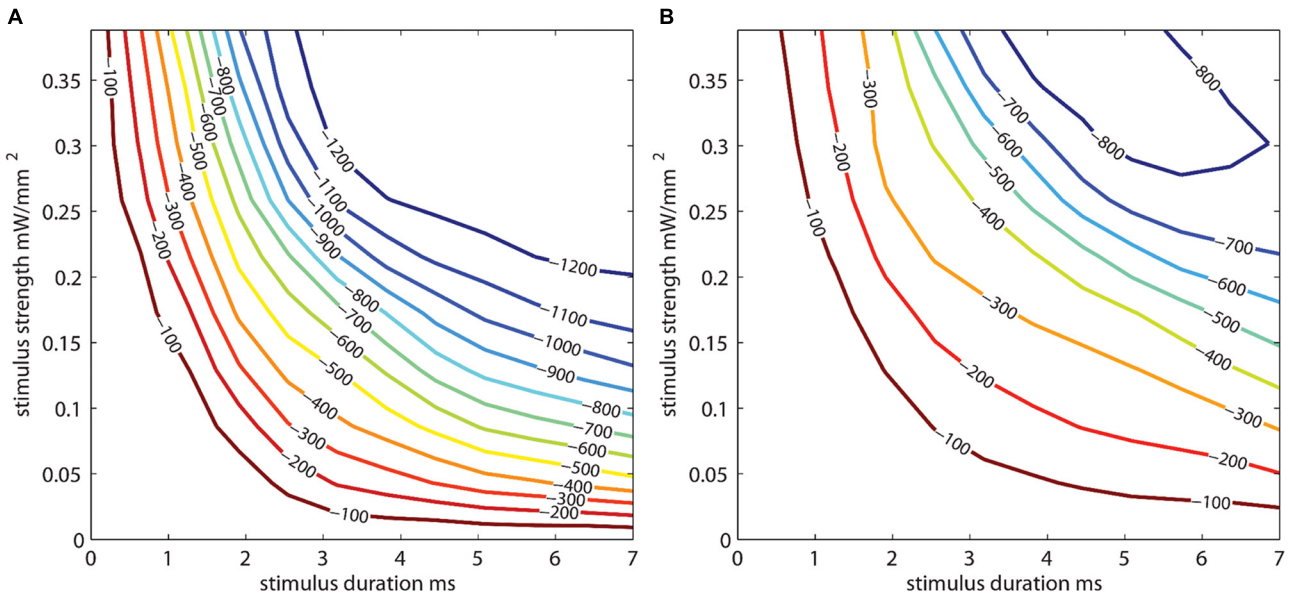

FIGURE 7 | Photostimulus duration vs. amplitude peak potential 2D interpolated contour plot. Stimulus strength is plotted against stimulus duration. Interpolated curves denoting the peak depolarization amplitudes (in μV) for the stimulus strength/duration are shown for **(A)** epidural and **(B)** thinned skull μECoG recordings in an acute terminal Thy1-ChR2 mouse. Longer stimulus durations and stimulus strength (power) are needed to evoke similar sized neural signal amplitudes in the thinned skull vs. epidural preparations. The stainless-steel skull screw reference was used for this analysis. No additional software referencing techniques were used.

of an optically transparent μECoG array with common thinned skull experiments for optical imaging would provide unique, complementary temporal information.

Chronic Periodic Impedance Spectra Recordings in Rats

To compare the electrical performance of epidural vs. thinned skull placed electrodes in rats over time, we measured the impedance spectra of electrodes on each array at 1 kHz periodically over the chronic implantation period (**Figure 5**). Impedance plots from μECoG arrays implanted on a thinned skull preparation showed slightly different patterns of change over time than those implanted epidurally (**Figure 5**). Initial electrode impedances were similar when measured in 0.9% w/v phosphate-buffered NaCl saline (∼25–125 mΩ at 1 KHz). After approximately 14 days of implantation as shown in **Figure 5**, the impedances of the electrodes on the epidural surface were higher on average than that of the electrodes on the thinned skull surface. The epidural impedance interpolation curve shows rise in impedance around 1 week after implantation and lasting for approximately 14 days, similar to other microelectrodes implanted in or on cortex in other studies (Ludwig et al., 2006; Williams et al., 2007). This may be attributed to a central nervous system immune response and new tissue formation and follows previous intracortical and epidural implantation impedance results (Williams et al., 2007; Park et al., 2014). Impedances of epidural implants reached a steady state between 2 and 4 weeks post-implant reflecting decelerated wound healing. In contrast, the thinned skull impedance interpolation curve remained relatively stable for the 30-day period, slowly rising throughout. The difference in shape of the impedance curves suggests the chronic thinned skull electrode/tissue interface is slightly different in composition than the epidural grids. Even though the curve shapes differed, the beginning and end point of data collection (days 0 and 30) between the thinned skull and epidural groups were similar (within ∼50 kΩ of each other). This demonstrates that bone regrowth/scarring under the thinned skull electrodes does not grossly increase the impedance by comparison. **Supplementary Figure S2** shows line plots of individually recorded impedance values from each rat over a time period of 1 month.

Decreased impedances during the first few weeks of thinned skull electrode implantation may suggest edema, and that fluid remained at the electrode/tissue interface without clearing. Extra fluid could have hypothetically caused shunting of current and increased distance between the electrode array and the thinned skull. Regardless, we were still able to record spatially and temporally accurate SSEPs and optogenetically induced field potentials from thinned skull electrodes in rats and mice with relatively low impedance values (impedance values not acquired post-implantation in acute mice studies).

Comparison of Thinned Skull vs. Epidural Recordings From Optogenetic Light Stimulation in Acute Terminal Mice

To further investigate the spatial resolution of information on nearby electrodes given a thinned skull recording approach, a light stimulus was applied through a clear parylene C μECoG array and thinned skull to optogenetically activate neurons expressing light sensitive proteins. Optogenetically

evoked potentials were recorded in ChR2 mice through a thinned skull (**Figure 6A**) and epidurally using a smaller 2 mm × 2 mm clear μECoG array to generate a consistent focal activation of cortex for comparison. Even though the array's substrate (parylene C) was clear, the metal electrodes and traces were not and blocked some portions of light. All optogenetic experiments used the same type of devices and had the same amount of light loss from metal. Using clear electrode sites and traces made of materials like In tin oxide, ITO, or graphene may help alleviate this problem in the future.

A comparison of signals from these two groups did present some confounds. Most likely there was a different scattering of light that arrived at the cortex in the thinned skull vs. the epidural cohorts. While quantifying this scattering of light through the thinned skull would be interesting, it would not be trivial to measure or model the light exiting the skull in each individual animal since the thinning technique which drills to the most transparent bone layer leaves the bone not completely uniform in thickness. Also, we wanted to demonstrate that even without an exact measurement of uniform bone, a simple thinning procedure could be performed to record useful neural signals.

Evoked responses through the thinned skull showed the highest peak responses near the foci of optogenetic stimulation after small Laplacian referencing, further demonstrating the spatial recording ability of the preparation (**Figure 6A**). Increasing 473 nm laser power also increased evoked potential peak amplitudes. A similar response paradigm occurs with epidural stimulation and recording (**Figure 6B**), however, we obtain a much larger signal possibly due to lack of spatial filtration of signal through the skull. The additional layer of thin bone also caused additional scattering of the blue light before it reached cortex, slightly changing the optogenetic stimulus between the two conditions. **Figures 6C,D** use a 2D interpolated heat map to show differences in peak to peak amplitudes at a stimulation laser power of 545.5 mW/mm^2. Both thinned skull and epidural heat maps display spatial distinct recordings on nearby electrode sites. Due to the presumed filtration/attenuation of signal through the skull and other tissues, the thinned skull recording (**Figure 6C**) is approximately 10 times less in peak-to-peak amplitude than the epidural recording (**Figure 6D**). The thinned skull signal also seems to be slightly more diffuse given appropriate referencing strategies. This may also be due to the scattering of light through the skull. Future studies could test different electrode diameter sizing and inter-site spacing to better specify the spatial properties of the signals recorded through a thinned skull.

One ChR2 mouse underwent an acute procedure where the skull was thinned, and a 465 nm LED was positioned 2 cm away from the thinned skull with the light power and duration values varied to generate photostimulus strength vs. duration curves (**Figure 7**). The resulting illumination covered most of the cortical area under the μECoG array. Stimuli strength and duration were applied randomly, and peak amplitudes of signals recorded. The thinned skull was then removed exposing the dural surface and stimulation procedure repeated. **Figure 7A** depicts a contour plots for signals recorded from the dura, whereas **Figure 7B** depicts the same plot from the thinned skull. The stainless-steel skull screw reference was used for **Figure 7** analysis. No additional software referencing techniques were used.

The optogenetically evoked μECoG signal on both the epidural and thinned skull grids demonstrated spatially distinct information, with waveform reversals often apparent on two adjacent sites. These reversals, in conjunction with the waveshape of the evoked response, demonstrated that the electrophysiological recordings were not photoelectric artifacts. Although the magnitude in μVolts of the evoked signal was approximately 10× less with the thinned skull preparation than with the epidurally placed grids, the spatial information as assessed by differences in recordings at adjacent electrode sites was highly similar after *post hoc* small Laplacian referencing.

Imaging of Immune Response in Neural Tissue to Thinned Skull and Epidural μECoG Implantations

Given the impedance responses over time in all animals, histology was performed on rat M32 to compare histology to the impedance measurement of approximately 50 kΩ at timepoint 32 days post-implantation. Histologic sectioning and immunochemical staining for glial fibrillary acidic protein (GFAP) for astrocytes and Iba-1 for microglia and/or infiltrating macrophages were performed with perfused neural tissue in the single rat with bilateral thinned skull/epidural μECoG arrays (**Supplementary Figure S3**). The cortical region directly beneath the epidural preparation showed putative increase in GFAP immunoreactivity and projection of astrocytic processes toward the cortical surface (**Supplementary Figure S3C**). Iba-1 staining did not reveal any obvious increases in microglial immunoreactivity within the brain tissue on either the epidural or thinned skull hemispheres (**Supplementary Figure S3D**). However, an apparent thickening of the dura on the epidural side was observed (**Supplementary Figure S3F**) which contained a higher density of Iba-1-positive cells, either microglia or infiltrating macrophages, that was not present on the thinned skull side of the animal (**Supplementary Figure S3E**). Previous studies have also reported thickening of the dura under the μECoG array consisting primarily of collagen (Schendel et al., 2014; Degenhart et al., 2016).

The main benefit of the thinned skull preparation is that the skull remains partially intact. When the skull is completely removed many side effects can occur which may impact the interpretation of behavioral results. Previous studies in the field of *in vivo* imaging have showed increased glial reaction (microglia and astrocytes) under an open craniotomy window preparation compared to a thinned skull window preparation in mice (Yang et al., 2010). Pneumocephalus can occur after craniotomy in a clinical setting which involves air being trapped in the cranial cavity (Reasoner et al., 1994). Also, dendritic spine plasticity has been shown to differ in thinned vs. open-skull window preparations, emphasizing that the neural environment under a craniotomy may be changed by the craniotomy itself (Xu et al., 2007; Yang et al., 2010).

Another benefit the thinned skull recording technique might offer is improved implant mechanical stability, and the lack of direct contact with the surface of the brain or dura. The latter may reduce the risk of injury to neural tissue or device failure due to the lack of device movement on the surface of the brain, although this will need to be investigated in further studies.

CONCLUSION

In summary, the studies described in this paper for the first time demonstrate that μECoG grids placed on a thinned skull can provide stable, spatially distinct electrophysiological information out to periods in excess of a month in rats. Mice implanted with a clear polymer μECoG array allowed for simultaneous electrophysiology and optical access through a thinned skull, although these studies were performed acutely. Chronic studies of these type would need to be performed to ensure similar results. Our chronic thinned skull neural recordings in conjunction with previously published chronic thinned skull window imaging (Shih et al., 2019) suggests that collecting these chronic data may be possible.

Neural recordings through a thinned skull is complementary to optical imaging techniques in a number of ways. First and perhaps foremost, ECoG is an established clinically viable diagnostic and therapeutic technique in human patients (Tripathi et al., 2010). The ability to combine optogenetics and optical recordings with μECoG allows for one to better understand and optimize the clinically viable ECoG system. Secondly, optical imaging is limited by the temporal resolution of the fluorescent indicator. This makes it difficult to infer number of synapses involved when a specific pathway is activated, such as is commonly done in SSEPs. Moreover, many studies look at pathological oscillations at higher frequencies, such as up to 30 Hz for tremor (Schnitzler and Gross, 2005), where the temporal resolution of the optical indicator becomes a potential confound due to undersampling the intrinsic oscillation. μECoG serves as a complement to more accurately measure the frequency component of intrinsic oscillations. Finally, unlike optical recording techniques that measure from superficial regions of cortex, ECoG is known to record activity originating from deeper areas of the brain (Ojemann et al., 2013; Richner et al., 2019). Future improvements to this method would include using optically transparent electrode sites and traces made out of transparent metals or other materials such as graphene. This would allow for complete light transmission through the μECoG array.

The ability to record neural signals through a thinned skull with μECoG recording grids may provide a useful balance between invasiveness, information content, and day to day stability that could be important for future neuroprosthetics applications. In addition, this novel method may be critically enabling for neuroscience studies in which minimizing the trauma to the underlying neural or non-neuronal cells of interest is necessary to avoid potential confounds given the fundamental hypothesis to be tested.

DATA AVAILABILITY STATEMENT

The datasets generated for this study are available on request to the corresponding author.

ETHICS STATEMENT

All animal procedures were approved by the Institutional Animal Care and Use Committee (IACUC) at the University of Wisconsin–Madison, Madison, WI, United States. All efforts were made to minimize animal discomfort.

AUTHOR CONTRIBUTIONS

SB, JPN, and TR: experimental design, data analysis, and manuscript preparation. AS, KL, and JW: experimental design and manuscript preparation. KC, MH, and JN: data collection and data analysis. ST: device fabrication and data collection. LK-H: manuscript preparation. All authors contributed to draft the manuscript and have read and approved the final manuscript.

FUNDING

This study is based upon the work supported by the Space and Naval Warfare Systems Center Pacific and Defense Advanced Research Projects Agency under Award Nos. N66001-11-1-4013 and N66001-12-C-4025. Any opinions, findings, and conclusions or recommendations expressed in this publication are those of the author(s) and do not necessarily reflect the views of the Defense Advanced Research Projects Agency or Space and Naval Warfare Systems Center Pacific.

ACKNOWLEDGMENTS

We acknowledge Brian Gosink for electrode array photography.

SUPPLEMENTARY MATERIAL

The Supplementary Material for this article can be found online at: https://www.frontiersin.org/articles/10.3389/fnins.2019.01017/full#supplementary-material

FIGURE S1 | Somatosensory evoked potentials (SSEPs) recorded on week 5 post-implantation from a rat implanted with a 16-channel μECoG array placed epidurally over right sensorimotor cortex. Biphasic current pulses (1 ms, varied amplitude) were used to stimulate the left hindlimb with surface electrodes over the sciatic nerve. **(A)** Stainless-steel bone screw, **(B)** Common average, and **(C)** small Laplacian referencing strategies are shown to increase the signal-to-noise ratio, and to reveal spatial signaling from the predicted hindlimb anatomical region. Dashed lines represent onset of electrical stimulus.

FIGURE S2 | Line plots of individual impedance values recorded at 1 kHz of rats implanted with μECoG arrays over **(A)** thinned skull and implanted **(B)** epidurally. Each color represents an individual animal. Data shown here is from the same animals as used in **Figure 5** main text.

FIGURE S3 | Immunohistology of astrocytes and microglia under a μECoG thinned skull implant (left hemisphere) and μECoG epidural implant (right hemisphere) after 1 month of implantation in the same rat. **(A)** GFAP (in green) shows astrocyte distribution and boxes indicate where the μECoG arrays were placed. **(B)** Astrocyte densities comparable to the area outside the implant are seen under a thinned skull implant. **(C)** Possible increased astrocyte densities and elongated processes are seen in the area beneath the epidural implant. **(D)** IBA-1 staining (in red) labeled microglia distribution. **(E)** Microglia staining comparable to the area outside the implant are seen under a thinned skull implant. **(F)** Possible increased microglia densities and thickened dura can be seen on the epidural implant hemisphere.

REFERENCES

Akhtari, M., Bryant, H. C., Mamelak, A. N., Flynn, E. R., Heller, L., Shih, J. J., et al. (2002). Conductivities of three-layer live human skull. *Brain Topogr.* 14, 151–167.

Bazley, F. A., Hu, C., Maybhate, A., Pourmorteza, A., Pashai, N., Thakor, N. V., et al. (2012). Electrophysiological evaluation of sensory and motor pathways after incomplete unilateral spinal cord contusion. *J. Neurosurg. Spine* 16, 414–423. doi: 10.3171/2012.1.SPINE11684

Bonder, D. E., and McCarthy, K. D. (2014). Astrocytic Gq-GPCR-Linked IP3R-Dependent Ca2+ signaling does not mediate neurovascular coupling in mouse visual cortex in vivo. *J. Neurosci.* 34, 13139–13150. doi: 10.1523/JNEUROSCI.2591-14.2014

Degenhart, A. D., Eles, J., Dum, R., Mischel, J. L., Smalianchuk, I., Endler, B., et al. (2016). Histological evaluation of a chronically-implanted electrocorticographic electrode grid in a non-human primate. *J. Neural. Eng.* 13:046019. doi: 10.1088/1741-2560/13/4/046019

Drew, P. J., Shih, A. Y., Driscoll, J. D., Knutsen, P. M., Blinder, P., Davalos, D., et al. (2010). Chronic optical access through a polished and reinforced thinned skull. *Nat. Methods* 7, 981–984. doi: 10.1038/nmeth.1530

Falcone, J. D., Carroll, S. L., Saxena, T., Mandavia, D., Clark, A., Yarabarla, V., et al. (2018). Correlation of mRNA expression and signal variability in chronic intracortical electrodes. *Front. Bioeng. Biotechnol.* 6:26. doi: 10.3389/fbioe.2018.00026

Fernández, E., Greger, B., House, P. A., Aranda, I., Botella, C., and Albisua, J. (2014). Acute human brain responses to intracortical microelectrode arrays: challenges and future prospects. *Front. Neuroeng.* 7:24. doi: 10.3389/fneng.2014.00024

Gefen, A., Gefen, N., Zhu, Q., Raghupathi, R., and Margulies, S. S. (2004). Age-dependent changes in material properties of the brain and braincase of the rat. *J. Neurotrauma* 20, 1163–1177. doi: 10.1089/089771503770802853

Goss-Varley, M., Dona, K. R., McMahon, J. A., Shoffstall, A. J., Ereifej, E. S., Lindner, S. C., et al. (2017). Microelectrode implantation in motor cortex causes fine motor deficit: implications on potential considerations to brain computer interfacing and human augmentation. *Sci. Rep.* 7:15254. doi: 10.1038/s41598-017-15623-y

Grill, W. M., Norman, S. E., and Bellamkonda, R. V. (2009). Implanted neural interfaces: biochallenges and engineered solutions. *Annu. Rev. Biomed. Eng.* 11, 1–24. doi: 10.1146/annurev-bioeng-061008-124927

Henle, C., Raab, M., Cordeiro, J. G., Doostkam, S., Schulze-Bonhage, A., Stieglitz, T., et al. (2011). First long term in vivo study on subdurally implanted micro-ECoG electrodes, manufactured with a novel laser technology. *Biomed. Microdevices* 13, 59–68. doi: 10.1007/s10544-010-9471-9

Khodagholy, D., Gelinas, J. N., Thesen, T., Doyle, W., Devinsky, O., Malliaras, G. G., et al. (2014). NeuroGrid: recording action potentials from the surface of the brain. *Nat. Neurosci.* 18, 310–315. doi: 10.1038/nn.3905

Kipke, D. R., Vetter, R. J., Williams, J. C., and Hetke, J. F. (2003). Silicon-substrate intracortical microelectrode arrays for long-term recording of neuronal spike activity in cerebral cortex. *IEEE Trans. Neural. Syst. Rehabil. Eng.* 11, 151–155. doi: 10.1109/tnsre.2003.814443

Leuthardt, E. C., Schalk, G., Moran, D., and Ojemann, J. G. (2006). The emerging world of motor neuroprosthetics: a neurosurgical perspective. *Neurosurgery* 59, 1–14. doi: 10.1227/01.neu.0000221506.06947.ac

Leuthardt, E. C., Schalk, G., Wolpaw, J. R., Ojemann, J. G., and Moran, D. W. (2004). A brain-computer interface using electrocorticographic signals in humans. *J. Neural. Eng.* 1, 63–71. doi: 10.1088/1741-2560/1/2/001

Ludwig, K. A., Miriani, R. M., Langhals, N. B., Joseph, M. D., Anderson, D. J., and Kipke, D. R. (2009). Using a common average reference to improve cortical neuron recordings from microelectrode arrays. *J. Neurophysiol.* 101, 1679–1689. doi: 10.1152/jn.90989.2008

Ludwig, K. A., Uram, J. D., Yang, J., Martin, D. C., and Kipke, D. R. (2006). Chronic neural recordings using silicon microelectrode arrays electrochemically deposited with a poly(3,4-ethylenedioxythiophene) (PEDOT) film. *J. Neural. Eng.* 3, 59–70. doi: 10.1088/1741-2560/3/1/007

Marin, C., and Fernández, E. (2010). Biocompatibility of intracortical microelectrodes: current status and future prospects. *Front. Neuroeng.* 3:8. doi: 10.3389/fneng.2010.00008

McFarland, D. J., McCane, L. M., David, S. V., and Wolpaw, J. R. (1997). Spatial filter selection for EEG-based communication. *Electroencephalogr. Clin. Neurophysiol.* 103, 386–394. doi: 10.1016/s0013-4694(97)00022-2

Myrden, A., and Chau, T. (2015). Effects of user mental state on EEG-BCI performance. *Front. Hum. Neurosci.* 9:308. doi: 10.3389/fnhum.2015.00308

Normann, R. A., and Fernandez, E. (2016). Clinical applications of penetrating neural interfaces and utah electrode array technologies. *J. Neural. Eng.* 13:061003. doi: 10.1088/1741-2560/13/6/061003

Ojemann, G. A., Ojemann, J., and Ramsey, N. F. (2013). Relation between functional magnetic resonance imaging (fMRI) and single neuron, local field potential (LFP) and electrocorticography (ECoG) activity in human cortex. *Front. Hum. Neurosci.* 7:34. doi: 10.3389/fnhum.2013.00034

Onal, C., Otsubo, H., Araki, T., Chitoku, S., Ochi, A., Weiss, S., et al. (2003). Complications of invasive subdural grid monitoring in children with epilepsy. *J. Neurosurg.* 98, 1017–1026. doi: 10.3171/jns.2003.98.5.1017

Osorio, I., Frei, M. G., Giftakis, J., Peters, T., Ingram, J., Turnbull, M., et al. (2002). Performance reassessment of a real-time seizure-detection algorithm on long ECoG series. *Epilepsia* 43, 1522–1535. doi: 10.1046/j.1528-1157.2002.11102.x

Park, D. W., Brodnick, S. K., Ness, J. P., Atry, F., Krugner-Higby, L., Sandberg, A., et al. (2016). Fabrication and utility of a transparent graphene neural electrode array for electrophysiology. *Nat. Protoc.* 11, 2201–2222. doi: 10.1038/nprot.2016.127

Park, D. W., Schendel, A. A., Mikael, S., Brodnick, S. K., Richner, T. J., Ness, J. P., et al. (2014). Graphene-based carbon-layered electrode array technology for neural imaging and optogenetic applications. *Nat. Commun.* 5:5258. doi: 10.1038/ncomms6258

Reasoner, D. K., Todd, M. M., Scamman, F. L., and Warner, D. S. (1994). The incidence of pneumocephalus after supratentorial craniotomy. Observations on the disappearance of intracranial air. *Anesthesiology* 80, 1008–1012. doi: 10.1097/00000542-199405000-00009

Richner, T. J., Brodnick, S. K., Thongpang, S., Sandberg, A. A., Krugner-Higby, L., and Williams, J. C. (2019). Phase relationship between micro-electrocorticography and cortical neurons. *J. Neural. Eng.* doi: 10.1088/1741-2552/ab335b [Epub ahead of print].

Richner, T. J., Thongpang, S., Brodnick, S. K., Schendel, A. A., Falk, R. W., Krugner-Higby, L. A., et al. (2014). Optogenetic micro-electrocorticography for modulating and localizing cerebral cortex activity. *J. Neural. Eng.* 11:016010. doi: 10.1088/1741-2560/11/1/016010

Sakatani, K., Iizuka, H., and Young, W. (1990). Somatosensory evoked potentials in rat cerebral cortex before and after middle cerebral artery occlusion. *Stroke* 21, 124–132. doi: 10.1161/01.str.21.1.124

Salatino, J. W., Ludwig, K. A., Kozai, T. D. Y., and Purcell, E. K. (2017). Glial responses to implanted electrodes in the brain. *Nat. Biomed. Eng.* 1, 862–877. doi: 10.1038/s41551-017-0154-1

Schendel, A. A., Nonte, M. W., Vokoun, C., Richner, T. J., Brodnick, S. K., Atry, F., et al. (2014). The effect of micro-ECoG substrate footprint on the meningeal tissue response. *J. Neural. Eng.* 11:046011. doi: 10.1088/1741-2560/11/4/046011

Schendel, A. A., Thongpang, S., Brodnick, S. K., Richner, T. J., Lindevig, B. D., Krugner-Higby, L., et al. (2013). A cranial window imaging method for monitoring vascular growth around chronically implanted micro-ECoG devices. *J. Neurosci. Methods* 218, 121–130. doi: 10.1016/j.jneumeth.2013.06.001

Schnitzler, A., and Gross, J. (2005). Normal and pathological oscillatory communication in the brain. *Nat. Rev. Neurosci.* 6, 285–296. doi: 10.1038/nrn1650

Shih, A. Y., Mateo, C., Drew, P. J., Tsai, P. S., and Kleinfeld, D. (2012). A polished and reinforced thinned-skull window for long-term imaging of the mouse brain. *J. Vis. Exp.* 7:3742. doi: 10.3791/3742

Shih, A. Y., Mateo, C., Drew, P. J., Tsai, P. S., and Kleinfeld, D. (2019). A polished and reinforced thinned-skull window for long-term imaging of the mouse brain. *J. Vis. Exp.* 7:3742. doi: 10.3791/3742

Shoffstall, A. J., Paiz, J. E., Miller, D. M., Rial, G. M., Willis, M. T., Menendez, D. M., et al. (2018). Potential for thermal damage to the blood-brain barrier during craniotomy: implications for intracortical recording microelectrodes. *J. Neural. Eng.* 15:034001. doi: 10.1088/1741-2552/aa9f32

Spuler, M., Walter, A., Ramos-Murguialday, A., Naros, G., Birbaumer, N., Gharabaghi, A., et al. (2014). Decoding of motor intentions from epidural ECoG recordings in severely paralyzed chronic stroke patients. *J. Neural. Eng.* 11:066008. doi: 10.1088/1741-2560/11/6/066008

Thongpang, S., Richner, T. J., Brodnick, S. K., Schendel, A., Kim, J., Wilson, J. A., et al. (2011). A micro-electrocorticography platform and deployment strategies for chronic BCI applications. *Clin. EEG Neurosci.* 42, 259–265. doi: 10.1177/155005941104200412

Tripathi, M., Garg, A., Gaikwad, S., Bal, C. S., Chitra, S., Prasad, K., et al. (2010). Intra-operative electrocorticography in lesional epilepsy. *Epilepsy Res.* 89, 133–141. doi: 10.1016/j.eplepsyres.2009.12.007

Uriguen, J. A., and Garcia-Zapirain, B. (2015). EEG artifact removal-state-of-the-art and guidelines. *J. Neural. Eng.* 12:031001. doi: 10.1088/1741-2560/12/3/031001

Viventi, J., Kim, D. H., Vigeland, L., Frechette, E. S., Blanco, J. A., Kim, Y. S., et al. (2011). Flexible, foldable, actively multiplexed, high-density electrode array for mapping brain activity in vivo. *Nat. Neurosci.* 14, 1599–1605. doi: 10.1038/nn.2973

Wang, W., Kim, C. K., and Ting, A. Y. (2019). Molecular tools for imaging and recording neuronal activity. *Nat. Chem. Biol.* 15, 101–110. doi: 10.1038/s41589-018-0207-0

Williams, J. C., Hippensteel, J. A., Dilgen, J., Shain, W., and Kipke, D. R. (2007). Complex impedance spectroscopy for monitoring tissue responses to inserted neural implants. *J. Neural. Eng.* 4, 410–423. doi: 10.1088/1741-2560/4/4/007

Wyler, A. R., Ojemann, G. A., Lettich, E., and Ward, A. A. Jr. (1984). Subdural strip electrodes for localizing epileptogenic foci. *J. Neurosurg.* 60, 1195–1200. doi: 10.3171/jns.1984.60.6.1195

Xu, H. T., Pan, F., Yang, G., and Gan, W. B. (2007). Choice of cranial window type for in vivo imaging affects dendritic spine turnover in the cortex. *Nat. Neurosci.* 10, 549–551. doi: 10.1038/nn1883

Yang, G., Pan, F., Parkhurst, C. N., Grutzendler, J., and Gan, W. B. (2010). Thinned-skull cranial window technique for long-term imaging of the cortex in live mice. *Nat. Protoc.* 5, 201–208. doi: 10.1038/nprot.2009.222

Conflict of Interest: JW and KL are scientific board members and have stock interests in NeuroOne Medical Inc., a company developing next generation epilepsy monitoring devices. JW also has an equity interest in NeuroNexus Technology Inc., a company that supplies electrophysiology equipment and multichannel probes to the neuroscience research community. KL is a co-founder and has an equity interest in Neuronoff, Inc. KL is also a paid member of the scientific advisory board of Cala Health, Blackfynn, and Battelle, and a paid consultant for Galvani. Outside of NeuroOne and NeuroNexus where the potential conflict is described in more detail here for transparency, none of these companies at present is developing technology that overlaps with the data discussed in this manuscript.

The remaining authors declare that the research was conducted in the absence of any commercial or financial relationships that could be construed as a potential conflict of interest.

frontiers in Neuroscience

ORIGINAL RESEARCH
published: 16 October 2019
doi: 10.3389/fnins.2019.01058

Sensorimotor ECoG Signal Features for BCI Control: A Comparison Between People With Locked-In Syndrome and Able-Bodied Controls

Zachary V. Freudenburg[1], Mariana P. Branco[1], Sacha Leinders[1], Benny H. van der Vijgh[1], Elmar G. M. Pels[1], Timothy Denison[2], Leonard H. van den Berg[1], Kai J. Miller[1], Erik J. Aarnoutse[1], Nick F. Ramsey[1] and Mariska J. Vansteensel[1]*

[1] UMC Utrecht Brain Center, Department of Neurology & Neurosurgery, University Medical Center Utrecht, Utrecht, Netherlands, [2] Department of Engineering Science, University of Oxford, Oxford, United Kingdom

The sensorimotor cortex is a frequently targeted brain area for the development of Brain-Computer Interfaces (BCIs) for communication in people with severe paralysis and communication problems (locked-in syndrome; LIS). It is widely acknowledged that this area displays an increase in high-frequency band (HFB) power and a decrease in the power of the low frequency band (LFB) during movement of, for example, the hand. Upon termination of hand movement, activity in the LFB band typically shows a short increase (rebound). The ability to modulate the neural signal in the sensorimotor cortex by imagining or attempting to move is crucial for the implementation of sensorimotor BCI in people who are unable to execute movements. This may not always be self-evident, since the most common causes of LIS, amyotrophic lateral sclerosis (ALS) and brain stem stroke, are associated with significant damage to the brain, potentially affecting the generation of baseline neural activity in the sensorimotor cortex and the modulation thereof by imagined or attempted hand movement. In the Utrecht NeuroProsthesis (UNP) study, a participant with LIS caused by ALS and a participant with LIS due to brain stem stroke were implanted with a fully implantable BCI, including subdural electrocorticography (ECoG) electrodes over the sensorimotor area, with the purpose of achieving ECoG-BCI-based communication. We noted differences between these participants in the spectral power changes generated by attempted movement of the hand. To better understand the nature and origin of these differences, we compared the baseline spectral features and task-induced modulation of the neural signal of the LIS participants, with those of a group of able-bodied people with epilepsy who received a subchronic implant with ECoG electrodes for diagnostic purposes. Our data show that baseline LFB oscillatory components and changes generated in the LFB power of the sensorimotor cortex by (attempted) hand movement differ between participants, despite consistent HFB responses in this area. We conclude that the etiology of LIS may have significant effects on the LFB spectral components in the sensorimotor cortex, which is relevant for the development of communication-BCIs for this population.

Keywords: brain-computer interface, implant, sensorimotor cortex, amyotrophic lateral sclerosis, brain stem stroke, electrocorticography, high-frequency band, low-frequency band

OPEN ACCESS

Edited by:
Christoph Guger, g.tec Medical Engineering GmbH, Austria

Reviewed by:
Tonio Ball, University Medical Center Freiburg, Germany
Sebastian Halder, University of Essex, United Kingdom

***Correspondence:**
Nick F. Ramsey
n.f.ramsey@umcutrecht.nl

Specialty section:
This article was submitted to Neuroprosthetics, a section of the journal Frontiers in Neuroscience

Received: *28 February 2019*
Accepted: *20 September 2019*
Published: *16 October 2019*

Citation:
Freudenburg ZV, Branco MP, Leinders S, Vijgh BHvd, Pels EGM, Denison T, Berg LHvd, Miller KJ, Aarnoutse EJ, Ramsey NF and Vansteensel MJ (2019) Sensorimotor ECoG Signal Features for BCI Control: A Comparison Between People With Locked-In Syndrome and Able-Bodied Controls. Front. Neurosci. 13:1058. doi: 10.3389/fnins.2019.01058

INTRODUCTION

The sensorimotor areas of the brain are a promising target area for the control of Brain-Computer Interfaces (BCIs) that aim to provide people with severe paralysis (locked-in syndrome, LIS) a channel for communication and environmental control. A wealth of electroencephalography (EEG) literature shows that movement is associated with decreases in the spectral power measured from the sensorimotor regions, specifically in the alpha/mu (8–12 Hz) and beta (13–30 Hz) frequency bands (Jasper and Penfield, 1949; Chatrian et al., 1959; Neuper and Pfurtscheller, 2001), commonly referred to as event-related desynchronization (ERD). The end of movement is typically associated with a short-lasting increase in beta power (event-related synchronization, ERS) (Pfurtscheller et al., 1996). These low-frequency band (LFB) EEG signal changes have been used to accomplish BCI control in able-bodied study participants (e.g., Wolpaw et al., 2000; Scherer et al., 2007; Blankertz et al., 2010; Thomas et al., 2013) as well as in several people with severe paralysis (e.g., Neuper et al., 2003; Kübler et al., 2005; Bai et al., 2010; Daly et al., 2013).

Over the past decades, subdural electrocorticography (ECoG) has received increasing attention as a signal acquisition technology for BCI purposes. In BCI research settings, ECoG signals are typically recorded from able-bodied people with refractory epilepsy who are temporarily fitted with these electrodes for clinical diagnostic purposes. Also in the ECoG-BCI research field, the sensorimotor cortex is recognized as an especially interesting source of signals to enable BCI control (Leuthardt et al., 2004; Hermes et al., 2011). Since ECoG allows one to capitalize on the detailed spatial organization of the sensorimotor cortex, multiple independent control signals may conceptually be extracted from this area using high-spatial-density ECoG grids (Slutzky et al., 2010; Branco et al., 2017). Importantly, research on implantable ECoG-based BCIs often focuses on movement-related increases in High-Frequency Band (HFB, >30 Hz) power (Crone et al., 1998; Chestek et al., 2013; Blakely et al., 2014; Branco et al., 2017), which are thought to reflect local processing and are considered to be more spatially focal than changes in LFB power (Miller et al., 2009; Hermes et al., 2012), potentially providing a more specific, and therefore more reliable, BCI control signal (Schalk and Leuthardt, 2011). Yet, it has also been shown that changes in LFB power may contribute to accurate decoding and reliable ECoG-BCI control (Schalk et al., 2007; Nakanishi et al., 2014; Vansteensel et al., 2016; Flint et al., 2017). Indeed, HFB activity in the sensorimotor cortex is thought to be highly correlated to lower frequency bands, with the amplitude of HFB activity being coupled to the phase of LFB oscillations during rest (Yanagisawa et al., 2012).

For sensorimotor BCIs to become of value for people with LIS, it is essential for them to be able to generate reliable responses in the sensorimotor cortex by imagining or attempting to move. Two common causes for LIS are amyotrophic lateral sclerosis (ALS) and brain stem stroke (Patterson and Grabois, 1986; Hayashi and Kato, 1989; Pels et al., 2017). Both of these conditions are associated with brain damage: ALS causes predominantly motor neuron loss in the motor cortex and spinal cord (see for review Agosta et al., 2018), whereas brain stem strokes that lead to LIS typically involve damage to the ventral pons (Patterson and Grabois, 1986; de Mendivil et al., 2013). It can be surmised that brain damage can result in changes in the sensorimotor neuroelectrical signal used for ECoG-BCI, potentially affecting the baseline spectral characteristics as well as the signal changes induced by attempts to move the hand. As stated above, most ECoG sensorimotor BCI research has so far been performed in able-bodied participants (i.e., people with epilepsy). Therefore, the extent to which the sensorimotor ECoG-BCI control signal is affected by ALS and by brain stem stroke remains unclear.

Within the Utrecht NeuroProsthesis (UNP) study, we aim to evaluate the usability of a fully implantable ECoG-based communication-BCI for daily life by people with LIS. Two participants with LIS (one due to ALS, see Vansteensel et al., 2016; one due to brain stem stroke) have been implanted with the system, including electrodes over the sensorimotor hand area. Interestingly, we noted differences between these participants in the spectral responses induced by attempted hand movement. Here, we aimed to evaluate whether or not the different ECoG response profiles observed in these two LIS participants are part of the normal distribution of response profiles in the general population. The implanted system provides extensive data on the controllability of the spectral signals, from which we can learn about the LFB and HFB spectral components in LIS. To investigate normalcy, ECoG data from the LIS participants need to be compared to those of a control group of able-bodied individuals. The only suitable population for this purpose consists of people who suffer from refractory epilepsy and temporarily receive subdural electrodes for diagnostic purposes. Therefore, we compared spectral oscillations during rest, and modulation of LFB and HFB features by (attempted) hand movement, between the LIS participants and able-bodied people with epilepsy.

MATERIALS AND METHODS

This study was carried out in accordance with the Declaration of World Medical Association (2013). Epilepsy participants gave written informed consent to participate in the study. LIS participants gave informed consent via a dedicated procedure (see Vansteensel et al., 2016 for details). The protocol was approved by the Medical Research and Ethics Committee Utrecht.

Participants

LIS Participants

The first participant with LIS (UNP1; described in Vansteensel et al., 2016) is a woman, 58 years old at the time of informed consent in 2015, who had been diagnosed with ALS in 2008. She is severely paralyzed and anarthric as a result of her disease, but sensibility was intact during pre- and post-surgical neurological evaluation. For communication, she uses an eye gaze device for typing, as well as eye blinks, and more recently small movements of the corner of her mouth, to answer closed

questions. In addition, she uses the implanted UNP device for communication. For that, she attempts to move the right hand and thereby generates reliable signal changes in the sensorimotor cortex, which are converted into "brain-clicks" to control communication software (Communicator 5, Tobii Dynavox, Danderyd, Sweden). The second participant with LIS (UNP4) is a woman who suffered from a brain stem stroke in 2004 and who has been severely paralyzed and anarthric as a result. Pre- and post-surgical neurological evaluation showed that sensibility was globally intact. She was 39 years old at the time of informed consent in August 2017. She uses a head switch to control scanning software for typing, and horizontal and vertical eye and head movements for answering closed questions. Both participants with LIS were implanted with subdural ECoG strips (Resume II, Medtronic, 4 circular contact points per strips, 1 cm inter-electrode distance, off-label use) over the left dorsolateral prefrontal cortex and over the hand region of the left sensorimotor cortex. The target location of the electrodes was determined using the results of an fMRI scan, which was conducted several weeks before surgery. Here, we describe results obtained from the sensorimotor electrodes (**Figure 1**). The participants have used the signal from sensorimotor electrodes for regular BCI training for 105 weeks (UNP1) and 61 weeks (UNP4), respectively, until the last datapoint included in this report. For analysis, the precise location of the subdural electrodes was assessed by co-registration of a post-operative CT scan with a pre-operative T1 MRI scan and a correction for brain shift, using the procedures described in Hermes et al. (2010) and Branco et al. (2018). Notably, two other LIS participants (UNP2 and UNP3) were included in this study, but died before surgery (Vansteensel et al., 2016).

Epilepsy Participants

Data from the participants with LIS were compared with data acquired from a group of 9 adult individuals (EP1-EP9; **Table 1**) with severe refractory epilepsy, who were temporarily implanted with subdural ECoG grids (Ad-Tech, Racine, United States, 1 cm inter-electrode distance) for clinical reasons. Individuals studied here had electrodes over the sensorimotor hand area (**Figure 1**), but the source of their epilepsy did not include this region in most cases. Note that in EP1 and EP8, the source of the epilepsy was located in the central areas, but the signal acquired during the Localizer task runs (see below) did not show interictal activity. All participants were MRI negative (i.e., no detectable structural or anatomical anomalies in the brain). Electrode localization was accomplished using a post-operative CT scan and a pre-operative T1 MRI scan, similarly as described for the LIS participants.

Signal Acquisition

LIS Participants

The implanted electrodes (1 dorsolateral prefrontal strip and 1 sensorimotor strip) were connected via subdural leads to an implantable amplifier/transmitter device (Activa PC + S, Medtronic; Rouse et al., 2011; Afshar et al., 2013; off-label use), which was placed subcutaneously under the clavicle. This device is able to relay filtered spectral power signals from multiple bipolar pairs of electrodes to a tablet computer at a rate of 5 Hz for BCI control (see Vansteensel et al., 2016 for more details). In addition, the raw time-domain signal of a single bipolar electrode pair of each strip can be transmitted at 200 Hz. This setting is more energy consuming and is therefore only used during research visits. Here, we report on analyses of the time-domain signal recorded from single pairs of the sensorimotor electrode strip during repeated Baseline and Localizer tasks (see below) performed by the LIS participants.

Epilepsy Participants

Time-domain data from all implanted ECoG electrodes was continuously and simultaneously recorded using a clinical recording system (Micromed, Treviso, Italy, band pass filter 0.15–134.4 Hz) at a sampling frequency of 512 Hz. Epilepsy participants performed one or more runs of a Localizer task (see below), during which the ECoG signal was spliced to a computer running the BCI2000 software package (Schalk et al., 2004), where it was stored for offline signal processing.

Tasks

Localizer Task

Locked-in syndrome participants periodically conducted a Localizer task that involved making repetitive attempted right hand movements or relaxing for alternating periods of 15 s. During each run of the Localizer task, the ECoG time-domain signal of one single electrode pair of the sensorimotor cortex strip was recorded (see **Tables 2**, **3** for the number of runs acquired per electrode pair). In both participants, one of the pairs was studied more frequently because it showed the most reliable responses (e1-e2 and e2-e3 for UNP1 and UNP4 respectively).

Five of the epilepsy participants performed a Localizer task that involved three different conditions in random order: rest, move (finger tapping of the hand contralateral to the implanted electrodes) and imagine (imagined finger tapping). Each trial had a duration of 15 s. For this study, only the move and rest conditions were analyzed. The other four epilepsy participants performed a task that contained alternating 30 s blocks of finger tapping and rest. Although the task performed by these four participants differed from the task performed by the other five participants in terms of the block-duration, the movement conditions of both tasks involved exactly the same action (finger tapping). Therefore, we did not distinguish between data acquired with the two paradigms. Instructions for the tasks were presented on a computer screen that was placed at the bedside (Presentation, Neurobehavioral Systems, Berkeley, CA, United States). Notably, the epilepsy participants were not involved in BCI feedback sessions before the Localizer task was acquired, except one participant, who did feedback sessions on 3 days.

Baseline Task

UNP1 and UNP4 regularly performed a Baseline task (2–5 min per run), in which they gazed at an image of a circle on a computer screen and were instructed to think of nothing in particular. Data from 52 to 32 runs (UNP1 and UNP4, respectively) recorded

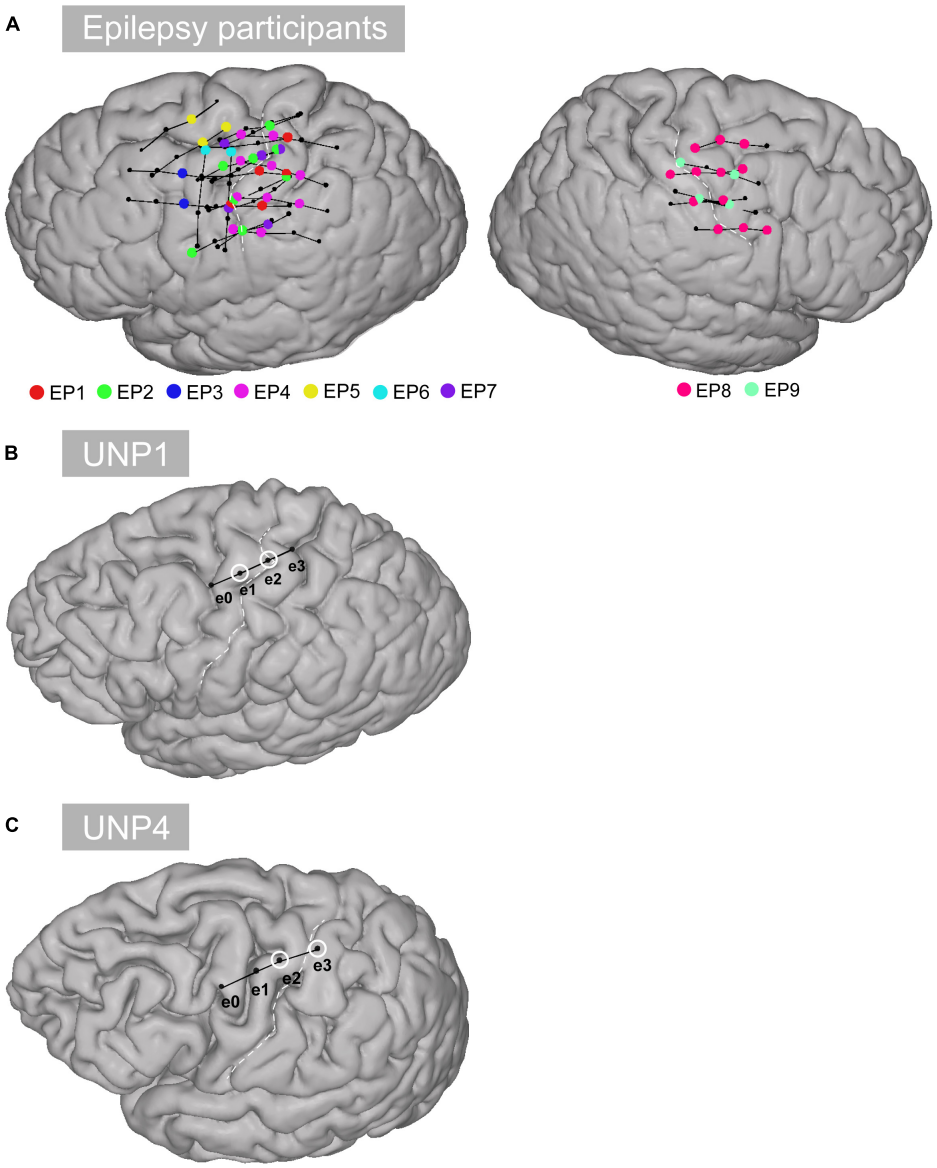

FIGURE 1 | Location of the electrodes. **(A)** All selected rows of sensorimotor electrodes (black circles connected by black lines) in all epilepsy participants (EP1-EP9). Single electrodes showing a significant HFB response ($p < 0.05$) are indicated in color. **(B)** Sensorimotor electrode strip of UNP1. The electrodes marked with a white circle represent the most frequently studied electrode pair (e1-e2). **(C)** Sensorimotor electrode strip of UNP4. The electrodes marked with a white circle represent the most frequently studied electrode pair (e2-e3).

from the most frequently studied pair (e1-e2 for UNP1 and e2-e3 for UNP4) were analyzed in terms of spectral content of the LFB (see below).

Signal Analysis: Presence and Consistency of LFB and HFB Features

LIS Participants

For every time sample of each time-domain data file, spectral power (6–100 Hz, 1 Hz bins) was computed using the real component of the convolution with a complex Gabor wavelet (Bruns, 2004; span 4 cycles at full width half max). The LFB and HFB responses over time where then computed as the sum over the log of the time varying amplitudes for two frequency ranges: 6–30 Hz (LFB) and 31–100 Hz (HFB). Subsequently, based on the well-described phenomena that occur in the sensorimotor cortex upon (attempted) movement (Jasper and Penfield, 1949; Chatrian et al., 1959; Pfurtscheller et al., 1996; Neuper and Pfurtscheller, 2001; Miller et al., 2007, 2010; Hermes et al., 2012; Vansteensel et al., 2016), we defined three movement-related signal features: (1) the increase in HFB (31–100 Hz; mean over time) power during active trials versus rest, (2) the decrease in LFB (6–30 Hz) power during active trials versus rest, and (3) the increase in LFB (6–30 Hz) power during the first 3 s following an active trial (i.e.,

TABLE 1 | Demographics of the able-bodied epilepsy participants.

Participant#	Hemi	Focus	# 4-electrode rows	# HFB significant single electrodes
EP1	L	L Central	3	5
EP2	L	L Superior Frontal	4	8
EP3	L	L Parietal-temporal-occipital	2	2
EP4	L	L Parietal	4	10
EP5	L	L Frontobasal	2	2
EP6	L	L Perisylvian	2	2
EP7	L	L Frontal Medial	4	5
EP8	R	R Central	4	12
EP9	R	R Frontal Parasagittal	2	4

Hemi, hemisphere covered by ECoG electrodes; Focus, Location of the source of the epilepsy. Notably, on request of the journal, age and gender of the epilepsy participants are not included in this table.

TABLE 2 | For UNP1, the number of Localizer tasks runs acquired per bipolar electrode pair and percentage of these runs with a significant response in each of the three features studied.

UNP1	Number of runs	% significant HFB increase	% significant LFB decrease	% significant LFB rebound
e0-e1	8	100	88	100
e0-e2	9	89	100	100
e0-e3	8	88	100	100
e1-e2	50	100	98	90
e1-e3	8	100	100	100
e2-e3	8	100	100	100

The most frequently studied electrode pair is highlighted in gray.

TABLE 3 | For UNP4, the number of Localizer tasks runs acquired per bipolar electrode pair and percentage of these runs with a significant response in each of the three features studied.

UNP4	Number of runs	% significant HFB increase	% significant LFB decrease	% significant LFB rebound
e0-e1	11	0	0	0
e0-e2	10	70	50	20
e0-e3	13	69	62	46
e1-e2	15	53	20	20
e1-e3	10	100	40	30
e2-e3	46	98	22	35

The most frequently studied electrode pair is highlighted in gray.

the rebound period) versus rest. In all cases, rest was taken as the period after the rebound period (i.e., from 3 s after the onset until the end of a rest-trial). For each of these features, we computed the coefficient of determination (signed R^2 value) per task run.

Epilepsy Participants

Data from all implanted subdual electrodes (excluding inter-hemispheric contacts and electrodes showing excessive noise or a flat signal, based on visual inspection) were common average re-referenced and evaluated in terms of response to the Localizer task, using the coefficient of determination (R^2) between the mean 65–95 Hz power log amplitudes (maximum entropy method; Schalk et al., 2004) per-trial and the active and rest trials of the task design. To compare the data of the epilepsy participants with those of the LIS participants, we selected for each epilepsy participant one or more sets of four neighboring electrodes that were comparable to the electrode strips of the LIS participants, located over the superior part of the sensorimotor cortex and more or less perpendicular to the central sulcus where possible. The sets additionally contained at least one single electrode with a significant positive signed R^2 ($p < 0.05$, Bonferroni corrected for multiple comparisons; see **Table 1** for the number of "rows" selected for each epilepsy participant and the number of single HFB significant electrodes; see **Figure 1** for the location of the selected rows). For each pair of selected rows of electrodes (i.e., six pairs per row), the LFB and HFB responses of the bipolar referenced signal were computed according to the same procedure as used for the participants with LIS.

Comparing LIS Participants With Epilepsy Participants

To investigate the co-occurrence of LFB with HFB power changes, we first determined the electrode pairs and runs that resulted in a significant change in the per-trial mean HFB power between active trials versus rest (significant positive signed R^2 value, $p < 0.05$). This screening resulted in 18, 14, 5, 17, 1, 4, 27, 22, and 13 data points (electrode pairs and runs) for epilepsy participants EP1-9, and 89 and 79 data points for UNP1 and UNP4, respectively. For these pairs and runs, we computed, per participant, the mean signed R^2 value for each of the three movement-related signal features, resulting in a single mean value per feature per participant. To evaluate whether the LFB responses of UNP1 and UNP4 fell in the normal range as observed in the epilepsy participants, we compared the mean signed R^2 per LFB feature of UNP1 and UNP4 to the distributions of mean signed R^2 values over epilepsy participants using z-scores.

Signal Analysis: Oscillatory Components

To further investigate the spectral changes that lead to the LFB functional responses, we analyzed the spectral content of the Baseline task of UNP1 and UNP4, and of the active and rest periods of the Localizer task of all participants.

For each run of the Baseline task of UNP1 and UNP4 (only recorded from the most frequently studied electrode pair of each participant), we computed the spectral amplitude (1–100 Hz) over time. Then, the mean and standard deviation of the amplitude profile was computed per run.

For each active and rest period of the Localizer task of all participants (UNP1, UNP4, and epilepsy participants, only runs/electrode pairs with significant HFB response), we separated the oscillatory spectral peaks, which are attributed to rhythmic local field potential fluctuations, from the scale-free or fractal component by applying irregular-resampling auto-spectral analysis (IRASA; Wen and Liu, 2016). This procedure corrects for differences in mixed spectra profiles, for example caused by differences in electrode impedance over runs or in

amplifiers between participants, and therefore allows for a direct comparison of the LFB oscillatory profiles. Rest and active data were split into smaller bins by applying a 3 s moving window with a step size of 1 s. Windows that overlapped the transition between active and rest or that included data from the rebound period (i.e., the first 3 s after the cue to stop moving) were excluded. The windows were irregularly resampled and for each resampling the auto-power spectra was computed, using methods described earlier (Wen and Liu, 2016). The fractal component was estimated by computing the median spectral profile for each of the resampled windows. The fractal component was subsequently subtracted from the non-resampled (or mixed) profile, resulting in the "oscillatory spectral profile" for each window. We then computed the means (over windows) of the mixed, fractal, and oscillatory profiles for both the active and rest task periods separately.

To compare the spectral content of the LFB of the LIS participants to those of the epilepsy participants, the difference between the normalized (z-scored over frequencies per participant) mean active and mean rest oscillatory profiles was computed and plotted. In this way the oscillatory functional changes of the UNP participants can be visually compared to those of the epilepsy participants. In addition, the UNP participants' LFB (6–30 Hz) oscillatory profiles were compared per 1 Hz frequency bin with a one-sample student's t-test to the mean epilepsy participant profiles.

RESULTS

Presence and Consistency of LFB and HFB Features

For all bipolar electrode pairs of UNP1 and for 5 out of 6 electrode pairs of UNP4, performance of the attempted hand movement Localizer task-induced a clear HFB response with high R^2 values (median R^2 value higher than 0.6; **Figure 2A**). For UNP1, these HFB responses were all accompanied by a consistent decrease in LFB power during the active trials and LFB rebound responses immediately thereafter. In contrast, the R^2 values of the LFB decreases and LFB rebound responses of UNP4 were more variable and closer to zero (median typically smaller than 0.6; **Figure 2C**), even in the electrode pairs that showed the highest HFB R^2 values. Notably, further splitting the LFB band into mu (8–12 Hz) and beta (13–30 Hz) frequency bands did not lead to larger or more consistent R^2 values (**Figures 2B,D**).

We subsequently studied the consistency of the LFB and HFB response features. In UNP1, all pairs showed a significant HFB increase, LFB decrease and LFB rebound in 88% or more of the runs (**Table 2**). In contrast, for UNP4, for the two pairs that showed the most consistent HFB responses (e1-e3 and e2-e3), a significant LFB decrease or LFB rebound was obtained in 40% or less of the runs (**Figure 3** and **Table 3**). Overall, a significant LFB response was obtained in only 62% or less of the runs.

Comparison of the mean R^2 values of the LFB decrease and LFB rebound responses of all runs/pairs with significant HFB changes between UNP1, UNP4, and the epilepsy participants revealed that the LFB decrease R^2 value of UNP4 was smaller (i.e., closer to 0) than the range of LFB decrease R^2 values observed in the epilepsy participants (z-score 2.14; **Figure 4A**). In addition, UNP1 and UNP4 had a rebound response that was among the 25% highest (UNP1; z-score 0.98) and 25% lowest (UNP4; z-score −1.04) values observed in able-bodied participants. Also looking at the (normalized) power traces reveals that UNP1 has large and UNP4 has small LFB responses (**Figure 4B**).

Oscillatory Components

The mean spectra of the Baseline runs of electrode pair e1-e2 of UNP1 showed a broad peak between ∼10 and 28 Hz (**Figure 5**). In addition, also the mixed spectra of the rest periods of the Localizer task (all runs/pairs with a significant HFB response) showed this clear and broad peak (**Figure 6**). Subtraction of the fractal component revealed the presence of a clear oscillatory component between 10 and 28 Hz that disappeared during the active periods of the Localizer task. In frequencies lower than 10 Hz, however, attempted hand movement did not seem to generate a decrease in power.

For UNP4, the Baseline spectra (electrode pair e2-e3) and the mixed spectra of the rest periods of the Localizer task (all pairs/run with a significant HFB response) showed a peak between 6 and 22 Hz (**Figure 6**). The oscillatory spectral profile, however, clearly peaked between 6 and 10 Hz during rest and, on average, did not show distinct peaks in low frequencies above 10 Hz. Importantly, the 6–10 Hz peak was hardly affected by attempted movement.

The oscillatory spectral profiles of the epilepsy participants typically included two peaks during the rest periods of the Localizer task, one between ∼5 and 8 Hz, and one between ∼12 and 22 Hz (**Figure 7**). During movement, power in both peaks decreased strongly (compare **Figure 7** with **Figure 8A**).

Visual comparison, between UNP1 and the epilepsy participants, of the difference between the active and rest spectra showed the absence (in UNP1) of task-modulation in the <10 Hz range and large amplitude differences between rest and attempted movement in a beta range that was broader than observed in the epilepsy participants. Indeed, a one-sample t-test showed a significantly higher normalized mean amplitude in UNP1 for the range 19–30 Hz ($p < 0.05$, Bonferroni corrected; **Figure 8B**). For UNP4, visual comparison revealed some level of task-related modulation in the 6–10 Hz range. The beta range seemed entirely devoid of task-related changes in power, in contrast to what was observed in the epilepsy participants (except EP5, who also showed only minor modulation in the beta range).

DISCUSSION

We investigated the characteristics of three different sensorimotor ECoG signal features that are regularly targeted for BCI control purposes, and compared these features between two participants with LIS from different etiologies and able-bodied participants with epilepsy. Our data reveal important differences between participants in the LFB changes generated in the

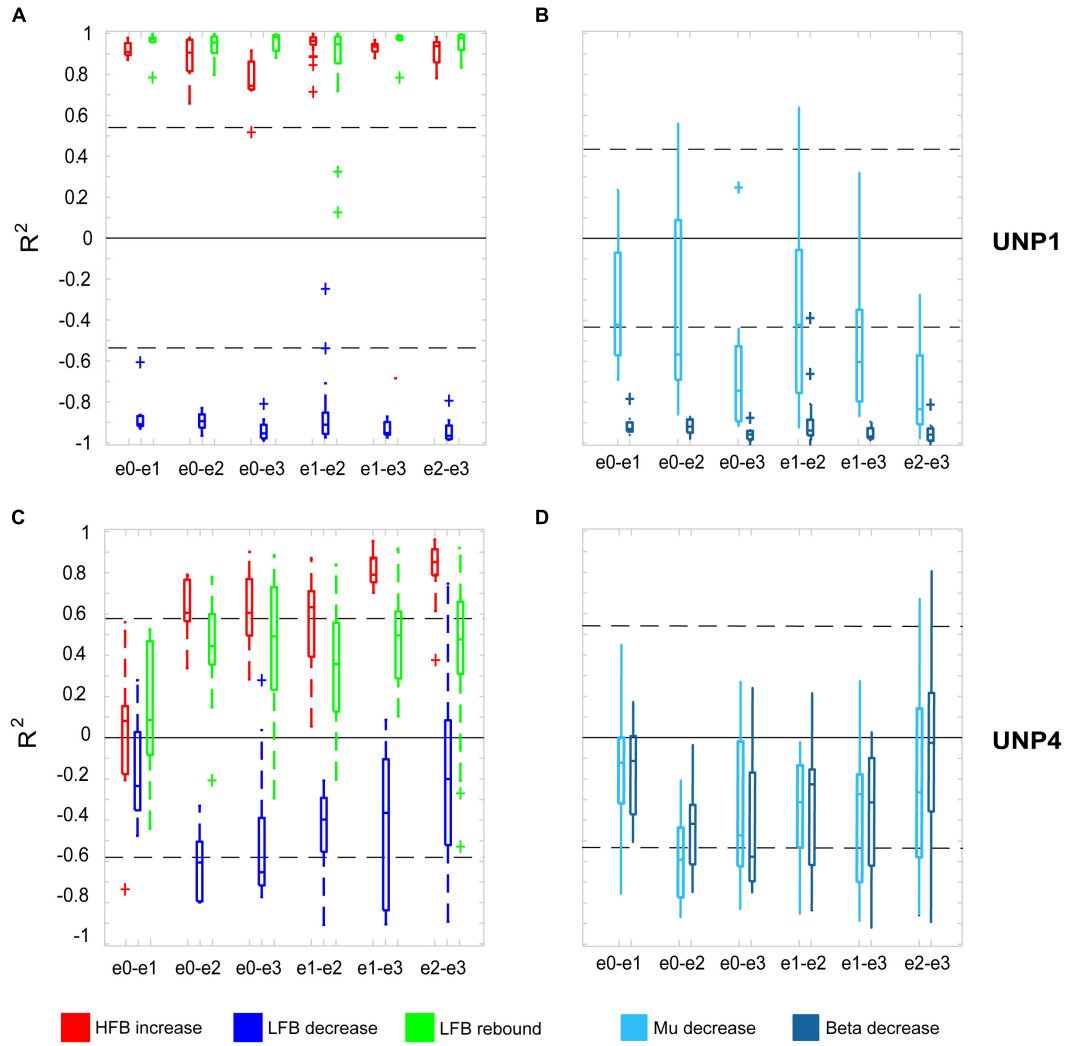

FIGURE 2 | R^2 values of HFB and LFB feature responses in UNP1 and UNP4. **(A,C)** Boxplot of the signed R^2 values of each of the three studied features for each of the six electrode pairs of the sensorimotor electrode strip of UNP1 **(A)** and UNP4 **(C)**. Red, HFB increase; Blue, LFB decrease; Green, LFB rebound. The number of runs per pair is described in **Tables 2**, **3**. The location of the electrodes is indicated in **Figures 1B,C**. **(B,D)** Boxplot of the signed R^2 values of mu (8–12 Hz, light blue) and beta (13–30 Hz, dark blue) power decrease of UNP1 **(B)** and UNP4 **(D)**, per electrode pair. **(A–D)** The horizontal dashed lines indicate the lowest (absolute value) R^2 value that was significant ($p < 0.05$) per participant. The solid black line indicates the value $R^2 = 0$.

sensorimotor cortex by (attempted) hand movement, despite consistent HFB responses in this area.

Two participants with LIS, UNP1, and UNP4, received a fully implantable ECoG-based BCI system, including a subdural electrode strip over the sensorimotor hand area, as part of a study that aims to evaluate the usability of the BCI for day-to-day communication at home. In both participants, most electrode pairs of the sensorimotor electrode strip showed a clear HFB power increase upon attempted hand movement. Yet, only for UNP1 this HFB response was consistently accompanied by a movement-related LFB decrease and a post-movement LFB rebound response. In UNP4, changes in LFB power were smaller on average and electrode pairs and runs that responded with a consistent HFB increase in UNP4 did not necessarily display a significant LFB decrease or rebound. These data suggest that there are important differences in the sensorimotor ECoG signal features between the individuals with LIS. Comparison of the LFB responses of UNP1 and UNP4 with those of a group of epilepsy participants revealed that electrode pairs and runs that display a significant increase in HFB power during (attempted) movement show, on average, a strong LFB decrease and LFB rebound in the epilepsy participants and in UNP1. In UNP4, however, the mean LFB decrease R^2 value was smaller (i.e., closer to 0) than the range of LFB decrease R^2 values observed in the epilepsy participants.

To further investigate the LFB responses, we examined the spectral changes underlying the LFB functional responses by computing the oscillatory spectral profiles during (attempted) hand movement and during rest, for all electrode pairs and runs with a significant HFB response. In the epilepsy participants,

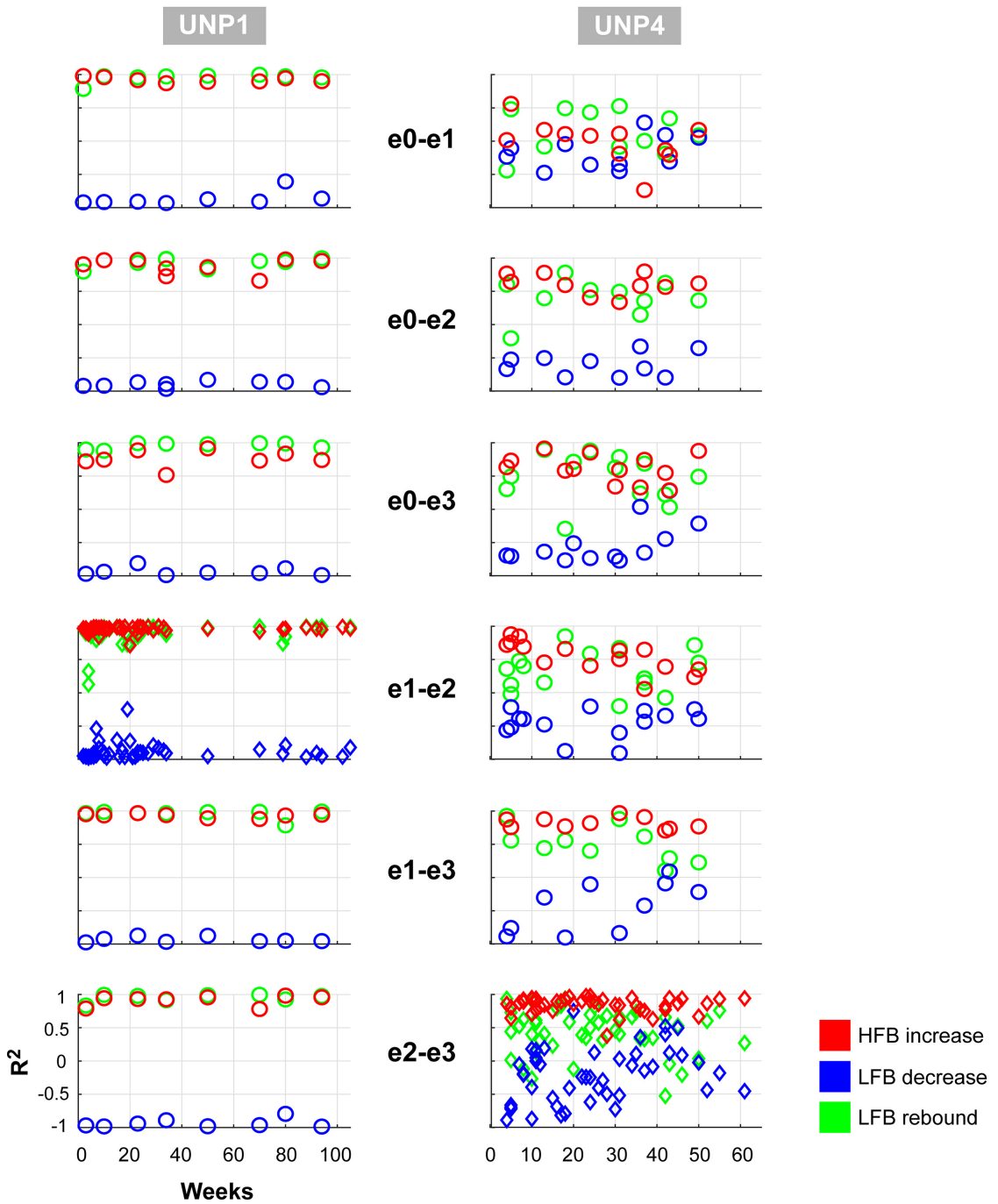

FIGURE 3 | Consistency of LFB and HFB feature responses. Each panel shows, for each electrode pair of UNP1 **(left column)** and UNP4 **(right column)**, the signed R^2 values of the three studied features for all runs acquired with that pair (1 symbol per run). Red, HFB increase; Blue, LFB decrease; Green, LFB rebound. Time on the *x*-axis indicates weeks since implantation. The panels with the diamond symbols indicate the data from the most frequently studied electrode pair.

two peaks were typically observed that were both strongly modulated by hand movement: one around 5–8 Hz and one around 12–22 Hz. Importantly, the center frequency of the 5–8 Hz peak was lower than classically reported in scalp EEG studies for the alpha/mu band oscillations over the central areas (Chatrian et al., 1959). This finding corresponds with results of a comprehensive investigation of the dominant frequencies in baseline ECoG recordings (Groppe et al., 2013). In that study, it was demonstrated that while beta (centered around 17 Hz) is clearly present in the ECoG measured from sensorimotor areas, alpha/mu activity is hardly observed in this region, and theta activity (4–8 Hz) is a dominant feature throughout the

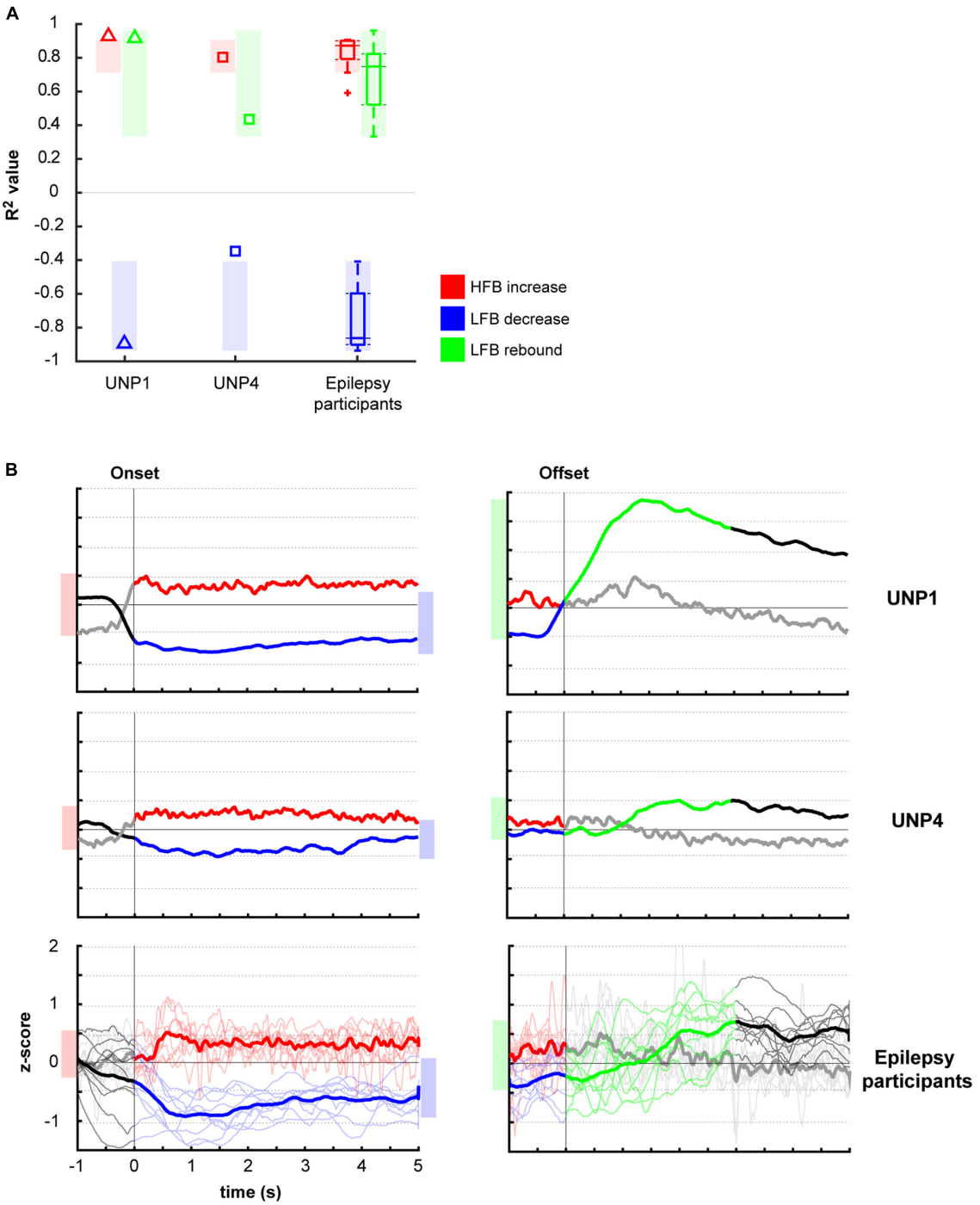

FIGURE 4 | Comparison of R^2 values of the HFB and LFB features between the LIS and epilepsy participants. **(A)** Per participant, the mean signed R^2 value of each of the three features was computed for all runs/electrodes with a significant HFB response. For UNP1 (triangles) and UNP4 (squares), this mean signed R^2 value is plotted. For the epilepsy participants, the distribution of the R^2 values is given in a boxplot: horizontal line represents the median; the rectangle indicates the 50% of the distribution; the dashed lines indicate the maximum and minimum values; and the outliers are indicated by crosses "+." The shaded areas indicate, per feature, the range of values observed among epilepsy participants. Red, HFB increase; Blue, LFB decrease; Green, LFB rebound. **(B)** Normalized (*z*-scored) power traces for each of the two UNP participants and the epilepsy participants (lower panels, where thin lines represent individual participants and the thick line the mean of all epilepsy participants). Left panels indicate HFB (red) and LFB decrease (blue) responses, locked to the onset of the active blocks in the Localizer task. Right panels indicate the LFB rebound responses (green), locked to the offset of the active blocks. Black and gray parts of the traces represent rest. Note that for the computation of the LFB rebound, only the first 3 s of the rest-trials were used, whereas for the HFB and LFB decrease responses, the entire active trial was included. Shaded bars next to the graphs are given for ease of comparison and indicate the variation of the (mean) responses (minimum until maximum value) for the given time window.

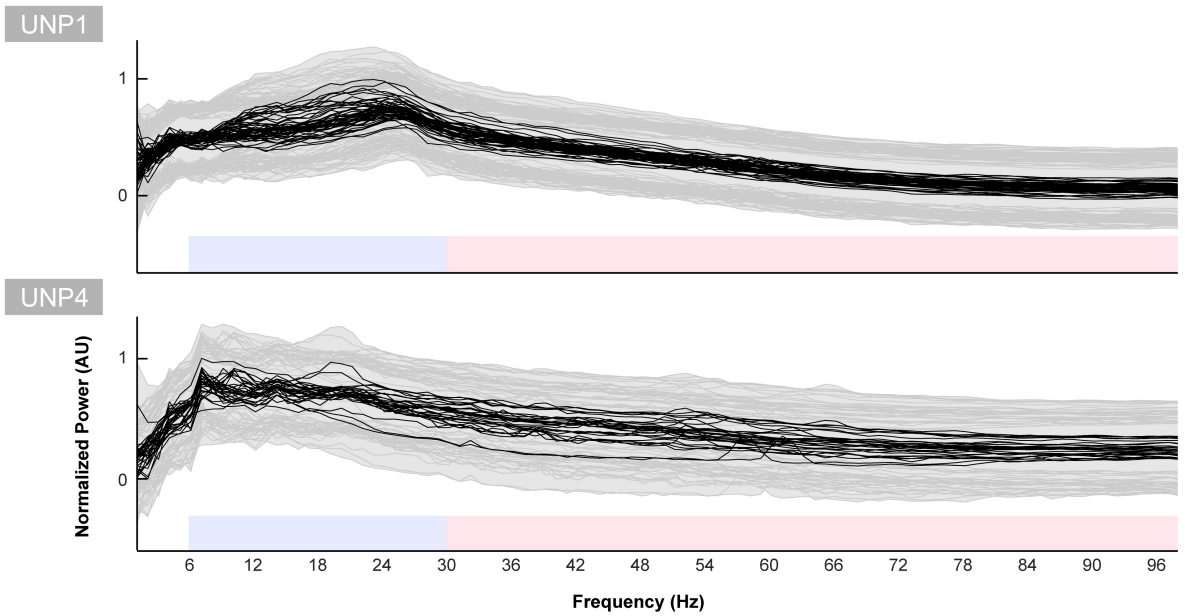

FIGURE 5 | Baseline spectra for UNP1 and UNP4. Each black line indicates the normalized mean power spectrum over time of one Baseline task run of UNP1 **(upper panel)** and UNP4 **(lower panel)** as a function of frequency (Hz). Each subplot was normalized (between 0 and 1) separately to the maximum and minimum value of the black lines. The gray shading and lines indicates the standard deviation over time of each run. The blue and red blocks indicate the frequency ranges used for the LFB and HFB analysis, respectively.

brain. Since hand movement by able-bodied people induced a clear power attenuation in the 5–8 Hz range in our data, it may be hypothesized that this ECoG feature represents the same phenomenon as described by the alpha/mu band in EEG studies. In contrast to the oscillatory spectral profiles of epilepsy participants, the rest profile of UNP1 showed a single, broad peak spanning a large part of the LFB range. In the beta band, power was strongly modulated by attempted movement, but not in lower frequencies. In UNP4, LFB oscillatory activity was limited to a peak in the 6–10 Hz range, which, however, was only minimally modulated by attempts to move the hand.

Our data suggest that the neuroelectrical ECoG features in the sensorimotor cortex of people with LIS display important differences with those of able-bodied people with epilepsy. Whereas both people with LIS were able to generate the well-described changes in the HFB upon attempted movement, LFB features were atypical. It could be surmised that the differences between the LIS participants and the epilepsy participants were related to the large differences in BCI training: both LIS participants have been involved in BCI feedback sessions for many months, whereas ECoG recordings in epilepsy patients typically last about one week and most participants did not have feedback training before the Localizer task was acquired. Importantly, however, already in the first measurements of the LIS participants, the differences in the LFB features were clear (**Figure 3**). In addition, we recently showed that long-term BCI use is not associated with significant changes in the control signal (Pels et al., 2019). Therefore, we believe that differences in training are unlikely to be associated with the atypical LFB features we observed. Instead, we postulate that these findings are suggestive of an effect of the underlying etiology of LIS on LFB baseline power in the sensorimotor cortex and on the modulation thereof by attempted hand movement. One important difference between ALS and brain stem stroke is the temporal aspect of the condition that leads to the locked-in state: whereas brain stem stroke is an event that suddenly disrupts motor function, ALS is a progressive disease that causes increasing muscle function loss over the course of months or years. Conceptually, there may be more room and time for adaptive changes and compensation in the case of ALS than for brain stem stroke, but it could also be reasoned that the longer period UNP4 has been in the locked-in state would allow for these changes. Alternatively, the difference in the location of the damage to the brain may underlie the different brain signal features we observed. Below, we discuss our results in the context of reported effects of brain stem stroke and ALS on the neuroelectrical signal.

Amyotrophic Lateral Sclerosis

Previous reports about the effects of ALS on the neuroelectrical signal are relatively scarce and equivocal. Some EEG studies have reported a decrease in baseline alpha (Mai et al., 1998; Santhosh et al., 2005) and theta (Jayaram et al., 2015) power in people with ALS compared to controls, while others indicated heightened baseline alpha/mu power (Iyer et al., 2015; Maležič et al., 2016) or no difference (Geronimo et al., 2016). In contrast to some EEG studies where modulation of the alpha/mu frequency band has been used for sensorimotor BCI control by individuals with ALS (Wolpaw et al., 1997; Kübler et al., 2005), we observed that frequencies lower than 10 Hz were not modulated by attempted hand movement in UNP1. Possibly, the level of disease

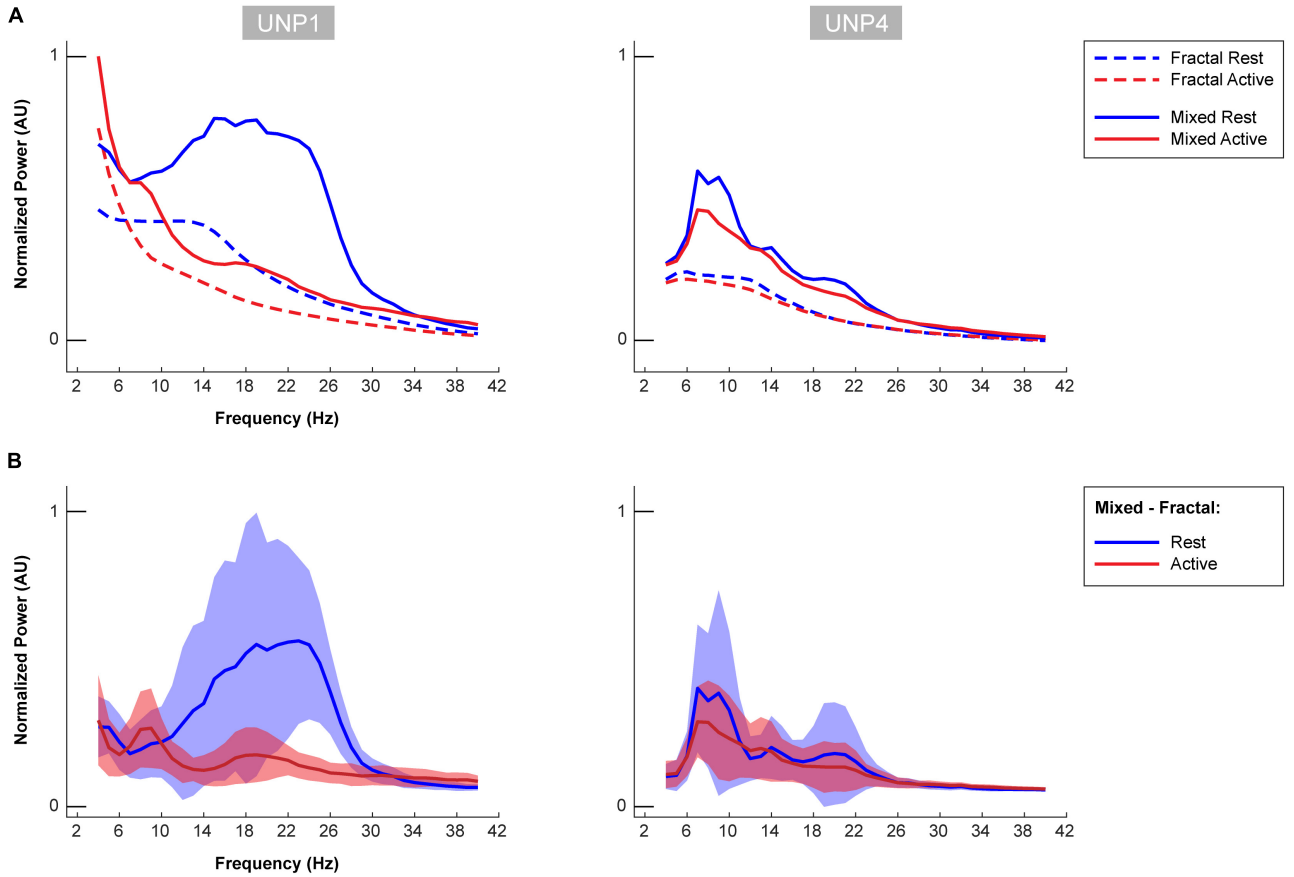

FIGURE 6 | Oscillatory components of UNP1 and UNP4. **(A)** For UNP1 and UNP4, the mixed normalized power profile of the active and rest periods of the Localizer tasks are plotted in solid red and blue lines, respectively. The fractal normalized power profiles of the active and rest periods are given with dashed red and blue lines, respectively. The power profiles are plotted as a function of frequency (in Hz). Fractal and mixed components were normalized (between 0 and 1) by the maximum and minimum of the traces of both subjects (UNP1 and UNP4). **(B)** Subtraction of the fractal from the mixed spectra results in the oscillatory spectra. Blue solid line denotes the mean oscillatory spectral profile (across runs/electrode pairs) of the rest period. Red indicates the mean oscillatory spectral profile of the attempted hand movement (active) periods. The shaded regions indicate the standard deviation (across runs/electrode pairs) of each trace. Plots were normalized (between 0 and 1) by the minimum and maximum of the mean ± standard deviation traces of both subjects (UNP1 and UNP4).

progression is related to this difference: the participants in the earlier studies were more recently diagnosed with ALS and still had some control over their limbs. Other possible explanations for the absence of modulation in frequencies lower than 10 Hz in UNP1, in the presence of clear ERD in higher LFB frequencies, is that the specific cortical area from which the electrode strip of UNP1 measures does not show this modulation or that there are individual differences in the modulation of this frequency range. Indeed, mu and beta desynchronization in the EEG signal often co-occur, but beta ERD may be observed without accompanying mu desynchronization and the two bands are thought to have distinct functional significance (Pfurtscheller, 1981).

Recently, Proudfoot et al. (2017) reported stronger movement-induced beta ERD in MEG recordings of people with ALS, compared to healthy controls. This result did not agree with earlier studies showing similar-sized beta ERD between patients and healthy controls (Riva et al., 2012) or a decreased ERD in patients (Kasahara et al., 2012), but does seem to correspond with our data of UNP1. Whereas the R^2 value of the total LFB decrease (6–30 Hz) of HFB significant channels/runs of UNP1 was within the range observed for the epilepsy participants, the results of the oscillatory component analysis suggest that the LFB response of UNP1 is largely driven by frequencies larger than 10 Hz, rather than by a combination of the 5–8 and 12–22 Hz changes, as was typically observed in the epilepsy participants.

With respect to the beta rebound, there is evidence for a delayed (Proudfoot et al., 2017) or a smaller amplitude response (Riva et al., 2012) in people with ALS, but also for a preservation of beta ERS (Bai et al., 2010). In our study, the R^2 value of the LFB rebound of UNP1 was among the 25% highest values observed in the epilepsy participants, which agrees with a preservation of beta ERS. Since we used the aggregate signal of the entire 3 s window post-movement-termination, we cannot draw any conclusions on the presence or absence of a delay in the LFB rebound response.

Previously, Jayaram et al. (2015) reported elevated baseline EEG HFB power in people with ALS, except in one, most severely motor impaired, patient. In another study, baseline ECoG HFB

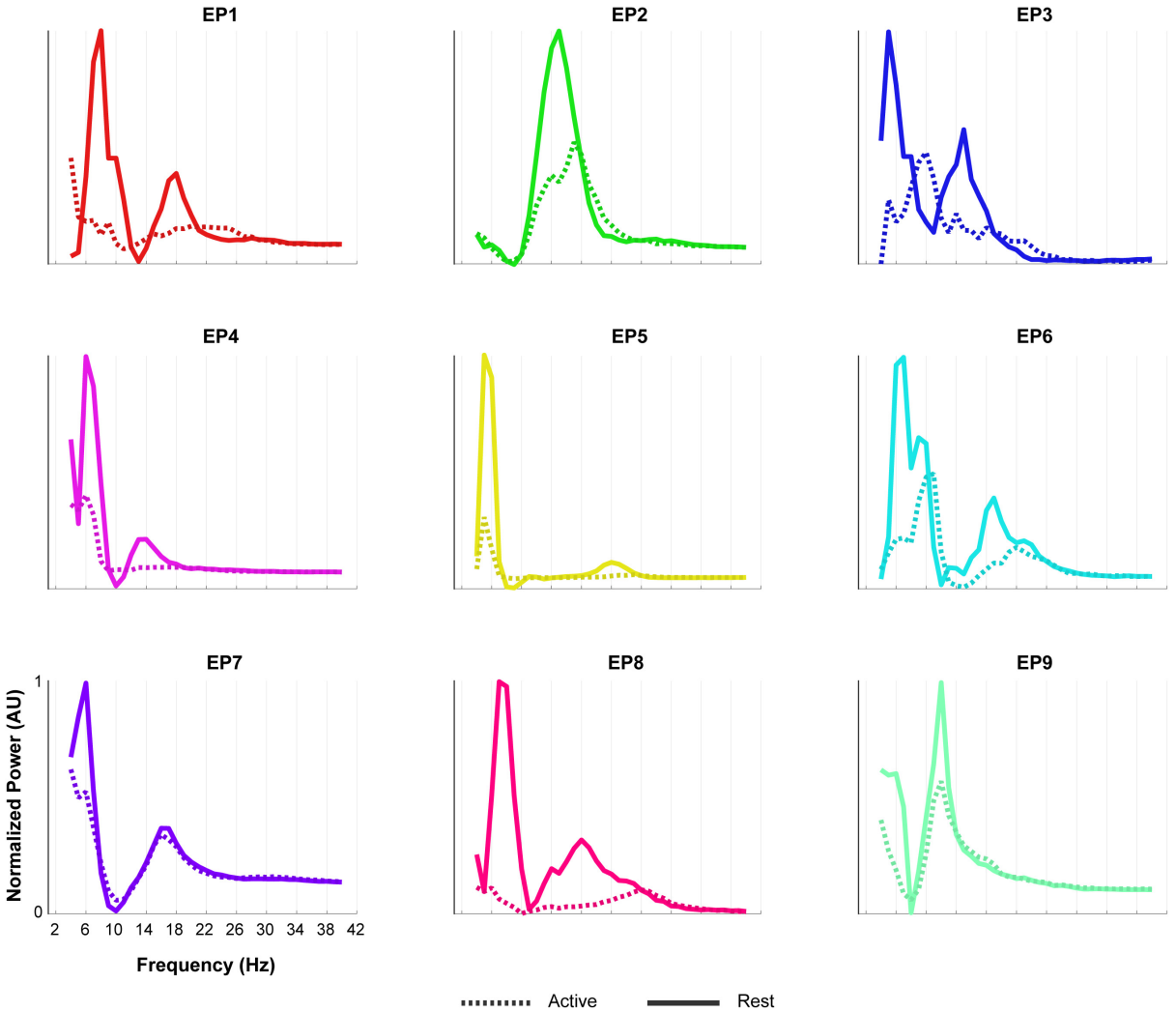

FIGURE 7 | Oscillatory components of epilepsy participants. For each of the epilepsy participants (EP1-9), normalized power of the oscillatory component of the rest (solid line) and the active (dashed line) period of the Localizer task is given. In order to compare the shape of the traces across subjects, each plot was normalized (between 0 and 1) separately by the minimum and maximum of each subjects trace. Note the presence of two LFB peaks during rest in most participants and the decrease in power during the active period.

power was studied in an individual with ALS who transitioned from LIS to Complete LIS (CLIS). HFB power was present during LIS, but the transition to CLIS was accompanied by a sharp drop in this feature (Bensch et al., 2014). Although we did not quantify baseline HFB power in this study, the earlier findings on measurable HFB signal in people with ALS are in general agreement with our findings of clear and consistent HFB responses to attempted movement in UNP1. Whether or not a decrease in baseline HFB power is a general aspect of very late stages of ALS and the transition to CLIS (or of possible changes in alertness or cognition in this state) remains to be determined.

Taken together, our results indicate that HFB and LFB responses may be preserved in at least part of the ALS population and, therefore, present highly usable neuroelectrical signal features that are relevant for BCI control in this population. Indeed, these features have been used to accomplish BCI control in several non-invasive (Wolpaw et al., 1997; Kübler et al., 2005; Bai et al., 2010) and implanted (Vansteensel et al., 2016; Milekovic et al., 2018) BCI studies in people with ALS.

Brain Stem Stroke

UNP4 showed a clear oscillation between 6 and 10 Hz, but oscillations between 10 and 30 Hz were virtually absent. In addition, none of the LFB frequency ranges showed consistent modulation by attempted hand movement in this LIS participant. One possible explanation for the small or absent modulation in LFB power may be an impaired ability to focus on the task, as a result of the brain stem lesion. Indeed, it has been reported that pontine lesions may lead to a deficit in mental imagery of hand rotation (Conson et al., 2008). However, since the analysis of the LFB oscillatory

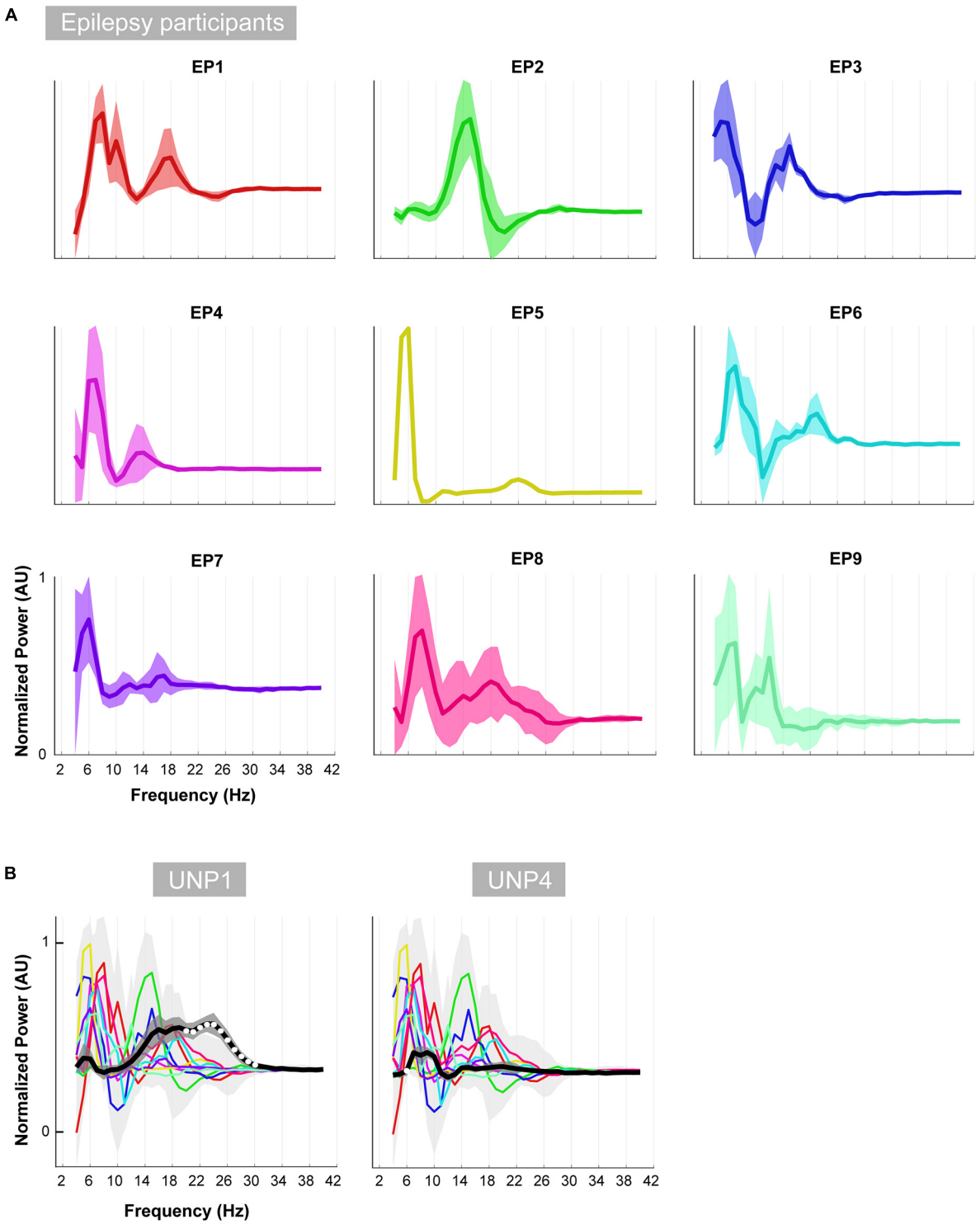

FIGURE 8 | Oscillatory differences. **(A)** For each of the epilepsy participants (EP1-9), the mean difference between the active and rest oscillatory profile across runs/electrode pairs is given. Shaded regions indicate the standard deviation. In order to compare the shape of the traces across subjects, each plot was normalized (between 0 and 1) separately by the minimum and maximum of each subjects trace. **(B)** Each colored line indicates the difference between the active and rest oscillatory profile of each epilepsy participant. Light gray shading indicates standard deviation. For comparison, the mean difference profile (across runs/electrode pairs) of UNP1 (left) and UNP4 (right) is plotted in black, with dark gray shading indicating standard deviation. All traces were normalized (between 0 and 1) by the minimum and maximum of the mean ± standard deviation of the traces of all subjects (EP1-EP9, UNP1 and UNP4). Frequency bins that showed significant (one-sample *t*-test; $p < 0.05$; Bonferroni corrected) difference between UNP participants (black line) and epilepsy participants (colored lines) are indicated with white dots.

components was conducted only using runs/electrode pairs that showed a significant HFB response, poor or variable (mental) task performance is unlikely to have caused the lack of clear LFB responses.

It should be considered that atypical baseline LFB oscillations and an inability to generate motor-related changes in LFB power may be generalized features of individuals who suffered from a brain stem stroke. Earlier studies of the effects of brain stem stroke on the baseline neural signal indicate a fairly normal EEG with a clear alpha peak and some slowing in the low frequencies (Chase et al., 1968; Hawkes and Bryan-Smyth, 1974; Markand, 1976; Patterson and Grabois, 1986; Babiloni et al., 2010; Kotchoubey and Lotze, 2013). Indeed, in our study, UNP4 presented a clear 6–10 Hz peak during rest, which is in agreement with these earlier findings. However, our finding that the spectrum of UNP4 does not contain a clear oscillation in the 12–22 Hz range, as opposed to what was typically observed in the epilepsy participants, does not agree with a previous report that showed no difference in beta power between people with brain stem stroke and healthy controls (Babiloni et al., 2010). Unfortunately, existing evidence on the consistency of LFB modulation in people with brain stem stroke is scarce. In one EEG study, a participant who was paralyzed because of a brain stem stroke (but could produce speech and had some control over the upper limbs) used the beta rebound for BCI control (Höhne et al., 2014). In addition, in two brain stem stroke participants of the BrainGate study, reliable offline decoding was accomplished using LFB and HFB power changes induced by attempted arm movements (Perge et al., 2014). Interestingly, both these studies reported that frequent calibration was necessary to maintain reliable decoding, as there was substantial variability in the anatomical location of the beta rebound (Höhne et al., 2014) or in the neural signals (Perge et al., 2014). Taken together, it seems that the characteristics of the LFB features of UNP4 are not entirely representative of the brain stem stroke population.

It may be hypothesized that the specific anatomic location of the brain stem damage is related to the presence or absence of cortical oscillation in the beta range. Indeed, beta oscillation has typically been attributed to the corticobasal ganglial-thalamic feedback loop (DeLong and Wichmann, 2007; McCarthy et al., 2011; Miller et al., 2012; Basha et al., 2014). Lack of this feature in the setting of brainstem stroke suggests that the wider motor circuit plays a role (**Figure 9**). We examined the specific anatomic lesion caused by the brain stem stroke of UNP4. Because both UNP1 and UNP4 exhibit a loss of functional connection with the spinal cord, it is not the likely reason for the virtual absence of oscillations in the beta range in only UNP4. The pedunculopontine nucleus (PPN) has reciprocal connections with cortical, basal ganglial, thalamic, and cerebellar structures, and it exhibits robust beta range oscillations (Shimamoto et al., 2010), making it a reasonable candidate structure. However, the PPN appears to be anatomically preserved in UNP4 (**Figure 9**). Ascending projections from the cerebellum to the thalamus (dentatothalamic/dentatorubrothalamic tract; Mollink et al., 2016) appear to be intact as well. However, descending cortical and thalamic projections to rostral and caudal pontine nuclei (which, in turn, project to the cerebellum via the middle cerebral peduncle; Evarts and Thach, 1969; Salmi et al., 2009; Kamali et al., 2010; Grimaldi and Manto, 2012) are completely obliterated in UNP4. We therefore consider it most likely that the absence of oscillations in the beta range in UNP4 are the result of the specific location of damage in the motor network.

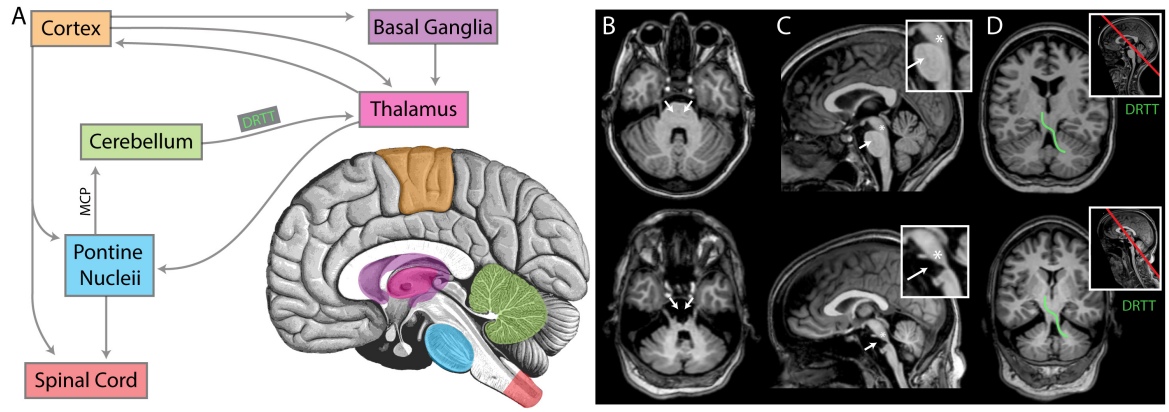

FIGURE 9 | An anatomic interpretation for the lack of beta oscillation in UNP4. **(A)** A simplified diagram of the relevant structures of the motor circuit. MCP denotes the middle cerebral peduncle. DRTT denotes dentatorubrothalamic tract. For panels **(B–D)**, the upper brain images are for participant UNP1 (ALS) and the lower are for participant UNP4 (pontine stroke). **(B)** Axial sections at the level of the MCP. White arrows indicate the location of pontine nuclei, receiving input from cortex and thalamus, and projecting (via the MCP) to the cerebellum. Note the absence of pontine structures in participant UNP4. **(C)** Midsagittal sections, with insets showing magnification of the brainstem. White arrows again indicate the location of pontine nuclei. The asterisks denote the approximate location of the pedunculopontine nucleus (PPN), a structure exhibiting prominent beta oscillations that is involved in movements and locomotion (amongst other modalities) with widespread projections. Note that the PPN appears structurally intact for both participants. **(D)** Sections through the DRTT (shown for one side in green), beginning in the dentate nucleus of the cerebellum, passing through the superior cerebellar peduncle and then the red nucleus, terminating in the ventrolateral nucleus of the thalamus. Section plane shown on midsagittal image with red line in inset. Note that the DRTT appears structurally intact for both participants.

Limitations

The present work has several limitations. First is the small number of people with LIS included in the study. It will be necessary to assess whether our findings on the LFB and HFB ECoG features are specific to the participants included here, or whether they present more generalized phenomena intrinsic to the different underlying etiologies of LIS. Yet, given the fact that our findings are corroborated by a substantial amount of data for each of the LIS participants, we believe that the results of this study are valuable for determining the most promising signal features for BCI control in people with LIS.

Second, intrinsic aspects of the reported ECoG data are the sparse sampling of the brain, due to the relatively large inter-electrode distance (1 cm) and the subject-specific electrode locations. As a result, there are inevitable differences in the exact neural populations recorded and used for the analyses across participants. Importantly, the location of the electrodes of UNP1 and UNP4 was driven by the fMRI activation pattern generated by attempted hand movement and the sampled neural populations should therefore be functionally comparable. The most frequently studied electrode pair of both UNP1 and UNP4 included an electrode over the precentral gyrus and one more posterior, over the central sulcus/postcentral gyrus. For the epilepsy participants, we attempted to sample the same functional region as for the LIS participants by using anatomical (the superior part of the sensorimotor cortex), directional (rows perpendicular as possible to the central sulcus) and signal (significant changes in HFB power induced by hand movement) constraints to select the electrode strips for analysis (see **Figure 1**). In addition, we studied a relatively large population of epilepsy participants. Despite these efforts, it cannot be entirely excluded that differences in the specific electrode locations over the sensorimotor hand area are associated with some level of variability in the LFB and HFB responses.

Third, it should be noted that the analyses conducted here are based on bipolar referenced signals. Since bipolar referencing is the method the implanted device of the LIS participants uses to measure signals from the subdural electrodes, the data of the epilepsy participants was analyzed using similar referencing, to make sure that the data of able-bodied and LIS participants could be accurately compared. It may be speculated that bipolar signals have fundamentally different characteristics than the unipolar signals typically reported in EEG and ECoG literature. In theory, the lack of a typical mu-oscillation in our bipolar ECoG data may even be explained by a complete in-phase synchronization of the area measured by the bipolar pair. However, since the LFB phenomena we observed in the bipolar referenced signals of the epilepsy participants largely corresponded with features observed for single ECoG electrodes in an earlier study (Groppe et al., 2013), we believe that the effect of the bipolar signal processing on our results is of limited significance.

Finally, as the low frequency band was the main focus of the current study, we did not investigate whether or not different aspects of the high-frequency band showed different responses. It will be interesting to investigate this topic in future work.

CONCLUSION

Attempted hand movement by two people with LIS generates consistent HFB power changes in the sensorimotor cortex, while baseline oscillations in the low frequencies, and modulation thereof by attempted hand movement, may be substantially affected by the underlying etiology of the motor impairment of people with LIS. These results bear relevance for the development of BCIs for this population, but should be confirmed in larger numbers of individuals.

DATA AVAILABILITY STATEMENT

The datasets for this study will not be made publicly available because some participants did not consent for public sharing of their data. Part of the data is available upon request.

ETHICS STATEMENT

This study was carried out in accordance with the Declaration of World Medical Association (2013). Epilepsy participants gave written informed consent to participate in the study. LIS participants gave informed consent via a dedicated procedure (see Vansteensel et al., 2016 for details). The protocol was approved by the Medical Research and Ethics Committee Utrecht.

AUTHOR CONTRIBUTIONS

ZF, MV, EA, and NR designed the study. TD led the team who designed the implanted device and provided technical support of the BCI system. SL and EP acquired the data. ZF, SL, and MB analyzed the data. ZF and MV drafted the manuscript. All authors interpreted the data and revised the manuscript.

FUNDING

This study was funded by grants from the European Union (ERC-Adv 320708), the Van Wagenen Foundation, the Dutch Technology Foundation STW (grant 14906), and the National Institute On Deafness and Other Communication Disorders of the National Institutes of Health (U01DC016686). The content is solely the responsibility of the authors and does not necessarily represent the official views of the National Institutes of Health.

ACKNOWLEDGMENTS

We thank the participants for their participation in this research. Also, we thank the clinical staff at the Department of Neurology and Neurosurgery for their contribution to our research, Stavrina Devetzoglou-Toliou for their help with data analysis and Eric Wolters for their help with literature research.

REFERENCES

Afshar, P., Khambhati, A., Stanslaski, S., Carlson, D., Jensen, R., Dani, S., et al. (2013). A translational platform for prototyping closed-loop neuromodulation systems. *Front. Neural Circuits* 6:117. doi: 10.3389/fncir.2012.00117

Agosta, F., Spinelli, E. G., and Filippi, M. (2018). Neuroimaging in amyotrophic lateral sclerosis: current and emerging uses. *Expert Rev. Neurother.* 18, 395–406. doi: 10.1080/14737175.2018.1463160

Babiloni, C., Pistoia, F., Sarà, M., Vecchio, F., Buffo, P., Conson, M., et al. (2010). Resting state eyes-closed cortical rhythms in patients with locked-in-syndrome: an eeg study. *Clin. Neurophysiol.* 121, 1816–1824. doi: 10.1016/j.clinph.2010.04.027

Bai, O., Lin, P., Huang, D., Fei, D.-Y., and Floeter, M. K. (2010). Towards a user-friendly brain–computer interface: initial tests in ALS and PLS patients. *Clin. Neurophysiol.* 121, 1293–1303. doi: 10.1016/j.clinph.2010.02.157

Basha, D., Dostrovsky, J. O., Lopez Rios, A. L., Hodaie, M., Lozano, A. M., and Hutchison, W. D. (2014). Beta oscillatory neurons in the motor thalamus of movement disorder and pain patients. *Exp. Neurol.* 261, 782–790. doi: 10.1016/j.expneurol.2014.08.024

Bensch, M., Martens, S., Halder, S., Hill, J., Nijboer, F., Ramos, A., et al. (2014). Assessing attention and cognitive function in completely locked-in state with event-related brain potentials and epidural electrocorticography. *J. Neural Eng.* 11:026006. doi: 10.1088/1741-2560/11/2/026006

Blakely, T. M., Olson, J. D., Miller, K. J., Rao, R. P. N., and Ojemann, J. G. (2014). Neural correlates of learning in an electrocorticographic motor-imagery brain-computer interface. *Brain Comput. Interfaces* 1, 147–157. doi: 10.1080/2326263X.2014.954183

Blankertz, B., Tangermann, M., Vidaurre, C., Fazli, S., Sannelli, C., Haufe, S., et al. (2010). The Berlin brain–computer interface: non-medical uses of BCI technology. *Front. Neurosci.* 4:198. doi: 10.3389/fnins.2010.00198

Branco, M. P., Freudenburg, Z. V., Aarnoutse, E. J., Bleichner, M. G., Vansteensel, M. J., and Ramsey, N. F. (2017). Decoding hand gestures from primary somatosensory cortex using high-density ECoG. *Neuroimage* 147, 130–142. doi: 10.1016/j.neuroimage.2016.12.004

Branco, M. P., Gaglianese, A., Glen, D. R., Hermes, D., Saad, Z. S., Petridou, N., et al. (2018). ALICE: a tool for automatic localization of intra-cranial electrodes for clinical and high-density grids. *J. Neurosci. Methods* 301, 43–51. doi: 10.1016/j.jneumeth.2017.10.022

Bruns, A. (2004). Fourier-, Hilbert- and wavelet-based signal analysis: are they really different approaches? *J. Neurosci. Methods* 137, 321–332. doi: 10.1016/j.jneumeth.2004.03.002

Chase, T. N., Moretti, L., and Prensky, A. L. (1968). Clinical and electroencephalographic manifestations of vascular lesions of the pons. *Neurology* 18, 357–368.

Chatrian, G. E., Petersen, M. C., and Lazarte, J. A. (1959). The blocking of the rolandic wicket rhythm and some central changes related to movement. *Electroencephalogr. Clin. Neurophysiol.* 11, 497–510. doi: 10.1016/0013-4694(59)90048-90043

Chestek, C. A., Gilja, V., Blabe, C. H., Foster, B. L., Shenoy, K. V., Parvizi, J., et al. (2013). Hand posture classification using electrocorticography signals in the gamma band over human sensorimotor brain areas. *J. Neural Eng.* 10:026002. doi: 10.1088/1741-2560/10/2/026002

Conson, M., Sacco, S., Sarà, M., Pistoia, F., Grossi, D., and Trojano, L. (2008). Selective motor imagery defect in patients with locked-in syndrome. *Neuropsychologia* 46, 2622–2628. doi: 10.1016/j.neuropsychologia.2008.04.015

Crone, N. E., Miglioretti, D. L., Gordon, B., and Lesser, R. P. (1998). Functional mapping of human sensorimotor cortex with electrocorticographic spectral analysis. II. Event-related synchronization in the gamma band. *Brain* 121, 2301–2315. doi: 10.1093/brain/121.12.2301

Daly, B. M., Laparra-Hernández, J., Aloise, F., García, M. L., and Faller, J. (2013). On the control of brain-computer interfaces by users with cerebral palsy. *Clin. Neurophysiol.* 124, 1787–1797. doi: 10.1016/j.clinph.2013.02.118

de Mendivil, A. O., Alcalá-Galiano, A., Ochoa, M., Salvador, E., and Millán, J. M. (2013). Brainstem stroke: anatomy, clinical and radiological findings. *Semin. Ultrasound CT MRI* 34, 131–141. doi: 10.1053/j.sult.2013.01.004

DeLong, M. R., and Wichmann, T. (2007). Circuits and circuit disorders of the basal ganglia. *Arch. Neurol.* 64, 20–24. doi: 10.1001/archneur.64.1.20

Evarts, E. V., and Thach, W. T. (1969). Motor mechanisms of the CNS: cerebrocerebellar interrelations. *Annu. Rev. Physiol.* 31, 451–498. doi: 10.1146/annurev.ph.31.030169.002315

Flint, R. D., Rosenow, J. M., Tate, M. C., and Slutzky, M. W. (2017). Continuous decoding of human grasp kinematics using epidural and subdural signals. *J. Neural Eng.* 14:016005. doi: 10.1088/1741-2560/14/1/016005

Geronimo, A., Simmons, Z., and Schiff, S. J. (2016). Performance predictors of brain–computer interfaces in patients with amyotrophic lateral sclerosis. *J. Neural Eng.* 13:026002. doi: 10.1088/1741-2560/13/2/026002

Grimaldi, G., and Manto, M. (2012). Topography of cerebellar deficits in humans. *Cerebellum* 11, 336–351. doi: 10.1007/s12311-011-0247-244

Groppe, D. M., Bickel, S., Keller, C. J., Jain, S. K., Hwang, S. T., Harden, C., et al. (2013). Dominant frequencies of resting human brain activity as measured by the electrocorticogram. *Neuroimage* 79, 223–233. doi: 10.1016/j.neuroimage.2013.04.044

Hawkes, C. H., and Bryan-Smyth, L. (1974). The electroencephalogram in the "locked-in" syndrome. *Neurology* 24, 1015–1018.

Hayashi, H., and Kato, S. (1989). Total manifestations of amyotrophic lateral sclerosis: ALS in the totally locked-in state. *J. Neurol. Sci.* 93, 19–35. doi: 10.1016/0022-510X(89)90158-90155

Hermes, D., Miller, K. J., Noordmans, H. J., Vansteensel, M. J., and Ramsey, N. F. (2010). Automated electrocorticographic electrode localization on individually rendered brain surfaces. *J. Neurosci. Methods* 185, 293–298. doi: 10.1016/j.jneumeth.2009.10.005

Hermes, D., Miller, K. J., Vansteensel, M. J., Aarnoutse, E. J., Leijten, F. S. S., and Ramsey, N. F. (2012). Neurophysiologic correlates of fMRI in human motor cortex. *Hum. Brain Mapp.* 33, 1689–1699. doi: 10.1002/hbm.21314

Hermes, D., Vansteensel, M. J., Albers, A. M., Bleichner, M. G., Benedictus, M. R., Orellana, C. M., et al. (2011). Functional MRI-based identification of brain areas involved in motor imagery for implantable brain–computer interfaces. *J. Neural Eng.* 8:025007. doi: 10.1088/1741-2560/8/2/025007

Höhne, J., Holz, E., Staiger-Sälzer, P., Müller, K.-R., Kübler, A., and Tangermann, M. (2014). Motor imagery for severely motor-impaired patients: evidence for brain-computer interfacing as superior control solution. *PLoS One* 9:e104854. doi: 10.1371/journal.pone.0104854

Iyer, P. M., Egan, C., Pinto-Grau, M., Burke, T., Elamin, M., Nasseroleslami, B., et al. (2015). Functional connectivity changes in resting-state EEG as potential biomarker for amyotrophic lateral sclerosis. *PLoS One* 10:e0128682. doi: 10.1371/journal.pone.0128682

Jasper, H., and Penfield, W. (1949). Electrocorticograms in man: effect of voluntary movement upon the electrical activity of the precentral gyrus. *Arch. Für Psychiatr. Nervenkr.* 183, 163–174. doi: 10.1007/BF01062488

Jayaram, V., Widmann, N., Förster, C., Fomina, T., Hohmann, M., Hagen, J. M., et al. (2015). "Brain-computer interfacing in amyotrophic lateral sclerosis: implications of a resting-state EEG analysis," in *Proceedings of the 2015 37th Annual International Conference of the IEEE Engineering in Medicine and Biology Society (EMBC)*, Milan.

Kamali, A., Kramer, L. A., Frye, R. E., Butler, I. J., and Hasan, K. M. (2010). Diffusion tensor tractography of the human brain cortico-ponto-cerebellar pathways: a quantitative preliminary study. *J. Magn. Reson. Imaging* 32, 809–817. doi: 10.1002/jmri.22330

Kasahara, T., Terasaki, K., Ogawa, Y., Ushiba, J., Aramaki, H., and Masakado, Y. (2012). The correlation between motor impairments and event-related desynchronization during motor imagery in ALS patients. *BMC Neurosci.* 13:66. doi: 10.1186/1471-2202-13-66

Kotchoubey, B., and Lotze, M. (2013). Instrumental methods in the diagnostics of locked-in syndrome. *Restor. Neurol. Neurosci.* 31, 25–40. doi: 10.3233/RNN-120249

Kübler, A., Nijboer, F., Mellinger, J., Vaughan, T. M., Pawelzik, H., Schalk, G., et al. (2005). Patients with ALS can use sensorimotor rhythms to operate a brain-computer interface. *Neurology* 64, 1775–1777. doi: 10.1212/01.WNL.0000158616.43002.6D

Leuthardt, E. C., Schalk, G., Wolpaw, J. R., Ojemann, J. G., and Moran, D. W. (2004). A brain–computer interface using electrocorticographic signals in humans. *J. Neural Eng.* 1, 63–71. doi: 10.1088/1741-2560/1/2/001

Mai, R., Facchetti, D., Micheli, A., and Poloni, M. (1998). Quantitative electroencephalography in amyotrophic lateral sclerosis. *Electroencephalogr. Clin. Neurophysiol.* 106, 383–386. doi: 10.1016/S0013-4694(97)00159-154

Maležič, T., Koritnik, B., Zidar, I., and Zidar, J. (2016). ID 339 – increases and decreases of power of EEG mu rhythm in patients with amyotrophic lateral sclerosis. *Clin. Neurophysiol.* 127:e92. doi: 10.1016/j.clinph.2015.11.309

Markand, O. N. (1976). Electroencephalogram in "locked-in" syndrome. *Electroencephalogr. Clin. Neurophysiol.* 40, 529–534. doi: 10.1016/0013-4694(76)90083-90083

McCarthy, M. M., Moore-Kochlacs, C., Gu, X., Boyden, E. S., Han, X., and Kopell, N. (2011). Striatal origin of the pathologic beta oscillations in Parkinson's disease. *Proc. Natl. Acad. Sci. U.S.A.* 108, 11620–11625. doi: 10.1073/pnas.1107748108

Milekovic, T., Sarma, A. A., Bacher, D., Simeral, J. D., Saab, J., Pandarinath, C., et al. (2018). Stable long-term BCI-enabled communication in ALS and locked-in syndrome using LFP signals. *J. Neurophysiol.* 120, 343–360. doi: 10.1152/jn.00493.2017

Miller, K. J., Hermes, D., Honey, C. J., Hebb, A. O., Ramsey, N. F., Knight, R. T., et al. (2012). Human motor cortical activity is selectively phase-entrained on underlying rhythms. *PLoS Comput. Biol.* 8:e1002655. doi: 10.1371/journal.pcbi.1002655

Miller, K. J., Leuthardt, E. C., Schalk, G., Rao, R. P. N., Anderson, N. R., Moran, D. W., et al. (2007). Spectral changes in cortical surface potentials during motor movement. *J. Neurosci.* 27, 2424–2432. doi: 10.1523/JNEUROSCI.3886-06.2007

Miller, K. J., Schalk, G., Fetz, E. E., Nijs, M., den Ojemann, J. G., and Rao, R. P. N. (2010). Cortical activity during motor execution, motor imagery, and imagery-based online feedback. *Proc. Natl. Acad. Sci. U.S.A.* 107, 4430–4435. doi: 10.1073/pnas.0913697107

Miller, K. J., Zanos, S., Fetz, E. E., den Nijs, M., and Ojemann, J. G. (2009). Decoupling the cortical power spectrum reveals real-time representation of individual finger movements in humans. *J. Neurosci.* 29, 3132–3137. doi: 10.1523/JNEUROSCI.5506-08.2009

Mollink, J., van Baarsen, K. M., Dederen, P. J. W. C., Foxley, S., Miller, K. L., Jbabdi, S., et al. (2016). Dentatorubrothalamic tract localization with postmortem MR diffusion tractography compared to histological 3D reconstruction. *Brain Struct. Funct.* 221, 3487–3501. doi: 10.1007/s00429-015-1115-1117

Nakanishi, Y., Yanagisawa, T., Shin, D., Chen, C., Kambara, H., Yoshimura, N., et al. (2014). Decoding fingertip trajectory from electrocorticographic signals in humans. *Neurosci. Res.* 85, 20–27. doi: 10.1016/j.neures.2014.05.005

Neuper, C., Müller, G. R., Kübler, A., Birbaumer, N., and Pfurtscheller, G. (2003). Clinical application of an EEG-based brain–computer interface: a case study in a patient with severe motor impairment. *Clin. Neurophysiol.* 114, 399–409. doi: 10.1016/S1388-2457(02)00387-385

Neuper, C., and Pfurtscheller, G. (2001). Event-related dynamics of cortical rhythms: frequency-specific features and functional correlates. *Int. J. Psychophysiol.* 43, 41–58. doi: 10.1016/S0167-8760(01)00178-177

Patterson, J. R., and Grabois, M. (1986). Locked-in syndrome: a review of 139 cases. *Stroke* 17, 758–764. doi: 10.1161/01.str.17.4.758

Pels, E. G. M., Aarnoutse, E. J., Leinders, S., Freudenburg, Z. V., Branco, M. P., van der Vijgh, B. H., et al. (2019). Stability of a chronic implanted brain-computer interface in late-stage amyotrophic lateral sclerosis. *Clin. Neurophysiol.* 130, 1798–1803. doi: 10.1016/j.clinph.2019.07.020

Pels, E. G. M., Aarnoutse, E. J., Ramsey, N. F., and Vansteensel, M. J. (2017). Estimated prevalence of the target population for brain-computer interface neurotechnology in the Netherlands. *Neurorehabil. Neural Repair* 31, 677–685. doi: 10.1177/1545968317714577

Perge, J. A., Zhang, S., Malik, W. Q., Homer, M. L., Cash, S., Friehs, G., et al. (2014). Reliability of directional information in unsorted spikes and local field potentials recorded in human motor cortex. *J. Neural Eng.* 11:046007. doi: 10.1088/1741-2560/11/4/046007

Pfurtscheller, G. (1981). Central beta rhythm during sensorimotor activities in man. *Electroencephalogr. Clin. Neurophysiol.* 51, 253–264. doi: 10.1016/0013-4694(81)90139-90135

Pfurtscheller, G., Stancák, A., and Neuper, C. (1996). Post-movement beta synchronization. A correlate of an idling motor area? *Electroencephalogr. Clin. Neurophysiol.* 98, 281–293. doi: 10.1016/0013-4694(95)00258-258

Proudfoot, M., Rohenkohl, G., Quinn, A., Colclough, G. L., Wuu, J., Talbot, K., et al. (2017). Altered cortical beta-band oscillations reflect motor system degeneration in amyotrophic lateral sclerosis. *Hum. Brain Mapp.* 38, 237–254. doi: 10.1002/hbm.23357

Riva, N., Falini, A., Inuggi, A., Gonzalez-Rosa, J. J., Amadio, S., Cerri, F., et al. (2012). Cortical activation to voluntary movement in amyotrophic lateral sclerosis is related to corticospinal damage: electrophysiological evidence. *Clin. Neurophysiol.* 123, 1586–1592. doi: 10.1016/j.clinph.2011.12.013

Rouse, A. G., Stanslaski, S. R., Cong, P., Jensen, R. M., Afshar, P., Ullestad, D., et al. (2011). A chronic generalized bi-directional brain–machine interface. *J. Neural Eng.* 8:036018. doi: 10.1088/1741-2560/8/3/036018

Salmi, J., Pallesen, K. J., Neuvonen, T., Brattico, E., Korvenoja, A., Salonen, O., et al. (2009). Cognitive and motor loops of the human cerebro-cerebellar system. *J. Cogn. Neurosci.* 22, 2663–2676. doi: 10.1162/jocn.2009.21382

Santhosh, J., Bhatia, M., Sahu, S., and Anand, S. (2005). Decreased electroencephalogram alpha band [8-13 Hz] power in amyotrophic lateral sclerosis patients: a study of alpha activity in an awake relaxed state. *Neurol. India* 53:99. doi: 10.4103/0028-3886.15071

Schalk, G., Kubánek, J., Miller, K. J., Anderson, N. R., Leuthardt, E. C., Ojemann, J. G., et al. (2007). Decoding two-dimensional movement trajectories using electrocorticographic signals in humans. *J. Neural Eng.* 4, 264–275. doi: 10.1088/1741-2560/4/3/012

Schalk, G., and Leuthardt, E. C. (2011). Brain-computer interfaces using electrocorticographic signals. *IEEE Rev. Biomed. Eng.* 4, 140–154. doi: 10.1109/RBME.2011.2172408

Schalk, G., McFarland, D. J., Hinterberger, T., Birbaumer, N., and Wolpaw, J. R. (2004). BCI2000: a general-purpose brain-computer interface (BCI) system. *IEEE Trans. Biomed. Eng.* 51, 1034–1043. doi: 10.1109/TBME.2004.827072

Scherer, R., Schloegl, A., Lee, F., Bischof, H., Janša, J., and Pfurtscheller, G. (2007). The self-paced graz brain-computer interface: methods and applications. *Comput. Intell. Neurosci.* 2007:79826. doi: 10.1155/2007/79826

Shimamoto, S. A., Larson, P. S., Ostrem, J. L., Glass, G. A., Turner, R. S., and Starr, P. A. (2010). Physiological identification of the human pedunculopontine nucleus. *J. Neurol. Neurosurg. Psychiatry* 81, 80–86. doi: 10.1136/jnnp.2009.179069

Slutzky, M. W., Jordan, L. R., Krieg, T., Chen, M., Mogul, D. J., and Miller, L. E. (2010). Optimal spacing of surface electrode arrays for brain–machine interface applications. *J. Neural Eng.* 7:026004. doi: 10.1088/1741-2560/7/2/026004

Thomas, E., Fruitet, J., and Clerc, M. (2013). Combining ERD and ERS features to create a system-paced BCI. *J. Neurosci. Methods* 216, 96–103. doi: 10.1016/j.jneumeth.2013.03.026

Vansteensel, M. J., Pels, E. G. M., Bleichner, M. G., Branco, M. P., Denison, T., Freudenburg, Z. V., et al. (2016). Fully implanted brain–computer interface in a locked-in patient with ALS. *N. Engl. J. Med.* 375, 2060–2066. doi: 10.1056/NEJMoa1608085

Wen, H., and Liu, Z. (2016). Separating fractal and oscillatory components in the power spectrum of neurophysiological signal. *Brain Topogr.* 29, 13–26. doi: 10.1007/s10548-015-0448-440

Wolpaw, J. R., Flotzinger, D., Pfurtscheller, G., and McFarland, D. J. (1997). Timing of EEG-based cursor control. *J. Clin. Neurophysiol. Off. Publ. Am. Electroencephalogr. Soc.* 14, 529–538. doi: 10.1097/00004691-199711000-00010

Wolpaw, J. R., McFarland, D. J., and Vaughan, T. M. (2000). Brain-computer interface research at the wadsworth center. *IEEE Trans. Rehabil. Eng.* 8, 222–226. doi: 10.1109/86.847823

World Medical Association (2013). World Medical Association Declaration of Helsinki: ethical principles for medical research involving human subjects. *JAMA* 310, 2191–2194. doi: 10.1001/jama.2013.281053

Yanagisawa, T., Yamashita, O., Hirata, M., Kishima, H., Saitoh, Y., Goto, T., et al. (2012). Regulation of motor representation by phase–amplitude coupling in the sensorimotor cortex. *J. Neurosci.* 32, 15467–15475. doi: 10.1523/JNEUROSCI.2929-12.2012

Conflict of Interest: TD was an employee of Medtronic Inc., which co-sponsored the STW-grant. He is a shareholder of Medtronic and holds patents related to patient directed therapy control (8,380,314), a chopper-stabilized instrumentation amplifier (8,354,881), and a therapy control based on a patient movement state (8,121,694), all licensed to Medtronic.

The remaining authors declare that the research was conducted in the absence of any commercial or financial relationships that could be construed as a potential conflict of interest.

frontiers in Neuroscience

ORIGINAL RESEARCH
published: 22 November 2019
doi: 10.3389/fnins.2019.01267

Generating Natural, Intelligible Speech From Brain Activity in Motor, Premotor, and Inferior Frontal Cortices

Christian Herff[1,2*], *Lorenz Diener*[2], *Miguel Angrick*[2], *Emily Mugler*[3], *Matthew C. Tate*[4], *Matthew A. Goldrick*[5], *Dean J. Krusienski*[6], *Marc W. Slutzky*[3,7,8†] *and Tanja Schultz*[2†]

[1] School of Mental Health & Neuroscience, Maastricht University, Maastricht, Netherlands, [2] Cognitive Systems Lab, University of Bremen, Bremen, Germany, [3] Department of Neurology, Northwestern University, Chicago, IL, United States, [4] Department of Neurosurgery, Northwestern University, Chicago, IL, United States, [5] Department of Linguistics, Northwestern University, Chicago, IL, United States, [6] Biomedical Engineering Department, Virginia Commonwealth University, Richmond, VA, United States, [7] Department of Physiology, Northwestern University, Chicago, IL, United States, [8] Department of Physical Medicine & Rehabilitation, Northwestern University, Chicago, IL, United States

OPEN ACCESS

Edited by:
Christoph Guger,
g.tec Medical Engineering GmbH, Austria

Reviewed by:
Peter Brunner,
Albany Medical College, United States
Vikash Gilja,
University of California, San Diego, United States

***Correspondence:**
Christian Herff
c.herff@maastrichtuniversity.nl

[†] These authors have contributed equally to this work

Specialty section:
This article was submitted to Neuroprosthetics, a section of the journal Frontiers in Neuroscience

Received: 03 May 2019
Accepted: 07 November 2019
Published: 22 November 2019

Citation:
Herff C, Diener L, Angrick M, Mugler E, Tate MC, Goldrick MA, Krusienski DJ, Slutzky MW and Schultz T (2019) Generating Natural, Intelligible Speech From Brain Activity in Motor, Premotor, and Inferior Frontal Cortices. Front. Neurosci. 13:1267. doi: 10.3389/fnins.2019.01267

Neural interfaces that directly produce intelligible speech from brain activity would allow people with severe impairment from neurological disorders to communicate more naturally. Here, we record neural population activity in motor, premotor and inferior frontal cortices during speech production using electrocorticography (ECoG) and show that ECoG signals alone can be used to generate intelligible speech output that can preserve conversational cues. To produce speech directly from neural data, we adapted a method from the field of speech synthesis called unit selection, in which units of speech are concatenated to form audible output. In our approach, which we call *Brain-To-Speech*, we chose subsequent units of speech based on the measured ECoG activity to generate audio waveforms directly from the neural recordings. *Brain-To-Speech* employed the user's own voice to generate speech that sounded very natural and included features such as prosody and accentuation. By investigating the brain areas involved in speech production separately, we found that speech motor cortex provided more information for the reconstruction process than the other cortical areas.

Keywords: ECoG, BCI, brain-computer interface, speech, synthesis, brain-to-speech

INTRODUCTION

Brain-computer interfaces (BCIs; Wolpaw et al., 2002) that process natural speech present a very intuitive paradigm for direct machine-mediated human communication and have the potential to restore intuitive communication for people unable to speak due to paralysis. In recent years, impressive advances in the decoding of speech processes from neural signals have been achieved. Electrocorticographic (ECoG) signals recorded from the cortical surface are well-suited for this purpose due to the broad coverage of multiple cortical areas (Herff and Schultz, 2016). Using ECoG, laryngeal activity (Dichter et al., 2018), phonetic features (Mesgarani et al., 2014; Lotte et al., 2015), articulatory gestures (Chartier et al., 2018; Mugler et al., 2018), phonemes (Mugler et al., 2014; Ramsey et al., 2017), words (Kellis et al., 2010; Milsap et al., 2019), and continuous sentences (Herff et al., 2015; Moses et al., 2016, 2018) have been investigated. To provide speech-impaired patients

with the full expressive power of speech, it is crucial to include acoustic, prosodic, and linguistic cues. These cues include, but are not limited to, pitch (intonation), timing, stress, emphasis, and pauses, which are required to discriminate statements from questions, differentiate words and meaning, carry emotions, and to convey humor and sarcasm, to name only a few. Furthermore, the decoding of sentences or words into textual representations always introduces a delay of at least the length of the smallest recognizable speech unit, which could potentially lead to severe articulatory disturbances (Stuart et al., 2002) when playing back the delayed audible feedback to the user. In contrast, the direct conversion of brain activity into audible speech can enable natural conversation, as it can provide rapid auditory feedback.

The speech production process has been widely studied (Tian and Poeppel, 2010; Tourville and Guenther, 2011; Hickok, 2012), and while it is not fully understood, a number of brain areas are known to be involved at the level of producing articulation. These areas include the inferior frontal gyrus (Okada et al., 2018), the pre-motor cortex (Glanz et al., 2018), and the speech motor cortex (Bouchard et al., 2013; Ramsey et al., 2017). Other areas such as superior temporal gyrus also show activity during speech production (Kubanek et al., 2013; Brumberg et al., 2016), but it is unclear whether these areas are involved in articulatory or semantic processing.

Previous studies have reconstructed perceived audio from ECoG (Pasley et al., 2012) and spectrotemporal modulations of real-life sounds from fMRI (Santoro et al., 2017). Martin et al. reconstructed spectrotemporal features of speech from speech production and perception areas (Martin et al., 2014), but did not synthesize audio waveforms from these features. Akbari and colleagues extended these findings and synthesized high quality audio from cortical areas involved in speech perception using Deep Neural Networks (Akbari et al., 2019). In an online study in motor-intact patients, Leuthardt and colleagues demonstrated one-dimensional cursor control using ECoG activity during the production of two isolated phonemes (Leuthardt et al., 2011). The first study presenting real-time, closed-loop synthesis of speech from cortical spikes in a paralyzed patient demonstrated accurate reconstruction of formant frequencies in attempted vowel production (Guenther et al., 2009) and thereby laid the foundations for speech neuroprostheses.

Recently, two different approaches synthesizing speech from neural activity during speech production have been presented. Both achieve very high quality audio by employing deep neural networks and an intermediate representation of speech, one study uses articulatory representations of the speech production process (Anumanchipalli et al., 2019), which are then transformed into audio output, the other (performed on the same dataset as this study) transforms the neural recordings to a spectral representation first, which is then transformed to an audio waveform with a second neural network (Angrick et al., 2019).

Here, we present an alternative approach which directly reconstructs intelligible, naturalistic speech (that is, speech with prosody and accentuation) from speech-related motor cortical activity using a very simple pattern matching approach from the speech synthesis community. The presented approach is simple to implement, requires little training data, is real-time ready, and does not require the design of deep learning architectures.

MATERIALS AND METHODS

Experiment Design

Participants in our study were asked to read words shown to them on a computer screen aloud (**Figure 1**). Most presented words were monosyllabic and followed a consonant-vowel-consonant (CVC) structure. This set of words primarily comprised of the Modified Rhyme Test presented in House et al. (1963) and supplemented with additional words to better reflect the phoneme distribution of American English (Mines et al., 1978). Words were displayed one at a time at rate of one word every 2 s in a randomized order. Participants read between 244 and 372 words resulting in 8.3 to 11.7 min of recordings each. **Table 1** summarizes recording length (in seconds) and number of repeated words for all participants. The data used in this study were also used in Mugler et al. (2018) and Angrick et al. (2019).

Participants

Patients undergoing awake craniotomy with cortical stimulation and recording as part of normal clinical care were selected for enrollment. All participants gave written informed consent to participate in the study prior to surgery. The study design was approved by the Institutional Review Board of Northwestern University. We recorded ECoG activity from six patients (1 female, 55.5 $\pm$ 10.1 yo) undergoing awake craniotomies for glioma resection. Tumors locations lay at least two gyri (2–3 cm) away from the recording sites. All participants were native English speakers.

Cortical Mapping

All participants were implanted with grids on the left hemisphere. The experimental grids were specifically placed to cover areas involved in the speech production process. Electrode grids were placed based on functional responses to cortical stimulation and on anatomical mapping. Final locations were confirmed using intraoperative navigation software (Brainlab), preoperative MRI, and intraoperative photography (Hermes et al., 2010).

To map the eloquent cortex, electrocortical stimulation was used. Areas producing speech or anomia arrest during stimulation were labeled as language associated, while areas producing movement of tongue and articulators during stimulation were labeled as functional speech motor areas.

Grid locations were different for each participants based on craniotomy location but always covered targeted areas of ventral motor cortex (M1v), premotor cortex (PMv), and inferior frontal gyrus pars opercularis (IFG). Since there is no clear cytoarchitectural difference between M1v and PMv, we defined PMv as the anterior half of the precentral gyrus and M1v as the posterior half of the precentral gyrus. **Table 1** provides information about the number of electrodes in each specific region for each participant. Grid locations for our six participants can be found in **Figure 2**.

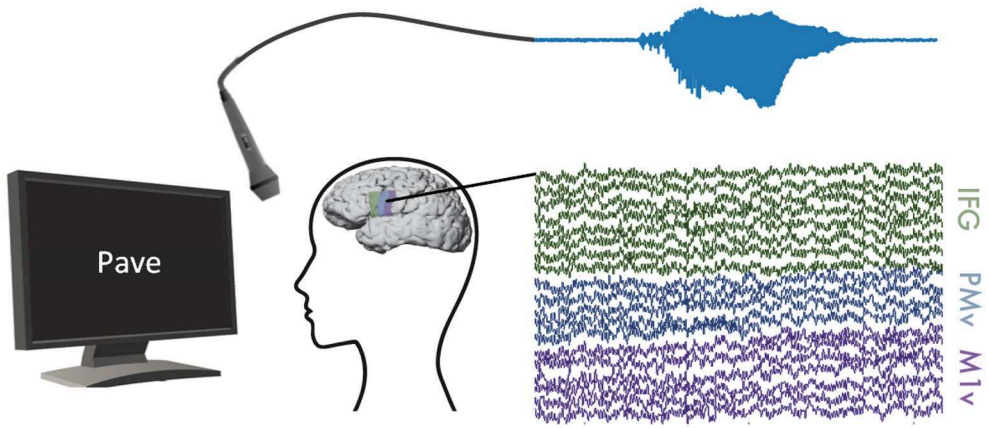

FIGURE 1 | Experimental Setup: ECoG and audible speech (light blue) were measured simultaneously while participants read words shown on a computer screen. We recorded ECoG data on inferior frontal (green), premotor (blue), and motor (purple) cortices.

TABLE 1 | Participant demographics and electrode information.

Participant	#Words	Recording time (s)	#IFG	#PMv	#M1v
1	368	752.8	12	19	18
2	370	761.7	8	15	19
3	249	509.2	16	21	20
4	249	571.5	11	29	18
5	244	499.2	0	19	19
6	372	760.8	15	18	12

Data Recording

We recorded ECoG using an 8 x 8, 64-channel electrode grid (Integra, 4 mm spacing) and a Neuroport data acquisition system (Blackrock Microsystems, Inc.). ECoG data was sampled at 2 kHz and bandpass-filtered between 0.5 and 300 Hz.

Audio data was recorded in parallel using a unidirectional lapel microphone (Sennheiser) and wirelessly transmitted to a recording station (Califone). Audio data was sampled at 48 kHz. Stimulus presentation and synchronous data recording was facilitated using BCI2000 (Schalk et al., 2004).

ECoG Signal Processing

To extract meaningful information from the recorded ECoG activity, we extracted logarithmic high-gamma power. The gamma-band is known to reflect ensemble spiking (Ray et al., 2008) and contain localized information for motor (Miller et al., 2007) and speech (Crone et al., 2001; Leuthardt et al., 2012) tasks. To remove slow drifts in the data, we first applied linear detrending to the raw ECoG data. The signal was then downsampled from 2 kHz to 600 Hz to reduce dataset size. We then forward-backward filtered the signals of all 64 electrodes using elliptic IIR low-pass (170 Hz cut-off, filter order 14) and high-pass (70 Hz cut-off, filter order 13) filters to represent the high-gamma band. To reduce the first harmonic of the 60 Hz line noise, we applied an elliptic IIR notch filter (118–122 Hz, filter order 13). Logarithmic high-gamma power was calculated by taking the logarithm of the squared signal. As the speech production process includes complex temporal dynamics (Sahin et al., 2009; Brumberg et al., 2016), a 450 ms long window centered on the current sample was considered and downsampled to 20 Hz. The resulting matrix of 64 channels $\times$ 9 time points was flattened to form a feature vector of 64 channels $\times$ 9 time points $=$ 576 features. Extracted features were normalized to zero mean and unit variance. To capture the fast dynamics of speech, a new feature vector was extracted every 10 ms. We generated speech using either all 64 electrodes or the electrodes from individual areas separately (IFG, PMv and M1v, mean of 12.4, 20.2 and 17.7 electrodes, respectively).

Audio Signal Processing

We downsampled the recorded audio data to 16 kHz and extracted raw waveforms in 150 ms windows centered on the corresponding frame of ECoG data. Windows were extracted with a 10 ms frameshift to maintain alignment to the intervals of neural activity. We extracted the 150 ms long windows using Hanning window functions to guarantee smooth transitions (Wu et al., 2013) even with the large overlap between neighboring windows. Each of these 150 ms windows of raw audio data were considered as one speech unit in our decoding approach. Due to the long speech unit size in combination with the windowing function, no problems with pitch synchronization arise, so more complex approaches such as pitch-synchronous overlap-add (PSOLA, Moulines and Charpentier, 1990) provided no increase in reconstruction quality. The shorter speech unit length in the audio data, as compared to the high-gamma windows, was chosen as it provides a good compromise between smoothness of output and capability to capture the fast dynamics of speech. The direct mapping between speech units and corresponding high-gamma windows is necessary for our reconstruction approach.

Decoding Approach

We reconstructed natural audio from the measured ECoG activity by applying a technique from the speech synthesis community called unit selection (Hunt and Black, 1996). Unit selection was originally used in text-to-speech (TTS) synthesis of

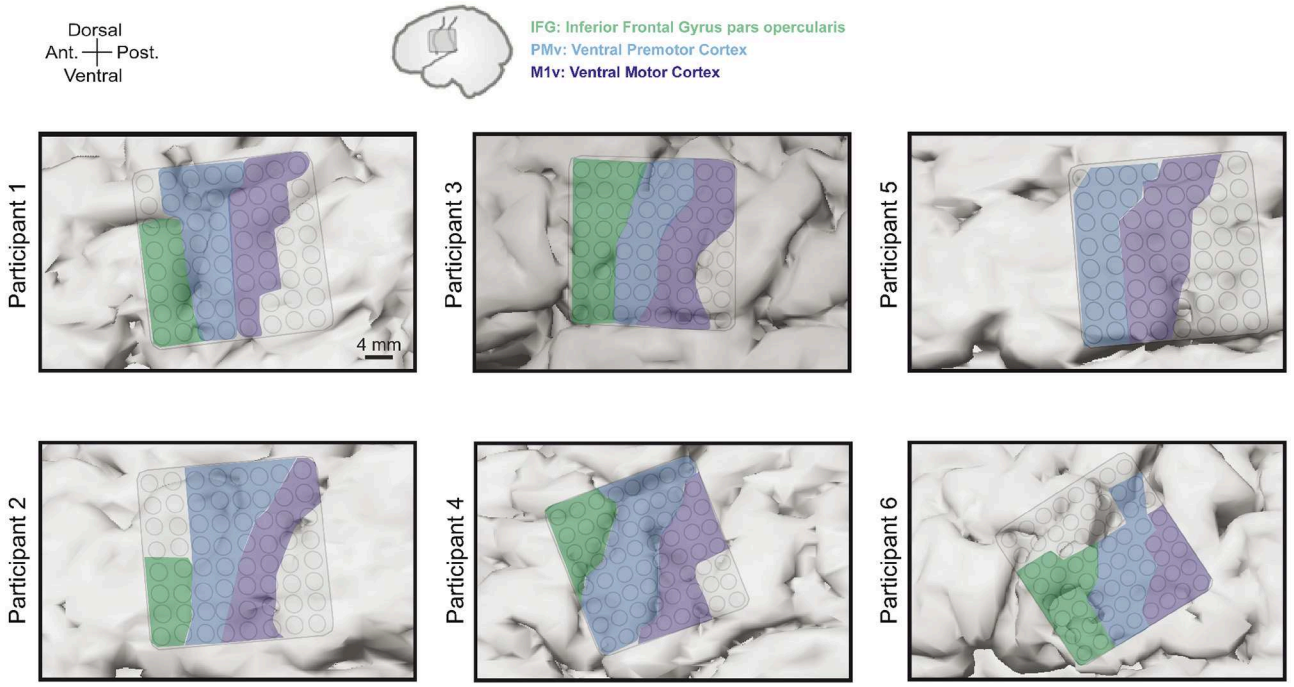

FIGURE 2 | Electrode grid positions for all six participants. Grids always covered areas in inferior frontal gyrus pars opercularis (IFG, green), ventral premotor cortex (PMv, blue), and ventral motor cortex (M1v, purple).

audio waveforms and relies on selecting and concatenating well-fitting units of speech from a large training database of speech units. The same approach was later used for voice conversion (Sundermann et al., 2006), where speech of one person is transformed to the voice of another speaker. Further extending upon this idea, unit selection was used in electromyography (EMG)-based silent speech interfaces (Zahner et al., 2014), where facial muscle movements are transformed into an audio waveform. The same approach can also be applied to other types of silent speech interfaces (Schultz et al., 2017). In all unit selection approaches, the next speech unit to concatenate to the output is chosen based on two different cost terms. The first one is how well the speech unit fits the current input, being the current phoneme in TTS or the current frame of EMG activity. This cost term is referred to as the *target cost*. The second cost function estimates how well the speech unit fits the previously selected speech units and is usually referred to as *concatenation cost*. Optimizing both cost functions together requires an iterative algorithm such as Viterbi decoding (Lou, 1995). Unit selection is known to perform well for small amounts of data, as is the case in our study. Limited datasets might not be sufficient to train more complex models with many free parameters.

In our decoding approach, we used unit selection to select the best fitting unit of speech, based on the high-gamma ECoG feature vectors (**Figure 3**). Our speech units were 150 ms intervals of plain audio waveforms extracted using a Hanning window function. To make sure that we selected speech units based only on the neural data and do not include any semantic information, we disregarded the *concatenation cost* for this proof-of-concept study. This speeds up the decoding process as new speech units can be selected based only on the current frame of high-gamma activity. Additionally, this allowed us to reformulate the selection approach as a maximization problem to find the ECoG feature vector $\hat{B}$ in the training data, that has the highest similarity with the current feature vector A:

$$\hat{B} = \arg\max_{B}\{\mathbf{similarity}(\mathbf{A}, \mathbf{B})\} \quad (1)$$

As ECoG data and audio data are aligned, the corresponding speech unit to $\hat{B}$, from the training data, could then be selected. **Figure 3** explains the decoding process: For each window of high-gamma power in the test data (top right), the cosine similarity with every window in the training data (bottom center) was computed. For the training data window A of high-gamma power with the highest cosine similarity to the test window $\hat{B}$, the corresponding speech unit of audio data in the training data (top center) was chosen. This process is repeated for all intervals in the test data. The chosen speech units (top right) were combined to form the generated speech (bottom right). The strongly overlapping audio data were combined by simply adding the waveforms; the Hanning windowing ensures that the resulting output is smooth. This approach is agnostic to categories of speech, such as phones, or any syntactic and semantic knowledge. It simply chooses the best fitting speech unit out of over 50,000 units (500 s / 0.01 s frameshift) instead of choosing a generalized representation, such as a phoneme or even word. This way, the speech unit with the best matching prosody and accentuation is

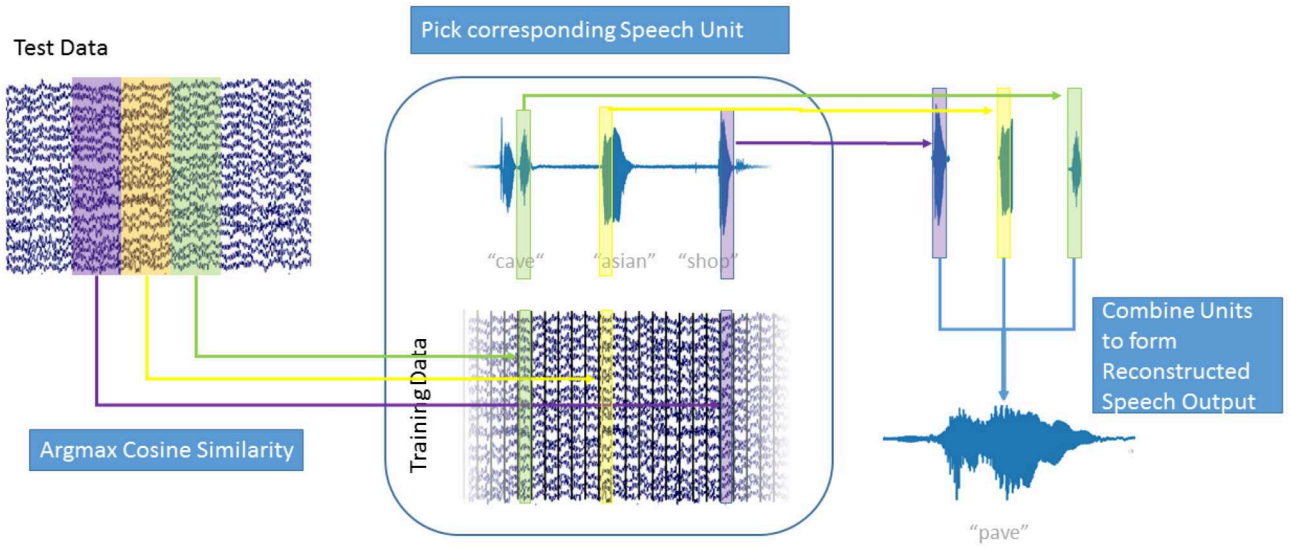

FIGURE 3 | Speech Generation Approach: For each window of high gamma activity in the test data (top left), the cosine similarity to each window in the training data (center bottom) was computed. The window in the training data that maximized the cosine similarity was determined and the corresponding speech unit (center top) was selected. The resulting overlapping speech units (top right) were combined using Hanning windows to form the generated speech output (bottom right). Also see **Supplementary Video 1**.

chosen and no labeling of the data with regards to phonemes, or words is used or necessary. As our approach concatenates units of natural speech, it conserves the spectrotemporal dynamics of human speech.

This decoding approach can be likened to a very simple pattern matching approach or nearest-neighbor regression, but provided superior results than more complex approaches for our limited dataset size.

While a number of different similarity measures can be used, we applied the cosine similarity that has proven to provide good results in a number of document clustering (Steinbach et al., 2000) and computer vision applications (Nguyen and Bai, 2010). The cosine similarity between vectors A and B is defined as :

$$\textbf{similarity}(\mathbf{A},\mathbf{B}) = \frac{\mathbf{A}\cdot\mathbf{B}}{\|\mathbf{A}\|\|\mathbf{B}\|} = \frac{\sum_{i=1}^{n} A_i B_i}{\sqrt{\sum_{i=1}^{n} A_i^2}\sqrt{\sum_{i=1}^{n} B_i^2}}$$

The cosine similarity is invariant to gamma scaling, only the power distribution between electrodes influences the similarity score. By precomputing the Euclidean norm $\|\mathbf{B}\| = \sqrt{\sum_{i=1}^{n} B_i^2}$ for all feature vectors in the training data, the cosine similarity can be computed fast enough on standard hardware to allow for real-time decoding for our data set sizes. This can be further sped up by clustering speech units together (Black and Taylor, 1997) resulting in fewer comparisons necessary. Once the high-gamma feature vector with the highest cosine similarity $\hat{B}$ was found, the corresponding speech unit in its original waveform was concatenated to the reconstructed output.

We applied our unit selection approach in a 5-fold cross-validation manner in which in each iteration 80% of the data were used as training data and the remaining 20% as testing data until all data were used as the test set exactly once. The set of spoken words in training and test set were always disjoint. To reduce the feature space, we used principal component analysis to select principal components that explain at least 70% of the total variance in the ECoG training data. The same feature space compression was than applied to the testing data, as well. This approach selected 108.1 $\pm$ 36.3 components for all electrodes, 15.9 $\pm$ 9.7 for IFG, 44 $\pm$ 15.5 for PMv, and 41.53 $\pm$ 6.8 for M1v.

Randomization Tests

To establish a baseline for our decoding approach, we used a randomization approach. Instead of using the speech unit corresponding to the high-gamma feature vector with the highest cosine similarity, we picked a random speech unit in the randomization condition. We combined the speech units in the same manner as the real decoding approach. We repeated this approach 1,000 times for each participant to establish a baseline of randomized reconstruction. We denoted the maximum of these randomizations as chance level in **Figure 6B**.

Correlation Analysis

To compare original and reconstructed audio waveforms, we transformed the waveforms into the spectral domain. This was done in 50 ms windows with 10 ms overlap. To only judge the frequency information that is important to human listeners, we transformed the magnitude spectrograms onto the mel-scale (Stevens et al., 1937) using 40 overlapping triangular filter banks. A logarithm was then applied to bring the distribution of spectral coefficients closer to a normal distribution. Pearson

correlation coefficients were then computed between the original and reconstruction for each logarithmic mel-scaled coefficient. We calculated the correlations for each word individually. Significance levels are established if resulting correlations were larger than 95, 99, or 99.9% of the randomized controls, respectively.

Averaging over all 40 logarithmic mel-scaled coefficients we can look at overall correlation coefficients for the reconstruction for each of the participants. **Figure 6A** shows correlation coefficient for all participants using all electrodes, only IFG electrodes, only PMv electrodes and only M1v electrodes.

Listening Tests

To evaluate the intelligibility of our synthesized audio, we conducted an online forced-choice listening test with 55 (15 female) healthy volunteers. In the test, volunteers heard the 30 synthesized words with the highest spectral correlations and were given four options, the correct answer plus three distractors, to choose from. Volunteers had to pick the option which they thought the synthesized audio resembled the most. One of the four answers always needed to be selected (forced-choice). Distractor words were chosen randomly from the complete set of words used in our study, resulting in similar word length (as most words follow the CVC structure) and similar distribution of phonemes. Word order and the order of the options was randomized for each volunteer individually. We used the beagleJS framework (Kraft and Zölzer, 2014) to build our listening test.

After the listening test, we asked the volunteers to give information about their gender (15 female, 40 male), age (34.9 ± 14.1) and whether they were English native speakers (27 native speakers).

All volunteers achieved accuracies well above chance level in identification of the correct word ($66.1\% \pm 6\%$) with relative low variance. These results show that our approach is very promising to generate natural, intelligible output for future voice prosthesis from neural data.

Objective Intelligibility Measure

In addition to the subjective listening tests, we calculated an objective intelligibility measure, namely the short-term objective intelligibility (STOI) measure (Taal et al., 2011) that is known to correlate well with subjective intelligibility. The STOI employs simple discrete Fourier transformation-based Time-frequency-decomposition. The STOI score (ranging from 0 to 1) can be mapped to an subjective intelligibility probability d in a transcription intelligibility test ($\rho = 0.95$). Taal et al. (2011) provides the formula:

$$STOI = \frac{100}{1 + exp(ad + b)}$$

with $a = -13.1903$ and $b = 6.5192$. Reformulating this, we can estimate the subjective intelligibility probability d in a transcription intelligibility test given the calculated *STOI* with:

$$d = \frac{\log_e(\frac{100}{STOI} - 1) - b}{a}$$

Objective measures of intelligibility, as well as spectral correlations, are notoriously unreliable in judging speech synthesis output for its intelligibility, we therefore believe our listening test provides a more realistic estimation of intelligibility for our data set, but report the STOI values for completeness. As our approach does not operate in the cepstral domain, we do not report Mel Cepstral Distortion (MCD) measures, which suffer from the same limitations as correlations.

RESULTS

Brain-to-Speech Reconstructs High-Quality Audio

The *Brain-To-Speech* approach concatenates natural units of speech and is thereby capable of creating completely unseen words, without the need to define a dictionary of recognizable words. The resulting waveforms sound very natural, as the user's own voice is employed. Many of the original spectrotemporal dynamics of speech are reconstructed. **Figure 4** shows examples of generated and actual speech in audio and spectral representations. The spectral representation is only used for illustration and analysis purposes, the approach concatenated speech units in their original waveform.

We evaluated the performance of *Brain-To-Speech* for each of the six participants by computing correlations between original and generated audio spectrograms using 5-fold cross-validation. Word lists in training and test set were disjoint. Models are trained participant dependent, as brain anatomy and electrode grid locations are strongly participant dependent.

To better represent the human perception of speech, we compressed the speech spectrogram to the Mel-scale (Stevens et al., 1937) using 40 logarithmically-spaced triangular filter banks. Correlations were calculated for each mel-scaled spectral coefficient between the original and reconstruction individually and then averaged across spectral coefficients.

High correlations were achieved for all of the six participants (best participant $r = 0.574 \pm 0.088$ STD, average $r = 0.246 \pm 0.075$) when using all electrodes (**Figure 5A**). Intelligible speech was obtained for many examples. To establish chance level correlations, we conducted randomization tests. A randomized baseline was established by selecting random speech intervals instead of the best fitting speech unit and repeating this procedure 1,000 times for each participant. Correlation coefficients were higher than chance level for all participants when using all electrodes (highest randomized $r = 0.04$). Our reconstruction resulted in significantly higher than chance level correlations across all spectral coefficients (**Figure 6B**).

M1v Provides Most Information to Decoding Process

Examining the three functional areas of interest independently, all three regions achieved correlations above the level of random chance. Ventral primary motor cortex (M1v) clearly outperformed the other two regions (significant differences, paired t-test $p < 0.001$), performing almost as well as all electrodes combined ($r = 0.235 \pm 0.012$). Inferior Frontal Cortex

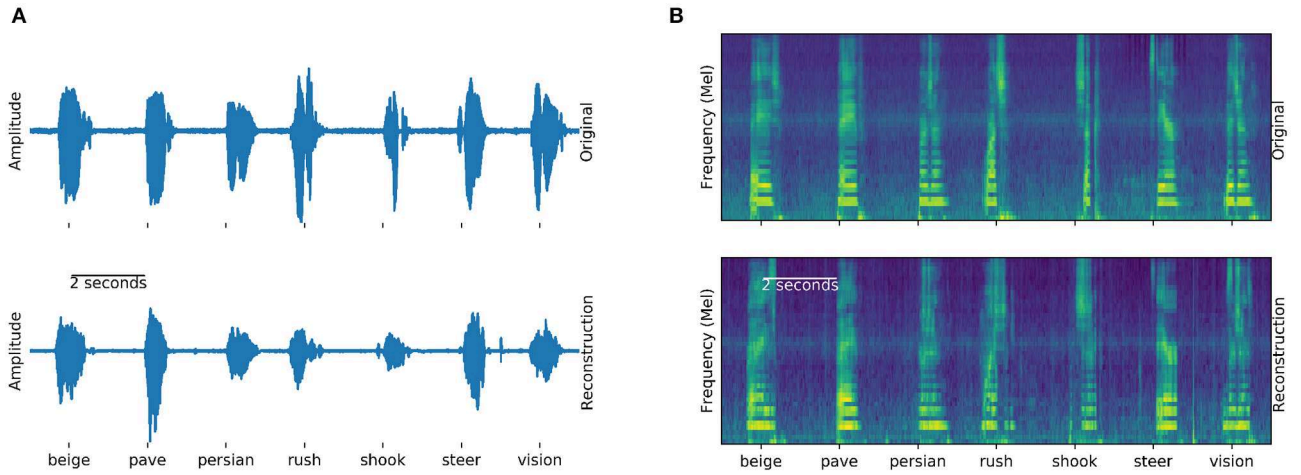

FIGURE 4 | Generation example: Examples of actual (top) and generated (bottom) audio waveforms **(A)** and spectrograms **(B)** of seven words spoken by participant 5. Similarities between the generation and actual speech are striking, especially in the spectral domain **(B)**. These generated examples can be found in the **Supplementary Audio 1**.

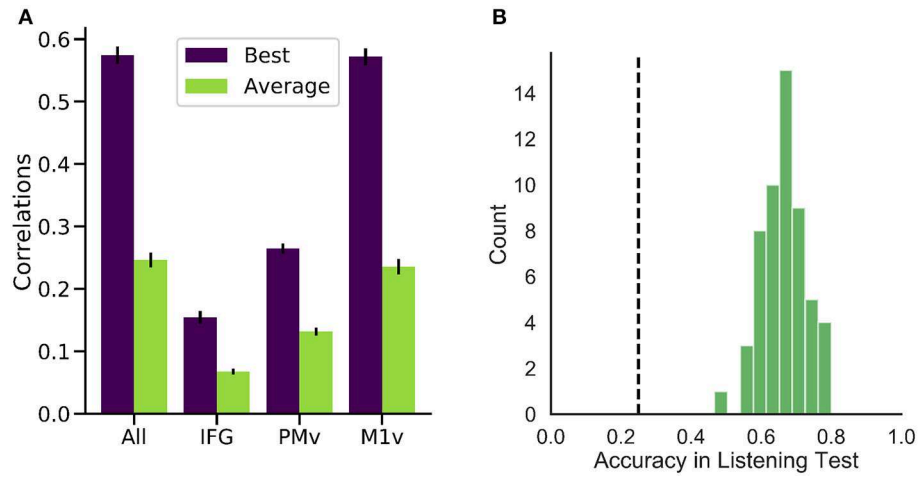

FIGURE 5 | Performance of our generation approach. **(A)** Correlation coefficients between the spectrograms of original and generated audio waveforms for the best (purple) and average (green) participant. While all regions yielded better than randomized results on average, M1v provided most information for our reconstruction process. **(B)** Results of listening test with 55 human listeners. Accuracies in the 4-option forced intelligibility test were above chance level (25%, dashed line) for all listeners.

yielded lowest results of $r = 0.067 \pm 0.004$. Activity from the premotor cortex yield an average of $r = 0.132 \pm 0.008$.

These results show that speech motor cortex (M1v) contains most information for our reconstruction approach. Comparing the correlation coefficients for each individual participant with the randomized baseline (**Figure 6A**), we can see that the reconstruction using all electrodes is significantly better than chance level ($p < 0.05$) for all participants and highly significant ($p < 0.001$) for all but one participant. The reconstruction from IFG is significantly better than randomized baseline for only two participants. Information from premotor cortex (PMv) could be used to significantly reconstruct speech from 4 participants and speech motor cortex (M1v) yielded the best results with highly significant reconstruction for all 6 participants. The results for the best participant (5) show no significant difference between using all electrodes and only using information from M1v. Given the small amount of training data, the similar levels of performance between all electrodes and only M1v could also be due to the larger feature space size in the first condition.

Reconstructed Speech Is Intelligible

To investigate the intelligibility of the *Brain-To-Speech* approach, we conducted a listening test with 55 human listeners. The listeners were presented with individual generated audio waveforms and were required to select the most likely perceived word from a list of four word options. All listeners achieved

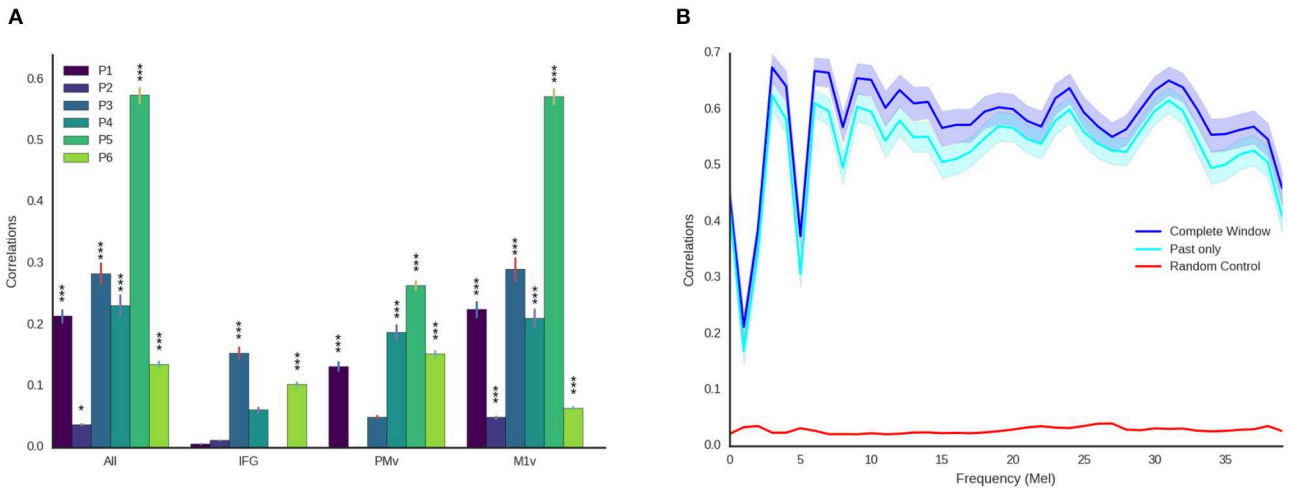

FIGURE 6 | Detailed decoding results. **(A)** Correlations between original and reconstructed spectrograms (melscaled) for all participants and electrode locations. Stars indicate significance levels (* Larger than 95% of random activations, *** Larger than 99.9% of random activations). M1v contains most information for our decoding approach. **(B)** Detailed results for best participant using all electrodes and the entire temporal context (blue) and only using activity prior to the current moment (cyan) across all frequency coefficients. Shaded areas denote 95% confidence intervals. Reconstruction is reliable across all frequency ranges and above chance level (maximum of all randomizations, red) for all frequency ranges.

well above chance level performance (25%) in this listening test (average of 66.1 $\pm$ 5.9%, **Figure 5B**).

In addition to the listening test, we calculated an objective measure of intelligibility. Our approach achieved an average Short-Term Objective intelligibility (STOI) measure (Taal et al., 2011) of 0.15, corresponding to an subjective intelligibility probability of 36%. This would mean that subjects would be able to identify the correct word in a transcription test 36% of the time. Our best participant reached a mean STOI of 0.25 corresponding to 41% intelligibility.

Approach Is Real-Time Ready

For future applications, it is important that our approach is real-time ready. While computing times for our limited dataset size are fast enough for real-time processing (less than 1ms for each new window every 10 ms), the long temporal context automatically induces an offset equivalent to the length of temporal context in the future. We therefore repeated our experiments using only ECoG features prior to the current time point (**Figure 6B**). We found that results only decreased mildly (best $r = 0.57$ for all temporal context, best $r = 0.528 \pm 0.088$ using only preceding feature vectors, **Figure 6B**) when using no information from the future. This emphasizes that our approach can be integrated into a closed-loop system, as preceding information is sufficient to reconstruct high-quality audio.

DISCUSSION

Brain-To-Speech generated speech from the user's own voice, leading to output that sounded very natural. Reconstructed audio was of high-quality and the best examples were intelligible to human listeners. Our simple approach, based on unit selection, made no assumptions about the form, syntax or even language of the reconstructed speech. It therefore should be able to reconstruct words other than the ones used in our experiment and even sentences and continuous speech. In fact, among the words that were correctly identified by all human listeners is "Persian," which does not follow the CVC structure. Nevertheless, *Brain-To-Speech* requires further testing with spontaneous, continuous speech in a closed-loop fashion. Our analyses are performed offline on previously collected data, but we show that *Brain-To-Speech* is capable of real-time processing, as information preceding the current moment is sufficient to generate high-quality audio. Comparing our results in terms of correlation coefficients to those achieved in the reconstruction of perceived speech from STG (Pasley et al., 2012), we achieve higher correlations for our best participants, but a lower mean r. However, we reconstructed articulated speech from motor areas, while Pasley et al. (2012) employed activity in auditory areas during speech perception for their approach. Martin et al. (2014) achieved higher mean correlations with their reconstruction of spectrotemporal features of speech, but lower correlations for their best participant. Their approach did not reproduce the audio waveform of the reconstruction, however. In our approach, the spectral correlations were only a secondary outcome, as we reconstructed audio waveforms directly, of which correlations were then calculated. This is distinctly different from using an approach that is directly tailored to maximize correlations.

Comparing the results of *Brain-To-Speech* to recent deep neural network based approaches (Akbari et al., 2019; Angrick et al., 2019; Anumanchipalli et al., 2019), our approach yields slightly lower correlations and STOI values, but does not require the huge computational costs of deep neural networks and is in fact fast enough for real-time processing. The formulation of our unit selection approach allows to easily integrate prior information about long term dependencies in speech

and language in the future, while not requiring bi-directional processing. This can allow the *Brain-To-Speech* approach to produce good quality output with very little data, while two of the other studies (Akbari et al., 2019; Anumanchipalli et al., 2019) used significantly more data per participant.

Primary motor cortex (M1v) provided the most informative activity for decoding speech and performed as highly as electrodes from all three cortices in our best participant. Recent studies showing robot arm control in paralyzed patients (Hochberg et al., 2006) utilize electrode arrays implanted into M1 and thereby purely relying on activity generated in attempted movement. We hope that our results are also extensible to attempted speech in patients with speech deficits. It is not surprising that M1v provided the most information about speech acoustics, given recent results showing M1v contains the most information about speech kinematics (Chartier et al., 2018; Mugler et al., 2018) and results showing that speech acoustics are highly correlated with articulation (Wang et al., 2015). Additionally, our results show that high quality speech generation can be achieved with a small number of electrodes (between 12 and 20). The rapid feedback of *Brain-To-Speech* is capable of could also enable the user to learn to operate the speech prosthesis in the future, as has been demonstrated for neural upper-limb prostheses (Hochberg et al., 2006).

The intelligibility analyses indicate that the generated speech can be intelligible to human listeners despite the fact that our synthesis approach ignores semantic and linguistic knowledge. Given more training data and the opportunity for listeners to gain more experience with perceiving the idiosyncrasies of the generation, we are confident that the *Brain-To-Speech* approach would allow a BCI to generate naturalistic speech. The inclusion of prior information is known to increase the intelligibility of unit selection approaches (Hunt and Black, 1996) and could also be beneficial to our approach. In the future, a closed-loop feedback of audible speech could put the speaker in the loop, thus giving paralyzed individuals the chance to adapt their brain activity to further improve the audio output.

LIMITATIONS

Currently, our approach relies on simultaneous recording of audible speech and ECoG activity. To adapt this approach for locked-in patients, we envision the following possibilities: Audible speech could be recorded before the patient loses the ability to speak, for example earlier in the course of a motor neuron disease. Alternatively, paralyzed patients could attempt to speak along with audio recordings of other people speaking (referred to as shadowing) and thereby generate a parallel recording of audio and brain activity data. This limitation highlights the long road toward usable BCIs based on speech processes. In the meantime, approaches based on typing activity (Pandarinath et al., 2017; Nuyujukian et al., 2018) already provide high performance communication for paralyzed patients, with an only slightly less natural paradigm.

A clear limitation of our study is the small dataset size and the intraoperative recording setup. The background noise levels and the patients' general state during an awake surgery will result in suboptimal data that are not directly transferable to the target population. However, the intraoperative setup allowed us to place the high-density grids on relevant areas for speech production and thereby investigate this process thoroughly. Longer term recordings of relevant areas, including spike recordings from intracortical arrays, are needed to bring the envisioned technology to patients. Especially recent findings of speech representations in the hand knob of the dorsal motor cortex (Stavisky et al., 2018a,b; Willett et al., 2019) might bring *Brain-To-Speech* to those in need.

Another limitation in our experimental design is the lack of control stimuli, including non-speech articulation and speech perception. The inclusion of these control stimuli in future experiments will help to identify aspects exclusive to speech production.

CONCLUSION

In conclusion, we present a simple pattern matching approach for the direct synthesis of comprehensible audible speech from cortical activity in motor, premotor and inferior frontal gyri. Our approach could restore a voice and natural means of conversation to completely paralyzed patients.

DATA AVAILABILITY STATEMENT

The raw data supporting the conclusions of this manuscript will be made available by the authors, without undue reservation, to any qualified researcher.

ETHICS STATEMENT

All participants gave written informed consent to participate in the study prior to surgery. The study design was approved by the Institutional Review Board of Northwestern University.

AUTHOR CONTRIBUTIONS

CH, LD, and MA analyzed the data. CH and TS evaluated the results. CH wrote the manuscript. EM, MT, and MS collected the data. EM, MT, MG, and MS designed the experiment. All authors commented on the manuscript.

FUNDING

CH, DK, and TS acknowledge funding by BMBF (01GQ1602) and NSF (1608140) as part of the NSF/NIH/BMBF Collaborative Research in Computational Neuroscience Program. MS acknowledges funding by the Doris Duke Charitable Foundation (Clinical Scientist Development Award, grant 2011039), a Northwestern Memorial Foundation Dixon Translational Research Award (including partial funding

from NIH National Center for Advancing Translational Sciences, UL1TR000150 and UL1TR001422), NIH grants F32DC015708 and R01NS094748, and NSF grant 1321015. EM acknowledges funding by the NIDCD (grant 1 F32 DC015708-01).

SUPPLEMENTARY MATERIAL

The Supplementary Material for this article can be found online at: https://www.frontiersin.org/articles/10.3389/fnins.2019.01267/full#supplementary-material

REFERENCES

Akbari, H., Khalighinejad, B., Herrero, J. L., Mehta, A. D., and Mesgarani, N. (2019). Towards reconstructing intelligible speech from the human auditory cortex. *Sci. Rep.* 9:874. doi: 10.1038/s41598-018-37359-z

Angrick, M., Herff, C., Mugler, E., Tate, M. C., Slutzky, M. W., Krusienski, D. J., et al. (2019). Speech synthesis from ecog using densely connected 3d convolutional neural networks. *J. Neural Eng.* 16:036019. doi: 10.1088/1741-2552/ab0c59

Anumanchipalli, G. K., Chartier, J., and Chang, E. F. (2019). Speech synthesis from neural decoding of spoken sentences. *Nature* 568, 493–498. doi: 10.1038/s41586-019-1119-1

Black, A. W., and Taylor, P. A. (1997). Automatically clustering similar units for unit selection in speech synthesis. *EUROSPEECH* (Rhodes), 601–604.

Bouchard, K. E., Mesgarani, N., Johnson, K., and Chang, E. F. (2013). Functional organization of human sensorimotor cortex for speech articulation. *Nature* 495, 327–332. doi: 10.1038/nature11911

Brumberg, J., Krusienski, D., Chakrabarti, S., Gunduz, A., Brunner, P., Ritaccio, A., et al. (2016). Spatio-temporal progression of cortical activity related to continuous overt and covert speech production in a reading task. *PLoS ONE* 11:e0166872. doi: 10.1371/journal.pone.0166872

Chartier, J., Anumanchipalli, G. K., Johnson, K., and Chang, E. F. (2018). Encoding of articulatory kinematic trajectories in human speech sensorimotor cortex. *Neuron* 98, 1042–1054. doi: 10.1016/j.neuron.2018.04.031

Crone, N. E., Boatman, D., Gordon, B., and Hao, L. (2001). Induced electrocorticographic gamma activity during auditory perception. *Clin. Neurophysiol.* 112, 565–582. doi: 10.1016/S1388-2457(00)00545-9

Dichter, B. K., Breshears, J. D., Leonard, M. K., and Chang, E. F. (2018). The control of vocal pitch in human laryngeal motor cortex. *Cell* 174, 21–31.e9. doi: 10.1016/j.cell.2018.05.016

Glanz, O., Derix, J., Kaur, R., Schulze-Bonhage, A., Auer, P., Aertsen, A., et al. (2018). Real-life speech production and perception have a shared premotor-cortical substrate. *Sci. Rep.* 8:8898. doi: 10.1038/s41598-018-26801-x

Guenther, F. H., Brumberg, J. S., Wright, E. J., Nieto-Castanon, A., Tourville, J. A., Panko, M., et al. (2009). A wireless brain-machine interface for real-time speech synthesis. *PLoS ONE* 4:e8218. doi: 10.1371/journal.pone.0008218

Herff, C., Heger, D., de Pesters, A., Telaar, D., Brunner, P., Schalk, G., et al. (2015). Brain-to-text: decoding spoken phrases from phone representations in the brain. *Front. Neurosci.* 9:217. doi: 10.3389/fnins.2015.00217

Herff, C., and Schultz, T. (2016). Automatic speech recognition from neural signals: a focused review. *Front. Neurosci.* 10:429. doi: 10.3389/fnins.2016.00429

Hermes, D., Miller, K. J., Noordmans, H. J., Vansteensel, M. J., and Ramsey, N. F. (2010). Automated electrocorticographic electrode localization on individually rendered brain surfaces. *J. Neurosci. Methods* 185, 293–298. doi: 10.1016/j.jneumeth.2009.10.005

Hickok, G. (2012). Computational neuroanatomy of speech production. *Nat. Rev. Neurosci.* 13, 135–145. doi: 10.1038/nrn3158

Hochberg, L. R., Serruya, M. D., Friehs, G. M., Mukand, J. A., Saleh, M., Caplan, A. H., et al. (2006). Neuronal ensemble control of prosthetic devices by a human with tetraplegia. *Nature* 442, 164–171. doi: 10.1038/nature04970

House, A. S., Williams, C., Hecker, M. H., and Kryter, K. D. (1963). Psychoacoustic speech tests: a modified rhyme test. *J. Acoust. Soc. Am.* 35, 1899–1899. doi: 10.21236/AD0411983

Hunt, A. J., and Black, A. W. (1996). "Unit selection in a concatenative speech synthesis system using a large speech database," in *Acoustics, Speech, and Signal Processing, 1996. ICASSP-96. Conference Proceedings., 1996 IEEE International Conference on*, Vol. 1 (Atlanta, GA: IEEE), 373–376.

Kellis, S., Miller, K., Thomson, K., Brown, R., House, P., and Greger, B. (2010). Decoding spoken words using local field potentials recorded from the cortical surface. *J. Neural Eng.* 7:056007. doi: 10.1088/1741-2560/7/5/056007

Kraft, S., and Zölzer, U. (2014). "Beaqlejs: Html5 and javascript based framework for the subjective evaluation of audio quality," in *Linux Audio Conference, Karlsruhe, DE* (Karlsruhe).

Kubanek, J., Brunner, P., Gunduz, A., Poeppel, D., and Schalk, G. (2013). The tracking of speech envelope in the human cortex. *PLoS ONE* 8:e53398. doi: 10.1371/journal.pone.0053398

Leuthardt, E., Pei, X.-M., Breshears, J., Gaona, C., Sharma, M., Freudenburg, Z., et al. (2012). Temporal evolution of gamma activity in human cortex during an overt and covert word repetition task. *Front. Hum. Neurosci.* 6:99. doi: 10.3389/fnhum.2012.00099

Leuthardt, E. C., Gaona, C., Sharma, M., Szrama, N., Roland, J., Freudenberg, Z., et al. (2011). Using the electrocorticographic speech network to control a brain–computer interface in humans. *J. Neural Eng.* 8:036004. doi: 10.1088/1741-2560/8/3/036004

Lotte, F., Brumberg, J. S., Brunner, P., Gunduz, A., Ritaccio, A. L., Guan, C., et al. (2015). Electrocorticographic representations of segmental features in continuous speech. *Front. Hum. Neurosci.* 9:97. doi: 10.3389/fnhum.2015.00097

Lou, H.-L. (1995). Implementing the viterbi algorithm. *IEEE Signal Process. Magaz.* 12, 42–52. doi: 10.1109/79.410439

Martin, S., Brunner, P., Holdgraf, C., Heinze, H.-J., Crone, N., Rieger, J., et al. (2014). Decoding spectrotemporal features of overt and covert speech from the human cortex. *Front. Neuroeng.* 7:14. doi: 10.3389/fneng.2014.00014

Mesgarani, N., Cheung, C., Johnson, K., and Chang, E. F. (2014). Phonetic feature encoding in human superior temporal gyrus. *Science* 343, 1006–1010. doi: 10.1126/science.1245994

Miller, K. J., Leuthardt, E. C., Schalk, G., Rao, R. P., Anderson, N. R., Moran, D. W., et al. (2007). Spectral changes in cortical surface potentials during motor movement. *J. Neurosci.* 27, 2424–2432. doi: 10.1523/JNEUROSCI.3886-06.2007

Milsap, G., Collard, M., Coogan, C., Rabbani, Q., Wang, Y., and Crone, N. E. (2019). Keyword spotting using human electrocorticographic recordings. *Front. Neurosci.* 13:60. doi: 10.3389/fnins.2019.00060

Mines, M. A., Hanson, B. F., and Shoup, J. E. (1978). Frequency of occurrence of phonemes in conversational english. *Lang. Speech* 21, 221–241. doi: 10.1177/002383097802100302

Moses, D. A., Leonard, M. K., and Chang, E. F. (2018). Real-time classification of auditory sentences using evoked cortical activity in humans. *J. Neural Eng.* 15:036005. doi: 10.1088/1741-2552/aaab6f

Moses, D. A., Mesgarani, N., Leonard, M. K., and Chang, E. F. (2016). Neural speech recognition: continuous phoneme decoding using spatiotemporal representations of human cortical activity. *J. Neural Eng.* 13:056004. doi: 10.1088/1741-2560/13/5/056004

Moulines, E., and Charpentier, F. (1990). Pitch-synchronous waveform processing techniques for text-to-speech synthesis using diphones. *Speech Commun.* 9, 453–467. doi: 10.1016/0167-6393(90)90021-Z

Mugler, E. M., Patton, J. L., Flint, R. D., Wright, Z. A., Schuele, S. U., Rosenow, J., et al. (2014). Direct classification of all american english phonemes using signals from functional speech motor cortex. *J. Neural Eng.* 11:035015. doi: 10.1088/1741-2560/11/3/035015

Mugler, E. M., Tate, M. C., Livescu, K., Templer, J. W., Goldrick, M. A., and Slutzky, M. W. (2018). Differential representation of articulatory gestures and phonemes in precentral and inferior frontal gyri. *J. Neurosci.* 38, 9803–9813. doi: 10.1523/JNEUROSCI.1206-18.2018

Nguyen, H. V., and Bai, L. (2010). "Cosine similarity metric learning for face verification," in *Asian Conference on Computer Vision* (Queenstown: Springer), 709–720.

Nuyujukian, P., Albites Sanabria, J., Saab, J., Pandarinath, C., Jarosiewicz, B., Blabe, C. H., et al. (2018). Cortical control of a tablet computer by people with paralysis. *PLoS One*. 13:e0204566. doi: 10.1371/journal.pone.0204566

Okada, K., Matchin, W., and Hickok, G. (2018). Phonological feature repetition suppression in the left inferior frontal gyrus. *J. Cogn. Neurosci.* 30, 1549–1557. doi: 10.1162/jocn_a_01287

Pandarinath, C., Nuyujukian, P., Blabe, C. H., Sorice, B. L., Saab, J., Willett, F. R., et al. (2017). High performance communication by people with paralysis using an intracortical brain-computer interface. *Elife* 6:e18554. doi: 10.7554/eLife.18554

Pasley, B. N., David, S. V., Mesgarani, N., Flinker, A., Shamma, S. A., Crone, N. E., et al. (2012). Reconstructing speech from human auditory cortex. *PLoS Biol.* 10:e1001251. doi: 10.1371/journal.pbio.1001251

Ramsey, N., Salari, E., Aarnoutse, E., Vansteensel, M., Bleichner, M., and Freudenburg, Z. (2017). Decoding spoken phonemes from sensorimotor cortex with high-density ecog grids. *Neuroimage* 180(Pt A), 301–311. doi: 10.1016/j.neuroimage.2017.10.011

Ray, S., Crone, N. E., Niebur, E., Franaszczuk, P. J., and Hsiao, S. S. (2008). Neural correlates of high-gamma oscillations (60–200 hz) in macaque local field potentials and their potential implications in electrocorticography. *J. Neurosci.* 28, 11526–11536. doi: 10.1523/JNEUROSCI.2848-08.2008

Sahin, N. T., Pinker, S., Cash, S. S., Schomer, D., and Halgren, E. (2009). Sequential processing of lexical, grammatical, and phonological information within brocas area. *Science* 326, 445–449. doi: 10.1126/science.1174481

Santoro, R., Moerel, M., De Martino, F., Valente, G., Ugurbil, K., Yacoub, E., et al. (2017). Reconstructing the spectrotemporal modulations of real-life sounds from fmri response patterns. *Proc. Natl. Acad. Sci. U.S.A.* 114, 4799–4804. doi: 10.1073/pnas.1617622114

Schalk, G., McFarland, D. J., Hinterberger, T., Birbaumer, N., and Wolpaw, J. R. (2004). Bci2000: a general-purpose brain-computer interface (bci) system. *IEEE Trans. Biomed. Eng.* 51, 1034–1043. doi: 10.1109/TBME.2004.827072

Schultz, T., Wand, M., Hueber, T., Krusienski, D. J., Herff, C., and Brumberg, J. S. (2017). Biosignal-based spoken communication: A survey. *IEEE ACM Trans. Audio Speech Lang. Process.* 25, 2257–2271. doi: 10.1109/TASLP.2017.2752365

Stavisky, S. D., Rezaii, P., Willett, F. R., Hochberg, L. R., Shenoy, K. V., and Henderson, J. M. (2018a). "Decoding speech from intracortical multielectrode arrays in dorsal arm/hand areas of human motor cortex," in *2018 40th Annual International Conference of the IEEE Engineering in Medicine and Biology Society (EMBC)* (Honululu, HI: IEEE), 93–97.

Stavisky, S. D., Willett, F. R., Murphy, B. A., Rezaii, P., Memberg, W. D., Miller, J. P., et al. (2018b). Neural ensemble dynamics in dorsal motor cortex during speech in people with paralysis. *bioRxiv* 505487. doi: 10.1101/505487

Steinbach, M., Karypis, G., and Kumar, V. (2000). "A comparison of document clustering techniques," in *KDD Workshop on Text Mining*, Vol. 400 (Boston, MA), 525–526.

Stevens, S. S., Volkmann, J., and Newman, E. B. (1937). A scale for the measurement of the psychological magnitude pitch. *J. Acoust. Soc. Am.* 8, 185–190. doi: 10.1121/1.1915893

Stuart, A., Kalinowski, J., Rastatter, M. P., and Lynch, K. (2002). Effect of delayed auditory feedback on normal speakers at two speech rates. *J. Acoust. Soc. Am.* 111, 2237–2241. doi: 10.1121/1.1466868

Sundermann, D., Hoge, H., Bonafonte, A., Ney, H., Black, A., and Narayanan, S. (2006). "Text-independent voice conversion based on unit selection," in *Acoustics, Speech and Signal Processing, 2006. ICASSP 2006 Proceedings. 2006 IEEE International Conference on*, Vol. 1 (Toulouse: IEEE).

Taal, C. H., Hendriks, R. C., Heusdens, R., and Jensen, J. (2011). An algorithm for intelligibility prediction of time–frequency weighted noisy speech. *IEEE Trans. Audio Speech Lang Process.* 19, 2125–2136. doi: 10.1109/TASL.2011.2114881

Tian, X., and Poeppel, D. (2010). Mental imagery of speech and movement implicates the dynamics of internal forward models. *Front. Psychol.* 1:166. doi: 10.3389/fpsyg.2010.00166

Tourville, J. A., and Guenther, F. H. (2011). The diva model: a neural theory of speech acquisition and production. *Lang. Cogn. Process.* 26, 952–981. doi: 10.1080/01690960903498424

Wang, W., Arora, R., Livescu, K., and Bilmes, J. A. (2015). "Unsupervised learning of acoustic features via deep canonical correlation analysis," in *Acoustics, Speech and Signal Processing (ICASSP), 2015 IEEE International Conference on* (Brisbane, QLD: IEEE), 4590–4594.

Willett, F. R., Deo, D. R., Avansino, D. T., Rezaii, P., Hochberg, L., Henderson, J., et al. (2019). Hand knob area of motor cortex in people with tetraplegia represents the whole body in a modular way. *bioRxiv* 659839. doi: 10.1101/659839

Wolpaw, J., Birbaumer, N., McFarland, D., Pfurtscheller, G., and Vaughan, T. (2002). Brain–computer interfaces for communication and control. *Clin. Neurophysiol.* 113, 767–791. doi: 10.1016/S1388-2457(02)00057-3

Wu, Z., Virtanen, T., Kinnunen, T., Chng, E., and Li, H. (2013). "Exemplar-based unit selection for voice conversion utilizing temporal information," in *INTERSPEECH* (Lyon), 3057–3061.

Zahner, M., Janke, M., Wand, M., and Schultz, T. (2014). "Conversion from facial myoelectric signals to speech: a unit selection approach," in *Fifteenth Annual Conference of the International Speech Communication Association* (Singapore).

Conflict of Interest: The authors declare that the research was conducted in the absence of any commercial or financial relationships that could be construed as a potential conflict of interest.

frontiers in Neuroscience

METHODS
published: 22 November 2019
doi: 10.3389/fnins.2019.01248

Discrimination of Movement-Related Cortical Potentials Exploiting Unsupervised Learned Representations From ECoGs

Carlos A. Loza[1,2]*, *Chandan G. Reddy*[3,4,5], *Shailaja Akella*[5] and *José C. Príncipe*[5]

[1] Department of Mathematics, Universidad San Francisco de Quito, Quito, Ecuador, [2] Instituto de Neurociencias, Universidad San Francisco de Quito, Quito, Ecuador, [3] Department of Neurosurgery, University of Iowa, Iowa City, IA, United States, [4] Department of Neurosurgery, University of Florida, Gainesville, FL, United States, [5] Computational NeuroEngineering Lab, Electrical and Computer Engineering Department, University of Florida, Gainesville, FL, United States

OPEN ACCESS

Edited by:
Mikhail Lebedev,
Duke University, United States

Reviewed by:
Alan Degenhart,
Carnegie Mellon University, United States
Andrey Eliseyev,
Columbia University, United States
Christoph Kapeller,
Guger Technologies OG, Austria

***Correspondence:**
Carlos A. Loza
cloza@usfq.edu.ec

Specialty section:
This article was submitted to Neuroprosthetics, a section of the journal Frontiers in Neuroscience

Received: 23 April 2019
Accepted: 05 November 2019
Published: 22 November 2019

Citation:
Loza CA, Reddy CG, Akella S and Príncipe JC (2019) Discrimination of Movement-Related Cortical Potentials Exploiting Unsupervised Learned Representations From ECoGs. Front. Neurosci. 13:1248. doi: 10.3389/fnins.2019.01248

Brain–Computer Interfaces (BCI) aim to bypass the peripheral nervous system to link the brain to external devices via successful modeling of decoding mechanisms. BCI based on electrocorticogram or ECoG represent a viable compromise between clinical practicality, spatial resolution, and signal quality when it comes to extracellular electrical potentials from local neuronal assemblies. Classic analysis of ECoG traces usually falls under the umbrella of Time-Frequency decompositions with adaptations from Fourier analysis and wavelets as its most prominent variants. However, analyzing such high-dimensional, multivariate time series demands for specialized signal processing and neurophysiological principles. We propose a generative model for single-channel ECoGs that is able to fully characterize reoccurring rhythm–specific neuromodulations as weighted activations of prototypical templates over time. The set of timings, weights and indexes comprise a temporal marked point process (TMPP) that accesses a set of bases from vector spaces of different dimensions—a dictionary. The shallow nature of the model admits the equivalence between latent variables and representations. In this way, learning the model parameters is a case of unsupervised representation learning. We exploit principles of Minimum Description Length (MDL) encoding to effectively yield a data-driven framework where prototypical neuromodulations (not restricted to a particular duration) can be estimated alongside the timings and features of the TMPP. We validate the proposed methodology on discrimination of movement-related tasks utilizing 32-electrode grids implanted in the frontal cortex of six epileptic subjects. We show that the learned representations from the high-gamma band (85–145 Hz) are not only interpretable, but also discriminant in a lower dimensional space. The results also underscore the practicality of our algorithm, i.e., 2 main hyperparameters that can be readily set via neurophysiology, and emphasize the need of principled and interpretable representation learning in order to model encoding mechanisms in the brain.

Keywords: brain-computer interfaces, electrocoticogram (ECoG), generative model, minimum description length (MDL), representation learning, temporal marked point process

1. INTRODUCTION

Brain-Computer Interfaces (BCI) strive to surpass the need for any measure of muscle control in order to provide patients suffering from severe neuromuscular disabilities with the ability to interact with the external world. These systems are anchored on principled analysis of the electrical activity of the brain during movement or movement intent; successful decoding of such neurophysiological processes is then relayed to external devices that execute the desired motor activity (Lebedev and Nicolelis, 2006). Recent technological and scientific advances in BCI systems have extended its application from enabling communication for completely "locked in" patients (Kübler et al., 2001; Vansteensel et al., 2016; Chaudhary et al., 2017), to restoration of motor control for patients with severe disabilities (Pfurtscheller et al., 2000; Hochberg et al., 2012; Yanagisawa et al., 2012; Ajiboye et al., 2017), and neurorehabilitation where BCIs are doubled as therapeutic devices (Dobkin, 2007; Soekadar et al., 2015; Bundy et al., 2017).

Current BCIs most commonly depend on scalp electroencephalogram (EEG) to record the combined electrical potentials of massive neuronal populations. While EEG is a non-invasive and cost-effective alternative, it is limited both in terms of spatial and temporal resolutions due to the overlapping activity of different cortical generators. In addition, the passive conductance through brain tissue, bone, and skin restrict the effective spectral support of the EEGs (Lebedev and Nicolelis, 2006). BCI systems depending on other non-invasive methods like magnetoencephalography (MEG) and functional magnetic resonance imaging (fMRI) provide finer spatiotemporal and spatial resolution, respectively (Weiskopf et al., 2004; Mellinger et al., 2007). However, besides being technically exhaustive, these methods are not cost effective. Moreover, the dependence of fMRI and positron emission tomography (PET) techniques on blood flow causes these systems to have very long time constants deeming them impractical for rapid communication and closed-loop applications (Vaughan, 2003).

Invasive methods involving single and multiunit recordings circumvent all the above mentioned drawbacks while delivering outstanding performance (Serruya et al., 2002; Taylor et al., 2002; Lebedev et al., 2005; Hochberg et al., 2012; Collinger et al., 2013; Bouton et al., 2016). However, these methods require that the cortex be penetrated which brings into question the safety of such technologies. Further, glial scars may develop overtime decreasing accessibility of units and inducing complex histological activity, simultaneously debilitating neural recordings. Finally, spatial resolution is inherently limited due to the restricted surface area covered by the recording electrodes (Abdulkader et al., 2015; Waldert, 2016).

Considering the disadvantages of both invasive and non-invasive BCIs and keeping in mind the ultimate aim of designing a durable, fully-implantable BCI system, many research groups have suggested Electrocorticogram (ECoG) as a more practical solution. These signals are acquired by implanting a grid of flat electrodes either above or below the dura mater, while never actually penetrating the brain parenchyma. Number of electrodes in these grids vary between 4 and 256, each having a diameter between 70 and 2 mm and an inter-electrode spacing between 1 and 10 mm depending on the extent of coverage and precision appropriate for analysis (Schalk and Leuthardt, 2011). Commonly used for invasive monitoring in patients with epilepsy (Reddy et al., 2009; Tangermann et al., 2012; Arya et al., 2017), these electrodes measure the cumulative activity of multiple neurons present in a small radius ($\sim$ 50–350 μm) around the tip of the electrode. Given their proximity to the brain surface, ECoG recordings not just provide better spatial resolution (1.2–1.4 mm compared to several cm in EEG), improved SNR and larger spectral support (0–500 vs. 0–40 Hz in EEG), they have also been found to be more robust to electrooculographic (EOG) and electromyographic (EMG) artifacts (Freeman et al., 2000; Ball et al., 2009). Moreover, while fidelity and durability of these electrodes have been positively tested in macaques for several months (Chao et al., 2010; Mestais et al., 2015; Degenhart et al., 2016), further evaluation on a group of patients implanted with subdural electrodes is under experimentation (Delavallée et al., 2008). ECoG recordings, therefore, strike a perfect balance between clinical practicality and signal quality, consequently delivering prominence in performance (Leuthardt et al., 2006; Schalk et al., 2008; Kubanek et al., 2009; Brunner et al., 2011; Yanagisawa et al., 2012; Hotson et al., 2016; Degenhart et al., 2018).

The broad spectral support available via ECoG recordings has important implications for BCI applications pertaining to encoding and decoding motor tasks. For instance, increased modulatory activity of faster rhythms (75–100 Hz) in the motor cortex of patients performing sustained muscle contractions has shown specific somatotopic organization (Crone et al., 1998; Miller et al., 2007). Several ECoG-based studies have confirmed the correlation between spatially focused gamma activity and motor function (Aoki et al., 1999; Miller et al., 2010; Leuthardt et al., 2012; Gunduz et al., 2016). Although advances in recording technology has allowed for similar EEG-based (Jokeit and Makeig, 1994; Darvas et al., 2010), the recordings usually suffer from severe contamination due to muscle artifacts (Goncharova et al., 2003).

In addition to the BCI recording paradigm, appropriate signal processing and feature extraction are paramount for designing effective BCIs. Extracellular electrical potentials from the brain—such as EEG, ECoG, and Local Field Potentials (LFP)—are usually deemed as either chaotic deterministic or stochastic non–stationary sequences; hence, they require principled and distinct processing that needs to incorporate neurophysiological principles into the modeling framework. Neuromodulations, also known as phasic events, wave packets, or micro-events constitute an order parameter of neuronal assemblies in the sense that the population imposes order by regulated synaptic interactions, i.e., they reflect the spatiotemporal interplay of local neuronal populations (Freeman and Quiroga, 2012). These textured images (as coined by Walter J. Freeman) appear in the recorded trace as organized, transient patterns and differ statistically from the featureless noisy background known to be characterized by a $1/f$ power spectrum (Freeman, 1975). Moreover, phasic events and deviation of Normality are the telltale signs of self-organized criticality—a metastable state of the brain that allows

shifting between dynamical states (Buzsaki, 2006). The goal of signal processing is, then, to discriminate between relevant neuromodulations and the temporally disorganized but spatially structured background activity in order to elucidate the encoding mechanisms that arise during BCI tasks.

A vast majority of ECoG-based BCIs exploit Time-Frequency (TF) decompositions to build multiscale representations (Dat et al., 2006; Zhao et al., 2010; Aydemir and Kayikcioglu, 2011; Herff et al., 2016), while the more advanced population algorithms incorporate spatial information to account for propagation and dependencies across electrodes (Ince et al., 2008; Chao et al., 2010; Onaran et al., 2011; Ramsey et al., 2018). However, TF methods are limited in their performance pertaining to the uncertainty principle (Gabor, 1946) which lower bounds the product of time and frequency resolutions. That is, in order to efficiently capture short locally stationary segments from non-stationary ECoGs, one must utilize small evolving windows, which, then, compromises the frequency resolution of the representation and blurs the phase information of potential phasic events inside the processing window in question. Although, wavelets attempt to alleviate this shortcoming (Unser and Aldroubi, 1996; Mallat, 1999), the output still suffers due to the imposition of fixed structures on the analysis of the input signal, i.e., the inference is generic by nature due to the templates of the underlying imposed generative model. Lastly, the background activity (which is sometimes deemed as "noise" by the signal processing algorithms applied to each lead) demands for application-specific frameworks that explicitly model the physiological regimes embedded in the temporal traces. The resolution constraints of TF methods and the inference on generic generative models that disregard the complex dynamics of ECoG (e.g., linear projections onto preset sinusoids in the case of Fourier analysis) are the two main deterrents of TF decompositions. It is imperative to exploit the neurophysiology behind ECoG in order to propose principled generative models that would not only advance signal processing applied to Neuroengineering, but also exploit the multivariate nature of the ensembles in order to improve performance and interpretability of ECoG-based BCIs.

We exploit a data-driven framework based on a generative model for single-channel ECoGs which is able to fully characterize each scale-specific neuromodulation by its timing, amplitude, and duration (Loza et al., 2017). One of the main advantages of the generative model is its exceptional temporal resolution limited only by the sampling rate, i.e., no windowing is necessary. Inference on the model can be viewed as either classic feature engineering or sampling of a Temporal Marked Point Process (TMPP) (Daley and Vere-Jones, 2007) fully characterized by the intensity function of the timings and the joint probability density function (pdf) of the amplitudes and durations—the "features" of the TMPP. This dual interpretation opens the door to uncover novel encoding mechanisms beyond the pervasive power-modulation-based techniques. Learning on the model invokes neurophysiological principles to restrict the search space of potential phasic events by isolating the pervasive background component of extracellular electrical potentials (Freeman and Quiroga, 2012). Then, the resulting vector space is partitioned in a top-down approach by means of a greedy clustering scheme based on the principle of Minimum Description Length (MDL) (Grünwald, 2007). The outcome is a set of prototypical vectors from different vector spaces (i.e., durations)—a collection of cluster centroids that represent bona fide transient events. Lastly, the learning process is virtually parameter free: it only requires two main hyperparameters; however, they are tightly connected to the oscillatory rhythm under consideration and, thus, can be selected based on empirical rules fully supported by clinical and research fields.

The present study integrates the advantages of an ECoG-based BCI and the proposed unsupervised learning framework to discriminate movement-related tasks in six patients. Each subject was requested to perform a motor task involving moving a joystick in one of four directions (up, down, left, or right) and an additional finger movement "trigger" task while ECoG activity from two main areas are recorded. Labeled single-channel, multi-trial ensembles go through the learning and inference processes on the generative model with a focus on the high-gamma band (85–145 Hz). The results in terms of movement direction separability not only confirm the plausibility of the methods, but they also reveal a novel cortical encoding mechanism taking place during movement-related tasks. The rest of the paper continues as follows: section 2 explains the generative model for ECoG alongside the proposed learning mechanisms. Section 3 details the experimental setting, while section 4 summarizes the main results. Section 5 offers discussion, limitations, and perspective. Lastly, section 6 concludes the paper and proposes future work.

2. EXPERIMENTAL SETTING

The study comprised of 3 male and 3 female participants in the age range of 22–40 years. All six subjects, suffering from medically intractable epilepsy, were undergoing invasive subdural electrode monitoring before resection. A standard (1 cm interelectrode spacing) 32-contact frontal grid and a high-density (0.5 cm interelectrode spacing) 96-contact temporal grid were used to ensure unilateral, frontotemporal, subdural grid coverage on the side corresponding to suspected seizure onset. Altogether, there were three patients with left coverage while the rest had right coverage. Patients did not incur additional risk by participating in these studies. Research protocols were approved by the University of Iowa Human Subjects Review Board.

During the trials, each participant was instructed to move a joystick in one of the four cardinal directions (up, down, left, right) in response to a visual display of an arrow pointing toward the target location. A fifth display in the form of a square was also included as a "trigger condition" where in response to the cue, the participant was required to click the trigger button on the joystick with the tip of the index finger. All cues were randomly interleaved and no bias was introduced during their presentation. Further, the patient was required to hold the joystick in the target location until the visual display was replaced with a blank screen, following which the patient was asked to either release the joystick or bring it to a neutral position (**Figure 1**).

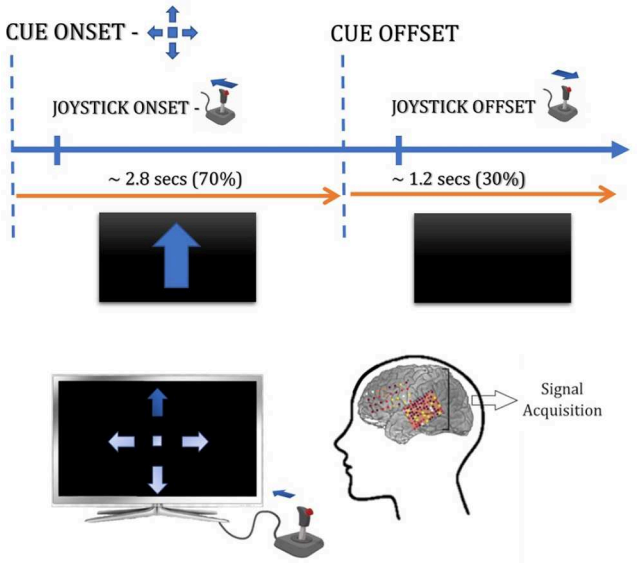

FIGURE 1 | Experimental paradigm of ECoG–based BCI.

All trials lasted ∼4 s. where the initial ∼2.8 s involved stimulus presentation and joystick maneuvers, while in the remaining ∼ 1.2 s the patient returned the joystick to its neutral position. All participants performed an average of 50 trials for each direction and "trigger" condition and all the trials were performed with the hand contralateral to the grid placement. **Table S1** details the number of trials for each joystick direction under consideration in our study. All signals were acquired at a sampling rate of 2034.5 Hz, which were later downsampled to 500 Hz for analysis.

3. METHODS

3.1. Generative Model for ECoG

Observable ECoG traces are the result of an underlying multiscale system that describes large-scale function of neuronal populations. One of the consequences of the structural fractal nature of the cortex is reflected on the very own fractal, scale-free nature of its observable variables (Buzsaki, 2006), being ECoG—with its characteristic $1/f$ law—one of the most representatives at a mesoscopic level. Self organized-criticality (Linkenkaer-Hansen et al., 2001; Freeman et al., 2003; Stam and De Bruin, 2004; Bak, 2013) further formalizes these concepts posing that brain dynamics remain at a complex state at the border between unpredictable chaos and predictable periodic behavior. The former representing a hypersensitive metastable state of the network near phase transitions, whereas the latter brings organization and transient stability by oscillations (Buzsaki, 2006). This type of micro-events have been well documented in the literature under the umbrella of induced potentials or event-related oscillations (Tallon-Baudry and Bertrand, 1999; Freeman and Quiroga, 2012), e.g., the occipital alpha rhythm (Berger, 1929), K-complexes, sleep spindles (Rechtschaffen et al., 1968), gamma oscillations in the olfactory bulb of cats and rabbits (Freeman, 1975), high-frequency oscillations correlated to the binding of perceptual information (Rodriguez et al., 1999), and hippocampal sharp-wave ripples (Buzsáki, 2015) to name a few. There are also so-called pathological patterns that are associated to particular states in a pathological setting, e.g., in epilepsy, interictal spikes and high-frequency oscillations (HFO) or ripples have been deemed as biomarkers and even potential predictors of seizures (Worrell et al., 2004; Staley et al., 2011; Jacobs et al., 2012). The challenge of principled signal analysis lies on the detection, modeling, and further unveiling of the behavioral correlates of said events.

Walter J. Freeman posited that the physiological regimes of the generating local neural assembly are reflected on the statistical properties of its observable EEG traces (Freeman and Quiroga, 2012). If the network is at rest, the resulting EEG is featureless, unorganized, and with amplitudes that closely resemble a Gaussian distribution—a critical state characterized by expectation in the form of hypersensitivity to perturbations, such as sensory stimuli or motor output. Transition to an active or work state shifts the network dynamics, which is revealed by transient stability, and, in turn, derives in deviation form Gaussianity (according to higher–order statistical moments). The generating mechanisms behind extracellular electrical potentials guarantees seamless translation of Freeman's theories from EEG to more local (and invasive) electrophysiology, such as ECoG and LFP (Niedermeyer and da Silva, 2005; Buzsáki et al., 2012). Let $\tilde{y}(t)$ be the result of linear filtering a single-channel, single-trial ECoG trace. Linear filtering is necessary so that the Gaussian/Non-Gaussian regimes are preserved through linear operators on the raw signal. According to Freeman's experimental results and the theory of self-organized criticality of neuronal assemblies, $\tilde{y}(t)$ can be decomposed into two sequences:

$$\tilde{y}(t) = \begin{cases} y(t) & \text{if Network is Active (Y State)} \\ z(t) & \text{if Network is at Rest (Z State)} \end{cases} \quad (1)$$

where $y(t)$ is the phasic event component—an ideal, noiseless sequence that includes scale-specific neuromodulations over time. On the other hand, $z(t)$ is the filtered version of the underlying ongoing activity, i.e., a background component.

The background component, $z(t)$, ongoing or spontaneous activity is associated to rest regimes of the generating neural network. From a signal processing point of view, it can be regarded as noise due to its featureless nature. However, it should not be confused with interfering and external sources usually mixed and superimposed in ECoG recordings—the so-called artifacts, e.g., ocular and muscle activity, movement-related activity, signal degradation as a byproduct of variable electrode impedance, and so on (Niedermeyer and da Silva, 2005). Also, noise might imply a complete divorce from behavior, yet, several studies have confirmed the encoding nature of the ongoing EEG by regulating response variability and imposing priors for induced potentials (Başar, 1980; Buzsaki, 2006; Hanslmayr et al., 2006; Busch et al., 2009; Luczak et al., 2009). Moreover, the background component is essential to maintain cortical functions in a linear dynamic range (Freeman and Quiroga, 2012).

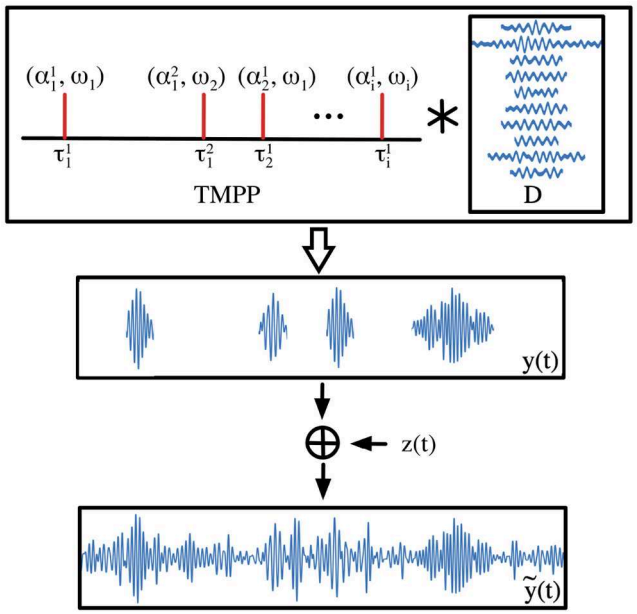

FIGURE 2 | Generative model for ECoG. A bandpassed, single–channel, single–trial ECoG trace, $\tilde{y}(t)$, is modeled as the noisy addition of weighted, scale–specific, shifted filters over time. Temporal Marked Point Process (TMPP) samples sparsely activate dictionary atoms to yield the phasic event component $y(t)$. Atom corresponding to ω_1 appears twice in the TMPP. * represents indexed convolution according to Equation (2).

The phasic event component is modeled taking inspiration from the shot noise model (Davenport and Root, 1958). $y(t)$ is the result of a Temporal Marked Point Process (TMPP) with timings τ and marks (features) α and ω activating filters, $\mathbf{d}$, over time:

$$y(t) = \sum_{\omega=1}^{K} \sum_{i=1}^{n_\omega} \alpha_i^\omega \mathbf{d}_\omega (t - \tau_i^\omega) + \epsilon(t) \tag{2}$$

where $\mathbf{D} = \{\mathbf{d}_\omega\}_{\omega=1}^K$ is a set of filters, kernels or atoms known as dictionary. τ_i^ω and α_i^ω are the timing and encoding coefficient of the i–th instance of filter $\mathbf{d}_\omega$, respectively. $\epsilon(t)$ is the additive noise sequence (possibly resulting from thermal noise, variation in electrode impedance, and propagation losses through tissue). n_ω indicates the number of instances of $\mathbf{d}_\omega$, which is not restricted to be the same across filters. ω basically constitutes an assigning set (i.e., index) between observed micro–events and modeled dictionary atoms, i.e., $\omega \in \{1, 2, 3, \ldots, K\}$. The resolution of τ is limited only by the recording sampling rate; for instance for 500 Hz, one can determine the occurrence of a neuromodulation with a 2 ms. resolution. In theory, the support of α is $\mathbb{R}$; however, practical constraints are imposed by the power of the rhythm under consideration. **Figure 2** illustrates the encoding from TMPP samples to noisy single-channel, bandpassed ECoG trace.

The model in (2) can be alternatively interpreted as $y(t)$ being the observable variable from a generative model with latent variables Y and Z. Y is parameterized as $\Theta_Y \triangleq \{\tau, \alpha, \omega, \mathbf{D}\}$, whereas Z, being Gaussian in nature, is fully characterized by the mean and standard deviation of the background EEG, i.e. $\Theta_Z \triangleq \{\mu_Z, \sigma_Z\}$. A multiple input single output (MISO) framework (Brockmeier and Príncipe, 2016) is the basis of the current generative model for ECoG; however, training was not scalable due to the amount of free hyperparameters. Then, a single-rhythm approach was adopted by Loza et al. (2017), where learning focused on scale-specific patterns of fixed duration by means of shift-invariant time series clustering techniques. The current work goes one step further and learns kernels of different lengths. Similar models have been proposed in neuroscience and statistics under the connotation of convolutional sparse coding (Lewicki, 2002; Smith and Lewicki, 2006; Balcan and Lewicki, 2009; Ekanadham et al., 2011). Their results highlight the need of principled priors and constraints to tackle an inherent combinatorial problem.

Given an ensemble of single-channel ECoG recordings, $\{\tilde{y}_i(t)\}_{i=1}^N$. Learning on the model implies estimating the dictionary $\mathbf{D}$ whose elements, in general, are not restricted in duration—they represent bases from vector spaces of different dimensions. On the other hand, inference or encoding is posed as learning the set of timings and marks of the TMPP, i.e., sampling from a point process. The shallow nature of the model admits the equivalence between latent variables and features or representations. $\mathbf{D}$ also encodes features of its own, such as duration, central frequency, and Q-factor. Estimating Θ_Y, then, can be posed as a case of unsupervised representation learning for ECoG (Bengio et al., 2013). The shallow generative framework and physiological-based constraints of the model guarantee that the learned dictionary and densities of timings, marks, and representations lead to meaningful and interpretable encoding mechanisms of the network without imposing handpicked signatures, as in the case of wavelets or Gabor bases.

3.2. Learning on the Model

Estimating the latent variables of this type of generative models usually falls into two categories depending whether the sources are explicitly estimated or not during learning. Bell and Sejnowski (1996), Davies and James (2007), Lucena et al. (2011), and Brockmeier and Príncipe (2016) showcase the potential of learning the bases without appealing to reconstruction cost functions or explicitly estimating the sources, i.e., marks of the TMPP, by using Independent Component Analysis off–the–shelf implementations, such as FastICA (Hyvarinen, 1999). The alternative approach (adopted here) is to exploit block coordinate descent optimization to iteratively estimate the sources while keeping the filters fixed, and then, learn the dictionary atoms while keeping $\{\tau, \alpha, \omega\}$ fixed. The result is a local optimum in solution space with the added bonus of less computational demands. For a comparison of both approaches applied to a MISO model on synthetic and real EEG, refer to Brockmeier and Príncipe (2016). Achieving the global optimum is impossible in practice because it would require combinatorial analysis, which is simply intractable, i.e., it would require checking all the possible different combinations of dictionary atoms (with different dimensionalities) until optima are found; hence, here we opt for the tractable, albeit suboptimal solution to the problem

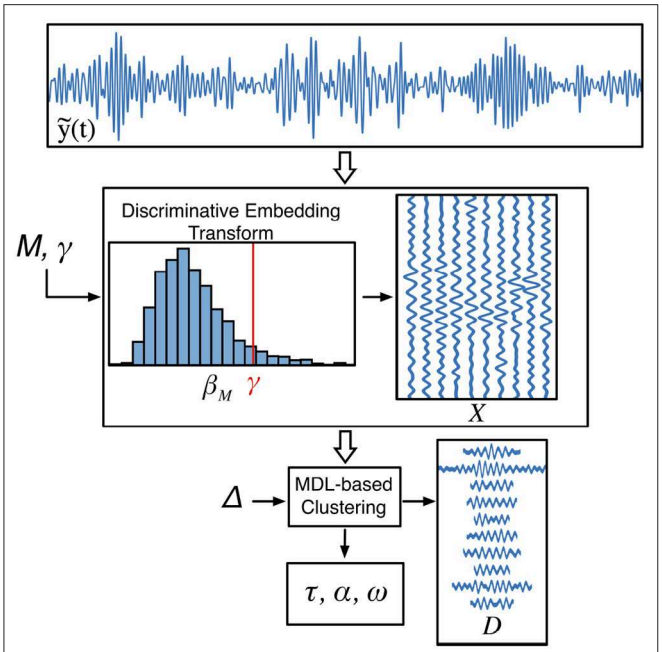

FIGURE 3 | Learning of generating dictionary and TMPP features. The discriminative embedding transform (DET) isolates potential *M*–snippets generated by the *Y* (active) state and collects them in the matrix **X**. MDL–based hierarchical clustering estimates TMPP timings and marks as well as bases from vector spaces of different dimensions, **D**.

at hand. For our case, learning takes place in two very distinctive sequential stages: discrimination between dynamical regimes and hierarchical partitioning of the data (**Figure 3**).

3.2.1. Discrimination of Dynamical Regimes: From Traces to M–Snippets

We take advantage of the architectural constraints and neurophysiology of the ECoG to render the learning more tractable, alleviate the computational complexity, and, most importantly, facilitate the interpretation of the learned prototypes. This is accomplished by bandpass filtering the traces according to the clinical EEG rhythms (Niedermeyer and da Silva, 2005). The result is a natural grouping of scale-specific neuromodulations. Then, sparsity is leveraged by associating a single dictionary atom to an observed, noisy micro-event. This will further prevent overfitting and overlapped occurrences of TMPP samples; it also emphasizes the temporal sparsity of the sources. Then, there is major deviation from the approaches adopted in classic convolutional sparse coding applied to time series (Lewicki, 2002; Smith and Lewicki, 2006; Mailhé et al., 2008; La Tour et al., 2018). Instead of performing iterative template matching over time, e.g., Matching Pursuit (Mallat and Zhang, 1993), that attempts to reconstruct the entire input, we exploit Freeman's theories and the concept of self-organized criticality to map the ECoG to a surrogate space of constrained ℓ_2-norms where discrimination between rest and active stages is plausible. Let the M-sample-long subsequence from $\tilde{y}[n]$ centered at the time instance $t = i$ be a M-snippet:

$$\begin{aligned} \tilde{y}_i &= \tilde{y}(i - M/2 : i + M/2) \\ \text{s.t} \quad & i = M/2, M/2 + 1, \ldots, \eta - M/2 \end{aligned} \tag{3}$$

where η is the number of sampled values in $\tilde{y}(t)$. One of the intermediate goals of learning on the generative model is to effectively discriminate between M-snippets generated by Z (background subsequences) and M-snippets with embedded phasic events generated by Y. The advantages of principled discrimination is two-fold: decrease likelihood of biased atoms and improved convergence rates by effective restriction of the input space to subsequences from the active stage, i.e., the learning is not reconstructive in nature because the entire ECoG trace, $\tilde{y}(t)$, is not worth encoding. The learning falls more into the hierarchical partitioning category. In this regard, the embedding transform (Loza and Principe, 2018)—introduced as a novel tool to assess non–stationarity of single-channel EEG ensembles—maps the input according to the ℓ_2-norms of its constituent M-snippets. The M-snippets are built sequentially: first, modulated patterns are extracted (peak detection via moving averages or instantaneous amplitudes), then, the rest of the unmodulated patters complete the set of M-snippets. The middle points from each sample is collected in the set $\Pi = \{\pi_i\}$. Powers of the M-dimensional vectors are calculated, and, the resulting ℓ_2-norms comprise the surrogate variable β_M. If $\tilde{y}(t)$ is strictly generated by Z, its amplitudes will resemble a Gaussian density, which derives in β_M being a chi-distribution with M degrees of freedom. Invoking the Central Limit Theorem, if M is large enough (which is satisfied for high sampling rates), the chi-distribution resolves to a Gaussian density. Conversely, M-snippets from Y interspersed between Z counterparts will drive the shape of β_M by enlarging the tails and skewing the distribution. β_M is then a surrogate variable of the dynamic stages of the network. The discriminative embedding transform (DET) goes one step further and proposes a threshold in the β_M space between potential M-snippets from different regimes. Specifically, the matrix $\mathbf{X}$ with columns $\mathbf{x}_i$ collects all the M-snippets larger than the hyperparameter γ:

$$\begin{aligned} \mathbf{x}_i &= \tilde{y}(\pi_i - M/2 : \pi_i + M/2)^T \\ \text{s.t.} \quad & ||\tilde{y}(\pi_i - M/2 : \pi_i + M/2)||_2 \geq \gamma \end{aligned} \tag{4}$$

The case for a set of multi-trial recordings is straightforward, i.e., $\mathbf{X} \in \mathbb{R}^{M \times \Psi}$ where Ψ is the total number of M-snippets from $\{\tilde{y}_i(t)\}_{i=1}^{N}$ generated by Y. In short, $\mathbf{X}$ collects potential embedded M-sample-long micro-events of single-channel, multi-trial traces according to a non-linear mapper with hyperparameters M and γ.

3.2.2. Learning Bases of Different Dimensions

After $\mathbf{X}$ is computed, the naive solution to extract centers of mass in $\mathbb{R}^M$ would involve classic static clustering algorithms, e.g., k-means. Yet, the shift-invariance of embedded phasic events would most likely derive in meaningless clusters as noted in Keogh and Lin (2005). Most importantly, if prototypes of different durations are present, k-means would blur their

contributions by grouping them in M-dimensional vectors. The former problem is addressed by cross-correlation operators: distances between prospective cluster centers and samples from $\mathbf{X}$ can now be estimated over lags (similar to Matching Pursuit implementations on time series). The latter problem is far more challenging; it demands for principled measures between centers, and vectors in general, of different dimensions, which is clearly prohibitive under Euclidean distance regimes. We exploit the parsimony principles of Minimum Description Length (MDL) coding to build a hierarchical partitioning in $\mathbb{R}^M$ where the learned atoms are not restricted to a fixed dimensionality.

The MDL principle is invoked to cluster reoccurring patterns embedded in the columns of $\mathbf{X}$. The goal is to attempt to compress the data in a lossless manner by finding repeated structures (or regularities) in it. Due to inherent noise and response variability, we practically aim to discover repeated structure and encode the differences. For instance, the conditional description length of a sequence A after being encoded with a hypothesis H is given by $DL(A|H) = DL(A - H)$; this can be interpreted as the cost of the encoding. $DL(T)$ is the bit level representation of time series T, which is defined as the entropy of T times its length m, i.e.,:

$$DL(T) = -m \sum_t P(T = t) \log_2 P(T = t) \tag{5}$$

We exploit a cost function based on bit level representations to decide among three basic clustering operations: creating a cluster, adding a subsequence to an existing cluster, and merging clusters. This approach was first introduced in Rakthanmanon et al. (2011) under the term *time series epenthesis* as a virtually parameter-free framework to find repeated subsequences in time series without necessarily explaining all the data. In a similar manner, we sequentially build a hierarchical partition of the patterns embedded in $\mathbf{X}$ by greedily selecting the clustering operation that reduces the total number of bits saved after being applied, i.e., the difference in the number of bits before and after applying an operator—a *bitsave* (*BS*) cost function. At each iteration, one operator is selected and the updated set goes through the same process until the set $\mathbf{X}$ is exhausted. The BS corresponding to the three clustering operators are:

BS after creating cluster C from subsequences A and B:

$$BS = DL(A) + DL(B) - DLC(C) \tag{6}$$

where $DLC(C) = DL(H) + \sum_{A \in C} DL(A|H) - \max_{A \in C} DL(A|H)$ is the number of bits needed to represent all subsequences assigned to cluster C. H is the center subsequence of the cluster under consideration.

BS after adding subsequence A to cluster C:

$$BS = DL(A) + DLC(C) - DLC(C') \tag{7}$$

where C' is the new cluster after adding A to C.

BS after merging clusters C_1 and C_2 into new cluster C':

$$BS = DLC(C_1) + DLC(C_2) - DLC(C') \tag{8}$$

Euclidean distance is used to initialize prospective clusters and find the closest subsequence from a given cluster center. Cross-correlation provides an intuitive extension to Euclidean distance over lags for both tasks and is, therefore, exploited in the current work. Consequently, the shift-invariance nature of the micro-events is explicitly modeled. Additional practical implementation details include quantizing the normalized inputs to a 64-bit representation so that *DL*s from different clusters and dimensions can be effectively compared. Also, the algorithm requires priors in the form of a set of prospective durations, $\delta \in \Delta$, in order to initialize cluster centers and initiate the optimization. Nevertheless, these priors are not rigid because cross-correlation operators are flexible enough to discover patterns beyond the grid imposed by Δ. Learning begins by finding the set of pairs mostly correlated in $\mathbf{X}$—a sort of motif finding routine—for each δ. Querying these sets can be effectively executed by building matrices of sizes $\mathbb{R}^{\delta \times \delta}$ with maximal pairwise cross–correlation as their elements. Initial cluster centers are merely the average between these motifs. Then, the operators of adding subsequences to existing clusters, merging clusters, and adding an existing motif to the active set are evaluated at each iteration. In summary, Δ are mere suggestions of dimensions to be explored initially, but, later during learning, the algorithm is free to venture into different dimensions up until the practical limit imposed by M. The timings, τ, are estimated as the lags corresponding to maximum cross–correlations with respect to the time stamp of $\mathbf{x}_i$ in the original time series. The encoding amplitudes or weights, α, are simply the aforementioned maximum cross-correlation values.

The proposed algorithm alternatively estimates the TMPP marks and learns bases from vector spaces of different dimensions. In this way, it resembles greedy block coordinate descent approaches. However, it is conceptually different from previous attempts to learn generating dictionaries for time series. First, it resembles the work in Rakthanmanon et al. (2011), in that we exploit MDL for hierarchical partitioning; yet, our implementation is significantly faster due to the pre-processing and discrimination of dynamical regimes provided by the DET. Second, clustering of shift-invariant patterns usually either fixes the support of possible discoverable patterns (Mailhé et al., 2008), or adapt this parameter in a semi-supervised manner (Lewicki, 2002; Smith and Lewicki, 2006; Loza et al., 2017). We propose a flexible initial grid that is free to be explored and shaped during learning as long as the bitsave is minimized. Lastly, and more importantly, the proposed clustering technique greedily selects the number of clusters, K, needed, i.e., model selection is a natural byproduct. This is a major improvement over classic convolutional sparse coders where K is left as a hyperparameter. The final implementation takes three main hyperparameters: γ, the threshold of dynamical regimes in the β_M space, M, the embedding dimension of the DET, and Δ, the duration prior. However, the last two are strictly tied to the rhythm under consideration; they can both be set according to previous studies, analysis of TF decompositions, or neurophysiology. γ is parameterized by the mean and standard deviation of the fitted Gaussian corresponding to Z in the β_M space, i.e., $\gamma = \mu_{Z_M} + \gamma' \times \sigma_{Z_M}$ where μ_{Z_M} and σ_{Z_M} are the mean and

standard deviation of the set of M–snippets generated from Z, respectively.

3.3. Additional Analysis Methods

Discriminability of movement direction is assessed via two methods: the one-way variant of multivariate analysis of variance (MANOVA) and the silhouette indicator.

Simply put, MANOVA (O'Brien and Kaiser, 1985) is the generalization of the well–known analysis of variance (ANOVA) methodology. While the latter performs statistical tests regarding univariate sample means, the former compares multivariate sample means. MANOVA exploits covariance matrices to unveil correlations between dependent variables instead of the sum of squares estimator in ANOVA, which is sufficient in the univariate case. In the present work, MANOVA is utilized to determine the discriminability of movement direction based on ECoG features (either power-based or representations derived from learning on the proposed model). In particular given the four movement directions under study, MANOVA poses the null hypothesis that the multivariate means either lie on a line, on a plane or on a 3-dimensional hyperplane, being this last alternative the most discriminant option.

Silhouette values (Rousseeuw, 1987) estimate the separability of clusters of points given their labels. In the present work, average silhouette values determine the separability of movement–related representations in a 3-dimensional space. In particular for the i-th point, its silhouette S_i, is defined as:

$$S_i = \frac{b_i - a_i}{\max\{a_i, b_i\}} \tag{9}$$

where b_i is the smallest average Euclidean distance of i to all points in any other cluster (where i is not a member), and a_i is the average distance between i and all other points belonging to the same cluster. S_i provides a bounded ($[-1, 1]$) measure of separability—average values close to -1 imply a poor clustering solution, i.e., low discrimination of features, while averages close to 1 guarantee high discriminability.

3.4. Parameter Selection

The proposed algorithm learns representations from ECoG ensembles in a single-channel, task-by-task basis per subject. Only the 32 channels across the frontal grid are part of the current study. To ensure a reliable baseline for the estimation of σ_{Z_M}, the processing comprises the interval starting at 0.5 s before visual cue to 4 s after; yet, the subsequent statistical tests consist of timings from -0.5 to 2 s relative visual cue to emphasize TMPP samples around motor tasks (see **Figure 6**). According to previous studies related to encoding of movement-related cortical potentials (Reddy et al., 2009; Zhao et al., 2010), we focus on bursts in the high-gamma band (85–145 Hz)—a Butterworth filter with quality factor $Q \sim 2$ is utilized for this purpose. Then, M is set equal to 50 samples, or 100 ms, $\Delta = [50 : 10 : 100]$ ms, and $\gamma' = 1$. The first two hyperparameters are set based on the physiology of cortical gamma rhythms and visual inspection of the traces in the time domain. The last hyperparameter is a recording-specific compromise between true and false positive detection rates in the β_M space, i.e., a value of $\gamma = \mu_{Z_M} + \sigma_{Z_M}$ guarantees a theoretical 66% of excluded M-snippets generated by Z from subsequent learning (according to an ideal Gaussian density for Z). All trials in the study are used for learning the prototypical high-gamma profiles. Lastly, for the present study we implement all the learning pipeline—bandpass filtering, hierarchical clustering per subject, task and channel, and feature engineering, e.g., neuromodulation rates and average timings and amplitudes—in an offline fashion.

4. RESULTS

First, we investigate the statistics of the TMPP samples and the descriptors of the learned generating dictionaries. **Table 1** emphasizes the data-driven nature of the framework: it enumerates the average number of dictionary atoms or clusters over electrodes learned by the proposed method in a subject-task-specific manner. It is worth noting that no further pruning nor post-processing of the cluster centers were performed. In terms of the learned dictionaries, **Figure 4** illustrates some of the learned prototypical high-gamma micro-events for a particular channel and all subjects (one waveform per movement direction). **Figure S1** highlights the variety of atoms in terms of estimated durations with respect to motor task type.

Next, spatial distributions are summarized; namely, **Figure 5B** shows the average rate of gamma bursts over channels for all movement directions. The rate statistic serves as a surrogate of the modulated power during motor tasks. This is readily confirmed in **Figure 5A** where average high–gamma power is illustrated instead (both features will be later used to assess and compare movement direction capabilities). **Figure 6A** illustrates exemplary raster plots of the timings from Subject 153, channel 113 (associated with left hand tingling according to functional mapping). An increase in *firing* of gamma events is clear around the 0.75 s—mark with respect to visual cue. **Figure 6B** corroborates such phenomenon by means of corresponding spectrograms (250 ms.–long segments with 50 % overlap). A clear increase in modulated high–frequency power is observed around the same 0.75 s—mark. For proper context, average joystick movement onsets are also depicted. We quantify the correlation between extracted TMPP timings and modulated

TABLE 1 | Average number of learned dictionary atoms per subject and task over recording electrodes.

Subject	Task			
	Up	Right	Down	Left
146	27.15	26.28	23.59	22.87
147	32.03	32.68	28.93	27.59
149	28.87	28.00	25.28	23.84
153	32.06	34.21	36.75	36.25
154	49.90	47.34	46.00	41.87
156	29.28	30.12	31.06	30.15

High–gamma rhythm (85–145 Hz).

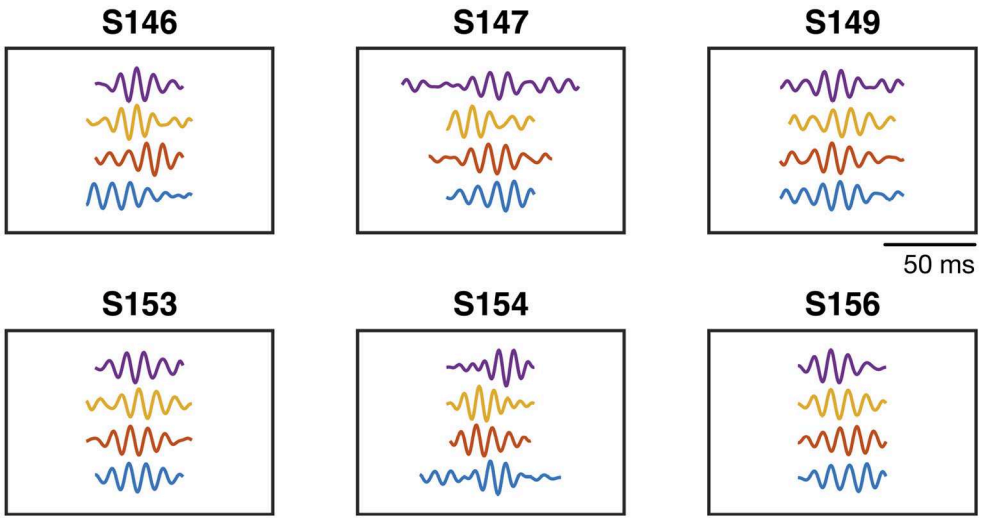

FIGURE 4 | Learned sample cluster centers from high–gamma generating dictionaries. SX stands for Subject X according to the identifiers of the study. One atom per movement direction. Channel 105. All atoms have unit ℓ_2–norm.

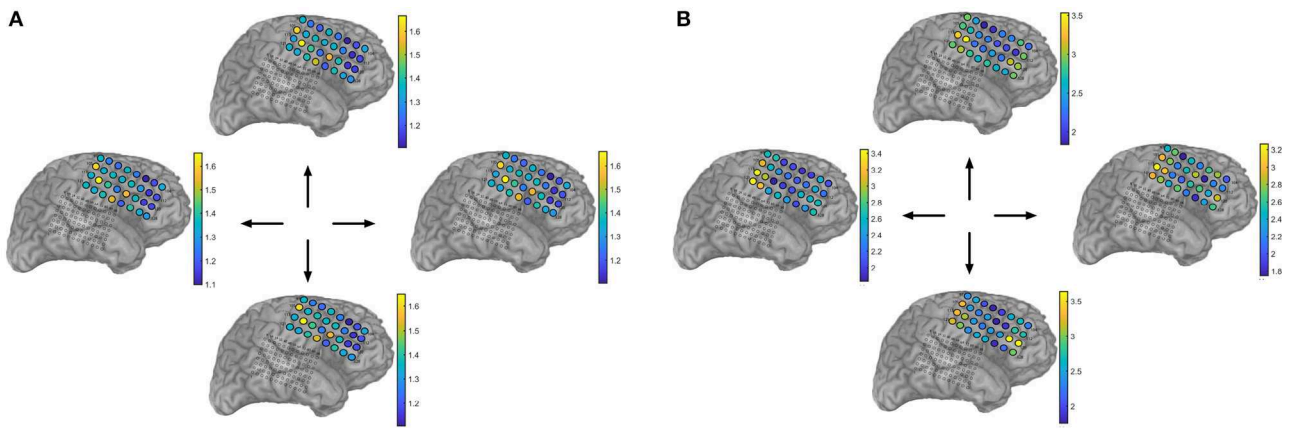

FIGURE 5 | Correlation between modulated power and rate of neuromodulations in the high–gamma band (85–145 Hz). **(A)** Average high–gamma power over sensor space for each movement direction. **(B)** Average rate of high–gamma micro–events (from proposed generative model) over sensor space for each movement direction. Anterior channels (e.g., 105) display relative increase in both descriptors, yet only rate appears to be modulated depending on the movement direction. Subject 153.

gamma power by means of normalized Pearson correlation coefficients across trials, electrodes, and tasks. In particular, the correlation is performed between running sums for τ and running variances for the bandpassed traces (sliding 250 ms). **Table 2** presents the means and standard deviations per subject alongside measures across patients. A similar correlation analysis (**Table S2**) between τ and the raw, unfiltered recordings confirm a statistically significant positive correlation between the extracted TMPP timings and the modulated high-gamma power (right-tailed two-sample t-test of Pearson correlation coefficients, $p = 7.71 \times 10^{-263}$). Lastly, the gamma firing seems to be spatially selective; for instance, channel 101 of the same subject does not display a bursting preference or clear increase in gamma power (**Figure 7**). This can be explained as τ being a proxy for modulated power (estimation of τ demands for power-based measures addressed in the DET).

Even though **Figure 5B** is informative, a more compelling picture needs to incorporate amplitude information in the form of the α feature. **Figure 8** summarizes the learned TMPP timings (τ) and weight marks (α) over electrodes for each movement direction task (Subject 153). The topographical plots depict the deviations from the globals means over space, i.e., a motor task-specific spatiotemporal marked point process over the ECoG recording grid. The figures are also a succinct summary of a multidimensional array or tensor: time × amplitude × electrodes × movement direction. Similar plots for the rest of the subjects are included as **Figures S2–S6**.

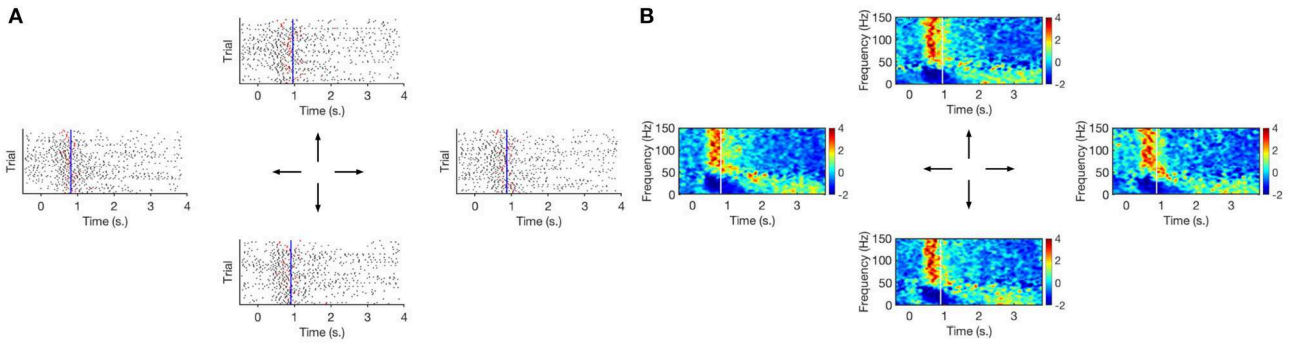

FIGURE 6 | (A) Raster plot of high–gamma bursts (timings of TMPP, τ) per movement direction. Red ticks signal joystick movement onset for each trial. Vertical blue line is the average joystick movement onset across trials. **(B)** Corresponding spectrogram (STFT). Vertical white line is the average joystick movement onset across trials. Zero–mark indicates visual cue before movement. Motor activity lasts $\sim$ 2.8 s. Higher rates of gamma micro–events around the 0.75 s–mark are reflected as larger densities of TMPP samples in the raster plots as well as increase of modulated high–frequency power in the spectrogram. Subject 153, channel 113.

TABLE 2 | Pearson correlation coefficients between extracted TMPP timings, τ, and modulated high–gamma power (85–145 Hz) across channels, trials, and tasks.

	Subject						Average
	146	**147**	**149**	**153**	**154**	**156**	
Mean	0.63	0.59	0.61	0.63	0.38	0.47	0.55
Standard deviation	0.18	0.25	0.19	0.29	0.27	0.26	0.26

We begin the discriminant analysis of the learned representations in an incremental fashion. First, we focus on the timings of gamma bursts, τ. One-way MANOVA confirms that the TMPP timings are not discriminative enough for the movement direction tasks under study. **Figure 9C** illustrates the linear projections from the original 32-channel space to a 2-dimensional space that maximizes the separation between groups or, in this case, directions (TMPP timings from each trial are collapsed as their mean in the design matrix). Two dimensions are plotted for visual purposes. In actuality, the MANOVA results fail to reject the null hypothesis that the group means lie on a line ($p = 0.90$).

Being a point process, the micro-events might encode information in timing-dependent measures, such as inter-event intervals (or IBI—inter-bursts interval), or event rates in a similar manner as spikes in units recordings (Reich et al., 2000). Average log-IBIs constitute the labeled design matrices for the MANOVA test (log-transform to encourage normality). In particular, IBIs are calculated as the intervals (in seconds) between consecutive gamma events for a given trial. Then, the average of the logarithm of such IBIs constitute the feature for the channel/trial/task under consideration. **Figure 9D** shows a similar 2–dimensional linear projection that maximizes separation according to the MANOVA test. The results effectively reject the null hypothesis that the group means lie on a line ($p = 0.0009$); yet, they fail to reject the coplanar null ($p = 0.19$). Similarly, **Figure 9E** summarizes the linear projections corresponding to the micro-event rates, i.e., the feature for a given channel/trial/task is defined as the number of gamma bursts over the 2.5 s—interval of interest. For this case, the test rejects the null hypothesis that the means lie on a 3-dimensional hyperplane ($p = 0.001$), which is the largest possible dimension for the case of four groups. Thus, high-gamma burst rates are the most discriminative timing–related features for movement directions.

Next, we incorporate α as an additional feature. From a generative model instance, α represents the inner product between observed micro-events and closest latent dictionary atoms. We now utilize the couple $\{\tau, \alpha\}$ as a 2-dimensional feature vector (TMPP timings and amplitudes from each trial are collapsed as their corresponding means in the design matrix). This novel feature can be rightfully regarded as a more refined measure of modulated power, i.e., usual TF-based feature vectors do not exploit the concept of sparse neuromodulations with localized modulated power with respect to the background and, therefore, are more likely to introduce noise to subsequent stages. **Figures 9A,B** confirm this limitation; the former exploits log–gamma power whereas the latter utilizes modulated gamma power over time after STFT (Short-Time Fourier Transform) decomposition (85-145 Hz for proper comparisons). On the other hand, **Figure 9F** shows the linear projections from the 64-bivariate ($\{\tau, \log(\alpha^2)\}$) feature space to a 2-dimensional space after the one-way MANOVA test. Classic log-gamma power features fail to reject the null hypothesis that the means lie on a 3-dimensional hyperplane ($p = 0.20$), the STFT case results in a value of $p = 0.51$, whereas a combination of timings and encoding amplitudes of the TMPP yields a rejection of said null ($p = 3 \times 10^{-5}$). **Table 3** summarizes the p-values from similar one-way MANOVAs for all subjects across movement directions. In general, high-gamma rates and bivariate TMPP features are the most discriminant approaches while STFT power is generally more discriminant than gamma power alone. In order to normalize results across subjects, **Table 4** outlines the average silhouette values for the same experiments and confirms the three most discriminant features (in descending order): bivariate TMPP features $\{\tau, \log(\alpha^2)\}$, neuromodulation rates, and Time-Frequency-based power.

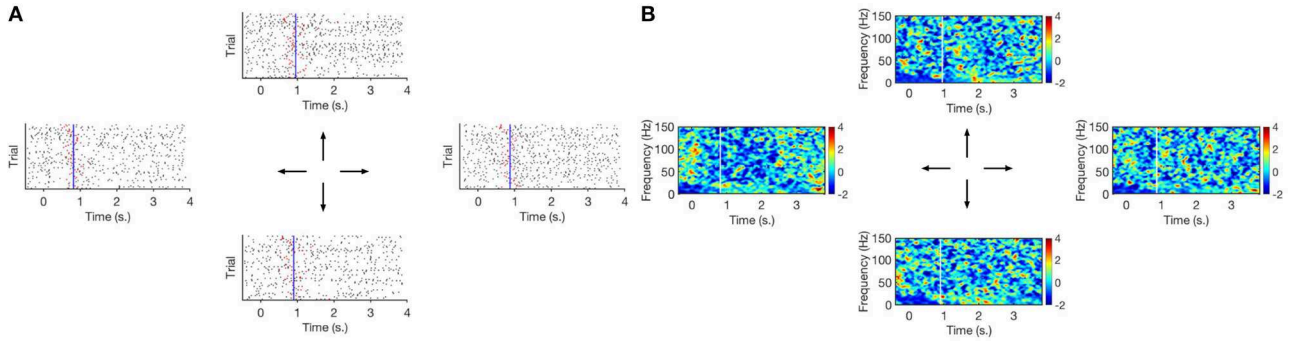

FIGURE 7 | (A) Raster plot of high–gamma bursts (timings of TMPP, τ) per movement direction. Red ticks signal joystick movement onset for each trial. Vertical blue line is the average joystick movement onset across trials. **(B)** Corresponding spectrogram (STFT). Vertical white line is the average joystick movement onset across trials. Zero–mark indicates visual cue before movement. Motor activity lasts $\sim$ 2.8 s. No clear indication of high–rates epochs in both raster plots and spectrograms. Subject 153, channel 101.

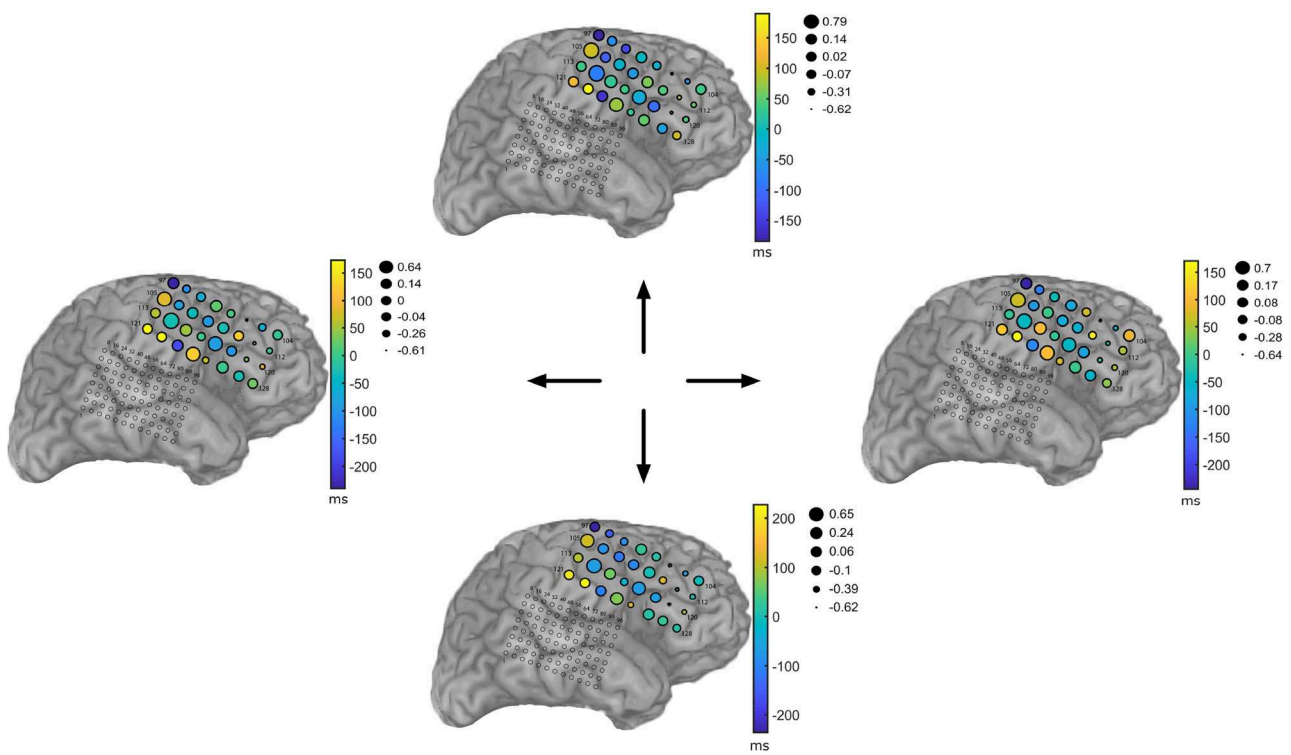

FIGURE 8 | Visualization of high–gamma (85–145 Hz) Temporal Marked Point Process (TMPP) statistics over sensor space for each movement direction. Subject 153. Color scale indicates the deviation of the timings τ from the global, task–specific mean over electrodes. Radii of circles represent deviations of the weights α from the global, task–specific mean over electrodes. Log–transform of squared weight feature to encourage normality, i.e., $\log(\alpha^2)$.

Lastly, sensitivity to hyperparameters is studied. Namely, γ' is varied in the interval [0:0.5:2] and the grand average of silhouette values are reported in **Table 5**. This is equivalent to modulate the sparsity of the resulting TMPP samples, i.e., smaller values of γ' will yield dense neuromodulations over time while a higher γ' further prunes the TMPP at expense of decreasing TPR. Yet once again, τ alone is not discriminant enough regardless of γ'. On the other hand, IBI, τ rate, and $\{\tau, \alpha\}$, show more discriminability and a slight dependency on γ' (especially for values on the extremes of the plausible threshold interval). However, the bivariate (τ, α) features remain the most discriminant case with respect to its peers for a given noise threshold γ'.

5. DISCUSSION

MDL principles are key in the current representation learning framework. Centroid-based clustering usually requires model selection techniques or hyperparameter tuning based on

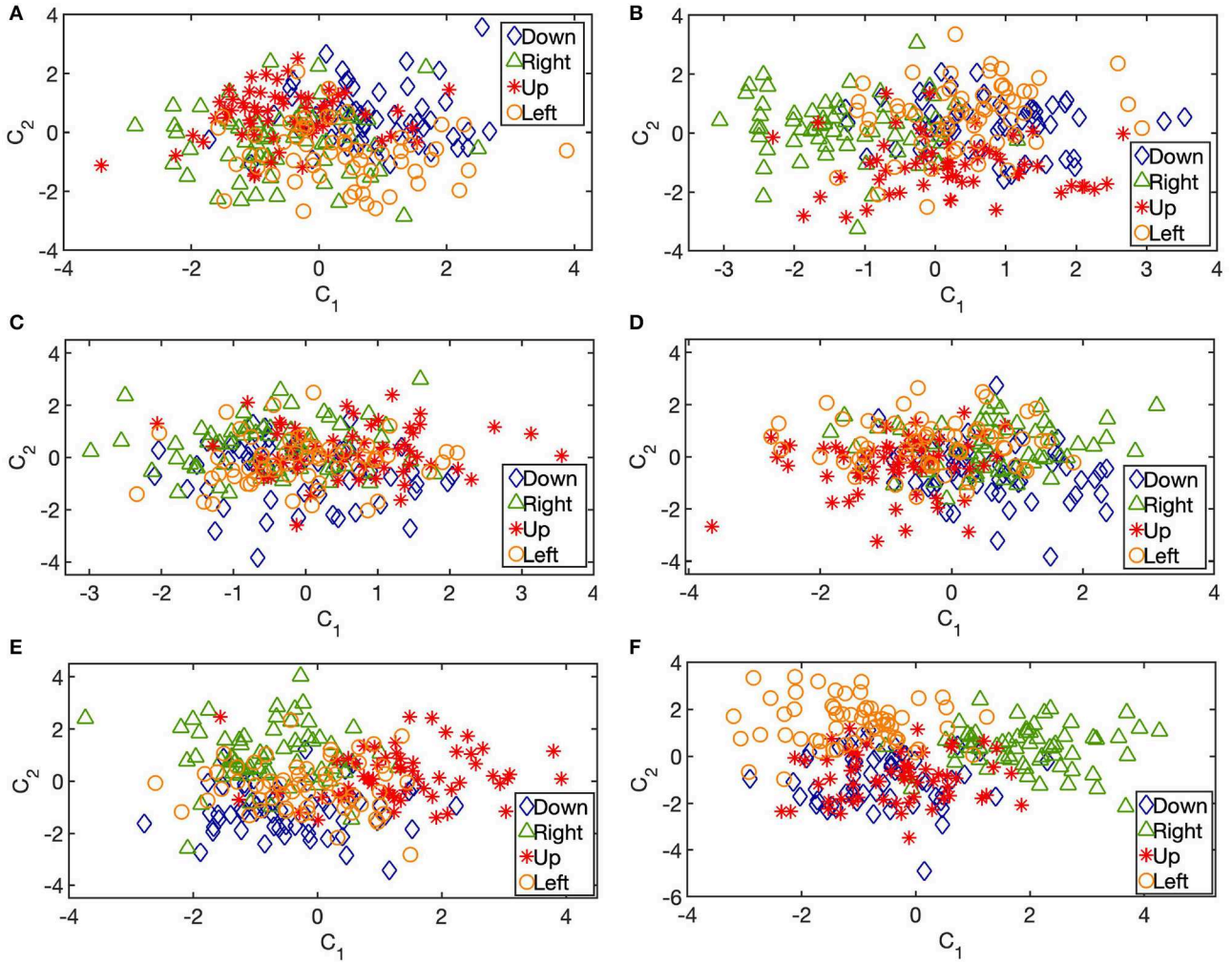

FIGURE 9 | Linear projections to a 2–dimensional space that maximizes Mahalanobis distance between groups (movement directions). Byproduct of multivariate analysis of variance (MANOVA) in the interval −0.5 to 2 s relative to visual cue. **(A)** 32–dimensional log gamma power features. **(B)** 64–dimensional STFT–based power features. **(C)** 32–dimensional TMPP timing (τ) features. **(D)** 32–dimensional TMPP inter–bursts intervals (IBI) features. **(E)** 32–dimensional TMPP phasic event rate features. **(F)** 64–dimensional TMPP timing and weight (τ, α) features. Subject 153. 2–dimensional projections presented for visual purposes only. **Tables 2**, **3** summarize the results of similar linear projections to 3–dimensional spaces.

performance measures. For our case, the latter option is impractical and intractable: reconstructive cost functions such as mean-squared error between inputs and reconstructions imply the need of encoding the entire sequences in $\mathbf{X} \in \mathbb{R}^{M \times \Psi}$ when, in reality, only subsequences embedded in each sample from $\mathbf{X}$ are worth encoding. In addition, hyperparameter tuning of such a large space would be infeasible, e.g., for 10 possible number of clusters per channel, there are a total of $10^{32} =$ possible hyperparameter settings for the frontal ECoG grid under analysis. MDL provides a principled model selection heuristic that is able to partition the input in a hierarchical manner. **Table 1** emphasizes this advantage, while at the same time, highlights the data-driven nature of the proposed algorithms. The fact that the number of dictionary atoms is different across subjects and tasks implies that diverse generative models are responsible for the inherent variability of the ECoG traces. Setting a fixed number of clusters (as is customary in centroid-based clustering) would certainly bias the learned representations. Another alternative is to compare solutions according to performance measures based on labels in a supervised fashion as in Loza et al. (2017).

5.1. Validation

The learning framework was initially proposed in Loza and Principe (2019) as a generalized sleep spindles detector for single-channel EEG recordings. Essentially, classic detectors either estimate the set of timings, $\{\tau\}$, and a surrogate of the set of durations of the micro-events in questions (sleep spindles) or obtain amplitude, $\{\alpha\}$, and duration features as a post-processing step (Huupponen et al., 2007; Devuyst et al., 2011; Purcell et al., 2017). Either way, both views lack the underlying generative nature the dictionary, $\mathbf{D}$, entails.

TABLE 3 | p-values from one–way MANOVA tests exploiting different types of features during the interval −0.5–2 s relative to visual cue.

Subject	Feature					
	Power	**STFT power**	τ	**IBI**	**Rate**	τ, α
146	8.7×10^{-1}	8.4×10^{-1}	9.9×10^{-1}	$\mathbf{8.2 \times 10^{-3}}$	$\mathbf{5.2 \times 10^{-6}}$	$\mathbf{2.8 \times 10^{-2}}$
147	7.3×10^{-1}	$\mathbf{3.7 \times 10^{-2}}$	6.9×10^{-1}	9.5×10^{-1}	$\mathbf{2.4 \times 10^{-3}}$	$\mathbf{3.2 \times 10^{-2}}$
149	5.8×10^{-1}	2.1×10^{-1}	7.6×10^{-1}	$\mathbf{2.2 \times 10^{-2}}$	$\mathbf{1.1 \times 10^{-9}}$	5.6×10^{-2}
153	2.0×10^{-1}	5.1×10^{-1}	9.9×10^{-1}	4.7×10^{-1}	$\mathbf{1.1 \times 10^{-3}}$	$\mathbf{3.0 \times 10^{-5}}$
154	5.5×10^{-1}	3.0×10^{-1}	7.8×10^{-1}	8.3×10^{-1}	4.9×10^{-1}	$\mathbf{4.3 \times 10^{-3}}$
156	9.6×10^{-1}	7.1×10^{-1}	9.2×10^{-1}	1.7×10^{-1}	$\mathbf{1.0 \times 10^{-5}}$	$\mathbf{3.3 \times 10^{-3}}$

Rate refers to high–gamma burst rate from TMPP framework. Null hypothesis: group (movement direction) multivariate means lie on the same 3–dimensional hyperplane. p*-values that lead to hypothesis rejection are marked in bold.*

TABLE 4 | Average silhouette values exploiting different types of features during the interval −0.5–2 s relative to visual cue.

Subject	Feature					
	Power	**STFT power**	τ	**IBI**	**Rate**	τ, α
146	0.39	0.72	0.20	0.46	0.70	0.88
147	0.02	0.34	−0.004	0.16	0.48	0.44
149	0.12	0.65	0.10	0.35	0.71	0.78
153	0.03	0.14	−0.05	0.01	0.16	0.36
154	−0.03	0.03	−0.05	−0.06	−0.03	0.12
156	−0.02	0.25	−0.003	0.16	0.49	0.46
Average	0.08	0.35	0.03	0.18	0.42	0.51

Rate refers to high–gamma burst rate from TMPP framework. Analysis on a three–dimensional space after MANOVA projections.

TABLE 5 | Grand average silhouette values of TMPP–based features during the interval −0.5–2 s relative to visual cue with respect to hyperparameter γ'.

Feature	γ'				
	0.0	**0.5**	**1.0**	**1.5**	**2.0**
τ	0.06	0.04	0.03	0.03	0.06
IBI	0.21	0.22	0.17	0.12	0.06
Rate	0.31	0.41	0.42	0.40	0.32
τ, α	0.47	0.44	0.51	0.51	0.51

The DREAMS database (Devuyst, 2011) was utilized to validate the methods. Single-channel (either CZ-A1 or C3-A1), 30-min-long EEG recordings from 8 subjects were made available with corresponding ground truth as visual scorings of sleep spindles from two different experts. M is set equal to the sample equivalent of 1.5 s while Δ is set to [0.5:0.1:1.5] s. according to scoring criteria of sleep spindles (Rechtschaffen et al., 1968; Niedermeyer and da Silva, 2005; Purcell et al., 2017). Lastly, detection performance with respect to γ' is compared to the visual scoring annotations of expert 1. Expert 2 did not provide scorings for two subjects; therefore, it is excluded from the analysis.

Receiver operating characteristics (ROC) curves quantify the grand averages of True Positive Rates (TPR) and False Positive Rates (FPR) across subjects for a γ' range of [−3:0.5:3] (Figure 3 in Loza and Principe, 2019). Namely, expert 1 provided ground truth as his assessment of the temporal timestamps and durations of each putative sleep spindle. On the other hand, our proposed learning algorithm returns the sets $\{\tau, \alpha, \omega, \mathbf{D}\}$ alongside the durations of each dictionary atom or kernel in an unsupervised fashion. A true positive (TP) appears when a time sample in the EEG recording is deemed as part of a micro–event by the visual scorer and our learning algorithm simultaneously. Conversely, a false negative (FN) occurs when a time sample is deemed as part of a sleep spindle by the expert, but it is missed by the learning method. False positives and true negatives can be defined analogously. Then, TPR and FPR are calculated as:

$$TPR = \frac{TP}{TP + FN} \tag{10}$$

$$FPR = \frac{FP}{FP + TN} \tag{11}$$

In addition due to the inherent noisy and artifact–prone nature of EEG, the sigma index (Huupponen et al., 2000, 2007) is exploited to further reduce the FPR by filtering alpha intrusions and Electromyography (EMG) interference. Best cases of our approach correspond to a global sensitivity of 67.7% and FPR = 0.154 compared to 70.2% and 0.264 from the original report (Devuyst et al., 2011), respectively. Essentially, the proposed algorithm is able to significantly improve specificity while compromising a few TPR percentage points. At the same time, the results go beyond classic detectors by estimating generating dictionaries and features in a completely data–driven fashion. The main scope of the current manuscript is not sleep spindles detection nor optimal conditions for learning on the generative model. Yet, interested readers are referred to Loza and Principe (2019) for further information and heuristics regarding the generalized sleep spindle detector as an application of the proposed model on single-channel EEG traces.

5.2. Analysis of Results

Before addressing the quantitative results of our study, we devote some time to a particular set of neuromodulations that usually appear in ECoG-based epileptic studies: high-frequency oscillations (HFO) or ripples—modulated activity in the 60–100 Hz range that has been used as a biomarker to localize seizure onset zones for potential subsequent resection in medicine resistant patients (Bragin et al., 1999; Worrell et al., 2004). Even though the HFO band is a subset of the high-gamma band under study here, we believe there is no real chance of HFO leaking into our detector. Namely, as mentioned in the Experimental Setting section, all of the epilepsy patients in our study had a temporal lobe onset of epilepsy and none had a frontal neocortical onset (our 32-channel analysis takes place in the frontal grid). Also, none of the patients had a Rolandic focus of their epilepsy, which is where the recordings were taken from. Lastly, it HFO were actually leaking into the learning framework, they likely would not be synchronized to the motor tasks and would serve more as

random background noise which would actually hurt, rather than strengthen our analysis.

Figure 4 underscores the data-driven solutions of the proposed methods. The learned filters are rich in terms of duration, symmetry, frequency, and modulatory patterns. This highlights the data-driven nature of the proposed framework; for instance, classic wavelets or complex sinusoids restrict the time-frequency plane to specific subsets; conversely, our learned dictionaries reflect the inherent non-stationarity of the ECoG with exceptional temporal resolution (only limited by the sampling frequency). The cluster centers depicted in **Figure 4** can also be regarded as the mean values of the distributions of a mixture model that gives rise to the phasic event component in Equation (2). MDL guarantees that said clusters will not merely fit the data, but they will capture the regularity of the ECoG traces, while at the same time, keeping the model as simple as possible (simplicity is quantified here in terms of compression-based measures). Classic shift-invariant dictionary learning solutions, also deemed as convolutional sparse coding, applied to time series either require careful hyperparameter tuning or fixing the number and dimensionality of the learned atoms (Lewicki, 2002; Smith and Lewicki, 2006; Mailhé et al., 2008; La Tour et al., 2018). Our approach provides an unsupervised framework where none of those constraints are required (as previously noted, Δ is a mere blueprint for the learning algorithm to explore different dimensions, however, it is not a restrictive grid of possible phasic event durations). The price we pay, though, comes in the specialization of the EEG spectrum, i.e., all the learning is rhythm-specific (high-gamma in this case). **Figure S1** summarizes the duration distributions and stands in stark contrast to traditional decomposition methods where the dictionary waveforms (e.g., complex sinusoids in Fourier analysis) have a predetermined set duration that is usually regarded as a free hyperparameter of the decomposition, e.g., window size in TF decompositions. Our proposed methods bypass this limitation by learning these duration profiles in a data-driven fashion. Further work will contemplate the potential of novel discriminative mechanisms based on the duration of gamma bursts.

Figure 5 illustrates the correlation between the high–gamma power profile and the rate of extracted micro-events over channels for each movement direction. While the power features suggest specialization over space, it does not fully indicate discriminant areas with respect to motor task type. On the other hand, the estimated rate provides a richer feature space where the neuromodulation density seems to be modulated according to movement direction. This is one of the main reasons why power-based features seem to fall short when compared to more elaborate descriptors that harness the inherent sparse nature of the phasic events (**Tables 3**, **4**). Also, **Figure 5** is a proof of concept of the proposed methods—a case in point is channel 105 where the power profile suggests an area of high local synchronization. The same channel displays high rate levels as well; however for the "up" direction, the high-gamma density slightly decreases suggesting potential discriminant behavior. Lastly, **Figure 5B** depicts smooth transitions in general, i.e., non-abrupt local spatial correlations that can further indicate discriminant regions (not only single electrodes) in terms of neuromodulation rates. This hypothesis is left as further work.

Figures 6A, **7A** suggest specialization of gamma bursting over the cortex. Some channels increase their bursting around specific time instances, while some others do not seem to display particular distinctive patterns. This suggests a selective spectral-spatiotemporal organization of local neuronal populations in order to encode motor tasks. Similar results are observed via averaged TF decompositions, such as STFT (**Figures 6B**, **7B**), however, the introduction of a windowing parameter blurs the temporal information encoded in the timings. Conversely, our approach provides a temporal resolution limited only by the sampling frequency: 2 ms for the current work, although the original 2034.5 Hz sampling frequency could have been used as well (yielding a $\sim$ 0.5 ms temporal resolution with the added computational load that comes with working on higher dimensions). The MANOVA results, silhouette values and exemplary 2-D projections in **Figure 9C** confirm that timing information alone is not sufficient to discriminate movement directions. Yet, further work will investigate if τ might be enough to distinguish between movement and rest stages.

Figures 6, **7** also illustrate the correlation between extracted TMPP timings, τ, and modulated high-gamma power over time. Even though the recordings are aligned to the visual cue, the density of estimated gamma micro-events grows larger around the average joystick movement onset (blue lines in **Figure 6**). This suggests that the rate of gamma neuromodulations increases before and around movement onset on a trial-by-trial basis (see red ticks in **Figure 6**). The measures in **Table 2** confirm the positive correlation between extracted TMPP timings and modulated high–gamma power. On the other hand, the estimated set of τ's bear no correlation (in a linear scheme) with the raw ECoG traces—average of -0.06. Comparison of these two samples (τ correlations with high-gamma filtered and raw recordings) by means of a right-tailed two-sample t-test confirms that the extracted phasic events follow the profile of actual high-gamma power.

A spatiotemporal marked point process succinctly summarizes the network dynamics during motor tasks. **Figure 8** exemplifies a novel graphical depiction of discrete micro-events in terms of their timings and weights. Unlike TF decompositions, the topographical plots quantitatively emphasize the concept of neuromodulations and gamma bursts. For instance, electrode 105 seems to encode motor activity via large timing and weight deviations (with respect to global mean over electrodes); yet, the activity does not seem to support discrimination of movement. On the other hand, electrode 124 modulates gamma burst firing with respect to movement while keeping the amplitudes relatively the same. Most sensors seem to fall into three categories, they resemble the activity of either electrode 105 or electrode 124, or they remain relatively unaffected by the motor task, e.g., electrode 97. However, there are no regions with clear weight modulation (variability of radii across tasks). If the weight α is devised as a surrogate of power with respect to normalized bases, then the results in **Tables 3**, **4** and **Figure 9A** are completely justified—power-based measures alone that disregard timing information are not discriminant when it comes to encoding

movement direction of motor tasks. This conclusion goes along the lines of Reddy et al. (2009) and Zhao et al. (2010). In the case of the two electrodes depicted in **Figures 6**, **7**, their TMPP representations emphasize the fact that channel 101 does not actively encode motor activity—both its τ and α deviations lie close to the zeros marks, i.e., electrode 101 resembles the average global activity of the grid. On the other hand, channel 113 clearly deviates from both global trends; namely, its smaller radii suggest relatively smaller α's (again with respect to the global average of the grid for a particular task). Similarly, positive deviations from the zero-timing-mark indicate slight latencies (roughly in the order of 50 ms) with respect to the entire local neuronal population under study. This empirical analysis highlights one of the main features of the proposed algorithm: the ability to analyze EEG recordings exploiting fine temporal resolutions only limited by the sampling frequencies. Similar plots from the remaining subjects are included as **Supplementary Material**.

IBI and micro-event rates seem to be more suitable features to linearly separate the classes. Both features are a direct consequence of working under the premise of discrete reoccurring wave packets throughout the cortex. These representations would be infeasible for classic TF decompositions where there is no explicit notion of micro-events. While IBI estimates the average interval between gamma bursts, micro-event rates indicate the density of neuromodulations during the specified 2.5 s window. The former seems to be more discriminant than τ alone; however, the latter is consistently superior. If **Figure 6** suggests a specialization in spectral-spatiotemporal organization of local assemblies, **Tables 3**, **4** and **Figure 9E** suggest a collaborative effort of the entire frontal network to modulate high-gamma burst densities at a macro level in order to sparsely encode movement direction. This conclusion could potentially lead to effective online classifiers where it would be only necessary to estimate the density of high-gamma bursts to predict motor tasks.

The incorporation of TMPP weight marks, α, into the modeling framework improves the separability of the classes and consistently outperforms all previous approaches, including classic TF-based frameworks. This last addition emphasizes the need of a generative model to encode neuromodulations as the noisy addition of weighted prototypical templates over time. STFT performs a similar generative assumption, however the basis is generic and not overcomplete; in addition, the unconstrained STFT decomposition does not encourage sparse solutions. Encoding high-gamma bursts as multimodal features not only reduces the dimensionality of the inputs, but also provides interpretable representations that can be fully validated. The bimodal representation (per channel) achieves the highest average silhouette values, signaling a proper clustering solution that can be further exploited in supervised learning frameworks, such as online BCI.

The main hyperparameter of the learning framework is the threshold γ' of the DET. **Table 5** summarizes the average silhouette values as a surrogate of the discriminability among movement directions (larger values imply better class separability). In general, τ–based results are unaffected by the choice of γ', i.e., they all yield a poor clustering solution. When IBIs are utilized as features there is an inverse relationship between performance and γ'; this is a direct consequence of the increase in sparseness that larger γ''s entail, i.e., temporally sparser events lead to biased IBI estimates (the same logic can be applied to τ rates). Lastly, bivariate features are not only the most discriminant solutions for a given γ' in a consistent manner, but they also register robust intervals of the hyperparameter; consequently, this combination of features should be preferred in practice.

Now we address the concept of overfitting, i.e., merely "memorizing" the data and fitting underlying noise rather than actual trends in the ECoG. First, one of MDL's main applications is model selection (Stine, 2004; Grünwald, 2007); hence, it provides a principled framework to choose an appropriate hypothesis (or set of hypotheses) that not only explains the regularities in the data, i.e., fit it properly according to a specified criterion, but also complies with a parsimony principle that controls the complexity of such hypothesis. In this way, MDL is an explicit tool to avoid overfitting. Second, we exploit a randomization test (1,000 independent runs) that randomly shuffles the labels and proceeds to compute the MANOVA p-values (null hypothesis that the means lie on a 3-dimensional hyperplane) and average silhouette values for each subject. **Table 6** summarizes the results and clearly indicates that no significant p-values emerge; silhouette-based measures are also lower than their counterparts on **Table 4**. In fact, the average silhouette values of **Table 4** surpass the 95th percentile of the corresponding randomization test distributions in all cases except for subject 154 exploiting IBI (**Table S3**). In this way, we provide a proof of concept that no overfitting takes place in our study.

In the previous paragraphs we glossed over an important concept for BCI deployment in real settings—online classifiers. Now, we explain in-depth how our framework can be adapted to the supervised learning setting alongside the associated theoretical and practical implications of such change. In this study, we basically clustered relevant subsequences of different lengths from single-channel, multi-trial ECoG traces. This

TABLE 6 | Mean p-values (from MANOVA) and average silhouettes (denoted by S) after randomization test.

Subject	Feature					
	IBI		Rate		τ, α	
	p	S	p	S	p	S
146	0.83	0.17	0.83	0.17	0.66	0.73
147	0.85	0.00	0.84	0.00	0.83	0.19
149	0.84	0.11	0.84	0.11	0.77	0.54
153	0.84	−0.04	0.85	−0.03	0.84	0.07
154	0.84	−0.07	0.83	−0.05	0.84	0.00
156	0.84	0.00	0.85	0.00	0.84	0.20
Average	0.84	0.02	0.84	0.03	0.79	0.28

Interval from −0.5 to 2 s relative to visual cue. One thousand runs of random trial shuffling were performed. $\gamma' = 1$.

learning is executed task by task, and the associated TMPP features and subsequent timing-related characteristics (IBI and rate) are found to be discriminant according to statistical tests and silhouette values. However, during learning, there is no cost function that maximizes discriminability (exploiting label information) and, at the same time, estimates the dictionaries and TMPP features; we only focused on the latter task. An apt analogy comes in handy here: in the computer vision field, dictionary learning is widely used; specifically, the K-SVD technique learns overcomplete, redundant dictionaries under the umbrella of sparse modeling (Aharon et al., 2006). This technique was initially utilized for compression, denoising, and demosaicking of digital images (Elad, 2010), i.e., unsupervised learning tasks similar to our framework in the present manuscript. Later, variations of K-SVD emerged in the supervised setting by exploiting label information and proposing novel cost functions (and consequently novel optimization techniques) (Zhang and Li, 2010; Jiang et al., 2013). We believe our contribution—likewise K-SVD—is the first step toward explicit discriminant models for ECoG-based BCI that exploit representation learning. To this end, the cost functions in Equations (6–8) should be modified to accommodate separability among classes (possibly via a linear classifier); then, appropriate optimization techniques (almost inevitably more complex than the algorithms presented here) would be proposed in order to estimate dictionaries that are not only adaptive, but also discriminant. If such dictionary is attainable, then online classifiers can be built on top of its atoms; for instance, a simple pipeline would assign any incoming trial to the class that minimizes the residual norm (after TMPP features estimation) according to a learned linear classifier. The computational burden and latency of said simple framework would be proportional to the added complexities of the following routines: online bandpass filtering, parallel convolutions with all of the dictionary atoms, online computation of the residue norm (per channel), and linear classifier. Clearly, more sophisticated classifiers can be built on top of such discriminant dictionary, but our goal here was to simply illustrate the point that our contribution focuses on fitting multivariate ECoG data to the proposed model (with the added model selection feature of MDL) in an unsupervised scheme, and yet, discriminability still arises as a property of the representation. In addition, this supervised learning framework would potentially allow the use of "global" dictionaries learned from a population of subjects in order to encode ECoG traces from a novel patient.

Lastly, as previously mentioned, the proposed learning algorithm is rhythm-specific. It was devised as an estimator of dictionary atoms that represent event–related oscillations at small time scales, i.e., higher frequencies. The DET exploits this constraint alongside the inherent sparsity of short-lived bursts to extract micro-events with prominent modulated envelopes. Even though the generative model of Equation (1) is general enough to explain the generative mechanisms of phasic events in the cortex, other learning frameworks are certainly needed to model non-oscillatory events (e.g., K-complexes), desynchronization type of activity (such as the decrease in beta and mu powers observed in **Figure 6** prior and during joystick movement onset), and dense low-frequency events at larger time scales (e.g., phase shifts in theta and delta waves). All these cases constitute attractive new avenues of research and are left as further work. In the spirit of openness and to encourage reproducibility, the MATLAB code corresponding to the proposed methods are available at https://github.com/carlosloza/EEGMDL.

6. CONCLUSION

We proposed a generative model and learning algorithm for single-channel, multi-trial ECoG recordings that can be either posed as a convolutional variant of the sparse modeling problem where both inference and learning are attained or as an estimation of temporal marked point processes and associated prototypical activation filters. MDL is successfully exploited to render a data-driven methodology where model selection and discovery of bases from vector spaces of different dimensions are plausible. Our approach learns representations per label and models the separability among classes via optimal linear projections that maximize the Mahalanobis distance between groups. Timings and weight features of the marked point process are the most discriminative representations and outperform methodologies that do not encourage sparsity and rely on power–based measures. Further work will expand the framework to predictive modeling, i.e., jointly learning the representations as well as a classifier to effectively generalize the encoding mechanisms at work during movement direction-related motor tasks.

DATA AVAILABILITY STATEMENT

The raw data supporting the conclusions of this manuscript will be made available by the authors, without undue reservation, to any qualified researcher.

ETHICS STATEMENT

This study was carried out in accordance with the recommendations of University of Iowa Human Subjects Review Board with written informed consent from all subjects. All subjects gave written informed consent in accordance with the Declaration of Helsinki. The protocol was approved by the University of Iowa Human Subjects Review Board.

AUTHOR CONTRIBUTIONS

CL was responsible for data analysis, methods, and manuscript preparation. CR was responsible for the acquisition, validation, and data sharing. SA worked on manuscript preparation and data analysis. JP collaborated with data analysis and manuscript preparation. All authors discussed the results.

FUNDING

This work was supported by grants to Matthew A. Howard III, M.D., from the National Institute on Deafness and other Communication Disorders (No. R01-DC04290), the General Clinical Research Centers Program (No. M01-RR-59) of the National Institutes of Health, the Hoover Fund, and the Carver

Trust. This work was also supported by Universidad San Francisco de Quito Collaboration Grant No. 10080 and NSF Grant No. 1631759.

ACKNOWLEDGMENTS

The authors would like to thank the patient volunteers for their generous scientific contributions, as well as numerous members of the Howard Lab who were instrumental in data collection at the University of Iowa.

SUPPLEMENTARY MATERIAL

The Supplementary Material for this article can be found online at: https://www.frontiersin.org/articles/10.3389/fnins.2019.01248/full#supplementary-material

REFERENCES

Abdulkader, S. N., Atia, A., and Mostafa, M.-S. M. (2015). Brain computer interfacing: applications and challenges. *Egypt. Inform. J.* 16, 213–230. doi: 10.1016/j.eij.2015.06.002

Aharon, M., Elad, M., and Bruckstein, A. (2006). K-SVD: An algorithm for designing overcomplete dictionaries for sparse representation. *IEEE Trans. Signal Process.* 54:4311. doi: 10.1109/TSP.2006.881199

Ajiboye, A. B., Willett, F. R., Young, D. R., Memberg, W. D., Murphy, B. A., Miller, J. P., et al. (2017). Restoration of reaching and grasping movements through brain-controlled muscle stimulation in a person with tetraplegia: a proof-of-concept demonstration. *Lancet* 389, 1821–1830. doi: 10.1016/S0140-6736(17)30601-3

Aoki, F., Fetz, E., Shupe, L., Lettich, E., and Ojemann, G. (1999). Increased gamma-range activity in human sensorimotor cortex during performance of visuomotor tasks. *Clin. Neurophysiol.* 110, 524–537. doi: 10.1016/S1388-2457(98)00064-9

Arya, R., Wilson, J. A., Fujiwara, H., Rozhkov, L., Leach, J. L., Byars, A. W., et al. (2017). Presurgical language localization with visual naming associated ECoG high-gamma modulation in pediatric drug-resistant epilepsy. *Epilepsia* 58, 663–673. doi: 10.1111/epi.13708

Aydemir, O., and Kayikcioglu, T. (2011). Wavelet transform based classification of invasive brain computer interface data. *Radioengineering* 20, 31–38. Available online at: https://www.radioeng.cz/fulltexts/2011/11_01_031_038.pdf

Bak, P. (2013). *How Nature Works: The Science of Self-Organized Criticality*. New York, NY: Springer Science & Business Media.

Balcan, D. C., and Lewicki, M. S. (2009). "Point coding: sparse image representation with adaptive shiftable-kernel dictionaries," in *SPARS'09-Signal Processing with Adaptive Sparse Structured Representations* (Saint Malo).

Ball, T., Kern, M., Mutschler, I., Aertsen, A., and Schulze-Bonhage, A. (2009). Signal quality of simultaneously recorded invasive and non-invasive eeg. *Neuroimage* 46, 708–716. doi: 10.1016/j.neuroimage.2009.02.028

Başar, E. (1980). *EEG-Brain Dynamics: Relation Between EEG and Brain Evoked Potentials*. Amsterdam: Elsevier-North-Holland Biomedical Press.

Bell, A. J., and Sejnowski, T. J. (1996). Learning the higher-order structure of a natural sound. *Network* 7, 261–266. doi: 10.1088/0954-898X_7_2_005

Bengio, Y., Courville, A., and Vincent, P. (2013). Representation learning: a review and new perspectives. *IEEE Trans. Pattern Anal. Mach. Intell.* 35, 1798–1828. doi: 10.1109/TPAMI.2013.50

Berger, H. (1929). Über das elektrenkephalogramm des menschen. *Eur. Arch. Psychiatry Clin. Neurosci.* 87, 527–570. doi: 10.1007/BF01797193

Bouton, C. E., Shaikhouni, A., Annetta, N. V., Bockbrader, M. A., Friedenberg, D. A., Nielson, D. M., et al. (2016). Restoring cortical control of functional movement in a human with quadriplegia. *Nature* 533:247. doi: 10.1038/nature17435

Bragin, A., Engel, J. Jr., Wilson, C. L., Fried, I., and Buzsáki, G. (1999). High-frequency oscillations in human brain. *Hippocampus* 9, 137–142. doi: 10.1002/(SICI)1098-1063(1999)9:2<137::AID-HIPO5>3.0.CO;2-0

Brockmeier, A. J., and Príncipe, J. C. (2016). Learning recurrent waveforms within EEGs. *IEEE Trans. Biomed. Eng.* 63, 43–54. doi: 10.1109/TBME.2015.2499241

Brunner, P., Ritaccio, A. L., Emrich, J. F., Bischof, H., and Schalk, G. (2011). Rapid communication with a p300 matrix speller using electrocorticographic signals (ECoG). *Front. Neurosci.* 5:5. doi: 10.3389/fnins.2011.00005

Bundy, D. T., Souders, L., Baranyai, K., Leonard, L., Schalk, G., Coker, R., et al. (2017). Contralesional brain–computer interface control of a powered exoskeleton for motor recovery in chronic stroke survivors. *Stroke* 48, 1908–1915. doi: 10.1161/STROKEAHA.116.016304

Busch, N. A., Dubois, J., and VanRullen, R. (2009). The phase of ongoing EEG oscillations predicts visual perception. *J. Neurosci.* 29, 7869–7876. doi: 10.1523/JNEUROSCI.0113-09.2009

Buzsaki, G. (2006). *Rhythms of the Brain*. Oxford, UK: Oxford University Press.

Buzsáki, G. (2015). Hippocampal sharp wave-ripple: a cognitive biomarker for episodic memory and planning. *Hippocampus* 25, 1073–1188. doi: 10.1002/hipo.22488

Buzsáki, G., Anastassiou, C. A., and Koch, C. (2012). The origin of extracellular fields and currents–EEG, ECoG, LFP and spikes. *Nat. Rev. Neurosci.* 13, 407–420. doi: 10.1038/nrn3241

Chao, Z. C., Nagasaka, Y., and Fujii, N. (2010). Long-term asynchronous decoding of arm motion using electrocorticographic signals in monkey. *Front. Neuroeng.* 3:3. doi: 10.3389/fneng.2010.00003

Chaudhary, U., Xia, B., Silvoni, S., Cohen, L. G., and Birbaumer, N. (2017). Brain–computer interface–based communication in the completely locked-in state. *PLoS Biol.* 15:e1002593. doi: 10.1371/journal.pbio.1002593

Collinger, J. L., Wodlinger, B., Downey, J. E., Wang, W., Tyler-Kabara, E. C., Weber, D. J., et al. (2013). High-performance neuroprosthetic control by an individual with tetraplegia. *Lancet* 381, 557–564. doi: 10.1016/S0140-6736(12)61816-9

Crone, N. E., Miglioretti, D. L., Gordon, B., and Lesser, R. P. (1998). Functional mapping of human sensorimotor cortex with electrocorticographic spectral analysis. II. Event-related synchronization in the gamma band. *Brain* 121, 2301–2315. doi: 10.1093/brain/121.12.2301

Daley, D. J., and Vere-Jones, D. (2007). *An Introduction to the Theory of Point Processes: Volume II: General Theory and Structure*. New York, NY: Springer Science & Business Media.

Darvas, F., Scherer, R., Ojemann, J. G., Rao, R., Miller, K. J., and Sorensen, L. B. (2010). High gamma mapping using EEG. *Neuroimage* 49, 930–938. doi: 10.1016/j.neuroimage.2009.08.041

Dat, T. H., Shue, L., and Guan, C. (2006). "Electrocorticographic signal classification based on time-frequency decomposition and nonparametric statistical modeling," in *Engineering in Medicine and Biology Society, 2006, EMBS'06. 28th Annual International Conference of the IEEE* (New York, NY: IEEE), 2292–2295.

Davenport, W. B., and Root, W. L. (1958). *An Introduction to the Theory of Random Signals and Noise, Vol. 159*. New York, NY: McGraw-Hill.

Davies, M. E., and James, C. J. (2007). Source separation using single channel ICA. *Signal Process.* 87, 1819–1832. doi: 10.1016/j.sigpro.2007.01.011

Degenhart, A. D., Eles, J., Dum, R., Mischel, J. L., Smalianchuk, I., Endler, B., et al. (2016). Histological evaluation of a chronically-implanted electrocorticographic electrode grid in a non-human primate. *J. Neural Eng.* 13:046019. doi: 10.1088/1741-2560/13/4/046019

Degenhart, A. D., Hiremath, S. V., Yang, Y., Foldes, S., Collinger, J. L., Boninger, M., et al. (2018). Remapping cortical modulation for electrocorticographic brain–computer interfaces: a somatotopy-based approach in individuals with upper-limb paralysis. *J. Neural Eng.* 15:026021. doi: 10.1088/1741-2552/aa9bfb

Delavallée, M., Abu-Serieh, B., De Tourchaninoff, M., and Raftopoulos, C. (2008). Subdural motor cortex stimulation for central and peripheral neuropathic pain: a long-term follow-up study in a series of eight patients. *Neurosurgery* 63, 101–108. doi: 10.1227/01.NEU.0000335076.24481.B6

Devuyst, S. (2011). *The DREAMS Databases*. The DREAMS Sleep Spindles Database.

Devuyst, S., Dutoit, T., Stenuit, P., and Kerkhofs, M. (2011). "Automatic sleep spindles detection overview and development of a standard proposal assessment method," in *Engineering in Medicine and Biology Society, EMBC, 2011 Annual International Conference of the IEEE* (Boston, MA: IEEE), 1713–1716. doi: 10.1109/IEMBS.2011.6090491

Dobkin, B. H. (2007). Brain–computer interface technology as a tool to augment plasticity and outcomes for neurological rehabilitation. *J. Physiol.* 579, 637–642. doi: 10.1113/jphysiol.2006.123067

Ekanadham, C., Tranchina, D., and Simoncelli, E. P. (2011). Recovery of sparse translation-invariant signals with continuous basis pursuit. *IEEE Trans. Signal Process.* 59, 4735–4744. doi: 10.1109/TSP.2011.2160058

Elad, M. (2010). *Sparse and Redundant Representations: From Theory to Applications in Signal and Image Processing*. New York, NY: Springer Science & Business Media.

Freeman, W., and Quiroga, R. Q. (2012). *Imaging Brain Function With EEG: Advanced Temporal and Spatial Analysis of Electroencephalographic Signals*. New York, NY: Springer Science & Business Media.

Freeman, W. J. (1975). *Mass Action in the Nervous System*. Cambridge, MA: Academic Press.

Freeman, W. J., Burke, B. C., and Holmes, M. D. (2003). Aperiodic phase re-setting in scalp EEG of beta–gamma oscillations by state transitions at alpha–theta rates. *Hum. Brain Mapp.* 19, 248–272. doi: 10.1002/hbm.10120

Freeman, W. J., Rogers, L. J., Holmes, M. D., and Silbergeld, D. L. (2000). Spatial spectral analysis of human electrocorticograms including the alpha and gamma bands. *J. Neurosci. Methods* 95, 111–121. doi: 10.1016/S0165-0270(99)00160-0

Gabor, D. (1946). Theory of communication. Part 1: The analysis of information. *J. Instit. Electr. Eng. Part III* 93, 429–441.

Goncharova, I. I., McFarland, D. J., Vaughan, T. M., and Wolpaw, J. R. (2003). EMG contamination of EEG: spectral and topographical characteristics. *Clin. Neurophysiol.* 114, 1580–1593. doi: 10.1016/s1388-2457(03)00093-2

Grünwald, P. D. (2007). *The Minimum Description Length Principle*. Cambridge, MA: MIT Press.

Gunduz, A., Brunner, P., Sharma, M., Leuthardt, E. C., Ritaccio, A. L., Pesaran, B., et al. (2016). Differential roles of high gamma and local motor potentials for movement preparation and execution. *Brain Comput. Interfaces* 3, 88–102. doi: 10.1080/2326263X.2016.1179087

Hanslmayr, S., Klimesch, W., Sauseng, P., Gruber, W., Doppelmayr, M., Freunberger, R., et al. (2006). Alpha phase reset contributes to the generation of ERPs. *Cereb. Cortex* 17, 1–8. doi: 10.1093/cercor/bhj129

Herff, C., Johnson, G., Diener, L., Shih, J., Krusienski, D., and Schultz, T. (2016). "Towards direct speech synthesis from ECoG: a pilot study," in *2016 IEEE 38th Annual International Conference of the Engineering in Medicine and Biology Society (EMBC)* (Orlando: IEEE), 1540–1543.

Hochberg, L. R., Bacher, D., Jarosiewicz, B., Masse, N. Y., Simeral, J. D., Vogel, J., et al. (2012). Reach and grasp by people with tetraplegia using a neurally controlled robotic arm. *Nature* 485:372. doi: 10.1038/nature11076

Hotson, G., McMullen, D. P., Fifer, M. S., Johannes, M. S., Katyal, K. D., Para, M. P., et al. (2016). Individual finger control of a modular prosthetic limb using high-density electrocorticography in a human subject. *J. Neural Eng.* 13:026017. doi: 10.1088/1741-2560/13/2/026017

Huupponen, E., Gómez-Herrero, G., Saastamoinen, A., Värri, A., Hasan, J., and Himanen, S.-L. (2007). Development and comparison of four sleep spindle detection methods. *Artif. Intell. Med.* 40, 157–170. doi: 10.1016/j.artmed.2007.04.003

Huupponen, E., Värri, A., Himanen, S.-L., Hasan, J., Lehtokangas, M., and Saarinen, J. (2000). Optimization of sigma amplitude threshold in sleep spindle detection. *J. Sleep Res.* 9, 327–334. doi: 10.1046/j.1365-2869.2000.00220.x

Hyvarinen, A. (1999). Fast and robust fixed-point algorithms for independent component analysis. *IEEE Trans. Neural Netw.* 10, 626–634.

Ince, N. F., Goksu, F., and Tewfik, A. H. (2008). An ECoG based brain computer interface with spatially adapted time-frequency patterns. *Biosignals* 25, 132–139. doi: 10.5220/0001068701320139

Jacobs, J., Staba, R., Asano, E., Otsubo, H., Wu, J., Zijlmans, M., et al. (2012). High-frequency oscillations (HFOs) in clinical epilepsy. *Prog. Neurobiol.* 98, 302–315. doi: 10.1016/j.pneurobio.2012.03.001

Jiang, Z., Lin, Z., and Davis, L. S. (2013). Label consistent K-SVD: Learning a discriminative dictionary for recognition. *IEEE Trans. Pattern Anal. Mach. Intell.* 35, 2651–2664. doi: 10.1109/TPAMI.2013.88

Jokeit, H., and Makeig, S. (1994). Different event-related patterns of gamma-band power in brain waves of fast-and slow-reacting subjects. *Proc. Natl. Acad. Sci. U.S.A.* 91, 6339–6343. doi: 10.1073/pnas.91.14.6339

Keogh, E., and Lin, J. (2005). Clustering of time-series subsequences is meaningless: implications for previous and future research. *Knowl. Inform. Syst.* 8, 154–177. doi: 10.1007/s10115-004-0172-7

Kubanek, J., Miller, K., Ojemann, J., Wolpaw, J., and Schalk, G. (2009). Decoding flexion of individual fingers using electrocorticographic signals in humans. *J. Neural Eng.* 6:066001. doi: 10.1088/1741-2560/6/6/066001

Kübler, A., Neumann, N., Kaiser, J., Kotchoubey, B., Hinterberger, T., and Birbaumer, N. P. (2001). Brain-computer communication: self-regulation of slow cortical potentials for verbal communication. *Arch. Phys. Med. Rehabil.* 82, 1533–1539. doi: 10.1053/apmr.2001.26621

La Tour, T. D., Moreau, T., Jas, M., and Gramfort, A. (2018). "Multivariate convolutional sparse coding for electromagnetic brain signals," in *Advances in Neural Information Processing Systems* (Montreal), 3296–3306.

Lebedev, M. A., Carmena, J. M., O'Doherty, J. E., Zacksenhouse, M., Henriquez, C. S., Principe, J. C., et al. (2005). Cortical ensemble adaptation to represent velocity of an artificial actuator controlled by a brain-machine interface. *J. Neurosci.* 25, 4681–4693. doi: 10.1523/JNEUROSCI.4088-04.2005

Lebedev, M. A., and Nicolelis, M. A. (2006). Brain–machine interfaces: past, present and future. *Trends Neurosci.* 29, 536–546. doi: 10.1016/j.tins.2006.07.004

Leuthardt, E., Pei, X.-M., Breshears, J., Gaona, C., Sharma, M., Freudenburg, Z., et al. (2012). Temporal evolution of gamma activity in human cortex during an overt and covert word repetition task. *Front. Hum. Neurosci.* 6:99. doi: 10.3389/fnhum.2012.00099

Leuthardt, E. C., Miller, K. J., Schalk, G., Rao, R. P., and Ojemann, J. G. (2006). Electrocorticography-based brain computer interface-the seattle experience. *IEEE Trans. Neural Syst. Rehabil. Eng.* 14, 194–198. doi: 10.1109/TNSRE.2006.875536

Lewicki, M. S. (2002). Efficient coding of natural sounds. *Nat. Neurosci.* 5:356. doi: 10.1038/nn831

Linkenkaer-Hansen, K., Nikouline, V. V., Palva, J. M., and Ilmoniemi, R. J. (2001). Long-range temporal correlations and scaling behavior in human brain oscillations. *J. Neurosci.* 21, 1370–1377. doi: 10.1523/JNEUROSCI.21-04-01370.2001

Loza, C. A., Okun, M. S., and Príncipe, J. C. (2017). A marked point process framework for extracellular electrical potentials. *Front. Syst. Neurosci.* 11:95. doi: 10.3389/fnsys.2017.00095

Loza, C. A., and Principe, J. C. (2018). "The embedding transform. A novel analysis of non-stationarity in the EEG," in *2018 IEEE 40th Annual International Conference of the Engineering in Medicine and Biology Society (EMBC)* (Honolulu: IEEE).

Loza, C. A., and Principe, J. C. (2019). "The generalized sleep spindles detector: a generative model approach on single-channel EEGs," in *International Work-Conference on Artificial Neural Networks* (New York, NY: Springer), 127–138.

Lucena, F., Barros, A. K., Príncipe, J. C., and Ohnishi, N. (2011). Statistical coding and decoding of heartbeat intervals. *PLoS ONE* 6:e20227. doi: 10.1371/journal.pone.0020227

Luczak, A., Barthó, P., and Harris, K. D. (2009). Spontaneous events outline the realm of possible sensory responses in neocortical populations. *Neuron* 62, 413–425. doi: 10.1016/j.neuron.2009.03.014

Mailhé, B., Lesage, S., Gribonval, R., Bimbot, F., and Vandergheynst, P. (2008). "Shift-invariant dictionary learning for sparse representations: extending K-SVD," in *2008 16th European Signal Processing Conference* (Lausanne: IEEE), 1–5.

Mallat, S. (1999). *A Wavelet Tour of Signal Processing*. San Diego, CA: Academic press.

Mallat, S. G., and Zhang, Z. (1993). Matching pursuits with time-frequency dictionaries. *IEEE Trans. Signal Process.* 41, 3397–3415. doi: 10.1109/78.258082

Mellinger, J., Schalk, G., Braun, C., Preissl, H., Rosenstiel, W., Birbaumer, N., et al. (2007). An MEG-based brain–computer interface (BCI). *Neuroimage* 36, 581–593. doi: 10.1016/j.neuroimage.2007.03.019

Mestais, C. S., Charvet, G., Sauter-Starace, F., Foerster, M., Ratel, D., and Benabid, A. L. (2015). Wimagine: wireless 64-channel ECoG recording implant for long term clinical applications. *IEEE Trans. Neural Syst. Rehabil. Eng.* 23, 10–21. doi: 10.1109/TNSRE.2014.2333541

Miller, K. J., Leuthardt, E. C., Schalk, G., Rao, R. P., Anderson, N. R., Moran, D. W., et al. (2007). Spectral changes in cortical surface potentials during motor movement. *J. Neurosci.* 27, 2424–2432. doi: 10.1523/JNEUROSCI.3886-06.2007

Miller, K. J., Schalk, G., Fetz, E. E., Den Nijs, M., Ojemann, J. G., and Rao, R. P. (2010). Cortical activity during motor execution, motor imagery, and imagery-based online feedback. *Proc. Natl. Acad. Sci. U.S.A.* 107, 4430–4435. doi: 10.1073/pnas.0913697107

Niedermeyer, E., and da Silva, F. L. (2005). *Electroencephalography: Basic Principles, Clinical Applications, and Related Fields*. Philadelphia, PA: Lippincott Williams & Wilkins.

O'Brien, R. G., and Kaiser, M. K. (1985). Manova method for analyzing repeated measures designs: an extensive primer. *Psychol. Bull.* 97:316. doi: 10.1037//0033-2909.97.2.316

Onaran, I., Ince, N. F., and Cetin, A. E. (2011). "Classification of multichannel ECoG related to individual finger movements with redundant spatial projections," in *Engineering in Medicine and Biology Society, EMBC, 2011 Annual International Conference of the IEEE* (Boston, MA: IEEE), 5424–5427.

Pfurtscheller, G., Guger, C., Müller, G., Krausz, G., and Neuper, C. (2000). Brain oscillations control hand orthosis in a tetraplegic. *Neurosci. Lett.* 292, 211–214. doi: 10.1016/S0304-3940(00)01471-3

Purcell, S., Manoach, D., Demanuele, C., Cade, B., Mariani, S., Cox, R., et al. (2017). Characterizing sleep spindles in 11,630 individuals from the national sleep research resource. *Nat. Commun.* 8:15930. doi: 10.1038/ncomms15930

Rakthanmanon, T., Keogh, E. J., Lonardi, S., and Evans, S. (2011). "Time series epenthesis: clustering time series streams requires ignoring some data," in *2011 IEEE 11th International Conference on Data Mining (ICDM)* (Vancouver: IEEE), 547–556.

Ramsey, N. F., Salari, E., Aarnoutse, E. J., Vansteensel, M. J., Bleichner, M. G., and Freudenburg, Z. (2018). Decoding spoken phonemes from sensorimotor cortex with high-density ECoG grids. *Neuroimage* 180, 301–311. doi: 10.1016/j.neuroimage.2017.10.011

Rechtschaffen, A., Kales, A., University of California, L. A. B. I. S., and Network, N. N. I. (1968). *A Manual of Standardized Terminology, Techniques and Scoring System for Sleep Stages of Human Subjects*. Publication. Brain Information Service; Brain Research Institute; University of California.

Reddy, C. G., Reddy, G. G., Kawasaki, H., Oya, H., Miller, L. E., and Howard, M. A. (2009). Decoding movement-related cortical potentials from electrocorticography. *Neurosurg. Focus* 27:E11. doi: 10.3171/2009.4.FOCUS0990

Reich, D. S., Mechler, F., Purpura, K. P., and Victor, J. D. (2000). Interspike intervals, receptive fields, and information encoding in primary visual cortex. *J. Neurosci.* 20, 1964–1974. doi: 10.1523/JNEUROSCI.20-05-01964.2000

Rodriguez, E., George, N., Lachaux, J.-P., Martinerie, J., Renault, B., and Varela, F. J. (1999). Perception's shadow: long-distance synchronization of human brain activity. *Nature* 397:430.

Rousseeuw, P. J. (1987). Silhouettes: a graphical aid to the interpretation and validation of cluster analysis. *J. Comput. Appl. Math.* 20, 53–65.

Schalk, G., and Leuthardt, E. C. (2011). Brain-computer interfaces using electrocorticographic signals. *IEEE Rev. Biomed. Eng.* 4, 140–154. doi: 10.1109/RBME.2011.2172408

Schalk, G., Miller, K. J., Anderson, N. R., Wilson, J. A., Smyth, M. D., Ojemann, J. G., et al. (2008). Two-dimensional movement control using electrocorticographic signals in humans. *J. Neural Eng.* 5:75. doi: 10.1088/1741-2560/5/1/008

Serruya, M. D., Hatsopoulos, N. G., Paninski, L., Fellows, M. R., and Donoghue, J. P. (2002). Brain-machine interface: instant neural control of a movement signal. *Nature* 416:141. doi: 10.1038/416141a

Smith, E. C., and Lewicki, M. S. (2006). Efficient auditory coding. *Nature* 439, 978–982. doi: 10.1038/nature04485

Soekadar, S. R., Birbaumer, N., Slutzky, M. W., and Cohen, L. G. (2015). Brain–machine interfaces in neurorehabilitation of stroke. *Neurobiol. Dis.* 83, 172–179. doi: 10.1016/j.nbd.2014.11.025

Staley, K. J., White, A., and Dudek, F. E. (2011). Interictal spikes: harbingers or causes of epilepsy? *Neurosci. Lett.* 497, 247–250. doi: 10.1016/j.neulet.2011.03.070

Stam, C. J., and De Bruin, E. A. (2004). Scale-free dynamics of global functional connectivity in the human brain. *Hum. Brain Mapp.* 22, 97–109. doi: 10.1002/hbm.20016

Stine, R. A. (2004). Model selection using information theory and the MDL principle. *Sociol. Methods Res.* 33, 230–260. doi: 10.1177/0049124103262064

Tallon-Baudry, C., and Bertrand, O. (1999). Oscillatory gamma activity in humans and its role in object representation. *Trends Cogn. Sci.* 3, 151–162. doi: 10.1016/S1364-6613(99)01299-1

Tangermann, M., Müller, K.-R., Aertsen, A., Birbaumer, N., Braun, C., Brunner, C., et al. (2012). Review of the BCI competition IV. *Front. Neurosci.* 6:55. doi: 10.3389/fnins.2012.00055

Taylor, D. M., Tillery, S. I. H., and Schwartz, A. B. (2002). Direct cortical control of 3D neuroprosthetic devices. *Science* 296, 1829–1832. doi: 10.1126/science.1070291

Unser, M., and Aldroubi, A. (1996). A review of wavelets in biomedical applications. *Proc. IEEE* 84, 626–638. doi: 10.1109/5.488704

Vansteensel, M. J., Pels, E. G., Bleichner, M. G., Branco, M. P., Denison, T., Freudenburg, Z. V., et al. (2016). Fully implanted brain–computer interface in a locked-in patient with ALS. *New Engl. J. Med.* 375, 2060–2066. doi: 10.1056/NEJMoa1608085

Vaughan, T. M. (2003). "Guest editorial brain-computer interface technology: a review of the second international meeting," in *IEEE Transactions on Neural Systems and Rehabilitation Engineering, Vol. 11* (IEEE), 94–109. doi: 10.1109/TNSRE.2003.814799

Waldert, S. (2016). Invasive vs. non-invasive neuronal signals for brain-machine interfaces: will one prevail? *Front. Neurosci.* 10:295. doi: 10.3389/fnins.2016.00295

Weiskopf, N., Mathiak, K., Bock, S. W., Scharnowski, F., Veit, R., Grodd, W., et al. (2004). Principles of a brain-computer interface (BCI) based on real-time functional magnetic resonance imaging (fMRI). *IEEE Trans. Biomed. Eng.* 51, 966–970. doi: 10.1109/TBME.2004.827063

Worrell, G. A., Parish, L., Cranstoun, S. D., Jonas, R., Baltuch, G., and Litt, B. (2004). High-frequency oscillations and seizure generation in neocortical epilepsy. *Brain* 127, 1496–1506. doi: 10.1093/brain/awh149

Yanagisawa, T., Hirata, M., Saitoh, Y., Kishima, H., Matsushita, K., Goto, T., et al. (2012). Electrocorticographic control of a prosthetic arm in paralyzed patients. *Ann. Neurol.* 71, 353–361. doi: 10.1002/ana.22613

Zhang, Q., and Li, B. (2010). "Discriminative K-SVD for dictionary learning in face recognition," in *2010 IEEE Computer Society Conference on Computer Vision and Pattern Recognition* (San Francisco, CA: IEEE), 2691–2698.

Zhao, H.-B., Yu, C.-Y., Liu, C., and Wang, H. (2010). "ECoG-based brain-computer interface using relative wavelet energy and probabilistic neural network," in *2010 3rd International Conference on Biomedical Engineering and Informatics (BMEI), Vol. 2* (Yantai: IEEE), 873–877.

Conflict of Interest: The authors declare that the research was conducted in the absence of any commercial or financial relationships that could be construed as a potential conflict of interest.

frontiers in Neuroinformatics

REVIEW
published: 03 December 2019
doi: 10.3389/fninf.2019.00074

Decoding Movement From Electrocorticographic Activity: A Review

Ksenia Volkova[1], *Mikhail A. Lebedev*[1], *Alexander Kaplan*[1,2,3] *and Alexei Ossadtchi*[1]*

[1] *Center for Bioelectric Interfaces, Higher School of Economics, National Research University, Moscow, Russia,* [2] *Center for Biotechnology Development, National Research Lobachevsky State University of Nizhny Novgorod, Nizhny Novgorod, Russia,* [3] *Laboratory for Neurophysiology and Neuro-Computer Interfaces, Faculty of Biology, Lomonosov Moscow State University, Moscow, Russia*

Electrocorticography (ECoG) holds promise to provide efficient neuroprosthetic solutions for people suffering from neurological disabilities. This recording technique combines adequate temporal and spatial resolution with the lower risks of medical complications compared to the other invasive methods. ECoG is routinely used in clinical practice for preoperative cortical mapping in epileptic patients. During the last two decades, research utilizing ECoG has considerably grown, including the paradigms where behaviorally relevant information is extracted from ECoG activity with decoding algorithms of different complexity. Several research groups have advanced toward the development of assistive devices driven by brain-computer interfaces (BCIs) that decode motor commands from multichannel ECoG recordings. Here we review the evolution of this field and its recent tendencies, and discuss the potential areas for future development.

Keywords: electrocorticography, ECoG, brain-computer interface, BCI, movement decoding

OPEN ACCESS

Edited by:
Gaute T. Einevoll, Norwegian University of Life Sciences, Norway

Reviewed by:
Wim Van Drongelen, University of Chicago, United States
Pierre Berthet, University of Oslo, Norway

***Correspondence:**
Alexei Ossadtchi
aossadtchi@hse.ru

Received: *03 May 2019*
Accepted: *14 November 2019*
Published: *03 December 2019*

Citation:
Volkova K, Lebedev MA, Kaplan A and Ossadtchi A (2019) Decoding Movement From Electrocorticographic Activity: A Review. Front. Neuroinform. 13:74. doi: 10.3389/fninf.2019.00074

1. INTRODUCTION

The brain is a unique organ of the human body. Containing myriads of neurons, the brain circuits continuously process multiple sensory, motor and cognitive signals, generate thoughts and decisions, and produce a subjective feeling of being conscious and free-willed. The brain enables us with the capacity to effortlessly control such complex behaviors as voluntary movements of body parts, maintenance of posture and balance, speech production, and perception of the external world. Unfortunately, neurological disease or trauma may cause dramatic disruptions of these neuronal mechanisms, making an individual unable to move, feel and communicate. Many of such devastating neurological conditions currently have no cure, including amyotrophic lateral sclerosis (ALS), stroke, and spinal cord injury (SCI).

BCIs, also called brain-machine interfaces (BMIs) and neural prostheses, hold promise to provide revolutionary solutions to the treatment of brain disorders. BCIs connect neural circuits to external devices, such as prosthetic limbs, means of communication, computers, appliances for functional electrical stimulation, and even the other parts of the brain (Lebedev and Nicolelis, 2006). Medical applications of BCIs strive to restore functions lost to neurological disorders and aid in rehabilitation. For example, BCI approach to SCI consists of directly connecting the unaffected brain regions, such as the sensorimotor cortex, to a limb prosthesis (Hochberg et al., 2006, 2012; Collinger et al., 2013; Bouton et al., 2016). Many neuroprosthetic components have been proposed and developed over the last two decades. These are biocompatible implants for neural recordings, devices for stimulating neural circuits, and wireless recording systems. BCIs can connect the brain

to computer cursors (Carmena et al., 2003; Lebedev et al., 2005), text generators (Pan et al., 2013; Akram et al., 2014), arm prostheses (Carmena et al., 2003; Velliste et al., 2008; Collinger et al., 2013), exoskeletons for assisted walking (Gancet et al., 2011; Contreras-Vidal and Grossman, 2013; Kwak et al., 2015), virtual-reality objects (Badia et al., 2013), powered wheelchairs (Galán et al., 2008; Chai et al., 2014), drones (LaFleur et al., 2013), and automobiles (Göhring et al., 2013). Recently, futuristic BCIs have emerged that merge several individual brains into a brain-net (Pais-Vieira et al., 2013; Rao et al., 2014).

Among different classes of BCIs, BCIs that operate in the motor domain have underwent a particularly extensive development because of the expectation that they could treat paralysis by enabling voluntary control of prosthetic limbs. Motor BCIs have been developed that enable movements of the arms (Wessberg et al., 2000; Carmena et al., 2003; Velliste et al., 2008; Collinger et al., 2013) and legs (Fitzsimmons et al., 2009). In addition to BCIs that enact movements, BCIs have emerged that handle cognitive functions, like executive control, attention, and decision making (Andersen et al., 2004, 2010; Mirabella and Lebedev, 2016). In the sensory domain, BCIs have been developed that apply stimulation to peripheral and central structures of the nervous system to evoke percepts mimicking natural senses, including hearing (House, 1976), vision (Dobelle, 2000; Normann et al., 2009), and touch (Bensmaia and Miller, 2014).

In this review, we focus on BCIs that are based on an invasive recording method called ECoG. We argue that ECoG could provide efficient solutions for many clinical cases because, first, ECoG grids sample neural signals with better spatial and temporal resolution compared to non-invasive recording methods, such as electroencephalography (EEG), and second, ECoG electrodes do not penetrate into the brain and thus offer a safer solution compared to the techniques that require insertion of recording sensors into the nervous tissue (Leuthardt et al., 2004; Hill et al., 2012; Petroff et al., 2016). The studies conducted up to date have demonstrated that ECoG-based BCIs are applicable to motor tasks. Yet, we suggest that accuracy of such motor BCIs could be improved by the implementation of more advanced neural decoding algorithms, particularly the ones based on deep neural networks.

We start with an overview of ECoG recording methods. Next, we review the motor tasks that have been utilized in ECoG decoding studies. Finally, we discuss the relevant decoding algorithms and software.

2. ECOG METHODOLOGY AND ITS ADVANTAGES COMPARED TO THE OTHER RECORDING METHODS

A multitude of methods for recording of brain activity have been developed during the last several decades. Depending on the biological and physical principles employed, these methods have different spatial and temporal resolution. The recording methods range from classical single-unit techniques, where microelectrodes are inserted into the brain tissue, to non-invasive approaches, such as EEG, magnetoencephalography (MEG), near-infrared spectroscopy and functional magnetic resonance imaging. The choice of method in each concrete case is based on a number of requirements, including an assessment of risk to human subjects.

With the advancement of BCIs, we have seen a development of multichannel recording methods that allow sampling signals from many brain regions simultaneously (Nicolelis and Lebedev, 2009). To build clinically relevant neural prostheses, such recording methods should be viable for long periods of time. Chronically implanted multielectrode arrays (MEAs) measure brain activity at high spatial (at the level of single neurons) and temporal (at the level of neuronal spikes) resolution. MEAs-based BCIs have been implemented in rats (Chapin et al., 1999; Song et al., 2009), non-human primates (Taylor et al., 2002; Carmena et al., 2003; Gilja et al., 2012; Schaffelhofer et al., 2015) and humans (Hochberg et al., 2006; Collinger et al., 2013; Gilja et al., 2015; Brandman et al., 2017). The number of motor degrees of freedom that such BCIs could handle has been steadily growing (Hochberg et al., 2012; Collinger et al., 2013; Wodlinger et al., 2014; Vaskov et al., 2018). Recordings with MEAs are, however, not without problems, particularly when utilized in humans, since intracortical electrodes may provoke infection, tissue damage and scarring – the factors that contribute to deterioration of recording quality over time (Perge et al., 2013; Nuyujukian et al., 2014; Murphy et al., 2016; Kim et al., 2018).

While non-invasive BCIs do not have appreciable health risks, they have limitations of their own. Thus, EEG-based BCIs, which are currently prevalent because of their ease of use (Nicolas-Alonso and Gomez-Gil, 2012), have a lower information transfer rate compared to invasive BCIs (Lebedev and Nicolelis, 2006). Signal to noise ratio and spatial resolution are low for EEG recordings because with this method electrical potentials are sampled at a distance from their source, get smeared due to propagation through brain meninges and skull, and are susceptible to contamination with mechanical, electrooculographic (EOG), and electromyographic (EMG) artifacts (Cooper et al., 1965). Classification of several discrete motor states can be achieved with EEG recordings (for example, detecting the presence or absence of an actual or imagined limb movement). However, accurate decoding of fine movement characteristics is difficult with this method.

ECoG alleviates several problems related to using the other recording methods. With ECoG, electrical signal is recorded from the surface of the brain either epidurally (i.e., the electrodes are placed on the surface of the dura mater), or subdurally (i.e., the electrodes are placed underneath the dura mater.) While ECoG signals resemble EEG data (Kellis et al., 2016), they have greater amplitude, higher spatial resolution and broader frequency range (Schalk and Leuthardt, 2011). ECoG is superior to EEG for recordings of both cortical low-frequency oscillations (Hughes and Crunelli, 2005) and high-frequency activity in the gamma-range (Manning et al., 2009; Schalk and Leuthardt, 2011). The superior spatial and frequency resolution of ECoG enables obtaining detailed cortical maps, for example motor and sensory maps of individual fingers, while sampling electrical activity from many cortical areas simultaneously. Additionally,

ECoG recordings are stable long-term (Blakely et al., 2009). By contrast, recordings of multiple single units with MEAs are not so stable, even though they could be considered a BCI control signal of superior quality. Although in the majority of studies ECoG grids have been implanted for a few days to minimize the infection risks associated to the use of tethered cables, it has been also shown that chronic ECoG implants are viable (Wyler et al., 1991; Weinand et al., 1994) and progress has been made toward the development of wireless, fully-implantable technologies (Vansteensel et al., 2016; Benabid et al., 2019). Based on these trends, it is reasonable to expect that clinically relevant, chronically implanted ECoG-based neural prostheses will emerge in the future for assisting patients suffering from neurological disorders. In summary, ECoG approach has multiple advantages for BCI applications, including an adequately high information transfer rate, stability of recordings, and a lower risk of medical complications. These features make ECoG method attractive for the developers of practical neuroprosthetic devices.

In clinical applications, ECoG electrodes are typically arranged into rectangular grids (for example, 6 × 8 or 8 × 8) or strips containing several electrodes in a single row. Platinum-iridium electrodes are often used, with the diameter of 4 mm most common for clinical applications. The commonly used 1-cm interelectrode distance yields an appropriate spatial resolution in many cases. Yet, the physical limit for resolution that could be achieved by decreasing the interelectrode distance is ∼1.25 mm for subdural recordings (Freeman et al., 2000) and ∼1.4 mm for epidural recordings (Slutzky et al., 2010). As a step toward reaching these limits of spatial resolution, ECoG grids with the spacing of 3–5 mm have been introduced and tested in a handful of studies conducted during the last decade (Wang et al., 2016). In such grids, neighboring electrodes carry sufficiently different information in the high gamma frequency range, as evident from the low coherence (∼ 0.3) between their signals (Wang et al., 2009). These grids have a superior spatial resolution compared to the 1-cm spaced grids not only because of the narrower inter-electrode spacing but also because of the smaller electrode size, which aids sampling local activity. With the 3–5 mm electrode spacing, accurate classification of finger movements and multiple hand gestures has been achieved, as well as real-time control of a hand prosthesis (Wang et al., 2013; Bleichner et al., 2016; Hotson et al., 2016). More recently, even denser micro-ECoG grids have emerged with 40–80-micron wires and 1–3 mm spacing; these grid can occasionally sample activity of single cortical neurons (Khodagholy et al., 2015).

ECoG grids implanted for clinical reasons have been used as a testbed for different types of BCIs. With epidural ECoG recordings (a safer option for clinical assessment), BCIs have been implemented for reliably detecting movements (Chavarriaga et al., 2016), recognizing different movement types (Spüler et al., 2014b) and decoding movement time-course (Flint et al., 2016). For widely spaced ECoG electrodes, decoding accuracy with epidural grids is similar to that achieved with subdural electrodes (Spüler et al., 2014a). Yet, if high-density ECoG grids are used, they work better when implanted subdurally (Bundy et al., 2014). In theory, it is desirable to place ECoG implants over as many cortical sites as possible because motor planning and execution engage multiple cortical areas. However, using many implants increases the health risk. Several studies have attempted to optimize the number and placement of ECoG electrodes (Bleichner et al., 2016; Li et al., 2017). Intraoperative assessment of electrical activity at different cortical sites, before an ECoG grid is implanted (Xie et al., 2015), is one way to decrease the implant size and reduce the health risk.

3. MOTOR PARADIGMS

Movements can be decoded from the brain electrical activity owing to the existence of correlation between neural modulations and motor parameters, for a range of motor tasks (Lebedev, 2014). Thus, ECoG modulations are correlated with the movements of both the upper and lower limbs (Toro et al., 1994b; McCrimmon et al., 2017). BCI decoding algorithms convert neural modulations into the output signals of interest, such as limb position in space. While decoding algorithms are often evaluated offline using previously collected neuronal data, their ultimate testing should be conducted in real-time settings, where subjects control actions performed by an external device directly with their brain activity.

The development of new decoding algorithms not only advances BCIs by improving their accuracy of performance and versatility, but also leads to new fundamental insights regarding the brain motor, sensory and cognitive mechanisms, the insights that emerge during BCI experiments and their trouble shooting (Nicolelis and Lebedev, 2009). Specifically, research on ECoG-based BCIs provides insights on the encoding of movements and sensations by the collective activity of cortical neuronal populations, functional significance of different cortical rhythms, somatotopic representation of body parts, as evident from ECoG activity at different cortical sites and frequency bands, and the capacity of the brain to plastically adapt to novel BCI tasks.

A variety of movement types can be decoded from ECoG signals. These are wrist flexion and extension (Satow et al., 2003; Gharabaghi et al., 2014; Spüler et al., 2014a; Jiang et al., 2015, 2017), various grasp types (Graimann et al., 2003; Miller et al., 2007; Pistohl et al., 2012; Chestek et al., 2013; Xie et al., 2015) hand gestures and postures (Graimann et al., 2003; Chestek et al., 2013; Bleichner et al., 2016; Li et al., 2017), individual finger movement (Graimann et al., 2003; Kubanek et al., 2009; Miller et al., 2009; Samiee et al., 2010; Wang et al., 2011; Elghrabawy and Wahed, 2012; Flamary and Rakotomamonjy, 2012; Liang and Bougrain, 2012; Chestek et al., 2013; Chen et al., 2014; Xie et al., 2018), tongue and lip protrusion (Graimann et al., 2003; Satow et al., 2003; Miller et al., 2007; Paul et al., 2017), and foot movements (Toro et al., 1994b; Satow et al., 2003). While cortical areas contralateral to the moving body part are usually used for decoding, the option of using ipsilateral cortex has been considered as well (Hotson et al., 2014).

In real-time BCIs, signals representing movements or their imagery are decoded from ECoG activity and sent as control signals to external devices, such as screen cursor. Cursor control has been implemented in one (Leuthardt et al., 2004, 2006), two

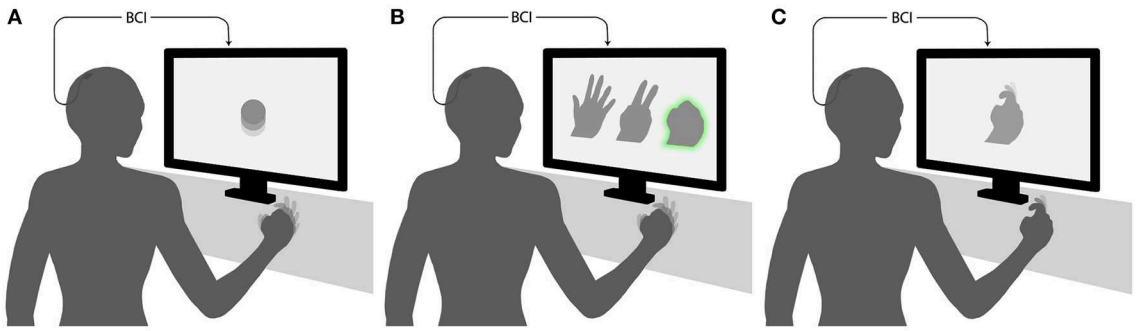

FIGURE 1 | Experimental paradigms for decoding of movements from ECoG. **(A)** An arbitrary mapping paradigm, where the task performed by the subject and BCI output are dissimilar. In the illustrated example, clenching of the fist produces an upward movement of the pointer. **(B)** A discrete classification paradigm, where a BCI recognizes a posture or movement performed by the subject and reproduces it with an external device. The case is illustrated, where a subjects shapes his/her hand in one of three gestures, and the BCI generates a gesture of a virtual hand shown on the screen. **(C)** Continuous decoding paradigm, where movement parameters are decoded continuously (as a function of time or some other parameter) and reproduced by an external device. In the illustrated example, a virtual finger reproduces the trajectory of the subject's finger.

(Schalk et al., 2008), and three (Wang et al., 2013) dimensions. Additionally, ECoG-based BCIs have been demonstrated for the tasks of controlling a prosthetic hand (Yanagisawa et al., 2011; Chestek et al., 2013; Wang et al., 2013; Hotson et al., 2016; Li et al., 2017), enabling exoskeleton-assisted walking (Benabid et al., 2019), and selecting font characters with a speller application (Vansteensel et al., 2016).

Here we focus on ECoG-based motor BCIs, which are BCIs where users modulate their cortical activity to generate movements of external devices. Such BCIs can be grouped into three main categories by the relationship between the task performed by the subject and BCI output (**Figure 1**) (while this classification can be applied to other types of BCIs, for example the ones based on EEG recordings, our review is restricted to ECoG-based systems). In the first category, there is an arbitrary relationship between the subject's action and the resulting movement of an external effector. For example, a subject imagines moving the hand to generate an upward movement of the pointer and imagines moving the tongue to move the pointer downward (Leuthardt et al., 2006). In the second category, a discrete classifier recognizes a motor action performed or imagined by the subject, for example moving one of the fingers. Next, an external device executes the same action. The third category of BCIs decode different motor parameters, such as movement direction, speed, acceleration, and force. The parameters are treated by the mathematical algorithm as continuous variables. An external device then reconstructs the movement from the decoded motor parameters.

3.1. Arbitrary-Mapping Paradigms

The arbitrary-mapping paradigm was the earliest to be implemented with ECoG recordings. The early studies employed event-related potentials for extracting motor commands (Toro et al., 1994b; Huggins et al., 1999; Levine et al., 1999). Later, ECoG spectral changes during real or imagined movements were used for BCI control (Leuthardt et al., 2004). In both groups of studies, actions performed by the subjects were mapped in an arbitrary way to actions executed by external devices.

To identify the most efficient control strategy for such an arbitrary-mapping BCI, Leuthardt et al. (2004) introduced a pre-screening procedure, which has become a common practice (Leuthardt et al., 2006; Miller et al., 2007; Schalk et al., 2008). During pre-screening, subjects perform a range of tasks so that ECoG features with the most prominent modulations could be identified and used for BCI control. The tasks are performed with the body parts represented by the cortical areas covered by the implanted ECoG electrodes (Schalk et al., 2008). Subjects perform or imagine motor acts like opening and closing the hand, protruding and retracting the tongue, flexing, and extending individual fingers, pursing and unpursing the lips, moving the arm, leg or foot (Miller et al., 2007), moving the jaw, shrugging the shoulders (Schalk et al., 2008), and pronouncing words (Leuthardt et al., 2004, 2006). Based on ECoG activity patterns exhibited during these tasks, subsets of ECoG features (e.g., frequency bands and electrodes with the most prominent modulations) are selected for implementing a BCI.

With the pre-screening approach, actions causing the largest ECoG modulations could be quickly selected to improve accuracy of BCI control. In a pioneering study (Leuthardt et al., 2004), subjects reached the success rates of 74–100% after 3–24 min of training in closed-loop experiments where they performed or imagined a preselected action (like opening and closing the hand, protruding the tongue or saying the word "move") to move a screen cursor in the vertical dimension. In these experiments, ECoG grids were placed over frontal, parietal and temporal cortical areas. In the next study (Leuthardt et al., 2006), the same group added to the experimental design an adjustment procedure, where the decoder settings were updated using the data from the initial online session. This adjustment accounted for the differences between ECoG modulations exhibited during the pre-screening procedure and the online control.

Schalk et al. (2008) designed an arbitrary-mapping approach for the case of two-dimensional cursor movements. ECoG

recordings were conducted from the frontal, temporal, and/or parietal cortex. During the pre-screening procedure, two tasks were selected that yielded the least correlated signal features (frequency bands and electrode locations) that were then used to independently control two coordinates of the cursor. After a training period of 12–26 min, five subjects achieved accuracy of 53–73% (with a 25% chance level) in a four-target task.

Wang et al. (2013) expanded the degrees of freedom of cursor movements to three dimensions. A tetraplegic subject with C4 level spinal cord injury underwent training for several weeks. ECoG activity was recorded using a high-density 32-electrode grid with 4-mm spacing; electrode diameter was 2 or 3 mm. The grid was implanted over the hand and arm representing areas of the left sensorimotor cortex. The subject learned to activate his sensorimotor cortex by attempting voluntary movements. Distinct cortical modulations occurred for attempted movements of different segments of the patient's upper limb. The BCI control consisted of assigning of each type of attempted movement to a particular direction of cursor movement. The decoder processed ECoG modulations in the gamma band. An adapting decoding scheme was used, where the decoder alternated between the periods when the decoder weights were fixed and when they underwent adjustments. The subject first learned a two-dimensional control of the cursor in a virtual environment, then the third dimension was added by gradually merging the weights calculated for the attempted three-dimensional task with the weights previously calculated for the two-dimensional control. The subject reached the success rate of 80% in the cursor control task, and also learned to control three-dimensional reaching movements performed by a prosthetic arm. In the next study conducted by the same group (Degenhart et al., 2018), two additional subjects with arm paralysis were tested, one with ALS and the other with brachial plexus injury. The subjects used a somatotopic control strategy to operate a virtual cursor in two or three dimensions. In this strategy, spatio-temporal patterns of gamma-band cortical activity evoked by different attempted upper-limb movements were converted into the direction of cursor movement. Cursor velocity was generated from ECoG gamma activity with an optimal linear estimator algorithm (Salinas and Abbott, 1994). Both subjects achieved control with up to three degrees of freedom.

Overall, the arbitrary-mapping approach has been shown suitable for building practical BCIs for the paralyzed patients capable of voluntarily modulating activity in the brain areas representing their paralyzed body parts (Spüler et al., 2014b; Chaudhary et al., 2016). Thus, Vansteensel et al. (2016) recently demonstrated a practical, a fully implanted ECoG-based BCI, where a patient with ALS learned to control a computer typing program by attempting voluntary hand movements. The ECoG grid was implanted subdurally over the motor cortex. This BCI enabled communication with a rate of two letters per minute. Notwithstanding the slow operation, BCIs of this kind offer a practical solution for functional restoration, communication and rehabilitation of neurologically impaired patients. As such, this approach needs to be further developed.

3.2. Classification and Reproduction of Movements

The second class of ECoG-based BCIs reproduces the same movements that subjects perform or imagine, which are recognized using a discrete classifier. High spatial and temporal resolution of ECoG allows recognizing a sufficiently large repertoire of movement types and executing them with an external device. Thus, areas corresponding to individual fingers can be discerned with ECoG recordings (Miller et al., 2009), which allows implementing a BCI that recognizes the finger being moved or imagined being moved with a classifier like Naïve Bayes (Chestek et al., 2013), linear discriminant analysis (LDA) (Wang et al., 2009; Hotson et al., 2016), or support vector machine (SVM) (Liu et al., 2010). Several studies have demonstrated that such classification can be performed with high accuracy based on ECoG recordings from the hemisphere contralateral to the working hand. Wang et al. (2009) decoded the finger being moved from the signals recorded with a micro-ECoG grid that was placed over the contralateral motor cortex. In this study, one subject performed self-paced finger flexions and extensions for ∼10 s. The active finger was identified with an accuracy of 73% with both LDA that processed the ECoG data reduced to the first eight principal components and an SVM classifier without dimensionality reduction. In the study by Kubanek et al. (2009) subjects responded to a cue by flexing an individual finger 3–5 times over a time period of 1.5–3 s. ECoG activity was recorded from the frontal or temporal cortical areas. The relationship between the poser in different ECoG spectral bands and finger trajectories was modeled using a linear decoder called PaceRegression. The active finger was then determined as the finger with the highest decoded flexion amplitude. The across-subject average classification accuracy was 77.1% when ECoG activity recorded at movement onset was analyzed. The accuracy increased to 80.3% when the analysis interval was optimized for each subject. Hotson et al. (2016) applied a hierarchical LDA classification scheme to detect the finger being moved, reaching an accuracy of 76%. Furthermore, Liu et al. (2010) showed that ECoG activity in the sensorimotor cortex ipsilateral to the working hand could be used to determine the finger being moved. Their decoder incorporated logistic regression (LR) and a binary SVM.

Several studies have classified hand configuration from ECoG recordings. Yanagisawa et al. (2011) recorded ECoG activity in the sensorimotor cortex of a subject performing three types of hand movements: grasping, hand-opening, and scissor-mimicking movements. With these tasks, they implemented online control of a prosthetic hand based on a two-step classification scheme, where the first step consisted of detecting movement intention and the second step was the decoding of movement type. Linear SVM was used as classification algorithm for both steps. The intention to move was detected on average 37 ms earlier than the actual movement onset. Movement type was classified with the accuracy of 69.2%, which significantly exceeded the 33.3% chance level. Pistohl et al. (2008) employed regularized LDA to decode two types of grasping movements from the ECoG recorded over the motor cortex. They decoded

the intention to move from ECoG 125-250 ms earlier than the actual movement onset. The subjects performed self-paced relocation of an object between several positions using either precision grip or whole-hand grasping. The grasp type was decoded with 93% accuracy based on the analysis of the time interval starting 1s before grasp till 0.5s after. Recording sites located anterior to the central sulcus were used for decoding whereas the sites posterior to the central sulcus were excluded as representing sensory responses.

Chestek et al. (2013) further increased the number of hand configurations decoded from the ECoG recorded over the sensorimotor-cortex. Their subjects configured the hands into one of four isometric postures: fist, pinch, point or five-finger spray. Additionally, the subjects flexed one or several fingers. The interval −0.5–1.5s relative to movement onset was used in this analysis. Classification was performed with a Naïve Bayes decoder applied to the gamma band of the ECoG. Four hand postures were classified with an accuracy of 68–81%, and 66–98% accuracy was achieved in a five-class classification, where classes represented four finger movements and a resting state. The same decoding methods were then utilized in the online sessions where subjects controlled a hand prosthesis with a BCI. Kapeller et al. (2014) classified three hand gestures: "open," "peace," and "fist." In their decoding method, the presence of hand movement was classified first with a two-class LDA classifier (with an accuracy of 86.6 and 97.7% in their first and second subjects, respectively), and then a multi-class LDA detected the gesture (with an accuracy of 93.8 and 98.8%).

Furthermore, hand-gesture tasks have been used to investigate the ways the number of implanted electrodes could be reduced and confined to a smaller cortical area. Bleichner et al. examined two subjects with high-density ECoG grids implanted over a small area (2.5–5.2 cm^2) in the hand-representing area. Four hand gestures corresponded to letters D, F, V, and Y of the American sign language (ASL) (Bleichner et al., 2016). Gesture classification was performed using a pattern-matching classification algorithm that was applied to ECoG spectral bands and local motor potentials (LMPs). An accuracy of 97 and 74% was reached for their first and second subjects, respectively. It was found that a selected electrode subset (two thirds of the total) was sufficient to reach the same classification accuracy as the accuracy achieved with all electrodes. In the study of Li et al. (2017), participants produced three hand gestures ("scissor," "rock," and "paper"). Classification accuracy with SVM classifier applied to spectral features was in the range 69.7–85.7% when performed offline and 80–82% during the online control of a prosthetic hand. The number of channels was reduced with a greedy algorithm. It was found that a subset of electrodes confined to a small cortical area was sufficient to maintain good decoding performance.

Xie et al. (2015) decoded different finger and hand movements from ECoG signals recorded intraoperatively in the motor cortex of awake subjects. They used an LDA classifier applied to the features extracted with an autoregressive model, and a waveform length feature that represented signal complexity. The intraoperative decoding accuracy (91.8 and 93.0% in two subjects) was comparable to the accuracy reached with the ECoG grids implanted for seizure monitoring (90.2 and 96.0% in the other two subjects). These results suggest that implementing BCI tasks during the implantation surgery could be useful for the adjustment of ECoG grid placement.

For proper reproduction of movements, movement onset needs to be decoded from neural activity in addition to the decoding of movement type. Early detection of the intention to move is important for BCI applications because it allows decreasing the delay between the brain activity and the response of the prosthetic device (Lebedev et al., 2008; Yanagisawa et al., 2011). Classification algorithms, such as LDA (Kapeller et al., 2014; Hotson et al., 2016) and SVM (Yanagisawa et al., 2011) have been used to detect movement onset based on ECoG recordings.

In conclusion, the classification and reproduction approach is suitable for neuroprosthetic applications where a finite set of motor outputs is sufficient, such as BCIs that enable sign language-like communications (Bleichner et al., 2016; Branco et al., 2017). Studies have shown that restoration of a finite set of movements is a practical BCI solution for amputees (Bruurmijn et al., 2017), and patients with hand paralysis (Shoham et al., 2001; Yanagisawa et al., 2012). Such BCIs could implement a shared control principle, where a general motor command is extracted from brain activity whereas the fine details of movements are handled by the controller of a prosthetic limb (Li et al., 2014).

3.3. Decoding of Motor Parameters as Continuous Variables

The third class of ECoG-based BCIs treats the parameters of movements, such as limb position and velocity, as continuous variables that are decoded from brain activity. Many studies have employed a center-out task for continuous decoding. During this task, subjects repeatedly perform cued or self-paced arm or hand movements from a center into different directions. These movements are usually converted into 2D or 3D movements of a cursor. The center-out task gained popularity after the studies of Georgopoulos et al. (1982) of the directional tuning properties of monkey motor cortical neurons. In ECoG studies with this design, four (Leuthardt et al., 2004; Reddy et al., 2009), six (Toro et al., 1994a), and eight (Leuthardt et al., 2004; Sanchez et al., 2008; Ball et al., 2009; Anderson et al., 2012; Wang et al., 2012; Nurse et al., 2015; Gunduz et al., 2016) targets locations have been used, all equidistant from the center. Center-out movements can be performed with a joystick (Reddy et al., 2009; Anderson et al., 2012; Wang et al., 2012), computer mouse (Kellis et al., 2012), stylus (Nurse et al., 2015), or the index finger moving on the surface of a touchscreen (Sanchez et al., 2008).

In a pioneering study that combined a center-out task with ECoG recordings in humans, Toro et al. (Toro et al., 1994a) evaluated tuning of ECoG in the 8–12 Hz band to the direction of arm movements. ECoG was sampled from the sensorimotor cortex and adjacent regions. Ten years later Leuthardt et al. (2004) analyzed a wider (0–200 Hz) range of frequencies and discovered directional tuning for various ECoG spectral bands. The center-out task was performed with a hand-held joystick and incorporated four or eight targets. Ball et al.

(2009) decoded movement direction from ECoG during the execution of a center-out task and assessed the representation of directional information in different cortical areas. Their subjects performed self-paced center-out movements with their arms to four target locations. Decoding was performed with regularized linear discriminant analysis (RLDA) applied to either smoothed ECoG signals or different frequency bands. Decoding accuracy of 75% was achieved using the features calculated over the movement-execution period whereas 45% accuracy was achieved using the pre-movement period. ECoG channels corresponding to the hand and arm representing areas of the primary motor cortex were the most informative for the decoding. The analysis of additional data from a subject performing an eight-target task showed that ECoG activity (in the low-frequency and high-gamma bands) was cosine-tuned to the direction of arm movements. Anderson et al. (2012) investigated ECoG tuning to movement speed and velocity for center-out and tracing tasks performed with a force feedback joystick. ECoG recordings were conducted in multiple cortical areas. The strongest modulations to direction, speed, and velocity were observed in the primary motor cortex.

Wang et al. (2012) decoded movement direction with a time-varying dynamic Bayesian network. Center-out movements were performed with a joystick toward eight targets. Accuracy was quantified as the mean angular error between the actual and decoded direction; it was $<90^\circ$ in all subjects. Gunduz et al. (2016) reported a similar experimental design with center-out movements performed with a joystick, and eight targets. The task incorporated a delay period when the subjects prepared to move while holding the joystick still, which allowed decoding a person's planned direction of movement. Direction was decoded with a stepwise multilinear regression applied to high gamma activity and/or LMPs. The median angular error was in the range 62–70° across subjects. The authors observed directionally specific modulations of both high-gamma ECoG and LMPs during the delay and movement periods. Directionally tuned high-gamma activity was most prominent in the sensorimotor cortex whereas LMP modulations occurred in prefrontal cortices. The authors concluded that sampling directionally tuned ECoG from multiple cortical areas could improve the decoding of both planned and executed movements.

Reddy et al. (2009) enriched the center-out task with a tapping condition, which allowed testing how well center-out movements could be distinguished from the other types of movements. Center-out movements were performed with a joystick in response to arrows pointing in four possible directions. Additionally, subjects responded to a trigger cue (a square shown on the screen) by clicking on top of the joystick with the index finger. Decoding was performed using Naïve Bayes classifier applied to time-frequency features. Decoding accuracy for movement direction was in the range 83–96% for the preparatory period and 58–86% for the movement period. The trigger condition was distinguished with 72–93% accuracy from the center-out conditions.

Bundy et al. (2016) added the third dimension to the center-out task. Their subjects performed arm reaching movements with the starting position located at the center of a cube and cube vertices serving as targets. The kinematic parameters of movements were decoded with a hierarchical partial-least squares regression model. Correlation coefficients between the true and predicted kinematic parameters ranged 0.31–0.80 across subjects for speed, 0.27–0.54 for velocity and 0.22–0.57 for position. The final position was reconstructed with an accuracy of 49.0–66.2%.

Several studies employed reaching tasks that differed from the classical center-out paradigm. In the study of Kellis et al. (2012), patients moved a cursor with a computer mouse from an initial position at the bottom of the screen to the upper right or upper left corner; trajectories were decoded from ECoG with a Kalman filter. Sanchez et al. (2008) continuously decoded kinematic parameters in two tasks: a center-out task where subjects tracked smoothly varying trajectories extending from the center to predefined locations, and a target selection task where subjects performed reaches toward color-coded targets placed along the top edge of the screen. Cursor movements were decoded from ECoG frequency bands with a Wiener filter. Pistohl et al. (2008) had subjects acquire targets randomly positioned on a plane; hand coordinates were decoded with a Kalman filter. Schalk et al. (2007) reported highly accurate decoding of position and velocity using linear models for the task, performed with a joystick, where subjects pursued a target that moved counterclockwise along a circular trajectory. ECoG activity was cosine tuned to target angle, and decoding accuracy was comparable to the accuracy reported for monkeys implanted with MEAs.

In several studies, kinematics of finger movements was decoded from ECoG. Kubanek et al. (2009) extracted the time-course of finger movements from motor cortical activity. The subjects repeatedly flexed individual fingers in response to a visual cue. Decoding was performed with PaceRegression algorithm. Several other decoding algorithms of different complexity have been used for reproducing finger movements from ECoG, including switching linear model (Flamary and Rakotomamonjy, 2012; Liang and Bougrain, 2012) empirical mode decomposition (Hazrati and Hofmann, 2012), logistic-weighted regression (Chen et al., 2014), and LSTM (Du et al., 2018; Xie et al., 2018).

In addition to the aforementioned reaching tasks and finger-movement tasks, more complex motor tasks have been used in ECoG-BCI studies. Hammer et al. (2013) employed a game-like continuous one-dimensional motor task where subjects controlled the horizontal position of a car with a steering wheel. Position, velocity and acceleration were decoded with a linear regression algorithm. In the study of Nakanishi et al. (2013), participants repositioned blocks on a board. ECoG features were transformed into a three-dimensional arm trajectory with a sparse linear regression algorithm. In the subsequent study by the same group, subjects repositioned blocks with three different masses (Nakanishi et al., 2017). With this design, representations of intrinsic (e.g., muscle force) and extrinsic (e.g., target location) parameters of movements could be compared. ECoG recorded in the primary motor cortex was correlated mostly with the intrinsic parameters whereas ECoG recorded in pre-motor cortex was correlated with the extrinsic parameters. Wang et al. (2014) varied movement duration to investigate whether the entire movement course could be decoded from ECoG or only the

values of motor parameters at movement onset. Wu et al. (2016) implemented a three-dimensional isometric force task where subjects exerted force in different directions without moving their arms. Directional information was extracted from the fronto-parietal ECoG recorded during both preparation and execution of the isometric task. The decoding algorithm incorporated a jPCA reduced-rank hidden Markov model (jPCA-RR-HMM), regularized shrunken centroid discriminant analysis, and LASSO regression.

Continuous-decoding BCIs based on ECoG recordings hold promise of eventually satisfying the requirements of paralyzed patients who need high-performance neuroprosthetic devices for restoration of mobility of their limbs. With a continuous-decoding neural prosthesis, patients would be able to execute a variety of movements in a near-normal way, where limb kinematics is constantly under the user's voluntary control and fine modifications of motor parameters could be done. Although a BCI with such an ideal control has not been demonstrated yet, recent advances in building fully implantable ECoG systems that perform continuous decoding (Vansteensel et al., 2016; Benabid et al., 2019) suggest that patients could improve in such BCI control through long-term practice that engages cortical plasticity mechanisms.

4. DECODING ALGORITHMS

In this section, we describe in more detail the decoding algorithms used in ECoG-based BCIs. These algorithms bear similarity to the decoders for EEG-based interfaces, which have been covered in several review articles (Lotte et al., 2007, 2018; McFarland and Wolpaw, 2017). Here we review only the literature on the decoding of movements from ECoG.

ECoG recordings capture electrical potentials of large neuronal populations formed by synchronous dendritic potentials and spikes (Buzsáki et al., 2012). Decoding of motor parameters from ECoG is possible because modulations of neuronal population activity are consistently correlated with task events and changes in motor parameters (Anderson et al., 2012; Lebedev, 2014). Multichannel ECoG data contains spatial (i.e., where in the cortex) and temporal (i.e., when and how) information that could be used for decoding of movement characteristics. Spatial ECoG components reflect, according to the somatotopic cortical map of the body, the body part engaged in a motor action. Temporal ECoG components reflect the time-dependent changes of motor parameters, such as limb position, speed, and acceleration.

An ECoG decoder takes multichannel ECoG data as the input and returns the signals of interest (the presence of movement, movement type, body part being moved, kinematic parameters, etc.) as the output. Many machine learning methods are applicable to this problem. The signal processing chain of a neural decoding algorithm comprises several blocks (**Figure 2A**). First, the raw data is transformed into features that contain information relevant to the BCI tasks. Ideally, these features should not contain redundant information. Next, a learning algorithm forms a decision rule that solves either a classification or regression problem. Classification algorithms solve the problem of matching an input with one of the predefined discrete classes. Regression algorithms match the input signals to the output continuously. For example, identification of the finger being moved is a classification problem, whereas decoding finger trajectory is a regression problem.

To properly set the decoder parameters, training data are needed that contain a sufficient number of examples of the inputs and their corresponding outputs. Based on the training data, a function is formed that, given the inputs from the dataset, returns values that are close to the corresponding desired outputs. A practicable decoder should be able to generalize to new data, that is, it should remain accurate when applied to the inputs not included in the training dataset. The case where decoding performs well for the training data but fails to work for the new data is called overfitting (Babyak, 2004). Overfitting often occurs when the decoder uses too many adjustable parameters, such as weights of the multiple linear regression. The presence of overfitting indicates that the transfer function is narrowly tuned to the anecdotal correlations between the input and output values taken from the training data rather than implements a generic transfer rule that reflects consistent input-output relationships. To avoid overfitting, feature space dimension reduction and appropriate regularization techniques should be employed. Thus, if an iterative approach is used to optimize decoder parameters, a proper stopping rule should be used to avoid overfitting.

Decoding algorithms have been developed that maintain generalization even when the sampled neural signals drift over time. Thus, Paul et al. (2017) used the higher-order statistics of ECoG bispectrum to overcome the difficulties decoding signals that were recorded during multiple task sessions. Their algorithm extracted signal features that were retained after a session-to-session transfer. This finding is consistent with the results of previous EEG-based studies (Shahid and Prasad, 2011; Das et al., 2016).

An additional important requirement is the versatility of training data, which means that the space of movements should be covered during sampling in such a way that the decoder interpolates to new data points rather than extrapolating to them. Practically, this means that experimental settings used to collect training data should be similar to the settings for online BCI control, including both the characteristics of movements and neural activity patterns. In the case of a mismatch between the training and online-BCI conditions, adjustments of the decoder may be needed to improve BCI performance.

4.1. Spectral Features

An important advantage of ECoG recordings compared to EEG is the wider range of signal frequencies that contain information useful for BCI control. ECoG activity comprises multiple frequency bands, from the low frequency activity (below 1 Hz) to high gamma (50–400 Hz). Some of these spectral components are clearly rhythmic, with clear peaks present in ECoG spectra (Miller et al., 2007). Each frequency band has specific functional correlates, which allows implementing decoders that capture different aspects of the behavioral tasks, such as responses to stimuli, transition from rest to movement, characteristics of limb

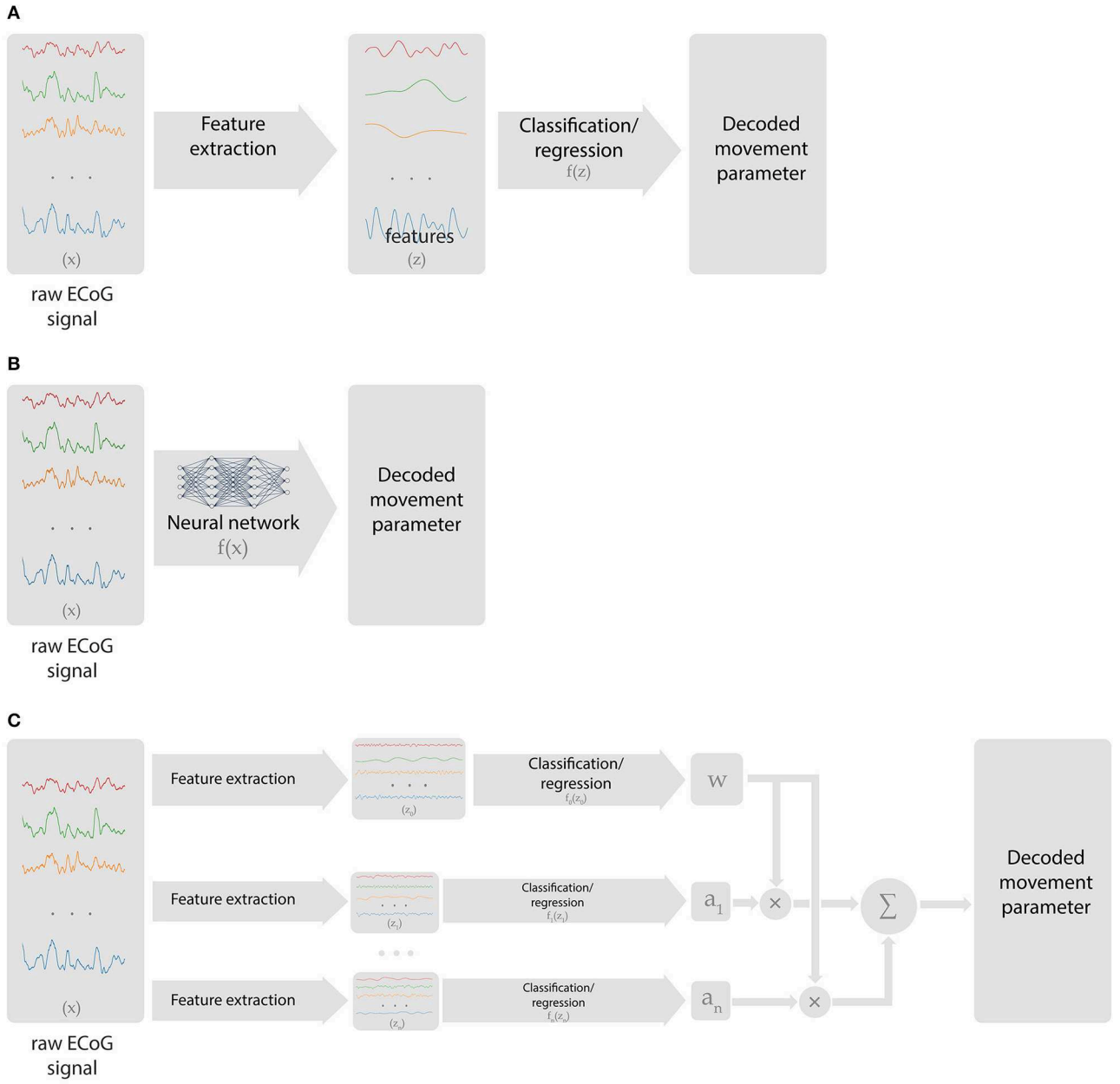

FIGURE 2 | Types of data processing chains employed in ECoG-based BCIs. **(A)** Classical approach, where preselected features are extracted from ECoG recordings, followed by a classification or regression algorithm that generates BCI output. **(B)** Deep learning approach that handles both feature selection and decoding. **(C)** Hierarchical scheme with multiple decoders and processing chains that perform switching or relative weights adjustment.

kinematics, and engaging different body parts. An ECoG decoder that uses multiple frequency bands simultaneously is potentially more accurate and versatile compared to the decoder based on a single spectral band.

To extract task-related spectral features, ECoG signal is either bandpass filtered (Liang and Bougrain, 2012; Chestek et al., 2013; Nakanishi et al., 2013) or converted into the frequency domain using non-parametric methods, such as Fourier transform (Chin et al., 2007; Miller et al., 2007; Blakely et al., 2009; Reddy et al., 2009; Ryun et al., 2014), multitaper methods (Ball et al., 2009; Kellis et al., 2012; Pistohl et al., 2012; Elgharabawy and Wahed, 2016), parametric techniques, such as autoregressive model estimation (Leuthardt et al., 2004; Schalk et al., 2007; Kubanek et al., 2009; Wang et al., 2012; Xie et al., 2015), and the maximum entropy approach (van Vugt et al., 2007; Collinger et al., 2014; Bundy et al., 2016; Gunduz et al., 2016). Spectral features can be also extracted with filter bank methods, such as Gabor filters (Liu et al., 2010; Elghrabawy and Wahed, 2012;

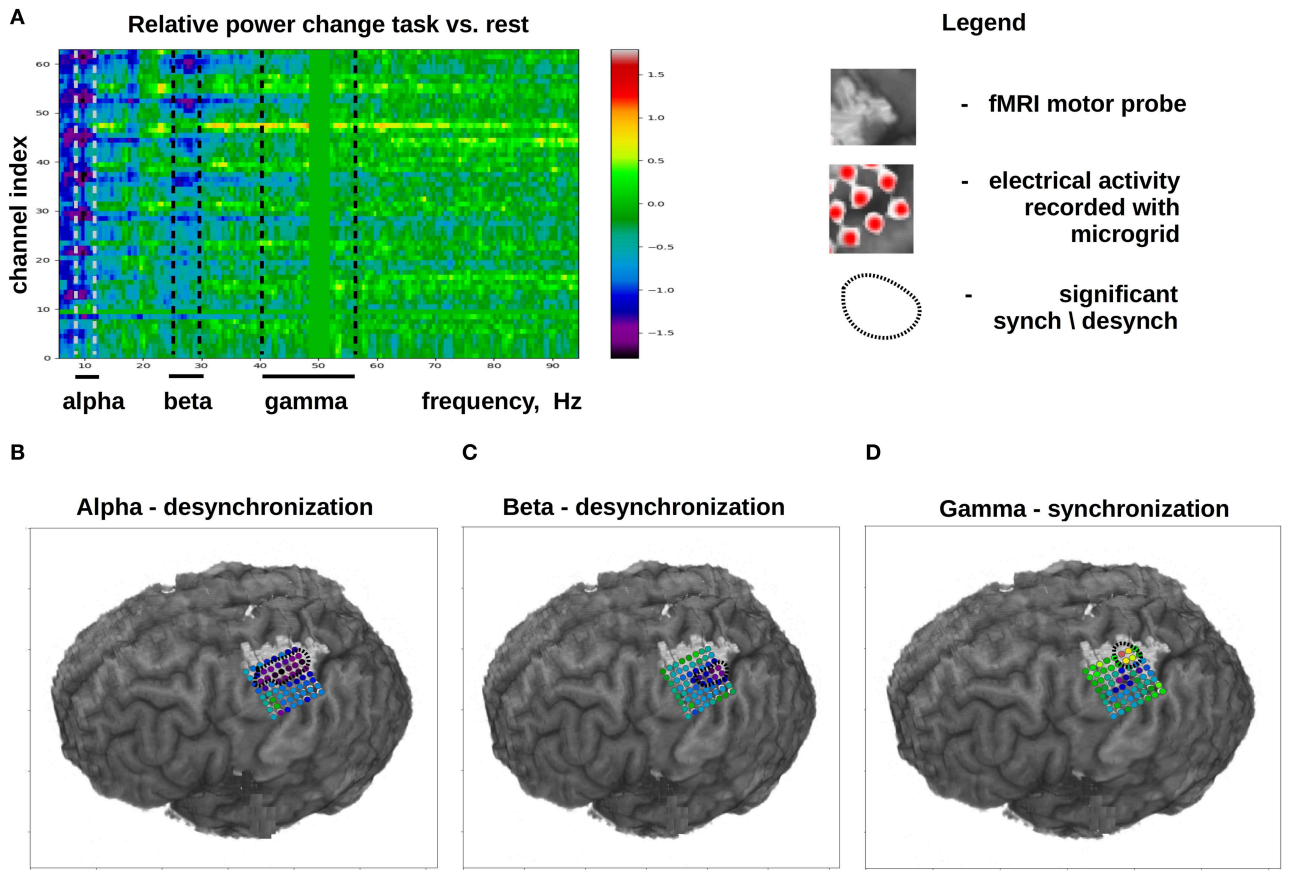

FIGURE 3 | Typical changes in ECoG activity that occur during the execution of a motor task (in this case, finger flexion). Task-related activity is compared to ECoG activity recorded during a rest period. **(A)** Channel index × spectral frequency diagram with the color-coded values representing desynchronization index calculated as $2\frac{P_{task}-P_{rest}}{P_{task}+P_{rest}}$. **(B–D)** Cortical distribution of desynchronization index for different ECoG frequency bands. **(B)** Data for the alpha band. It can be seen that, during a motor task, alpha-band activity is desynchronized over a large portion of the sensorimotor cortex. **(C)** Data for the beta band. Beta band activity is desychronization over a more compact cortical area as compared to the alpha-band. **(D)** Data for the beta band for the high frequency gamma activity (40–60 Hz), which exhibits a pronounced synchronization over a small cortical area. The light-gray shaded spot shows the localization of the hand-related sensorimotor are obtained with fMRI.

Elgharabawy and Wahed, 2016; Wu et al., 2016). Ideally, neural signals should be processed in such a way that an optimal trade-off is reached between the temporal and spectral resolution.

ECoG mu (8–12 Hz) and beta (18–26 Hz) rhythms recorded in the sensorimotor are commonly used for decoding movements from ECoG. These oscillations are thought to reflect the activity in corticothalamic loops (Schalk and Leuthardt, 2011). The mu and beta rhythms are typically not confined to local cortical areas but rather occur over large surfaces (Brunner et al., 2009). Movement and motor imagery cause desynchronization (i.e., decrease in amplitude) of these rhythms, which allows implementing BCIs that detect movement onset and time course. While ECoG recordings are useful for measuring the mu and beta activity, approximately the same measurements, albeit with a lower spatial resolution, could be accomplished with EEG recordings, which are suitable for monitoring cortical rhythms below 40 Hz. By contrast, gamma-band activity (40 Hz and higher) cannot be reliably recorded with EEG due to signal contamination by facial EMG activity that belongs to the same frequency range. Yet, gamma activity is reliably sampled with ECoG. ECoG activity in the gamma band matches the activity of single neurons in the same area (Buzsáki et al., 2012) and, unlike the slower rhythms, it is not widespread but rather occurs in local cortical areas (Schalk and Leuthardt, 2011). These properties make ECoG gamma activity suitable for decoding based on cortical location and for decoding specific aspects of movement planning and execution with the accuracy comparable to the decoding from neuronal spikes (Anderson et al., 2012; Gunduz et al., 2016). ECoG gamma recordings are also useful to study cognitive mechanisms (Sturm et al., 2014). Thus, high-frequency ECoG components are especially valuable for implementing BCIs of different kinds. **Figure 3** shows the typical changes that occur in different ECoG frequency bands during the execution of a motor task.

At the lower end of ECoG spectrum (<2 Hz), ECoG low-frequency component (LFC) has been shown to be applicable for BCI decoding because it contains information about movement timecourse and kinematics (Mehring et al., 2003; Rickert et al.,

2005; Pistohl et al., 2008; Ball et al., 2009; Hammer et al., 2013). LFC can be extracted, for example, by smoothing the signal with Savitzky-Golay filters (Pistohl et al., 2008, 2012; Ball et al., 2009). Schalk et al. (2007) called this component local motor potential (LMP) and computed it as a running average. LMP is modulated during motor behaviors, so it can be used for decoding limb kinematics (Kubanek et al., 2009; Acharya et al., 2010; Fifer et al., 2012; Wang et al., 2012; Chen et al., 2014; Hotson et al., 2014; Bleichner et al., 2016; Bundy et al., 2016; Wu et al., 2016). Hammer et al. suggested that LFC phase is more informative for motor decoding than LFC magnitude (Hammer et al., 2013). While LFC is highly informative for decoding, it can be easily contaminated by mechanical and electrical artifacts caused by the movements of the limbs and recording equipment. Because of this issue, a special care should be taken to minimize the artifacts, remove them from the data programmatically and ensure that they are not utilized for decoding.

Besides spectral band power modulations, within-band and across-band coupling features appear to be informative on movement intentions. Thus, Brunner et al. (2005) found extra information in the phase coupling between different ECoG channels, measured as phase locking value (PLV). This method worked well when applied to the beta and gamma bands.

Several connectivity measures have been applied to the analysis of ECoG. Bayesian networks (TV-DBN) and eigenvector centrality analysis have been used to identify brain regions relevant to motor tasks (Newman et al., 2015). Benz et al. (2012) used TV-DBN to quantify task-related changes in connectivity and to decode hand kinematics. With this approach, higher accuracy was achieved compared to spectral feature decoders. Babiloni et al. (2017) utilized lagged linear connectivity (LLC) between several cortical areas in the delta-theta (<8 Hz) band to distinguish action execution from action observation.

4.2. Spatial Features

Decoder accuracy is known to improve with increasing number of recording channels (Nicolelis and Lebedev, 2009). In addition to the mere number of channels, improvements in decoding can be gained by accounting for the spatial arrangement of recording sensors, such as the arrangement of electrodes in an ECoG grid. The procedure that improves decoding using the information about the electrode locations is referred to as spatial filtering. Spatial filters treat different ECoG channels as coordinates for multivariate data sampling. This coordinate system is transformed by the filter to improve decoding. For example, spatial filtering could be used to reduce data dimensionality or improve separability of different observations.

The initial spatial filtering is usually accomplished with the reference schemes utilized during ECoG recordings. Common average reference (CAR) is typically used as a simple denoising technique (Schalk et al., 2007; Kubanek et al., 2009; Wang et al., 2012). This method reduces noise that is common to all recording channels but it does not handle channel-specific noise and it may also introduce noise into otherwise clean channels. Several alternative filtering techniques have been proposed to address these problems. Morales-Flores et al. (2014) developed a non-supervised algorithm where the spatial filter coefficients are adjusted using a steepest descent method that minimizes the variance on differences of the linear combination of ECoG channels. This approach improved the decoding of finger flexions from ECoG when compared to the data produced by CAR. Liu et al. (2015) considered the problem of the introduction of channel-specific noise when CAR is applied to the channel sets containing noisy channels. They tested several types of unsupervised spatial filters and techniques for detecting artifacts. After the noisy channels were automatically removed, data contamination was reduced. Moreover, they developed a median average reference filter that reduced channel-specific noise even when the noisy channels remained in the set.

Principal component analysis (PCA) is widely used in conjunction with spatial filtering, primarily for dimensionality reduction (Freeman et al., 2000; Boye et al., 2008). This method transforms the original data into principal components, which are uncorrelated with each other and are created in such a way that the first several components capture the largest possible amount of variance in the data. The principal components are quantitatively characterized in terms of how much variance (i.e., information contained in the data) they comprise. After the PCA transformation, the least informative (or least powerful) components can be discarded, reducing data dimensionality. This approach is, however, not optimal in the cases where information is present in the low-power features of the ECoG signal. In some cases, dimensionality reduction techniques, such as PCA, are applied not only to ECoG signals but also to motor parameters (Liu et al., 2010; Samiee et al., 2010; Hotson et al., 2014). This is particularly useful when movements are unconstrained. In this algorithm, the decoder first generates output in PCA coordinates, and this output is then converted into the original coordinates. Canonical correlation analysis is another technique that can handle high multidimensionality of both ECoG and movement data. This method performs a linear transformation that maximizes the correlation between the ECoG activity and movements (Spüler et al., 2016).

Common spatial patterns (CSP) is a spatial filtering technique that is often used in EEG- and ECoG-based BCIs to extract features that are useful for classification (Kapeller et al., 2014, 2015; Xie et al., 2015; Jiang et al., 2017). When two classes of observations are used, CSP maximizes the ratio of their variances to increase the separability of the two classes. After the CSP transformation, dimensionality reduction can be carried out based on the separability of the two classes in different dimensions. Additionally, CSP performs more robustly and exhibits better generalization properties when preceded by a separate dimension reduction step (Nicolae et al., 2017).

Source reconstruction methods are applicable to improve the performance of ECoG-based BCIs. The use of dynamical spatial features obtained from the reconstructed cortical current source density has been already shown to drastically improve the decoding accuracy in the MEG and EEG based BCIs where subjects generate outputs using motor imagery (Lin et al., 2013; Edelman et al., 2019). Raw ECoG recordings better reflect the surface distribution of cortical sources compared to non-invasive measurements (Schalk and Leuthardt, 2011). Yet, the activity of sources located deep in the sulci spreads into several recording

channels and therefore can not be assessed selectively in the raw data. As a solution to this problem, a sufficiently fine model can be built that describes the relationship between the activity of neuronal sources and the ECoG measurements (Gramfort et al., 2010). Based on such forward model, reasonably accurate current source density reconstructions can be obtained for neuronal sources located within 1 cm from the cortical surface (Zhang et al., 2008; Pascarella et al., 2016; Todaro et al., 2018). We foresee that such reconstruction of sources from ECoG will be useful for BCI decoding by providing decoding algorithms with the inputs that discern the activity of more compact cortical areas compared raw ECoG data. To fully benefit from this approach, care needs to be taken to accurately determine grid location with respect to the cortical surface. In addition to geometric calculations, the techniques exploiting functional data-driven methods based on maximizing model evidence (Henson et al., 2009) could improve the performance of these methods.

In addition to the methods described above that perform spatial filtering and/or reduce data dimensionality (Gu et al., 2012), the decoding accuracy benefits from techniques to determine the most informative features for classification, such as requesting a certain separation in power for a certain ECoG spectral band for different movements (Ryun et al., 2014), choosing features strongly correlated with the task (Leuthardt et al., 2004), successively adding features correlated to the class and not correlated to the previously selected features (Schalk et al., 2007), or choosing features according to a scatter-matrix based separability (Samiee et al., 2010). Several filter selection algorithms utilize a wrapper-based approach, where features are scored using the learning algorithm that is then used for regression or classification (Gu et al., 2012). In this approach, the feature set is enhanced in consecutive steps, where features are added to the previous feature set to improve decoding accuracy estimated with cross-validation (Liang and Bougrain, 2012; Wang et al., 2012; Elgharabawy and Wahed, 2016; Li et al., 2017). When following these strategies, one should bear in mind that ECoG features assumed to be useful could be contaminated by noise that is accidentally correlated to the parameters being decoded.

4.3. Classification and Regression

Starting with the report of Levine et al. (1999) on movement-related ECoG patterns, pattern matching techniques have been applied to derive motor commands from ECoG recordings. Thus, movement-related ECoG desynchronization was detected using an average ECoG template and cross-correlating it with ECoG samples (Huggins et al., 1999). More complex features can be used for the same purpose (Graimann et al., 2003). Such pattern-matching approach has been successfully used to classify multiple movement types (Bleichner et al., 2016) and to implement BCI control (Levine et al., 2000).

As explained above, the capacity to generalize to new data is essential for both classification and regression algorithms. Since the number of features is often large, regularization methods are applied to prevent overfitting. Algorithms with fewer parameters are less susceptible to overfitting and often perform no worse than more complex algorithms (Marjaninejad et al., 2017).

For decoding ECoG into discrete classes, linear discriminant analysis (LDA) is often used (Ball et al., 2009; Samiee et al., 2010; Pistohl et al., 2012; Xie et al., 2015; Bleichner et al., 2016; Jiang et al., 2017). Classification can be performed as well using other algorithms, such as k-nearest neighbor method (Chin et al., 2007; Samiee et al., 2010; Paul et al., 2017) and Naïve Bayes classifier (Chestek et al., 2013).

Support vector machines (SVM) is another class of models that solve the problem of separating samples of different classes by maximizing the margin between them. This group of algorithms is versatile and allows constructing highly non-linear decision surfaces. Linear kernel is often used to prevent overfitting and ensure robustness (Yanagisawa et al., 2009, 2011; Ryun et al., 2014; Elgharabawy and Wahed, 2016). Additionally, radial basis functions can be employed (Wang et al., 2012). The disadvantage of this approach is that kernel selection remains largely heuristic and is usually performed via some sort of cross-validation that requires additional data.

For continuous decoding of motor parameters from ECoG, linear models are often used, including linear regression (Schalk et al., 2007; Liang and Bougrain, 2012; Hammer et al., 2013; Hotson et al., 2014; Gunduz et al., 2016) and its modifications designed to reduce overfitting (Kubanek et al., 2009; Nakanishi et al., 2013). Sanchez et al. used the Wiener filter, a linear model, to decode movement trajectory (Sanchez et al., 2008). Pistohl et al. (2008) and Kellis et al. (2012) utilized the Kalman filter, which better handles non-stationary inputs. Wang et al. (2012) employed a modification of dynamic Bayesian network to capture non-stationarity in the temporal and spatial ECoG characteristics.

Several studies utilized prior knowledge of the task performance to improve decoding. Schalk and Leuthardt (2011) developed a Bayesian decoding model that incorporated constraints on finger flexion. Wu et al. (2016) employed a hidden Markov model that highlighted rhythmic task behavior. Saa et al. (2016) enhanced their decoding algorithms with the assumption that subjects do not perform rapid changes between movement and rest.

Hierarchical algorithms (i.e., the ones that stack several models) are often used to enable online BCI tasks. In these schemes, different regression and classification tasks are performed in a certain order (**Figure 2C**). Yanagisawa et al. (2011) and Hotson et al. (2016) used a hierarchical algorithm, where one model classified between rest and movement and detected movement onset and the second model classifies movement type. In several studies, switching between regression models was performed based on a classification algorithm (Flamary and Rakotomamonjy, 2012; Bundy et al., 2016; Elgharabawy and Wahed, 2016). Additionally, Chen et al. developed an algorithm where the output of one model was used to weigh the output of the other model to improve prediction accuracy (Chen et al., 2014).

Artificial neural networks are the class of algorithms that handle complex, non-stationary patterns of brain activity. They can be applied to both classification and regression problems. The primary advantage of artificial neural networks is their versatility. With sufficient number of model parameters (units or neurons),

complex neural patterns can be processed. While shallow neural networks with few layers are useful for decoding, during the last several years deep neural networks containing many layers have significantly advanced. Advantages of deep learning models include their ability to automatically extract features useful for decoding rather than hand-engineering them (**Figure 2B**) and to generate representations at multiple levels of abstraction.

Deep learning is rapidly gaining popularity as a BCI decoding method. In the last few years, deep learning algorithms have been applied to ECoG data processing (Roy et al., 2019), seizure forecasting (Meisel and Bailey, 2019), language mapping (RaviPrakash et al., 2018), and speech decoding (Livezey et al., 2018; Angrick et al., 2019a,b). Several studies have already employed deep learning for decoding movements from ECoG. Xie et al. (2018) decoded finger trajectory with high accuracy using LSTM recurrent neural network. Du et al. (2018) applied LSTM to the same data and implemented real-time control of a robotic arm. Wang et al. (2018) employed a deep model to detect the upper body joints movement based on both ECoG recordings and video data. Pan et al. used recurrent neural networks that recognized temporal dependencies in ECoG signal for rapid and robust gesture decoding (Pan et al., 2018). We foresee further and fruitful development of deep learning approaches for ECoG-based BCIs. This is because of several advantages of this approach. Deep learning architectures applied to electrophysiological data (Roy et al., 2019) perform on par or slightly better than the classical algorithms and do not require neural features to be defined upfront. While such automated processing can be considered as an advantage, BCI researchers still would want to better understand the processing chain performed by a deep learning algorithm, and ideally to relate the processing steps to certain physiological characteristics of the recorded neural signals. Such understanding of the representation of information deep architectures employed for decoding purposes is crucial in order to assess validity of the obtained solutions (Hammer et al., 2013). Thus, it is important to understand the contribution to decoding from different types of neuronal activity, such high-frequency ECoG components better corresponding to neuronal discharges and low-frequency ECoG reflecting synchronization of large neuronal populations (Aoki et al., 1999; Chestek et al., 2013). Additionally, one needs to be able to distinguish causal decoding that captures commands generated by the brain from the decoding based on the peripheral reafferent signals resulting from overt behaviors (Livezey et al., 2019). With a better understanding of these functional relationships, BCI developers can make full use of the information carried by the neural signals, avoid inadvertent uses of informational confounds, establish practical utility of their algorithmic solutions, and gain fundamental neurophysiological insights.

5. SOFTWARE

ECoG-based BCIs can be implemented using several currently available software packages that perform real-time processing of multichannel neural data. OpenVIBE (Renard et al., 2010) is one popular project that offers tools for visual programming and scripting signal processing pipelines. Experimental task descriptions are saved as XML files. OpenVIBE is closed source software. Another popular closed source package for implementing BCIs is BCI2000 (Schalk et al., 2004). BCI2000 is written in C/C++. It incorporates several algorithms for processing multichannel recordings. In our laboratory, we have recently developed NFBLab[1], an open-source software written in Python for implementing a variety of BCI designs (Smetanin et al., 2018b). This software accepts ECoG signals as inputs, as well as EEG and MEG recordings and synchronizes them with motion-tracking information and other multimodal data. Lab Streaming Layer[2] protocol is used to interface NFBLab to data acquisition devices. NFBLab implements temporal and spatial filters for selecting signal feature and removing artifacts. Inverse solvers that generate source-space representation of multichannel inputs are implemented via an interface to MNE-Python software (Gramfort et al., 2014). Additionally, NFBLab incorporates algorithms that reduce processing latency (Smetanin et al., 2018a).

Several standard general purpose libraries are available for implementing deep learning approaches, such as *PyTorch*, *TensorFlow*, and *Keras*. Currently, only a few wrappers are available implementing specific functions that facilitate electrophysiological data processing. The *Braindecode* toolbox by Schirrmeister et al. (2017) is based on *PyTorch* and supports trial-wise and cropped decoding of raw EEG data. This toolbox is applicable to ECoG data. A novel software package *MNEFlow* for dealing with EEG/MEG data is currently being developed[3] with three architectures implemented so far: *LFCNN*, *VARCNN* (Zubarev et al., 2018), and *EEGNet*. The latter architecture (Lawhern et al., 2018) implements a compact convolutional network; it is available for download[4]. While these libraries have not been developed to specifically process ECoG, they can be rapidly adapted to process ECoG data.

The developers of decoding algorithms can utilize open ECoG datasets containing data from movement and motor imagery tasks. For instance, dataset 4 from international BCI competition IV[5] contains data for finger movements. This dataset is often used as a benchmark for BCI decoders that classify the finger being moved and/or perform continuous reconstruction of finger movements. The other ECoG dataset from BCI competition III[6] contains recordings from several experimental sessions, so it is useful for testing how well a BCI decoder generalizes from one session to another. Researches from Brunton Lab made available a large annotated dataset[7] containing long-term ECoG recording along with joint kinematics. Stanford Collection of ECoG Data[8] includes recordings from 250 subjects conducted over an 8-years period. This dataset includes ECoG

[1]https://github.com/nikolaims/nfb/wiki/Experiment-file-structure
[2]https://github.com/sccn/labstreaminglayer
[3]https://mneflow.readthedocs.io
[4]https://github.com/vlawhern/arl-eegmodels
[5]http://www.bbci.de/competition/iv/
[6]http://www.bbci.de/competition/iii/
[7]https://www.bingbrunton.com/data
[8]https://purl.stanford.edu/zk881ps0522

recordings from the sensorimotor cortex in patients performing motor tasks.

6. DISCUSSION

Over the last two decades we observe a growing number of ECoG-based BCI studies in patients who underwent implantation for clinical purposes. This research is clinically relevant and holds promise to provide new treatments for people suffering from severe motor and sensory disabilities caused by such conditions as spinal cord injury, stroke and amyotrophic lateral sclerosis. At the same time, these studies have already provided benefits to the patients and materialized in take-home BCI systems for text-dialing purposes (Brunner et al., 2011), novel safer solutions for passive speech mapping of eloquent cortex during neurosurgery (Taplin et al., 2016; Sinkin et al., 2019) and wireless ECoG devices (Matsushita et al., 2018) that reduce septic risks and can be employed for chronic monitoring of patients with epilepsy. In recent years, it has become clear that ECoG-based BCIs are a viable approach to restoration and rehabilitation of motor functions. ECoG recordings are useful for decoding such motor parameters as movement onset (Wang et al., 2012; Pistohl et al., 2013), movement type (Pistohl et al., 2012; Ryun et al., 2014), and limb trajectory (Pistohl et al., 2008; Nakanishi et al., 2013; Eliseyev and Aksenova, 2014; Xie et al., 2018). These decoded signals can be then sent to external devices, such as hand prosthesis with many degrees of freedom (Yanagisawa et al., 2011; Hotson et al., 2016) or a lower-limb exoskeleton (Vansteensel et al., 2016; Benabid et al., 2019). ECoG-based BCIs can control two-dimensional and three-dimensional movements of a cursor or a prosthetic arm (Anderson et al., 2012; Yanagisawa et al., 2012). Several kinematic parameters can be extracted from ECoG, including position, velocity, and acceleration (Hammer et al., 2013). Extrinsic variables, such as target location, can also be also decoded from ECoG and utilized for BCI control (Nakanishi et al., 2017). The recently developed fully implantable ECoG-based BCIs (Vansteensel et al., 2016; Benabid et al., 2019) have extended the functionality of such systems as they enable long-term operations and engage cortical plasticity. With the rapid development of new technologies for high-fidelity ECoG recordings (Viventi et al., 2011; Akinwande et al., 2014; Khodagholy et al., 2015) and of neural decoding methods (Faust et al., 2018; Richards et al., 2019), ECoG-based BCIs will likely continue to improve.

ECoG-based BCIs are clinically relevant due to their safety as compared to the intracortical implants (e.g., Utah array) and have a better spatial and temporal resolution than non-invasive, EEG-based BCIs. At the same time, the ECoG grids cover relatively cortical areas which allows to take advantage of the spatial-temporal encoding principles implemented by the brain. Such large-scale recordings improve BCI accuracy by allowing for simultaneous access to the information processed by many brain regions involved in programming and execution of movements.

Broad spectral and spatial extent of ECoG recordings open the opportunity to explore at various scales interregional interactions between and within several frequency bands from delta-band (Gunduz et al., 2016) correlates of movement, desynchronization in the alpha and beta bands in spatially distributed task-relevant cortical areas to more localized synchronization in the high gamma range and cross-frequency coupling between bands and specific cytoarchitectonic assemblies. This flexibility leads to significant variability in the choice of features, decoded parameters and decoding models witnessed in the range of described ECoG studies. Thus, depending on the clinical needs, different ECoG components and associated neurophysiological phenomena can be utilized in practical BCI system.

In recent years, an active development of the decoding algorithms is underway. Several strategies have been particularly useful, including switching models, adapting algorithms, and the decoders utilizing prior information on movement characteristics and the nature of physiological processes. Even more versatile methods are currently being developed, such as those based on deep learning which allows for capturing complex relationship between motor parameters and ECoG characteristics.

We foresee that the next series of major advances will be made in bidirectional BCI technology that combines motor-control loops with sensory feedback provided by cortical stimulation and/or sensory substitution methods (Wilson et al., 2012; Cronin et al., 2016; Hiremath et al., 2017). The development of bidirectional ECoG-based BCIs will bring new challenges for modeling the complex relationships between ECoG signals and different motor and sensory parameters. Previous studies have reported a range of promising results regarding the possibility of building BCIs that employ ECoG recordings to enable motor functions. With the rapid developments in ECoG technologies (Shokoueinejad et al., 2019), surgical implantation procedures and mathematical algorithms for neural decoding, it is reasonable to expect that a variety of practical, fully-implantable (Vansteensel et al., 2016) ECoG-based neural prostheses will emerge for enabling motor and sensory functions to neurologically impaired patients.

AUTHOR CONTRIBUTIONS

KV wrote the first draft of the manuscript. KV, ML, AK, and AO revised the manuscript. All authors contributed to the final revision, read, and approved the submitted version.

FUNDING

This study has been funded by the Center for Bioelectric Interfaces NRU Higher School of Economics, RF Government grant, AG. No. 14.641.31.0003.

REFERENCES

Acharya, S., Fifer, M. S., Benz, H. L., Crone, N. E., and Thakor, N. V. (2010). Electrocorticographic amplitude predicts finger positions during slow grasping motions of the hand. *J. Neural Eng.* 7:046002. doi: 10.1088/1741-2560/7/4/046002

Akinwande, D., Petrone, N., and Hone, J. (2014). Two-dimensional flexible nanoelectronics. *Nat. Commun.* 5:5678. doi: 10.1038/ncomms6678

Akram, F., Han, H.-S., and Kim, T.-S. (2014). A p300-based brain computer interface system for words typing. *Comput. Biol. Med.* 45, 118–125. doi: 10.1016/j.compbiomed.2013.12.001

Andersen, R. A., Burdick, J. W., Musallam, S., Pesaran, B., and Cham, J. G. (2004). Cognitive neural prosthetics. *Trends Cogn. Sci.* 8, 486–493. doi: 10.1016/j.tics.2004.09.009

Andersen, R. A., Hwang, E. J., and Mulliken, G. H. (2010). Cognitive neural prosthetics. *Annu. Rev. Psychol.* 61, 169–190. doi: 10.1146/annurev.psych.093008.100503

Anderson, N. R., Blakely, T., Schalk, G., Leuthardt, E. C., and Moran, D. W. (2012). Electrocorticographic (ECoG) correlates of human arm movements. *Exp. Brain Res.* 223, 1–10. doi: 10.1007/s00221-012-3226-1

Angrick, M., Herff, C., Johnson, G., Shih, J., Krusienski, D., and Schultz, T. (2019a). Interpretation of convolutional neural networks for speech spectrogram regression from intracranial recordings. *Neurocomputing* 342, 145–151. doi: 10.1016/j.neucom.2018.10.080

Angrick, M., Herff, C., Mugler, E., Tate, M. C., Slutzky, M. W., Krusienski, D. J., et al. (2019b). Speech synthesis from ECoG using densely connected 3d convolutional neural networks. *J. Neural Eng.* 16:036019. doi: 10.1088/1741-2552/ab0c59

Aoki, F., Fetz, E. E., Shupe, L., Lettich, E., and Ojemann, G. A. (1999). Increased gamma-range activity in human sensorimotor cortex during performance of visuomotor tasks. *Clin. Neurophysiol.* 110, 524–537. doi: 10.1016/S1388-2457(98)00064-9

Babiloni, C., Del Percio, C., Lopez, S., Di Gennaro, G., Quarato, P. P., Pavone, L., et al. (2017). Frontal functional connectivity of electrocorticographic delta and theta rhythms during action execution versus action observation in humans. *Front. Behav. Neurosci.* 11:20. doi: 10.3389/fnbeh.2017.00020

Babyak, M. A. (2004). What you see may not be what you get: a brief, nontechnical introduction to overfitting in regression-type models. *Psychosom. Med.* 66, 411–421. doi: 10.1097/00006842-200405000-00021

Badia, S. B., García Morgade, A., Samaha, H., and Verschure, P. F. (2013). Using a hybrid brain computer interface and virtual reality system to monitor and promote cortical reorganization through motor activity and motor imagery training. *IEEE Trans. Neural Syst. Rehabil. Eng.* 21, 174–181. doi: 10.1109/TNSRE.2012.2229295

Ball, T., Schulze-Bonhage, A., Aertsen, A., and Mehring, C. (2009). Differential representation of arm movement direction in relation to cortical anatomy and function. *J. Neural Eng.* 6:016006. doi: 10.1088/1741-2560/6/1/016006

Benabid, A. L., Costecalde, T., Eliseyev, A., Charvet, G., Verney, A., Karakas, S., et al. (2019). An exoskeleton controlled by an epidural wireless brain–machine interface in a tetraplegic patient: a proof-of-concept demonstration. *Lancet Neurol.* 18, P1112–1122. doi: 10.1016/S1474-4422(19)30321-7

Bensmaia, S. J., and Miller, L. E. (2014). Restoring sensorimotor function through intracortical interfaces: progress and looming challenges. *Nat. Rev. Neurosci.* 15:313. doi: 10.1038/nrn3724

Benz, H. L., Zhang, H., Bezerianos, A., Acharya, S., Crone, N. E., Zheng, X., et al. (2012). Connectivity analysis as a novel approach to motor decoding for prosthesis control. *IEEE Trans. Neural Syst. Rehabil. Eng.* 20, 143–152. doi: 10.1109/TNSRE.2011.2175309

Blakely, T., Miller, K. J., Zanos, S. P., Rao, R. P., and Ojemann, J. G. (2009). Robust, long-term control of an electrocorticographic brain-computer interface with fixed parameters. *Neurosurg. Focus* 27:E13. doi: 10.3171/2009.4.FOCUS0977

Bleichner, M. G., Freudenburg, Z. V., Jansma, J. M., Aarnoutse, E. J., Vansteensel, M. J., and Ramsey, N. F. (2016). Give me a sign: decoding four complex hand gestures based on high-density ECoG. *Brain Struct. Funct.* 221, 203–216. doi: 10.1007/s00429-014-0902-x

Bouton, C. E., Shaikhouni, A., Annetta, N. V., Bockbrader, M. A., Friedenberg, D. A., Nielson, D. M., et al. (2016). Restoring cortical control of functional movement in a human with quadriplegia. *Nature* 533:247. doi: 10.1038/nature17435

Boye, A. T., Kristiansen, U. Q., Billinger, M., do Nascimento, O. F., and Farina, D. (2008). Identification of movement-related cortical potentials with optimized spatial filtering and principal component analysis. *Biomed. Signal Process. Control* 3, 300–304. doi: 10.1016/j.bspc.2008.05.001

Branco, M. P., Freudenburg, Z. V., Aarnoutse, E. J., Bleichner, M. G., Vansteensel, M. J., and Ramsey, N. F. (2017). Decoding hand gestures from primary somatosensory cortex using high-density ECoG. *Neuroimage* 147, 130–142. doi: 10.1016/j.neuroimage.2016.12.004

Brandman, D. M., Cash, S. S., and Hochberg, L. R. (2017). human intracortical recording and neural decoding for brain–computer interfaces. *IEEE Trans. Neural Syst. Rehabil. Eng.* 25, 1687–1696. doi: 10.1109/TNSRE.2017.2677443

Brunner, C., Graimann, B., Huggins, J. E., Levine, S. P., and Pfurtscheller, G. (2005). Phase relationships between different subdural electrode recordings in man. *Neurosci. Lett.* 375, 69–74. doi: 10.1016/j.neulet.2004.11.052

Brunner, P., Ritaccio, A. L., Emrich, J. F., Bischof, H. and Schalk, G. (2011). Rapid communication with a "p300" matrix speller using electrocorticographic signals (ECoG). *Front. Neurosci.* 5:5. doi: 10.3389/fnins.2011.00005

Brunner, P., Ritaccio, A. L., Lynch, T. M., Emrich, J. F., Wilson, J. A., Williams, J. C., et al. (2009). A practical procedure for real-time functional mapping of eloquent cortex using electrocorticographic signals in humans. *Epilepsy Behav.* 15, 278–286. doi: 10.1016/j.yebeh.2009.04.001

Bruurmijn, M. L. C. M., Pereboom, I. P. L., Vansteensel, M. J., Raemaekers, M. A. H., and Ramsey, N. F. (2017). Preservation of hand movement representation in the sensorimotor areas of amputees. *Brain* 140, 3166–3178. doi: 10.1093/brain/awx274

Bundy, D. T., Pahwa, M., Szrama, N., and Leuthardt, E. C. (2016). Decoding three-dimensional reaching movements using electrocorticographic signals in humans. *J. Neural Eng.* 13:026021. doi: 10.1088/1741-2560/13/2/026021

Bundy, D. T., Zellmer, E., Gaona, C. M., Sharma, M., Szrama, N., Hacker, C., et al. (2014). Characterization of the effects of the human dura on macro-and micro-electrocorticographic recordings. *J. Neural Eng.* 11:016006. doi: 10.1088/1741-2560/11/1/016006

Buzsáki, G., Anastassiou, C. A., and Koch, C. (2012). The origin of extracellular fields and currents—EEG, ECoG, LFP and spikes. *Nat. Rev. Neurosci.* 13:407. doi: 10.1038/nrn3241

Carmena, J. M., Lebedev, M. A., Crist, R. E., O'Doherty, J. E., Santucci, D. M., Dimitrov, D. F., et al. (2003). Learning to control a brain–machine interface for reaching and grasping by primates. *PLoS Biol.* 1:e42. doi: 10.1371/journal.pbio.0000042

Chai, R., Tran, Y., Craig, A., Ling, S. H., and Nguyen, H. T. (2014). Enhancing accuracy of mental fatigue classification using advanced computational intelligence in an electroencephalography system. *Conf. Proc. IEEE Eng. Med. Biol. Soc.* 2014, 1318–1341. doi: 10.1109/EMBC.2014.6943846

Chapin, J. K., Moxon, K. A., Markowitz, R. S., and Nicolelis, M. A. (1999). Real-time control of a robot arm using simultaneously recorded neurons in the motor cortex. *Nat. Neurosci.* 2:664. doi: 10.1038/10223

Chaudhary, U., Birbaumer, N., and Ramos-Murguialday, A. (2016). Brain–computer interfaces in the completely locked-in state and chronic stroke. *Prog. Brain Res.* 228, 131–161. doi: 10.1016/bs.pbr.2016.04.019

Chavarriaga, R., Sobolewski, A., Leeb, R., Pralong, E., Bloch, J., and Millán, J. D. R. (2016). "Reliable BMI control using epidural ECoG by an hemiplegic user," in *Proceedings of the 6th International Brain-Computer Interface Meeting Number EPFL-CONF-218936* (Asilomar, CA), 86.

Chen, W., Liu, X., and Litt, B. (2014). Logistic-weighted regression improves decoding of finger flexion from electrocorticographic signals. *Conf. Proc. IEEE Eng. Med. Biol. Soc.* 2014, 2629–2632. doi: 10.1109/EMBC.2014.6944162

Chestek, C. A., Gilja, V., Blabe, C. H., Foster, B. L., Shenoy, K. V., Parvizi, J., et al. (2013). Hand posture classification using electrocorticography signals in the gamma band over human sensorimotor brain areas. *J. Neural Eng.* 10:026002. doi: 10.1088/1741-2560/10/2/026002

Chin, C. M., Popovic, M. R., Thrasher, A., Cameron, T., Lozano, A., and Chen, R. (2007). Identification of arm movements using correlation of electrocorticographic spectral components and kinematic recordings. *J. Neural Eng.* 4:146. doi: 10.1088/1741-2560/4/2/014

Collinger, J. L., Vinjamuri, R., Degenhart, A. D., Weber, D. J., Sudre, G. P., Boninger, M. L., et al. (2014). Motor-related brain activity during action observation: a neural substrate for electrocorticographic brain-computer interfaces after spinal cord

injury. *Front. Integr. Neurosci.* 8:17. doi: 10.3389/fnint.2014.00017

Collinger, J. L., Wodlinger, B., Downey, J. E., Wang, W., Tyler-Kabara, E. C., Weber, D. J., et al. (2013). High-performance neuroprosthetic control by an individual with tetraplegia. *Lancet* 381, 557–564. doi: 10.1016/S0140-6736(12)61816-9

Contreras-Vidal, J. L., and Grossman, R. G. (2013). Neurorex: a clinical neural interface roadmap for EEG-based brain machine interfaces to a lower body robotic exoskeleton. *Conf. Proc. IEEE Eng. Med. Biol. Soc.* 2013, 1579–1582. doi: 10.1109/EMBC.2013.6609816

Cooper, R., Winter, A. L., Crow, H. J., and Walter, W. G. (1965). Comparison of subcortical, cortical and scalp activity using chronically indwelling electrodes in man. *Clin. Neurophysiol.* 18, 217–228. doi: 10.1016/0013-4694(65)90088-X

Cronin, J. A., Wu, J., Collins, K. L., Sarma, D., Rao, R. P., Ojemann, J. G., et al. (2016). Task-specific somatosensory feedback via cortical stimulation in humans. *IEEE Trans. Haptics* 9, 515–522. doi: 10.1109/TOH.2016.2591952

Das, B., Talukdar, M., Sarma, R., and Hazarika, S. M. (2016). Multiple feature extraction of electroencephalograph signal for motor imagery classification through bispectral analysis. *Proc. Comput. Sci.* 84, 192–197. doi: 10.1016/j.procs.2016.04.086

Degenhart, A. D., Hiremath, S. V., Yang, Y., Foldes, S., Collinger, J. L., Boninger, M., et al. (2018). Remapping cortical modulation for electrocorticographic brain–computer interfaces: a somatotopy-based approach in individuals with upper-limb paralysis. *J. Neural Eng.* 15:026021. doi: 10.1088/1741-2552/aa9bfb

Delgado Saa, J. F., De Pesters, A., and Cetin, M. (2016). Asynchronous decoding of finger movements from ECoG signals using long-range dependencies conditional random fields. *J. Neural Eng.* 13:036017. doi: 10.1088/1741-2560/13/3/036017

Dobelle, W. H. (2000). Artificial vision for the blind by connecting a television camera to the visual cortex. *ASAIO J.* 46, 3–9. doi: 10.1097/00002480-200001000-00002

Du, A., Yang, S., Liu, W., and Huang, H. (2018). "Decoding ECoG signal with deep learning model based on LSTM," in *TENCON 2018–2018 IEEE Region 10 Conference* (Jeju: IEEE), 430–435.

Edelman, B. J., Meng, J., Suma, D., Zurn, C., Nagarajan, E., Baxter, B. S., et al. (2019). Noninvasive neuroimaging enhances continuous neural tracking for robotic device control. *Sci. Robot.* 4:eaaw6844. doi: 10.1126/scirobotics.aaw6844

Elgharabawy, A., and Wahed, M. A. (2016). "Decoding of finger movement using kinematic model classification and regression model switching," in *2016 8th Cairo International Biomedical Engineering Conference (CIBEC)* (Cairo: IEEE), 84–89.

Elghrabawy, A., and Wahed, M. (2012). "Prediction of five-class finger flexion using ECoG," in *Cairo International Biomedical Engineering Conference* (Giza).

Eliseyev, A., and Aksenova, T. (2014). Stable and artifact-resistant decoding of 3d hand trajectories from ECoG signals using the generalized additive model. *J. Neural Eng.* 11:066005. doi: 10.1088/1741-2560/11/6/066005

Faust, O., Hagiwara, Y., Hong, T. J., Lih, O. S., and Acharya, U. R. (2018). Deep learning for healthcare applications based on physiological signals: a review. *Comput. Methods Programs Biomed.* 161, 1–13. doi: 10.1016/j.cmpb.2018.04.005

Fifer, M. S., Acharya, S., Benz, H. L., Mollazadeh, M., Crone, N. E., and Thakor, N. V. (2012). Toward electrocorticographic control of a dexterous upper limb prosthesis: building brain-machine interfaces. *IEEE Pulse* 3, 38–42. doi: 10.1109/MPUL.2011.2175636

Fitzsimmons, N. A., Lebedev, M. A., Peikon, I. D., and Nicolelis, M. A. (2009). Extracting kinematic parameters for monkey bipedal walking from cortical neuronal ensemble activity. *Front. Integr. Neurosci.* 3:3. doi: 10.3389/neuro.07.003.2009

Flamary, R., and Rakotomamonjy, A. (2012). Decoding finger movements from ECoG signals using switching linear models. *Front. Neurosci.* 6:29. doi: 10.3389/fnins.2012.00029

Flint, R. D., Rosenow, J. M., Tate, M. C., and Slutzky, M. W. (2016). Continuous decoding of human grasp kinematics using epidural and subdural signals. *J. Neural Eng.* 14:016005. doi: 10.1088/1741-2560/14/1/016005

Freeman, W. J., Rogers, L. J., Holmes, M. D., and Silbergeld, D. L. (2000). Spatial spectral analysis of human electrocorticograms including the alpha and gamma bands. *J. Neurosci. Methods* 95, 111–121. doi: 10.1016/S0165-0270(99)00160-0

Galán, F., Nuttin, M., Lew, E., Ferrez, P. W., Vanacker, G., Philips, J., et al. (2008). A brain-actuated wheelchair: asynchronous and non-invasive brain–computer interfaces for continuous control of robots. *Clin. Neurophysiol.* 119, 2159–2169. doi: 10.1016/j.clinph.2008.06.001

Gancet, J., Ilzkovitz, M., Cheron, G., Ivanenko, Y., Van Der Kooij, H., Van Der Helm, F., et al. (2011). "Mindwalker: a brain controlled lower limbs exoskeleton for rehabilitation. potential applications to space," in *11th Symposium on Advanced Space Technologies in Robotics and Automation* (Noordwijk), 12–14.

Georgopoulos, A. P., Kalaska, J. F., Caminiti, R., and Massey, J. T. (1982). On the relations between the direction of two-dimensional arm movements and cell discharge in primate motor cortex. *J. Neurosci.* 2, 1527–1537.

Gharabaghi, A., Naros, G., Walter, A., Roth, A., Bogdan, M., Rosenstiel, W., et al. (2014). Epidural electrocorticography of phantom hand movement following long-term upper-limb amputation. *Front. Hum. Neurosci.* 8:285. doi: 10.3389/fnhum.2014.00285

Gilja, V., Nuyujukian, P., Chestek, C. A., Cunningham, J. P., Byron, M. Y., Fan, J. M., et al. (2012). A high-performance neural prosthesis enabled by control algorithm design. *Nat. Neurosci.* 15:1752. doi: 10.1038/nn.3265

Gilja, V., Pandarinath, C., Blabe, C. H., Nuyujukian, P., Simeral, J. D., Sarma, A. A., et al. (2015). Clinical translation of a high-performance neural prosthesis. *Nat. Med.* 21:1142. doi: 10.1038/nm.3953

Göhring, D., Latotzky, D., Wang, M., and Rojas, R. (2013). "Semi-autonomous car control using brain computer interfaces," in *Intelligent Autonomous Systems 12* (Jeju Island: Springer), 393–408.

Graimann, B., Huggins, J. E., Schlögl, A., Levine, S. P., and Pfurtscheller, G. (2003). Detection of movement-related patterns in ongoing single-channel electrocorticogram. *IEEE Trans. Neural Syst. Rehabil. Eng.* 11, 276–281. doi: 10.1109/TNSRE.2003.816863

Gramfort, A., Luessi, M., Larson, E., Engemann, D. A., Strohmeier, D., Brodbeck, C., et al. (2014). Mne software for processing MEG and EEG data. *Neuroimage* 86, 446–460. doi: 10.1016/j.neuroimage.2013.10.027

Gramfort, A., Papadopoulo, T., Olivi, E., and Clerc, M. (2010). Openmeeg: opensource software for quasistatic bioelectromagnetics. *Biomed. Eng. Online* 9:45. doi: 10.1186/1475-925X-9-45

Gu, Q., Li, Z., and Han, J. (2012). Generalized fisher score for feature selection. *arXiv [Preprint]. arXiv:1202.3725.*

Gunduz, A., Brunner, P., Sharma, M., Leuthardt, E. C., Ritaccio, A. L., Pesaran, B., et al. (2016). Differential roles of high gamma and local motor potentials for movement preparation and execution. *Brain Comput. Interfaces* 3, 88–102. doi: 10.1080/2326263X.2016.1179087

Hammer, J., Fischer, J., Ruescher, J., Schulze-Bonhage, A., Aertsen, A., and Ball, T. (2013). The role of ECoG magnitude and phase in decoding position, velocity, and acceleration during continuous motor behavior. *Front. Neurosci.* 7:200. doi: 10.3389/fnins.2013.00200

Hazrati, M. K., and Hofmann, U. G. (2012). Decoding finger movements from ECoG signals using empirical mode decomposition. *Biomed. Eng.* 57, 650–653. doi: 10.1515/bmt-2012-4489

Henson, R. N., Mattout, J., Phillips, C., and Friston, K. J. (2009). Selecting forward models for MEG source-reconstruction using model-evidence. *Neuroimage* 46, 168–176. doi: 10.1016/j.neuroimage.2009.01.062

Hill, N. J., Gupta, D., Brunner, P., Gunduz, A., Adamo, M. A., Ritaccio, A., et al. (2012). Recording human electrocorticographic (ECoG) signals for neuroscientific research and real-time functional cortical mapping. *J. Vis. Exp.* 64:e3993. doi: 10.3791/3993

Hiremath, S. V., Tyler-Kabara, E. C., Wheeler, J. J., Moran, D. W., Gaunt, R. A., Collinger, J. L., et al. (2017). Human perception of electrical stimulation on the surface of somatosensory cortex. *PLoS ONE* 12:e0176020. doi: 10.1371/journal.pone.0176020

Hochberg, L. R., Bacher, D., Jarosiewicz, B., Masse, N. Y., Simeral, J. D., Vogel, J., et al. (2012). Reach and grasp by people with tetraplegia using a neurally controlled robotic arm. *Nature* 485:372. doi: 10.1038/nature11076

Hochberg, L. R., Serruya, M. D., Friehs, G. M., Mukand, J. A., Saleh, M., Caplan, A. H., et al. (2006). Neuronal ensemble control of prosthetic devices by a human with tetraplegia. *Nature* 442:164. doi: 10.1038/nature04970

Hotson, G., Fifer, M. S., Acharya, S., Benz, H. L., Anderson, W. S., Thakor, N. V., et al. (2014). Coarse electrocorticographic decoding of ipsilateral reach in patients with brain lesions. *PLoS ONE* 9:e115236. doi: 10.1371/journal.pone.0115236

Hotson, G., McMullen, D. P., Fifer, M. S., Johannes, M. S., Katyal, K. D., Para, M. P., et al. (2016). Individual finger control of a modular prosthetic limb using high-density electrocorticography in a human subject. *J. Neural Eng.* 13:026017. doi: 10.1088/1741-2560/13/2/026017

House, W. F. (1976). Cochlear implants. *Ann. Otol. Rhinol. Laryngol.* 85, 3–3.

Huggins, J. E., Levine, S. P., BeMent, S. L., Kushwaha, R. K., Schuh, L. A., Passaro, E. A., et al. (1999). Detection of event-related potentials for development of a direct brain interface. *J. Clin. Neurophysiol.* 16:448.

Hughes, S. W., and Crunelli, V. (2005). Thalamic mechanisms of EEG alpha rhythms and their pathological implications. *Neuroscientist* 11, 357–372. doi: 10.1177/1073858405277450

Jiang, T., Ince, N. F., Jiang, T., Wang, T., Mei, S., Li, Y., et al. (2015). "Investigation of the spatial and spectral patterns of hand extension/flexion using high-density ECoG," in *2015 7th International IEEE/EMBS Conference on Neural Engineering (NER)* (Milan: IEEE), 589–592.

Jiang, T., Jiang, T., Wang, T., Mei, S., Liu, Q., Li, Y., et al. (2017). Characterization and decoding the spatial patterns of hand extension/flexion using high-density ECoG. *IEEE Trans. Neural Syst. Rehabil. Eng.* 25, 370–379. doi: 10.1109/TNSRE.2016.2647255

Kapeller, C., Gergondet, P., Kamada, K., Ogawa, H., Takeuchi, F., Ortner, R., et al. (2015). Online control of a humanoid robot through hand movement imagination using CSP and ECoG based features. *Conf. Proc. IEEE Eng. Med. Biol. Soc.* 2015, 1765–1768. doi: 10.1109/EMBC.2015.7318720

Kapeller, C., Schneider, C., Kamada, K., Ogawa, H., Kunii, N., Ortner, R., et al. (2014). Single trial detection of hand poses in human ECoG using CSP based feature extraction. *Conf. Proc. IEEE Eng. Med. Biol. Soc.* 2014, 4599–4602. doi: 10.1109/EMBC.2014.6944648

Kellis, S., Hanrahan, S., Davis, T., House, P. A., Brown, R., and Greger, B. (2012). Decoding hand trajectories from micro-electrocorticography in human patients. *Conf. Proc. IEEE Eng. Med. Biol. Soc.* 2012, 4091–4094. doi: 10.1109/EMBC.2012.6346866

Kellis, S., Sorensen, L., Darvas, F., Sayres, C., O'Neill, K., Brown, R. B., et al. (2016). Multi-scale analysis of neural activity in humans: implications for micro-scale electrocorticography. *Clin. Neurophysiol.* 127, 591–601. doi: 10.1016/j.clinph.2015.06.002

Khodagholy, D., Gelinas, J. N., Thesen, T., Doyle, W., Devinsky, O., Malliaras, G. G., et al. (2015). Neurogrid: recording action potentials from the surface of the brain. *Nat. Neurosci.* 18:310. doi: 10.1038/nn.3905

Kim, G. H., Kim, K., Lee, E., An, T., Choi, W., Lim, G., et al. (2018). Recent progress on microelectrodes in neural interfaces. *Materials* 11:1995. doi: 10.3390/ma11101995

Kubánek, J., Miller, K. J., Ojemann, J. G., Wolpaw, J. R., and Schalk, G. (2009). Decoding flexion of individual fingers using electrocorticographic signals in humans. *J. Neural Eng.* 6:066001. doi: 10.1088/1741-2560/6/6/066001

Kwak, N.-S., Müller, K.-R., and Lee, S.-W. (2015). A lower limb exoskeleton control system based on steady state visual evoked potentials. *J. Neural Eng.* 12:056009. doi: 10.1088/1741-2560/12/5/056009

LaFleur, K., Cassady, K., Doud, A., Shades, K., Rogin, E., and He, B. (2013). Quadcopter control in three-dimensional space using a noninvasive motor imagery-based brain–computer interface. *J. Neural Eng.* 10:046003. doi: 10.1088/1741-2560/10/4/046003

Lawhern, V. J., Solon, A. J., Waytowich, N. R., Gordon, S. M., Hung, C. P., and Lance, B. J. (2018). EEGNet: a compact convolutional neural network for EEG-based brain–computer interfaces. *J. Neural Eng.* 15:056013. doi: 10.1088/1741-2552/aace8c

Lebedev, M. (2014). Brain-machine interfaces: an overview. *Transl. Neurosci.* 5, 99–110. doi: 10.2478/s13380-014-0212-z

Lebedev, M. A., Carmena, J. M., O'Doherty, J. E., Zacksenhouse, M., Henriquez, C. S., Principe, J. C., et al. (2005). Cortical ensemble adaptation to represent velocity of an artificial actuator controlled by a brain-machine interface. *J. Neurosci.* 25, 4681–4693. doi: 10.1523/JNEUROSCI.4088-04.2005

Lebedev, M. A., and Nicolelis, M. A. (2006). Brain–machine interfaces: past, present and future. *Trends Neurosci.* 29, 536–546. doi: 10.1016/j.tins.2006.07.004

Lebedev, M. A., O'doherty, J. E., and Nicolelis, M. A. (2008). Decoding of temporal intervals from cortical ensemble activity. *J. Neurophysiol.* 99, 166–186. doi: 10.1152/jn.00734.2007

Leuthardt, E. C., Miller, K. J., Schalk, G., Rao, R. P., and Ojemann, J. G. (2006). Electrocorticography-based brain computer interface-the seattle experience. *IEEE Trans. Neural Syst. Rehabil. Eng.* 14, 194–198. doi: 10.1109/TNSRE.2006.875536

Leuthardt, E. C., Schalk, G., Wolpaw, J. R., Ojemann, J. G., and Moran, D. W. (2004). A brain–computer interface using electrocorticographic signals in humans. *J. Neural Eng.* 1:63. doi: 10.1088/1741-2560/1/2/001

Levine, S. P., Huggins, J. E., BeMent, S. L., Kushwaha, R. K., Schuh, L. A., Passaro, E. A., et al. (1999). Identification of electrocorticogram patterns as the basis for a direct brain interface. *J. Clin. Neurophysiol.* 16:439.

Levine, S. P., Huggins, J. E., BeMent, S. L., Kushwaha, R. K., Schuh, L. A., Rohde, M. M., et al. (2000). A direct brain interface based on event-related potentials. *IEEE Trans. Rehabil. Eng.* 8, 180–185. doi: 10.1109/86.847809

Li, T., Hong, J., Zhang, J., and Guo, F. (2014). Brain–machine interface control of a manipulator using small-world neural network and shared control strategy. *J. Neurosci. Methods* 224, 26–38. doi: 10.1016/j.jneumeth.2013.11.015

Li, Y., Zhang, S., Jin, Y., Cai, B., Controzzi, M., Zhu, J., et al. (2017). Gesture decoding using ECoG signals from human sensorimotor cortex: a pilot study. *Behav. Neurol.* 2017:3435686. doi: 10.1155/2017/3435686

Liang, N., and Bougrain, L. (2012). Decoding finger flexion from band-specific ECoG signals in humans. *Front. Neurosci.* 6:91. doi: 10.3389/fnins.2012.00091

Lin, P. T., Sharma, K., Holroyd, T., Battapady, H., Fei, D.-Y., and Bai, O. (2013). "A high performance MEG based BCI using single trial detection of human movement intention," in *Functional Brain Mapping and the Endeavor to Understand the Working Brain* (Norderstedt: IntechOpen).

Liu, Y., Coon, W. G., de Pesters, A., Brunner, P., and Schalk, G. (2015). The effects of spatial filtering and artifacts on electrocorticographic signals. *J. Neural Eng.* 12:056008. doi: 10.1088/1741-2560/12/5/056008

Liu, Y., Sharma, M., Gaona, C., Breshears, J., Roland, J., Freudenburg, Z., et al. (2010). "Decoding ipsilateral finger movements from ECoG signals in humans," in *Advances in Neural Information Processing Systems* (Vancouver, BC), 1468–1476.

Livezey, J. A., Bouchard, K. E., and Chang, E. F. (2018). Deep learning as a tool for neural data analysis: speech classification and cross-frequency coupling in human sensorimotor cortex. *arXiv [Preprint]. arXiv:1803.09807.*

Livezey, J. A., Bouchard, K. E., and Chang, E. F. (2019). Deep learning as a tool for neural data analysis: speech classification and cross-frequency coupling in human sensorimotor cortex. *PLoS Comput. Biol.* 15:e1007091. doi: 10.1371/journal.pcbi.1007091

Lotte, F., Bougrain, L., Cichocki, A., Clerc, M., Congedo, M., Rakotomamonjy, A., et al. (2018). A review of classification algorithms for EEG-based brain–computer interfaces: a 10 year update. *J. Neural Eng.* 15:031005. doi: 10.1088/1741-2552/aab2f2

Lotte, F., Congedo, M., Lécuyer, A., Lamarche, F., and Arnaldi, B. (2007). A review of classification algorithms for EEG-based brain–computer interfaces. *J. Neural Eng.* 4:R1. doi: 10.1088/1741-2560/4/2/R01

Manning, J. R., Jacobs, J., Fried, I., and Kahana, M. J. (2009). Broadband shifts in local field potential power spectra are correlated with single-neuron spiking in humans. *J. Neurosci.* 29, 13613–13620. doi: 10.1523/JNEUROSCI.2041-09.2009

Marjaninejad, A., Taherian, B., and Valero-Cuevas, F. J. (2017). Finger movements are mainly represented by a linear transformation of energy in band-specific ECoG signals. In *Conf. Proc. IEEE Eng. Med. Biol. Soc.* 2017, 986–989. doi: 10.1109/EMBC.2017.8036991

Matsushita, K., Hirata, M., Suzuki, T., Ando, H., Yoshida, T., Ota, Y., et al. (2018). A fully implantable wireless ecog 128-channel recording device for human brain—machine interfaces: W-herbs. *Front. Neurosci.* 12:511. doi: 10.3389/fnins.2018.00511

McCrimmon, C. M., Wang, P. T., Heydari, P., Nguyen, A., Shaw, S. J., Gong, H., et al. (2017). Electrocorticographic encoding of human gait in the leg primary motor cortex. *Cereb. Cortex* 28, 2752–2762. doi: 10.1093/cercor/bhx155

McFarland, D., and Wolpaw, J. (2017). EEG-based brain–computer interfaces. *Curr. Opin. Biomed. Eng.* 4, 194–200. doi: 10.1016/j.cobme.2017.11.004

Mehring, C., Rickert, J., Vaadia, E., de Oliveira, S. C., Aertsen, A., and Rotter, S. (2003). Inference of hand movements from local field potentials in monkey motor cortex. *Nat. Neurosci.* 6:1253. doi: 10.1038/nn1158

Meisel, C., and Bailey, K. A. (2019). Identifying signal-dependent information about the preictal state: a comparison across ECoG, EEG and EKG using deep learning. *EBioMedicine* 45, 422–431. doi: 10.1016/j.ebiom.2019.07.001

Miller, K. J., Leuthardt, E. C., Schalk, G., Rao, R. P., Anderson, N. R., Moran, D. W., et al. (2007). Spectral changes in cortical surface potentials during motor movement. *J. Neurosci.* 27, 2424–2432. doi: 10.1523/JNEUROSCI.3886-06.2007

Miller, K. J., Zanos, S., Fetz, E. E., Den Nijs, M., and Ojemann, J. G. (2009). Decoupling the cortical power spectrum reveals real-time representation of individual finger movements in humans. *J. Neurosci.* 29, 3132–3137. doi: 10.1523/JNEUROSCI.5506-08.2009

Mirabella, G., and Lebedev, M. A. (2016). Interfacing to the brain's motor decisions. *J. Neurophysiol.* 117, 1305–1319. doi: 10.1152/jn.00051.2016

Morales-Flores, E., Schalk, G., and Ramirez-Cortes, J. M. (2014). Non-supervised technique to adapt spatial filters for ECoG data analysis. in *2014 IEEE Symposium on Computational Intelligence in Brain Computer Interfaces (CIBCI)* (Orlando, FL: IEEE), 43–48.

Murphy, M. D., Guggenmos, D. J., Bundy, D. T., and Nudo, R. J. (2016). Current challenges facing the translation of brain computer interfaces from preclinical trials to use in human patients. *Front. Cell. Neurosci.* 9:497. doi: 10.3389/fncel.2015.00497

Nakanishi, Y., Yanagisawa, T., Shin, D., Fukuma, R., Chen, C., Kambara, H., et al. (2013). Prediction of three-dimensional arm trajectories based on ECoG signals recorded from human sensorimotor cortex. *PLoS ONE* 8:e72085. doi: 10.1371/journal.pone.0072085

Nakanishi, Y., Yanagisawa, T., Shin, D., Kambara, H., Yoshimura, N., Tanaka, M., et al. (2017). Mapping ECoG channel contributions to trajectory and muscle activity prediction in human sensorimotor cortex. *Sci. Rep.* 7:45486. doi: 10.1038/srep45486

Newman, G., Fifer, M., Benz, H., Crone, N., and Thakor, N. (2015). "Eigenvector centrality reveals the time course of task-specific electrode connectivity in human ECoG," in *2015 7th International IEEE/EMBS Conference on Neural Engineering (NER)* (Montpellier: IEEE), 336–339.

Nicolae, I.-E., Acqualagna, L., and Blankertz, B. (2017). Assessing the depth of cognitive processing as the basis for potential user-state adaptation. *Front. Neurosci.* 11:548. doi: 10.3389/fnins.2017.00548

Nicolas-Alonso, L. F., and Gomez-Gil, J. (2012). Brain computer interfaces, a review. *Sensors* 12, 1211–1279. doi: 10.3390/s120201211

Nicolelis, M. A., and Lebedev, M. A. (2009). Principles of neural ensemble physiology underlying the operation of brain–machine interfaces. *Nat. Rev. Neurosci.* 10:530. doi: 10.1038/nrn2653

Normann, R. A., Greger, B., House, P., Romero, S. F., Pelayo, F., and Fernandez, E. (2009). Toward the development of a cortically based visual neuroprosthesis. *J. Neural Eng.* 6:035001. doi: 10.1088/1741-2560/6/3/035001

Nurse, E. S., Freestone, D. R., Oxley, T. J., Ackland, D. C., Vogrin, S. J., Murphy, M., et al. (2015). "Movement related directional tuning from broadband electrocorticography in humans," in *2015 7th International IEEE/EMBS Conference on Neural Engineering (NER)* (Montpellier: IEEE), 33–36.

Nuyujukian, P., Kao, J. C., Fan, J. M., Stavisky, S. D., Ryu, S. I., and Shenoy, K. V. (2014). Performance sustaining intracortical neural prostheses. *J. Neural Eng.* 11:066003. doi: 10.1088/1741-2560/11/6/066003

Pais-Vieira, M., Lebedev, M., Kunicki, C., Wang, J., and Nicolelis, M. A. (2013). A brain-to-brain interface for real-time sharing of sensorimotor information. *Sci. Rep.* 3:1319. doi: 10.1038/srep01319

Pan, G., Li, J.-J., Qi, Y., Yu, H., Zhu, J.-M., Zheng, X.-X., et al. (2018). Rapid decoding of hand gestures in electrocorticography using recurrent neural networks. *Front. Neurosci.* 12:555. doi: 10.3389/fnins.2018.00555

Pan, J., Li, Y., Gu, Z., and Yu, Z. (2013). A comparison study of two p300 speller paradigms for brain–computer interface. *Cogn. Neurodyn.* 7, 523–529. doi: 10.1007/s11571-013-9253-1

Pascarella, A., Todaro, C., Clerc, M., Serre, T., and Piana, M. (2016). Source modeling of electrocorticography (ECoG) data: stability analysis and spatial filtering. *J. Neurosci. Methods* 263, 134–144. doi: 10.1016/j.jneumeth.2016.02.012

Paul, S., Zabir, I., Sarker, T., Fattah, S. A., and Shahnaz, C. (2017). Higher order statistics of bispectrum and MRP of ECoG signals for motor imagery tasks classification. in *IEEE Region 10 Symposium (TENSYMP), 2017* (Cochin: IEEE), 1–4.

Perge, J. A., Homer, M. L., Malik, W. Q., Cash, S., Eskandar, E., Friehs, G., et al. (2013). Intra-day signal instabilities affect decoding performance in an intracortical neural interface system. *J. Neural Eng.* 10:036004. doi: 10.1088/1741-2560/10/3/036004

Petroff, O. A., Spencer, D. D., Goncharova, I. I., and Zaveri, H. P. (2016). A comparison of the power spectral density of scalp EEG and subjacent electrocorticograms. *Clin. Neurophysiol.* 127, 1108–1112. doi: 10.1016/j.clinph.2015.08.004

Pistohl, T., Ball, T., Schulze-Bonhage, A., Aertsen, A., and Mehring, C. (2008). Prediction of arm movement trajectories from ECoG-recordings in humans. *J. Neurosci. Methods* 167, 105–114. doi: 10.1016/j.jneumeth.2007.10.001

Pistohl, T., Schmidt, T. S., Ball, T., Schulze-Bonhage, A., Aertsen, A., and Mehring, C. (2013). Grasp detection from human ECoG during natural reach-to-grasp movements. *PLoS ONE* 8:e54658. doi: 10.1371/journal.pone.0054658

Pistohl, T., Schulze-Bonhage, A., Aertsen, A., Mehring, C., and Ball, T. (2012). Decoding natural grasp types from human ECoG. *Neuroimage* 59, 248–260. doi: 10.1016/j.neuroimage.2011.06.084

Rao, R. P., Stocco, A., Bryan, M., Sarma, D., Youngquist, T. M., Wu, J., et al. (2014). A direct brain-to-brain interface in humans. *PLoS ONE* 9:e111332. doi: 10.1371/journal.pone.0111332

RaviPrakash, H., Korostenskaja, M., Castillo, E. M., Lee, K. H., Salinas, C. M., Baumgartner, J., et al. (2018). Deep learning provides exceptional accuracy to ECoG-based functional language mapping for epilepsy surgery. *bioRxiv [Preprint]*. doi: 10.1101/497644

Reddy, C. G., Reddy, G. G., Kawasaki, H., Oya, H., Miller, L. E., and Howard, M. A. III. (2009). Decoding movement-related cortical potentials from electrocorticography. *Neurosurg. Focus* 27:E11. doi: 10.3171/2009.4.FOCUS0990

Renard, Y., Lotte, F., Gibert, G., Congedo, M., Maby, E., Delannoy, V., et al. (2010). Openvibe: an open-source software platform to design, test, and use brain–computer interfaces in real and virtual environments. *Presence Teleoper. Virtual Environ.* 19, 35–53. doi: 10.1162/pres.19.1.35

Richards, B. A., Lillicrap, T. P., Beaudoin, P., Bengio, Y., Bogacz, R., Christensen, A., et al. (2019). A deep learning framework for neuroscience. *Nat. Neurosci.* 22, 1761–1770. doi: 10.1038/s41593-019-0520-2

Rickert, J., de Oliveira, S. C., Vaadia, E., Aertsen, A., Rotter, S., and Mehring, C. (2005). Encoding of movement direction in different frequency ranges of motor cortical local field potentials. *J. Neurosci.* 25, 8815–8824. doi: 10.1523/JNEUROSCI.0816-05.2005

Roy, Y., Banville, H., Albuquerque, I., Gramfort, A., Falk, T. H., and Faubert, J. (2019). Deep learning-based electroencephalography analysis: a systematic review. *J. Neural Eng.* 16:051001. doi: 10.1088/1741-2552/ab260c

Ryun, S., Kim, J. S., Lee, S. H., Jeong, S., Kim, S.-P., and Chung, C. K. (2014). Movement type prediction before its onset using signals from prefrontal area: an electrocorticography study. *BioMed Res. Int.* 2014:783203. doi: 10.1155/2014/783203

Salinas, E., and Abbott, L. (1994). Vector reconstruction from firing rates. *J. Comput. Neurosci.* 1, 89–107.

Samiee, S., Hajipour, S., and Shamsollahi, M. B. (2010). "Five-class finger flexion classification using ECoG signals," in *2010 International Conference on Intelligent and Advanced Systems (ICIAS)* (Kuala Lumpur: IEEE), 1–4.

Sanchez, J. C., Gunduz, A., Carney, P. R., and Principe, J. C. (2008). Extraction and localization of mesoscopic motor control signals for human ecog neuroprosthetics. *J. Neurosci. Methods* 167, 63–81. doi: 10.1016/j.jneumeth.2007.04.019

Satow, T., Matsuhashi, M., Ikeda, A., Yamamoto, J., Takayama, M., Begum, T., et al. (2003). Distinct cortical areas for motor preparation and execution in human identified by bereitschaftspotential recording and ECoG-EMG coherence analysis. *Clin. Neurophysiol.* 114, 1259–1264. doi: 10.1016/S1388-2457(03)00091-9

Schaffelhofer, S., Agudelo-Toro, A., and Scherberger, H. (2015). Decoding a wide range of hand configurations from macaque motor, premotor, and parietal cortices. *J. Neurosci.* 35, 1068–1081. doi: 10.1523/JNEUROSCI.3594-14.2015

Schalk, G., Kubánek, J., Miller, K. J., Anderson, N. R., Leuthardt, E. C., Ojemann, J. G., et al. (2007). Decoding two-dimensional movement trajectories using electrocorticographic signals in humans. *J. Neural Eng.* 4:264. doi: 10.1088/1741-2560/4/3/012

Schalk, G., and Leuthardt, E. C. (2011). Brain-computer interfaces using electrocorticographic signals. *IEEE Rev. Biomed. Eng.* 4, 140–154. doi: 10.1109/RBME.2011.2172408

Schalk, G., McFarland, D. J., Hinterberger, T., Birbaumer, N., and Wolpaw, J. R. (2004). Bci2000: a general-purpose brain-computer interface (BCI) system. *IEEE Trans. Biomed. Eng.* 51, 1034–1043. doi: 10.1109/TBME.2004.827072

Schalk, G., Miller, K., Anderson, N., Wilson, J., Smyth, M., Ojemann, J., et al. (2008). Two-dimensional movement control using electrocorticographic signals in humans. *J. Neural Eng.* 5:75. doi: 10.1088/1741-2560/5/1/008

Schirrmeister, R. T., Springenberg, J. T., Fiederer, L. D. J., Glasstetter, M., Eggensperger, K., Tangermann, M., et al. (2017). Deep learning with convolutional neural networks for EEG decoding and visualization. *Hum. Brain Mapp.* 38, 5391–5420. doi: 10.1002/hbm.23730

Shahid, S., and Prasad, G. (2011). Bispectrum-based feature extraction technique for devising a practical brain–computer interface. *J. Neural Eng.* 8:025014. doi: 10.1088/1741-2560/8/2/025014

Shoham, S., Halgren, E., Maynard, E. M., and Normann, R. A. (2001). Motor-cortical activity in tetraplegics. *Nature* 413:793. doi: 10.1038/35101651

Shokoueinejad, M., Park, D.-W., Jung, Y. H., Brodnick, S. K., Novello, J., Dingle, A., et al. (2019). Progress in the field of micro-electrocorticography. *Micromachines* 10:62. doi: 10.3390/mi10010062

Sinkin, M., Osadchiy, A., Lebedev, M., Volkova, K., Kondratova, M., Trifonov, I., et al. (2019). High resolution passive speech mapping in dominant hemisphere glioma surgery. *Russ. J. Neurosurg.* 21, 12–18. doi: 10.17650/1683-3295-2019-21-3-37-43

Slutzky, M. W., Jordan, L. R., Krieg, T., Chen, M., Mogul, D. J., and Miller, L. E. (2010). Optimal spacing of surface electrode arrays for brain–machine interface applications. *J. Neural Eng.* 7:026004. doi: 10.1088/1741-2560/7/2/026004

Smetanin, N., Lebedev, M. A., and Ossadtchi, A. (2018a). Towards zero-latency neurofeedback. *bioRxiv [preprint]*. doi: 10.1101/424846

Smetanin, N., Volkova, K., Zabodaev, S., Lebedev, M., and Ossadtchi, A. (2018b). NFBLab–a versatile software for neurofeedback and brain-computer interface research. *Front. Neuroinform.* 12:100. doi: 10.3389/fninf.2018.00100

Song, W., Ramakrishnan, A., Udoekwere, U. I., and Giszter, S. F. (2009). Multiple types of movement-related information encoded in hindlimb/trunk cortex in rats and potentially available for brain–machine interface controls. *IEEE Trans. Biomed. Eng.* 56, 2712–2716. doi: 10.1109/TBME.2009.2026284

Spüler, M., Grimm, F., Gharabaghi, A., Bogdan, M., and Rosenstiel, W. (2016). "Comparing methods for decoding movement trajectory from ECoG in chronic stroke patients," in *Advances in Neurotechnology, Electronics and Informatics* (Rome: Springer), 125–139.

Spüler, M., Rosenstiel, W., and Bogdan, M. (2014a). "Predicting wrist movement trajectory from ipsilesional ECoG in chronic stroke patients," in *Proceedings of 2nd International Congress on Neurotechnology, Electronics and Informatics (NEUROTECHNIX)* (Rome), 38–45.

Spüler, M., Walter, A., Ramos-Murguialday, A., Naros, G., Birbaumer, N., Gharabaghi, A., et al. (2014b). Decoding of motor intentions from epidural ECoG recordings in severely paralyzed chronic stroke patients. *J. Neural Eng.* 11:066008. doi: 10.1088/1741-2560/11/6/066008

Sturm, I., Blankertz, B., Potes, C., Schalk, G., and Curio, G. (2014). Ecog high gamma activity reveals distinct cortical representations of lyrics passages, harmonic and timbre-related changes in a rock song. *Front. Hum. Neurosci.* 8:798. doi: 10.3389/fnhum.2014.00798

Taplin, A. M., de Pesters, A., Brunner, P., Hermes, D., Dalfino, J. C., Adamo, M. A., et al. (2016). Intraoperative mapping of expressive language cortex using passive real-time electrocorticography. *Epilepsy Behav. Case Rep.* 5, 46–51. doi: 10.1016/j.ebcr.2016.03.003

Taylor, D. M., Tillery, S. I. H., and Schwartz, A. B. (2002). Direct cortical control of 3d neuroprosthetic devices. *Science* 296, 1829–1832. doi: 10.1126/science.1070291

Todaro, C., Marzetti, L., Sosa, P. A. V., Valdés-Hernández, P. A., and Pizzella, V. (2018). Mapping brain activity with electrocorticography: resolution properties and robustness of inverse solutions. *Brain Topogr.* 32, 583–598. doi: 10.1007/s10548-018-0623-1

Toro, C., Cox, C., Friehs, G., Ojakangas, C., Maxwell, R., Gates, J. R., et al. (1994a). 8–12 Hz rhythmic oscillations in human motor cortex during two-dimensional arm movements: evidence for representation of kinematic parameters. *Electroencephalogr. Clin. Neurophysiol.* 93, 390–403.

Toro, C., Deuschl, G., Thatcher, R., Sato, S., Kufta, C., and Hallett, M. (1994b). Event-related desynchronization and movement-related cortical potentials on the ECoG and EEG. *Electroencephalogr. Clin. Neurophysiol.* 93, 380–389.

van Vugt, M. K., Sederberg, P. B., and Kahana, M. J. (2007). Comparison of spectral analysis methods for characterizing brain oscillations. *J. Neurosci. Methods* 162, 49–63. doi: 10.1016/j.jneumeth.2006.12.004

Vansteensel, M. J., Pels, E. G., Bleichner, M. G., Branco, M. P., Denison, T., Freudenburg, Z. V., et al. (2016). Fully implanted brain–computer interface in a locked-in patient with als. *N. Engl. J. Med.* 375, 2060–2066. doi: 10.1056/NEJMoa1608085

Vaskov, A. K., Irwin, Z. T., Nason, S. R., Vu, P. P., Nu, C. S., Bullard, A. J., et al. (2018). Cortical decoding of individual finger group motions using refit kalman filter. *Front. Neurosci.* 12:751. doi: 10.3389/fnins.2018.00751

Velliste, M., Perel, S., Spalding, M. C., Whitford, A. S., and Schwartz, A. B. (2008). Cortical control of a prosthetic arm for self-feeding. *Nature* 453:1098. doi: 10.1038/nature06996

Viventi, J., Kim, D.-H., Vigeland, L., Frechette, E. S., Blanco, J. A., Kim, Y.-S., et al. (2011). Flexible, foldable, actively multiplexed, high-density electrode array for mapping brain activity *in vivo*. *Nat. Neurosci.* 14:1599. doi: 10.1038/nn.2973

Wang, N. X., Farhadi, A., Rao, R. P., and Brunton, B. W. (2018). "Ajile movement prediction: multimodal deep learning for natural human neural recordings and video," in *Thirty-Second AAAI Conference on Artificial Intelligence* (New Orleans, LA).

Wang, P. T., King, C. E., McCrimmon, C. M., Lin, J. J., Sazgar, M., Hsu, F. P., et al. (2016). Comparison of decoding resolution of standard and high-density electrocorticogram electrodes. *J. Neural Eng.* 13:026016. doi: 10.1088/1741-2560/13/2/026016

Wang, P. T., King, C. E., McCrimmon, C. M., Shaw, S. J., Millett, D. E., Liu, C. Y., et al. (2014). Electrocorticogram encoding of upper extremity movement duration. *Conf. Proc. IEEE Eng. Med. Biol. Soc.* 2014, 1243–1246. doi: 10.1109/EMBC.2014.6943822

Wang, W., Collinger, J. L., Degenhart, A. D., Tyler-Kabara, E. C., Schwartz, A. B., Moran, D. W., et al. (2013). An electrocorticographic brain interface in an individual with tetraplegia. *PLoS ONE* 8:e55344. doi: 10.1371/journal.pone.0055344

Wang, W., Degenhart, A. D., Collinger, J. L., Vinjamuri, R., Sudre, G. P., Adelson, P. D., et al. (2009). Human motor cortical activity recorded with micro-ecog electrodes, during individual finger movements. *Conf. Proc. IEEE Eng. Med. Biol. Soc.* 2009, 586–589. doi: 10.1109/IEMBS.2009.5333704

Wang, Z., Gunduz, A., Brunner, P., Ritaccio, A. L., Ji, Q., and Schalk, G. (2012). Decoding onset and direction of movements using electrocorticographic (ECoG) signals in humans. *Front. Neuroeng.* 5:15. doi: 10.3389/fneng.2012.00015

Wang, Z., Ji, Q., Miller, K. J., and Schalk, G. (2011). Prior knowledge improves decoding of finger flexion from electrocorticographic signals. *Front. Neurosci.* 5:127. doi: 10.3389/fnins.2011.00127

Weinand, M. E., Hermann, B., Wyler, A. R., Carter, L. P., Oommen, K., Labiner, D., et al. (1994). Long-term subdural strip electrocorticographic monitoring of ictal déjà vu. *Epilepsia* 35, 1054–1059.

Wessberg, J., Stambaugh, C. R., Kralik, J. D., Beck, P. D., Laubach, M., Chapin, J. K., et al. (2000). Real-time prediction of hand trajectory by ensembles of cortical neurons in primates. *Nature* 408:361. doi: 10.1038/35042582

Wilson, J. A., Walton, L. M., Tyler, M., and Williams, J. (2012). Lingual electrotactile stimulation as an alternative sensory feedback pathway for brain–computer interface applications. *J. Neural Eng.* 9:045007. doi: 10.1088/1741-2560/9/4/045007

Wodlinger, B., Downey, J., Tyler-Kabara, E., Schwartz, A., Boninger, M., and Collinger, J. (2014). Ten-dimensional anthropomorphic arm control in a human brain–machine interface: difficulties, solutions, and limitations. *J. Neural Eng.* 12:016011. doi: 10.1088/1741-2560/12/1/016011

Wu, J., Shuman, B. R., Brunton, B. W., Steele, K. M., Olson, J. D., Rao, R. P., et al. (2016). Multistep model for predicting upper-limb 3d isometric force application from pre-movement electrocorticographic features. *Conf. Proc. IEEE Eng. Med. Biol. Soc.* 2016, 1564–1567. doi: 10.1109/EMBC.2016.7591010

Wyler, A. R., Walker, G., and Somes, G. (1991). The morbidity of long-term seizure monitoring using subdural strip electrodes. *J. Neurosurg.* 74, 734–737.

Xie, T., Zhang, D., Wu, Z., Chen, L., and Zhu, X. (2015). Classifying multiple types of hand motions using electrocorticography during intraoperative awake

craniotomy and seizure monitoring processes—case studies. *Front. Neurosci.* 9:353. doi: 10.3389/fnins.2015.00353

Xie, Z., Schwartz, O., and Prasad, A. (2018). Decoding of finger trajectory from ECoG using deep learning. *J. Neural Eng.* 15:036009. doi: 10.1088/1741-2552/aa9dbe

Yanagisawa, T., Hirata, M., Saitoh, Y., Goto, T., Kishima, H., Fukuma, R., et al. (2011). Real-time control of a prosthetic hand using human electrocorticography signals. *J. Neurosurg.* 114, 1715–1722. doi: 10.3171/2011.1.JNS101421

Yanagisawa, T., Hirata, M., Saitoh, Y., Kato, A., Shibuya, D., Kamitani, Y., et al. (2009). Neural decoding using gyral and intrasulcal electrocorticograms. *Neuroimage* 45, 1099–1106. doi: 10.1016/j.neuroimage.2008.12.069

Yanagisawa, T., Hirata, M., Saitoh, Y., Kishima, H., Matsushita, K., Goto, T., et al. (2012). Electrocorticographic control of a prosthetic arm in paralyzed patients. *Ann. Neurol.* 71, 353–361. doi: 10.1002/ana.22613

Zhang, Y., van Drongelen, W., Kohrman, M., and He, B. (2008). Three-dimensional brain current source reconstruction from intra-cranial ecog recordings. *Neuroimage* 42, 683–695. doi: 10.1016/j.neuroimage.2008.04.263

Zubarev, I., Zetter, R., Halme, H.-L., and Parkkonen, L. (2018). Adaptive neural network classifier for decoding MEG signals. *Neuroimage* 197, 425–434. doi: 10.1016/j.neuroimage.2019.04.068

Conflict of Interest: The authors declare that the research was conducted in the absence of any commercial or financial relationships that could be construed as a potential conflict of interest.

frontiers in Neuroscience

ORIGINAL RESEARCH
published: 13 February 2020
doi: 10.3389/fnins.2020.00035

ECoG Beta Suppression and Modulation During Finger Extension and Flexion

Julian Unterweger[1†], *Martin Seeber*[2], *Stavros Zanos*[3], *Jeffrey G. Ojemann*[4] *and Reinhold Scherer*[5*†]

[1] Institute of Neural Engineering, Graz University of Technology, Graz, Austria, [2] Functional Brain Mapping Laboratory, Department of Fundamental Neurosciences, University of Geneva, Geneva, Switzerland, [3] Translational Neurophysiology Laboratory, Institute of Bioelectronic Medicine, Feinstein Institutes for Medical Research, Manhasset, NY, United States, [4] Department of Neurological Surgery, University of Washington, Seattle, WA, United States, [5] Brain-Computer Interfaces and Neural Engineering Laboratory, School of Computer Science and Electronic Engineering, University of Essex, Colchester, United Kingdom

Neural oscillations originate predominantly from interacting cortical neurons and consequently reflect aspects of cortical information processing. However, their functional role is not yet fully understood and their interpretation is debatable. Amplitude modulations (AMs) in alpha (8–12 Hz), beta (13–30 Hz), and high gamma (70–150 Hz) band in invasive electrocorticogram (ECoG) and non-invasive electroencephalogram (EEG) signals change with behavior. Alpha and beta band AMs are typically suppressed (desynchronized) during motor behavior, while high gamma AMs highly correlate with the behavior. These two phenomena are successfully used for functional brain mapping and brain-computer interface (BCI) applications. Recent research found movement-phase related AMs (MPA) also in high beta/low gamma (24–40 Hz) EEG rhythms. These MPAs were found by separating the suppressed AMs into sustained and dynamic components. Sustained AM components are those with frequencies that are lower than the motor behavior. Dynamic components those with frequencies higher than the behavior. In this paper, we study ECoG beta/low gamma band (12–30 Hz/30–42 Hz) AM during repetitive finger movements addressing the question whether or not MPAs can be found in ECoG beta band. Indeed, MPA in the 12–18 Hz and 18–24 Hz band were found. This additional information may lead to further improvements in ECoG-based prediction and reconstruction of motor behavior by combining high gamma AM and beta band MPA.

Keywords: electrocorticogram, brain-computer interface, beta band, high gamma, movement-phase related amplitude modulation

OPEN ACCESS

Edited by:
Mikhail Sinkin,
Research Institute of Emergency Care, Russia

Reviewed by:
Robert D. Flint,
Northwestern University, United States
Sabato Santaniello,
University of Connecticut, United States

***Correspondence:**
Reinhold Scherer
r.scherer@essex.ac.uk

[†] *These authors have contributed equally to this work*

Specialty section:
This article was submitted to Neuroprosthetics, a section of the journal Frontiers in Neuroscience

Received: *15 June 2019*
Accepted: *13 January 2020*
Published: *13 February 2020*

Citation:
Unterweger J, Seeber M, Zanos S, Ojemann JG and Scherer R (2020) ECoG Beta Suppression and Modulation During Finger Extension and Flexion. Front. Neurosci. 14:35. doi: 10.3389/fnins.2020.00035

1. INTRODUCTION

Functional brain mapping (fBM) and brain-computer interface (BCI) technologies identify behavior—cognitive and motor—by interpretation of brain signal patterns. For example, invasive electrocorticogram (ECoG) high gamma band (70–150 Hz) activity (γ^H) strongly correlates with motor behavior (Crone et al., 1998; Edwards et al., 2005; Miller et al., 2007, 2014; Schalk et al., 2007; Scherer et al., 2009; Martin et al., 2016) and was suggested to contain similar information as firing rates on a intermediate spatial scale (Ray et al., 2008; Manning et al., 2009; Miller et al., 2009b). The single-trial signal-to-noise ratio (SNR) of γ^H is high, which is essential for robust and timely

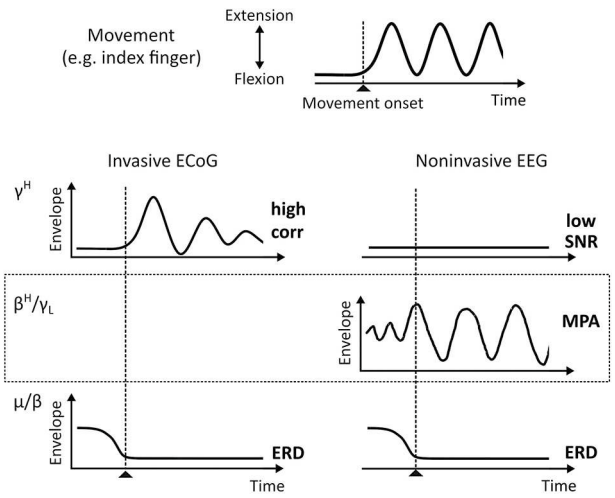

FIGURE 1 | ECoG and EEG envelopes of known oscillatory phenomena during single-trial motor behavior (idealized). The top plot shows a typical times series recorded from data glove sensors during, for example, index finger extension and flexion movements. Below characteristic γ^H (70–150 Hz) and μ/β (8–12 Hz/13–30 Hz) activities for invasive ECoG and noninvasive EEG, respectively, are shown. EEG β_H-γ_L (24–40 Hz) MPA is shown in the dotted box. *corr*, Pearson Correlation Coefficient; ERD, Event-Related Desynchronization; MPA, Movement Phase related Amplitude modulation.

online BCI performance. γ^H can also be found in the noninvasive electroencephalogram (EEG) (Ball et al., 2008; Darvas et al., 2010; Grosse-Wentrup et al., 2011; Seeber et al., 2015); However, the single-trial SNR is low in non-invasive EEG. In contrast, oscillations over sensorimotor areas in the μ (8–12 Hz) and β (13–30 Hz) frequency range are much more pronounced in EEG recordings on a single-trial level. The suppression of theses rhythms—a phenomenon known as event-related desynchronization (ERD) (Pfurtscheller and Da Silva, 1999)—were suggested to represent increased excitability in underlying neural circuitry (Neuper and Pfurtscheller, 2001) or a release of inhibition facilitating movement initiation (Hermes et al., 2012). Sensorimotor μ and β band suppression during motor behavior is also characteristic for ECoG. A simplified, idealized representation of event-related μ, β, and γ^H activity patterns during movement are summarized in **Figure 1**. Since these patterns are well described in the literature, they are commonly used in BCI. Currently a precise reconstruction of the behavior from these macroscopic recordings is, however, only possible to a limited extent. To improve fBM/BCI performance, it is essential to deepen our understanding of signals recorded as local field potentials (LFP), ECoG, and EEG.

Recently, we started to systematically study EEG source dynamics during upright gait (Wagner et al., 2012; Seeber et al., 2014). Results confirmed a sustained μ and β band ERD and γ^H activity during walking when compared to standing. Additionally, we found EEG source amplitudes in the high β-low γ (β^H-γ_L) frequency range (24–40 Hz) that are modulated in relation to the gait cycle (Wagner et al., 2012, 2016; Seeber et al., 2014, 2015). These movement-phase related amplitude modulations (MPA, see **Figure 1**) showed different spectral profiles than classical ERD and event-related synchronization (ERS) phenomena (Pfurtscheller and Da Silva, 1999; Neuper and Pfurtscheller, 2001). We found β^H-γ_L MPA being present during rhythmic finger extension and flexion movements using EEG source reconsturction (Seeber et al., 2016). Because spectral profiles were suggested to be characteristic for specific large-scale networks (Donner and Siegel, 2011; Siegel et al., 2012), we interpreted MPA to represent different frequency-specific networks than classical ERD/ERS (Seeber et al., 2014, 2016). Moreover, following previous literature (Neuper and Pfurtscheller, 2001; Hermes et al., 2012) sustained ERD/ERS phenomena, i.e., different synchrony states in sensorimotor populations, during repetitive movements indicate the contrast between non-movement and active movement states. The functional meaning of MPA is less clear so far. Based on their time-frequency properties and cortical location we suggested that they might reflect processes linked to the prediction and integration of sensorimotor information (Seeber et al., 2016). Yet, more work is needed to falsify or support this viewpoint.

Since μ, β, and γ^H are phenomena found during repetitive finger extension and flexion movements in both ECoG and EEG, in this work, we investigate whether MPA in β_H-γ_L range can also be found in ECoG. This would complement the gap in **Figure 1**. As outlined above, our hypothesis is that β_H-γ_L envelopes, i.e., band-pass filtered power signals tat are commonly used for movement decoding, are composed by superposition of functionally different frequency-specific cortical networks. The first class of networks provides information on the movement state (motor system "active" or "inactive"). These networks contribute elements of sustained amplitude modulation during repetitive movements and are linked to classical ERD/ERS. The second class of networks provide information on functional aspects of the motor behavior (movement phases). These networks contribute elements of dynamic amplitude modulations and are linked to MPAs. Note that interpretation of MPAs is only meaningful when the motor system is "active." To test this perspective, we split up β and γ envelopes in sustained and dynamic components, and compare their correlation with behavior, precisely movement trajectories recorded with a data glove. Sustained and dynamic components can be decomposed by low and high pass filters, respectively. The movement pace defines the filter cut-off frequency. Modulation frequencies close to, but below the movement pace reflect ERD/ERS. Modulation frequencies close to, but above the movement pace might show MPAs.

2. METHODS

2.1. Patients, Data Acquisition, and Experimental Paradigm

The study participants were six neurosurgical patients with intractable epilepsy (Patient ID: BP, CC, MN, OJ, ES, and DJ). They underwent temporary placement of a subdural electrode array (8 × 8 grid, 1 cm horizontal and vertical inter-electrode distance) to localize the epileptic seizure focus and map brain function prior to surgical resection. Electrode placement was

determined by clinical considerations, with the necessity and location of the electrodes determined by the interdisciplinary conference of the Regional Epilepsy Center, Harborview Medical Center, University of Washington. The patients gave informed consent prior to participation in a manner approved by the Human Studies Division (Institutional Review Board) of the University of Washington.

ECoG signals were recorded on a Synamp2 amplifier (Compumedics Neuroscan) at a sampling rate of 2,000 samples per second (1,000 for patients BP and CC) and band-pass filtered between 1 and 500 (200 for patients BP and CC) Hz. The position of each finger was registered through a 5-degrees of freedom data glove device (Fifth Dimension Technologies, Inc.) with a rate of 25 samples per second.

Participants were asked to perform a cue-guided repetitive motion task of individual finger movements. Two-second-long visual cues for thumb, index finger and a pinching motion (involving thumb and index finger movement as well as middle finger, ring finger and pinky) were randomly interleaved and separated by 2-s rest intervals. The cues were delivered visually on a 10 by 10-cm presentation window at a distance of 70 cm from the subject, using the BCI2000 software (Schalk et al., 2004). In total there were 29–31 cue presentations per type of visual cue (except for one subject which was only presented with 23–26 cues per type of visual cue). The results in this paper focus on thumb and index finger movements only.

2.2. Data Analysis

ECoG time series were down-sampled to 1,000 samples per second and visually inspected for the presence of artifacts. Noisy segments and malfunctioning channels were removed. Overall, 92.6% of channels and 91.5% of movement trials were retained for further analysis. The down-sampled ECoG data was band pass filtered between 0.1 and 200 Hz (8*th* order Butterworth IIR filter) and re-referenced with respect to the common average. Data glove recordings were up-sampled by zero-order-hold interpolation to 1000 samples per second. Thumb and index finger movement onset and movement duration were selected by visual inspection.

The β-γ_L frequency range was subdivided into five non-overlapping sub-bands $\beta_1 = 12 - 18\ Hz$, $\beta_2 = 18 - 24\ Hz$, $\beta_3 = 24 - 30\ Hz$, $\gamma_1 = 30 - 36\ Hz$, $\gamma_2 = 36 - 42\ Hz$. The Hilbert transform was applied to the β_i and γ_i band pass filtered re-referenced ECoG signals (6^{th} order Butterworth IIR filter) to compute the time varying analytical amplitude $\hat{A}_j$ ($j = [thumb, index]$), which is a measure of amplitude modulation (AM). Additionally, the analytical amplitude $\hat{A}_j$ in the high $\gamma^H = 70 - 150\ Hz$ frequency band was computed. This resulted in six (frequency band $fb = [\beta_1, \beta_2, \beta_3, \gamma_1, \gamma_2, \gamma^H]$) analytical amplitude $\hat{A}_{j,ch,fb}$ time series per channel $ch = 1, 2, \ldots 64$.

Study participants performed between 1 and 6 finger movement cycles per trial (see **Figure 2A** for finger movement trajectories). This corresponds to movement frequencies from 0.5 to 3 Hz. In order to sufficiently separate sustained (condition SUS) and dynamic (condition DYN) components, a cut-off frequency of 0.4 Hz was selected. Hence, each $\hat{A}_{j,ch,fb}$ was further divided into sustained $\hat{A}^{SUS}_{j,ch,fb}$ and dynamic $\hat{A}^{DYN}_{j,ch,fb}$ AM components by applying a 0.4 *Hz* low pass and high pass filter, respectively. Data glove time series G_j ($j = [thumb, index]$) was also subdivided into sustained G^{SUS}_j ($\leq$ 0.4 Hz) and dynamic G^{DYN}_j ($>$ 0.4 Hz) elements. A 6*th* order Butterworth IIR low (high) pass filter was used. From each of the calculated time series, 4 s segments were extracted from $\left[-1.0 \ \ldots \ 3.0 \right] s$ with respect to movement onset $t = 0$ and concatenated. Further analyses were made with these new time series. **Figure 2B** summarizes the signal processing pipeline.

Pearson correlation coefficients $corr(G^{SUS}_j, \hat{A}^{SUS}_{j,ch,fb})$, and $corr(G^{DYN}_j, \hat{A}^{DYN}_{j,ch,fb})$ were computed for each finger *j*, frequency band *fb* and channel *ch*. As reference, gold standard correlations $corr(G_j, \hat{A}_{j,ch,fb})$ were calculated, without separating sustained and dynamic AM.

The entire correlation-analysis was repeated with $N = 1,000$ random time-domain permutations of common-average re-referenced channel data. The obtained correlation values where then pooled and permutation distribution for the different conditions and frequency bands was evaluated. Permutation distribution showed to be normal for all patients for each frequency band and condition. Nonetheless sub-band standard deviation showed to be higher compared to γ^H and random permutations of $corr(G_j, \hat{A}_{j,ch,fb})$ exhibited the lowest and $corr(G^{SUS}_j, \hat{A}^{SUS}_{j,ch,fb})$ the highest standard deviations over-all. To gain comparability between frequency bands and conditions, Pearson-correlation coefficients were converted into z-scores $z_{j,ch,fb}$, $z^{SUS}_{j,ch,fb}$ and $z^{DYN}_{j,ch,fb}$ by subtracting the mean and dividing by the standard deviation of the underlying pooled permutation distribution. Z-scores give the distance from the mean and are measured in standard deviations. The 2.5% and 97.5% quantile were selected as subject-specific chance level for negative and positive z-scores, respectively, conforming with two times the standard deviation, hence a z-score of approximately two.

Z-scores that exceed chance level show a significant relation between ECoG AM envelopes and finger movement trajectories. We defined these AM envelopes as MPAs. For visual presentation envelopes of the channel with the highest z-score located over movement-related areas were averaged after trial-wise segmentation for each patient and frequency band.

3. RESULTS

ERD/ERS time-frequency maps (Graimann et al., 2002) were computed for each patient to obtain a reference image of β and γ^H activity. ERD/ERS maps are time-frequency plots that display significant ERD and ERS in predefined frequency bands. Topographically arranged, they give a clear overview of the movement-related behavior of the non-phase locked activity over a broad frequency range. **Figure 3A** shows example ERD/ERS maps for patient BP index finger and thumb movement. The maps show widespread β band ERD during finger flexion and extension over sensorimotor areas and more focal high γ activity over cortical index finger and thumb representation areas. This

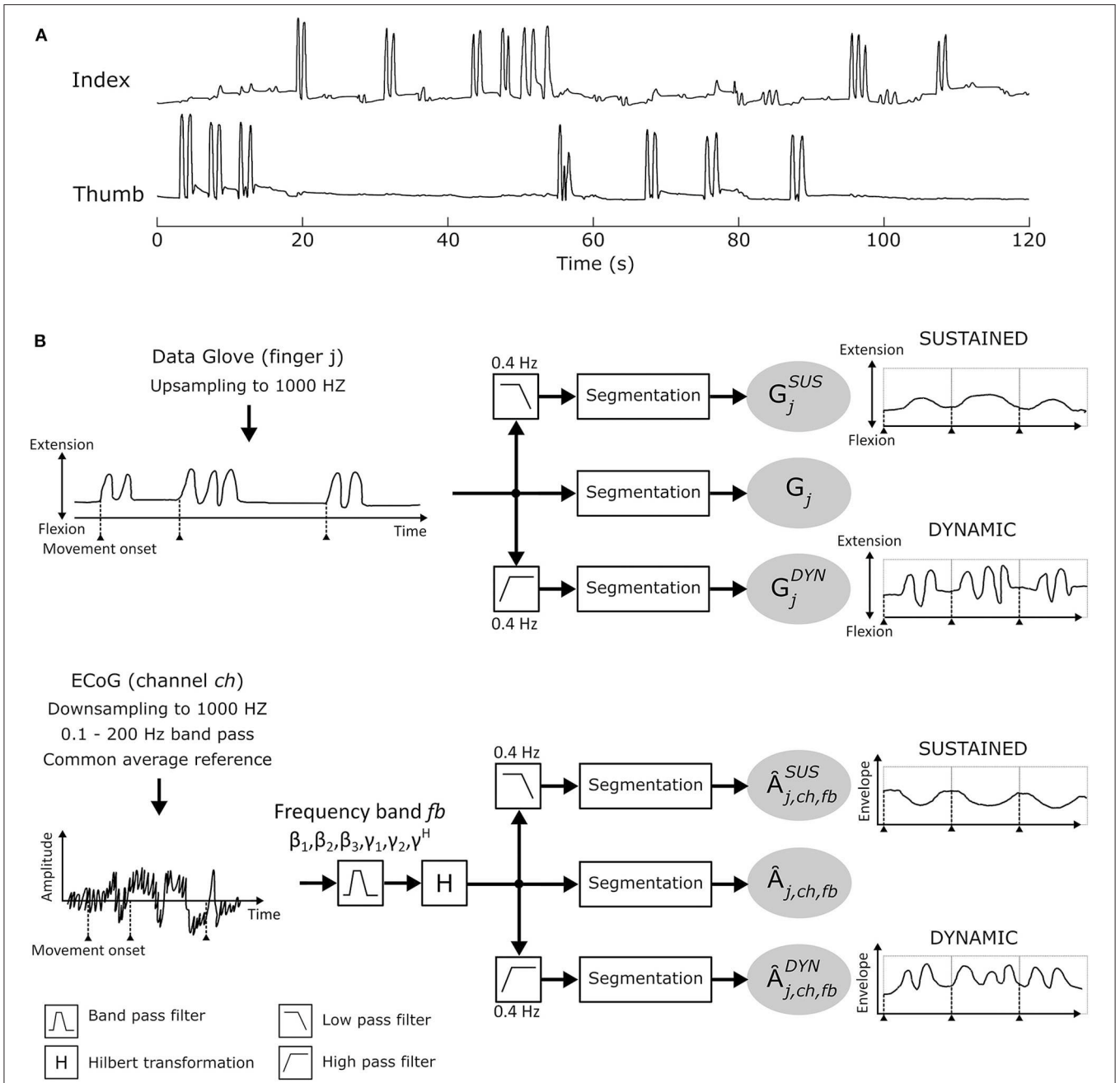

FIGURE 2 | (A) Individual thumb and index finger trajectories recorded with the 5-DOF data-glove for one patient in a time window of 120 s. **(B)** Signal analysis pipeline.

pattern was visible in all patients. For patient ES the pattern was widespread and distributed over the whole grid.

For all patients and conditions significant negative z-scores were calculated for β_1, β_2, β_3, γ_1, and γ_2 sub-bands. High positive z-scores were found in γ^H. $z^{DYN}_{j,ch,fb}$ showed to be much more focal than $z^{SUS}_{j,ch,fb}$ and $z_{j,ch,fb}$; $z^{SUS}_{j,ch,fb}$ values were comparably lower. Overall z-score magnitude decreases and spatial distribution gets more focal with increasing frequency. The spatial distribution of positive and negative z-scores conforms with the spatial location of ERD and ERS activity. **Figure 3B** summarizes these findings in detail for patients BP. For each frequency band and condition z-scores are topographically arranged in form of bubble plots. For the remaining subjects only bubble plots for γ^H and the sub-band with the highest negative z-score over sensorimotor areas are presented (**Figures 4**, **5**). Bubble plots for the remaining frequency bands can be found as **Supplementary Information**.

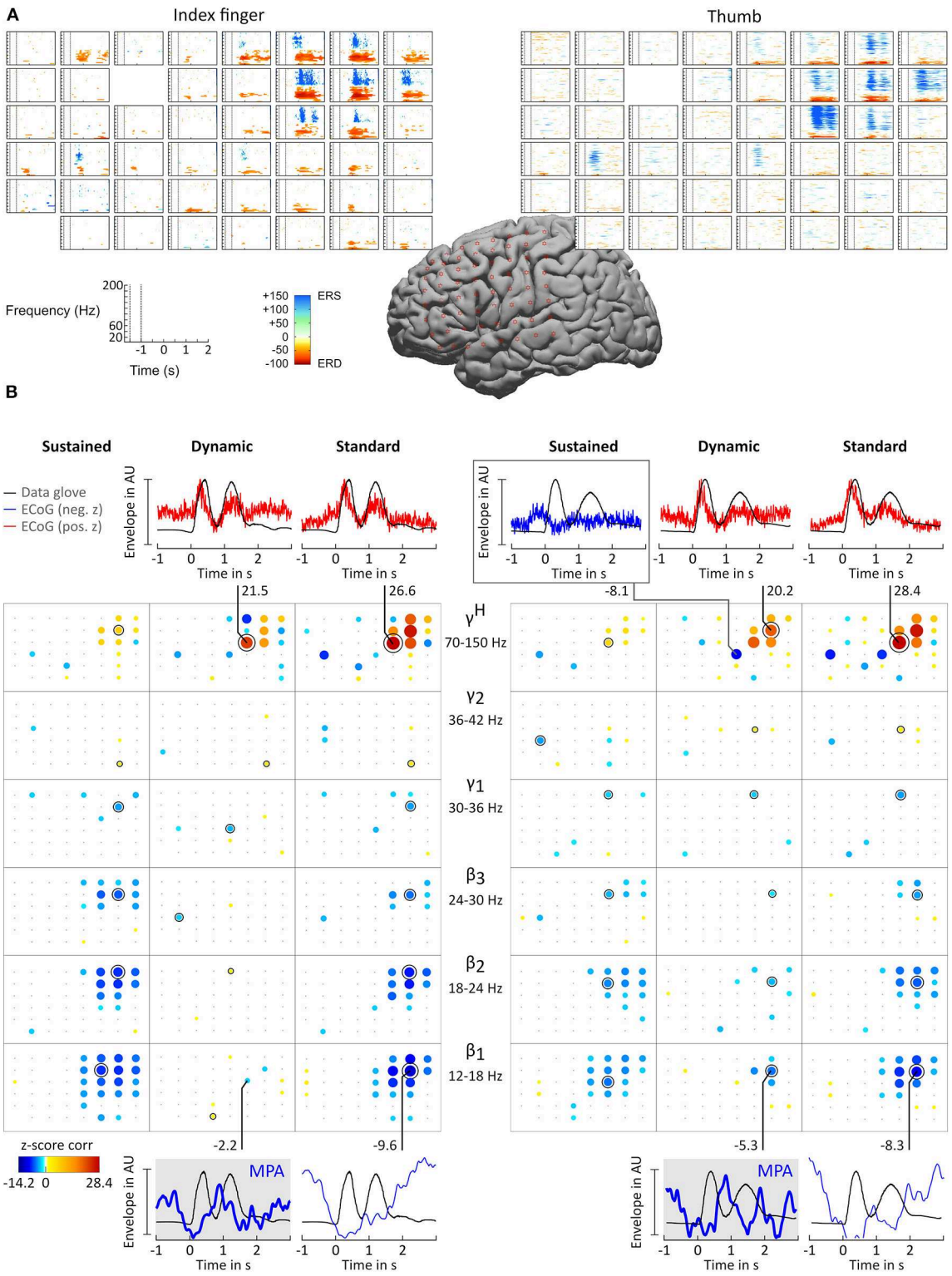

FIGURE 3 | Results for subject BP. **(A)** ERD/ERS time-frequency maps. The plots show, topographically arranged (8 × 8 grid), significant ERD and ERS activity plots for index finger (left) and thumb (right). Electrode locations are marked by star symbol on standard brain. **(B)** Correlation analysis and MPA. Significant z-score transformed Pearson correlation coefficients, computed between corresponding digit trajectory and ECoG envelope components, are displayed for index finger (left) and thumb (right) movements. Z-scores are topographically arranged for each condition (columns, sustained, dynamic, and standard) and frequency band (rows,

(Continued)

FIGURE 3 | $\beta_1 = 12-18$ Hz, $\beta_2 = 18-24$ Hz, $\beta_3 = 24-30$ Hz, $\gamma_1 = 30-36$ Hz, $\gamma_2 = 36-42$ Hz, and $\gamma^H = 70-150$ Hz) independently. Size and color of bubbles correspond to z-score values. A black "x" symbol marks channels with z-scores below chance level. A black annulus marks channels with the highest absolute value for each frequency band. Blank spaces in the 8 × 8 electrode grid mark channels excluded from the analysis. Note that negative correlations were smaller than positive correlations. To enhance readability of the bubble plots negative correlations are doubled in size. For selected sensorimotor channels curves of averaged amplitude envelopes of filtered ECoG and averaged data-glove trajectory for β_1 (bottom) and γ^H (top) frequency bands are plotted. The number next to the line connecting channels and plots are the corresponding z-scores. β_1 MPAs are drawn with thicker lines and highlighted in gray background color.

Averaged amplitude envelope curves for selected channels and the conditions standard and dynamic are shown in **Figures 3B**, **4**, **5**. Channel selection was based on location (only channels located over sensorimotor areas were considered) and maximum absolute z-score magnitude. As reference the averaged original data glove trajectories are visualized. The curves for the standard condition show a sustained decrease during movement. The curves for the dynamic condition show β_1 MPA and β_2 MPA. Corresponding z-score values for $z^{DYN}_{j,ch,fb}$ are summarized in **Table 1**.

4. DISCUSSION

The aim of this study is to investigate whether $\beta^H - \gamma_L$ MPA, previously observed in EEG (Seeber et al., 2016), are similarly present in ECoG recordings during finger extension and flexion. To tackle this question, ECoG activity and data glove trajectories were split into sustained and dynamic components. The latter was expected to show MPA. Correlations between ECoG and corresponding data glove components were computed. In addition to prominent ERD/ERS phenomena, we indeed found significant correlation between the dynamic ECoG and the dynamic glove data component as shown in **Figures 3–5** for index finger and thumb movement, respectively.

ERD/S time-frequency maps (**Figure 3A**) show the well established patterns of β ERD and high γ ERS (Crone et al., 1998; Pfurtscheller et al., 2003; Scherer et al., 2003; Miller et al., 2007). High gamma activity shows movement related modulation patterns in agreement with previous literature (Schalk et al., 2007; Miller et al., 2009a; Scherer et al., 2009; Hermes et al., 2012).

The position of channels showing significant correlation with behavior were determined based on Talairach coordinates and are located over sensorimotor areas. Using the classical approach of using solely band pass filtered envelope ECoG AMs $\hat{A}_{ch,fb}$, represented by our standard condition, results in higher z-scores compared to sustained $\hat{A}^{SUS}_{ch,fb}$ and dynamic $\hat{A}^{DYN}_{ch,fb}$ AMs. For the interpretation of the reported z-scores it is relevant to take into account which component (condition) of the data glove signal is compared to which frequency-specific brain feature. For instance, one can find that the high positive correlation for γ^H standard condition mostly stem from the dynamic movement components. High z-scores in the sub bands standard condition are mainly caused by the rather strong sustained suppression. For the latter high z-scores represent the similarity of the ERD/ERS feature and glove data in general. This distinctions are only possible by decomposing AMs in different components (conditions). There is considerable variability between subjects, but as shown in **Figures 3–5** dynamic condition, not only in γ^H, but also in β range sub-bands are modulated by movement. This is in agreement with findings from EEG studies investigating walking (Wagner et al., 2012) and finger tapping (Seeber et al., 2016).

All z-score normalized correlation values reported above were computed at zero-lag between amplitude envelopes and glove data. The impact of time lags on the robustness of the results was analyzed by computing cross-correlation at varying lags. For sustained and standard condition 0s lag showed to result in the highest z-scores whereas for dynamic condition no clear relation could be obtained for all frequency bands. Thus temporal dynamics were analyzed by averaging with 0 s lag. Because of the variability in task execution (high variability in timing and number of finger movements per trial, as can be seen in **Figure 2A** and in the averaged data glove trajectories $\bar{\hat{G}}_j$ in **Figures 4**, **5** for patients CC and DJ) we shall focus our interpretation of results to the period from 0.5 s before start of movement and during the first finger movement cycle. As excepted γ^H AMs show clear modulation with the movement pace and are thereby highly positively correlated with the finger trajectories. Interestingly for every subject individual electrodes were found with high negative z-values. Corresponding γ^H AM curves peak directly before movement onset and resemble a rather flat line during the rest of the movement period. An example of an averaged amplitude envelope curve illustrating this phenomena for subject BP thumb movement is presented in **Figure 3B**. This activity seems to coincide with movement planning. β_1 AMs in subjects BP, MN and OJ and β_2 AMs in subjects CC and ES anticipate the motor behavior and are negatively correlated to the first cycle of thumb and index finger movement. These results suggest that β rhythms not only show sustained decrease in amplitude, but that they are superimposed with dynamic modulations that are somewhat correlated with behavior and thus indeed show MPA.

Data analyzed in this paper were originally recorded to study temporal dynamics of γ^H activity during movement (Scherer et al., 2010) and not to research MPAs. This results in some limitations. Limitations include the short movement duration ($\sim$ 2 s), the high variability of motor execution and small number of movement cycles per finger movement (1–6 cycles per trial), the small number of movement trials (23–31) and the short inter-cue interval. We expect that longer trials and larger number of rhythmic finger movements per trial would result in visually much clearer and more consistent dynamic modulations. The use of a general cut-off frequency of 0.4 Hz based on movement speed for low- and high-pass filtering with such a high variability in movement-speed holds another

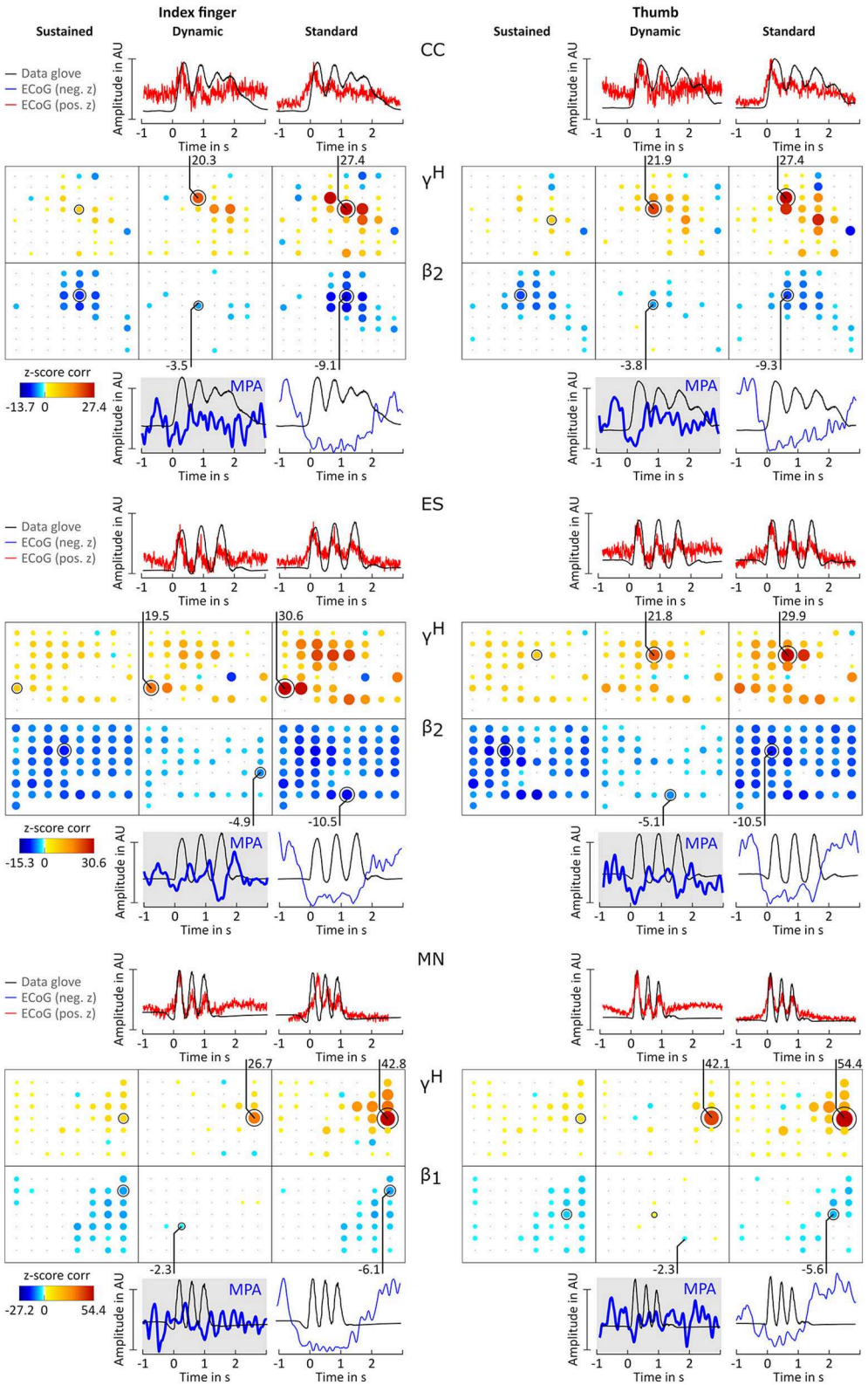

FIGURE 4 | Correlation analysis results and MPA for subjects CC, ES, and MN. Significant z-score transformed Pearson correlation coefficients for each channel, topographically arranged in bubble plots, for index finger (left) and thumb (right) are displayed. For each subject all conditions (columns, sustained, dynamic, and standard) of $\gamma^H = 70 - 150$ *Hz* and the sub-band $\beta_1 = 12 - 18$ Hz or $\beta_2 = 18 - 24$ Hz with the highest significant z-scores are displayed. Bubble size and color is not directly comparable from subject to subject due to different color-bar ranges. For more detailed description see **Figure 3**.

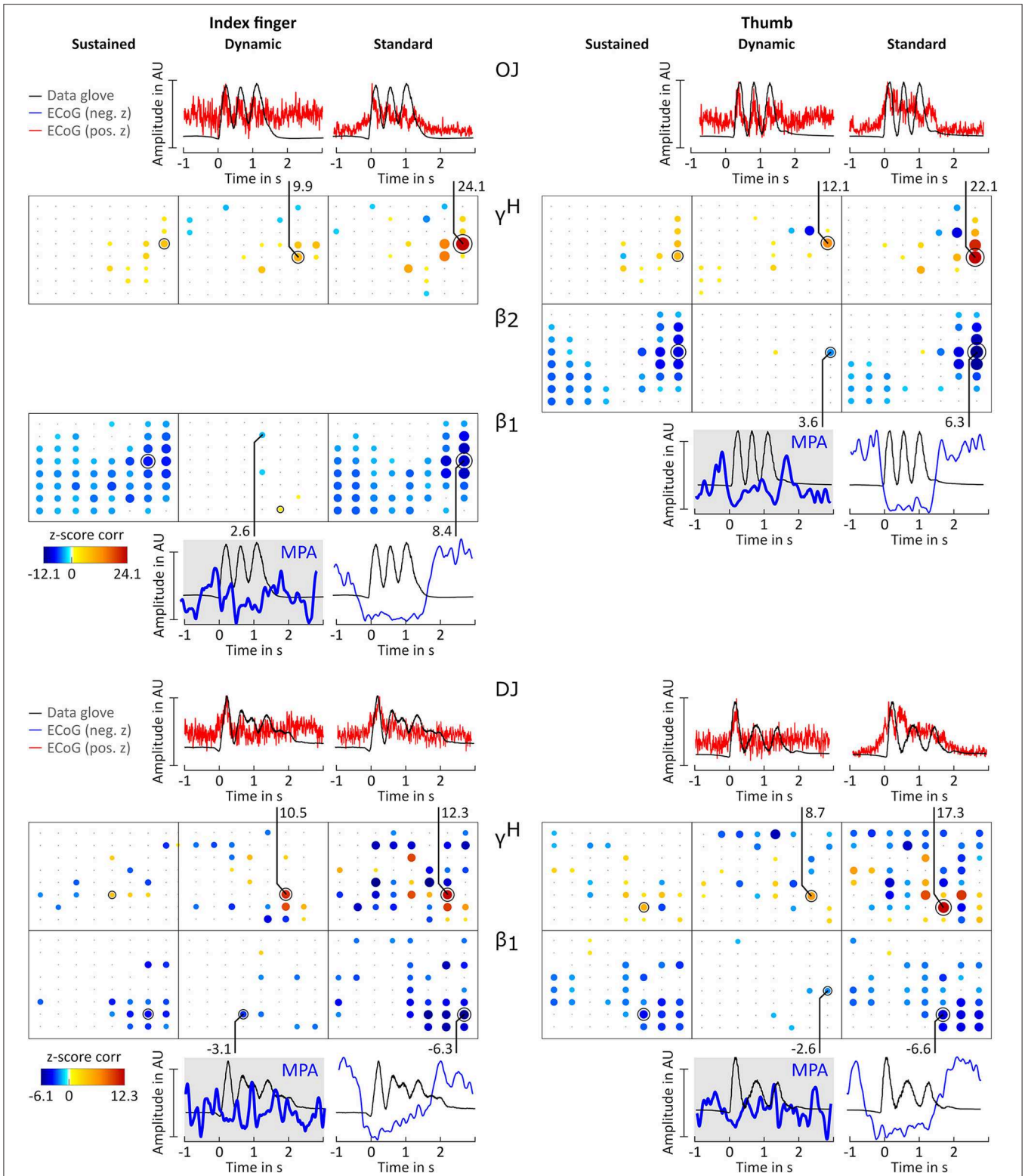

FIGURE 5 | Correlation analysis results and MPA for subjects OJ and DJ. Significant z-score transformed Pearson correlation coefficients for each channel, topographically arranged in bubble plots, for index finger (left) and thumb (right) are displayed. For each subject all conditions (columns, sustained, dynamic, and standard) of $\gamma^H = 70 - 150$ *Hz* and the sub-band $\beta_1 = 12 - 18$ Hz or $\beta_2 = 18 - 24$ Hz with the highest significant z-scores are displayed. Bubble size and color is not directly comparable from subject to subject due to different color-bar ranges. For more detailed description see **Figure 3**.

TABLE 1 | Highest most significant negative z-score for dynamic condition ($z^{DYN}_{j,ch,fb}$) and corresponding frequency band (fb) for each subject and finger movement.

Subject	Index finger	Thumb
	($z^{DYN}_{j,ch,fb}$, fb)	($z^{DYN}_{j,ch,fb}$, fb)
BP	−2.2, β_1	−5.3, β_1
CC	−3.5, β_2	−3.8, β_2
ES	−4.9, β_2	−5.1, β_2
MN	−2.3, β_1	−2.3, β_1
OJ	−2.6, β_1	−3.6, β_2
DJ	−3.1, β_1	−2.6, β_1

limitation and could further be improved by individualized selection of filter stop/pass bands likely resulting in higher correlation values.

Nonetheless we find and report for the first time dynamic β_1 and β_2 modulations that are significantly, but rather loosely, correlated with finger flexion and extension. Yet, their time course and location suggest that they contain information that is different and potentially supplementary to the information that γ^H modulations provide. Additionally to these novel findings in ECoG, we replicated activity patterns in β and γ^H that are in agreement to previous literature (Schalk et al., 2007; Miller et al., 2009a; Scherer et al., 2009; Hermes et al., 2012). The model of interpretation of β activity we suggest in this paper may pave the way to gaining a more comprehensive understanding of brain activity in the context of motor behavior. Sound in-depth knowledge of brain activity will lead to more informative BCI features, which represents one essential component toward the improvement of BCI pattern recognition performance in BCI and fBM applications.

DATA AVAILABILITY STATEMENT

The datasets generated for this study are available on request to the corresponding author.

ETHICS STATEMENT

The studies involving human participants were reviewed and approved by Human Studies Division (Institutional Review Board) of the University of Washington, Seattle, WA, USA. The patients/participants provided their written informed consent to participate in this study.

AUTHOR CONTRIBUTIONS

SZ, JO, and RS designed the research. SZ collected the data. JU, MS, and RS analyzed the data. JU, MS, SZ, JO, and RS wrote the manuscript.

SUPPLEMENTARY MATERIAL

The Supplementary Material for this article can be found online at: https://www.frontiersin.org/articles/10.3389/fnins.2020.00035/full#supplementary-material

REFERENCES

Ball, T., Demandt, E., Mutschler, I., Neitzel, E., Mehring, C., Vogt, K., et al. (2008). Movement related activity in the high gamma range of the human EEG. *Neuroimage* 41, 302–310. doi: 10.1016/j.neuroimage.2008.02.032

Crone, N. E., Miglioretti, D. L., Gordon, B., and Lesser, R. P. (1998). Functional mapping of human sensorimotor cortex with electrocorticographic spectral analysis. II. Event-related synchronization in the gamma band. *Brain* 121, 2301–2315. doi: 10.1093/brain/121.12.2301

Darvas, F., Scherer, R., Ojemann, J. G., Rao, R. P., Miller, K. J., and Sorensen, L. B. (2010). High gamma mapping using EEG. *Neuroimage* 49, 930–938. doi: 10.1016/j.neuroimage.2009.08.041

Donner, T. H., and Siegel, M. (2011). A framework for local cortical oscillation patterns. *Trends Cogn. Sci.* 15, 191–199. doi: 10.1016/j.tics.2011.03.007

Edwards, E., Soltani, M., Deouell, L. Y., Berger, M. S., and Knight, R. T. (2005). High gamma activity in response to deviant auditory stimuli recorded directly from human cortex. *J. Neurophysiol.* 94, 4269–4280. doi: 10.1152/jn.00324.2005

Graimann, B., Huggins, J. E., Levine, S. P., and Pfurtscheller, G. (2002). Visualization of significant ERD/ERS patterns in multichannel EEG and ecog data. *Clin. Neurophysiol.* 113, 43–47. doi: 10.1016/s1388-2457(01)00697-6

Grosse-Wentrup, M., Schölkopf, B., and Hill, J. (2011). Causal influence of gamma oscillations on the sensorimotor rhythm. *NeuroImage* 56, 837–842. doi: 10.1016/j.neuroimage.2010.04.265

Hermes, D., Siero, J. C., Aarnoutse, E. J., Leijten, F. S., Petridou, N., and Ramsey, N. F. (2012). Dissociation between neuronal activity in sensorimotor cortex and hand movement revealed as a function of movement rate. *J. Neurosci.* 32, 9736–9744. doi: 10.1523/JNEUROSCI.0357-12.2012

Manning, J. R., Jacobs, J., Fried, I., and Kahana, M. J. (2009). Broadband shifts in local field potential power spectra are correlated with single-neuron spiking in humans. *J. Neurosci.* 29, 13613–13620. doi: 10.1523/JNEUROSCI.2041-09.2009

Martin, S., Brunner, P., Iturrate, I., Millán Jdel, R., Schalk, G., Knight, R. T., et al. (2016). Word pair classification during imagined speech using direct brain recordings. *Sci. Rep.* 6:25803. doi: 10.1038/srep25803

Miller, K. J., Honey, C. J., Hermes, D., Rao, R. P., denNijs, M., and Ojemann, J. G. (2014). Broadband changes in the cortical surface potential track activation of functionally diverse neuronal populations. *Neuroimage* 85, 711–720. doi: 10.1016/j.neuroimage.2013.08.070

Miller, K. J., Leuthardt, E. C., Schalk, G., Rao, R. P., Anderson, N. R., Moran, D. W., et al. (2007). Spectral changes in cortical surface potentials during motor movement. *J. Neurosci.* 27, 2424–2432. doi: 10.1523/JNEUROSCI.3886-06.2007

Miller, K. J., Sorensen, L. B., Ojemann, J. G., and Den Nijs, M. (2009b). Power-law scaling in the brain surface electric potential. *PLoS Comput. Biol.* 5:e1000609. doi: 10.1371/journal.pcbi.1000609

Miller, K. J., Zanos, S., Fetz, E., Den Nijs, M., and Ojemann, J. G. (2009a). Decoupling the cortical power spectrum reveals real-time representation of individual finger movements in humans. *J. Neurosci.* 29, 3132–3137. doi: 10.1523/JNEUROSCI.5506-08.2009

Neuper, C., and Pfurtscheller, G. (2001). Event-related dynamics of cortical rhythms: frequency-specific features and functional correlates. *Int. J. Psychophysiol.* 43, 41–58. doi: 10.1016/s0167-8760(01)00178-7

Pfurtscheller, G., Graimann, B., Huggins, J. E., Levine, S. P., and Schuh, L. A. (2003). Spatiotemporal patterns of beta desynchronization and gamma synchronization in corticographic data during self-paced movement. *Clin. Neurophysiol.* 114, 1226–1236. doi: 10.1016/s1388-2457(03)00067-1

Pfurtscheller, G., and Lopes da Silva, F. H. (1999). Event-related EEG/MEG synchronization and desynchronization: basic principles. *Clin. Neurophysiol.* 110, 1842–1857. doi: 10.1016/s1388-2457(99)00141-8

Ray, S., Crone, N. E., Niebur, E., Franaszczuk, P. J., and Hsiao, S. S. (2008). Neural correlates of high-gamma oscillations (60–200 hz) in macaque local field

potentials and their potential implications in electrocorticography. *J. Neurosci.* 28, 11526–11536. doi: 10.1523/JNEUROSCI.2848-08.2008

Schalk, G., Kubánek, J., Miller, K. J., Anderson, N. R., Leuthardt, E. C., Ojemann, J. G., et al. (2007). Decoding two-dimensional movement trajectories using electrocorticographic signals in humans. *J. Neural Eng.* 4:264. doi: 10.1088/1741-2560/4/3/012

Schalk, G., McFarland, D. J., Hinterberger, T., Birbaumer, N., and Wolpaw, J. R. (2004). Bci2000: a general-purpose brain-computer interface (BCI) system. *IEEE Trans. Biomed. Eng.* 51, 1034–1043. doi: 10.1109/TBME.2004.827072

Scherer, R., Darvas, F., Zanos, S., Miller, K., Sorensen, L., Hebb, A., et al. (2010). "Temporal dynamics of high-frequency (>75 hz) power increase in electrocorticographic brain signals during cue-guided movement of individual digits. Program No. 383.7/ZZ7," in *2010 Neuroscience Meeting Planner*. San Diego, CA: Society for Neuroscience, 2010. Available online at: https://www.abstractsonline.com/Plan/ViewAbstract.aspx?mID=2554&sKey=1e679379-6353-4016-a610-f89d5404d16e&cKey=2e4e24de-e0d3-4025-bf1a-0c4fe2e5100c&mKey=e5d5c83f-ce2d-4d71-9dd6-fc7231e090fb

Scherer, R., Graimann, B., Huggins, J. E., Levine, S. P., and Pfurtscheller, G. (2003). Frequency component selection for an ECoG-based brain-computer interface. *Biomedizinische Technik. Biomed. Eng.* 48, 31–36. doi: 10.1515/bmte.2003.48.1-2.31

Scherer, R., Zanos, S. P., Miller, K. J., Rao, R. P., and Ojemann, J. G. (2009). Classification of contralateral and ipsilateral finger movements for electrocorticographic brain-computer interfaces. *Neurosurg. Focus* 27:E12. doi: 10.3171/2009.4.FOCUS0981

Seeber, M., Scherer, R., and Müller-Putz, G. R. (2016). EEG oscillations are modulated in different behavior-related networks during rhythmic finger movements. *J. Neurosci.* 36, 11671–11681. doi: 10.1523/JNEUROSCI.1739-16.2016

Seeber, M., Scherer, R., Wagner, J., Solis-Escalante, T., and Müller-Putz, G. R. (2014). EEG beta suppression and low gamma modulation are different elements of human upright walking. *Front. Hum. Neurosci.* 8:485. doi: 10.3389/fnhum.2014.00485

Seeber, M., Scherer, R., Wagner, J., Solis-Escalante, T., and Müller-Putz, G. R. (2015). High and low gamma EEG oscillations in central sensorimotor areas are conversely modulated during the human gait cycle. *Neuroimage* 112, 318–326. doi: 10.1016/j.neuroimage.2015.03.045

Siegel, M., Donner, T. H., and Engel, A. K. (2012). Spectral fingerprints of large-scale neuronal interactions. *Nat. Rev. Neurosci.* 13:121. doi: 10.1038/nrn3137

Wagner, J., Makeig, S., Gola, M., Neuper, C., and Müller-Putz, G. (2016). Distinct β band oscillatory networks subserving motor and cognitive control during gait adaptation. *J. Neurosci.* 36, 2212–2226. doi: 10.1523/JNEUROSCI.3543-15.2016

Wagner, J., Solis-Escalante, T., Grieshofer, P., Neuper, C., Müller-Putz, G., and Scherer, R. (2012). Level of participation in robotic-assisted treadmill walking modulates midline sensorimotor EEG rhythms in able-bodied subjects. *Neuroimage* 63, 1203–1211. doi: 10.1016/j.neuroimage.2012.08.019

Conflict of Interest: The authors declare that the research was conducted in the absence of any commercial or financial relationships that could be construed as a potential conflict of interest.

frontiers in Neuroscience

MINI REVIEW
published: 27 February 2020
doi: 10.3389/fnins.2020.00123

The Potential of Stereotactic-EEG for Brain-Computer Interfaces: Current Progress and Future Directions

Christian Herff[1]*, *Dean J. Krusienski*[2] and *Pieter Kubben*[3]

[1] Department of Neurosurgery, School of Mental Health and Neurosciences, Maastricht University, Maastricht, Netherlands,
[2] ASPEN Lab, Biomedical Engineering Department, Virginia Commonwealth University, Richmond, VA, United States,
[3] Department of Neurosurgery, Maastricht University Medical Center, Maastricht, Netherlands

Stereotactic electroencephalography (sEEG) utilizes localized, penetrating depth electrodes to measure electrophysiological brain activity. It is most commonly used in the identification of epileptogenic zones in cases of refractory epilepsy. The implanted electrodes generally provide a sparse sampling of a unique set of brain regions including deeper brain structures such as hippocampus, amygdala and insula that cannot be captured by superficial measurement modalities such as electrocorticography (ECoG). Despite the overlapping clinical application and recent progress in decoding of ECoG for Brain-Computer Interfaces (BCIs), sEEG has thus far received comparatively little attention for BCI decoding. Additionally, the success of the related deep-brain stimulation (DBS) implants bodes well for the potential for chronic sEEG applications. This article provides an overview of sEEG technology, BCI-related research, and prospective future directions of sEEG for long-term BCI applications.

Keywords: electrocorticography, ECoG, brain-computer interface, BCI, stereotactic EEG, depth electrodes, intracranial, iEEG

OPEN ACCESS

Edited by:
Alessandro Vato,
Italian Institute of Technology (IIT), Italy

Reviewed by:
Disha Gupta,
Langone Medical Center, New York University, United States
Juan Álvaro Gallego,
Northwestern University, United States

***Correspondence:**
Christian Herff
c.herff@maastrichtuniversity.nl

Specialty section:
This article was submitted to Neuroprosthetics, a section of the journal Frontiers in Neuroscience

Received: *05 July 2019*
Accepted: *30 January 2020*
Published: *27 February 2020*

Citation:
Herff C, Krusienski DJ and Kubben P (2020) The Potential of Stereotactic-EEG for Brain-Computer Interfaces: Current Progress and Future Directions. Front. Neurosci. 14:123. doi: 10.3389/fnins.2020.00123

1. INTRODUCTION

Brain-Computer Interfaces (BCIs, Wolpaw et al., 2002) have rapidly advanced in recent years, employing a wide variety of communication and control paradigms (Huggins et al., 2017). Notably, BCIs based on electrocorticography (ECoG, Schalk and Leuthardt, 2011) have demonstrated reliable decoding of a number of cortical processes. Compared to surface electroencephalography (EEG), the superior decoding results of ECoG can be attributed to its millimeter-spatial and millisecond-temporal resolution (Parvizi and Kastner, 2018). Furthermore, ECoG is unaffected by movement artifacts and allows for the measurement of higher-frequency activity, such as the high gamma-band (>70 Hz), as it is unfiltered by dura, skull and scalp tissues. The high-gamma band might correlate with ensemble spiking (Ray et al., 2008) and contain very localized information for a variety of motor (Miller et al., 2007) (including smiling Kern et al., 2019) and speech tasks (Crone et al., 2001; Leuthardt et al., 2012).

ECoG is routinely utilized for monitoring of medication-resistant epilepsy in which the electrodes are implanted for the localization of the seizure origin. The procedure involves a craniotomy to place strips or grids of electrodes directly on the cortex. The electrodes generally remain implanted for a period of one to two weeks during which the brain signals are recorded and monitored to localize the seizure origin. The ECoG electrodes are also used for functional mapping of the eloquent cortex via electrical cortical stimulation (Arya et al., 2018). In addition

to epilepsy procedures, ECoG can also be collected intraoperatively during awake craniotomies for brain tumor resection surgeries.

Patients undergoing these procedures are recruited to voluntarily participate in neuroscientific research and, more recently, BCI research. These investigations have allowed for tremendous advances both in the understanding of cortical processes as well as BCI technology. However, as ECoG electrodes are typically placed over specific, localized regions of the cortex based on the clinical needs of the patients, broad coverage is generally not achieved. Furthermore, ECoG only provides access to the cortical surface and not key deeper structures such as the hippocampus, insula, Herschl's gyrus and basal ganglia.

Another method for intracranial seizure localization employs penetrating depth electrodes that are implanted through small burr holes in the skull. These electrodes are positioned using stereotactic guidance, thus the modality is referred to as stereotactic EEG (sEEG). sEEG allows for the measurement of neural activity in deeper structures of the brain. The cortical sampling of sEEG is generally much sparser than ECoG, leading to regular combined implantation of sEEG and ECoG in the same patient. However, it is believed that sEEG alone leads to fewer surgical complications than the craniotomies required for ECoG (Iida and Otsubo, 2017). As in ECoG, the usage in epilepsy monitoring opens a window to conduct neuroscientific or BCI research with these intracranial recordings without putting any additional burden on the patient. In fact, many patients welcome participation in the experiments as a diversion from the tedium of waiting in the hospital room for the occurrence of a spontaneous seizure. While sEEG is being increasingly utilized for neuroscientific research, it has received relatively little attention for BCI research. This article provides an overview of sEEG technology, BCI-related research, and prospective future directions of sEEG for long-term BCI applications.

2. STEREOTACTIC EEG

The implantation of depth electrodes guided by a stereotactic frame is called stereotactic/stereo electroencephalography (sEEG) and was first developed by Talairach and Bancaud in Paris in the late 1950s (Bancaud, 1959; Talairach and Bancaud, 1966). The procedure has become a common practice to identify epileptogenic zones in refactory elipepsy (Chassoux et al., 2018). After the patient has been identified as a candidate for invasive recordings, the epileptologist and neurosurgeon plan the trajectory of typically 5–15 cylindrical sEEG electrode shafts containing 8–18 contacts, each. Typical contacts are made from platinum/iridium, have a length of roughly 2 mm, a diameter of 1 mm and a resulting total surface area of 10 mm^2 (suppliers include e.g., Dixi Medical, Beçanson, France and Ad-tech Medical, Oak Creek, U.S.A.). The typical inter-electrode distance is roughly 1.5–3.5 mm (van der Loo et al., 2017), which generally provides localized sampling of sparse brain regions. This can result in a total of hundreds of distinct recording sites across the brain, allowing for simultaneous recording within and across various brain structures. Less sEEG electrodes are usually implanted when sEEG is used in combination with ECoG. **Figure 1** shows an example of the implantation of 8 sEEG electrode shafts.

sEEG electrodes are generally preferred over ECoG grids when the lateralization of the seizures is unknown or is expected to be in deeper brain structures, such as insula or hippocampus (Parvizi and Kastner, 2018). This preference results in regular targeting of limbic structures including the medial temporal, orbitofrontal, cingulate, and insular regions. As the electrode positioning along the trajectory spans from the skull to these deeper areas, cortical regions can also be captured. This sampling of very different areas along one electrode shaft results in special requirements for electrode referencing (Li et al., 2018). **Figure 1** shows an example of a typical sEEG implantation. Red electrodes are planned (**Figure 1A**) to target the hippocampus and a heterotopia in the right hemisphere. Other trajectories are mainly targeting a heterotopia. Electrodes positioned along the trajectory of the planned surgical target (**Figure 1B**) can also capture other brain regions which can be effective for BCI applications. For example, the blue electrode trajectory is proximal to the primary motor cortex. Such coverage highlights one of the major differences between sEEG and ECoG. While ECoG provides higher density coverage over a limited cortical region (typically unilateral), sEEG provides sparser coverage spanning more, bilateral brain regions including deeper structures. As with ECoG, because the targeted areas for the electrode implants are solely determined based on clinical needs, BCI investigations in sEEG must be designed to accommodate the patient-specific montages.

Because the clinical intent is to capture epileptic activity, sampling rates between 1 and 3 kHz are commonly used, giving a temporal resolution in the sub-millisecond range. In addition to the standard frequency ranges investigated in surface EEG, namely delta (1–3 Hz), theta (4–7 Hz), alpha (8–12 Hz), beta (13–20 Hz), and gamma (21–50 Hz), sEEG allows the measurement of the high gamma band ($>$ 70 Hz), which is highly attenuated by skull and scalp in surface EEG recordings. The high-gamma band activity has been shown to be highly correlated with task-related signals (Miller et al., 2007) and ensemble spiking of cells in the close proximity of the electrode contact (Ray et al., 2008). The high-gamma band is also known to be strongly correlated to the BOLD signal (Logothetis et al., 2001; Mukamel et al., 2005). In addition to the access to the high-gamma band, sEEG also provides higher signal amplitude (about ten times higher) and a resulting increase in Signal-Noise-Ratio up to 100 times higher (Ball et al., 2009) compared to scalp EEG. Additionally, sEEG provides very localized information, with superior spatial resolution compared to surface EEG (Parvizi and Kastner, 2018). Estimates place the number of cells measurable by an individual contact at ~500,000 (Miller et al., 2009). Artifacts such as electrocardiogram, movement artifacts and skin potentials are also significantly attenuated or even absent in sEEG recordings. While surface EEG recordings can degrade over time and show large inter-session variability due to impedance issues, intracranial recordings appear to be much more stable over extended periods of time (Chao et al., 2010).

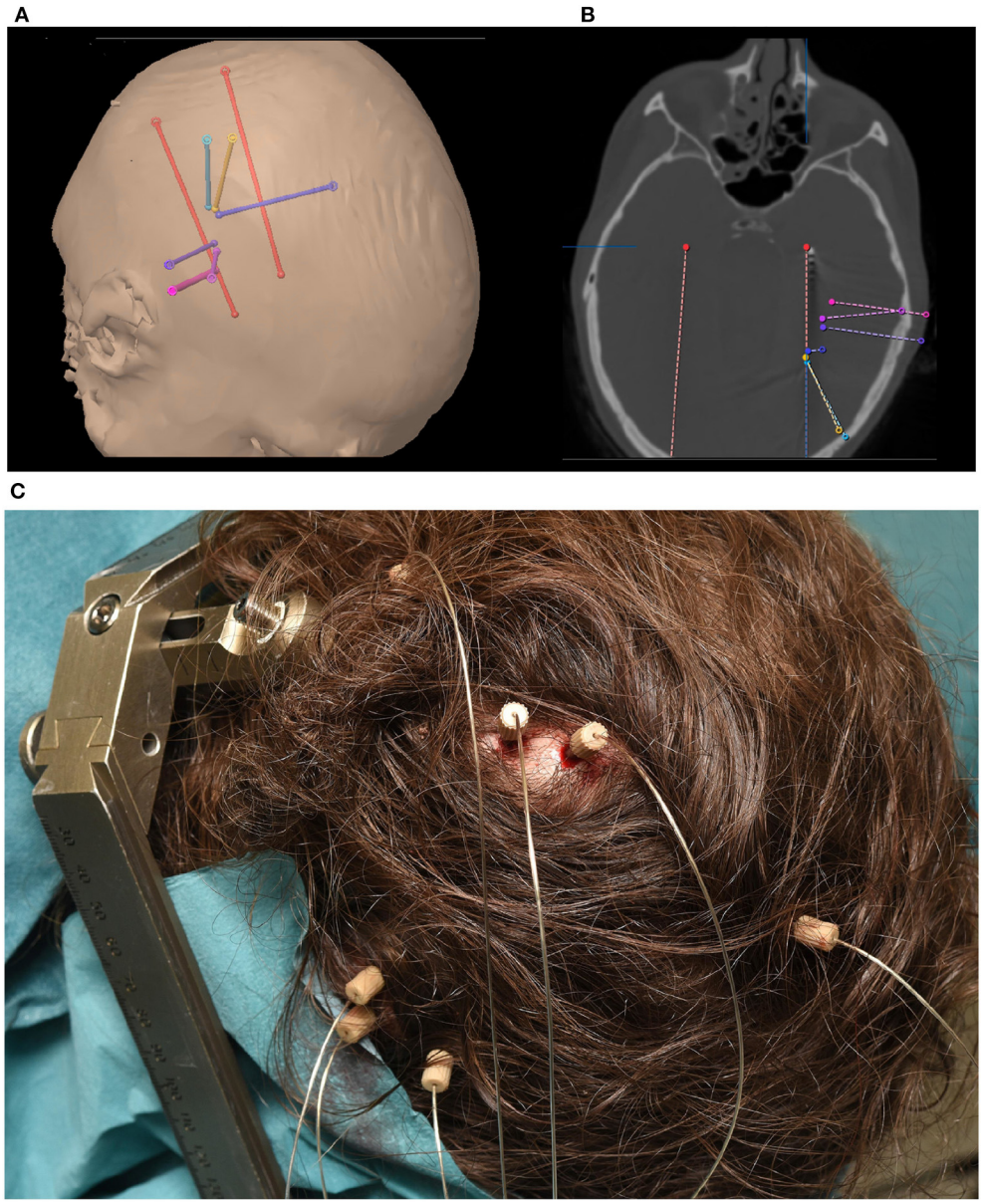

FIGURE 1 | (A) Trajectory planning for 8 sEEG electrode shafts. **(B)** Computer Tomography showing implanted electrode shaft locations. **(C)** Implanted electrode shafts. sEEG requires only small, localized burr holes compared to the comparatively large craniotomies required for ECoG implants.

These advantages of sEEG combined with the relative low risk profile (Cardinale et al., 2012; Hader et al., 2013; Mullin et al., 2016) associated with the small burr holes (diameter of 1.2 mm) as opposed to the full craniotomy necessary for ECoG, make sEEG a desirable modality for electrophysiological investigations. The leads employed in sEEG and the associated surgery are akin to those used for Deep Brain Stimulation (DBS) procedures, which is widely-used as a treatment for tremors, dystonia and Parkinson's Disease, with more recent application to obsessive-compulsive disorder (Greenberg et al., 2006), Tourette's syndrome (Martinez-Ramirez et al., 2018), and epilepsy (Pycroft et al., 2018). While DBS electrodes are primarily used for electric stimulation of the brain, the demonstrated long-term efficacy of chronic DBS electrodes suggests the possibility of chronic sEEG for BCI applications.

3. DECODING SEEG SIGNALS FOR BCI

Significant BCI advances have been achieved with other intracranial (Schalk and Leuthardt, 2011) and intracortical (Bensmaia and Miller, 2014) recording modalities. Penetrating microarrays implanted on the cortex have achieved robust control of commercial tablets (Nuyujukian et al., 2018), robotic

arms (Hochberg et al., 2006, 2012) and even allowed paralyzed patients to regain control of their own arms using functional electric stimulation (Ajiboye et al., 2017). ECoG arrays implanted over the cortex have achieved remarkable results in a wide variety of BCI tasks. See Schalk and Leuthardt (2011) for a review. While it is unlikely that the standard sparse sEEG implants will exhibit superior decoding performance to microarrays and ECoG for the aforementioned applications, sEEG recordings can be used in isolation or to uniquely complement these cortical recording modalities to access information from multiple sub-cortical regions. Specific regions of interest for BCI that cannot be accessed with other modalities are the limbic system and insula for memory, emotion, place cells, etc. and deeper brain regions such as the basal ganglia and subthalamic nucleus that might help to further define motor decoding. sEEG also has the unique potential to simultaneously target multiple brain networks, bilaterally. Initial investigations in the decoding of mental processes highlight the potential for targeting unique, bilateral combinations of cortical and deeper brain structures. In the following sections, we will highlight decoding results achieved with sEEG.

3.1. Motor BCI

A number of studies have demonstrated decoding of motor signals for BCI using sEEG. Vadera et al. (2013) demonstrate two-dimensional cursor control from depth electrodes implanted in hand and foot cortical areas. While imagined movements were not investigated, this study highlights one of the advantages of sEEG - the opportunity to record foot cortical areas that reside in the longitudinal fissure that cannot be attained with surface measurements.

Another study (Li et al., 2017b) investigates the control of a prosthetic hand using sEEG electrodes in the central sulcus. The investigators were able to decode three different hand gestures and a resting state with good accuracies. Another robotic upper limb prosthetic employed a hybrid BCI using ECoG and sEEG, eye tracking and computer vision in two patients (McMullen et al., 2014). Two recent studies investigated the decoding of grip strength for potential use in hand prosthesis. In Murphy et al. (2016), the investigators decoded the grip strength of imagined and executed grip movements from subsurface sEEG electrodes in the central sulcus and the insular cortex and conclude that "depth electrodes could be useful tools for investigating the functions of deeper brain structures as well as showing that central sulcus and insular cortex may contain neural signals that could be used for control of a grasp force BMI." Fischer et al. (2017) also showed that beta and gamma activity in the STN is modulated depending on the level of imagined grip force. Their study is based on electrodes implanted for DBS in the treatment of Parkinson's disease.

3.2. Visual Speller BCI

Studies have successfully decoded different visual-evoked potentials from sEEG recordings. In Krusienski and Shih (2011) depth electrodes in and adjacent to the hippocampus were used to successfully operate a visual speller using the P300 response. With decoding accuracies at or near 100% using less than 15 visual stimulations, achieved results were similar to those achieved with ECoG (Krusienski and Shih, 2011). This performance can be attributed to the existence of the P300 in the hippocampus (McCarthy et al., 1989) and that several of the posterior electrodes were bordering the occipital lobe. Additionally, the same group showed that similar performance could also be achieved using electrodes that were located in the lateral ventricle (Shih and Krusienski, 2012). By employing a motion-onset VEP (Kuba et al., 2007) and sEEG electrodes in middle temporal regions, Li et al. (2017a) showed that up to 14 characters per minute could be typed.

3.3. Speech BCI

Another type of BCI that has rapidly developed are interfaces that aim to restore the ability to speak (Herff and Schultz, 2016; Schultz et al., 2017). Studies have shown that it is possible to decode ECoG activity into text (Herff et al., 2015; Moses et al., 2016, 2019) and speech output (Herff et al., 2016; Angrick et al., 2019; Anumanchipalli et al., 2019). Using depth electrodes, Chrabaszcz et al. (2019) showed that STN is also active during speech production. Two recent advances showed that decoding of speech perception from depth electrodes is also possible. In Akbari et al. (2019) perceived speech was decoded from sEEG electrodes in auditory cortex into an audible waveform. In this approach, sEEG electrodes even yielded slightly better results than ECoG recordings. In Han et al. (2019), the authors decoded the attended speaker for intelligent hearing aids. In this study, one participant was implanted with bilateral temporal depth electrodes covering left and right auditory cortex. The goal of this line of research it to be able to increase intelligibility of attended speaker for smart hearing aids.

3.4. Navigational BCI

The discovery of place and grid cells in the hippocampus (Maguire et al., 1998; Moser et al., 2008) has greatly advanced our understanding of human spatial navigation. As sEEG electrodes can sample from the hippocampus and epilepsy monitoring often requires electrodes in the hippocampus, an unparalleled opportunity to decode navigational parameters from sEEG activity arises. Several different aspects of navigation have been decoded from sEEG electrodes in the hippocampus. Aghajan et al. (2017) used neural networks to decode movement speed. Another study (Vass et al., 2016) showed successful decoding of teleportation distance from hippocampus, highlighting that location is well-represented in these recordings. Watrous et al. (2018) extended these findings by showing that even the navigational goal can be decoded from single united activity recorded from microelectrodes at the tip of sEEG electrodes.

3.5. Passive BCI

Instead of directly controlling computers, the idea of passive BCIs (Zander and Kothe, 2011) is to adapt interfaces to a user's mental state such as stress, workload, drowsiness, or emotion, which the user may or may not be consciously aware of. As sEEG targets deeper brain structures including limbic regions such as the amygdala, it is well-suited to detect and decode brain activity associated with such user states. Alasfour et al. (2019)

demonstrated the classification of abstract naturalistic behavioral contexts from ECoG and sEEG recordings, which could be used to adapt interfaces to the coarse behavioral context of users in the future. Sani et al. (2018) showed that mood variations during natural behavior can be decoded from intracranial recordings (including sEEG). Their classifiers relied mostly on electrodes in limbic regions. These findings could one day help in the development of closed-loop systems to treat neuropsychiatric disorders. Yamin et al. (2017) investigate online neurofeedback in depth electrodes with a virtual reality interface. Their preliminary results show that users were able to reliably downregulate their amygdala activity.

Another aspect of cognition that could be useful for passive BCI is the encoding and retrieval of memory that could for example inform an interface which information needs to be presented again. Initial investigations highlight the feasibility of decoding aspects of memory from sEEG recordings (Song et al., 2016, 2017). Hampson et al. (2018) extended these findings and demonstrated that the typical activity pattern during successful memory encoding could also be used in stimulation to increase memory performance.

4. FUTURE DIRECTIONS

Despite the impressive results achieved in decoding of mental processes from sEEG recordings, there are still numerous practical issues that must be addressed before sEEG BCIs can be considered for long-term, clinical applications. **Figure 2** shows the standard processing pipeline of an sEEG-based BCI. At each individual stage of this pipeline there are unique challenges and opportunities for achieving a practical BCI.

For *data acquisition*, current clinical sEEG implants can be modified in a multitude of ways to improve the spatial resolution and target sampling. By maintaining the same shaft size, the contact size and density can be reduced to be able to record local field potentials along the entire length of the shaft (Pothof et al., 2016). Additionally, microwires can be placed at the tip of the shaft for recording single-units (Pothof et al., 2016). Such modifications are expected to yield significant improvements in BCI decoding performance as observed when using micro-ECoG in comparison to standard clinical ECoG (Slutzky et al., 2010; Wang et al., 2013; Kellis et al., 2016; Muller et al., 2016). Furthermore, the sEEG shafts can be designed to have custom electrode placement or directional electrodes (Tinkhauser et al., 2018) to strategically target multiple brain locations or networks using a single shaft and trajectory planning. Such sampling of multiple brain networks, including cortical and subcortical targets, would significantly increase the decoding potential for many complex functions such as language and memory. Since sEEG is well-suited for bilateral implantation, there is significant potential for investigating network coordination across hemispheres. Leveraging the clinical success of DBS based on electrical stimulation, there is also the possibility of developing bidirectional BCIs using sEEG (Wander and Rao, 2014). Additionally, the long term stability of sEEG recordings needs to be investigated. While studies show that ECoG grids provide reliable long-term measurements (Vansteensel et al., 2016; Pels et al., 2019), similar evidence for sEEG is currently lacking.

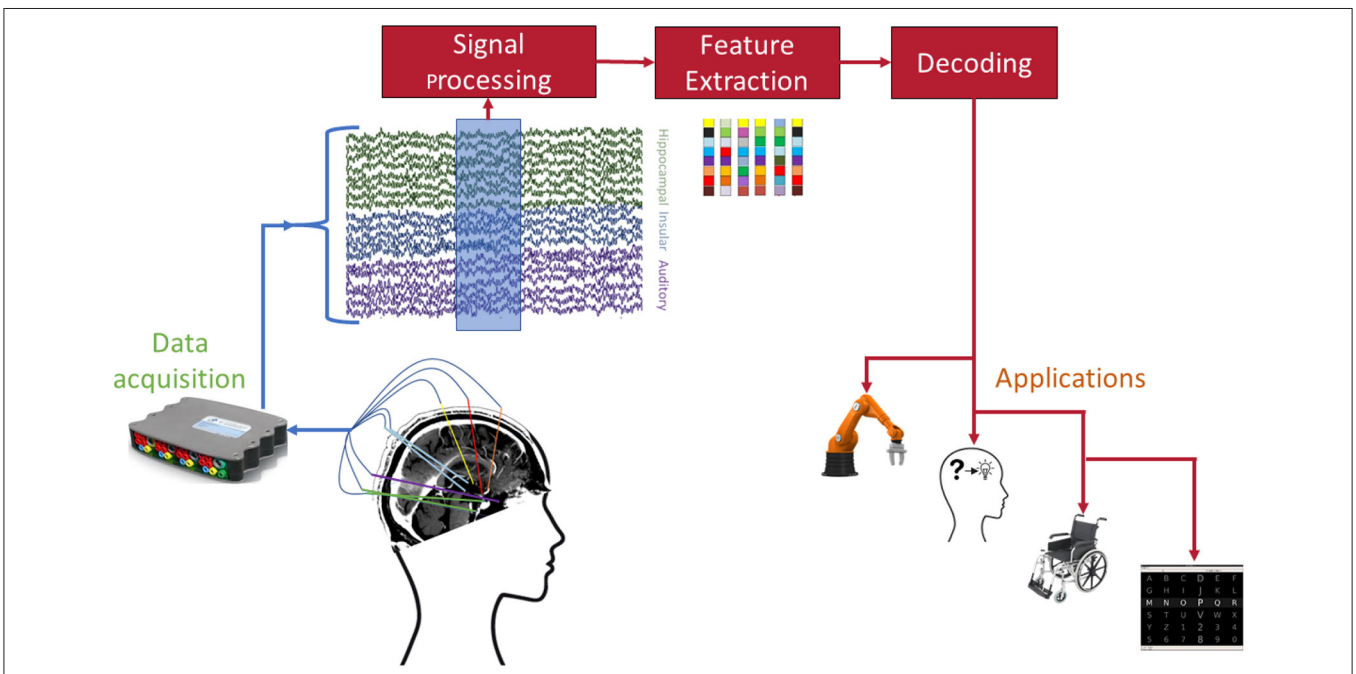

FIGURE 2 | Envisioned pipeline for sEEG BCI. Each of the involved stages poses open challenges before successful dissemination to patients. Example applications include (from left to right) robotic arm control, memory prosthesis, wheelchair control, and speller interfaces.

While DBS devices present fully implanted solutions, sEEG measurements still rely on externalized leads connected to bulky amplifiers. For realistic BCI applications, a fully implanted solution should be targeted placing new requirements on (wireless) amplifiers. Advances from other types of neural implants might be harnessed for these *data acquisition* challenges (Eftekhar et al., 2010; Liu et al., 2017).

The sparse sampling of sEEG across different brain regions requires specific *signal processing*, as well as *feature extraction*. For example, while high-gamma has been the focus of many intracranial BCI studies and are also found in e.g., hippocampus (Colgin and Moser, 2010), other frequency ranges such as theta might be better suited for decoding activity (Stavisky et al., 2015) from deeper structures (Buzsáki, 2002). Furthermore, sEEG provides an excellent opportunity to explore more global phenomena such as traveling waves (Nunez and Srinivasan, 2006; Muller et al., 2018), connectivity (Van Mierlo et al., 2013), and frequency-coupling (Maris et al., 2011).

In addition to the common *applications* mentioned in **Figure 2**, sEEG provides a unique opportunity to enhance existing or develop new applications by harnessing brain activity from limbic and memory-related brain activity. For instance, this information could conceivably be used to convey emotion or affect in a speech neuroprosthetic. As with other measurement modalities, different requirements for the *decoding* procedures will arise depending on the envisioned *application* (Borton et al., 2013; Bensmaia and Miller, 2014).

Overall, sEEG exhibits several unique advantages of other intracranial monitoring methods. In addition to the capability of sampling subcortical regions, sEEG implantation is a less traumatic procedure that exhibits a lower risk of infection. Since the hardware and procedures for sEEG and DBS implantation are effectively identical, the success and precedent established by DBS suggests that sEEG could also be chronically implanted for BCIs. Ultimately, the BCI field needs to further develop and test new sEEG electrode/shaft designs and develop paradigms that exploit sEEG's unique capability of recording from multiple cortical and subcortical targets. It is also prudent to explore sEEG in conjunction with microarrays and ECoG to evaluate whether the addition of subcortical targets and networks can further refine the decoding performance and capabilities of these already-successful approaches. It is feasible that future BCIs will require a hybrid of cortical (Microarrays and ECoG) and subcortical (sEEG) sampling on the path to achieving fully-transparent and natural operation.

5. CONCLUSION

In this review article, we briefly introduced sEEG and compared its characteristics with ECoG, another intracranial measurement modality. We reviewed initial decoding work using sEEG and highlighted further potential and future directions of BCI research using sEEG.

We believe that sEEG holds great potential for BCI as it offers the measurement of brain structures that are not reachable with ECoG and supplying a very broad sampling of neural activity. In particular, sEEG provides an unparalleled opportunity for the decoding of memory-related processes and limbic activity, which can also be incorporated to supplement or further enhance decoding of other cognitive processes.

AUTHOR CONTRIBUTIONS

All authors contributed to the final version of the manuscript.

FUNDING

This work was part of the research project Decoding Speech In SEEG (DESIS) with project number VI.Veni.194.021, which was financed by the Dutch Research Council (NWO).

REFERENCES

Aghajan, Z. M., Schuette, P., Fields, T. A., Tran, M. E., Siddiqui, S. M., Hasulak, N. R., et al. (2017). Theta oscillations in the human medial temporal lobe during real-world ambulatory movement. *Curr. Biol.* 27, 3743–3751. doi: 10.1016/j.cub.2017.10.062

Ajiboye, A. B., Willett, F. R., Young, D. R., Memberg, W. D., Murphy, B. A., Miller, J. P., et al. (2017). Restoration of reaching and grasping movements through brain-controlled muscle stimulation in a person with tetraplegia: a proof-of-concept demonstration. *Lancet* 389, 1821–1830. doi: 10.1016/S0140-6736(17)30601-3

Akbari, H., Khalighinejad, B., Herrero, J. L., Mehta, A. D., and Mesgarani, N. (2019). Towards reconstructing intelligible speech from the human auditory cortex. *Sci. Rep.* 9:874. doi: 10.1038/s41598-018-37359-z

Alasfour, A., Gabriel, P., Jiang, X., Shamie, I., Melloni, L., Thesen, T., et al. (2019). Coarse behavioral context decoding. *J. Neural Eng.* 16:016021. doi: 10.1088/1741-2552/aaee9c

Angrick, M., Herff, C., Mugler, E., Tate, M. C., Slutzky, M. W., Krusienski, D. J., et al. (2019). Speech synthesis from ecog using densely connected 3d convolutional neural networks. *J. Neural Eng.* 16:036019. doi: 10.1088/1741-2552/ab0c59

Anumanchipalli, G. K., Chartier, J., and Chang, E. F. (2019). Speech synthesis from neural decoding of spoken sentences. *Nature* 568:493. doi: 10.1038/s41586-019-1119-1

Arya, R., Horn, P. S., and Crone, N. E. (2018). Ecog high-gamma modulation versus electrical stimulation for presurgical language mapping. *Epilepsy Behav.* 79, 26–33. doi: 10.1016/j.yebeh.2017.10.044

Ball, T., Kern, M., Mutschler, I., Aertsen, A., and Schulze-Bonhage, A. (2009). Signal quality of simultaneously recorded invasive and non-invasive eeg. *Neuroimage* 46, 708–716. doi: 10.1016/j.neuroimage.2009.02.028

Bancaud, J. (1959). Apport de l'exploration fonctionnelle par voie stéréotaxique à la chirurgie de l'épilepsie. *Neurochirurgie* 5, 55–112.

Bensmaia, S. J., and Miller, L. E. (2014). Restoring sensorimotor function through intracortical interfaces: progress and looming challenges. *Nat. Rev. Neurosci.* 15:313. doi: 10.1038/nrn3724

Borton, D., Micera, S., Millán, J. d. R., and Courtine, G. (2013). Personalized neuroprosthetics. *Sci. Transl. Med.* 5:210rv2. doi: 10.1126/scitranslmed.3005968

Buzsáki, G. (2002). Theta oscillations in the hippocampus. *Neuron* 33, 325–340. doi: 10.1016/S0896-6273(02)00586-X

Cardinale, F., Cossu, M., Castana, L., Casaceli, G., Schiariti, M. P., Miserocchi, A., et al. (2012). Stereoelectroencephalography: surgical methodology, safety, and stereotactic application accuracy in 500 procedures. *Neurosurgery* 72, 353–366. doi: 10.1227/NEU.0b013e31827d1161

Chao, Z. C., Nagasaka, Y., and Fujii, N. (2010). Long-term asynchronous decoding of arm motion using electrocorticographic signals in monkey. *Front. Neuroeng.* 3:3. doi: 10.3389/fneng.2010.00003

Chassoux, F., Navarro, V., Catenoix, H., Valton, L., and Vignal, J.-P. (2018). Planning and management of seeg. *Neurophysiol. Clin.* 48, 25–37. doi: 10.1016/j.neucli.2017.11.007

Chrabaszcz, A., Neumann, W. J., Stretcu, O., Lipski, W. J., Bush, A., Dastolfo-Hromack, C., et al. (2019). Subthalamic nucleus and sensorimotor cortex activity during speech production. *J. Neurosci.* 39, 2698–2708. doi: 10.1523/JNEUROSCI.2842-18.2019

Colgin, L. L., and Moser, E. I. (2010). Gamma oscillations in the hippocampus. *Physiology* 25, 319–329. doi: 10.1152/physiol.00021.2010

Crone, N., Hao, L., Hart, J., Boatman, D., Lesser, R., Irizarry, R., et al. (2001). Electrocorticographic gamma activity during word production in spoken and sign language. *Neurology* 57, 2045–2053. doi: 10.1212/WNL.57.11.2045

Eftekhar, A., Sivylla, E. P., and Timothy, G. C. (2010). "Towards a next generation neural interface: Optimizing power, bandwidth and data quality," in *2010 Biomedical Circuits and Systems Conference (BioCAS)* (Paphos: IEEE), 122–125.

Fischer, P., Pogosyan, A., Cheeran, B., Green, A. L., Aziz, T. Z., Hyam, J., et al. (2017). Subthalamic nucleus beta and gamma activity is modulated depending on the level of imagined grip force. *Exp. Neurol.* 293, 53–61. doi: 10.1016/j.expneurol.2017.03.015

Greenberg, B. D., Malone, D. A., Friehs, G. M., Rezai, A. R., Kubu, C. S., Malloy, P. F., et al. (2006). Three-year outcomes in deep brain stimulation for highly resistant obsessive–compulsive disorder. *Neuropsychopharmacology* 31:2384. doi: 10.1038/sj.npp.1301165

Hader, W. J., Tellez-Zenteno, J., Metcalfe, A., Hernandez-Ronquillo, L., Wiebe, S., Kwon, C.-S., et al. (2013). Complications of epilepsy surgery–a systematic review of focal surgical resections and invasive eeg monitoring. *Epilepsia* 54, 840–847. doi: 10.1111/epi.12161

Hampson, R. E., Song, D., Robinson, B. S., Fetterhoff, D., Dakos, A. S., Roeder, B. M., et al. (2018). Developing a hippocampal neural prosthetic to facilitate human memory encoding and recall. *J. Neural Eng.* 15:036014. doi: 10.1088/1741-2552/aaaed7

Han, C., O'Sullivan, J., Luo, Y., Herrero, J., Mehta, A. D., and Mesgarani, N. (2019). Speaker-independent auditory attention decoding without access to clean speech sources. *Sci. Adv.* 5:eaav6134. doi: 10.1126/sciadv.aav6134

Herff, C., Heger, D., De Pesters, A., Telaar, D., Brunner, P., Schalk, G., and Schultz, T. (2015). Brain-to-text: decoding spoken phrases from phone representations in the brain. *Front. Neurosci.* 9:217. doi: 10.3389/fnins.2015.00217

Herff, C., Johnson, G., Diener, L., Shih, J., Krusienski, D., and Schultz, T. (2016). "Towards direct speech synthesis from ecog: a pilot study," in *2016 38th Annual International Conference of the IEEE Engineering in Medicine and Biology Society (EMBC)* (Orlando, FL: IEEE), 1540–1543.

Herff, C., and Schultz, T. (2016). Automatic speech recognition from neural signals: a focused review. *Front. Neurosci.* 10:429. doi: 10.3389/fnins.2016.00429

Hochberg, L. R., Bacher, D., Jarosiewicz, B., Masse, N. Y., Simeral, J. D., Vogel, J., et al. (2012). Reach and grasp by people with tetraplegia using a neurally controlled robotic arm. *Nature* 485:372. doi: 10.1038/nature11076

Hochberg, L. R., Serruya, M. D., Friehs, G. M., Mukand, J. A., Saleh, M., Caplan, A. H., et al. (2006). Neuronal ensemble control of prosthetic devices by a human with tetraplegia. *Nature* 442:164. doi: 10.1038/nature04970

Huggins, J. E., Guger, C., Ziat, M., Zander, T. O., Taylor, D., Tangermann, M., et al. (2017). Workshops of the sixth international brain–computer interface meeting: brain–computer interfaces past, present, and future. *Brain Computer Interfaces* 4, 3–36. doi: 10.1080/2326263X.2016.1275488

Iida, K., and Otsubo, H. (2017). Stereoelectroencephalography: indication and efficacy. *Neurol. Medico-chirurgica* 57, 375–385. doi: 10.2176/nmc.ra.2017-0008

Kellis, S., Sorensen, L., Darvas, F., Sayres, C., O'Neill, K., Brown, R. B., et al. (2016). Multi-scale analysis of neural activity in humans: implications for micro-scale electrocorticography. *Clin. Neurophysiol.* 127, 591–601. doi: 10.1016/j.clinph.2015.06.002

Kern, M., Bert, S., Glanz, O., Schulze-Bonhage, A., and Ball, T. (2019). Human motor cortex relies on sparse and action-specific activation during laughing, smiling and speech production. *Commun. Biol.* 2:118. doi: 10.1038/s42003-019-0360-3

Krusienski, D. J., and Shih, J. J. (2011). Control of a visual keyboard using an electrocorticographic brain–computer interface. *Neurorehabil. Neural Rep.* 25, 323–331. doi: 10.1177/1545968310382425

Kuba, M., Kubová, Z., Kremláček, J., and Langrová, J. (2007). Motion-onset veps: characteristics, methods, and diagnostic use. *Vis. Res.* 47, 189–202. doi: 10.1016/j.visres.2006.09.020

Leuthardt, E., Pei, X.-M., Breshears, J., Gaona, C., Sharma, M., Freudenburg, Z., et al. (2012). Temporal evolution of gamma activity in human cortex during an overt and covert word repetition task. *Front. Hum. Neurosci.* 6:99. doi: 10.3389/fnhum.2012.00099

Li, D., Han, H., Xu, X., Ling, Z., and Hong, B. (2017a). "Minimally invasive brain computer interface for fast typing," in *2017 8th International IEEE/EMBS Conference on Neural Engineering (NER)* (Shanghai: IEEE), 477–480.

Li, G., Jiang, S., Paraskevopoulou, S. E., Wang, M., Xu, Y., Wu, Z., Chen, L., et al. (2018). Optimal referencing for stereo-electroencephalographic (seeg) recordings. *NeuroImage* 183, 327–335. doi: 10.1016/j.neuroimage.2018.08.020

Li, G., Jiang, S., Xu, Y., Wu, Z., Chen, L., and Zhang, D. (2017b). "A preliminary study towards prosthetic hand control using human stereo-electroencephalography (seeg) signals," in *2017 8th International IEEE/EMBS Conference on Neural Engineering (NER)* (IEEE), 375–378.

Liu, Y., Luan, S., Williams, I., Rapeaux, A., and Constandinou, T. G. (2017). A 64-channel versatile neural recording soc with activity-dependent data throughput. *IEEE Trans. Biomed. Circ. Syst.* 11, 1344–1355. doi: 10.1109/TBCAS.2017.2759339

Logothetis, N. K., Pauls, J., Augath, M., Trinath, T., and Oeltermann, A. (2001). Neurophysiological investigation of the basis of the fmri signal. *Nature* 412:150. doi: 10.1038/35084005

Maguire, E. A., Burgess, N., Donnett, J. G., Frackowiak, R. S., Frith, C. D., and O'keefe, J. (1998). Knowing where and getting there: a human navigation network. *Science* 280, 921–924. doi: 10.1126/science.280.5365.921

Maris, E., van Vugt, M., and Kahana, M. (2011). Spatially distributed patterns of oscillatory coupling between high-frequency amplitudes and low-frequency phases in human ieeg. *Neuroimage* 54, 836–850. doi: 10.1016/j.neuroimage.2010.09.029

Martinez-Ramirez, D., Jimenez-Shahed, J., Leckman, J. F., Porta, M., Servello, D., Meng, F.-G., et al. (2018). Efficacy and safety of deep brain stimulation in tourette syndrome: the international tourette syndrome deep brain stimulation public database and registry. *JAMA Neurol.* 75, 353–359. doi: 10.1001/jamaneurol.2017.4317

McCarthy, G., Wood, C. C., Williamson, P. D., and Spencer, D. D. (1989). Task-dependent field potentials in human hippocampal formation. *J. Neurosci.* 9, 4253–4268. doi: 10.1523/JNEUROSCI.09-12-04253.1989

McMullen, D. P., Hotson, G., Katyal, K. D., Wester, B. A., Fifer, M. S., McGee, T. G., et al. (2014). Demonstration of a semi-autonomous hybrid brain–machine interface using human intracranial eeg, eye tracking, and computer vision to control a robotic upper limb prosthetic. *IEEE Trans. Neural Syst. Rehabil. Eng.* 22, 784–796. doi: 10.1109/TNSRE.2013.2294685

Miller, K. J., Leuthardt, E. C., Schalk, G., Rao, R. P., Anderson, N. R., Moran, D. W., et al. (2007). Spectral changes in cortical surface potentials during motor movement. *J. Neurosci.* 27, 2424–2432. doi: 10.1523/JNEUROSCI.3886-06.2007

Miller, K. J., Sorensen, L. B., Ojemann, J. G., and Den Nijs, M. (2009). Power-law scaling in the brain surface electric potential. *PLoS Comput. Biol.* 5:e1000609. doi: 10.1371/journal.pcbi.1000609

Moser, E. I., Kropff, E., and Moser, M.-B. (2008). Place cells, grid cells, and the brain's spatial representation system. *Annu. Rev. Neurosci.* 31, 69–89. doi: 10.1146/annurev.neuro.31.061307.090723

Moses, D. A., Leonard, M. K., Makin, J. G., and Chang, E. F. (2019). Real-time decoding of question-and-answer speech dialogue using human cortical activity. *Nat. Commun.* 10, 1–14. doi: 10.1038/s41467-019-10994-4

Moses, D. A., Mesgarani, N., Leonard, M. K., and Chang, E. F. (2016). Neural speech recognition: continuous phoneme decoding using spatiotemporal representations of human cortical activity. *J. Neural Eng.* 13:056004. doi: 10.1088/1741-2560/13/5/056004

Mukamel, R., Gelbard, H., Arieli, A., Hasson, U., Fried, I., and Malach, R. (2005). Coupling between neuronal firing, field potentials, and fmri in human auditory cortex. *Science* 309, 951–954. doi: 10.1126/science.1110913

Muller, L., Chavane, F., Reynolds, J., and Sejnowski, T. J. (2018). Cortical travelling waves: mechanisms and computational principles. *Nat. Rev. Neurosci*. 19:255. doi: 10.1038/nrn.2018.20

Muller, L., Hamilton, L. S., Edwards, E., Bouchard, K. E., and Chang, E. F. (2016). Spatial resolution dependence on spectral frequency in human speech cortex electrocorticography. *J. Neural Eng.* 13:056013. doi: 10.1088/1741-2560/13/5/056013

Mullin, J. P., Shriver, M., Alomar, S., Najm, I., Bulacio, J., Chauvel, P., et al. (2016). Is seeg safe? a systematic review and meta-analysis of stereo-electroencephalography–related complications. *Epilepsia* 57, 386–401. doi: 10.1111/epi.13298

Murphy, B. A., Miller, J. P., Gunalan, K., and Ajiboye, A. B. (2016). Contributions of subsurface cortical modulations to discrimination of executed and imagined grasp forces through stereoelectroencephalography. *PLoS ONE* 11:e0150359. doi: 10.1371/journal.pone.0150359

Nunez, P. L., and Srinivasan, R. (2006). A theoretical basis for standing and traveling brain waves measured with human eeg with implications for an integrated consciousness. *Clin. Neurophysiol.* 117, 2424–2435. doi: 10.1016/j.clinph.2006.06.754

Nuyujukian, P., Sanabria, J. A., Saab, J., Pandarinath, C., Jarosiewicz, B., Blabe, C. H., et al. (2018). Cortical control of a tablet computer by people with paralysis. *PLoS ONE* 13:e0204566. doi: 10.1371/journal.pone.0204566

Parvizi, J., and Kastner, S. (2018). Promises and limitations of human intracranial electroencephalography. *Nat. Neurosci.* 21, 474–483. doi: 10.1038/s41593-018-0108-2

Pels, E. G., Aarnoutse, E. J., Leinders, S., Freudenburg, Z. V., Branco, M. P., van der Vijgh, B. H., et al. (2019). Stability of a chronic implanted brain-computer interface in late-stage amyotrophic lateral sclerosis. *Clin. Neurophysiol.* 130, 1798–1803. doi: 10.1016/j.clinph.2019.07.020

Pothof, F., Bonini, L., Lanzilotto, M., Livi, A., Fogassi, L., Orban, G. A., et al. (2016). Chronic neural probe for simultaneous recording of single-unit, multi-unit, and local field potential activity from multiple brain sites. *J. Neural Eng.* 13:046006. doi: 10.1088/1741-2560/13/4/046006

Pycroft, L., Stein, J., and Aziz, T. (2018). Deep brain stimulation: An overview of history, methods, and future developments. *Brain Neurosci. Adv.* 2:2398212818816017. doi: 10.1177/2398212818816017

Ray, S., Crone, N. E., Niebur, E., Franaszczuk, P. J., and Hsiao, S. S. (2008). Neural correlates of high-gamma oscillations (60–200 hz) in macaque local field potentials and their potential implications in electrocorticography. *J. Neurosci.* 28:11526–11536. doi: 10.1523/JNEUROSCI.2848-08.2008

Sani, O. G., Yang, Y., Lee, M. B., Dawes, H. E., Chang, E. F., and Shanechi, M. M. (2018). Mood variations decoded from multi-site intracranial human brain activity. *Nat. Biotechnol.* 36:954. doi: 10.1038/nbt.4200

Schalk, G., and Leuthardt, E. C. (2011). Brain-computer interfaces using electrocorticographic signals. *IEEE Rev. Biomed. Eng.* 4, 140–154. doi: 10.1109/RBME.2011.2172408

Schultz, T., Wand, M., Hueber, T., Krusienski, D. J., Herff, C., and Brumberg, J. S. (2017). Biosignal-based spoken communication: A survey. *IEEE/ACM Trans. Audio Speech Lang. Process.* 25, 2257–2271. doi: 10.1109/TASLP.2017.2752365

Shih, J. J., and Krusienski, D. J. (2012). Signals from intraventricular depth electrodes can control a brain–computer interface. *J. Neurosci. Methods* 203, 311–314. doi: 10.1016/j.jneumeth.2011.10.012

Slutzky, M. W., Jordan, L. R., Krieg, T., Chen, M., Mogul, D. J., and Miller, L. E. (2010). Optimal spacing of surface electrode arrays for brain-machine interface applications. *J. Neural Eng.* 7:26004. doi: 10.1088/1741-2560/7/2/026004

Song, D., Hampson, R. E., Robinson, B. S., Marmarelis, V. Z., Deadwyler, S. A., and Berger, T. W. (2016). "Decoding memory features from hippocampal spiking activities using sparse classification models," in *2016 38th Annual International Conference of the IEEE Engineering in Medicine and Biology Society (EMBC)* (Orlando, FL), 1620–1623.

Song, D., She, X., Hampson, R. E., Deadwyler, S. A., and Berger, T. W. (2017). "Multi-resolution multi-trial sparse classification model for decoding visual memories from hippocampal spikes in human," in *2017 39th Annual International Conference of the IEEE Engineering in Medicine and Biology Society (EMBC)* (Jeju Island), 1046–1049.

Stavisky, S. D., Kao, J. C., Nuyujukian, P., Ryu, S. I., and Shenoy, K. V. (2015). A high performing brain–machine interface driven by low-frequency local field potentials alone and together with spikes. *J. Neural Eng.* 12:036009. doi: 10.1088/1741-2560/12/3/036009

Talairach, J., and Bancaud, J. (1966). Lesion," irritative" zone and epileptogenic focus. *Stereot. Funct. Neurosurg.* 27, 91–94. doi: 10.1159/000103937

Tinkhauser, G., Pogosyan, A., Debove, I., Nowacki, A., Shah, S. A., Seidel, K., et al. (2018). Directional local field potentials: a tool to optimize deep brain stimulation. *Mov. Disord.* 33, 159–164. doi: 10.1002/mds.27215

Vadera, S., Marathe, A. R., Gonzalez-Martinez, J., and Taylor, D. M. (2013). Stereoelectroencephalography for continuous two-dimensional cursor control in a brain-machine interface. *Neurosurg. Focus* 34:E3. doi: 10.3171/2013.3.FOCUS1373

van der Loo, L. E., Schijns, O. E., Hoogland, G., Colon, A. J., Wagner, G. L., Dings, J. T., et al. (2017). Methodology, outcome, safety and *in vivo* accuracy in traditional frame-based stereoelectroencephalography. *Acta Neurochirurg.* 159, 1733–1746. doi: 10.1007/s00701-017-3242-9

Van Mierlo, P., Carrette, E., Hallez, H., Raedt, R., Meurs, A., Vandenberghe, S., et al. (2013). Ictal-onset localization through connectivity analysis of intracranial eeg signals in patients with refractory epilepsy. *Epilepsia* 54, 1409–1418. doi: 10.1111/epi.12206

Vansteensel, M. J., Pels, E. G., Bleichner, M. G., Branco, M. P., Denison, T., Freudenburg, Z. V., et al. (2016). Fully implanted brain–computer interface in a locked-in patient with als. *N. Engl. J. Med.* 375, 2060–2066. doi: 10.1056/NEJMoa1608085

Vass, L. K., Copara, M. S., Seyal, M., Shahlaie, K., Farias, S. T., Shen, P. Y., et al. (2016). Oscillations go the distance: low-frequency human hippocampal oscillations code spatial distance in the absence of sensory cues during teleportation. *Neuron* 89, 1180–1186. doi: 10.1016/j.neuron.2016.01.045

Wander, J. D., and Rao, R. P. (2014). Brain–computer interfaces: a powerful tool for scientific inquiry. *Curr. Opin. Neurobiol.* 25, 70–75. doi: 10.1016/j.conb.2013.11.013

Wang, W., Collinger, J. L., Degenhart, A. D., Tyler-Kabara, E. C., Schwartz, A. B., Moran, D. W., et al. (2013). An electrocorticographic brain interface in an individual with tetraplegia. *PLoS ONE.* 8:e55344. doi: 10.1371/journal.pone.0055344

Watrous, A. J., Miller, J., Qasim, S. E., Fried, I., and Jacobs, J. (2018). Phase-tuned neuronal firing encodes human contextual representations for navigational goals. *eLife* 7:e32554. doi: 10.7554/eLife.32554

Wolpaw, J. R., Birbaumer, N., McFarland, D. J., Pfurtscheller, G., and Vaughan, T. M. (2002). Brain–computer interfaces for communication and control. *Clin. Neurophysiol.* 113, 767–791. doi: 10.1016/S1388-2457(02)00057-3

Yamin, H. G., Gazit, T., Tchemodanov, N., Raz, G., Jackont, G., Charles, F., et al. (2017). Depth electrode neurofeedback with a virtual reality interface. *Brain-Computer Interfaces* 4, 201–213. doi: 10.1080/2326263X.2017.1338008

Zander, T. O., and Kothe, C. (2011). Towards passive brain–computer interfaces: applying brain–computer interface technology to human–machine systems in general. *J. Neural Eng.* 8:025005. doi: 10.1088/1741-2560/8/2/025005

Conflict of Interest: The authors declare that the research was conducted in the absence of any commercial or financial relationships that could be construed as a potential conflict of interest.

frontiers in Neuroscience

ORIGINAL RESEARCH
published: 25 May 2021
doi: 10.3389/fnins.2021.517316

Prediction of Successful Memory Encoding Based on Lateral Temporal Cortical Gamma Power

Soyeon Jun[1,3], June Sic Kim[2] and Chun Kee Chung[1,3]**

[1] Department of Brain and Cognitive Sciences, Seoul National University, Seoul, South Korea, [2] Research Institute of Basic Sciences, Seoul National University, Seoul, South Korea, [3] Department of Neurosurgery, Seoul National University Hospital, Seoul, South Korea

Prediction of successful memory encoding is important for learning. High-frequency activity (HFA), such as gamma frequency activity (30–150 Hz) of cortical oscillations, is induced during memory tasks and is thought to reflect underlying neuronal processes. Previous studies have demonstrated that medio-temporal electrophysiological characteristics are related to memory formation, but the effects of neocortical neural activity remain underexplored. The main aim of the present study was to evaluate the ability of gamma activity in human electrocorticography (ECoG) signals to differentiate memory processes into remembered and forgotten memories. A support vector machine (SVM) was employed, and ECoG recordings were collected from six subjects during verbal memory recognition task performance. Two-class classification using an SVM was performed to predict subsequently remembered vs. forgotten trials based on individually selected frequencies (low gamma, 30–60 Hz; high gamma, 60–150 Hz) at time points during pre- and during stimulus intervals. The SVM classifier distinguished memory performance between remembered and forgotten trials with a mean maximum accuracy of 87.5% using temporal cortical gamma activity during the 0- to 1-s interval. Our results support the functional relevance of ECoG for memory formation and suggest that lateral temporal cortical HFA may be utilized for memory prediction.

Keywords: memory prediction, successful memory encoding, electrocorticography, high-frequency activity, memory formation, gamma frequency

OPEN ACCESS

Edited by:
Christoph Guger, g.tec medical engineering GmbH, Austria

Reviewed by:
Kazutaka Takahashi, University of Chicago, United States
Antonino Casile, Italian Institute of Technology (IIT), Italy

****Correspondence:***
June Sic Kim
Jskim@hbf.re.kr
Chun Kee Chung
chungc@snu.ac.kr

Specialty section:
This article was submitted to Neuroprosthetics, a section of the journal Frontiers in Neuroscience

Received: *03 December 2019*
Accepted: *30 March 2021*
Published: *25 May 2021*

Citation:
Jun S, Kim JS and Chung CK (2021) Prediction of Successful Memory Encoding Based on Lateral Temporal Cortical Gamma Power. Front. Neurosci. 15:517316. doi: 10.3389/fnins.2021.517316

INTRODUCTION

Memory formation is an important cognitive process that enables the identification of traces of individual episodic memories and learning from experiences to guide behavior (Chadwick et al., 2010). Understanding the neural correlates of memory formation is essential to identify the brain mechanisms underpinning memory processes, which can be further applied to predict subsequent memories or even improve memory (Ezzyat et al., 2017). The decoding of neural activity during memory processing has garnered substantial interest in the cognitive neuroscience community. Neural activity relevant to memory formation measured with electrocorticography (ECoG) provides a valuable window into the neural correlates of underlying cognitive processes (Fell et al., 2011). The field potential of ECoG activity interacts with neural membrane potentials and, thus, modulates the degree of neuronal excitability and influences their discharge times

(Anastassiou et al., 2010; Hohne et al., 2016). As such, these studies have provided evidence for the role of the amplitude of cortical oscillatory activities in neural processing.

There has been growing interest in human brain oscillations and their possible role in memory processes. Low-frequency activity (i.e., theta rhythm, 4–8 Hz) and high-frequency activity (HFA) (i.e., gamma rhythm, >30 Hz) have received attention in the context of understanding human memory function (Sederberg et al., 2003, 2007; Kahana, 2006). In particular, HFA is a brain response with ECoG signals for episodic memory formation, which provides spatiotemporal properties of memory encoding with millisecond temporal resolution. The neural substrates that produce such fast activity is a topic of ongoing research. HFA has been linked to asynchronous signals related to increased multi-unit activity (Manning et al., 2009; Milstein et al., 2009; Ray and Maunsell, 2011). An increasing number of studies have leveraged HFA as a marker of underlying neural activation (Miller et al., 2008; Shenoy et al., 2008; Lachaux et al., 2012), and HFA is, thus, considered to reflect regional activation during memory encoding (Burke et al., 2014). HFA has been reported to be a potential biomarker for mapping, targeting, and modulating neuronal assemblies at a high temporal resolution during memory formation (Lachaux et al., 2012; Burke et al., 2015; Johnson and Knight, 2015). In particular, these oscillations spanning a 30- to 150-Hz range were proposed to set an ideal frame for neuronal interactions underlying memory formation (Jensen et al., 2007; Duzel et al., 2010). Thus, studies investigated to detect discrete events induced during memory formation of word encoding in different gamma band activities—low gamma (30–60 Hz) and high-gamma (>60 Hz) (Colgin et al., 2009; Buzsaki and Silva, 2012). Separating different types of gamma activities (30–150 Hz) is a crucial electrophysiological biomarker of memory formation and applications (Kucewicz et al., 2017).

Extant evidence suggests that prevalent HFA from structures outside the medial temporal lobe (MTL) is critical for memory formation (Buzsaki, 1996; Eichenbaum, 2000; Poldrack et al., 2001; Ritchey et al., 2015; Moscovitch et al., 2016). Neuroimaging studies have provided evidence for the neural correlates of episodic encoding within the hippocampus and functional networks spanning prefrontal, medial temporal, lateral temporal, and parietal cortical regions (Kim et al., 2010). Similarly, successful memory processing relies on coherent oscillations of multiple temporal and neocortical regions at varying frequencies. For instance, increased coherence between brain regions, particularly the hippocampus and prefrontal cortex, is associated with better memory (Fell et al., 2008; Benchenane et al., 2010; Watrous et al., 2013). Especially, gamma oscillatory power increases with memory task in the hippocampus, and this gamma pattern (28–40 Hz and 90–100 Hz) was observed in other memory-related regions such as frontal and temporal cortical regions (van Vugt et al., 2010). The neural correlates of HFA of successful memory processing in neocortical regions may, therefore, provide insight into the roles of specific regions in memory performance, and characterizing these features may facilitate the evaluation of memory performance. However, the effect of HFA in human ECoG signals to differentiate memory prediction has been little explored.

The core aim in this study is to provide novel evidence on how HFA in the temporal cortex is associated with success of memory formation in human ECoG signals and to differentiate memory process into remembered and forgotten memories with HFA. We evaluated temporal cortical HFA, which was accompanied by successful memory formation relative to unsuccessful encoding. We hypothesized that the difference in HFA would enable differentiation of successful encoding trials from unsuccessful ones. In the first step, we identified time windows (i.e., pre-stimulus vs. during-stimulus) referenced by the human single-unit activity and HFA with statistically significant power clustering across subjects. We delegated the HFA to low gamma (30–60 Hz) and high gamma (60–150 Hz) based on previous literature, revealing a sequential memory effect (SME) during the encoding phase (Sederberg et al., 2007; van Vugt et al., 2010). We then determined the brain regions and frequencies for which the amplitude differences differed between the remembered and forgotten conditions in order to analyze encoding-related activities for subsequently remembered and forgotten words. Finally, a support vector machine (SVM) was trained using the power in the selected time windows and frequencies.

MATERIALS AND METHODS

Subjects

The present study included six subjects (four women; mean age: 34.2 ± 11.6 years) with drug-resistant epilepsy who had been implanted with intracranial electrodes to determine the area of the seizure onset zone. The local institutional review board (IRB) approved the study protocol (H-1407-115-596). All subjects provided written informed consent to participate in the present study. Subject characteristics are presented in **Table 1**. Most of the subjects underwent neuropsychological assessments including IQ and MQ to confirm that the subjects were within a normal cognitive category.

Electrode Localization

The locations of the electrodes were determined by clinical diagnosis. The electrodes (AdTech Medical Instrument Corporation, Racine, WI, United States) were positioned for subdural electrocorticography (ECoG) on the cortical surface (diameter of 4 mm, placed 10-mm apart) with stainless steel contacts. Prior to electrode implantation, each subject underwent a preoperative magnetic resonance imaging (MRI) scan in a Magnetom Trio, Magnetim Verio 3-tesla (Siemens, München, Germany) or Signa 1.5-Tesla scanner (GE, Boston, MA, United States). Computed tomography (CT) scans were performed following electrode implantation using a Somatom sensation device (64 eco; Siemens München, Germany). For visualization, CT and MRI images were co-registered as previously described (Avants et al., 2008). The brain model and implanted electrodes were reconstructed from individual preoperative MRI and postoperative CT images using CURRY software version 7.0 (Compumedics Neuroscan, Charlotte, NC, United States) (**Figure 1**). A neuroradiologist and neurosurgeon

TABLE 1 | Subject demographics, clinical characteristics, and electrode locations.

Subject	Demographics		Clinical characteristics				
	Age	IQ/MQ	Seizure onset	Pathology	Resection	Seizure type	Electrode Type
Sub1	50–55	77/94	ATG, TP	PHG reactive gliosis	PHG	TLE	Subdural
Sub2	30–35	N/A	TP, STG	Temporal lobe Focal cortical dysplasia	L. ITG	Bilateral TLE	Subdural
Sub3	20–25	89/92	Amygdala	FCD Heteropia	PHG, Amygdala	TLE	Subdural
Sub4	40–45	85/85	STG	HP neuronal loss	ATL, AH	TLE	Subdural
Sub5	25–30	N/A	PHG	DG dispersion, HP neuronal loss	HP	TLE	Subdural
Sub6	25–30	N/A	ATG, TP	PHG reactive gliosis	PHG	TLE	Depth

IQ, intelligence quotient; MQ, memory quotient; R, right; L, left; HP, hippocampus; mHP, middle hippocampus; LWM, limbic white matter; PHG, parahippocampal gyrus; DG, dentate gyrus; aTG, anterior temporal gyrus; STG, superior temporal gyrus; ITG, inferior temporal gyrus; TP, temporal pole; TLE, temporal lobe epilepsy; FCD, focal cortical dysplasia; N/A, not applicable.

Subject demographic data are presented together with clinical observations from clinically identified seizure onset zones, pathology in subjects who underwent corresponding surgery and showed neuropsychological results. A clinical psychologist employed the Wechsler Adult Intelligence Scale—Korean version (K-WAIS-IV) and the MQ of the Rey–Kim Memory test to assess IQ. Most of the subjects underwent neuropsychological assessment including IQ and MQ, providing that the subjects were within a normal cognitive category.

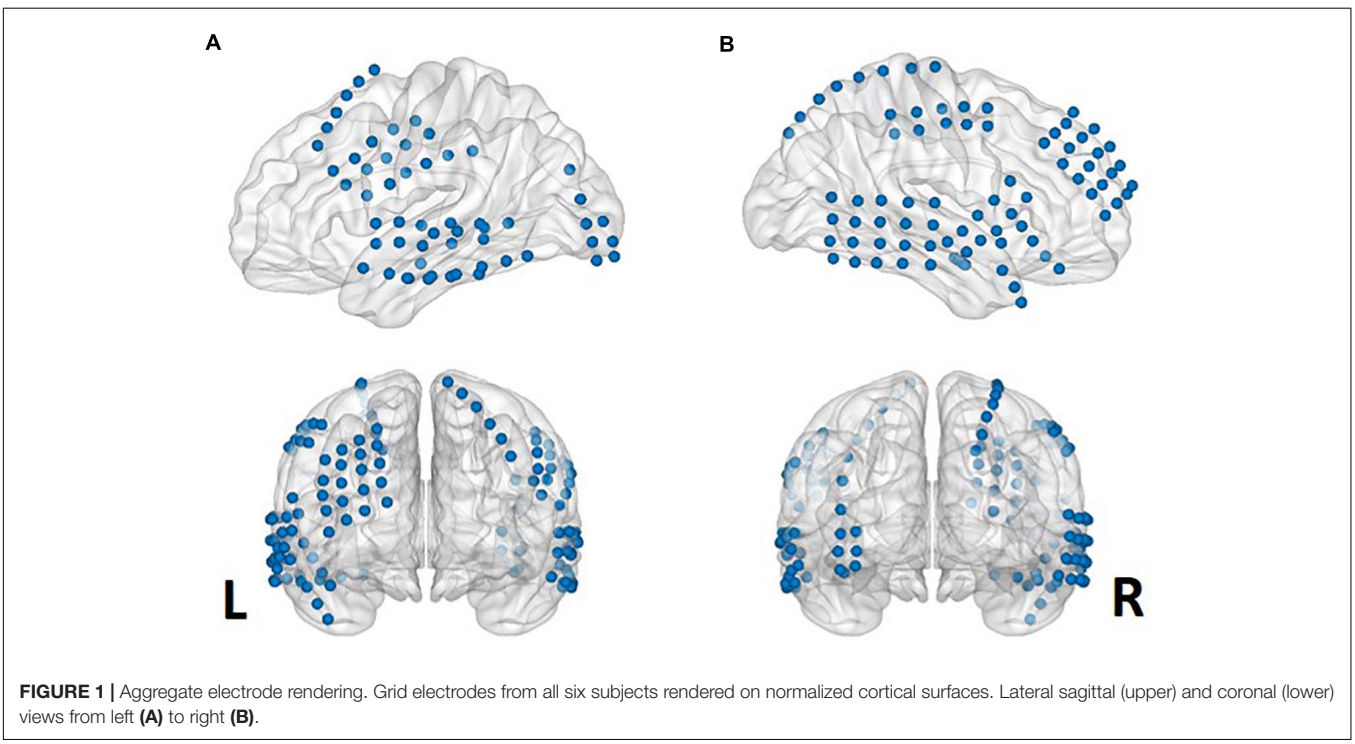

FIGURE 1 | Aggregate electrode rendering. Grid electrodes from all six subjects rendered on normalized cortical surfaces. Lateral sagittal (upper) and coronal (lower) views from left **(A)** to right **(B)**.

performed electrode localization based on thin-section post-implantation CT scans and co-registered MR images. BrainNet Viewer (Xia et al., 2013) was used to visualize the electrodes.

Verbal Memory Task

All stimuli were presented on a laptop computer with a Stim 2 Gentask (Neuroscan, Charlotte, NC, United States). We used a word memory task (**Figure 2**), which is known to recruit the medial temporal lobe during memory encoding (Axmacher et al., 2008; Hamani et al., 2008; Jun et al., 2020). All words consisted of concrete Korean nouns according to the Korean Category Norms: Survey on Exemplar Frequency Norm, Typicality, and Features (Rhee, 1991) and the second version of the Modern Korean Words database (Kim, 2005). Prior to the main experiment, a brief practice set of trials was conducted to ensure that the subjects understood the task. For the task, subjects were instructed to memorize the presented words. The subjects were instructed to study 60 words across two sessions. Each session consisted of 30 words. In total, 60 concrete nouns were individually presented in a random manner. The presentation of each word commenced with a fixation cross appearing on the screen for 1 s during the pre-stimulus time period, followed by the word that was displayed for 4 s. To ensure deep encoding, subjects were instructed to report whether they judged the word on the screen as "pleasant" or "unpleasant" by pressing a keyboard button with their index finger (de Vanssay-Maigne et al., 2011). Following presentation of the final word of the encoding block, subjects were allowed a 10-min break and

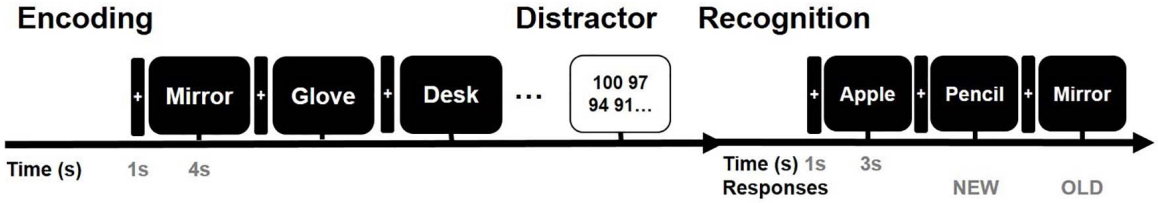

FIGURE 2 | Verbal memory task paradigm. Example of the timeline of the word memory paradigm. The entire task consisted of three study periods: encoding, rest (distractor), and retrieval.

subsequently performed a 30 s distractor task consisting of a series of arithmetic problems for "A − B = ?" where A and B were randomly chosen integers ranging from 1 to 100. In the item task, a total of 90 words were used, including 30 new words and 60 old words. Subjects were instructed to respond whether the word had been presented before ("old"; button #1), new ("new"; button #2), or no idea ("no idea"; button #3). For the main experimental session, none of the words were presented twice, and subjects were not exposed to the same experimental task more than once.

Data Acquisition and Analysis

ECoG and depth electrodes were recorded using a 64-channel digital video monitoring system (Telefactor Beehive Horizon with an AURA LTM 64- and 128-channel amplifier system; Natus Neurology, West Warwick, RI, United States) digitized at a sampling rate of 1,600 Hz and filtered from 0.1 to 150 Hz. These ECoG data were analyzed using MATLAB software (version 2015b, Mathworks, Natick, MA, United States). The depth electrode was implanted only in Subject 6, and it covered the temporal white matter. The depth electrode did not cover the region of interest in the present study, and we excluded the depth electrode from further analysis. We first performed manual artifact rejection of the signal for every electrode. Channels affected by artifacts were excluded from subsequent analyses. Individual stimulus response trials were marked and precluded if motion artifacts were present. Signals exhibiting motion artifacts and epileptic-form spikes were also marked and excluded from further analyses. The recorded data were re-referenced to the common average reference. To quantify specific changes in frequency bands during stimulation for the encoding period of the memory task, time-frequency analysis with Morlet wavelet transformation (wave number: 2.48) was applied to obtain a continuous-time complex value representation of the signal. The effective window length (95% confidence interval of the Gaussian kernel, seven cycles) was 80 ms at 50 Hz. Transformed data were squared to calculate the power value and normalized by the mean of the pre-stimulus baseline power (i.e., resting periods prior to the task) for each frequency. The resting periods prior to the memory task was 5-min duration, and it was equal to every subject. During the resting periods, the subjects were instructed to keep their eyes open, while fixating a white cross in the notebook. A fixation cross, on which subjects were instructed to focus their gaze, was presented to minimize eye movement. The electrophysiological data were divided into epochs that onset 1 s pre-stimulus and continued to 1 and 1.5 s of during stimulus from the onset of the word trials and sorted according to subsequent memory performance. The averaged power of each condition was compared across a frequency range of 30–150 Hz for correctly and incorrectly encoded memory items. Normalized data were averaged across all trials for correct and incorrect trials according to each condition. To test the significance between subsequently remembered and subsequently forgotten words at encoding, independent two-sample t-tests were performed.

Feature Selection

Figure 3 presents the selected features for each phase and frequency band. **Table 2** presents the t-statistic values and regions of the selected features. The most informative frequency values with the top 20% of t-statistics were selected as the features in each phase and frequency band.

Classification Problem

The classification problem was set up. Trials that were presented in the encoding phase were labeled according to the results of recognition phase. Remembered and forgotten were labeled. There were two labels: remembered and forgotten. The remembered class consisted of trials where the subjects pressed the buttons "Old" (old words correctly recognized as old), and the forgotten class consisted of trials where the subjected pressed the buttons "New" (old words incorrectly recognized as new). Since all subjects only responded as "old" and "new," we could not get "no idea" trials. Furthermore, new trials were not included to maximize the difference in encoding process. Sets of labeled trials were acquired from two different periods: pre- and during stimulus. These spectral classifier learned the power differences between the remembered and forgotten trials from the three separate time windows (i.e., −500 to stimulus onset, stimulus onset to 1 s, and stimulus onset to 1.5 s).

Classification

For classification between remembered and forgotten trials from low- and high-gamma band signals, features from the single-trial low- and high-gamma power (dashed line in **Figures 3A,B**) of all electrodes located in **Figures 3A,B** were first extracted. The *p*-values were then calculated by comparing the remembered and forgotten items. To confirm whether the features based on the HFA difference in the single-trial conditions represented their

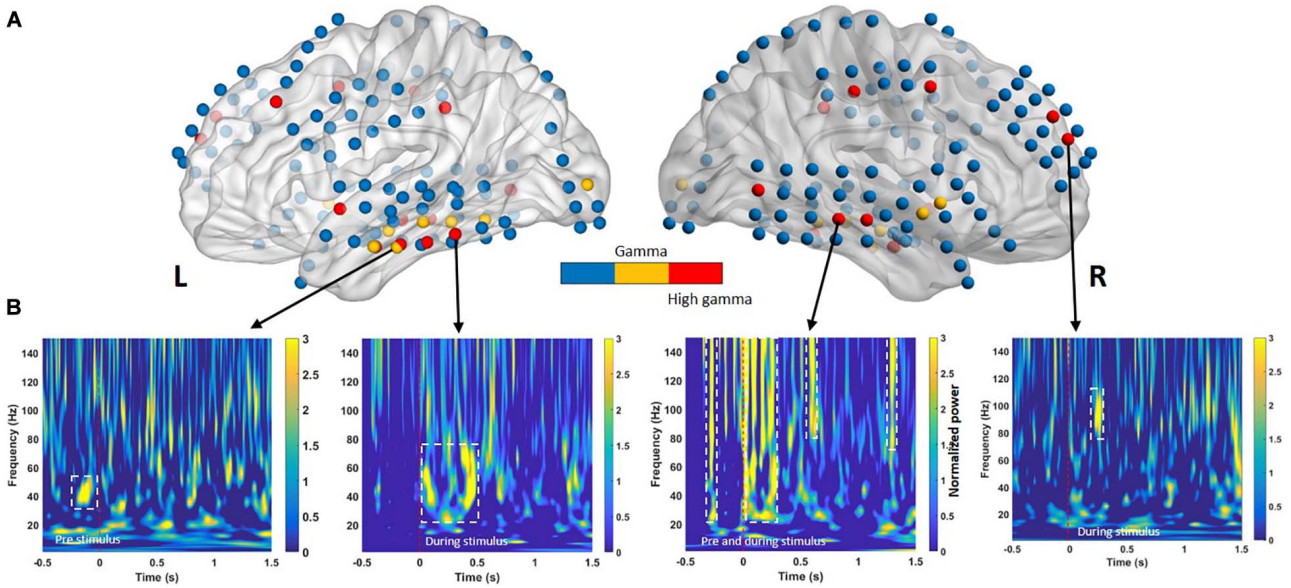

FIGURE 3 | (A) Electrodes in cortical regions exhibiting across-subject differences between successful memory encoding (SME) for the −0.5- to 1.5-s time bins. The color intensity indicates the direction of the effect (yellow = low gamma, red = high gamma) with a significance threshold of $p < 0.05$. Blue denotes regions that did not exhibit a significant effect among subjects. **(B)** Time course of significant oscillatory activity in SMEs for lateral temporal cortices from four individuals (Subject 1 to Subject 4, left to right, respectively). Each panel shows the *t*-transformed significance value of the difference in power between remembered and forgotten memories. The left and right temporal cortices both exhibit heightened low-gamma power (30–60 Hz) and high-gamma oscillation (∼150 Hz) increases during pre- and during-stimulus intervals in SME. The dashed white line indicates $p < 0.05$ significance threshold.

respective successful memory encoding (SME), simple linear SVM analyses were performed. The selected feature sets were entered into a supervised linear classification procedure using an SVM algorithm to assess whether subsequently remembered trials could differentiate subsequently forgotten trials. A data-driven feature-filtering step was performed before SVM learning. The most informative power with statistical significance was within the high-frequency power (low gamma, 30–60 Hz; high gamma, 60–150 Hz) as identified using the subsequent memory effect (SME) procedure in the encoding phase (Sederberg et al., 2007; van Vugt et al., 2010). The most informative power was selected as a candidate feature for SVM learning to identify the optimal classifier modified from a previous study (Jin and Chung, 2017). SVM group classification analyses were performed using the Statistics Toolbox in Matlab software (version R2018b; MathWorks Inc., Natick, MA, United States). The nonlinear radial basis function kernel (sigma = 2) and constant soft margin (cost = 1) were applied for the SVM training, as recommended previously, showing high gamma time features with an SVM model that classified individual words from a pair of words (Martin et al., 2016). In the SVM training procedure, the decision boundary formulated using a candidate feature set was optimized to maximize group classification accuracy using 80% of trials randomly selected from the total trials (Dosenbach et al., 2010). All SVM procedures, testing, and iterative group classifier performance evaluation (with random permutation of subjects into training and testing sets for cross-validation) were repeated 10,000 times per candidate feature set. The most accurate group classifier with the highest overall mean accuracy across the 10,000 cross-validation procedures was selected as the optimal SVM group classifier.

Statistical Analysis

Statistical tests were performed using the Statistical Package for Social Sciences v12.0 K (SPSS) and MATLAB (Mathworks). Our primary measurement of memory performance was the percentage of correctly recognized trials in each block. Paired non-parametric rank-sum tests were used to compare behavioral performance between conditions. For activity in the lateral temporal cortex, independent two-sample t-statistics ($^{**}p < 0.01$ or $^{*}p < 0.05$) were used to compare the average power amplitudes of ECoG waveforms between correctly and incorrectly recognized trials. Prior to significance testing, normality was assessed using the Lilliefors test ($p > 0.01$, for all datasets). For multiple comparisons among gamma power levels, the Bonferroni correction procedure was employed. The level of statistical significance was set at $p < 0.05$.

RESULTS

On average, subjects successfully remembered 81.19 ±5.79% (standard error of the mean; SEM) of the words, with a mean response time of 1,277.45 ± 315.28 ms (1,076.26 ±181.82 ms for remembered trials and 1,478.64 ± 475.34 ms for forgotten trials, $p > 0.05$). Full-scale IQ (FSIQ) and memory quotation (MQ) were measured in six subjects before electrode implantation as part of the routine clinical preoperative

TABLE 2 | Results of the t-test for the difference between the remembered and forgotten conditions.

Time	Band	Feature set	t-value
Pre-stimulus interval	Low gamma (30–60 Hz)	ITG (L)	2.828**
		MTG (R)	1.618*
		MTG (L)	1.315*
		STG (R)	2.358*
	High gamma (60–150 Hz)	ITG (R)	2.158**
		PFC (R)	1.785*
		MTG (R)	2.215**
		IPL (R)	1.582*
Time	**Band**	**Feature set**	**t-value**
During-stimulus interval	Low gamma (30–60 Hz)	ITG (L)	3.515*
		MTG (R)	2.357**
		MTG (L)	1.298**
		STG (R)	1.685*
	High gamma (60–150 Hz)	ITG (R)	2.553**
		PFC (R)	1.699*
		MTG (R)	2.288*
		IPL (R)	1.453*

*$p < 0.05$, **$p < 0.01$.
ITC, inferior temporal cortex; PFC, prefrontal cortex; IFG, inferior frontal gyrus; IPL, inferior parietal lobule; L, left; R, right.
The t-statistic values and regions of the selected features. The most informative frequency values with the top four ranked of t-statistics were selected as the features in each phase and frequency band. The pre-stimulus interval showed positive spectral SME in the low-gamma bands (i.e., 38–50, 35–48, 32–40, and 38–54 Hz, respectively) and in the high-gamma band (65–70, 81–90, 78–95, and 81–93 Hz, respectively). The during-stimulus interval showed positive spectral SME in the low-gamma (38–59, 35–54, 42–54, and 38–55 Hz) and high-gamma band (82–90, 78–150, 80–150, and 82–109 Hz, respect.

evaluation. Subjects had an average preoperative FSIQ of 83 ± 8 (mean ± SEM) and MQ of 85.6 ± 8.45. No significant correlations were observed between preoperative FSIQ and accuracy during the task ($r = -0.300$, $p = 0.624$, N = 5) ($r = -0.200$, $p = 0.747$, N = 5) across all sessions for each subject, suggesting that task performance was associated with normal psychometric measurements.

Temporal and Spectral Successful Memory Effects

Previous memory studies have compared signals during learning of visual items that are subsequently remembered to items that will be forgotten to assess differences in brain activity, yielding an outcome termed the SME. Positive and negative SMEs have been reported in different frequency bands (Hanslmayr et al., 2012). Interpretation of these effects suggests that the power increase for remembered items typically occurs in positive high-frequency SMEs (Sederberg et al., 2003; Burke et al., 2014, 2015). In our study, SMEs in the pre- and during-stimulus intervals were identified using the methods described in the *Classification* section. Oscillatory power in the pre- and during-stimulus intervals was examined separately for two nonoverlapping sub-bands (low gamma, 30–60 Hz; high gamma, 60–150 Hz). For a given sub-band, within-subject averages of the power difference between the remembered and forgotten trials were calculated for all electrode positions. An independent two-sample *t*-test was performed to identify differences in gamma power between the remembered and forgotten trials. Multiple comparisons confirmed that the during-stimulus period exhibited consistent positive spectral SME across subjects in the low- and high-gamma bands in the left and right temporal cortical electrodes, as shown in **Figure 3B**.

Predictive Performance of Pre- and During-Stimulus Intervals

We next evaluated the type of ECoG signals that contributed to memory performance prediction. ECoG signals from the two different intervals were considered separately as input from all electrodes for the classification of statistical differences in gamma power from left to right hemispheres (**Figure 3A**; yellow and red dots, respectively). Performance during the pre-stimulus interval (−0.5 to 0 s) was compared with that for the first and second during-stimulus epochs (0–1 and 0–1.5 s, respectively) (**Table 3**), revealing the predictive accuracy and final included number of trials for each participant. The optimal SVM group classifier with the top 10 ranked features among the 20 significantly different frequency bands according to the averaged *t*-statistics distinguished correct versus incorrect trials. The overall predictive performance with pre-stimulus signals was 78.5% (averaged over six subjects) (**Figure 4A**) and that of the during-stimulus intervals was approximately 88.5% (**Figure 4B**) and 85.5% for the first and second epochs, respectively (averaged over six subjects). The accuracy of each subject was significantly greater than chance levels (50%) for the entire period. Compared with the average accuracy using the pre-stimulus interval of ECoG data, the average accuracy using the first epoch of the during-stimulus interval increased to 88.5%, which was similar to that for the second epoch of the during-stimulus interval.

Comparison With Other Approaches

Four other approaches were implemented and tested on the outperformed data set of the during-stimulus interval (0–1 s) using the same experimental protocols for comparison. As shown

TABLE 3 | Prediction accuracy using two different periods of during stimulus.

Subject	Pre-stimulus interval	During-stimulus interval		# trials (REM/FOR)
	−0.5 to 0 s	0 to 1 s	0 to 1.5 s	
Sub1	80	91	80	45/10
Sub2	78	95	96	41/11
Sub3	97	81	97	40/16
Sub4	66	95	70	36/9
Sub5	84	97	84	49/9
Sub6	66	72	86	48/5
Average	78.5 (10.7)	88.5 (9.05)	85.5 (9.27)	43/10

The mean scores given by high-frequency power spectral classifiers trained from the pre- and two during-stimulus intervals in each subject. Overall accuracy given in the last row are the accuracies over all subjects considered for classification. REM, remembered; FOR, forgotten.

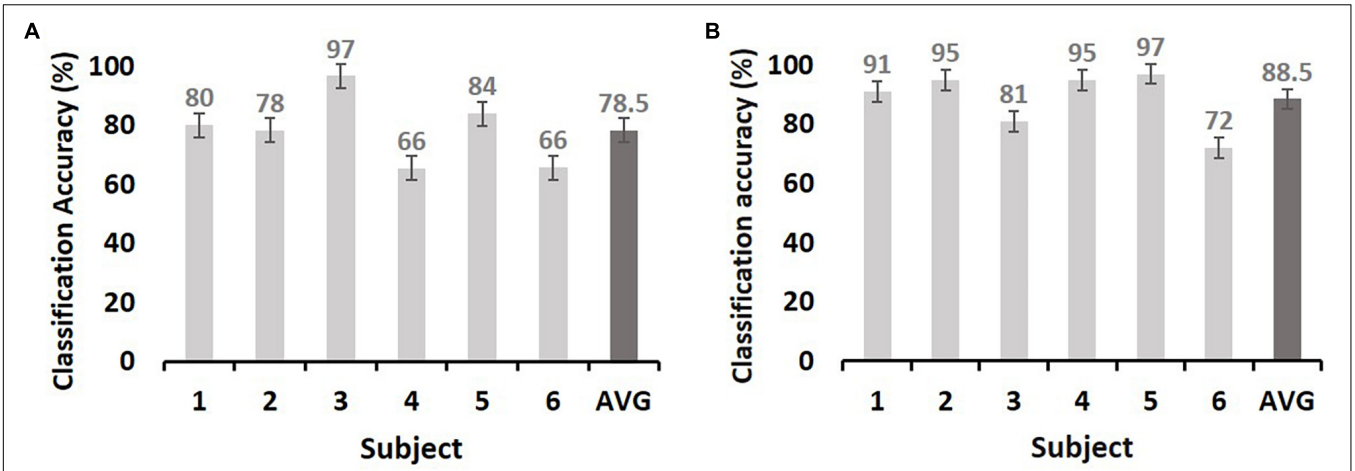

FIGURE 4 | The maximum accuracy of successful memory classification by simple SVM using the pre-stimulus interval [**(A):** −0.5–0 s] and during-stimulus interval [**(B)**: 0–1 s]. The x-axis indicates subjects, and y-axis indicates the classification accuracy (%). The chance level is 50% (dashed line). The dark gray bars in both **(A)** and **(B)** indicate the average accuracy. Error bars indicate the standard error of the mean.

in **Supplementary Table 1**, two different classifiers performed over chance level predictions. Among these approaches, SVM achieved higher accuracy but was similar to linear discriminant analysis (LDA) and Fisher linear discriminant analysis (FLDA), which are effective methods that classify features with linear separability.

DISCUSSION

This study demonstrated that neocortical HFA (i.e., gamma power) predicted successful memory encoding, with average prediction accuracies of 78.5 and 88.5% for the pre-stimulus and during-stimulus intervals, respectively. The prediction rate improved by 10% when using during-stimulus intervals from the pre-stimulus interval. The majority of above-chance predictions were associated with activity in lateral temporal cortical regions, suggesting that cortical HFA values predict memory encoding.

To date, there have been no studies comparing data from pre- and during-stimulus intervals to predict subsequent memory formation using cortical ECoG activity. In accordance with our findings, several scalp EEG studies have demonstrated that pre- or during-stimulus electrophysiological brain activity predicted memory formation or subsequent memory. For instance, both neural signals before (Otten et al., 2010) and during an event (Sun et al., 2016) enabled the distinction of remembered events from forgotten ones. Indeed, by combining information from pre- and during-stimulus periods with single-trial-based classification methods, high-resolution surface EEG recordings predicted subsequent memory (Noh et al., 2014).

This is the first study to demonstrate the efficacy of HFA in cortical regions for memory prediction. Our data revealed specific gamma activity from different sub-bands (low gamma, 30–60 Hz; high gamma, 60–150 Hz) depending on cortical region during the 200–300 ms after stimulus presentation or later, which typically indicates induced activity (Basar-Eroglu et al., 1996; Tallon-Baudry et al., 1998). Studies have demonstrated that HFA may play a role in encoding information. A previous study reported an increase in gamma power (20–80 Hz) in subjects performing a visual delayed-matching-to-sample task while memorizing information, particularly in the occipitotemporal and frontal regions (Tallon-Baudry et al., 1998). In fMRI studies, the positive gamma SME in lateral temporal regions mirrors the localization of the positive SME (Wagner et al., 1998; Davachi et al., 2001; Reber et al., 2002). Similar to our findings, iEEG recordings of subjects during the encoding of a verbal noun memory task revealed that gamma oscillations (44–64 Hz) in the left temporal and frontal cortices predicted successful encoding of new verbal memory (Sederberg et al., 2007).

The majority of significant HFA during pre- and during-stimulus periods was observed in the lateral temporal cortices. The functional relevance of lateral temporal cortical activity in memory formation is unclear. The lateral temporal cortical regions play a functional role in memory formation, as this is a critical region in episodic memory processing (Chao et al., 1999). In humans, neuronal activity in the lateral temporal cortex subserves the encoding of verbal material networks (Ojemann and Schoenfield-McNeill, 1998; Ojemann et al., 2002, 2009). Previous functional imaging studies support temporal changes in cortical activity during the encoding stage of explicit verbal memory (Casasanto et al., 2002; Fletcher and Tyler, 2002). In line with this, a recent direct human brain stimulation study demonstrated causality between the direct stimulation of the lateral temporal cortices and verbal memory encoding (Kucewicz et al., 2018). Our recent hippocampal stimulation study also revealed that successful memory encoding involves the temporal cortex, which may act in concert with the hippocampus (Jun et al., 2019). Collectively, these findings suggest that the lateral cortex supports the functional connectivity underpinning memory formation.

The present study demonstrated that the pre- and during-stimulus brain activity in the lateral cortex could be used

to distinguish subsequently remembered trials from forgotten trials. This indicates that the characterized high-frequency neural correlates of the lateral temporal cortex can predict subsequent memory. In this regard, investigating neural high-frequency oscillatory changes in memory-related temporal neocortical regions that modulate memory processes may provide insight into our understanding of the neural basis of episodic memory.

DATA AVAILABILITY STATEMENT

The datasets generated for this study are available on request to the corresponding author.

ETHICS STATEMENT

The studies involving human participants were reviewed and approved by Seoul National University Hospital. The patients/participants provided their written informed consent to participate in this study.

AUTHOR CONTRIBUTIONS

SJ, JK, and CC contributed to the study design and wrote the article. SJ and CC performed the study. SJ and JK analyzed the data. JK and CC obtained funding. All authors contributed to the article and approved the submitted version.

FUNDING

This research was supported by a grant (2018M3C7A1022317, 2021R1A4A2001803, and 2020R1A6A3A01100654) of the Basic Science Research Program through the National Research Foundation (NRF) funded by the Ministry of Science & ICT, Republic of Korea.

SUPPLEMENTARY MATERIAL

The Supplementary Material for this article can be found online at: https://www.frontiersin.org/articles/10.3389/fnins.2021.517316/full#supplementary-material

REFERENCES

Anastassiou, C. A., Montgomery, S. M., Barahona, M., Buzsaki, G., and Koch, C. (2010). The effect of spatially inhomogeneous extracellular electric fields on neurons. *J. Neurosci.* 30, 1925–1936. doi: 10.1523/JNEUROSCI.3635-09.2010

Avants, B. B., Epstein, C. L., Grossman, M., and Gee, J. C. (2008). Symmetric diffeomorphic image registration with cross-correlation: evaluating automated labeling of elderly and neurodegenerative brain. *Med. Image Anal.* 12, 26–41. doi: 10.1016/j.media.2007.06.004

Axmacher, N., Schmitz, D. P., Weinreich, I., Elger, C. E., and Fell, J. (2008). Interaction of working memory and long-term memory in the medial temporal lobe. *Cereb. Cortex* 18, 2868–2878. doi: 10.1093/cercor/bhn045

Basar-Eroglu, C., Struber, D., Schurmann, M., Stadler, M., and Basar, E. (1996). Gamma-band responses in the brain: a short review of psychophysiological correlates and functional significance. *Int. J. Psychophysiol.* 24, 101–112. doi: 10.1016/s0167-8760(96)00051-7

Benchenane, K., Peyrache, A., Khamassi, M., Tierney, P. L., Gioanni, Y., Battaglia, F. P., et al. (2010). Coherent theta oscillations and reorganization of spike timing in the hippocampal- prefrontal network upon learning. *Neuron* 66, 921–936. doi: 10.1016/j.neuron.2010.05.013

Burke, J. F., Long, N. M., Zaghloul, K. A., Sharan, A. D., Sperling, M. R., and Kahana, M. J. (2014). Human intracranial high-frequency activity maps episodic memory formation in space and time. *Neuroimage* 85(Pt 2), 834–843. doi: 10.1016/j.neuroimage.2013.06.067

Burke, J. F., Ramayya, A. G., and Kahana, M. J. (2015). Human intracranial high-frequency activity during memory processing: neural oscillations or stochastic volatility? *Curr. Opin. Neurobiol.* 31, 104–110. doi: 10.1016/j.conb.2014.09.003

Buzsaki, G. (1996). The hippocampo-neocortical dialogue. *Cereb. Cortex* 6, 81–92.

Buzsaki, G., and Silva, F. L. (2012). High frequency oscillations in the intact brain. *Prog. Neurobiol.* 98, 241–249. doi: 10.1016/j.pneurobio.2012.02.004

Casasanto, D. J., Killgore, W. D., Maldjian, J. A., Glosser, G., Alsop, D. C., Cooke, A. M., et al. (2002). Neural correlates of successful and unsuccessful verbal memory encoding. *Brain Lang.* 80, 287–295. doi: 10.1006/brln.2001.2584

Chadwick, M. J., Hassabis, D., Weiskopf, N., and Maguire, E. A. (2010). Decoding individual episodic memory traces in the human hippocampus. *Curr. Biol.* 20, 544–547. doi: 10.1016/j.cub.2010.01.053

Chao, L. L., Haxby, J. V., and Martin, A. (1999). Attribute-based neural substrates in temporal cortex for perceiving and knowing about objects. *Nat. Neurosci.* 2, 913–919. doi: 10.1038/13217

Colgin, L. L., Denninger, T., Fyhn, M., Hafting, T., Bonnevie, T., Jensen, O., et al. (2009). Frequency of gamma oscillations routes flow of information in the hippocampus. *Nature* 462, 353–357. doi: 10.1038/nature08573

Davachi, L., Maril, A., and Wagner, A. D. (2001). When keeping in mind supports later bringing to mind: neural markers of phonological rehearsal predict subsequent remembering. *J. Cogn. Neurosci.* 13, 1059–1070. doi: 10.1162/089892901753294356

de Vanssay-Maigne, A., Noulhiane, M., Devauchelle, A. D., Rodrigo, S., Baudoin-Chial, S., Meder, J. F., et al. (2011). Modulation of encoding and retrieval by recollection and familiarity: mapping the medial temporal lobe networks. *Neuroimage* 58, 1131–1138. doi: 10.1016/j.neuroimage.2011.06.086

Dosenbach, N. U., Nardos, B., Cohen, A. L., Fair, D. A., Power, J. D., Church, J. A., et al. (2010). Prediction of individual brain maturity using fMRI. *Science* 329, 1358–1361. doi: 10.1126/science.1194144

Duzel, E., Penny, W. D., and Burgess, N. (2010). Brain oscillations and memory. *Curr. Opin. Neurobiol.* 20, 143–149. doi: 10.1016/j.conb.2010.01.004

Eichenbaum, H. (2000). A cortical-hippocampal system for declarative memory. *Nat. Rev. Neurosci.* 1, 41–50. doi: 10.1038/35036213

Ezzyat, Y., Kragel, J. E., Burke, J. F., Levy, D. F., Lyalenko, A., Wanda, P., et al. (2017). Direct brain stimulation modulates encoding states and memory performance in humans. *Curr. Biol.* 27, 1251–1258. doi: 10.1016/j.cub.2017.03.028

Fell, J., Ludowig, E., Rosburg, T., Axmacher, N., and Elger, C. E. (2008). Phase-locking within human mediotemporal lobe predicts memory formation. *Neuroimage* 43, 410–419. doi: 10.1016/j.neuroimage.2008.07.021

Fell, J., Ludowig, E., Staresina, B. P., Wagner, T., Kranz, T., Elger, C. E., et al. (2011). Medial temporal theta/alpha power enhancement precedes successful memory encoding: evidence based on intracranial EEG. *J. Neurosci.* 31, 5392–5397. doi: 10.1523/JNEUROSCI.3668-10.2011

Fletcher, P., and Tyler, L. (2002). Neural correlates of human memory. *Nat. Neurosci.* 5, 8–9. doi: 10.1038/nn0102-8

Hamani, C., McAndrews, M. P., Cohn, M., Oh, M., Zumsteg, D., Shapiro, C. M., et al. (2008). Memory enhancement induced by hypothalamic/fornix deep brain stimulation. *Ann. Neurol.* 63, 119–123. doi: 10.1002/ana.21295

Hanslmayr, S., Staudigl, T., and Fellner, M. C. (2012). Oscillatory power decreases and long-term memory: the information via desynchronization hypothesis. *Front. Hum. Neurosci.* 6:74. doi: 10.3389/fnhum.2012.00074

Hohne, M., Jahanbekam, A., Bauckhage, C., Axmacher, N., and Fell, J. (2016). Prediction of successful memory encoding based on single-trial rhinal and

hippocampal phase information. *Neuroimage* 139, 127–135. doi: 10.1016/j.neuroimage.2016.06.021

Jensen, O., Kaiser, J., and Lachaux, J. P. (2007). Human gamma-frequency oscillations associated with attention and memory. *Trends Neurosci.* 30, 317–324. doi: 10.1016/j.tins.2007.05.001

Jin, S. H., and Chung, C. K. (2017). Electrophysiological resting-state biomarker for diagnosing mesial temporal lobe epilepsy with hippocampal sclerosis. *Epilepsy Res.* 129, 138–145. doi: 10.1016/j.eplepsyres.2016.11.018

Johnson, E. L., and Knight, R. T. (2015). Intracranial recordings and human memory. *Curr. Opin. Neurobiol.* 31, 18–25. doi: 10.1016/j.conb.2014.07.021

Jun, S., Kim, J. S., and Chung, C. K. (2019). Direct stimulation of human hippocampus during verbal associative encoding enhances subsequent memory recollection. *Front. Hum. Neurosci.* 13:23. doi: 10.3389/fnhum.2019.00023

Jun, S., Lee, S. A., Kim, J. S., Jeong, W., and Chung, C. K. (2020). Task-dependent effects of intracranial hippocampal stimulation on human memory and hippocampal theta power. *Brain Stimul.* 13, 603–613. doi: 10.1016/j.brs.2020.01.013

Kahana, M. J. (2006). The cognitive correlates of human brain oscillations. *J. Neurosci.* 26, 1669–1672. doi: 10.1523/JNEUROSCI.3737-05c.2006

Kim, H., Daselaar, S. M., and Cabeza, R. (2010). Overlapping brain activity between episodic memory encoding and retrieval: roles of the task-positive and task-negative networks. *Neuroimage* 49, 1045–1054. doi: 10.1016/j.neuroimage.2009.07.058

Kim, H. S. (2005). *Modern Korean Words version 2*. 780p National Institute of Korean Language.

Kucewicz, M. T., Berry, B. M., Kremen, V., Brinkmann, B. H., Sperling, M. R., Jobst, B. C., et al. (2017). Dissecting gamma frequency activity during human memory processing. *Brain* 140, 1337–1350. doi: 10.1093/brain/awx043

Kucewicz, M. T., Berry, B. M., Miller, L. R., Khadjevand, F., Ezzyat, Y., Stein, J. M., et al. (2018). Evidence for verbal memory enhancement with electrical brain stimulation in the lateral temporal cortex. *Brain* 141, 971–978. doi: 10.1093/brain/awx373

Lachaux, J. P., Axmacher, N., Mormann, F., Halgren, E., and Crone, N. E. (2012). High-frequency neural activity and human cognition: past, present and possible future of intracranial EEG research. *Prog. Neurobiol.* 98, 279–301. doi: 10.1016/j.pneurobio.2012.06.008

Manning, J. R., Jacobs, J., Fried, I., and Kahana, M. J. (2009). Broadband shifts in local field potential power spectra are correlated with single-neuron spiking in humans. *J. Neurosci.* 29, 13613–13620. doi: 10.1523/JNEUROSCI.2041-09.2009

Martin, S., Brunner, P., Iturrate, I., Millan Jdel, R., Schalk, G., Knight, R. T., et al. (2016). Word pair classification during imagined speech using direct brain recordings. *Sci. Rep.* 6:25803. doi: 10.1038/srep25803

Miller, K. J., Shenoy, P., den Nijs, M., Sorensen, L. B., Rao, R. N., and Ojemann, J. G. (2008). Beyond the gamma band: the role of high-frequency features in movement classification. *IEEE Trans. Biomed. Eng.* 55, 1634–1637. doi: 10.1109/TBME.2008.918569

Milstein, J., Mormann, F., Fried, I., and Koch, C. (2009). Neuronal shot noise and Brownian 1/f2 behavior in the local field potential. *PLoS One* 4:e4338. doi: 10.1371/journal.pone.0004338

Moscovitch, M., Cabeza, R., Winocur, G., and Nadel, L. (2016). Episodic memory and beyond: the hippocampus and neocortex in transformation. *Annu. Rev. Psychol.* 67, 105–134. doi: 10.1146/annurev-psych-113011-143733

Noh, E., Herzmann, G., Curran, T., and de Sa, V. R. (2014). Using single-trial EEG to predict and analyze subsequent memory. *Neuroimage* 84, 712–723. doi: 10.1016/j.neuroimage.2013.09.028

Ojemann, G. A., and Schoenfield-McNeill, J. (1998). Neurons in human temporal cortex active with verbal associative learning. *Brain Lang.* 64, 317–327. doi: 10.1006/brln.1998.1982

Ojemann, G. A., Schoenfield-McNeill, J., and Corina, D. (2009). The roles of human lateral temporal cortical neuronal activity in recent verbal memory encoding. *Cereb. Cortex* 19, 197–205. doi: 10.1093/cercor/bhn071

Ojemann, G. A., Schoenfield-McNeill, J., and Corina, D. P. (2002). Anatomic subdivisions in human temporal cortical neuronal activity related to recent verbal memory. *Nat. Neurosci.* 5, 64–71. doi: 10.1038/nn785

Otten, L. J., Quayle, A. H., and Puvaneswaran, B. (2010). Prestimulus subsequent memory effects for auditory and visual events. *J. Cogn. Neurosci.* 22, 1212–1223. doi: 10.1162/jocn.2009.21298

Poldrack, R. A., Clark, J., Pare-Blagoev, E. J., Shohamy, D., Creso Moyano, J., Myers, C., et al. (2001). Interactive memory systems in the human brain. *Nature* 414, 546–550. doi: 10.1038/35107080

Ray, S., and Maunsell, J. H. (2011). Different origins of gamma rhythm and high-gamma activity in macaque visual cortex. *PLoS Biol.* 9:e1000610. doi: 10.1371/journal.pbio.1000610

Reber, P. J., Siwiec, R. M., Gitelman, D. R., Parrish, T. B., Mesulam, M. M., and Paller, K. A. (2002). Neural correlates of successful encoding identified using functional magnetic resonance imaging. *J. Neurosci.* 22, 9541–9548.

Rhee, K. Y. (1991). Korean category norms: survey on exemplar frequency norm, typicality, and features. *Korean J. Exp. Cogn. Psychol.* 3, 131–160.

Ritchey, M., Libby, L. A., and Ranganath, C. (2015). Cortico-hippocampal systems involved in memory and cognition: the PMAT framework. *Prog. Brain Res.* 219, 45–64. doi: 10.1016/bs.pbr.2015.04.001

Sederberg, P. B., Kahana, M. J., Howard, M. W., Donner, E. J., and Madsen, J. R. (2003). Theta and gamma oscillations during encoding predict subsequent recall. *J. Neurosci.* 23, 10809–10814.

Sederberg, P. B., Schulze-Bonhage, A., Madsen, J. R., Bromfield, E. B., McCarthy, D. C., Brandt, A., et al. (2007). Hippocampal and neocortical gamma oscillations predict memory formation in humans. *Cereb. Cortex* 17, 1190–1196. doi: 10.1093/cercor/bhl030

Shenoy, P., Miller, K. J., Ojemann, J. G., and Rao, R. P. (2008). Generalized features for electrocorticographic BCIs. *IEEE Trans. Biomed. Eng.* 55, 273–280. doi: 10.1109/TBME.2007.903528

Sun, X., Qian, C., Chen, Z., Wu, Z., Luo, B., and Pan, G. (2016). Remembered or forgotten?-An EEG-based computational prediction approach. *PLoS One* 11:e0167497. doi: 10.1371/journal.pone.0167497

Tallon-Baudry, C., Bertrand, O., Peronnet, F., and Pernier, J. (1998). Induced gamma-band activity during the delay of a visual short-term memory task in humans. *J. Neurosci.* 18, 4244–4254.

van Vugt, M. K., Schulze-Bonhage, A., Litt, B., Brandt, A., and Kahana, M. J. (2010). Hippocampal gamma oscillations increase with memory load. *J. Neurosci.* 30, 2694–2699. doi: 10.1523/JNEUROSCI.0567-09.2010

Wagner, A. D., Schacter, D. L., Rotte, M., Koutstaal, W., Maril, A., Dale, A. M., et al. (1998). Building memories: remembering and forgetting of verbal experiences as predicted by brain activity. *Science* 281, 1188–1191. doi: 10.1126/science.281.5380.1188

Watrous, A. J., Tandon, N., Conner, C. R., Pieters, T., and Ekstrom, A. D. (2013). Frequency-specific network connectivity increases underlie accurate spatiotemporal memory retrieval. *Nat. Neurosci.* 16, 349–356. doi: 10.1038/nn.3315

Xia, M., Wang, J., and He, Y. (2013). BrainNet viewer: a network visualization tool for human brain connectomics. *PLoS One* 8:e68910. doi: 10.1371/journal.pone.0068910

Conflict of Interest: The authors declare that the research was conducted in the absence of any commercial or financial relationships that could be construed as a potential conflict of interest.

frontiers in Neuroscience

ORIGINAL RESEARCH
published: 02 July 2021
doi: 10.3389/fnins.2021.683784

Optimization of Task Allocation for Collaborative Brain–Computer Interface Based on Motor Imagery

Bin Gu[1†], Minpeng Xu[1,2†], Lichao Xu[2], Long Chen[2], Yufeng Ke[2], Kun Wang[2], Jiabei Tang[1] and Dong Ming[1,2]*

[1] Neural Engineering & Rehabilitation Laboratory, Department of Biomedical Engineering, College of Precision Instruments and Optoelectronics Engineering, Tianjin University, Tianjin, China, [2] Academy of Medical Engineering and Translational Medicine, Tianjin University, Tianjin, China

Objective: Collaborative brain–computer interfaces (cBCIs) can make the BCI output more credible by jointly decoding concurrent brain signals from multiple collaborators. Current cBCI systems usually require all collaborators to execute the same mental tasks (common-work strategy). However, it is still unclear whether the system performance will be improved by assigning different tasks to collaborators (division-of-work strategy) while keeping the total tasks unchanged. Therefore, we studied a task allocation scheme of division-of-work and compared the corresponding classification accuracies with common-work strategy's.

Approach: This study developed an electroencephalograph (EEG)-based cBCI which had six instructions related to six different motor imagery tasks (MI-cBCI), respectively. For the common-work strategy, all five subjects as a group had the same whole instruction set and they were required to conduct the same instruction at a time. For the division-of-work strategy, every subject's instruction set was a subset of the whole one and different from each other. However, their union set was equal to the whole set. Based on the number of instructions in a subset, we divided the division-of-work strategy into four types, called "2 Tasks" … "5 Tasks." To verify the effectiveness of these strategies, we employed EEG data collected from 19 subjects who independently performed six types of MI tasks to conduct the pseudo-online classification of MI-cBCI.

Main results: Taking the number of tasks performed by one collaborator as the horizontal axis (two to six), the classification accuracy curve of MI-cBCI was mountain-like. The curve reached its peak at "4 Tasks," which means each subset contained four instructions. It outperformed the common-work strategy ("6 Tasks") in classification accuracy (**72.29** ± **4.43** vs. 58.53 ± 4.36%).

Significance: The results demonstrate that our proposed task allocation strategy effectively enhanced the cBCI classification performance and reduced the individual workload.

Keywords: collaborative brain-computer interfaces, task allocation, division-of-work, common-work, motor imagery

OPEN ACCESS

Edited by:
Alessandro Vato, National Center for Adaptive Neurotechnologies, United States

Reviewed by:
Mario Ortiz, Miguel Hernández University of Elche, Spain
Jing Jin, East China University of Science and Technology, China

***Correspondence:**
Dong Ming
richardming@tju.edu.cn

[†] These authors have contributed equally to this work

Specialty section:
This article was submitted to Neuroprosthetics, a section of the journal Frontiers in Neuroscience

Received: *22 March 2021*
Accepted: *31 May 2021*
Published: *02 July 2021*

Citation:
Gu B, Xu M, Xu L, Chen L, Ke Y, Wang K, Tang J and Ming D (2021) Optimization of Task Allocation for Collaborative Brain–Computer Interface Based on Motor Imagery. Front. Neurosci. 15:683784. doi: 10.3389/fnins.2021.683784

INTRODUCTION

Brain–computer interface (BCI) systems could use human brain signals for the direct control of external devices (Wang and Jung, 2011; Jiang et al., 2018). Compared with other ways of human machine interaction (HCI), such as voice or gesture (Karpov and Yusupov, 2018), BCI systems have the potential to provide more efficient HCI channels by encoding brain signals directly. It could express intended human actions and monitor human physiological states by detecting and analyzing neural activity. Brain–computer interface systems can be differentiated based on the brain-sensing modality employed, such as functional magnetic resonance imaging (fMRI) (Sokunbi et al., 2014), near infra-red spectroscopy (NIRS) (Naseer and Hong, 2015), and electroencephalography (EEG) (Abiri et al., 2019). Each of these modalities has certain advantages, which render it more suitable for specific applications. Due to the high time resolution and portability of EEG-based BCI, it is usually employed in the control of external devices (Luu et al., 2017; McCrimmon et al., 2018).

For control purposes, it can be divided into two types: (A) active BCI systems that do not require external stimuli which only use consciously intended brain signals. Motor imagery BCI (MI-BCI) is one of the mature representatives (Vourvopoulos et al., 2019; Zapała et al., 2020). (B) Reactive BCI systems are driven by indirectly modulated brain signals related to specific exxternal stimulation, such as steady-state visually evoked potential BCI (SSVEP-BCI) (Ma et al., 2017). However, most of them have not been widely used so far in social and productive activities mainly due to the following two reasons:

(1) Low information transmission rate: due to volume conduction effects of the brain, the EEG signal-to-noise ratio is relatively low (Liu, 2019; Wei et al., 2019). Hence, EEG-based BCI systems are generally incapable of extracting sufficiently effective neural features in a short time window, which results in poor decoding performance. On the other hand, for a high level of human–computer hybrid intelligence, elaborate control operations with high precision, short time delays, and long-term reliability are needed. These performance requirements are hardly met by current EEG-based BCI systems.
(2) Poor interpersonal collaboration: currently, the majority of BCI systems are designed for a single user, which are hard to meet the demands of social interactions and the large-scale collaboration of social groups. Human social interactions suggest that BCI systems should involve forms of collaboration with multiple persons and computers (Mattout, 2012).

To overcome the above limitations, collaborative BCI (cBCI) systems have been proposed. It is defined as BCIs where data from multiple users are integrated to achieve a common purpose (Valeriani et al., 2017). The classification performance and robustness could be effectively improved by fusing group EEG features. Therefore, cBCI systems are more suitable for advanced tasks of hybrid human–computer intelligence, especially group interactions (Valeriani et al., 2015).

Current cBCI systems can be divided into two categories based on their goals. One kind of cBCI systems is utilized to perform visual target matching or search tasks, which seeks to improve the system decision-making ability based on human visual information (Matran-Fernandez and Poli, 2014; Valeriani et al., 2015, 2017). The other kind of cBCI systems focuses on the output by movement intentions, which can carry out active control instructions much faster and more conveniently (Wang and Jung, 2011; Zhou et al., 2019). These studies show that BCI performance can be effectively improved by fusing the neural responses of multiple users for the same task. However, they did not explore how to design a better system architecture to achieve more efficient fusion of multiple sources of human brain information. We believe that two improvements are of vital importance in optimizing system design:

(1) Task allocation strategy: for existing cBCI systems, collaborators follow a common-work strategy, i.e., users perform the same task together. Nevertheless, this strategy does not fully consider the rationality of task allocation and the differences in individual capabilities. It may result in wasteful use of collaborative resources, without effectively improving the overall performance. By contrast, group performance might be improved through division-of-work strategy. In fact, Adam Smith, one of the key founders of free-market economics, suggested in his book "The Wealth of Nations" (Smith, 1848) that division-of-work greatly improves labor productivity. Hence, we designed the cBCI system with an optimizing task allocation strategy of division-of-work, in order to enhance the overall system performance and reduce the individual workload as well.
(2) Data-fusing method: Wang and Jung (2011) presented two paradigms of cBCI—centralized and distributed systems. The biggest distinction between the two is whether the brain information of multiple persons is processed centrally on one data server (centralization) or not (distribution). Different paradigms dictate distinct requirements of data fusion methods. Thus, we designed a *feature fusion method* for centralized paradigm which conducts unified modeling and recognition through integrating the EEG features of all collaborators. Besides, a *decision fusion method* was developed to compute an overall decision value of classification in the distributed paradigm. For the classification performance of cBCI, a comparison was undertaken between the two methods under multiple strategies of task allocation in this work.

Motor imagery is the mental representation of movement without any body movement (Dickstein and Deutsch, 2007). In our previous research (Zhou et al., 2019), a MI-cBCI system was successfully implemented by decoding event-related de-/synchronization (ERD/ERS) features from multiusers. This study still adopted the motor imagery paradigm, which is suitable for active control. Through the pseudo-online process of MI-cBCI, we explored the impact of two key factors: (1)

TABLE 1 | Categories of motor imagery instructions for the MI-cBCI system.

Name	Both hands	Both feet	Left hand	Right hand	Right hand left foot	Left hand right foot
Abbreviation	BH	BF	LH	RH	RHLF	LHRF
Diagram						
Symbol	↑	↓	←	→	↗	↘
No.	1	2	3	4	5	6

task allocation strategy and (2) data fusion method on system classification performance.

MATERIALS AND METHODS

Subjects

The study involved 19 healthy volunteering subjects (11 females, 23–27 years). None of these participants had cognitive or physical dysfunction. Nine subjects had previously participated in MI-BCI studies. The rest of the subjects had no BCI experience prior to this study. All participants read and signed the informed consent form approved by the Institutional Research Ethics Committee of Tianjin People's Hospital before the experiment.

Paradigm Design

In this study, we aim to address the problem of classifying six types of motor imagery instructions, namely, moving both hands (BH), both feet (BF), the left hand (LH), the right hand (RH), the right hand and the left foot (RHLF), and finally the left hand and the right foot (LHRF). **Table 1** shows the details for these categories. For example, the name of the first type is "both hands." Participants were required to perform MI of both wrist extensions. The command abbreviation is BH, the symbol is ↑ and the instruction number is 1. The motion associated with the foot task is ankle dorsiflexion.

All 19 subjects independently performed the above six types of motor imagery tasks with EEG data collected simultaneously. Then, the MI-cBCI system based on the division-of-work strategy was simulated by using offline EEG data from users. The whole experiment for a single subject was divided into 14 blocks, consisting of 36 trials (6 types × 6 trials) each, which led to 84 trials of each type of MI task. There was a break of about 5 min between the consecutive three blocks. Within each block, MI tasks were performed in a random order. The task paradigm is shown in **Figure 1**, which mainly includes a period of motor imagery that lasts 4 s. The experiment was programmed using Psychtoolbox on MATLAB platform.

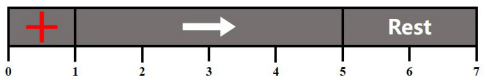

FIGURE 1 | Experimental paradigm of a motor imagery task. At the beginning of each trial, a red fixation cross was presented at the center of the screen to remind subjects to prepare for the following task. At the first second, a symbol of instruction appeared on the screen for 4 s, subjects were instructed to perform the indicated motor imagery (MI) task up to the fifth second. This time period of 4 s was defined as a MI epoch. Then, "Rest" was displayed for 2 s to remind participants to have a rest.

Data Acquisition and Preprocessing

The EEG signal was recorded using a SynAmps2 system (Neuroscan Inc., Charlotte, NC, United States) with a 64-channel quick-cap at a sampling rate of 1,000 Hz, whose electrode positioning follows the international 10/20 system. The reference and ground electrode were placed at the vertex and on the prefrontal lobe, respectively. A band-pass filter between 0.5 and 100 Hz and a 50-Hz notch filter were enabled during the data acquisition. All raw data were downsampled to 200 Hz and re-referenced by the common average reference (CAR). According to data labels, the EEG data of all trials were extracted as data samples. Then, data samples were band-pass filtered to obtain interested frequency (8–28 Hz) by a fourth-order Butterworth filter. All 84 samples of each class of MI are divided into two parts randomly. One part is for offline training, including 72 samples, and the other part includes 12 samples for the pseudo-online classification of cBCI.

Algorithms

All the main algorithms applied in this study are described here, in order to avoid disrupting the continuity of the introduction of the overall workflow. The preprocessed EEG data collected from the motor imagery tasks were analyzed in the succeeding sections.

Event-Related Spectral Perturbation

Event-related spectral perturbation can provide detailed information about temporal and spatial ERD/ERS features of various MI categories (Yi et al., 2017). It is a useful tool to select the MI task with stronger feature separability from six instructions as the reference instruction, rather than for classification. The average event-related spectral perturbation (ERSP) across the input data is defined as follows:

$$\mathrm{ERSP}\left(f,t\right) = \frac{1}{n}\sum_{k=1}^{n}\left(F_k\left(f,t\right)^2\right) \quad (1)$$

where n is the number of trials, and $F_k(f, t)$ indicates the spectral estimation of the kth trial at frequency f and time t. To produce the baseline-normalized ERSP, the spectral estimation of a baseline period (1 s before the MI epoch) is subtracted from the ERSP of tasks. To observe time–frequency domain features, plots of the mean ERSP from two key electrodes C3 and C4 were displayed from -1 to 6 s between 8 and 28 Hz for analysis. To investigate the topographical distributions of ERD features, the average ERD values were computed within

the specific frequency range and time window for each channel according to the following equation:

$$\mathrm{ERD}_{\mathrm{value}} = \frac{1}{N}\sum_{f\in F}\sum_{t\in T}(\mathrm{ERSP}(f,t)) \quad (2)$$

where F is the α band (8–13 Hz) or β band (14–25 Hz), and T is the whole MI task duration of 4 s. N is the total number of time–frequency bins decided by F and T.

Multiclass Common Spatial Patterns

Multiclass common spatial patterns (multi-CSP) was applied to extract features from multichannel EEG data of MI epochs (Qian et al., 2011; Yi et al., 2013). For the analysis, a single MI epoch data is represented as an N by T matrix X_i, where $i\epsilon\{1,2,\ldots,6\}$ indicates the ith class of MI, N is the number of channels ($N = 60$), and T is the number of samples per channel ($T = 800$). We firstly calculated the average covariance matrix R_i of every MI pattern. The whitening matrix can be formed by

$$P = \Lambda^{-1/2}U_0^T \quad (3)$$

where U_0 is the $N \times N$ matrix of eigenvectors and Λ is the diagonal matrix of eigenvalues from

$$R = \sum_{i=1}^{6} R_i = U_0\Lambda U_0^T \quad (4)$$

The strategy of one-versus-rest is adopted to acquire spatial filter matrices. For the first class, we let$R_1{}' = \sum 6_{i=2}R_i$. Then R_1 and $R_1{}'$ can be translated as

$$Y_1 = PR_1P^T$$

$$Y_1' = PR_1{}'P^T \quad (5)$$

And Y_1 and $Y_1{}'$ share common eigenvectors

$$Y_1 = U_1\Lambda_1U_1^T$$

$$Y_1' = U_1\Lambda_1{}'U_1^T \quad (6)$$

With the projection matrix $W_1 = U_1^TP$ consisting of spatial filters corresponding to the first class, the other five projection matrices also can be computed in a similar way.

Mutual Information Maximization

Mutual information maximization (MIM) (Khaleghi et al., 2015) was used in the feature fusion method to select features from the integrating features of all single users. The mutual information (MI) between every feature and its class label separately was calculated. Then features were ranked according to a decrease of MI. MI is defined as:

$$\mathrm{MI}(Y,X) = H(Y) + H(X) - H(Y,X)$$

$$= -\sum_{i,j} P(y_i,x_i)\log_2\frac{P(y_i,x_i)}{P(y_i)\,P(x_i)} \quad (7)$$

where H function is the information theory,

$$H(X) = -\sum_{i=1}^{K} P(x_i)\log_2P(x_i) \quad (8)$$

$$H(Y) = -\sum_{j=1}^{K} P(y_i)\log_2P(y_i) \quad (9)$$

$$H(Y,X) = -\sum_{i=1}^{K}\sum_{j=1}^{K} P(y_i,x_i)\log_2P(y_i,x_i) \quad (10)$$

$P(x_i)$ and $P(y_i)$ are the ith priori probability of feature vector X and label Y in all K values, respectively. $P(y_i,x_i)$ is the joint probability of them. After ranking the features, the first four features are reserved for processing in this work.

Multiclass Classification Support Vector Machines

Multiclass classification support vector machines (multi-class SVM) were employed to classify multiclass of features (Duan and Keerthi, 2005; Aboalayon et al., 2015). It constructs M binary classifiers, where M is the number of classes. Each classifier is trained to separate one class as positive from the rest of the k - 1 classes as negative.

Next, we describe in detail the concepts of task allocation and data processing flow in MI-cBCI systems.

Task Allocation Schemes Based on the Division-of-Work Strategy

We propose an optimized task allocation scheme based on the division-of-work strategy for MI-cBCI systems. This strategy generates a feasible scheme to assign different MI tasks to collaborators. The MI-cBCI system has the same instruction set as a single-user MI-BCI system which has six MI instructions. A collaborative group consisted of five users, denoted by the letters A–E. In other words, the MI-cBCI system is operated by five persons controlling six instructions together. All of the users were randomly selected from 19 subjects. The workflow of the division-of-work strategy in MI-cBCI is divided into four steps:

(A) Selection of the division-of-work strategy. As shown in **Figure 2A**, there are four types of division-of-work strategies. Based on the size of the instruction subset for one person, they are categorized into "2 Tasks," "3 Tasks," and so on until "5 Tasks." In addition, "6 Tasks" is the common-work strategy where each of the five users executes the identical six MI tasks. Both feet (BF) instruction is selected as the reference instruction that is involved in every single users' instruction set. Here, we choose the "3 Tasks" strategy (in the solid black box) as an example to illustrate the following workflow.

(B) Setting of the collaborative mode. The input of the MI-cBCI system is defined as the required MI task, and the output is the instruction obtained by decoding the EEG information of all users. As shown in **Figure 2B**, six collaborative modes are set up to indicate the designated tasks to users in line with the input instructions. In most modes, two users are

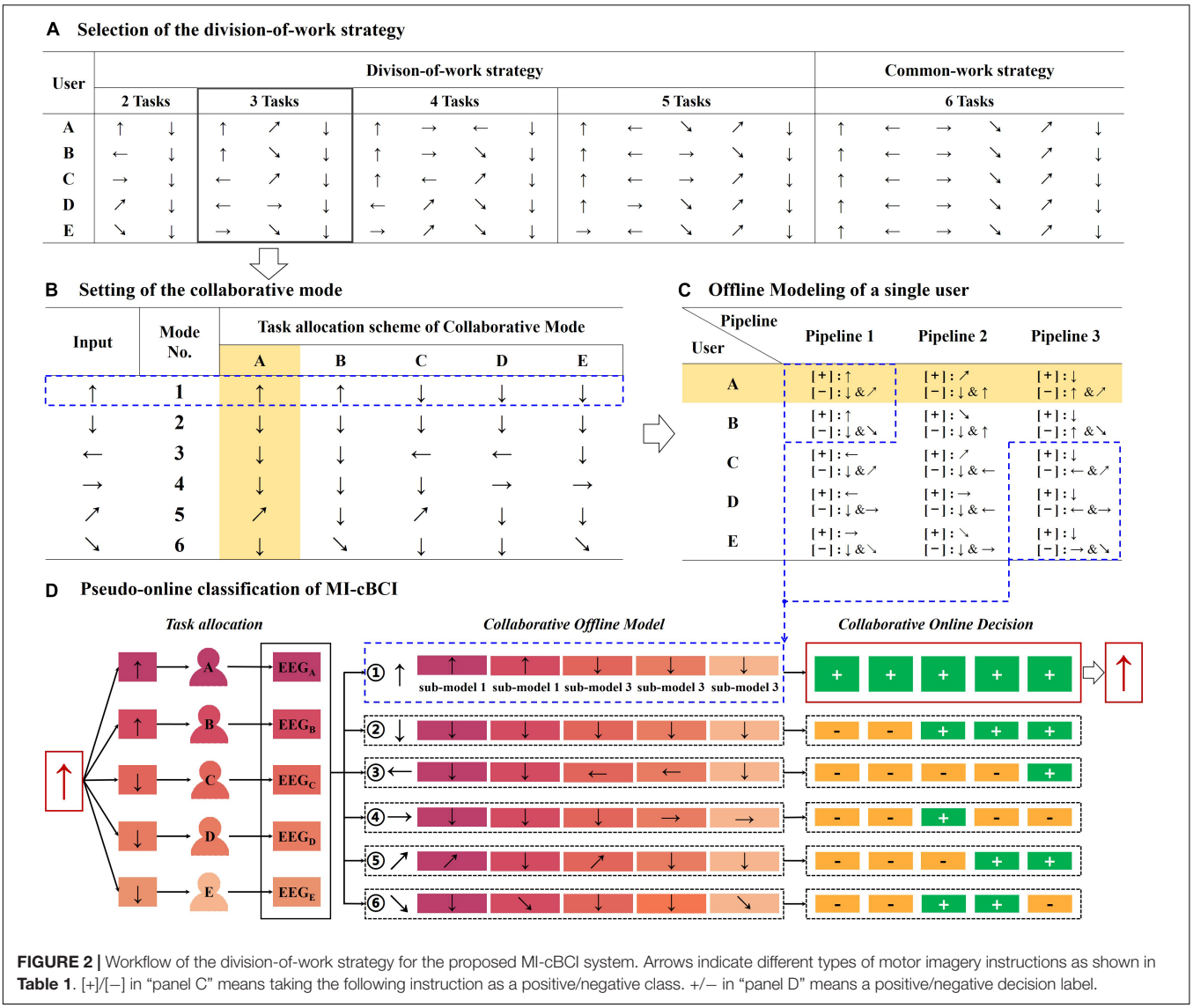

FIGURE 2 | Workflow of the division-of-work strategy for the proposed MI-cBCI system. Arrows indicate different types of motor imagery instructions as shown in **Table 1**. [+]/[−] in "panel C" means taking the following instruction as a positive/negative class. +/− in "panel D" means a positive/negative decision label.

required to complete the tasks consistent with the system input, while others execute the both feet task. Only mode 2 requires all users to perform both feet tasks together. As an example, in the blue dashed box, the system input is ↑. According to the task allocation scheme of mode 1, users A and B should perform both hands MI (↑) and the remaining users perform both feet MI (↓).

(C) Offline modeling of a single user. Across all modes, each user executes a total of three types of tasks represented by arrows, which is in accordance with the "3 Tasks" strategy. Each arrow in **Figure 2B** matches a single-user offline modeling pipeline in **Figure 2C**. For instance, in the yellow shading area in **Figure 2B**, user A executes three kinds of MI tasks (↑ ↗ ↓). For these tasks, three data processing pipelines have been established, as shown in the yellow shading area in **Figure 2C**. Each pipeline is to complete the corresponding offline modeling of EEG data in the light of the one-versus-rest strategy. It means that one type of MI data is taken as the positive class [+], and the other two types of data became the negative class [−]. Features of two classes EEG data are extracted by the CSP algorithm and classified by a SVM classifier. In all pipelines of a single user, a total of three pairs of CSP filters and SVM classifiers have been trained. In the next offline phase of cBCI, they would be used as the submodels for the collaborative model. Detailed information about data processing of a single user have been described in the *Offline modeling of a single user* section.

(D) Pseudo-online classification. The pseudo-online classification of MI-cBCI is composed of two processes: the offline phase for cBCI modeling and the pseudo-online phase for recognition. In the offline phase, we established six collaborative models for feature extraction and classification, one for each of the collaborative modes in **Figure 2B**. For each collaborative model (①-⑥) in **Figures 2B,D** shows what submodels it should entail. Every

collaborative model is assembled from five submodels. The submodels are generated by offline modeling of the users in step (C). Take the collaborative model ① as an example; it is set up with two submodels from pipeline 1 (users A and B) and three submodels from pipeline 3 (users C, D, and E), as shown in the blue dashed box in **Figures 2C,D**. Other collaborative models are built in the same way. There are two alternative fusion methods applied in constructing collaborative models called feature fusion and decision fusion, which are described in the *Feature fusion method* and *Decision fusion method* sections.

In the pseudo-online phase, EEG data collected from five collaborators are sent to the six collaborative models sequentially for classification. The collaboration model that has the highest number of submodels matched to the multiperson input data is the winner, and its corresponding mode (i.e., the arrow that immediately follows numbers ①-⑥ in **Figure 2D**) is selected as the final system output. To illustrate the process of pseudo-online recognition more specifically, we take the system input of ↑ as an example in **Figure 2D**. It shows that users A and B need to imagine both hands (↑) while the other users are required to imagine both feet (↓) as defined in the task allocation scheme in **Figure 2B**. Subsequently, pseudo-online EEG data from all five users (marked as different colors) are processed by the six collaborative models in sequence. Because the input EEG data match to the positive classes of all five submodels of collaborative model ①, it should contain the largest number of positive decision labels among all six collaborative models. Therefore, the system output is both hands instruction (↑).

Data Processing of MI-cBCI

After describing the overall workflow, we will concentrate on the details of data processing. Two data fusion methods for MI-cBCI have been proposed in this study, which are called feature fusion and decision fusion. The implementation of both methods is based on the single-user modeling process and differed on the subsequent cBCI offline modeling and pseudo-online validation.

Offline Modeling of a Single User

The purpose of single-person offline modeling is to provide the required submodels for cBCI, mainly including CSP filters and SVM classifiers. Here, we continue with the example of the "3 Tasks" strategy. According to the task allocation scheme in **Figure 2C**, subject A should perform BH, BF, and RHLF tasks (numbered 1, 5, and 2, respectively). **Figure 3** illustrates the offline modeling process of EEG data related to these instructions. Each class of EEG data is taken in turn as a positive class [+], while others represent the negative class [−]. All three data processing pipelines are made to accomplish binary classifications. For example, in pipeline 1, x_{A1} represents the data of executing instruction 1 and x_{RA1} represents two remaining data (x_{A5} and x_{A2}). Feature matrices $\mathbf{F_{A1}} \epsilon \mathbb{R}^{72 \times 4}$ and $\mathbf{F_{RA1}} \epsilon \mathbb{R}^{144 \times 4}$ are obtained by filtering 72 samples of x_{A1} and 144 samples of x_{RA1}, respectively. A SVM classifier with linear kernel function is trained using the two classes of features. Leave-one-out cross-validation is applied to obtain the offline accuracy acc_{A1}, and an accuracy-based weight coefficient $\lambda_{\mathrm{A1}} = {\mathrm{acc}_{A1}}^2$ is computed to guide subsequent offline processing of cBCI.

Feature Fusion Method

Figure 4 demonstrates the data processing procedure of the feature fusion method for MI-cBCI. In the multiperson cBCI offline phase, **X** represents the EEG training dataset for five collaborators. The selection of data processing pipelines of users depends on the collaborative modes. We describe here the offline and pseudo-online process of mode 1. The data processing pipeline of each user is executed independently using training datasets. As described in the previous section, all submodels containing feature matrices of the two classes $\mathbf{F_i}$ and $\mathbf{F_{R}}_i$, CSP filters, and weight coefficients λ_i are all obtained from five collaborators, i = {A1,B1,C3,D3,E3}. $\mathbf{F_i} \epsilon \mathbb{R}^{72 \times 4}$ and $\mathbf{F_{R}}_i \epsilon \mathbb{R}^{144 \times 4}$ are multiplied by their respective coefficients λ_i and concatenated into matrices $\mathbf{F_X} \epsilon \mathbb{R}^{72 \times 20}$ and $\mathbf{F_{R}}_X \epsilon \mathbb{R}^{144 \times 20}$ in the column direction. After that, the features are sorted in descending order by the mutual information criterion, and the achieved feature ranking R_{f} is recorded. Only the top 4 features are pick up as $\mathbf{F'_X} \epsilon \mathbb{R}^{72 \times 4}$ and $\mathbf{F'_{R}}_X \epsilon \mathbb{R}^{144 \times 4}$, respectively. Finally, a SVM classifier is trained for offline modeling of mode 1 by taking $\mathbf{F'_X}$ and $\mathbf{F'_{R}}_X$ as positive/negative class.

In the cBCI pseudo-online phase, $\boldsymbol{Y}$ contains single-trial data extracted from five users' testing dataset. The CSP filters from the offline modeling phase are applied to filter $\boldsymbol{Y}$ to calculate single-user features $\mathbf{f_i} \epsilon \mathbb{R}^{1 \times 4}$. Then, the multiuser features are combined (following the offline processing approach) to gain the selected features $\mathbf{f_Y} \epsilon \mathbb{R}^{1 \times 20}$. According to the feature ranking R_{f}, the fusing features are rearranged and the first four features are selected as $\mathbf{f'_Y} \epsilon \mathbb{R}^{1 \times 4}$. Then, the optimized features are classified by the trained classifier SVM_{model1} to export the decision value Dv_{model1}. Using the same method, we process $\boldsymbol{Y}$ with the other five models and subsequently acquire the outputs Dv_{model2}... Dv_{model6}. The label associated with the maximum positive decision value is considered to be the predicted label.

Decision Fusion Method

Figure 5 shows the data processing procedure of the decision fusion method for MI-cBCI. It fuses information on the decision value level, while the feature fusion method is on the feature level. Specifically, in the offline phase, the training dataset X is processed with different pipelines from collaborators. The CSP filters and SVM classifiers are reserved, and the accuracy-based weights λ_i are also calculated. In the pseudo-online phase, multiple pairs of CSP filters and SVM classifiers are utilized to conduct spatial filtering and classification on the multiusers' EEG testing data. The corresponding decision value vector $\mathrm{dv}_i \epsilon \mathbb{R}^{1 \times 1}$ is calculated. In addition, decision values from multiple users are fused to get the decision value vector of model 1 $\mathrm{Dv}_{\mathrm{model\ 1}} = \frac{1}{5} \sum \lambda_i \mathrm{dv}_i$. In turn, the output value $\mathrm{Dv}_{\mathrm{model}}$ of each model is calculated, and then the label corresponding to the maximum positive value is chosen as the predicted label.

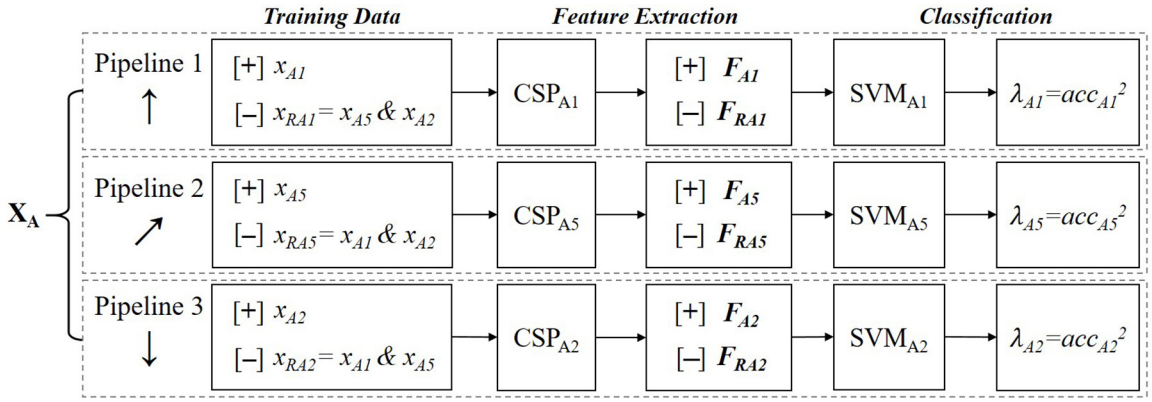

FIGURE 3 | The data processing procedure of a single user for offline modeling. X_A represents the training dataset of subject A. *x* means a certain class of data. [+]/[−] means taking the following data as a positive/negative class. CSP and SVM indicate CSP filters and SVM classifiers, respectively. We use the symbol ***F*** to represent the feature matrix. acc is the abbreviation of accuracy.

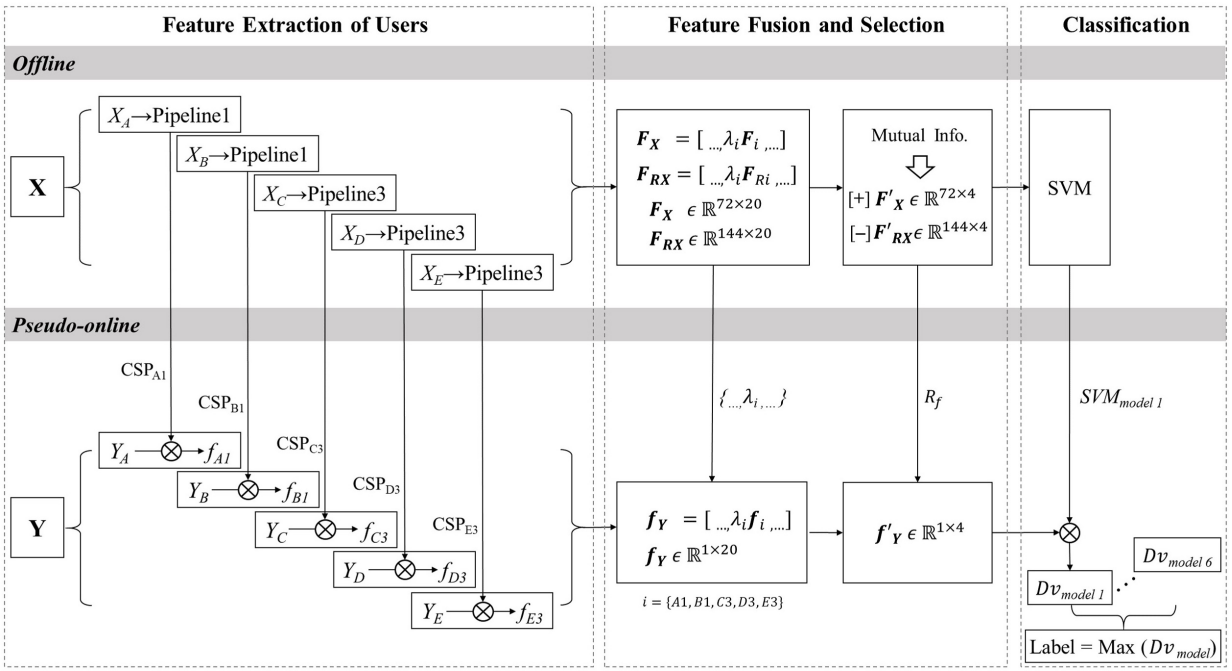

FIGURE 4 | The data processing procedure for the feature fusion method. $m \xrightarrow{k} n$ means that *m* is processed by component *k* (a filter or a classifier) to obtain data *n*. Mutual Info and Dv are the abbreviations of mutual information and decision value, respectively.

RESULTS

Event-Related Spectral Perturbation

The C3 and C4 electrodes are located in the sensorimotor cortex of the brain (Li et al., 2019). As preliminary knowledge, they are the primary electrodes for the neural response features induced by MI (Tangwiriyasakul et al., 2013). **Figure 6** shows the averaged ERSP time–frequency maps of two electrodes across 19 subjects performing six types of MI tasks. The two black dotted lines at time points 0 and 4 represent the start and stop time of MI, respectively. The color bar from blue to red represents the energy ratio from low to high compared with the baseline energy. The map presents clear spectral powers of ERD at α (8–13 Hz) and β (14–28 Hz) bands under various MI tasks. They last until the end of the MI task phase, especially for instruction 3-LH, 4-RH, 5-RHLF, and 6-LHRF. The ERD on both feet is the weakest, as shown in **Figure 6**. It also could be seen that the ERD in the α band is more obvious, and it has laterality with different instructions. In order to explore spatial distribution, averaged topographical maps of ERD are drawn in this study as well.

Figure 7 is the average topographic map of all 19 subjects, and α (the first row) and β (the second row) bands for

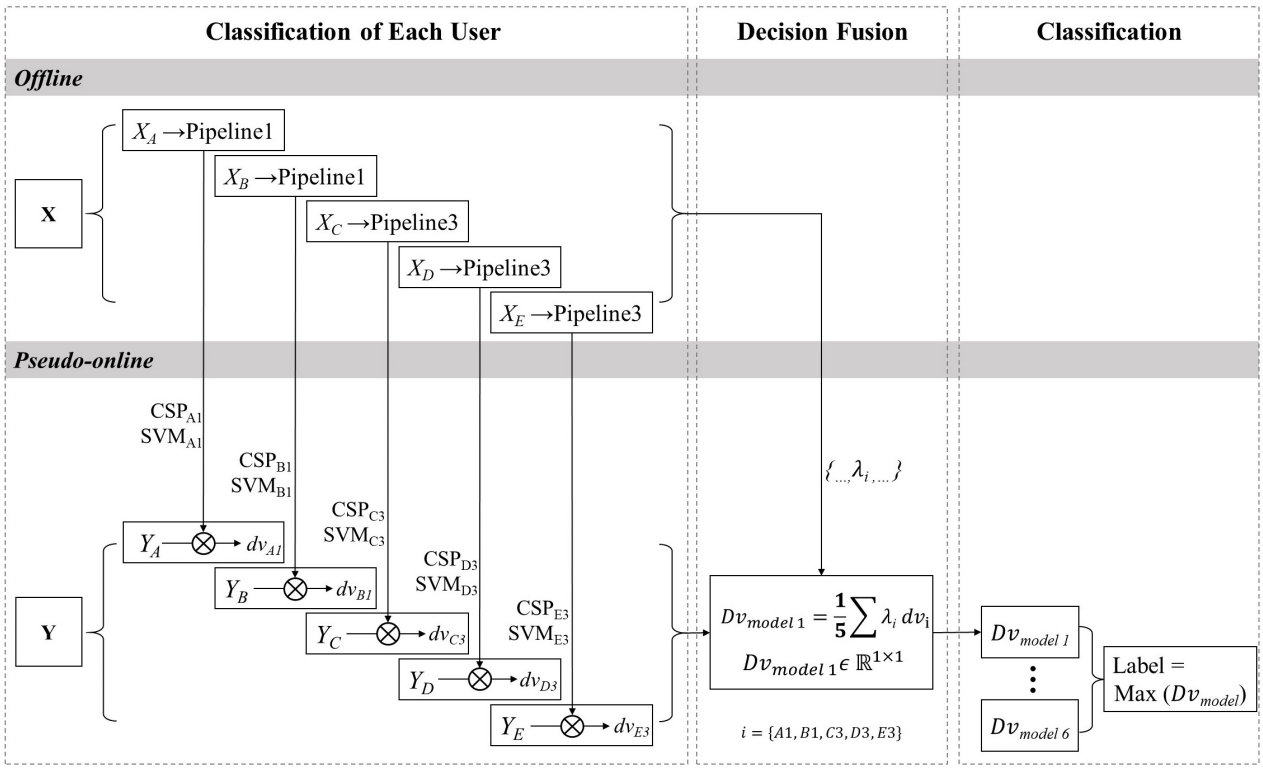

FIGURE 5 | The data processing procedure for the decision fusion method.

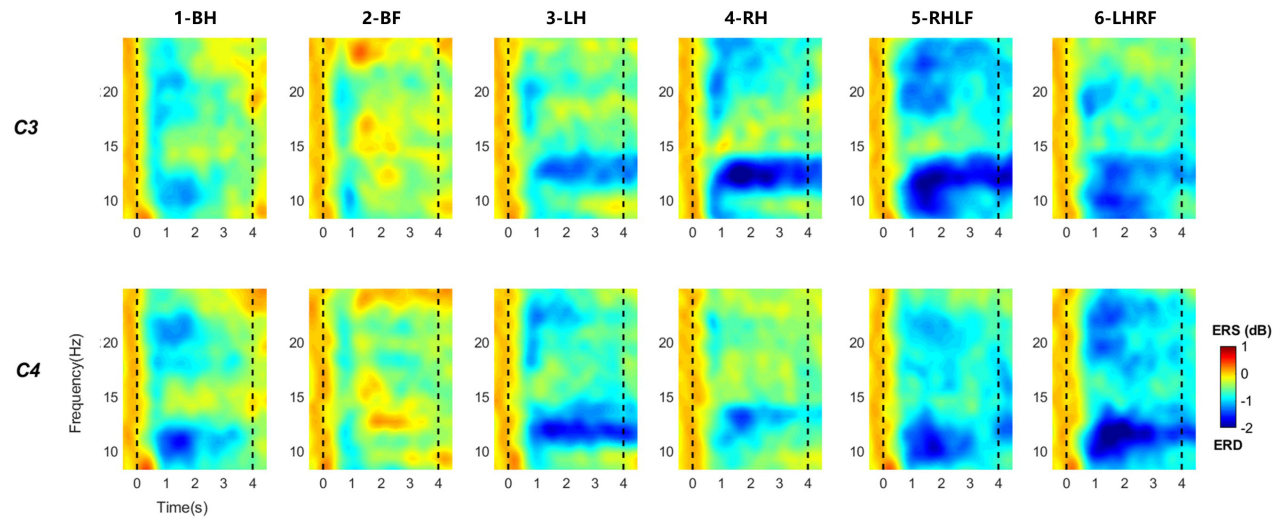

FIGURE 6 | Averaged time–frequency maps across 19 subjects for six types of MI tasks at the location of C3 and C4 electrodes. Blue indicates ERD; red indicates ERS. Black dashed line indicates the onset and offset of motor imagery.

the MI period (4 s) are selected. It can be clearly observed that the ERD of unilateral upper limb MI has obvious contralateral dominance. Both hands' movement induces marked enhancement of ERD on both sides. As we can view in the second column, the ERD of both feet is the weakest in the six types of MI, which is consistent with the time–frequency plot. The compound MI composed of one hand and one foot had significant ERD enhancement on both sides. Moreover, the whole brain has more significant energy attenuation than other types of MI. By contrast, the contralateral activation of the hand is stronger than that of foot MI, and the activation area is larger.

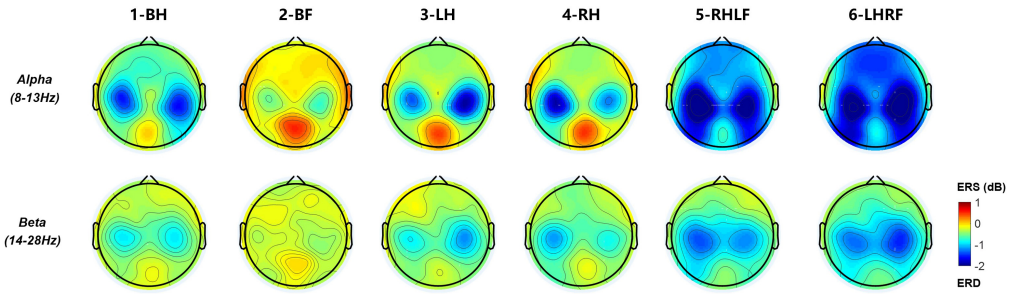

FIGURE 7 | Averaged topographical distribution for six types of MI tasks at α (8–13 Hz) and β (14–28 Hz) bands. Blue regions indicate the involved areas where ERD occurs during the MI period.

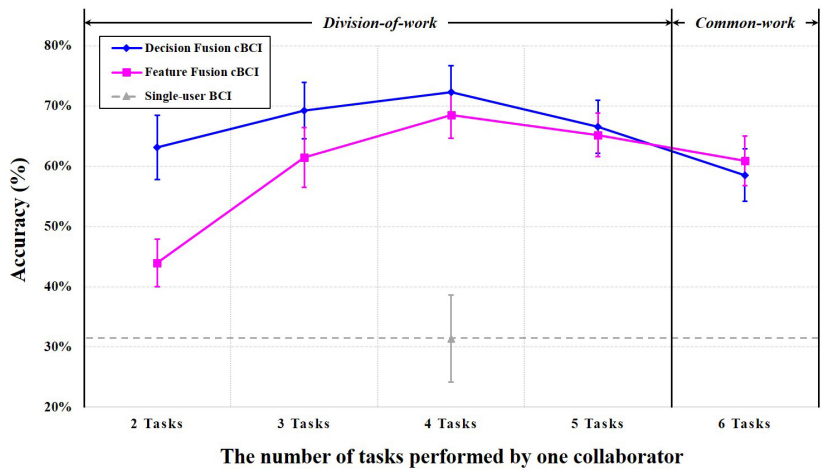

FIGURE 8 | Classification accuracy curves of the feature and decision fusion methods for cBCI and single-user BCI.

By superimposing the averages of multiple trials of ERSP, we can find that ERD features of 19 participants are actually induced in general, and the ERD of six types of MI is mainly located in the α and β bands with contralateral dominance, which is consistent with the results of previous studies (Sollfrank et al., 2015; Collazos-Huertas et al., 2020). Among the six types of MI tasks, the ERD of both feet MI task is the weakest, which could have the largest difference from other tasks. This is the reason why we chose it as a reference instruction.

Classification Performance

In this work, we collected EEG data from 19 subjects who independently performed the abovementioned six types of MI tasks. We should select five persons as users A–E from 19 subjects to conduct the pseudo-online classification of MI-cBCI. The maximum number of possible selections is the number of five permutations of 19. To reduce the complexity, we randomly picked 300 selections among them, and the average classification accuracy of MI-cBCI was obtained for simulated online classification, as shown in **Figure 8**. The vertical coordinate shows the average classification accuracy of six instructions, and the horizontal coordinate represents the number of tasks performed by one collaborator; "2 Tasks" to "5 Tasks" belong to the division-of-work strategy, while the "6 Tasks" strategy is the conventional common-work strategy. The classification accuracies of the cBCI systems using feature fusion and decision fusion methods are depicted by the pink and blue lines, respectively. The gray dotted line shows the six-class average classification accuracy of 19 subjects by the single-user BCI system. This accuracy is independent of the task allocation and does not change with the horizontal coordinate.

These results show the following: (1) even at the lowest point of the cBCI performance curves, the cBCI average classification accuracy is more than 10% higher than the single-user BCI (feature fusion cBCI at "2 Tasks": 43.97 ± 3.96%, decision fusion cBCI at "6 Tasks": 58.53 ± 4.36%, single-user BCI: 31.37 ± 7.21%); (2) accuracy peaks of both classification curves are at "4 Tasks" (division-of-work), which is higher than "6 Tasks" (common work): feature fusion cBCI (68.48 ± 3.85 vs. 60.93 ± 4.13%) and decision fusion cBCI (72.29 ± 4.43 vs. 58.53 ± 4.36%); (3) comparison of the cBCI performance curves indicates the superiority of the decision fusion cBCI system over the feature fusion for most of the division-of-work strategies; (4) the standard deviation of the classification accuracy is reasonably small which almost remains within 5%. This low standard deviation shows that the subject selection

may have little impact on the cBCI system performance. Therefore, these results obtained by randomly selected users are representative and authentic.

CONCLUSION AND DISCUSSION

In this work, a novel task allocation based on division-of-work strategy for MI-cBCI system is proposed. The recognition performance metrics indicated that the division-of-work systems outperform the common-work system, and showed better accuracy than the single-user BCI system. We believe that the main reason for this is due to that division-of-work strategy effectively reduced the number of classes in multiclassification for single person, thereby improving the accuracy of it. Generally speaking, the classification performance of cBCI is positively correlated to the single-person performance and the number of users executing the common tasks. Although the division-of-work strategy reduces the number of users recognizing the same instructions, it improves the classification performance of a single person. The influences of these two factors on the system are the reasons why the shape of the classification accuracy curves are mountain-like in both methods. In the current system, the accuracy peak is at the "4 Tasks" strategy.

Moreover, this paper compares the recognition performance of two data-fusing methods and shows that the decision fusion algorithm is generally superior to the feature fusion. Currently, the literature suffers from the lack of extensive discussions on this problem. We are aware of little relevant work on this problem, except for the cBCI based on rapid serial visual presentation (RSVP) which was designed by Matran-Fernandez and Poli (2014). Moreover, they came to similar conclusions to ours in spite of the employment of different potential features.

We are here to discuss the reasons for the difference in performance between the two methods. Specifically, decision fusion for distributed architecture is more direct, while feature fusion for centralized architecture retains more EEG information of individuals and may lead to degraded performance. If more efficient multiperson EEG feature extraction algorithms can be applied, e.g., algorithms based on deep learning or transfer learning, feature fusion cBCI could capture more relevant information and may thus have greater research potential.

We believe that future cBCI research should have more hybridization and collaboration in the following aspects: (1) *hybrid tasks*: the current cBCI tasks are usually single tasks, which are basically enhancement tasks for motion control or visual recognition (Liu et al., 2020). However, cBCI systems may perform better in hybrid high-load tasks and have greater advantages of collaboration; (2) *Joint task allocation strategies and data-fusing methods*: more tasks lead to inferior performance under a standalone task allocation scheme. Therefore, cBCI systems should be adjusted continuously according to operation characteristics and user capabilities. More specifically, cBCI systems may be created with hybrid common-work and division-of-work strategies, as well as hybrids of centralized and distributed architectures. It can assign dynamic specific tasks and data processing methods according to the status of each collaborator; (3) *fusion of multimodal signals*: multiple neural response features (e.g., potential and energy) should be deeply mined and fused (Wang et al., 2020). Also, cBCI systems with other physiological or behavioral signals might be exploited. Furthermore, fusion strategies can be adjusted to achieve automatic performance optimization.

On one hand, the development of the cBCI technology indicates that the performance of existing BCI systems can be substantially improved. On the other hand, cBCI technology evolution promises the development of a new generation of human–computer interaction systems with energy-saving and networking modes. In addition to the abovementioned cBCI systems, passive cBCI systems whose operation is based on monitoring the interaction between multiple persons and the external environment have been gradually emerging. This technology is also known as hyperscanning. In recent years, hyperscanning systems based on EEG, functional near-infrared spectroscopy (fNIRS), and magnetoencephalography (MEG) have been rapidly developed. Through designing joint tasks to explore the brain activation characteristics and causality (Konvalinka and Roepstorff, 2012; Sänger et al., 2012; Babiloni and Astolfi, 2014; Nam et al., 2020), the conventional interaction between individual subjects, tasks, and the environment has been gradually transformed into the interaction between multiple persons, multiple tasks, and different environments. Hence, the cBCI technology is expected to spread more widely and be more successful in novel and diverse engineering applications.

DATA AVAILABILITY STATEMENT

The raw data supporting the conclusions of this article will be made available by the authors, without undue reservation.

ETHICS STATEMENT

The studies involving human participants were reviewed and approved by the institutional research ethics committee of Tianjin People's Hospital. The patients/participants provided their written informed consent to participate in this study.

AUTHOR CONTRIBUTIONS

BG and MX designed the study. BG, LC, KW, and JT performed research. BG and MX analyzed data. BG, YK, MX, LX, and DM wrote the manuscript. All authors contributed to the article and approved the submitted version.

FUNDING

This work was supported by the National Natural Science Foundation of China (Grant Numbers 81925020, 61976152, and 81671861) and the Young Elite Scientist Sponsorship Program by CAST (Grant Number 2018QNRC001).

REFERENCES

Abiri, R., Borhani, S., Sellers, E. W., Jiang, Y., and Zhao, X. (2019). A comprehensive review of EEG-based brain-computer interface paradigms. *J. Neural Eng.* 16, 1–43. doi: 10.1088/1741-2552/aaf12e

Aboalayon, K. A. I, Almuhammadi, W. S., and Faezipour, M. (2015). "A comparison of different machine learning algorithms using single channel EEG signal for classifying human sleep stages," in *Proceedings of the 2015 Long Island Systems, Applications and Technology*, (Farmingdale, NY: IEEE), doi: 10.1109/LISAT.2015.7160185

Babiloni, F., and Astolfi, L. (2014). Social neuroscience and hyperscanning techniques: past, present and future. *Neurosci. Biobehav. Rev.* 44, 76–93. doi: 10.1016/j.neubiorev.2012.07.006

Collazos-Huertas, D., Caicedo-Acosta, J., Castaño-Duque, G. A., and Acosta-Medina, C. D. (2020). Enhanced multiple instance representation using time-frequency atoms in motor imagery classification. *Front. Neurosci.* 14:155. doi: 10.3389/fnins.2020.00155

Dickstein, R., and Deutsch, J. E. (2007). Physical therapist practice. *Phys. Ther.* 87, 942–953.

Duan, K., and Keerthi, S. S. (2005). "Which is the best multiclass SVM method? An empirical study," in *Multiple Classifier Systems*, eds N. C. Oza, R. Polikar, J. Kittler, and F. Roli (Berlin: Springer), 278–285.

Jiang, J., Yin, E., Wang, C., Xu, M., and Ming, D. (2018). Incorporation of dynamic stopping strategy into the high-speed SSVEP-based BCIs. *J. Neural Eng.* 15:aac605. doi: 10.1088/1741-2552/aac605

Karpov, A. A., and Yusupov, R. M. (2018). Multimodal interfaces of human–computer interaction. *Her. Russ. Acad. Sci.* 88, 67–74. doi: 10.1134/S1019331618010094

Khaleghi, A., Sheikhani, A., Mohammadi, M. R., Nasrabadi, A. M., Vand, S. R., Zarafshan, H., et al. (2015). EEG classification of adolescents with type I and type II of bipolar disorder. *Australas. Phys. Eng. Sci. Med.* 38, 551–559. doi: 10.1007/s13246-015-0375-0

Konvalinka, I., and Roepstorff, A. (2012). The two-brain approach: how can mutually interacting brains teach us something about social interaction? *Front. Hum. Neurosci.* 6:215. doi: 10.3389/fnhum.2012.00215

Li, F., Peng, W., Jiang, Y., Song, L., Liao, Y., Yi, C., et al. (2019). The dynamic brain networks of motor imagery: time-varying causality analysis of scalp EEG. *Int. J. Neural Syst.* 29:1850016. doi: 10.1142/S0129065718500168

Liu, L. (2019). Recognition and analysis of motor imagery EEG signal based on improved BP neural network. *IEEE Access* 7, 47794–47803. doi: 10.1109/ACCESS.2019.2910191

Liu, S., Wang, W., Sheng, Y., Zhang, L., Xu, M., and Ming, D. (2020). Improving the cross-subject performance of the ERP-based brain–computer interface using rapid serial visual presentation and correlation analysis rank. *Front. Hum. Neurosci.* 14:296. doi: 10.3389/fnhum.2020.00296

Luu, T. P., Nakagome, S., He, Y., and Contreras-Vidal, J. L. (2017). Real-time EEG-based brain-computer interface to a virtual avatar enhances cortical involvement in human treadmill walking. *Sci. Rep.* 7:8895. doi: 10.1038/s41598-017-09187-0

Ma, T., Li, H., Deng, L., Yang, H., Lv, X., Li, P., et al. (2017). The hybrid BCI system for movement control by combining motor imagery and moving onset visual evoked potential. *J. Neural Eng.* 14:026015. doi: 10.1088/1741-2552/aa5d5f

Matran-Fernandez, A., and Poli, R. (2014). "Collaborative brain-computer interfaces for target localisation in rapid serial visual presentation," in *Proceedings of the 2014 6th Computer Science and Electronic Engineering Conference (CEEC)*, (Colchester: IEEE), 127–132. doi: 10.1109/CEEC.2014.6958567

Mattout, J. (2012). Brain-computer interfaces: a neuroscience paradigm of social interaction? A matter of perspective. *Front. Hum. Neurosci.* 6:114. doi: 10.3389/fnhum.2012.00114

McCrimmon, C. M., Fu, J. L., Wang, M., Lopes, L. S., Wang, P. T., Karimi-Bidhendi, A., et al. (2018). Performance assessment of a custom, portable, and low-cost brain-computer interface platform. *Physiol. Behav.* 176, 139–148. doi: 10.1117/12.2549369.Hyperspectral

Nam, C. S., Choo, S., Huang, J., and Park, J. (2020). Brain-to-brain neural synchrony during social interactions: a systematic review on hyperscanning studies. *Appl. Sci.* 10, 1–23. doi: 10.3390/APP10196669

Naseer, N., and Hong, K. S. (2015). fNIRS-based brain-computer interfaces: a review. *Front. Hum. Neurosci.* 9:3. doi: 10.3389/fnhum.2015.00003

Qian, T., Wu, W., Zhou, W., Gao, S., and Hong, B. (2011). One-versus-the rest(OVR) AlgorithmAn extension of common spatial patterns(CSP) Algorithm to multi-class case. *Proc. Annu. Int. Conf. IEEE Eng. Med. Biol. Soc. EMBS* 2011, 2347–2350. doi: 10.1109/IEMBS.2011.6090656

Sänger, J., Müller, V., and Lindenberger, U. (2012). Intra- and interbrain synchronization and network properties when playing guitar in duets. *Front. Hum. Neurosci.* 6:312. doi: 10.3389/fnhum.2012.00312

Smith, A. (2005). *The Wealth of Nations[M]*. Penguin Books.

Sokunbi, M. O., Linden, D. E. J., Habes, I., Johnston, S., and Ihssen, N. (2014). Real-time fMRI brain-computer interface: development of a 'motivational feedback' subsystem for the regulation of visual cue reactivity. *Front. Behav. Neurosci.* 8:392. doi: 10.3389/fnbeh.2014.00392

Sollfrank, T., Hart, D., Goodsell, R., Foster, J., and Tan, T. (2015). 3D visualization of movements can amplify motor cortex activation during subsequent motor imagery. *Front. Hum. Neurosci.* 9:463. doi: 10.3389/fnhum.2015.00463

Tangwiriyasakul, C., Verhagen, R., Van Putten, M. J., and Rutten, W. L. (2013). Importance of baseline in event-related desynchronization during a combination task of motor imagery and motor observation. *J. Neural Eng.* 10:026009. doi: 10.1088/1741-2560/10/2/026009

Valeriani, D., Poli, R., and Cinel, C. (2015). "A collaborative brain-computer interface for improving group detection of visual targets in complex natural environments," in *Proceedings of the 7th International IEEE EMBS Neural Engineering Conference*, (Montpellier: IEEE), 25–28. doi: 10.1109/NER.2015.7146551

Valeriani, D., Poli, R., and Cinel, C. (2017). Enhancement of group perception via a collaborative brain-computer interface. *IEEE Trans. Biomed. Eng.* 64, 1238–1248. doi: 10.1109/TBME.2016.2598875

Vourvopoulos, A., Jorge, C., Abreu, R., Figueiredo, P., Fernandes, J. C., and Bermúdez I Badia, S. (2019). Efficacy and brain imaging correlates of an immersive motor imagery BCI-driven VR system for upper limb motor rehabilitation: a clinical case report. *Front. Hum. Neurosci.* 13:244. doi: 10.3389/fnhum.2019.00244

Wang, K., Xu, M., Wang, Y., Zhang, S., Chen, L., and Ming, D. (2020). Enhance decoding of pre-movement EEG patterns for brain–computer interfaces. *J. Neural Eng.* 17:016033. doi: 10.1088/1741-2552/ab598f

Wang, Y., and Jung, T. P. (2011). A collaborative brain-computer interface for improving human performance. *PLoS One* 6:e20422. doi: 10.1371/journal.pone.0020422

Wei, Q., Zhu, S., Wang, Y., Gao, X., Guo, H., and Wu, X. (2019). Maximum signal fraction analysis for enhancing signal-to-noise ratio of EEG signals in SSVEP-based BCIs. *IEEE Access* 7, 85452–85461. doi: 10.1109/ACCESS.2019.2925078

Yi, W., Qiu, S., Qi, H., Zhang, L., Wan, B., and Ming, D. (2013). EEG feature comparison and classification of simple and compound limb motor imagery. *J. Neuroeng. Rehabil.* 10:106. doi: 10.1186/1743-0003-10-106

Yi, W., Qiu, S., Wang, K., Qi, H., Zhao, X., He, F., et al. (2017). Enhancing performance of a motor imagery based brain-computer interface by incorporating electrical stimulation-induced SSSEP. *J. Neural Eng.* 14:026002. doi: 10.1088/1741-2552/aa5559

Zapała, D., Zabielska-Mendyk, E., Augustynowicz, P., Cudo, A., Jaśkiewicz, M., Szewczyk, M., et al. (2020). The effects of handedness on sensorimotor rhythm desynchronization and motor-imagery BCI control. *Sci. Rep.* 10, 1–11. doi: 10.1038/s41598-020-59222-w

Zhou, Y., Gu, B., Dai, T., Wang, Z., Song, X., Xu, M., et al. (2019). "A multiuser collaborative strategy for MI-BCI system," in *Proceedings of the 2018 IEEE 23rd International Conference on Digital Signal Processing (DSP)*, (Shanghai: IEEE), doi: 10.1109/ICDSP.2018.8631864

Conflict of Interest: The authors declare that the research was conducted in the absence of any commercial or financial relationships that could be construed as a potential conflict of interest.

Advantages of publishing in Frontiers

OPEN ACCESS
Articles are free to read for greatest visibility and readership

FAST PUBLICATION
Around 90 days from submission to decision

HIGH QUALITY PEER-REVIEW
Rigorous, collaborative, and constructive peer-review

TRANSPARENT PEER-REVIEW
Editors and reviewers acknowledged by name on published articles

Frontiers
Avenue du Tribunal-Fédéral 34
1005 Lausanne | Switzerland

Visit us: www.frontiersin.org
Contact us: frontiersin.org/about/contact

REPRODUCIBILITY OF RESEARCH
Support open data and methods to enhance research reproducibility

DIGITAL PUBLISHING
Articles designed for optimal readership across devices

FOLLOW US
@frontiersin

IMPACT METRICS
Advanced article metrics track visibility across digital media

EXTENSIVE PROMOTION
Marketing and promotion of impactful research

LOOP RESEARCH NETWORK
Our network increases your article's readership